

Dissertation zur Erlangung des Doktorgrades
der Fakultät für Chemie und Pharmazie
der Ludwig-Maximilians-Universität München

Development of Functional
Covalent Organic Frameworks with
Extended Heteroaromatic Building Blocks

Derya Daniel Bessinger

aus

München, Deutschland

2022

Erklärung

Diese Dissertation wurde im Sinne von § 7 der Promotionsordnung vom 28. November 2011 von Herrn Prof. Dr. Thomas Bein betreut.

Eidesstattliche Versicherung

Diese Dissertation wurde eigenständig und ohne unerlaubte Hilfe erarbeitet.

München, den 26.10.2022

.....

(Derya Bessinger)

Dissertation eingereicht am 03.11.2022

1. Gutachter: Prof. Dr. Thomas Bein
2. Gutachter: Prof. Dr. Achim Hartschuh

Mündliche Prüfung am 21.11.2022

Abstract

With advancing research on porous materials, a new emerging class has been developed: covalent organic frameworks (COFs). These frameworks are constructed from rigid organic building blocks which are connected through strong covalent bonds and are arranged in an orderly manner giving rise to new highly crystalline, permanently porous, and stable structures. The deliberate assembly of building blocks for the construction of ordered frameworks follows the principle of reticular chemistry, enabling additional control over the pre-designed frameworks. The ability to rationally synthesize these highly crystalline and organic polymers is thereby enabled by the introduced reversibility of bond formation, allowing to self-repair structural defects during synthesis. The manifold toolbox of organic chemistry additionally allows to chemically modify the implemented building blocks in order to tune the various characteristics of the resulting COFs, such as pore geometry, optical features, and optoelectronic properties. The combination of rational design and synthetic organic chemistry thus provides access to a variety of tailor-made and functional materials which then fulfill the prerequisites of potential applications, such as gas storage and separation, optoelectronics or sensing.

The impact of judicious building block modifications on the properties of COFs was demonstrated by the development of new isoindigo- and thienoisindigo-based building blocks, which are already established in the field of functional polymers. The strongly electron-withdrawing (thieno)isoindigo core was therefore combined with electron-donating moieties to enforce the donor-acceptor character of the resulting building blocks. This electronic configuration provides strong optical effects through intramolecular charge transfer (ICT) between the moieties, shifting the absorption onset well into the longer wavelength-region of the electromagnetic spectrum. The structural changes made for the thienoisindigo (TII) building block allowed to further enhance the optical features by extending its effective π -conjugation. This was accomplished by overcoming the structural drawbacks of isoindigo, which affect the intramolecular co-planarity due to steric hindrance. Employing the extended thienoisindigo building block with a truly planar conformation in 2D COF synthesis transferred its superior light absorption properties to the resulting highly crystalline and porous framework. This near-infrared-absorbing material grown as an oriented thin film was then processed as the active material in an interdigitated heterojunction, which was then applied as the first COF-based UV- to NIR-responsive photodetector. The new device additionally

featured a completely invertible photoresponse that can be reversibly switched from blue- and red-sensitive to green- and NIR-responsive.

The advantages of the strong structural and optical characteristics of thienoisindigo-based building blocks and their respective 2D COFs motivated us to expand the series by combining the TII core with larger thienothiophene (tt) and naphthalene (n) moieties. The increase in molecular length of the linear bridging units while still maintaining the strong absorption features owing to the ICT gave rise to novel COF materials with optimal requirements for electrochromic applications. The deliberate structural design of the linear TII building block thus provided crystalline structures combining pore size sufficiently large for the unimpeded diffusion of counterions, enhanced framework stability while maintaining the electrochromic performance over repeated cycles, and strong vis-NIR absorption bands that can be significantly shifted in response to an external electronic stimulus. Oriented thin films of the best-performing COF, incorporating the extended building block, ttTII, with the highest coplanarity and rigidity, therefore achieved highly efficient and fully reversible color changes with super-fast switching speeds, outperforming many other electrochromic frameworks.

The concept of precise building block modification was further explored with the development of extended oligothiophene bridges in the third part of the thesis. For the integration of linear quaterthiophenes into 2D COFs, the solubilizing alkyl chains were attached asymmetrically to the backbone in order to promote their alternating orientation and avoid steric repulsion in the closely stacked arrangement of COFs. With this functionalization strategy, the first highly crystalline quaterthiophene-containing COFs were constructed and further modifications to the backbone could be introduced to tune their electronic properties. Optical investigations of the COF materials revealed for the first time the formation of a charge transfer state between the imine-linked building blocks. The new asymmetric modification strategy demonstrated the possibility to construct highly ordered COFs from extended linear molecular bridges, expanding the range of applicable building blocks and accessible COFs.

This developed strategy allowed us to design and implement a set of oligothiophenes with two types of modifications in order to investigate the influence of selective backbone changes on the resulting COFs. To this end, the length of the backbone and the alkyl chains was varied. Backbone length variation allowed us to tune the structural COF parameters almost independently of the attached alkyl chains, owing to their sufficient spacing in the close-packed

arrangement. Investigating the optical properties of the oligothiophene-based COF series indicated that the modifications of the bridging units induce changes of the photoluminescence lifetimes with two opposing trends with respect to the alkyl chain and backbone length. Alkyl chain elongation thus shortened the photoluminescence lifetimes, while the further extended backbone increased the decay times. These results demonstrate that already small variations influence the framework properties and emphasize the importance of deliberate building block design. With the findings of our studies, we could derive guiding principles on how to fine-tune the characteristics of COFs by backbone modifications.

The last chapter of this thesis focuses on the development of fully conjugated three-dimensional COFs based on a modified variant of a novel pseudo-tetrahedral cyclooctatetrathiophene (COTh) building block. The extended π -conjugation is achieved by the saddle-shaped annulene COTh backbone formed by four fused thiophenes and thus providing a sp^2 carbon-conjugated structure. Through the direct attachment of functional groups to the COTh core, a new compact derivative was synthesized and incorporated into 3D COFs. The formation of a highly crystalline framework was supported by the utilization of a modulation approach with mono-functionalized modulators. Furthermore, this synthesis strategy allowed for the homogenous growth of the first ordered 3D COF thin film on various substrates without previous surface preparation. The promising intrinsic conductivity results of these films provided a first insight regarding the great potential of the well-ordered arrangement of electronically coupled and fully conjugated 3D frameworks, thus allowing direct transfer of their intriguing electronic features to functional coatings, and paving the way for future applications.

Table of Contents

1	Introduction	1
1.1	Metal Organic Frameworks.....	1
1.2	Covalent Organic Frameworks	3
1.3	Linkage types in Covalent Organic Frameworks	7
1.4	Indigo isomers: Powerful Building Blocks for COFs	10
1.5	References	15
2	Characterization Techniques	21
2.1	X-ray Diffraction.....	21
2.2	Grazing-Incidence Wide-Angle X-ray Scattering (GIWAXS)	23
2.3	Nitrogen Physisorption.....	24
2.4	Nuclear Magnetic Resonance (NMR).....	29
2.5	UV-Vis Spectroscopy.....	33
2.6	Photoluminescence (PL) Spectroscopy	35
2.7	Electron Microscopy	36
2.7.1	Scanning Electron Microscopy (SEM)	37
2.7.2	Transmission Electron Microscopy (TEM).....	38
2.8	Infrared Spectroscopy (IR).....	41
2.9	Cyclic Voltammetry (CV).....	42
2.10	References	45
3	Spectrally Switchable Photodetection with Near-Infrared-Absorbing Covalent Organic Frameworks.....	47
3.1	Abstract	48
3.2	Introduction	48
3.3	Results and Discussion.....	49
3.4	Conclusion.....	58
3.5	Supporting Information.....	60
3.6	References	88
4	Fast-Switching Vis-IR Electrochromic Covalent Organic Frameworks.....	91
4.1	Abstract	93
4.2	Introduction	93
4.3	Results	94
4.4	Discussion	101
4.5	Conclusion.....	101
4.6	Supporting Information.....	103
4.7	References	142
5	Oligothiophene-Bridged Conjugated Covalent Organic Frameworks	145

5.1	Abstract	146
5.2	Introduction	146
5.3	Results and Discussion.....	148
5.4	Conclusion.....	154
5.5	Supporting Information.....	155
5.6	References	196
6	Extension of Oligothiophene Backbones in Covalent Organic Frameworks.....	199
6.1	Abstract	200
6.2	Introduction	200
6.3	Results and Discussion.....	202
6.4	Conclusion.....	212
6.5	Supporting Information.....	214
6.6	References	243
7	Highly Crystalline and Fully Conjugated 3D Cyclooctatetrathiophene-based Covalent Organic Frameworks as Bulk and Thin Film Materials.....	245
7.1	Abstract	246
7.2	Introduction	246
7.3	Results and Discussion.....	249
7.4	Conclusion.....	256
7.5	Supporting Information.....	258
7.6	References	276
8	Conclusion.....	280
9	Publications and Presentations	284
9.1	Publications	284
9.2	Oral Presentations	286
9.3	Poster Presentations	286

1 Introduction

The increasing demand for porous and at the same time stable materials underlines their great importance and functionality in everyday life. Naturally occurring and synthetically produced zeolites with porous framework structures already show their excellent potential for many different applications, whether they are industrial or household-related. To name but a few, zeolites are promising and commonly used materials for petrochemistry,^[1, 2] catalysis,^[3] gas storage and separation,^[4, 5] water softening and purification,^[6] cat litter,^[7] and thermal energy storage.^[8] The advantages of crystalline nanostructured frameworks with their defined and permanent porosity, such as high surface area, molecular selectivity, stability, and uptake of guest molecules, motivated the scientific community to intensify their efforts in finding pathways that provide access to families of novel porous materials with additional or complementary characteristics. This led to the development of porous organic frameworks which feature access to large stable pores and advanced organic functionalities allowing precise pore wall modifications.

1.1 Metal Organic Frameworks

Crystalline porous organic frameworks entail the advantages of exact control over the pore size, pore shape, chemical functionality, and intrinsic properties. Polymerization of the subunits to form the respective framework material must therefore involve a controlled degree of reversibility to provide an effective error correction mechanism. One of the approaches to achieve this with organic building blocks is to rely on complexation with metal ions. Complexation is generally reversible with the equilibrium between bound and free ligands depending on various factors, such as ligand strength and synthesis parameters.

This was realized by the development of metal-organic frameworks (MOFs) that combine – as the name implies – inorganic and organic chemistry components. The term ‘metal-organic framework’ initially described coordination networks comprised of single metal ions and organic linkers and was established for the first time in 1995.^[9] This new class of porous materials advanced and gained more stability with stronger bonds via charged chelating linkers in the same year.^[10] Further developments substituted the metal ions and introduced metal-clusters, leading to even more rigid coordination networks and marking a turning point in the evolution of MOFs in 1998.^[11] Employing polynuclear metal nodes, widely termed secondary building units (SBUs), in the construction of MOFs combined with the use of charged organic

1 Introduction

linkers provided enhanced framework stabilization and therefore led to the first framework, MOF-2, with permanent porosity and reversible gas adsorption behavior. A major breakthrough in the field of MOFs was the discovery of MOF-5, a periodic and three-dimensional network with permanent porosity that preserved its initial stability after the removal of guest molecules.^[12] This extended framework consisting of tetrahedral $[\text{Zn}_4\text{O}]^{6+}$ clusters that are connected by chelating 1,4-benzenedicarboxylate linkers not only exhibited exceptionally high surface area and pore volume but also paved the way for a new synthesis concept that was later named ‘reticular chemistry’.^[13] In the 3D cubic net of MOF-5, the nodes are occupied by octahedral secondary building units (SBUs), which are comprised of four ZnO_4 tetrahedrons with central Zn^{2+} ions sharing an O^{2-} vertex at the core of the SBUs. The edges of the clusters are formed by six carboxylate groups of the ditopic organic linkers which constitute the links of the primitive cubic net (Figure 1.1).

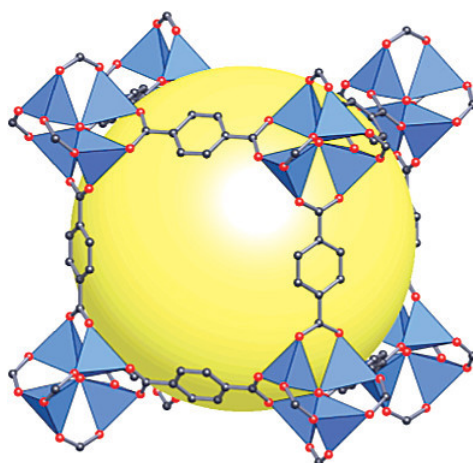


Figure 1.1. Structure of MOF-5 constructed from octahedral $\text{Zn}_4\text{O}(\text{COO})_6$ secondary building units and linear benzene dicarboxylate linkers. The SBUs consist of four ZnO_4 units (blue tetrahedra) with an O^{2-} ion at the core position. The cavity originating from eight linked SBUs is accessible from all sides and is illustrated by the yellow sphere. Color scheme: oxygen red, carbon grey. Zinc atoms not visible due to their position in the center of the tetrahedra. Adapted with permission.^[14] Copyright (2007) American Chemical Society.

The novel approach of synthesizing porous materials utilizing SBUs introduced hitherto unknown framework control and flexibility due to their directionality and defined geometrical shapes dependent on the number and orientation of extension points. In the case of the pioneering MOF-5 for example, this is achieved by the carboxylate carbon atoms. This reticular synthesis principle therefore allowed for the designed construction of rigid extended frameworks by combining various SBUs of different geometries, accessing a staggering structural diversity of more than 100,000 different MOF structures to date.^[15] And with

judicious choice of SBUs, it became possible to assemble predetermined frameworks with specific properties by rational design.

A great demonstration of the advantages of reticular chemistry can be found in the isorecticular framework series (IRMOF) of MOF-5 (Figure 1.2).^[16] Here, the original cubic topology was kept constant, but the pore size and functionality could be deliberately changed by varying the ditopic carboxylate linkers. All structures of this IRMOF series contain the same octahedral SBU at the vertices, allowing for the design of new expanded networks with tailor-made pore metrics by targeted elongation of the linear linkers. This synthesis strategy according to a ‘construction blueprint’ also allows for pore functionalization by attaching functional groups to the benzene links.

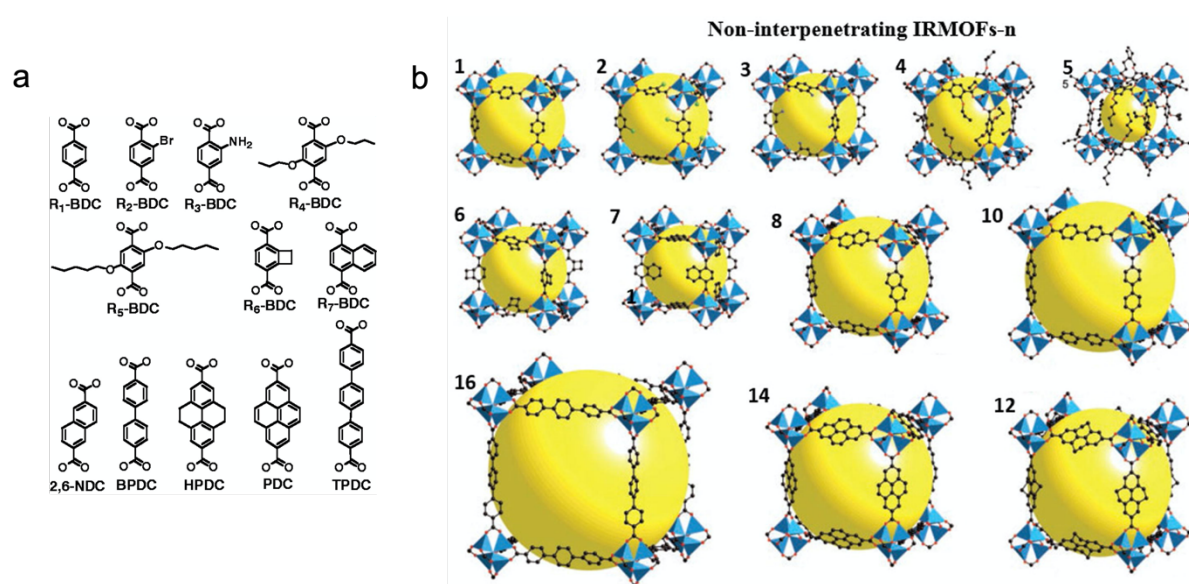


Figure 1.2. Isorecticular MOF (IRMOF) series of the cubic MOF-5 (IRMOF-1). **(a)** Variations of the linear ditopic linkers at the edges alter the pore dimensions and functionalities.^[16] Reprinted with permission from AAAS. **(b)** Every framework of the series exhibits a 3D primitive cubic topology and the same octahedral SBUs at the vertices. Reprinted with permission.^[17] Copyright (2017) Elsevier. Modifications of the linkers are indicated by the subscripts of the R₂ – R₇-BDC molecules in **(a)** and lead to the respective IRMOF-2 to IRMOF-7 structures in **(b)**. The expanded linkers 2,6-NDC, BPDC, HPDC, PDC, and TPDC produced the IRMOF-8, -10, -12, -14, and -16 structures with increasing pore cavities (yellow spheres), respectively. Color scheme: Zn blue (tetrahedra), O red, C grey, Br green (in **2**), NH₂ blue (in **3**).

1.2 Covalent Organic Frameworks

The abovementioned reversibility, which is a prerequisite for the formation of crystalline porous organic frameworks since it allows for error correction during the synthesis, also applies

1 Introduction

to the concept of linking organic molecules through strong covalent bonds. In order to achieve this, the reaction conditions must be adjusted in a way that thermodynamic control and building block integrity is ensured during framework formation.

The challenge of covalently linking organic building blocks in a highly ordered fashion, which was believed to be nearly impossible at that time and known as the ‘crystallization problem’,^[18] was overcome for the first time in 2005. Omar Yaghi and coworkers showed that it was indeed possible to build extended crystalline organic materials by covalent bonds with the first two covalent organic frameworks (COFs), COF-1 and COF-5 (Figure 1.3).^[19] Consequently, a new class of porous and lightweight materials evolved by transferring the modular construction principle of reticular chemistry to the field of organic chemistry.

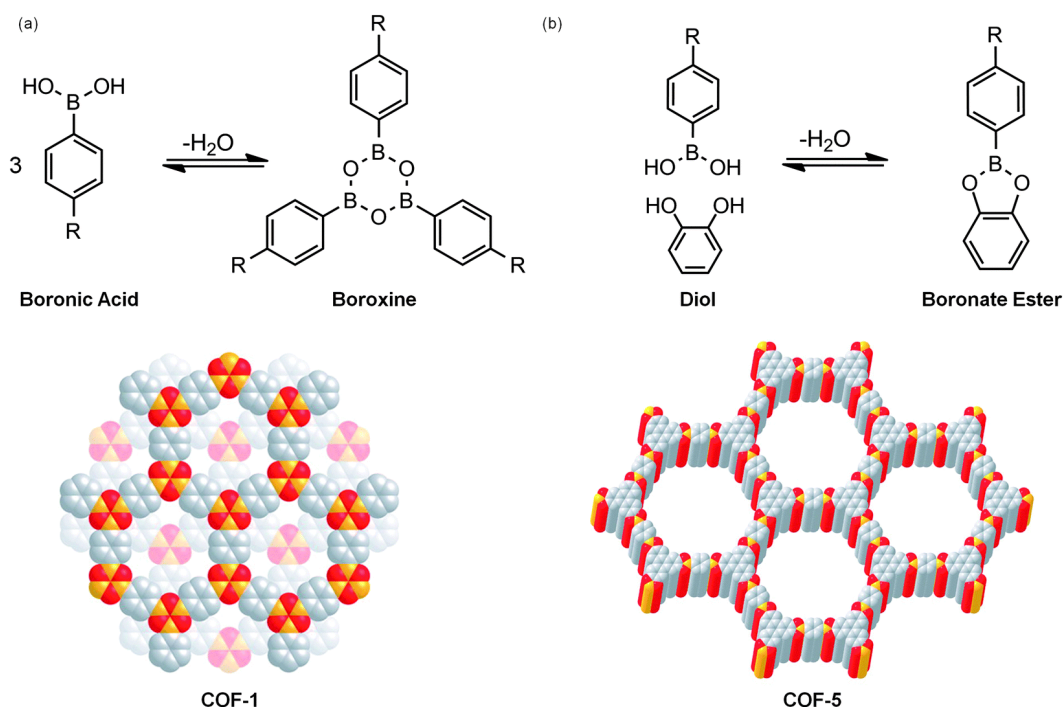


Figure 1.3. Reversible self-condensation reaction of benzenediboronic acid leads to the novel COF-1 which is covalently linked via boroxine rings and stacked in staggered arrangement (a). The reversible co-condensation of boronic acid and the diols of the hexahydroxytriphenylene (HHTP) building block formed the crystalline COF-5 in an eclipsed fashion (b). Color scheme: O red, B orange, C grey. Reproduced with permission from the Royal Society of Chemistry.^[20]

In the first COFs, the organic building blocks were connected by strong covalent bonds via the self-condensation of 1,4-benzenediboronic acid (COF-1) and its co-condensation with hexahydroxytriphenylene (COF-5). For the construction of highly crystalline frameworks, mild reaction conditions were identified that ensure bond formation reversibility during the synthesis. This enabled the ability of error correction through the reversible formation of boroxine or boronate ester linkages to promote the uninterrupted crystalline growth of periodic

nets. The microscopic reversibility is crucial for the formation of highly ordered crystalline COFs since the postsynthetic purification of the insoluble material is unfeasible. Therefore, the synthesis conditions must be adjusted in a way that reversibility is promoted and thus error correction processes *in situ* are enabled.^[21]

With the newly found ability to build ordered extended frameworks applying the toolbox of reticular chemistry and the immense manifold of organic molecules, this new generation of rigid, lightweight, and porous materials has experienced enormous growth ever since. And with the extensive toolset of organic chemistry, it became possible to blueprint and fabricate suitable organic building units that were then implemented into new COFs with tailor-made characteristics. The conceptual procedure of designing a new framework mostly follows a similar principle: the intended structure is first fragmented into the fundamental geometric building blocks. Then, the underlying constituents are examined and molecular equivalents are found which are made accessible and functionalized through organic chemistry. The next step employs these rigid precursors with attached functional groups in reactions under synthetic conditions that enable microscopic reversibility, producing crystalline COFs with specific and pre-designed properties.^[22]

Stitching together building units of predetermined symmetry and connectivity leads to different COF topologies, such as hexagonal, tetragonal, trigonal, rhombic/pseudosquare, and star-shaped/dual-pore (Figure 1.4). This way, the pore shape and metrics of COFs can be adjusted to specific needs, enabling their great structural diversity.

1 Introduction

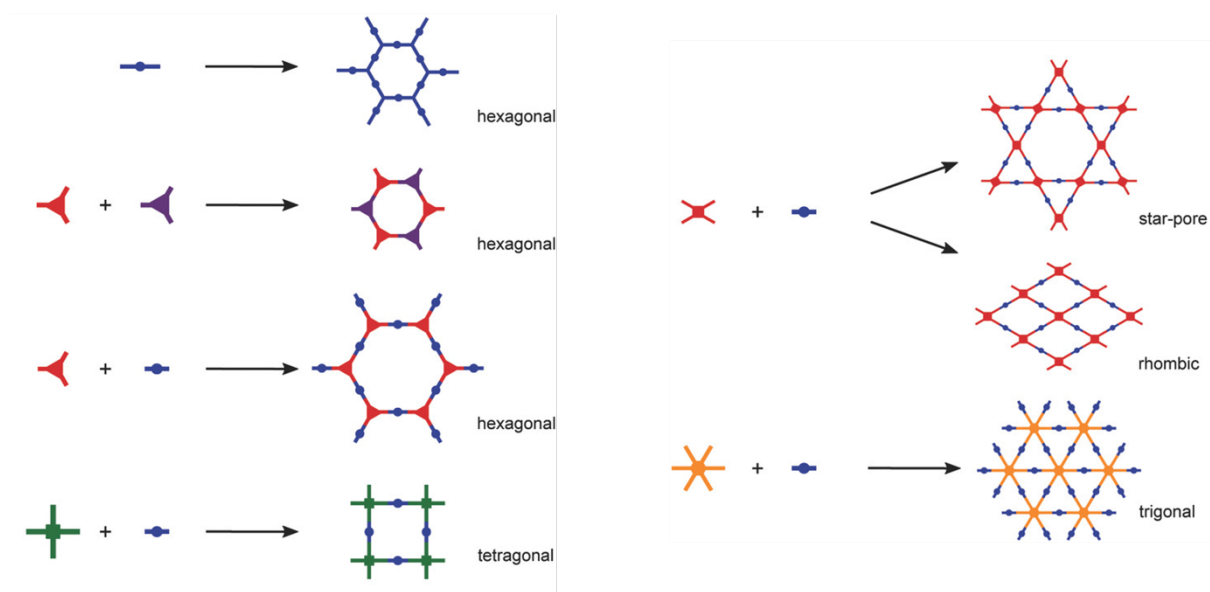


Figure 1.4. Reticular chemistry allows for the combination of building blocks with specific geometries, leading to various COF topologies and structural diversity. Adapted with permission.^[23] Copyright (2018) Maria Lohse and Thomas Bein. Publisher: WILEY-VCH Verlag GmbH & Co.

Subsequently, a broad range of various COFs was developed by the judicious combination of various building blocks of different size, geometry, and functionality. While the first COFs were solely composed of covalently-connected two-dimensional layers which were then π -stacked in the third dimension and therefore exhibited non-covalent bonds in one direction, a new subspecies joined the emergent field of COFs in 2007: three-dimensional COFs.^[24] In 3D COFs, the molecular building blocks are connected via covalent bonds in all three dimensions.

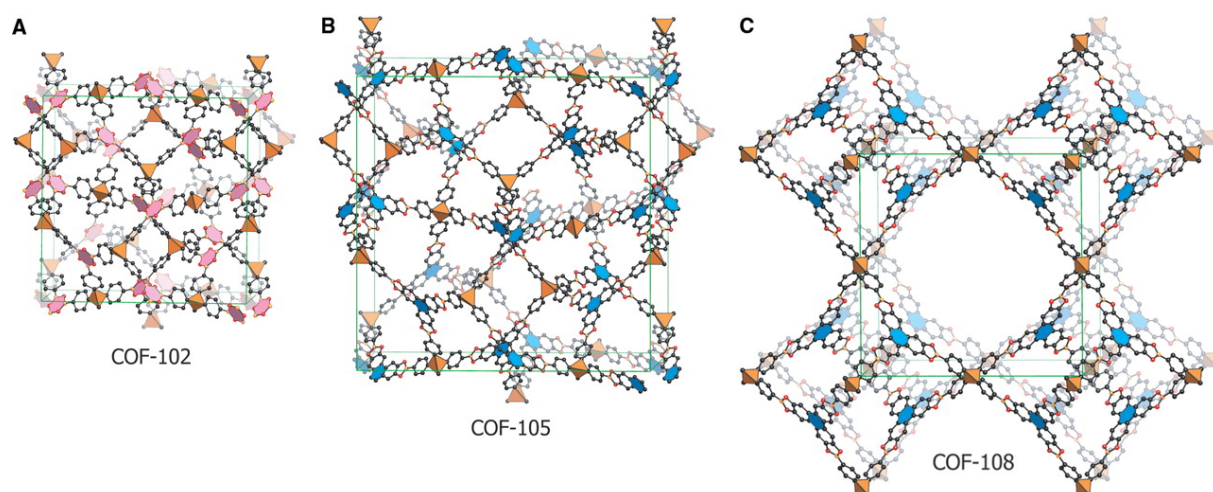


Figure 1.5. Structure models of the first 3D COFs. The self-condensation of a tetrahedral tetra-functionalized methane building block yielded COF-102 (a), while its co-condensation with the triangular hexahydroxytriphenylene yielded COF-105 (b). Co-condensation of the tetrahedral silane analog with the same triangular counterpart produced COF-108 (c).^[24] Reprinted with permission from AAAS.

This was accomplished by the reversible self-condensation reactions of tetrahedral building blocks and their co-condensation with triangular counterparts (Figure 1.5). The tetrasubstituted methane and silane derivatives enabled the growth of crystalline COF material linked by strong covalent bonds in three dimensions. The 3D COFs constructed this way offered high thermal stabilities and surface areas while their densities were exceptionally low.^[24]

1.3 Linkage types in Covalent Organic Frameworks

In addition to the composing building blocks, also the linkages between them can be altered in order to build novel covalent organic frameworks. In organic chemistry, this is achieved by equipping the components with suitable functional groups. While the first COFs employed covalent boron-oxygen-based bond types with the formation of boroxine and boronate esters,^[19, 24] a variety of many different linkage motifs followed thereafter (Figure 1.6). The sensitivity of both linkages towards hydrolysis limits their fields of application and thus has necessitated the development of more stable linkage types,^[25] always taking into account mandatory reversibility during bond formation. As a consequence, COFs with their building blocks linked via spiroborates were developed in 2016, revealing enhanced stability towards water and basic solution.^[26]

Further research with focus on more stable and π -conjugated bond types led to nitrogen-containing linkages. Triazine-linked COFs show great stability with large surface areas, rendering them as promising materials for gas storage and catalysis.^[27] However, their harsh synthesis conditions at high temperatures to increase the reversibility and thus produce crystalline material require extremely rigid and thermostable building blocks. As a consequence, the choice of suitable building units is limited.

1 Introduction

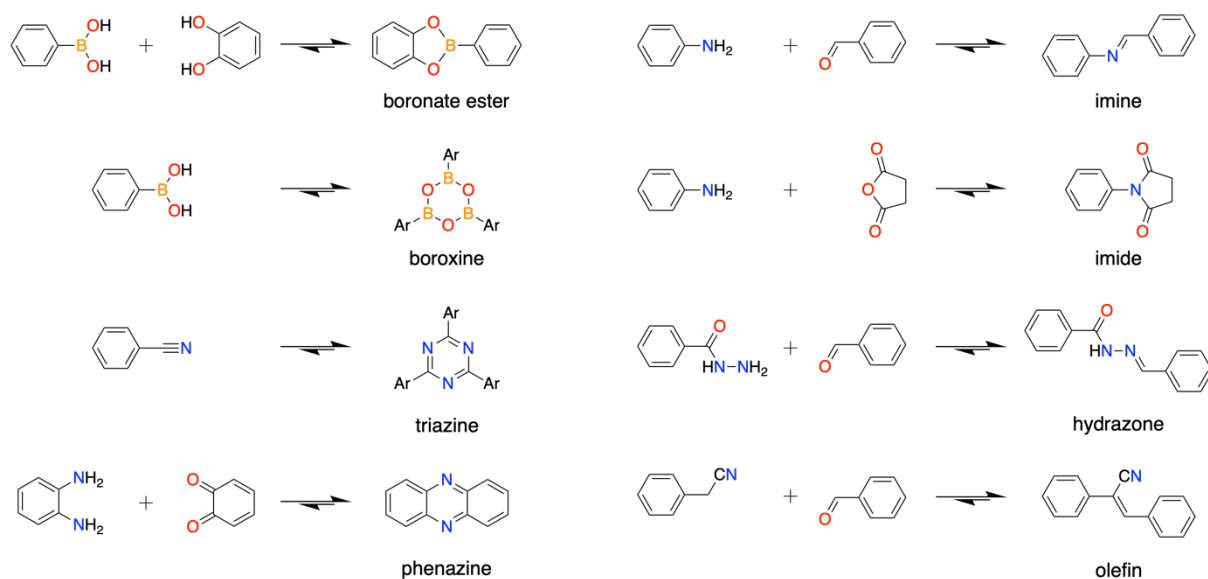


Figure 1.6. Common linkages developed for the formation of various COFs based on reversible condensation reactions.

Forming stable covalent bonds with simultaneous microscopic reversibility could also be achieved by acid-catalyzed Schiff-base chemistry under relatively mild solvothermal conditions. This allows the use of a great variety of different building blocks and therefore applies to a wide range of COFs. The first linkage of this reaction class was introduced in 2009 with a highly ordered 3D COF based on imine bonds, named COF-300.^[28] This COF laid the foundation for an ever-expanding number of subsequent imine-linked COFs, making this linkage motif by now the most commonly used in a great variety of frameworks.^[21] The imine bonds exhibit an overall higher stability over the boron-containing linkages and are very versatile through the straightforward condensation of amine and aldehyde functional groups, which can be attached to a broad range of monomers via the extended toolset of organic chemistry, at moderate conditions. Therefore, the imine linkage was also applied for the various frameworks developed in this thesis.

The mechanism of the acid-catalyzed imine formation starts with the protonation of the carbonyl oxygen, followed by the nucleophilic addition of the primary amine to the now more electrophilic carbonyl carbon (Figure 1.7).

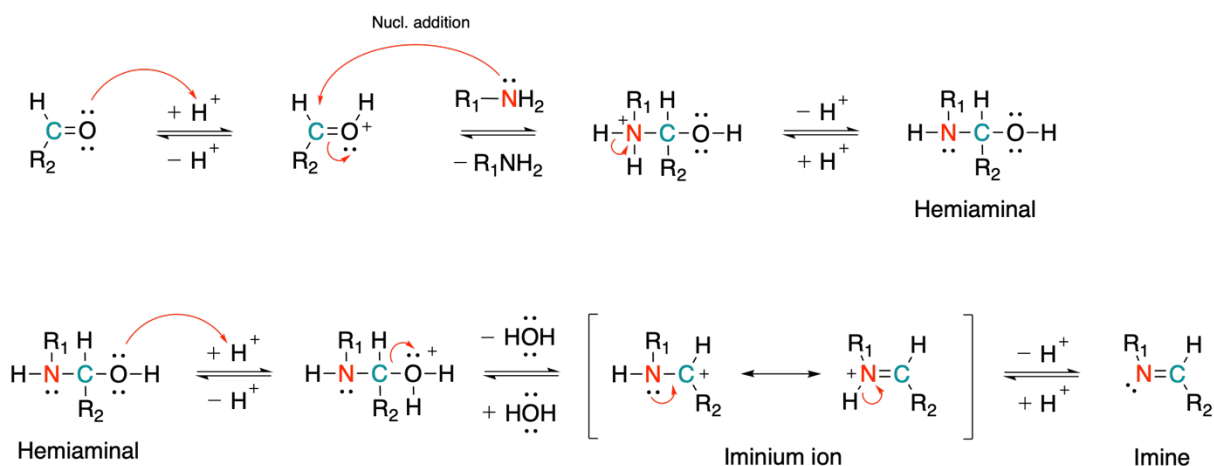


Figure 1.7. Mechanism of the acid-catalyzed imine formation from aldehydes and primary amines via the hemiaminal intermediate.

Deprotonation at the nitrogen of the secondary ammonium ion leads to the neutral hemiaminal intermediate. The subsequent protonation of the hydroxy group furnishes H_2O as a good leaving group and thus induces the dehydration of the hemiaminal. The resonance-stabilized iminium ion is then formed and its deprotonation produces the imine linkage, which is also termed Schiff base. The acidity of this condensation reaction must be adjusted in a way that enough catalytic acid is present to promote the rate-determining dehydration step. However, too much acid will counteract the imine formation since then the basic amine will be protonated forming the ammonium salt and hence decreasing the concentration of the free amine for the initial nucleophilic addition. Therefore, the pH of the synthesis must be taken into account and should be around 4 – 5 for the maximum rate.^[29]

Further C=N-linkage development applying the reversible Schiff base chemistry led to hydrazone COFs^[30] with good chemical stability and squaraine-linked COFs^[31] with a zwitterionic resonance structure. With the aim to further increase the stability and conjugation, the aromatic phenazine linkage via the condensation of di-ketones and 1,2-diamines was developed.^[32] Other condensation reactions developed for the construction of COFs encompass azine,^[33] imide,^[34] and β -ketoenamine linkages.^[35]

In order to construct fully π -conjugated 2D COFs, olefin linkages based on sp^2 -hybridized carbon were implemented into the periodic frameworks in 2016.^[36] The C=C bonds were realized by the Knoevenagel condensation of polyfunctional building blocks containing aryl acetonitrile and aromatic aldehyde moieties. Since then, a growing number of sp^2 -carbon linked COFs were reported with enhanced chemical stability and extended conjugation.^[37-39] While the first COFs of this category employed nitrile-substituted sp^2 -carbon bonds ($-\text{CH}=\text{C}(\text{CN})-$), further development produced the COF-701 with unsubstituted olefin linkages ($-\text{CH}=\text{CH}-$) and

exceptionally high stability.^[40] These continuing developments in the field of COFs underline the inexhaustible versatility of constructing new crystalline framework materials with specific characteristics.

Altering the single constituents of COFs by chemically modifying their linkage and building block design produced a wide range of different materials until now, each with bespoke functionalities that render them suitable for specific application fields. This way, COFs have drawn attention as promising candidates for gas storage and separation,^[41-47] catalysis and photocatalysis,^[48-54] and optoelectronics and electronics.^[32, 55-62]

1.4 Indigo isomers: Powerful Building Blocks for COFs

In the development of new molecular building blocks for the incorporation into COFs, a novel ditopic member with intriguing properties joined the growing construction kit: isoindigo. Isoindigo is an isomer of the world-famous blue indigo dye, which can be directly extracted from nature and is one of the oldest and most important natural dyes, earning this molecule the name ‘king of dyes’.^[63] Although indigo was utilized as an organic colorant for textiles, among others, for thousands of years,^[64] the synthetic production was first possible at the end of the 19th century when Adolf v. Baeyer succeeded with the first full laboratory synthesis of indigo in 1878.^[65] Later on, in 1883, he successfully determined the chemical structure of this molecule,^[66] which already took the center stage of the scientific community and industry.

Structural modifications of the indigo skeleton led to a diverse range of differently colored dyes, including the red indirubin, the purple 6,6'-dibromoindigo, or the brown isoindigo.^[65] Besides their use as indigoid dyes, these bis-indoles were also applied in the field of pharmacology.^[67] In the research for new building blocks for organic electronics, ancient and strongly colored dyes and pigments have experienced a revival since they feature promising properties for modern applications, such as organic photovoltaics (OPVs) and organic field effect transistors (OFETs).^[68] For an enhanced performance, these application fields often require constituents with suitable optical absorption, processability, stability, and charge transport capabilities.

Isoindigo exhibits electron-deficient γ -lactam rings and therefore structurally differs from indigo by the relative position of the nitrogen atoms and the carbonyl groups of the heterocycles (Figure 1.8).

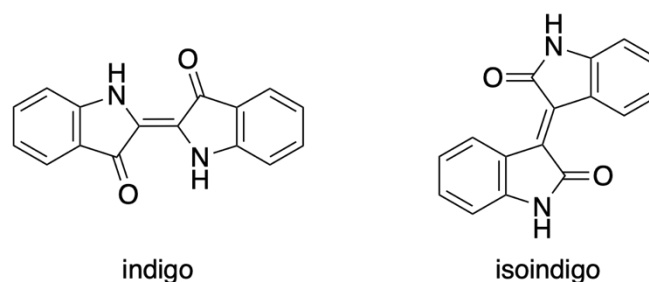


Figure 1.8. Chemical structures of the well-known blue indigo dye and its isomer isoindigo.

The five-membered lactam rings in isoindigo are fused to phenyl groups, leading to an extended delocalized π -system throughout the bis-oxindole skeleton and rendering these molecules ideally suited building blocks for organic semiconductors.^[69] The strong electron-withdrawing character of isoindigo was first utilized in molecular bulk-heterojunction solar cells by John R. Reynolds and coworkers in 2010.^[70] Here, the isoindigo core was *N*-alkylated to provide solubility in common organic solvents and functionalized at the 6,6'-carbons to enable the Suzuki-coupling with electron-donating bithiophenes. The resulting oligomeric donor-acceptor (D-A) systems showed a broad optical absorption and performed successfully in the first isoindigo-based solar cells. Subsequently, isoindigo-containing polymers with strong absorption capabilities were developed by coupling functionalized isoindigo with various donor moieties, paving the way for donor-acceptor polymer solar cells.^[71]

The strong optical absorption capabilities of isoindigo-based polymers that encompass the whole visible light spectrum and range into the NIR region derive from the concept of combining electron-rich and -deficient units in materials with extended π -conjugation along the backbone.^[72] The broad two-band spectral absorption characteristic for polymers that are designed according to the donor-acceptor approach comprises two main contributions: an absorption band at higher energies that can be assigned to the π - π^* transitions, whereas the second band at lower energies is attributed to intramolecular charge transfer (ICT) transitions.^[71, 73] By systematically varying the electron-donating or -withdrawing character of the single co-monomers, the ICT effects of the D-A materials can be modulated and their absorption profile can be tuned.^[74] Therefore, the absorption can be red-shifted by adjusting the implemented donor- or acceptor-moieties in a way that the ICT character is enhanced.^[71, 75]

The strong light absorption features, which cover the whole visible spectrum owing to their low band gap, combined with the versatile tunability and the suitable HOMO (highest occupied molecular orbital) and LUMO (lowest unoccupied molecular orbital) energy levels made isoindigo-based polymers promising materials for photovoltaic applications and consequently led to the first solar cells based on these donor-acceptor-type polymers in 2011.^[76-78] With

While initial research on the crystal structure of isoindigo claimed a perfectly planar molecule with the two oxindole moieties coplanar to each other,^[86, 87] later studies however suggested a slightly twisted conformation.^[88-90] Here, the structural investigations and calculations resulted in an energetically favored rotation of the two oxindole units relative to each other along the central double bond. The coexistence of planar and twisted crystal structures of isoindigo is attributed to the rather small energy barrier that could be overcome by thermal energy and packing interactions in the solid state to yield a planar conformation.^[91] Nevertheless, the global minimum based on theoretical calculations was found for the twisted geometry, especially when isoindigo is disubstituted at the 6,6'-positions.^[92] This twisted conformation is caused by the steric repulsion between the hydrogen atoms of the outer phenyl rings and the carbonyl oxygen atoms of the lactam groups, negatively affecting π -conjugation and stacking interactions.^[93, 94] Following the strategy applied in diketopyrrolopyrrole-containing polymers, where the torsional backbone twist was significantly reduced by switching the flanking moieties from phenyl to thiophene rings,^[95] the structure of the isoindigo core was similarly fine-tuned.^[73] The outer phenyl rings of isoindigo were replaced with fusing thiophenes producing the novel derivative thienoisindigo.^[96] With this modification strategy, the structural drawbacks are overcome and coplanarity is enforced since the steric repulsion is now avoided and replaced by favorable sulfur-oxygen interactions of the thiophene and carbonyl groups (Figure 1.9).^[93, 97, 98] Additionally, the steric hindrance between the isoindigo core and flanking electron-donating moieties is reduced in the case of thienoisindigo, leading to an even stronger improved backbone planarity.^[99, 100]

The optimized coplanar structure of thienoisindigo implies an extended π -conjugated system throughout the entire molecule and promotes close packing and thus improved intermolecular interaction.^[96, 101, 102] These factors are favorable for effective charge carrier transport and enhanced charge delocalization and promote the light absorption capabilities.^[103] The reduced optical band gap of the strongly π -conjugated thienoisindigo and its derivatives induces a broad and distinctly red-shifted light absorption. Donor-acceptor polymers based on thienoisindigo moieties therefore exhibit strong absorption features that range far into the near infrared region of the electromagnetic spectrum.^[102, 104]

With its improved structural, optical, and electronic features, the thienoisindigo building unit showed its great potential for high performing applications, such as OFETs and OPVs.^[93, 99, 103, 105-107] Based on its outstanding properties and suitable features, thienoisindigo recently found its way into the highly ordered environment of conjugated COFs, showing its impact on potential COF-based applications.^[108, 109]

1 Introduction

This exemplary advancement and modification of molecular building blocks based on the powerful toolbox of organic chemistry, accompanied by the constant improvements of the respective materials employing them, demonstrates the great potential of reticular chemistry. Depending on specific needs, the building units are chemically adjusted and implemented into custom-made functional materials whose properties are mainly controlled by the synthesized subunits. This synergy of shape and function enables the possibility to design and synthesize variable products that fulfill diverse requirements for modern applications.

The crystalline character of COFs additionally increases the structural control and therefore facilitates the fine-tuning of properties. Furthermore, their tunable porosity with the possibility of additional functionalization expands their constantly growing fields of application.

1.5 References

- [1] T. F. Degnan, *Top. Catal.* **2000**, *13*, 349-356.
- [2] W. Vermeiren, J. P. Gilson, *Top. Catal.* **2009**, *52*, 1131-1161.
- [3] A. Khaleque, M. M. Alam, M. Hoque, S. Mondal, J. B. Haider, B. Xu, M. A. H. Johir, A. K. Karmakar, J. L. Zhou, M. B. Ahmed, M. A. Moni, *Environmental Advances* **2020**, *2*, 100019.
- [4] R. E. Morris, P. S. Wheatley, *Angew. Chem. Int. Ed.* **2008**, *47*, 4966-4981.
- [5] Y. Cui, H. Kita, K.-i. Okamoto, *J. Mater. Chem.* **2004**, *14*, 924-932.
- [6] J. Wen, H. Dong, G. Zeng, *J. Clean. Prod.* **2018**, *197*, 1435-1446.
- [7] T. Armbruster, in *Minerals as Advanced Materials I* (Ed.: S. V. Krivovichev), Springer Berlin Heidelberg, Berlin, Heidelberg, **2008**, pp. 1-6.
- [8] Y. Li, L. Li, J. Yu, *Chem* **2017**, *3*, 928-949.
- [9] O. M. Yaghi, H. Li, *J. Am. Chem. Soc.* **1995**, *117*, 10401-10402.
- [10] O. M. Yaghi, G. Li, H. Li, *Nature* **1995**, *378*, 703-706.
- [11] H. Li, M. Eddaoudi, T. L. Groy, O. M. Yaghi, *J. Am. Chem. Soc.* **1998**, *120*, 8571-8572.
- [12] H. Li, M. Eddaoudi, M. O'Keeffe, O. M. Yaghi, *Nature* **1999**, *402*, 276-279.
- [13] O. M. Yaghi, M. O'Keeffe, N. W. Ockwig, H. K. Chae, M. Eddaoudi, J. Kim, *Nature* **2003**, *423*, 705-714.
- [14] S. S. Kaye, A. Dailly, O. M. Yaghi, J. R. Long, *J. Am. Chem. Soc.* **2007**, *129*, 14176-14177.
- [15] R. Freund, O. Zaremba, G. Arnauts, R. Ameloot, G. Skorupskii, M. Dincă, A. Bavykina, J. Gascon, A. Ejsmont, J. Goscianska, M. Kalmutzki, U. Lächelt, E. Ploetz, C. S. Diercks, S. Wuttke, *Angew. Chem. Int. Ed.* **2021**, *60*, 23975-24001.
- [16] M. Eddaoudi, J. Kim, N. Rosi, D. Vodak, J. Wachter, M. O'Keeffe, O. M. Yaghi, *Science* **2002**, *295*, 469-472.
- [17] W. Xu, K. B. Thapa, Q. Ju, Z. Fang, W. Huang, *Coord. Chem. Rev.* **2018**, *373*, 199-232.
- [18] M. O'Keeffe, *Chem. Soc. Rev.* **2009**, *38*, 1215-1217.
- [19] A. P. Côté, A. I. Benin, N. W. Ockwig, M. O'Keeffe, A. J. Matzger, O. M. Yaghi, *Science* **2005**, *310*, 1166-1170.
- [20] M. Dogru, T. Bein, *Chem. Commun.* **2014**, *50*, 5531-5546.

- [21] O. M. Yaghi, M. J. Kalmutzki, C. S. Diercks, *Introduction to Reticular Chemistry: Metal-Organic Frameworks and Covalent Organic Frameworks*, 1 ed., Wiley-VCH, Weinheim, **2019**.
- [22] C. S. Diercks, O. M. Yaghi, *Science* **2017**, *355*, eaal1585.
- [23] M. S. Lohse, T. Bein, *Adv. Funct. Mater.* **2018**, *28*, 1705553.
- [24] H. M. El-Kaderi, J. R. Hunt, J. L. Mendoza-Cortés, A. P. Côté, R. E. Taylor, M. O'Keeffe, O. M. Yaghi, *Science* **2007**, *316*, 268-272.
- [25] C. R. DeBlase, W. R. Dichtel, *Macromolecules* **2016**, *49*, 5297-5305.
- [26] Y. Du, H. Yang, J. M. Whiteley, S. Wan, Y. Jin, S.-H. Lee, W. Zhang, *Angew. Chem. Int. Ed.* **2016**, *55*, 1737-1741.
- [27] P. Kuhn, M. Antonietti, A. Thomas, *Angew. Chem. Int. Ed.* **2008**, *47*, 3450-3453.
- [28] F. J. Uribe-Romo, J. R. Hunt, H. Furukawa, C. Klöck, M. O'Keeffe, O. M. Yaghi, *J. Am. Chem. Soc.* **2009**, *131*, 4570-4571.
- [29] P. Vollhardt, N. Schore, *Organic Chemistry: Structure and Function* 8ed., W. H. Freeman and Company, New York, **2018**.
- [30] F. J. Uribe-Romo, C. J. Doonan, H. Furukawa, K. Oisaki, O. M. Yaghi, *J. Am. Chem. Soc.* **2011**, *133*, 11478-11481.
- [31] A. Nagai, X. Chen, X. Feng, X. Ding, Z. Guo, D. Jiang, *Angew. Chem. Int. Ed.* **2013**, *52*, 3770-3774.
- [32] J. Guo, Y. Xu, S. Jin, L. Chen, T. Kaji, Y. Honsho, M. A. Addicoat, J. Kim, A. Saeki, H. Ihee, S. Seki, S. Irlé, M. Hiramoto, J. Gao, D. Jiang, *Nat. Commun.* **2013**, *4*, 2736.
- [33] S. Dalapati, S. Jin, J. Gao, Y. Xu, A. Nagai, D. Jiang, *J. Am. Chem. Soc.* **2013**, *135*, 17310-17313.
- [34] Q. Fang, Z. Zhuang, S. Gu, R. B. Kaspar, J. Zheng, J. Wang, S. Qiu, Y. Yan, *Nat. Commun.* **2014**, *5*, 4503.
- [35] C. R. DeBlase, K. E. Silberstein, T.-T. Truong, H. D. Abruña, W. R. Dichtel, *J. Am. Chem. Soc.* **2013**, *135*, 16821-16824.
- [36] X. Zhuang, W. Zhao, F. Zhang, Y. Cao, F. Liu, S. Bi, X. Feng, *Polym. Chem.* **2016**, *7*, 4176-4181.
- [37] E. Jin, M. Asada, Q. Xu, S. Dalapati, M. A. Addicoat, M. A. Brady, H. Xu, T. Nakamura, T. Heine, Q. Chen, D. Jiang, *Science* **2017**, *357*, 673-676.
- [38] E. Jin, J. Li, K. Geng, Q. Jiang, H. Xu, Q. Xu, D. Jiang, *Nat. Commun.* **2018**, *9*, 4143.
- [39] X. Li, *Mater. Chem. Front.* **2021**, *5*, 2931-2949.
- [40] H. Lyu, C. S. Diercks, C. Zhu, O. M. Yaghi, *J. Am. Chem. Soc.* **2019**, *141*, 6848-6852.

- [41] M. G. Rabbani, A. K. Sekizkardes, Z. Kahveci, T. E. Reich, R. Ding, H. M. El-Kaderi, *Chem. Eur. J.* **2013**, *19*, 3324-3328.
- [42] C. J. Doonan, D. J. Tranchemontagne, T. G. Glover, J. R. Hunt, O. M. Yaghi, *Nat. Chem.* **2010**, *2*, 235-238.
- [43] S. S. Han, H. Furukawa, O. M. Yaghi, W. A. Goddard, *J. Am. Chem. Soc.* **2008**, *130*, 11580-11581.
- [44] H. Furukawa, O. M. Yaghi, *J. Am. Chem. Soc.* **2009**, *131*, 8875-8883.
- [45] A. Nagai, Z. Guo, X. Feng, S. Jin, X. Chen, X. Ding, D. Jiang, *Nat. Commun.* **2011**, *2*, 536.
- [46] X. Guan, H. Li, Y. Ma, M. Xue, Q. Fang, Y. Yan, V. Valtchev, S. Qiu, *Nat. Chem.* **2019**, *11*, 587-594.
- [47] X. Guan, Y. Ma, H. Li, Y. Yusran, M. Xue, Q. Fang, Y. Yan, V. Valtchev, S. Qiu, *J. Am. Chem. Soc.* **2018**, *140*, 4494-4498.
- [48] S.-Y. Ding, J. Gao, Q. Wang, Y. Zhang, W.-G. Song, C.-Y. Su, W. Wang, *J. Am. Chem. Soc.* **2011**, *133*, 19816-19822.
- [49] Q. Fang, S. Gu, J. Zheng, Z. Zhuang, S. Qiu, Y. Yan, *Angew. Chem. Int. Ed.* **2014**, *53*, 2878-2882.
- [50] H. Xu, J. Gao, D. Jiang, *Nat. Chem.* **2015**, *7*, 905-912.
- [51] H. Li, Q. Pan, Y. Ma, X. Guan, M. Xue, Q. Fang, Y. Yan, V. Valtchev, S. Qiu, *J. Am. Chem. Soc.* **2016**, *138*, 14783-14788.
- [52] S. Yang, W. Hu, X. Zhang, P. He, B. Pattengale, C. Liu, M. Cendejas, I. Hermans, X. Zhang, J. Zhang, J. Huang, *J. Am. Chem. Soc.* **2018**, *140*, 14614-14618.
- [53] V. S. Vyas, F. Haase, L. Stegbauer, G. Savasci, F. Podjaski, C. Ochsenfeld, B. V. Lotsch, *Nat. Commun.* **2015**, *6*, 8508.
- [54] L. Stegbauer, K. Schwinghammer, B. V. Lotsch, *Chem. Sci.* **2014**, *5*, 2789-2793.
- [55] M. Dogru, M. Handloser, F. Auras, T. Kunz, D. Medina, A. Hartschuh, P. Knochel, T. Bein, *Angew. Chem. Int. Ed.* **2013**, *52*, 2920-2924.
- [56] M. Calik, F. Auras, L. M. Salonen, K. Bader, I. Grill, M. Handloser, D. D. Medina, M. Dogru, F. Löbermann, D. Trauner, A. Hartschuh, T. Bein, *J. Am. Chem. Soc.* **2014**, *136*, 17802-17807.
- [57] S.-L. Cai, Y.-B. Zhang, A. B. Pun, B. He, J. Yang, F. M. Toma, I. D. Sharp, O. M. Yaghi, J. Fan, S.-R. Zheng, W.-G. Zhang, Y. Liu, *Chem. Sci.* **2014**, *5*, 4693-4700.
- [58] L. Ascherl, E. W. Evans, M. Hennemann, D. Di Nuzzo, A. G. Hufnagel, M. Beetz, R. H. Friend, T. Clark, T. Bein, F. Auras, *Nat. Commun.* **2018**, *9*, 3802.
- [59] X. Feng, L. Chen, Y. Honsho, O. Saengsawang, L. Liu, L. Wang, A. Saeki, S. Irlle, S. Seki, Y. Dong, D. Jiang, *Adv. Mater.* **2012**, *24*, 3026-3031.

- [60] S. Jin, X. Ding, X. Feng, M. Supur, K. Furukawa, S. Takahashi, M. Addicoat, M. E. El-Khouly, T. Nakamura, S. Irle, S. Fukuzumi, A. Nagai, D. Jiang, *Angew. Chem. Int. Ed.* **2013**, *52*, 2017-2021.
- [61] X. Li, Q. Gao, J. Wang, Y. Chen, Z.-H. Chen, H.-S. Xu, W. Tang, K. Leng, G.-H. Ning, J. Wu, Q.-H. Xu, S. Y. Quek, Y. Lu, K. P. Loh, *Nat. Commun.* **2018**, *9*, 2335.
- [62] N. Keller, T. Bein, *Chem. Soc. Rev.* **2021**, *50*, 1813-1845.
- [63] H. Schmidt, *Chem. unserer Zeit* **1997**, *31*, 121-128.
- [64] W. C. Fernelius, E. E. Renfrew, *J. Chem. Educ.* **1983**, *60*, 633.
- [65] M. Puchalska, K. Połęcz-Pawlak, I. Zadrożna, H. Hryszko, M. Jarosz, *J. Mass Spectrom.* **2004**, *39*, 1441-1449.
- [66] A. Baeyer, *Ber. Dtsch. Chem. Ges.* **1883**, *16*, 2188-2204.
- [67] F. Erben, D. Kleeblatt, M. Sonneck, M. Hein, H. Feist, T. Fahrenwaldt, C. Fischer, A. Martin, J. Iqbal, M. Plötz, J. Eberle, P. Langer, *Org. Biomol. Chem.* **2013**, *11*, 3963-3978.
- [68] M. J. Robb, S.-Y. Ku, F. G. Brunetti, C. J. Hawker, *J. Polym. Sci., Part A: Polym. Chem.* **2013**, *51*, 1263-1271.
- [69] E. D. Głowacki, G. Voss, N. S. Sariciftci, *Adv. Mater.* **2013**, *25*, 6783-6800.
- [70] J. Mei, K. R. Graham, R. Stalder, J. R. Reynolds, *Org. Lett.* **2010**, *12*, 660-663.
- [71] R. Stalder, J. Mei, J. R. Reynolds, *Macromolecules* **2010**, *43*, 8348-8352.
- [72] P. M. Beaujuge, C. M. Amb, J. R. Reynolds, *Acc. Chem. Res.* **2010**, *43*, 1396-1407.
- [73] R. Stalder, J. Mei, K. R. Graham, L. A. Estrada, J. R. Reynolds, *Chem. Mater.* **2014**, *26*, 664-678.
- [74] A. P. Kulkarni, Y. Zhu, A. Babel, P.-T. Wu, S. A. Jenekhe, *Chem. Mater.* **2008**, *20*, 4212-4223.
- [75] S. A. Jenekhe, L. Lu, M. M. Alam, *Macromolecules* **2001**, *34*, 7315-7324.
- [76] G. Zhang, Y. Fu, Z. Xie, Q. Zhang, *Macromolecules* **2011**, *44*, 1414-1420.
- [77] B. Liu, Y. Zou, B. Peng, B. Zhao, K. Huang, Y. He, C. Pan, *Polym. Chem.* **2011**, *2*, 1156-1162.
- [78] E. Wang, Z. Ma, Z. Zhang, P. Henriksson, O. Inganäs, F. Zhang, M. R. Andersson, *Chem. Commun.* **2011**, *47*, 4908-4910.
- [79] E. Wang, Z. Ma, Z. Zhang, K. Vandewal, P. Henriksson, O. Inganäs, F. Zhang, M. R. Andersson, *J. Am. Chem. Soc.* **2011**, *133*, 14244-14247.
- [80] C.-C. Ho, C.-A. Chen, C.-Y. Chang, S. B. Darling, W.-F. Su, *J. Mater. Chem. A* **2014**, *2*, 8026-8032.

- [81] Y. Deng, J. Liu, J. Wang, L. Liu, W. Li, H. Tian, X. Zhang, Z. Xie, Y. Geng, F. Wang, *Adv. Mater.* **2014**, *26*, 471-476.
- [82] S.-F. Liao, C.-F. Lu, A. D. Fenta, C.-T. Chen, C.-Y. Chao, W.-F. Su, *J. Mater. Chem. A* **2019**, *7*, 21309-21320.
- [83] T. Lei, Y. Cao, Y. Fan, C.-J. Liu, S.-C. Yuan, J. Pei, *J. Am. Chem. Soc.* **2011**, *133*, 6099-6101.
- [84] T. Lei, Y. Cao, X. Zhou, Y. Peng, J. Bian, J. Pei, *Chem. Mater.* **2012**, *24*, 1762-1770.
- [85] T. Lei, J.-H. Dou, Z.-J. Ma, C.-H. Yao, C.-J. Liu, J.-Y. Wang, J. Pei, *J. Am. Chem. Soc.* **2012**, *134*, 20025-20028.
- [86] H. Von Eller-Pandraud, *Acta Cryst.* **1960**, *13*, 936-938.
- [87] M.-S. Yuan, Q. Fang, L. Ji, W.-T. Yu, *Acta Cryst.* **2007**, *E63*, o4342.
- [88] E. A. Perpète, J. Preat, J.-M. André, D. Jacquemin, *J. Phys. Chem. A* **2006**, *110*, 5629-5635.
- [89] Y. K. Voronina, D. B. Krivolapov, A. V. Bogdanov, V. F. Mironov, I. A. Litvinov, *J. Struct. Chem.* **2012**, *53*, 413-416.
- [90] J. Huang, Z. Mao, Z. Chen, D. Gao, C. Wei, W. Zhang, G. Yu, *Chem. Mater.* **2016**, *28*, 2209-2218.
- [91] J. Huang, G. Yu, *Chem. Mater.* **2021**, *33*, 1513-1539.
- [92] L. A. Estrada, R. Stalder, K. A. Abboud, C. Risko, J.-L. Brédas, J. R. Reynolds, *Macromolecules* **2013**, *46*, 8832-8844.
- [93] G. K. Dutta, A.-R. Han, J. Lee, Y. Kim, J. H. Oh, C. Yang, *Adv. Funct. Mater.* **2013**, *23*, 5317-5325.
- [94] Y. Koizumi, M. Ide, A. Saeki, C. Vijayakumar, B. Balan, M. Kawamoto, S. Seki, *Polym. Chem.* **2013**, *4*, 484-494.
- [95] C. B. Nielsen, M. Turbiez, I. McCulloch, *Adv. Mater.* **2013**, *25*, 1859-1880.
- [96] R. S. Ashraf, A. J. Kronemeijer, D. I. James, H. Sirringhaus, I. McCulloch, *Chem. Commun.* **2012**, *48*, 3939-3941.
- [97] X. Guo, N. Zhou, S. J. Lou, J. W. Hennek, R. Ponce Ortiz, M. R. Butler, P.-L. T. Boudreaault, J. Strzalka, P.-O. Morin, M. Leclerc, J. T. López Navarrete, M. A. Ratner, L. X. Chen, R. P. H. Chang, A. Facchetti, T. J. Marks, *J. Am. Chem. Soc.* **2012**, *134*, 18427-18439.
- [98] X. Wei, W. Zhang, G. Yu, *Adv. Funct. Mater.* **2021**, *31*, 2010979.
- [99] T. Odajima, M. Ashizawa, Y. Konosu, H. Matsumoto, T. Mori, *J. Mater. Chem. C* **2014**, *2*, 10455-10467.

1 Introduction

- [100] M. S. Chen, J. R. Niskala, D. A. Unruh, C. K. Chu, O. P. Lee, J. M. J. Fréchet, *Chem. Mater.* **2013**, *25*, 4088-4096.
- [101] W. Yue, R. S. Ashraf, C. B. Nielsen, E. Collado-Fregoso, M. R. Niazi, S. A. Yousaf, M. Kirkus, H.-Y. Chen, A. Amassian, J. R. Durrant, I. McCulloch, *Adv. Mater.* **2015**, *27*, 4702-4707.
- [102] G. W. P. Van Pruissen, F. Gholamrezaie, M. M. Wienk, R. A. J. Janssen, *J. Mater. Chem.* **2012**, *22*, 20387-20393.
- [103] D. Yoo, T. Hasegawa, M. Ashizawa, T. Kawamoto, H. Masunaga, T. Hikima, H. Matsumoto, T. Mori, *J. Mater. Chem. C* **2017**, *5*, 2509-2512.
- [104] M. Karakawa, Y. Aso, *Macromol. Chem. Phys.* **2013**, *214*, 2388-2397.
- [105] G. Kim, S.-J. Kang, G. K. Dutta, Y.-K. Han, T. J. Shin, Y.-Y. Noh, C. Yang, *J. Am. Chem. Soc.* **2014**, *136*, 9477-9483.
- [106] P. Han, X. Gong, B. Lin, Z. Jia, S. Ye, Y. Sun, H. Yang, *RSC Advances* **2015**, *5*, 50098-50104.
- [107] H. Kang, S. Y. An, B. Walker, S. Song, T. Kim, J. Y. Kim, C. Yang, *J. Mater. Chem. A* **2015**, *3*, 9899-9908.
- [108] D. Bessinger, L. Ascherl, F. Auras, T. Bein, *J. Am. Chem. Soc.* **2017**, *139*, 12035-12042.
- [109] D. Bessinger, K. Muggli, M. Beetz, F. Auras, T. Bein, *J. Am. Chem. Soc.* **2021**, *143*, 7351-7357.

2 Characterization Techniques

2.1 X-ray Diffraction

Working with crystalline materials, such as COFs, requires a fast and non-destructive characterization method to immediately evaluate the degree of crystallinity after the synthesis. For sufficiently crystalline samples and good data quality, X-ray diffraction (XRD) provides access to structural insights of the new materials and is of great importance for refining and simulating the unit cell of a periodic structure.

This analytical technique is based on X-rays that are generated in a tube with an anode target material and are focused onto the sample. The tube emits an intense X-ray radiation of a characteristic wavelength when voltage-accelerated electrons collide with the anode material. Here, the atoms of the target metal are ionized by the kinetically energized electrons and the vacancies of the inner shell are subsequently refilled by electrons from shells with a higher quantum number. Taking the K -transition as an example, an electron of the inner K -shell is ejected by the inbound electron. When an electron of the outer L -shell then refills the resulting vacancy, an X-ray photon whose energy corresponds to the energy differences of both shells is emitted, generating the characteristic K_α radiation. Refilling by an electron of the higher M -shell emits the K_β radiation. This also applies to the L radiation where an electron of the L -shell is ejected and the vacant position is then filled with an electron from an outer shell (Figure 2.1).^[1]

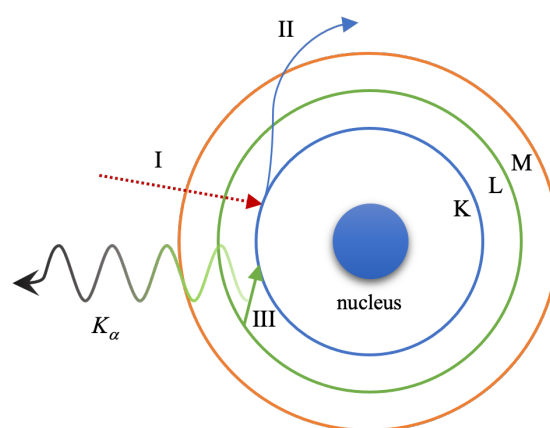


Figure 2.1. Collision of an accelerated electron with a target metal atom (I) leads to the ejection of an electron of the inner K -shell (II). The vacancy is then refilled by an electron of the outer L -shell (III) emitting an X-ray photon in the form of the characteristic K_α radiation.

The foundation of the principle of X-ray diffraction is attributed to the discoveries of Laue and Bragg at the beginning of the 20th century. They found that diffraction occurs when X-ray

2 Characterization Techniques

beams are directed onto the highly ordered periodic structures of crystals.^[1] The theory behind their observations relies on the constructive interference of X-rays through scattering events at the crystal lattice. The conditions that must be fulfilled for the X-ray reflection on lattice planes are given by the Bragg equation

$$n \lambda = 2d \sin \theta$$

with n being the order of the reflection, λ the wavelength of the monochromatic X-ray beam, d the lattice plane spacing and θ the Bragg angle between the X-ray beam and the lattice planes.^[2] Diffraction in crystalline materials requires wavelengths of the incident beam that are of a similar order of magnitude as the lattice distances. Therefore, X-rays with typical wavelengths from 0.01 to 10 nm are the preferred radiation type for this purpose.^[3] From the Bragg equation it can be derived that with fixed spacing d and wavelength λ , constructive interference only occurs if the incident angle θ possesses such values that the path length difference $2d \sin \theta$ of the adjacent lattice plane is an integer multiple of the wavelength (Figure 2.2).^[2]

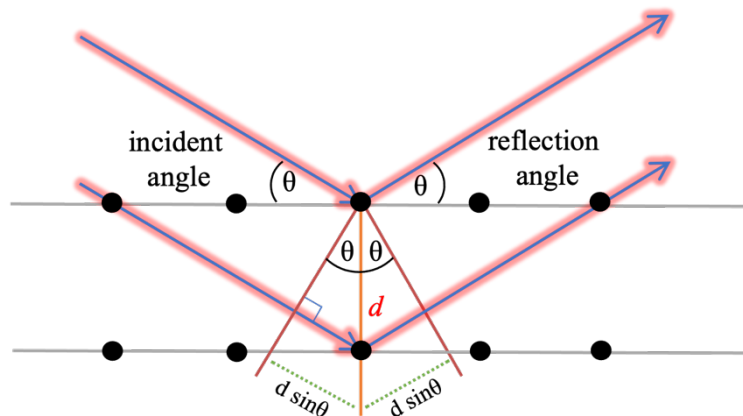


Figure 2.2. Visualization of the reflection of X-rays at a crystal lattice meeting the Bragg conditions for constructive interference.

In this case, the diffracted beams are in alignment and can be detected as a diffraction peak. If the Bragg angle θ is changed to a value at which the equation is not fulfilled, the diffracted beams are out of sync and the resulting destructive interference prevents the detection of a reflection signal.^[1] Furthermore, the Bragg equation illustrates that, assuming constant values of λ , the angle θ determines the lattice plane distance d , since d must be smaller for higher values of θ . Although the first discoveries of X-ray diffraction described the scattering behavior of single crystals, this technique has by now become a very common characterization tool not

only for polycrystalline powder samples but also for thin films of crystalline materials grown on substrates.

The powder XRD measurements were carried out using the Bragg-Brentano reflection geometry on a Bruker D8 Discover diffractometer with a Ni-filtered Cu-K α radiation source and a Lynx-Eye position-sensitive detector. The simulated COF structure models based on the experimental XRD data were generated using the Accelrys Materials Studio software package and the implemented Rietveld and Pawley structure refinement methods.

2.2 Grazing-Incidence Wide-Angle X-ray Scattering (GIWAXS)

For many applications of COFs, preferentially oriented thin films are of great interest. Their high degree of order and their permanent porosity fulfill the requirements to serve as an active host material, e.g. for electron acceptors such as fullerenes, or for charge-balancing counterions in an electrolyte solution. Since the thickness of these functional COF layers homogeneously grown on top of specific substrates can be very small and therefore the signal intensities are very weak in relation to the background signal if measured with common X-ray scattering geometries, the grazing-incidence X-ray scattering method is utilized to gain information about the crystallinity and the orientation of the nanostructured thin films.

In the GIWAXS experiment, an incident monochromatic X-ray beam of a defined wavelength λ probes the thin sample layer with a small incident angle α_i . The beam is scattered in vertical direction at the exit angle α_f and in horizontal direction at the in-plane angle $2\theta_f$ (Figure 2.3).^[4]

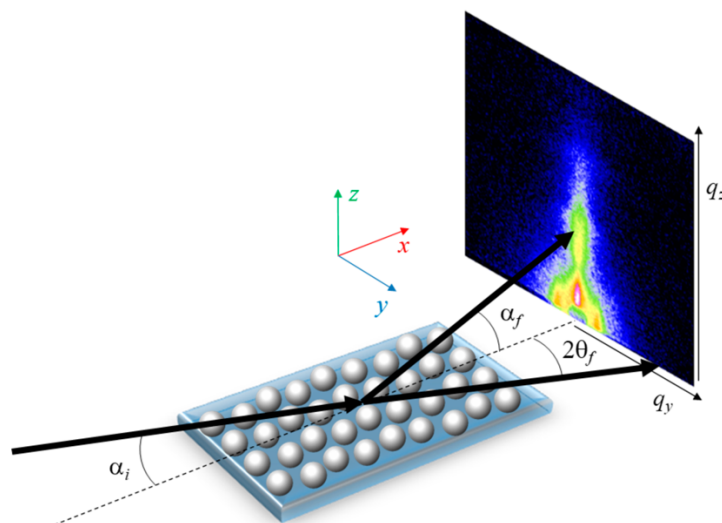


Figure 2.3. Schematic representation of grazing-incidence scattering on a thin sample surface.^[4]

In this surface-sensitive diffraction technique, the chosen angle of the incident X-ray beam onto the sample is below the critical angle. Under these conditions, the X-ray beam is totally externally reflected at the surface and the exponentially decreasing evanescent wave is only penetrating a short distance into the bulk of the material. The detected Bragg reflections are thus mainly from scattering events at the crystal lattices close to the surface.^[5]

The data of the resulting patterns are indicated by the magnitude of the scattering vector q with units of \AA^{-1} or nm^{-1} . With the given wavelength λ of the monochromatic X-ray beam, the q -values correlate with half of the scattering angle 2θ by the equation:^[5]

$$q = \frac{4\pi}{\lambda} \sin \theta$$

Particularly in the case of conjugated two-dimensional COFs, where an orientation of the π -stacked sheet-like layers parallel to the substrate surface is highly desirable since the pores then extend towards the film surface, the grazing-incidence scattering technique is a great tool to evaluate the growth of the COF layer. The distribution of diffraction intensities on the GIWAXS images reveals whether and in which direction there is a preferential orientation of the COF crystallites.

The GIWAXS measurements were mostly performed using an Anton Paar SAXSpoint 2.0 system equipped with a Primux 100 micro Cu K_{α} source and a Dectris EIGER R 1M 2D detector.

2.3 Nitrogen Physisorption

For the evaluation of porous materials such as COFs, nitrogen physisorption is a key analytical method. Probing the samples with inert gas molecules, with nitrogen gas being one of the most common ones in the field of COFs, enables insights about their pore accessibility and characteristics including the pore size, pore volume, and surface area. The method is based on reversible interactions between the adsorbent which is the respective sample surface and the adsorptive, the adsorbable gas. In contrast to chemisorption where strong chemical bonds are formed between the two abovementioned species, interactions in physisorption analyses are mainly relatively weak van-der-Waals forces including the London dispersion forces and the intermolecular repulsion component.^[6]

If the ambient temperature is kept constant below the critical point of the adsorptive throughout the measurement (i.e. at 77 K for nitrogen sorption measurements), its relative pressure is given by p/p° , which indicates the fraction of the equilibrium pressure p and the saturation vapor pressure p° . At each predetermined relative pressure value of the gas admitted to the sample, the volume of adsorbed gas is recorded with adequate equilibration conditions taken into account.^[7] The relative gas pressure is increased stepwise, allowing more gas molecules to adsorb on the surface until the gas nearly reaches the saturation pressure p° , and is subsequently decreased whilst gradually desorbing the adsorptive from the surface. Due to the constant temperature, the recorded data are then plotted as adsorption and desorption isotherms, respectively.

The original IUPAC recommendation from 1985 categorizes the different pore sizes into three types:

- I.) *macropores* for pores exceeding the width of about 50 nm,
- II.) *mesopores* for pores with a width between 2 nm and 50 nm,
- III.) *micropores* for pores with a width smaller than 2 nm;

and furthermore includes the classification of the different physisorption isotherm shapes into six types based on the pore type and structure.^[8] The IUPAC categories were recently further specified and now comprise eight types of isotherms shown in Figure 2.4.

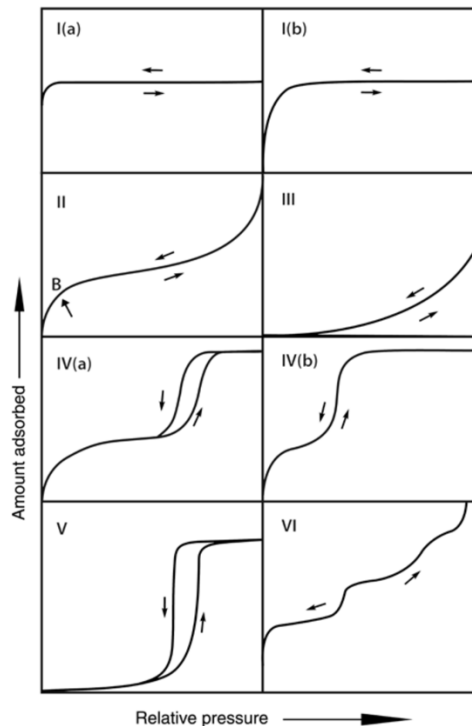


Figure 2.4. Classification of physisorption isotherms according to specified IUPAC reports. Reprinted with permission.^[7] Copyright (2015) IUPAC & De Gruyter.

2 Characterization Techniques

The reversible Type I isotherms reach the maximum amount of adsorbable gas molecules at relatively low p/p° values and typically occur for microporous materials due to increased interactions in the narrow pores. Type I(a) represent micropores with widths below ~ 1 nm whereas Type I(b) is characteristic for wider micropores and narrow mesopores with width below ~ 2.5 nm.

Type II isotherms are received from nonporous or microporous solids and refer to the unrestricted monolayer-multilayer adsorption. The inflection point B usually indicates the beginning of multilayer formation after the completion of monolayer coverage.

This shoulder is missing in the Type III isotherm that also represents nonporous or microporous samples, however with rather weak interactions between the adsorbent and the adsorbate which defines the gas molecules in an adsorbed state. Hence, there is no clear information concerning the monolayer coverage.

Mesoporous materials yield Type IV isotherms that can be divided into Type IV(a), featuring a distinct hysteresis, and the reversible Type IV(b) with similar shapes of the adsorption and the desorption branches. The shape of the isotherm at low relative pressures is similar to that of Type II illustrating the initial monolayer formation. Besides the monolayer and subsequent multilayer adsorption at higher relative pressure values, additional capillary condensation occurs in mesopores. This phenomenon describes the process where the probing gas condenses to a liquid-like phase at a pressure that is lower than the saturation pressure p° . Type IV isotherms indicate a saturation of adsorbed molecules with a plateau of the curve shape at increasing p/p° values. The hysteresis of Type IV(a) isotherms can be found for larger mesopores exceeding a critical width while mesopores of smaller widths typically show the reversible Type IV(b) curve shape.

The Type V isotherms without an identifiable monolayer coverage, similar to Type III, are received from micro- and mesoporous materials. Here, the interactions between the adsorbent and adsorbate are also very weak. The hysteresis in the multilayer range and the plateau at higher relative pressures stems from condensation and pore filling.

Type VI isotherms with a cascade curve exclusively applies to nonporous adsorbents with smooth surface. Here, the steps indicate the formation of single layers of the adsorbate on the sample surface. The step shapes are governed by the capacity of each layer and furthermore the adsorption system and the temperature.^[7]

With the majority of COFs being classified as mesoporous materials, their physisorption measurements typically show Type IV isotherms. For pore widths exceeding a certain value,

the capillary condensation is accompanied by a hysteresis loop between the adsorption and desorption branches (Figure 2.5).

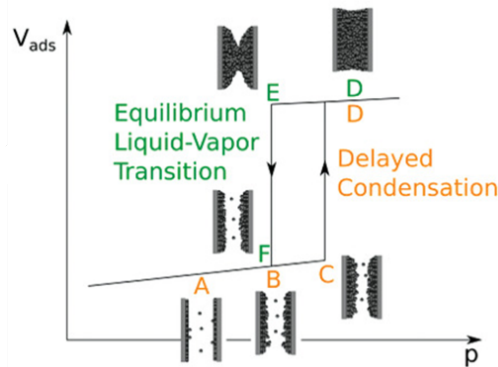


Figure 2.5. Schematic illustration of a Type IV(a) isotherm with capillary condensation leading to hysteresis due to delayed condensation in the adsorption branch. Adapted with permission.^[9] Copyright (2021) Carola Schlumberger and Matthias Thommes. Publisher: WILEY-VCH GmbH.

The hysteresis located in the multilayer region originates from the delayed pore condensation of the adsorption process (B – D) due to metastable adsorption multilayer films on the pore walls accompanied by the hindered nucleation of liquid bridges.^[10] In contrast, the desorption follows a liquid-vapor transition in the thermodynamic equilibrium (D – F). The removal of adsorbate during the desorption proceeds from a liquid meniscus without nucleation.^[9] If the material deviates from a rather simple pore structure, like uniform cylindrical pores or ordered three-dimensional frameworks, the desorption branch is influenced by pore blocking or cavitation, hence leading to different types of hystereses.^[11]

The theoretical evaluation of the experimental physisorption data contains the assessment of the surface area using the Brunauer-Emmett-Teller (BET) method. For materials exhibiting Type II or Type IV isotherms, the calculated BET area under controlled conditions describes the accessible area for the probing adsorbate. The BET method requires a transformation of the isotherm into a BET plot. The BET monolayer capacity n_m , indicating the amount of adsorbate necessary to build a complete monolayer on the sample surface, can then be derived from the BET equation

$$\frac{\frac{p}{p^0}}{n \left(1 - \frac{p}{p^0}\right)} = \frac{1}{n_m C} + \frac{C - 1}{n_m C} \left(\frac{p}{p^0}\right)$$

2 Characterization Techniques

with n as the amount adsorbed at the relative pressure p/p° and the BET parameter C that is exponentially related to the monolayer adsorption energy.^[7, 9]

For a correct derivation of n_m based on the BET equation, it is essential that the linear range of the BET plot is considered where the linear relation between $\frac{\frac{p}{p^\circ}}{n\left(1-\frac{p}{p^\circ}\right)}$ and $\frac{p}{p^\circ}$ applies. For most of the Type II and IV(a) isotherms, the linear BET range is in the relative pressure range between 0.05 and 0.30.^[12] The slope of $\frac{C-1}{n_m C}$ and the intercept of $\frac{1}{n_m C}$ from the extrapolated linear BET plot lead to the monolayer capacity.

The BET surface area $A_s(\text{BET})$ can then be derived using the equation

$$A_s(\text{BET}) = n_m \cdot N_A \cdot \sigma_m$$

with the known molecular cross-sectional area σ_m of the adsorbate, which is widely used with the value 16.2 \AA^2 for nitrogen,^[13] and the Avogadro constant N_A .^[7]

Taking into account the mass of the adsorbent (m), the specific surface area $a_s(\text{BET})$ can be calculated as:

$$a_s(\text{BET}) = \frac{A_s}{m}$$

The nitrogen physisorption isotherms were measured on Quantachrome Autosorb 1 and Autosorb iQ instruments at 77 K. Before measurement, the COFs were extracted with supercritical CO₂ and degassed at temperatures up to 120 °C under high vacuum.

2.4 Nuclear Magnetic Resonance (NMR)

For the characterization of organic molecules, an analysis via nuclear magnetic resonance (NMR) spectroscopy is highly desirable. In the field of COFs, this especially applies to synthesized building blocks that have to be evaluated in terms of structural information and phase-purity. An important prerequisite for using this analytical tool is the existence of isotopes with a nuclear magnetic moment and therefore a total nuclear spin (I) exceeding 0 in half-integer steps. Depending on the atom's number of protons (Z) and number of neutrons (N), the following three categories can be found for isotopes:

Class 1: Nuclei with even numbers of Z and N – *all proton and neutron spins are paired* – nuclear spin $I = 0$ – Invisible to NMR – Example isotopes: ¹²C, ¹⁶O, and ¹⁸O.

Class 2: Nuclei with odd numbers of Z and N – *odd number of unpaired proton ($I = \frac{1}{2}$) spins and unpaired neutron ($I = \frac{1}{2}$) spins* – nuclear spin $I = \text{non-zero integer}$ – Visible to NMR – Example isotopes: ²H ($I = 1$), ¹⁰B ($I = 3$), and ¹⁴N ($I = 1$).

Class 3: Nuclei with even Z and odd N , or odd Z and even N – *even number of paired proton spins and odd number of neutron spins, or vice versa* – nuclear spin $I = \text{odd integer multiple of } \frac{1}{2}$ – Visible to NMR – Example isotopes: ¹H ($I = \frac{1}{2}$), ¹¹B ($I = \frac{3}{2}$), ¹³C ($I = \frac{1}{2}$), ¹⁵N ($I = \frac{1}{2}$), and ³¹P ($I = \frac{1}{2}$).^[14]

2 Characterization Techniques

Most of the investigated nuclei in NMR spectroscopy, including ^1H and ^{13}C , possess the nuclear spin $I = \frac{1}{2}$ with a spherical and symmetrical spinning charge distribution. For nuclei with a higher spin number, an electric quadrupole moment is present with a non-spherical and non-symmetrical charge distribution. This has an effect on the NMR, leading to broadened NMR signals of the respective isotopes, as in case of the abundant ^{14}N nuclei with a spin of 1.^[15]

The spin states of the nuclei are degenerate without an external magnetic field. If a magnetic field is applied, the degeneracy is broken and the different nuclear spin states are energetically separated due to the interaction with the magnetic field referred to as the *Zeeman-splitting* (Figure 2.6). In contrast to atomic particles, i.e. protons, electrons and neutrons, with only two magnetic spin orientations, the more complex nuclei exhibit even more magnetic spin quantum numbers m .^[14] The number of these available spin levels is calculated by the multiplicity $2I + 1$ and can take values in the range of:

$$m = -I, -I + 1, \dots, I - 1, I$$

If applied to the ^1H nucleus with a nuclear spin of $I = \frac{1}{2}$, the spin state multiplicity is 2 with the magnetic spin quantum values $m = -\frac{1}{2}$ and $m = +\frac{1}{2}$.

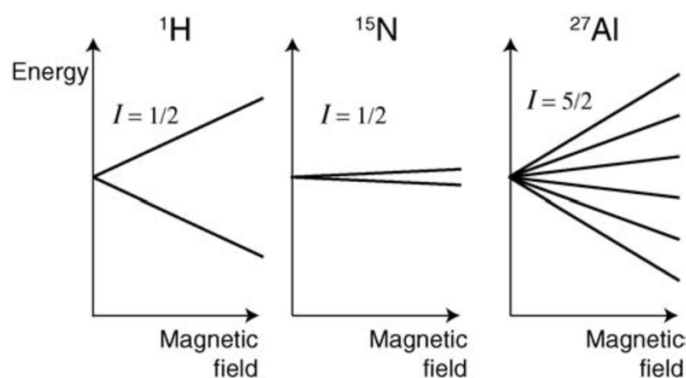


Figure 2.6. Nuclear Zeeman-splitting of the isotopes ^1H , ^{15}N , and ^{27}Al in an external magnetic field revealing the different energy levels of the spin states. Reprinted with permission.^[15] Copyright (2008) John Wiley and Sons.

Since nuclei with a non-zero spin angular momentum \mathbf{p} show a magnetic moment $\boldsymbol{\mu}$ proportional to the spin, their relation can be defined as follows:

$$\boldsymbol{\mu} = \gamma \mathbf{p}$$

Here, γ describes the gyromagnetic ratio which is a unique proportionality constant of the respective isotope. The ratio also indicates the effect of an external magnetic field on the energy levels of the nuclear spin states.

In a homogenous and static external magnetic field \mathbf{B}_0 along the z-direction, the angular momentum is quantized and the z-component of the angular momentum is $p_z = m\hbar$ which then leads to the z-component of the magnetic moment:^[16]

$$\mu_z = \gamma m\hbar$$

The energy E of a particular nuclear spin state is given by

$$E = -\mu_z \mathbf{B}_0$$

and is directly proportional to the magnetic quantum number m and the magnetic field \mathbf{B}_0 :

$$E = -\gamma m\hbar \mathbf{B}_0$$

When an external magnetic field is applied to the sample, the randomly oriented magnetic moments align with or against the magnetic field. As a result, the magnetic moment $\boldsymbol{\mu}$ of the nucleus with an apparent angular momentum then precesses around the axis of \mathbf{B}_0 with the Larmor frequency:^[14]

$$\nu = \frac{\gamma \mathbf{B}_0}{2\pi}$$

For the sake of simplicity, the most studied and simplest nucleus ^1H with a positive gyromagnetic ratio γ and a nuclear spin $I = \frac{1}{2}$ will be considered in the further course of this chapter. Based on the Boltzmann distribution according to which the energy levels are populated, the lower energy spin states with the magnetic moments parallel to the static magnetic field, also named α -states, are slightly stronger populated than the higher energy spin states with antiparallel magnetic moment orientation, the β -states, due to the thermal equilibrium. Hence, this leads to a net nuclear magnetization along the axis of the magnetic field (Figure 2.7).

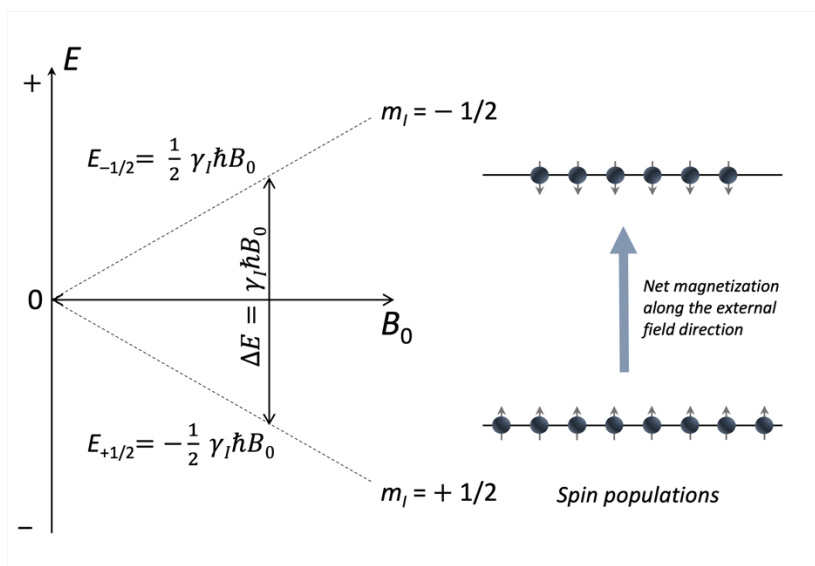


Figure 2.7. Zeeman splitting and spin state distribution of ^1H nuclei in a static external magnetic field. Higher population of states with magnetic moments parallel to the magnetic field yielding a longitudinal magnetization along the magnetic field (blue arrow). Reproduced with permission from the Royal Society of Chemistry.^[17]

The energy difference ΔE between the two adjacent spin states $m = -\frac{1}{2}$ and $m = +\frac{1}{2}$ is given as

$$\Delta E = E_{(m=-1/2)} - E_{(m=1/2)} = -\left[\left(-\frac{1}{2}\right) - \left(\frac{1}{2}\right)\right] \gamma \hbar \mathbf{B}_0 = \gamma \hbar \mathbf{B}_0$$

and is dependent on the magnitude of the applied magnetic field \mathbf{B}_0 .

For NMR analysis, a second oscillating magnetic field \mathbf{B}_1 perpendicular to \mathbf{B}_0 is now applied to the sample in order to perturb the longitudinal magnetization. If the frequency of the oscillating field \mathbf{B}_1 matches the Larmor frequency of the precessing magnetic moments, it will induce a transition between the two spin states and lead to a system with equally populated α - and β -states. As a consequence, the macroscopic magnetization is reduced in z-direction. Additionally, the precessing magnetic moments become phase coherent which hinders the spins from randomly precessing around \mathbf{B}_0 . The perpendicularly applied radio frequency pulse at the Larmor frequency ultimately rotates the net magnetization away from the z-axis towards the transverse x,y-plane after a 90° -pulse. The angle of rotation can be controlled by the irradiation time of the magnetic field \mathbf{B}_1 .^[14, 18]

The radio frequency pulse is then switched off, allowing for the relaxation of the system back to the initial state of thermal equilibrium in a static magnetic field \mathbf{B}_0 . This includes two types of relaxation processes: On the one hand, the population of nuclear spin states relax back following the Boltzmann distribution and the slight excess of nuclei in the lower energy α -states resumes the predominant magnetization of the system along the z-axis. This process is

called longitudinal or spin-lattice relaxation and is indicated by the relaxation time T_1 . On the other hand, the phase coherence of the precessing magnetic moments is decreasing and the spins return to precess in random order around \mathbf{B}_0 which is referred to as transverse or spin-spin relaxation. The time necessary for this relaxation mechanism is defined as the relaxation time T_2 . From a macroscopic perspective, these processes lead to a precessional motion of net magnetization from the transverse plane back to the z-axis.^[14]

The detection of the NMR signal is realized by Faraday induction in a receiver coil. Here, an alternating current is induced in a wire loop by the oscillation of the precessing magnetization after the pulse. The signal decreasing exponentially due to the abovementioned relaxation is then recorded and gives a time-domain spectrum or the so-called free induction decay (FID). Processing the FID by means of Fourier transformation converts the signal into the conventional frequency-domain NMR-spectrum.^[15]

The ^1H and ^{13}C NMR measurements were performed with Bruker Avance III HD spectrometers.

2.5 UV-Vis Spectroscopy

The optical analysis of yet unexplored building blocks and COFs is part of the basic characterization set that is applied to new materials. In UV-Vis spectroscopy, the absorption capabilities of liquids and solids are determined by irradiating the sample with monochromatic light of the ultraviolet (UV, 100 – 400 nm), visible (400 – 760 nm) and near-infrared (NIR, > 780 nm) regions of the electromagnetic spectrum.^[19] In the field of COFs, the comparison of the optical properties between the monomeric building blocks and their combination in conjugated periodic frameworks, between specific COFs themselves, and the optical response to an external stimulus is of special interest.

Since the absorption of photons in organic molecules is based on the excitation of electrons from the ground state \mathbf{S}_0 to excited states \mathbf{S}_n ($n > 0$) in the investigated compound, it is possible to gain insights regarding the optical band structure. The energy of the absorbed photon with its frequency ν must therefore match the energy difference between the specific charge carrier energy levels of the ground and excited states, respectively.^[16] A simplified illustration of the molecular absorption process and the resulting transition of electrons from the ground state \mathbf{S}_0 to the excited states \mathbf{S}_1 or \mathbf{S}_2 can be visualized by the Jablonski diagram (Figure 2.8, blue arrows).

2 Characterization Techniques

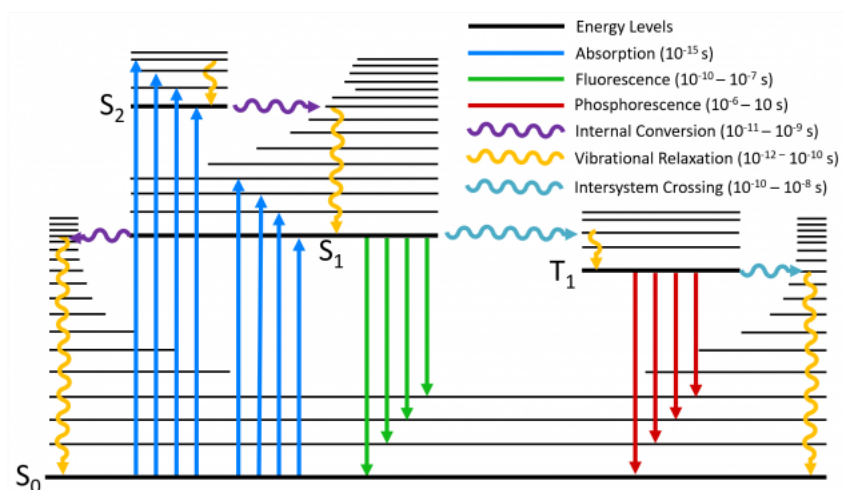


Figure 2.8. Visualization of the different radiation and non-radiation processes after photoexcitation of a molecule via the Jablonski diagram.^[20]

In general, the optical band gap decreases with higher π -conjugation which directly affects the absorption characteristics. The absorption onset of larger conjugated π -systems is consequently red-shifted since less energy is required for the lowest-energy electron transition to the excited state $S_0 \rightarrow S_1$.^[21]

If a monochromatic light beam of an initial intensity $I_0(\lambda)$ passes a homogeneously diluted sample, it will be attenuated by the absorption of the compound. The transmitted beam then possesses an intensity reduced by $I_{\text{abs}}(\lambda)$:

$$I(\lambda) = I_0(\lambda) - I_{\text{abs}}(\lambda)$$

Subsequently, the wavelength-dependent absorbance $A(\lambda)$ can be calculated based on the correlation

$$A(\lambda) = \log \frac{I_0(\lambda)}{I(\lambda)} = \varepsilon(\lambda) \cdot c \cdot d$$

with the molar extinction coefficient $\varepsilon(\lambda)$, the optical path length d and the concentration of the sample c according to the Lambert-Beer law.^[16]

For the optical characterization of insoluble samples, diffuse reflectance measurements with slight measuring setup modifications of the UV-Vis spectrometer have to be conducted. Here, a praying mantis diffuse reflectance accessory was installed, which replaces the classical cuvette holder, and the measured powder material is diluted in a white standard, such as barium

sulfate. The diffuse reflectance R is measured with the white standard as the reference and the spectrum is subsequently converted to a spectrum that estimates the absorption characteristics of the sample using the Kubelka-Munk equation:^[22]

$$Kubelka - Munk = \frac{(1 - R)^2}{2R}$$

The UV-Vis spectra were recorded on a Perkin-Elmer Lambda 1050 spectrometer that is equipped with a 150 mm integrating sphere and photomultiplier and InGaAs detectors. COF thin films were measured in transmission geometry. Diffuse reflectance spectra were collected with a Praying Mantis (Harrick) accessory kit and referenced to barium sulfate as white standard.

2.6 Photoluminescence (PL) Spectroscopy

In addition to UV-Vis spectroscopy, the measurement of photoluminescence is an essential optical characterization of newly synthesized compounds. Here, the relaxation process of previously excited electrons by light absorption is of special interest; it can be accompanied by the spontaneous emission of radiation. In terms of the re-emitted radiation, two types are to be distinguished: the much quicker fluorescence that occurs within a few nanoseconds and the phosphorescence that can last over a longer period of time, in some cases even for several hours.^[23] Since the electronic transition from the excited state back to the ground state only occurs from the energetically lowest vibrational level of a given multiplicity following Kasha's rule, non-radiative relaxation occurs prior to the return to the ground state, which then leads to the emission of photoluminescent light with lower energy than the energy of the absorbed photons (Figure 2.8, green and red arrows). This generally causes a shift of the emission spectrum in respect to the absorption spectrum, known as the Stokes shift.^[24] If the electrons are photoexcited to higher electronic states of the same spin multiplicity, e.g. to the singlet state S_2 , radiationless internal conversion to the lowest excited electronic state S_1 occurs. Non-radiative internal conversion can also take place to the ground state S_0 but is controlled by the energy gap between the ground and excited state. With a smaller energy gap between S_1 and S_0 , the probability of internal conversion and transition to the ground state without emission increases. In contrast, fluorescence involves the rapid return to the ground state of the same spin multiplicity with emission of photons (Figure 2.8, green arrows). Another possible radiative de-excitation from the lowest vibrational level of S_1 results in the delayed

phosphorescence. This phenomenon is preceded by intersystem crossing, a non-radiative transition between two degenerate electronic states of different spin multiplicities (Figure 2.8, light blue arrow). This transition is in fact formally forbidden since a change of the total electron spin is required, which contradicts the preservation of the angular momentum. In the rare cases in which this unpairing of electron spins is enabled, the transition from the lowest vibrational level of S_1 to an iso-energetic vibrational level of the triplet state T_1 is for example possible. Subsequently, the electron relaxes vibrationally to the ground energy level of T_1 . The again spin-forbidden but partly possible transition $T_1 \rightarrow S_0$ can then involve the emission of photons, which is defined as phosphorescence, or can take place via non-radiative intersystem crossing. In the case of phosphorescence, the life-time of the excited triplet state can be much longer than that of the excited singlet state of fluorescence leading to a potentially longer timescale of radiative emission. The molecular surroundings determine if $T_1 \rightarrow S_0$ is radiative or non-radiative: while the intersystem crossing is predominant in a solution at room temperature, phosphorescence is favored in solutions of low temperature and/or in solid media. In comparison to the absorption and fluorescence spectra, the photoluminescence spectrum is furthest red-shifted to lower energies due to the lower energy level of the T_1 vibrational ground state.^[21, 24, 25]

One part of the PL measurements was conducted on a home-built setup consisting of a Horiba Jobin Yvon iHR 320 monochromator equipped with a photomultiplier tube and a liquid N_2 -cooled InGaAs detector. The other samples were measured on a PicoQuant FluoTime 300 with a high-resolution monochromator and a photomultiplier detector assembly. For both, a 378 nm pulsed laser was used for photoexcitation.

2.7 Electron Microscopy

Gaining nanostructural and morphological information about the crystal growth of COFs requires imaging techniques on the nanoscale. The spatial resolution of conventional light microscopy is restricted to approximately 200 nm by the wavelength-dependent Abbe diffraction limit and is therefore insufficient for the visualization of nanostructures. With electrons exhibiting much shorter wavelengths in the range of picometers depending on the acceleration voltage, the enhanced spatial resolution of less than 1 nm enables the visual examination of nanostructures.^[26] The different types of electron microscopy are dependent on the electron-matter interaction and therefore also the electron acceleration voltage and the

electron range, i.e. the penetration depth of the primary electron of a given energy in the specimen.^[27] The incident electron beam that is focused onto the sample surface through electromagnetic lenses produces different signals, such as secondary electrons (SE), backscattered electrons (BSE), X-rays or transmitted electrons which can then be detected and contain diverse information about the specimen (Figure 2.9).

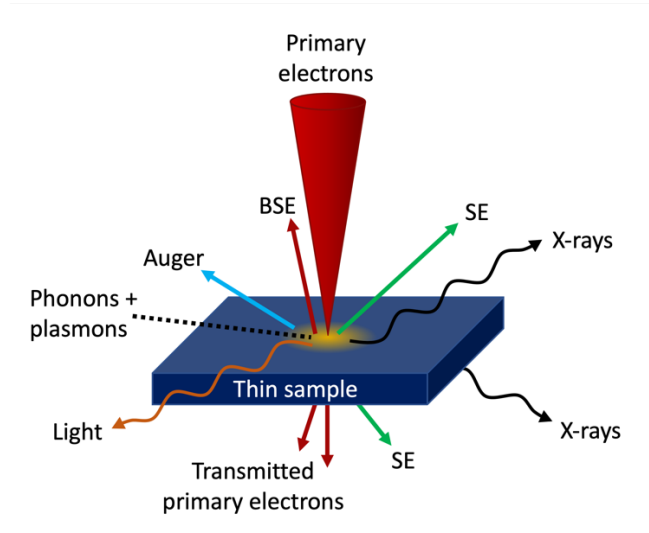


Figure 2.9. Different types of signals produced by electron-matter interactions between the sample and an incident electron beam of specific energy. Adapted with permission.^[27] Copyright (2016) Elsevier

2.7.1 Scanning Electron Microscopy (SEM)

In scanning electron microscopy (SEM), the focused electron beam rasters the sample to analyze the surface topology. The SEM microscope in its basic operation mode mainly detects secondary electrons (SE) from the sample surface with energies below 10 eV. SE are electrons from the specimen that are ejected from the atoms as a result of inelastic collision with incident beam electrons. This inelastic scattering is most probable for outer-shell or valence electrons that are excited above the vacuum energy level and therefore only requires lower acceleration voltages below 30 kV. Backscattered electrons (BSE) are defined as primary electrons that are scattered in an angle above 90° with respect to the incident beam and possess a kinetic energy above 50 eV. Since the number of BSE is proportional to the sample's atomic number, it is possible to see the compositional contrast in the microscopic images. Here, heavier elements with higher Z numbers appear brighter because the number of emitted BSE is higher. Another signal that can be detected by an SEM is X-ray emission. In this operating mode, the characteristic X-rays of different energies are used for elemental analysis and reveal the local chemical composition. If electrons of the inner or core shell are ejected by the collision with

the high-energy primary electrons, the sample atom is ionized. This vacancy is subsequently filled by a second electron from a higher shell which is accompanied by the emission of X-rays of a characteristic energy, i.e. the energy difference between the two shell energy levels (see Chapter 2.1). The detected X-rays of different energies are then processed for energy-dispersive X-ray spectroscopy (EDX).^[28, 29]

A typical SEM architecture comprises an electron source which can be a thermionic emitter (consisting of W or LaB₆) or a field emission gun (FEG, typically made of W). The electron beam is accelerated by the anode and focused onto the sample by an electromagnetic lens array. The various detectors then collect the specific emitted signals in the respective measuring mode (Figure 2.10).^[27]

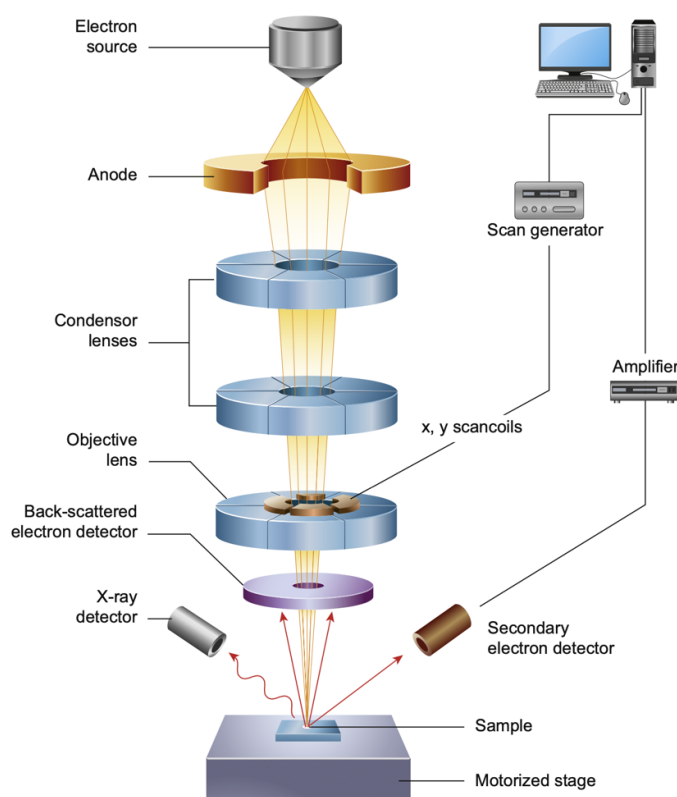


Figure 2.10. Schematic illustration of a generic SEM architecture. Reprinted with permission.^[27] Copyright (2016) Elsevier.

The SEM images were obtained with an FEI Helios NanoLab G3 UC microscope equipped with a Schottky field emitter operated at 1 – 30 kV.

2.7.2 Transmission Electron Microscopy (TEM)

In contrast to SEM, which is mainly based on the detection of SE and BSE, Transmission Electron Microscopy (TEM) focuses on the transmitted primary electrons. Therefore, the

sample preparation, i.e. the thickness of the specimen, and a sufficient energy of the electron beam are critical. The primary electrons with energies of up to 400 keV are scattered by the specimen and are then processed depending on the TEM operating mode. As for conventional transmission electron microscopy (CTEM), there are different imaging modes: dark-field (DF), bright-field (BF), and high-resolution TEM (HRTEM). The thermionic or field emission electron source similar to those in SEM (see Chapter 2.7.1) is adjusted by condenser lenses to form a parallel beam illuminating a wider field of the specimen (Figure 2.11).^[29]

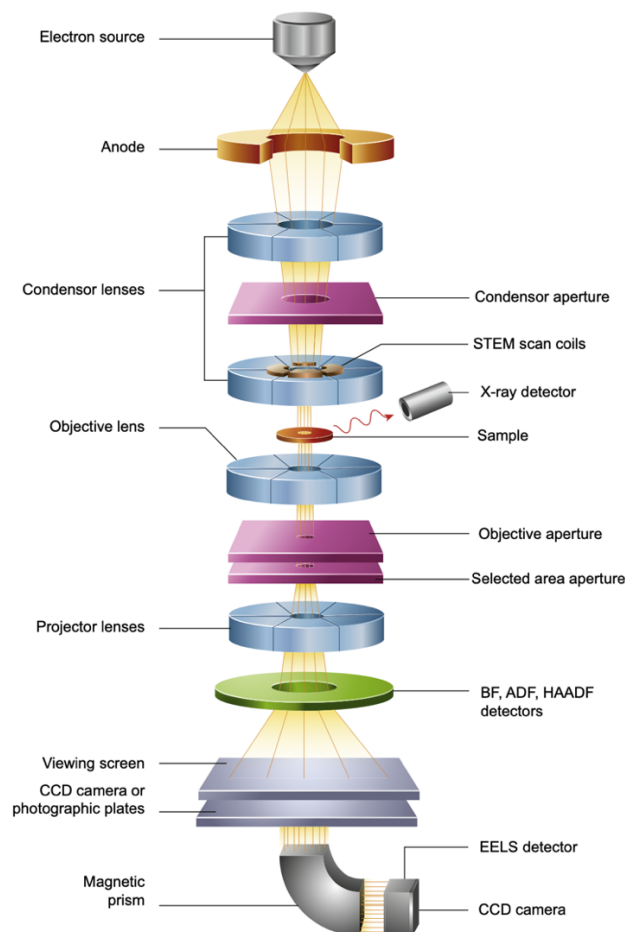


Figure 2.11. Simplified schematic illustration of a TEM instrument. Reprinted with permission.^[27] Copyright (2016) Elsevier.

The objective lens behind the sample focuses the transmitted beam and creates a diffraction pattern in the back-focal plane by dispersion. The objective aperture in the back-focal plane determines the imaging mode. If the position of the aperture allows solely the direct beam with unscattered electrons to pass, a BF image will be projected onto the viewing screen. As a result, the sample domains that significantly scatter the primary electrons, e.g. containing heavier atoms or increased thickness, appear dark in the BF image. In contrast, if the direct electron

2 Characterization Techniques

beam is blocked and only diffracted electrons are selected by the objective aperture, they appear as brighter spots in DF imaging mode. HRTEM images require a wider objective aperture that allows the collection not only of transmitted primary electrons but also of diffracted beams to generate interference. That way, HRTEM images enable resolution on an atomic level, but the complex image processing also requires the consideration of a variety of parameters, such as sample thickness and crystallinity. Apart from the imaging modes, the TEM can also be operated in diffraction mode that projects the diffraction pattern on the viewing screen. Instead of the objective aperture, a selected-area diffraction (SAD) aperture is inserted into the image plane of the objective lens to view the diffraction pattern of a selected area of the sample.^[29, 30]

A convergent electron beam is necessary in the scanning transmission electron microscopy (STEM) mode; it can be created by additional lenses above the specimen. The focused electron beam rasters across the specimen and the specific transmitted electrons are detected, hence combining the main features of both techniques, SEM and TEM. The scattered electrons are then collected by different detectors depending on their scattering angles. Like TEM, the STEM-BF images visualize the direct beam electrons, whereas the STEM-DF images contain the scattered electrons at higher angles which are usually recorded by an annular dark field (ADF) detector. Strongly scattered electrons which exit the sample at very high scattering angles are detected by the high angle annular dark field (HAADF) detector. The number of electrons collected at high scattering angles is dependent on the atomic number Z and the sample thickness. Therefore, the so-called Z -contrast images obtained by this technique contain information about the elemental composition with higher-mass regions appearing brighter due to their higher angle of elastic scattering.^[26, 29, 30]

Well-equipped TEM microscopes are also capable of analytical measurement modes that are based on inelastic scattering processes and therefore the generation of characteristic X-rays and energy-loss of primary electrons. With suitable spectrometers, it is then possible to perform energy-dispersive X-ray spectroscopy (EDX) and electron energy-loss spectroscopy (EELS) to chemically analyze the sample material.^[31]

TEM images were recorded with an FEI Titan Themis microscope equipped with a FEG operated at 300 kV.

2.8 Infrared Spectroscopy (IR)

The absorption of electromagnetic radiation of the infrared spectral region is utilized in infrared (IR) spectroscopy. The absorbed radiation of a specific frequency leads to excitations of the molecules' vibrational and rotational energy levels, if the excitation energy matches the energy differences of the respective quantum numbers. As a consequence, the molecules start moving in different vibrational and rotational modes. The wavenumber region that is generally scanned in IR spectroscopy covers 4000 cm^{-1} to 400 cm^{-1} .^[16] The advantage of using wavenumbers instead of wavelengths (like in UV-Vis spectroscopy) lies in the direct proportionality of wavenumbers to the frequency and therefore the energy.

A prerequisite for the absorption of IR radiation is a change of the dipole-moment during the vibration, which is then IR-active. This means that the vibrations of a symmetric molecule without a dipole-moment in the ground state (e.g. CO_2) are only visible in IR spectroscopy if their vibrations are antisymmetric to their center of symmetry and the dipole-moment therefore is induced. Otherwise, the vibrations are IR-inactive and there is no interaction between the IR light and the specimen molecules and hence no absorption in the IR-spectrum. Since many functional groups of organic molecules show distinct absorption bands in defined wavenumber ranges of the IR spectrum due to their characteristic vibrations, this spectroscopy method is widely used for the structural classification of the investigated sample.^[32] In imine-linked COFs, for example, the successful reaction of their building blocks is indicated by the appearance of $\text{C}=\text{N}$ vibrations, which are characteristic for imine-bonds, accompanied by the attenuation of aldehyde and amine vibrations of the starting materials.

In a first simplified approximation, a diatomic molecule is described by the model of a classical harmonic oscillator with two different masses m_1 and m_2 which are connected via an elastic spring. The vibration frequency ν_{osc} of the harmonic oscillator is calculated as

$$\nu_{\text{osc}} = \frac{1}{2\pi} \sqrt{\frac{k}{\mu}}$$

with the force constant k describing the bond strength between the atoms and the reduced mass μ .^[16] The above-mentioned equation indicates that the frequency increases with higher bond strengths and lower atomic masses, allowing a first classification of the absorption band positions in an IR spectrum. This simple model does not take into account dissociation or repulsion of atoms if their distances reach a threshold value. Therefore, the model of an

anharmonic oscillator with asymmetric potential curves is the more realistic description since it also considers the dissociation energy that leads to bond breaking (Figure 2.12).^[32]

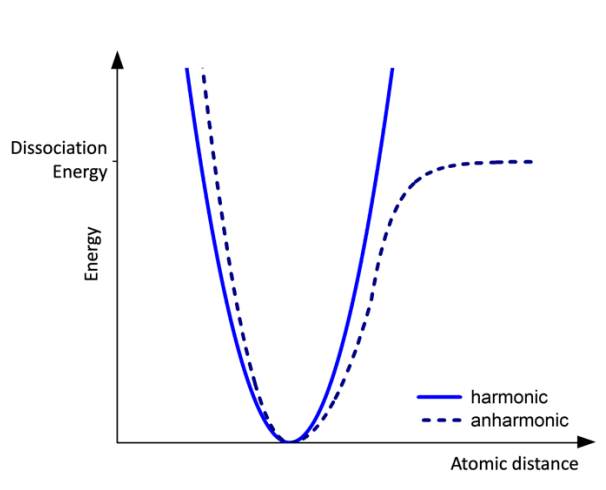


Figure 2.12. Potential curves of a harmonic oscillator and an anharmonic oscillator. The curve of the anharmonic oscillator reaches a maximum energy value with increasing atomic distances if a limit value is reached (dissociation energy).^[32]

The model of an anharmonic oscillator also involves a different selection rule allowing overtones that lead to transitions between non-adjacent vibrational states.^[32]

IR spectra were measured on a Thermo Scientific Nicolet iN10 FT-IR spectrometer equipped with a MicroTip attenuated total reflection (ATR) unit and an MCT-detector.

2.9 Cyclic Voltammetry (CV)

Cyclic voltammetry (CV) is a useful measurement technique to learn about the electrochemical processes in a material. The cyclic voltammogram provides information on the reversibility and electrode kinetics of the materials' redox reactions during the electrochemical experiment. The setup to perform the CV measurements usually comprises three electrodes immersed into an electrolyte solution. The working electrode oxidizes and reduces the analyte by an applied voltage, the reference electrode with a stable equilibrium potential functions as the reference point and is used to measure the applied potential, and the counter electrode, which balances the reactions at the working electrode, completes the electrical circuit and allows current to flow. The potential is cycled by a potentiostat between two set points with a fixed scan speed resulting in a triangular potential waveform (Figure 2.13, a). During the potential sweep, the

current flow is recorded with respect to the applied voltage, generating the cyclic voltammogram (Figure 2.13, b).^[33, 34]

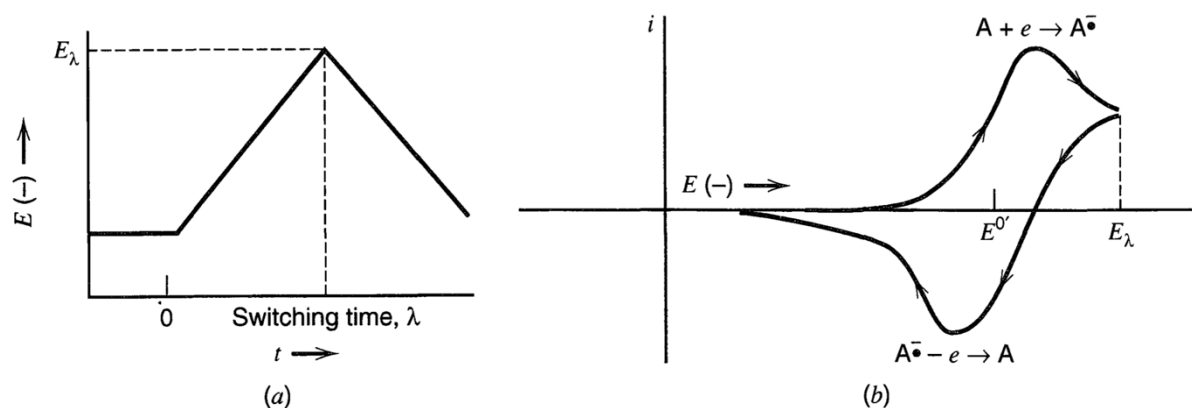


Figure 2.13. (a) Triangular potential waveform of the applied potential as a function of time. (b) Cyclic voltammogram of an analyte A with the applied potential E and the measured current i . Reprinted with permission.^[33] Copyright (2000) John Wiley and Sons.

With increasing negative potentials E , the material of interest is reduced at the working electrode which is indicated by a distinct reduction peak. Upon beginning depletion of the analyte A illustrated by the descending curve after peak, the scanning direction is reversed at the applied voltage E_λ . This leads to an oxidation of the radical anion $A^{\bullet-}$ back to the neutral state A with a sharp oxidation step due to the anodic current flow. The shift of these cathodic and anodic peak positions, the so-called peak-to-peak-separation, is a direct indication for the reversibility of the redox reaction.^[33]

There are two common conventions applied for plotting the CV curves: following the US convention, the higher applied potentials are assigned to the left side of the x-axis and the cathodic current is upward along the ordinate axis. In contrast, the IUPAC convention plots the potential increase from left to right on the abscissa and the anodic currents are declared positive with the oxidation peak above the x-axis (Figure 2.14).^[35, 36]

2 Characterization Techniques

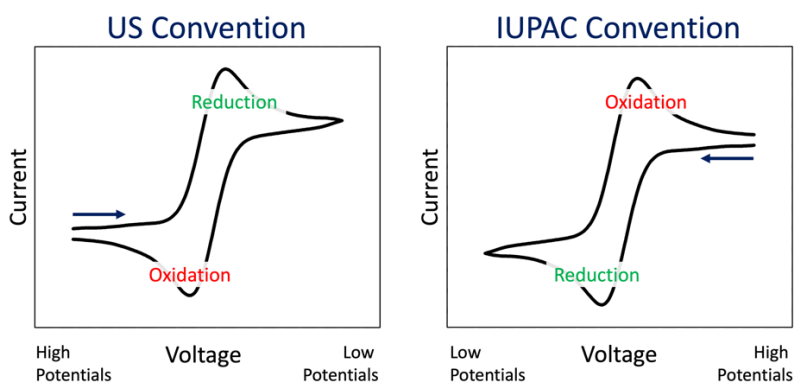


Figure 2.14. Plotting a cyclic voltammogram according to the US convention (left) and the IUPAC convention (right).^[34]

The CV curves in this work are uniformly plotted according to the IUPAC convention.

The respective COF which was electrochemically characterized was previously grown as a thin film on the conductive coating of a glass substrate. This architecture was then applied as the working electrode in the three-electrode setup with an inert platinum wire used as the counter electrode. A Ag/AgCl electrode and a silver wire were used as the reference electrode and the quasi-reference electrode, respectively. The electrolyte solution of the electrochemical cell consisted of 0.1 M tetrabutylammonium hexafluorophosphate (TBAPF₆) in acetonitrile. The electrochemical measurements were performed on a Metrohm Autolab PGSTAT potentiostat/galvanostat.

2.10 References

- [1] B. D. Cullity, *Elements of X-ray Diffraction*, 2 ed., Addison-Wesley Publishing Company, Reading, Massachusetts, **1978**.
- [2] Y. Waseda, E. Matsubara, K. Shinoda, *X-Ray Diffraction Crystallography*, Springer-Verlag, Berlin Heidelberg, **2011**.
- [3] N. Stribeck, *X-Ray Scattering of Soft Matter*, Springer-Verlag, Berlin Heidelberg, **2007**.
- [4] V. Saxena, G. Portale, *Nanomaterials* **2020**, *10*, 2240.
- [5] M. Birkholz, *Thin Film Analysis by X-Ray Scattering*, Wiley-VCH, Weinheim, **2006**.
- [6] M. Thommes, *Chem. Ing. Tech.* **2010**, *82*, 1059-1073.
- [7] M. Thommes, K. Kaneko, A. V. Neimark, J. P. Olivier, F. Rodriguez-Reinoso, J. Rouquerol, K. S. W. Sing, *Pure Appl. Chem.* **2015**, *87*, 1051-1069.
- [8] K. S. W. Sing, *Pure Appl. Chem.* **1985**, *57*, 603-619.
- [9] C. Schlumberger, M. Thommes, *Adv. Mater. Interfaces* **2021**, *8*, 2002181.
- [10] M. Thommes, K. A. Cychosz, *Adsorption* **2014**, *20*, 233-250.
- [11] K. A. Cychosz, M. Thommes, *Engineering* **2018**, *4*, 559-566.
- [12] S. Brunauer, P. H. Emmett, E. Teller, *J. Am. Chem. Soc.* **1938**, *60*, 309-319.
- [13] J. Zou, C. Fan, X. Liu, *Langmuir* **2020**, *36*, 14656-14665.
- [14] R. S. Macomber, *A Complete Introduction to Modern NMR Spectroscopy*, John Wiley & Sons, Inc., New York, NY, **1998**.
- [15] M. H. Levitt, *Spin Dynamics - Basics of Nuclear Magnetic Resonance*, 2 ed., John Wiley & Sons Ltd, Chichester, **2008**.
- [16] M. Hesse, H. Meier, B. Zeeh, *Spektroskopische Methoden in der organischen Chemie*, 7 ed., Georg Thieme Verlag, Stuttgart, **2005**.
- [17] L. Peng, R. J. Clément, M. Lin, Y. Yang, in *NMR and MRI of Electrochemical Energy Storage Materials and Devices*, The Royal Society of Chemistry, **2021**, pp. 1-70.
- [18] A. Tampieri, M. Szabó, F. Medina, H. Gulyás, *Phys. Sci. Rev.* **2021**, *6*, 20190086.
- [19] S. E. Braslavsky, *Pure Appl. Chem.* **2007**, *79*, 293-465.
- [20] Edinburgh Instruments. <https://www.edinst.com/wp-content/uploads/2019/02/Jablonski-Diagram-1-e1551188553773.png> (accessed: 14.09.2022).
- [21] P. J. Walla, *Modern Biophysical Chemistry: Detection and Analysis of Biomolecules*, 2 ed., Wiley-VCH, Weinheim, **2014**.

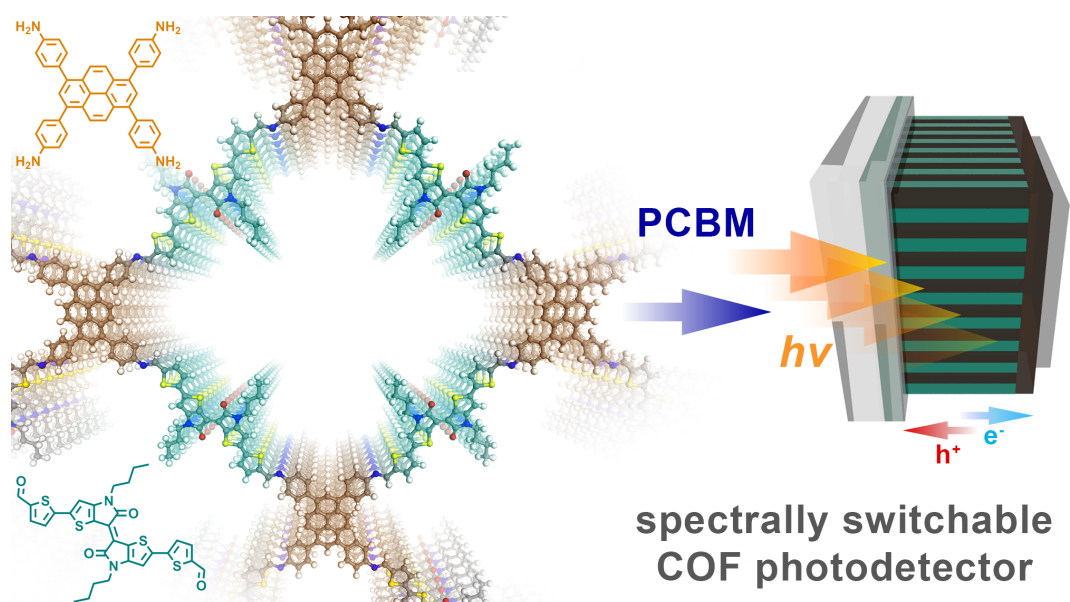
- [22] H. G. Hecht, *J. Res. Natl. Bur. Stand. Sect. A Phys. Chem.* **1976**, *80A*, 567-583.
- [23] P. Atkins, J. d. Paula, *Atkins' Physical Chemistry*, 8 ed., Oxford University Press, Oxford, **2006**.
- [24] B. Valeur, *Molecular Fluorescence: Principles and Applications*, 1 ed., Wiley-VCH, Weinheim, **2002**.
- [25] M. Sauer, J. Hofkens, J. Enderlein, *Handbook of Fluorescence Spectroscopy and Imaging*, 1 ed., Wiley-VCH, Weinheim, **2011**.
- [26] G. V. Tendeloo, D. V. Dyck, S. J. Pennycook, *Handbook of Nanoscopy*, 1 ed., Wiley-VCH, Weinheim, **2012**.
- [27] B. J. Inkson, in *Materials Characterization Using Nondestructive Evaluation (NDE) Methods*, Woodhead Publishing, **2016**, pp. 17-43.
- [28] C. Scheu, W. D. Kaplan, in *In-Situ Electron Microscopy*, **2012**, pp. 1-37.
- [29] D. B. Williams, C. B. Carter, *Transmission Electron Microscopy: A Textbook for Materials Science*, 2 ed., Springer, New York, **2009**.
- [30] B. Fultz, J. Howe, *Transmission Electron Microscopy and Diffractometry of Materials*, 4 ed., Springer, Berlin, Heidelberg, **2013**.
- [31] L. Reimer, H. Kohl, *Transmission Electron Microscopy: Physics of Image Formation*, 5 ed., Springer, New York, **2008**.
- [32] H. Günzler, H.-U. Gremlich, *IR-Spektroskopie: Eine Einführung*, 4 ed., Wiley-VCH, Weinheim, **2003**.
- [33] A. J. Bard, L. R. Faulkner, *Electrochemical Methods: Fundamentals and Applications*, 2 ed., John Wiley & Sons, Inc., New York, **2001**.
- [34] N. Elgrishi, K. J. Rountree, B. D. McCarthy, E. S. Rountree, T. T. Eisenhart, J. L. Dempsey, *J. Chem. Educ.* **2018**, *95*, 197-206.
- [35] R. G. Bates *et al.*, *Pure Appl. Chem.* **1976**, *45*, 131-134.
- [36] R. G. Compton, C. E. Banks, *Understanding Voltammetry*, 3 ed., World Scientific, New Jersey, **2018**.

3 Spectrally Switchable Photodetection with Near-Infrared-Absorbing Covalent Organic Frameworks

This chapter is based on the following publication:

Derya Bessinger, Laura Ascherl, Florian Auras*, and Thomas Bein*

J. Am. Chem. Soc. **2017**, *139*, 12035–12042



Copyright 2017, American Chemical Society

* corresponding authors

3.1 Abstract

Most covalent organic frameworks (COFs) to date are made from relatively small aromatic sub-units, which can only absorb the high-energy part of the visible spectrum. We have developed near-infrared-absorbing low bandgap COFs by incorporating donor-acceptor-type isoindigo- and thienoisindigo-based building blocks. The new materials are intensely colored solids with a high degree of long-range order and a pseudo-quadratic pore geometry. Growing the COF as a vertically oriented thin film allows for the construction of an ordered interdigitated heterojunction through infiltration with a complementary semiconductor. Applying a thienoisindigo-COF:fullerene heterojunction as the photoactive component, we realized the first COF-based UV- to NIR-responsive photodetector. We found that the spectral response of the device is reversibly switchable between blue- and red-sensitive, and green- and NIR-responsive. To the best of our knowledge, this is the first time that such nearly complete inversion of spectral sensitivity of a photodetector has been achieved. This effect could lead to potential applications in information technology or spectral imaging.

3.2 Introduction

Constructing covalent organic frameworks (COFs) from rigid organic building blocks has opened a synthetic route to a broad range of tailor-made porous materials,^[1-3] whereby key properties such as the pore structure, optical properties and electronic coupling between the individual sub-units can be tuned via the selection of suitable building blocks.^[4-6] The materials realized this way offer a unique combination of high thermal and mechanical stability,^[7] very high surface areas,^[8, 9] and high density and accessibility of the functional organic building blocks,^[10] thus rendering them suitable for potential applications in gas storage and separation,^[11] catalysis and photocatalysis,^[12, 13] and optoelectronics.^[14-16]

The geometry of stacked two-dimensional (2D) COFs can be designed to tune the π -overlap between the individual layers,^[17, 18] thus creating conductive columns and/or facilitating long-range exciton transport.^[19-21] Initial studies have shown that COFs can act as the active component in interdigitated heterojunction photovoltaic devices.^[22-24] Due to the limited absorption capabilities of the building blocks used in these studies, however, the devices could only harvest light in the blue and green spectral regions with appreciable quantum efficiency. Extension of the absorption capabilities into the red and near infrared (NIR) spectral regions that encompass most of the solar photons would therefore be highly desirable.

Since the maximum length of COF building blocks to date is limited to only 1-2 nm due to the increasing flexibility of more extended molecules, shifting the building block absorption into the NIR cannot be achieved by simply extending the length of the π -conjugated backbone. However, combining electron-rich and -deficient moieties within the same building block can lead to additional charge-transfer transitions at energies well below the fundamental π - π^* transition.^[25]

One of the most effective components in this context is the highly electron-deficient isoindigo (II), an isomer of the naturally occurring indigo dye. Pairing isoindigo with an appropriate electron-rich counterpart leads to a strong intramolecular donor-acceptor charge delocalization in conjugated polymeric semiconductors, hence shifting the absorption onset well into the NIR regime.^[26] Bulk heterojunction solar cells with isoindigo-based low-band gap co-polymers recently exceeded a power conversion efficiency of 9% with very high short-circuit currents of above 17 mA cm⁻².^[27] The planarity and the highly polar nature of the isoindigo unit facilitate aggregation and give rise to exceptionally crystalline polymers, leading to high charge carrier mobilities and thus rendering isoindigo-containing polymers interesting candidates for organic field-effect transistor applications.^[28, 29] Given these excellent electronic and optoelectronic properties, it would be highly desirable to be able to incorporate and study isoindigo-based building blocks in the precisely defined environment of a COF.^[30]

In this work, we have developed a series of isoindigo- and thienoisindigo-based building blocks and have applied them in the synthesis of highly crystalline imine-linked 2D COFs. The resulting materials are porous and intensely colored solids that absorb light throughout the visible and NIR spectral region. Growing vertically oriented thin films of these materials allows for the subsequent infiltration of the pores with a complementary semiconductor. The resulting ordered interdigitated heterojunction was employed as the active layer in the first COF-based NIR-sensitive and voltage-switchable photodetector.

3.3 Results and Discussion

To create an isoindigo-bridged COF, we designed a new 6,6'-bis(4-formylphenyl)-*N,N'*-dibutyl-isoindigo (**pII**) building block. The terminal aldehyde hereby provides the chemical functionality for reversible imine formation, while the butyl chains ensure sufficient solubility during COF synthesis (Figure 3.1a).

3 Spectrally Switchable Photodetection with Near-Infrared-Absorbing Covalent Organic Frameworks

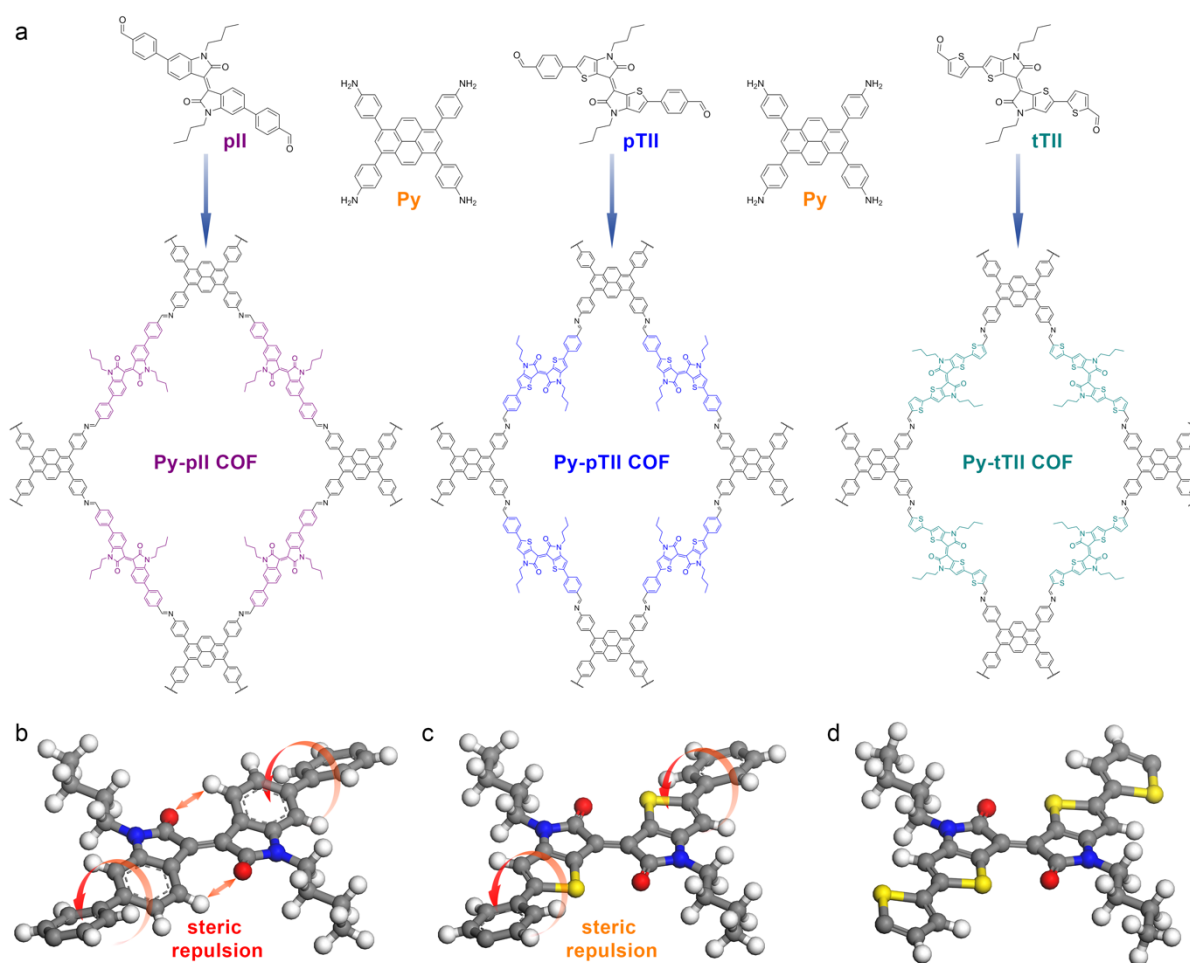


Figure 3.1. (a) Co-condensation of 1,3,6,8-tetrakis(4-aminophenyl)pyrene (Py) with 2 equivalents of the (thieno-)isoindigo-bridged dialdehydes **pII**, **pTII**, and **tTII** leads to the formation of the respective imine-linked 2D COFs. (b) The cut-out of the simulated **Py-pII** COF structure reveals that the **pII** building block is not entirely flat. Steric repulsion causes a rotation of the terminal phenyls vs. the isoindigo core. Additionally, the repulsion between the ketones and adjacent hydrogen atoms leads to a slight distortion of the core itself. (c) These steric constraints are considerably relaxed when the benzene rings are replaced by thiophenes, resulting in a planar thioisoindigo core. While the terminal phenyl rings remain slightly rotated vs. the core in the case of **pTII**, exchanging them for thiophenes (d) yields the virtually planar **tTII** building block.

In solution, the optical absorption spectrum of the **pII** building block exhibits two main absorption bands that are typical for donor-acceptor molecules (Supporting Information, Figure 3.9a). The band at 370 – 470 nm has been attributed to the isoindigo π - π^* transitions, whereas the lower-energy band between 470 and 620 nm is due to an intramolecular charge transfer (ICT) between the electron-deficient isoindigo moiety and the more electron-rich phenylenes.^[31] The optical band gap, estimated from the corresponding Tauc plot for a direct allowed transition, is 2.06 eV (SI, Figure 3.9b).

Given the geometry of the building block (Figure 3.1b) and the strong tendency of isoindigo-based molecules to form closely-packed, slightly offset cofacial aggregates,^[32] the construction of a geometrically compatible framework is crucial for obtaining a highly crystalline COF. Force-field- and density functional theory (DFT) based simulations indicate that a synchronized

slip-stacked arrangement in a pseudo-quadratic network, as induced by 1,3,6,8-tetrakis(4-aminophenyl)pyrene (**Py**), could match the geometric requirements of the **pII** unit very well.^[17] Among the known multidentate amine building blocks, **Py** has proven to produce some of the closest-packed COFs with significant π -overlap within the self-assembled columns of both subunits and excellent crystallinity.^[16, 33, 34]

The imine-linked **Py-pII** COF was obtained via acid-catalyzed solvothermal synthesis as a dark purple powder (see the SI for experimental details).

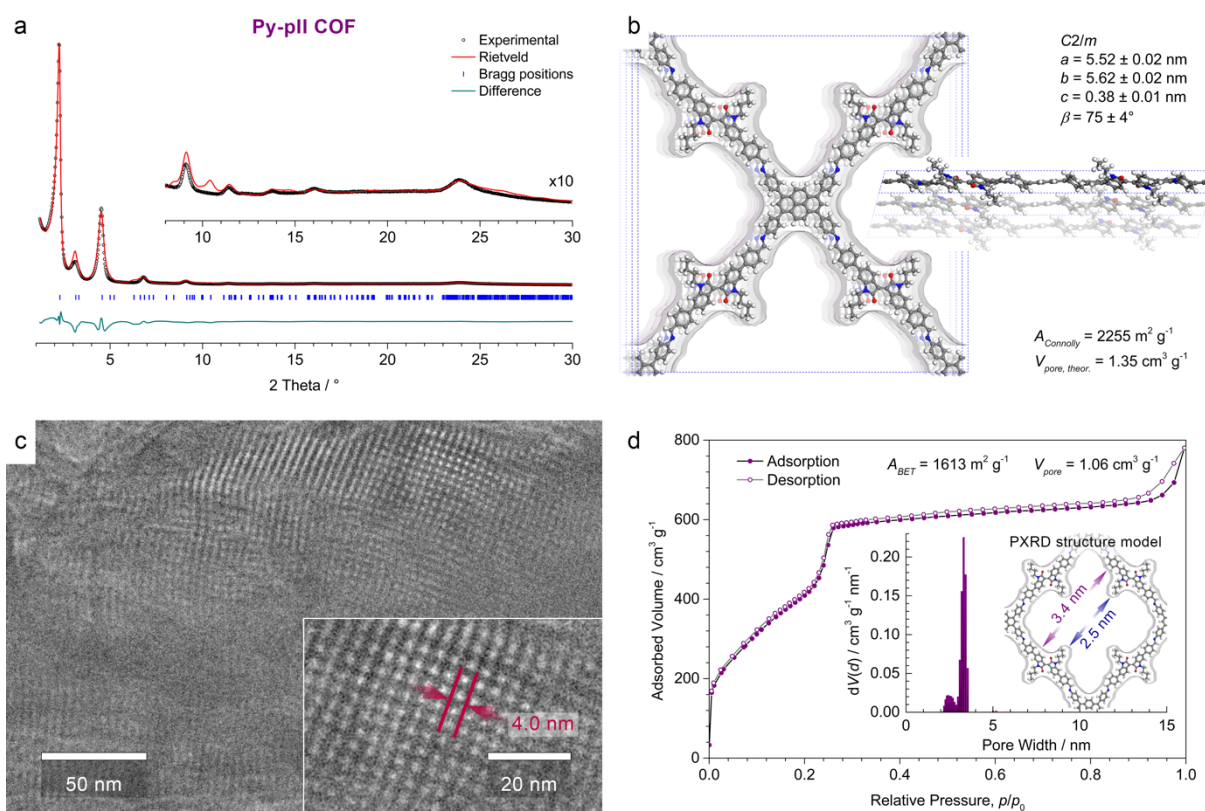


Figure 3.2. (a) Experimental PXRD pattern (black dots) of the **Py-pII** COF. Rietveld refinement (red line) using the $C2/m$ symmetric DFT-optimized structure model shown in (b) provides a very good fit to the experimental data with only minimal differences (the green line shows the difference plot between the experimental and the Rietveld-refined PXRD patterns; $R_{wp} = 7.86\%$, $R_p = 13.9\%$). Bragg positions are indicated by blue ticks. Inset, magnified view of the $2\theta > 8^\circ$ region. (b) The **Py-pII** COF unit cell with the viewing direction normal to the a - b plane (left) and along b (right), and the Connolly surface calculated for a nitrogen-sized probe molecule. Crystallographic data are available as Supporting Information. (c) High-resolution TEM image of a polycrystalline **Py-pII** COF sample showing the pseudo-quadratic arrangement of the mesopores (top right), and the parallel alignment of the pore channels (top and bottom left). Inset, magnified view onto a COF domain showing the pseudo-quadratic geometry with a periodicity of 4.0 ± 0.2 nm. (d) Nitrogen sorption isotherm recorded at 77 K. Insets, QSDFT calculation using an equilibrium model yields a very narrow pore size distribution centered at 3.3 nm with an additional porosity at around 2.5 nm due to the **pII** alkyl chains. These values agree very well with the wall-to-wall distance and the reduced pore diameter due to the alkyl chains derived from the Rietveld-refined structure model (purple and blue arrows).

Successful formation of a crystalline framework was confirmed by powder X-ray diffraction (PXRD; Figure 3.2a). The diffraction pattern exhibits a number of well-defined reflections and only weak background, highlighting the high degree of long-range order in this material. Rietveld refinement in the monoclinic space group $C2/m$ using a DFT optimized structure model reproduced the experimental pattern very well and yielded the lattice parameters $a = 5.52 \pm 0.02$ nm, $b = 5.62 \pm 0.02$ nm, $c = 0.38 \pm 0.01$ nm, and $\beta = 75 \pm 4^\circ$ (Figure 3.2b). Owing to the large number of light atoms in the unit cell and the peak broadening due to the inherent flexibility of the COF network it is not possible to refine the coordinates of individual atoms. We therefore observe some deviations in the intensities of higher-index reflections that are primarily attributed to slight differences between the DFT-optimized structure model and the actual COF structure.

High-resolution transmission electron microscopy (TEM) further confirms the formation of a periodic, porous framework (Figure 3.2c). Domains that are oriented along the crystallographic c axis show the pseudo-quadratic arrangement with a periodicity of 4.0 ± 0.2 nm, in excellent agreement with the in-plane pyrene-to-pyrene distance of 3.93 nm in the Rietveld-refined COF structure.

The nitrogen sorption isotherm of the **Py-pII** COF exhibits a type IV isotherm shape with a sharp step around $p/p_0 = 0.24$ (Figure 3.2d). Pore size analysis by quenched solid density functional theory (QSDFT) using an equilibrium model for cylindrical pores reveals a distribution ranging from 2.1 to 3.4 nm with a main pore diameter of 3.3 nm and a second maximum at 2.5 nm. Unlike most COFs reported to date, the **Py-pII** COF features butyl chains that extend into the pore, giving rise to a shamrock-shaped cross-section and resulting in more than one pore size. We notice that the maximum of the pore size distribution is in excellent agreement with the simulated wall-to-wall distance of 3.4 nm, while the porosity at smaller pore diameter coincides with the reduced pore width of 2.5 nm due to the alkyl chains.^[35] The Brunauer-Emmett-Teller (BET) surface area is $1613 \text{ m}^2 \text{ g}^{-1}$ with a total pore volume of $1.06 \text{ cm}^3 \text{ g}^{-1}$, in reasonable agreement with the Connolly surface of $2255 \text{ m}^2 \text{ g}^{-1}$ and a theoretical pore volume of $1.35 \text{ cm}^3 \text{ g}^{-1}$, confirming that the pores are open and accessible. Due to the alkyl chains that split the pore into smaller compartments with highly concave surfaces, the Connolly surface tends to be systematically higher than the surface that can be occupied by nitrogen molecules during the sorption experiment.^[36]

Recent studies on N,N' -dimethyl-isoindigo showed that due to the steric repulsion between the protons of the benzene ring and the oxygen atoms of the ketopyrrole, the molecule crystallizes

in a slightly twisted configuration with a rotation of the two oxindole rings along the central double bond.^[32] In a COF, such deviation from a truly planar conformation might not only reduce the effective π -conjugation in the molecule, but could also affect the crystallinity and stability of the framework.

Attempting to overcome these potential structural drawbacks, thieno-modified versions of the isoindigo core have been developed.^[37] In thienoisindigo (TII), the unfavorable repulsion between the ketones and the adjacent hydrogen atoms is replaced by a favorable electrostatic attraction between the sufficiently spaced ketones and sulfur atoms, thus rendering the molecule entirely planar.^[38] In order to test the influence of this added planarity on the structure and electronic properties of our COFs, we constructed two TII-based building blocks (Figure 3.1a). According to our structure simulations, the 5,5'-bis(4-formylphenyl)-*N,N'*-dibutyl-thienoisindigo (**pTII**) features a planar core that is flanked by slightly tilted phenyl rings (Figure 3.1c). Replacing the latter by thiophenes results in an entirely planar conformation of the 5,5'-bis(2-formylthiophen-5-yl)-*N,N'*-dibutyl-thienoisindigo (**tTII**) building block (Figure 3.1d).

The UV-VIS spectra of **pTII** and **tTII** feature strong absorption bands in the blue and the red-to-NIR regions (SI, Figure 3.9a). While the π - π^* transitions appear slightly blue-shifted compared to the **pII**, the ICT bands of the TII building blocks are much stronger and considerably red-shifted to 480 – 730 nm and 500 – 750 nm for **pTII** and **tTII**, respectively. The corresponding optical band gaps, estimated from Tauc plots for direct allowed transitions, are 1.75 eV and 1.68 eV, respectively (SI, Figures 3.9c, d).

3 Spectrally Switchable Photodetection with Near-Infrared-Absorbing Covalent Organic Frameworks

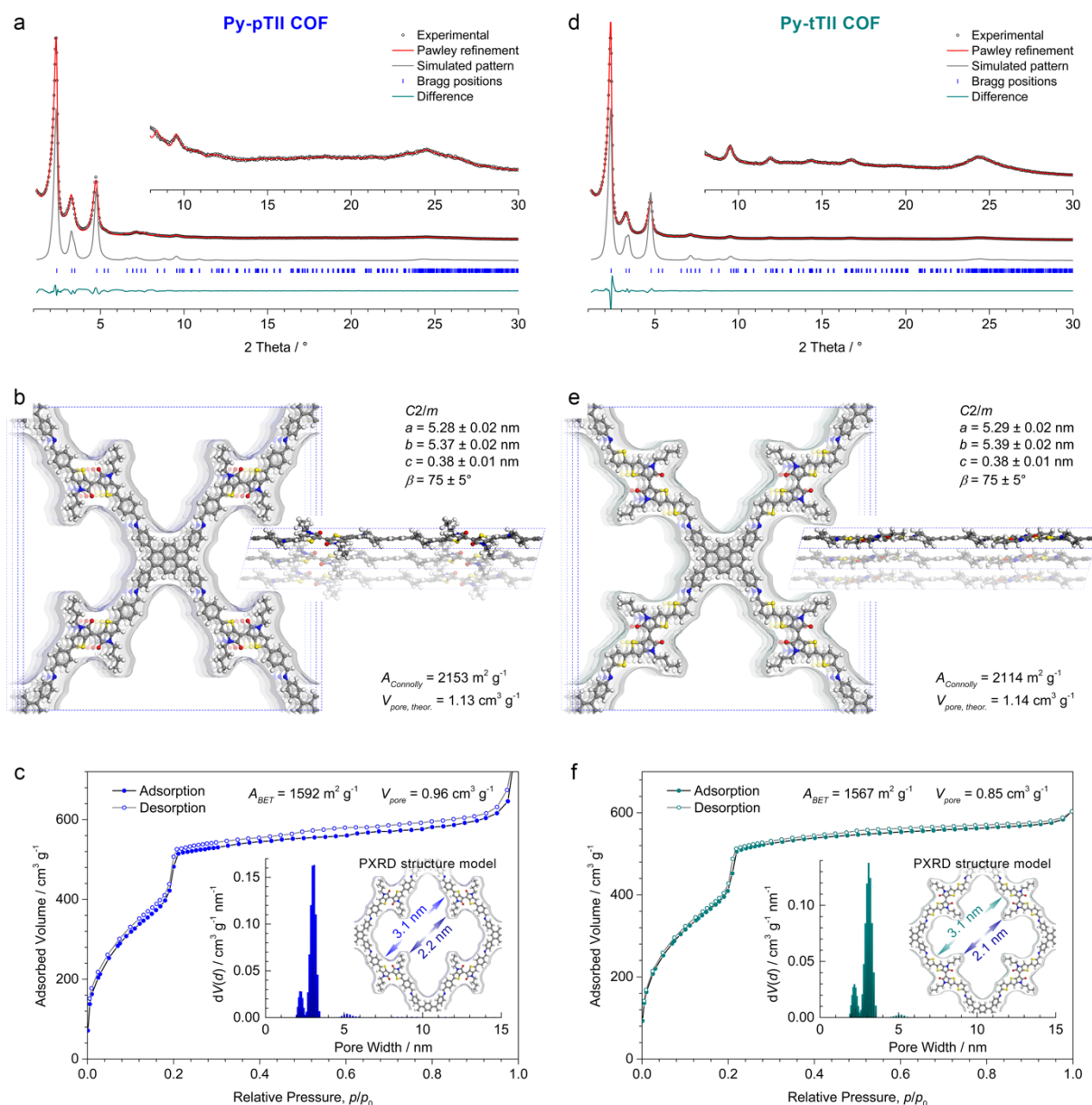


Figure 3.3. (a, d) Experimental PXRD patterns (black dots) of the thienoisindigo-bridged **Py-pTII** and **Py-tTII** COFs, respectively. For both COFs, Pawley refinements (red lines) in the space group $C2/m$ provide an excellent fit to the experimental data. Insets, magnified view of the $2\theta > 8^\circ$ region. The simulated PXRD patterns (grey lines) based on the structure models shown in (b) and (e), respectively, agree very well with the experimental and refined patterns of the frameworks. Differences in the peak intensities might stem from slight differences between the simulations and the actual COF structures. (b, e) The **Py-pTII** and **Py-tTII** COF unit cells with the viewing direction normal to the a - b plane (left) and along b (right), and the Connolly surfaces calculated for a nitrogen-sized probe molecule. (c, f) Nitrogen sorption isotherms recorded at 77 K. Insets, QSDFT calculations using an equilibrium model yield very narrow pore size distributions with maxima at 3.0 nm and 3.1 nm, respectively, and an additional porosity at around 2.2 nm due to the alkyl chains of the thienoisindigo moieties. These values agree very well with the wall-to-wall distances and the reduced pore diameters due to the alkyl chains derived from the refined structure models (blue and green arrows).

Acid-catalyzed co-condensation of **Py** with two equivalents of the TII building blocks yielded the **Py-pTII** and **Py-tTII** COFs as dark blue- and green-colored powders, respectively. Pawley refinement of the **Py-pTII** and **Py-tTII** COF PXRD patterns (Figures 3.3a, d), using the force-field-optimized structure models displayed in Figures 3.3b and 3.3e, respectively, matched the

experimental patterns very well. The refined unit cell parameters are $a = 5.28 \pm 0.02$ nm, $b = 5.37 \pm 0.02$ nm, $c = 0.38 \pm 0.01$ nm, and $\beta = 75 \pm 5^\circ$ for the **Py-pTII** COF, and $a = 5.29 \pm 0.02$ nm, $b = 5.39 \pm 0.02$ nm, $c = 0.38 \pm 0.01$ nm, and $\beta = 75 \pm 5^\circ$ for the **Py-tTII** COF. In both COFs, the shorter length and slightly different geometry of the TII building blocks give rise to a more contracted framework compared to the **Py-pII** COF.

The nitrogen sorption isotherms and corresponding QSDFT-derived pore size distributions are qualitatively similar to the **Py-pII** COF, but are, as anticipated from the refined COF structures, slightly shifted towards smaller pore diameters (Figures 3.3c, f). The pore size distribution exhibits again two maxima that stem from the shamrock-shaped pore cross-section. For both COFs, the main peak corresponds to the wall-to-wall distance of 3.1 nm, and the smaller one relates to the reduced pore diagonal due to the alkyl chains. The Brunauer-Emmett-Teller (BET) surface areas are $1592 \text{ m}^2 \text{ g}^{-1}$ and $1567 \text{ m}^2 \text{ g}^{-1}$ with total pore volumes of $0.96 \text{ cm}^3 \text{ g}^{-1}$ and $0.85 \text{ cm}^3 \text{ g}^{-1}$ for the **Py-pTII** and **Py-tTII** COFs, respectively. As discussed above for the **Py-pII** COF, differences between these values and the Connolly surface areas and theoretical pore volumes might arise from the pore geometry.^[36]

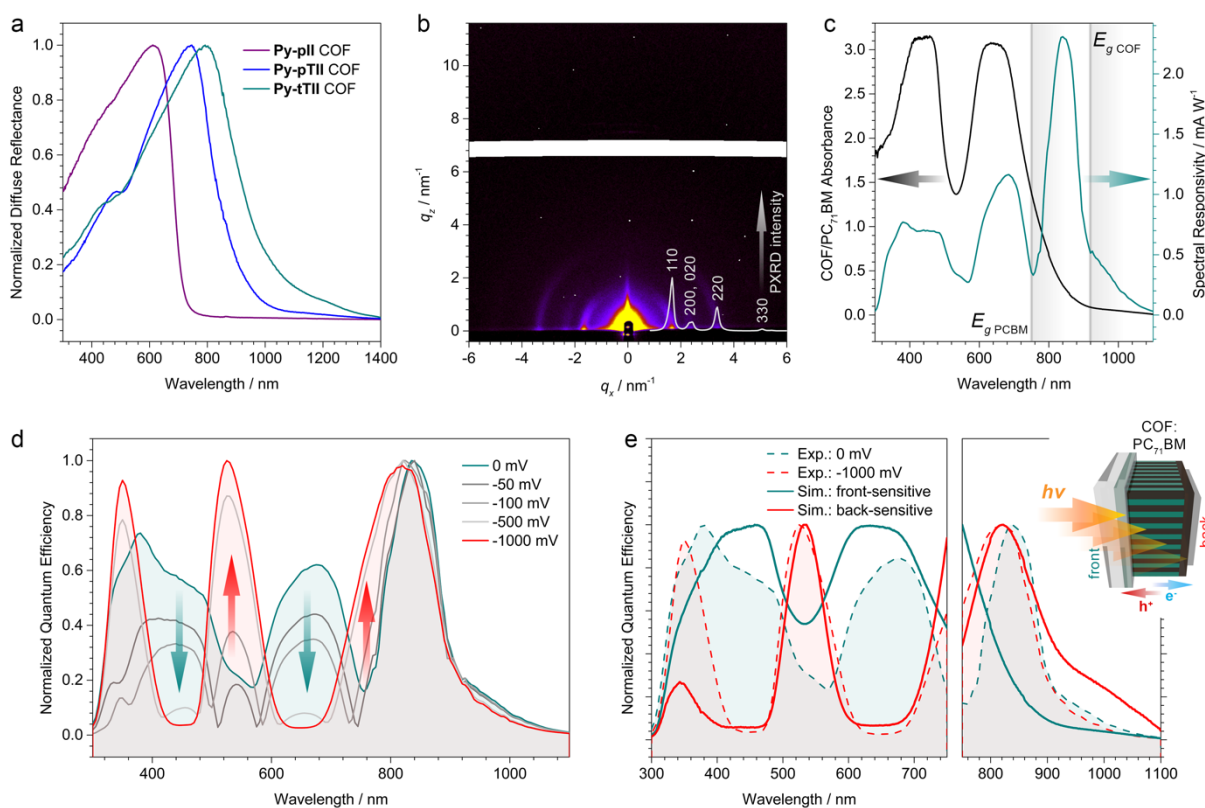


Figure 3.4. (a) UV-VIS-NIR diffuse reflectance spectra of the **Py-pII**, **Py-pTII**, and **Py-tTII** COF powders dispersed in BaSO₄. (b) GISAXS pattern of a **Py-tTII** COF film grown on ITO/MoO_x indicating a predominant orientation of the COF domains with their a - b plane parallel to the substrate. Inset, the simulated **Py-tTII** COF PXR D pattern. The reflections observed in the GISAXS pattern correspond to the 110, 020 and 200, 220, and 330 sets of lattice planes. (c) Spectral responsivity of the **Py-tTII** COF-based photodetector without external voltage

bias (green) and the transmission absorbance of the COF:PC₇₁BM active layer (black). Grey lines indicate the optical band gaps of PC₇₁BM and the COF. **(d)** Upon applying an external voltage to the photodetector, the quantum efficiency in the green and NIR regions up to 750 nm is greatly enhanced. This is accompanied by a reduced sensitivity to blue and red light, eventually leading to an inversion of the sensitivity profile across the visible spectrum at 1000 mV reverse bias. **(e)** A qualitative description of these characteristics can be derived from modelling the spectral distributions of collected charge carriers. While without voltage bias the device responds mostly to photons absorbed close to the front electrode (green line), the photoresponse at -1000 mV indicates a predominant sensitivity toward photons that penetrate deep into the active layer and are absorbed close to the back electrode (red line). Inset, illustration of the photodetector device layout.

The integration of the isoindigo- and thienoisindigo-containing building blocks produces strongly colored frameworks that absorb light across the visible and parts of the NIR spectrum (Figure 3.4a). The optical band gaps, estimated from the corresponding Tauc plots for direct allowed transitions, are 1.78, 1.48, and 1.36 eV, for the **Py-pII**, **Py-pTII**, and **Py-tTII** COFs, respectively (SI, Figure 3.10).

2D COFs possess very anisotropic electronic properties with the highest conductivity typically being along the π -stacked molecular columns. For application as an active component in a photodiode structure, these columns should therefore be aligned vertically to the substrate. The growth of oriented films on non-epitaxial substrates, during which the inherent anisotropy of the COF structure itself generates the preferred vertical orientation, has previously been achieved for boronate ester-linked COFs.^[19] We adapted this strategy for the growth of the imine-linked **Py-tTII** COF on MoO_x-modified indium-tin oxide (ITO) transparent electrodes (see the SI for details).

Grazing-incidence small angle X-ray scattering (GISAXS) measurements confirm that the resulting COF films are highly textured (Figure 3.4b). The intensity of the reflections corresponding to the 110, 020 and 200, 220, and 330 sets of lattice planes is highest directly above the sample horizon, indicating that most COF domains are oriented with their *a-b* plane parallel to the substrate (SI, Figure 3.11). Taking into account the monoclinic unit cell, the π -stacked columns thus extend away from the substrate at an angle of $\beta = 75^\circ$. This orientation also ensures that the pores are open towards the film surface and can be used for the subsequent infiltration with a complementary semiconductor.

For the construction of a COF-based NIR photodetector, we infiltrated a 450 nm thick oriented **Py-tTII** COF film grown on a hole-selective ITO/MoO_x electrode with [6,6]-phenyl C₇₁ butyric acid methyl ester (PC₇₁BM), thus forming an ordered interdigitated heterojunction. The device was completed by deposition of an electron-selective back contact consisting of poly[(9,9-bis(3-(*N,N*-dimethylamino)propyl)fluorene)-*alt*-(9,9-dioctylfluorene)] (PFN) and Ag. While the degree of infiltration cannot be assessed via photoluminescence (PL) quenching^[19, 22] for

this particular COF due to its very low PL quantum yield, comparing the COF:PC₇₁BM photodetection capabilities with a non-infiltrated COF-only device provides evidence for a predominant filling of the COF pores (SI, Figures 3.12d-f).

At short-circuit conditions the COF:PC₇₁BM device exhibits a panchromatic photoresponse ranging from 300 to 1100 nm (Figure 3.4c, green line). For photon energies above the optical band gap of PC₇₁BM (i.e. $\lambda < 750$ nm), the spectral responsivity follows the absorbance of the COF:PC₇₁BM heterojunction (Figure 3.4c, black line). The strong absorption and responsivity bands centered at 450 and 650 nm, respectively, are mainly attributed to the π - π^* transitions and the ICT band of **tTII**. At longer wavelengths, however, the photodetector exhibits an additional sensitivity peak around 840 nm that does not reflect an absorption feature of the COF:PC₇₁BM heterojunction. This might be a first indication that the photophysics of the device change at photon energies at which only the COF can be photoexcited (see the discussion below).

In the absence of an external voltage bias, the peak responsivity is 2.3 mA W⁻¹ at 840 nm. When applying a reverse bias to aid the extraction of the photogenerated charge carriers, this can be increased to above 12 mA W⁻¹ at -1000 mV (SI, Figure 3.12a).

Besides increasing responsivity and external quantum efficiency (EQE), applying a reverse bias has a profound effect on the photoresponse spectrum (Figure 3.4d). At 0 mV bias, the photodetector is sensitive towards blue and red light, and relatively insensitive to green and NIR light shorter than 750 nm. With increasing reverse bias, the relative and absolute sensitivities in the blue and red spectral region drop, while they improve in the green and NIR regions, ultimately inverting the sensitivity characteristics of the device throughout the 400 – 750 nm range. At longer wavelengths, where only the COF can be photoexcited, the shape of the EQE spectrum is hardly affected by applying a reverse bias.

In order to derive a qualitative description of these observations, we modelled the spectral distribution of the absorbed photons and hence the photogenerated charge carriers throughout the active layer (see the SI, Section J for a detailed discussion). Considering the inevitable transport losses in thick organic bulk heterojunctions, the probability of a charge carrier pair to be collected at the respective electrodes, η_{coll} , depends on where in the active layer it has been generated. η_{coll} is hereby limited by the carrier species (electron or hole) that has the shorter transport distance. Comparing the measured EQE spectra to the simulated spectral distributions of absorbed photons thus allows us to conclude from where inside the active layer the collected charge carriers originate. For the sake of simplicity, we focus our discussion on the two extreme cases of a front-sensitive (η_{coll} decreases with distance from front electrode, i.e. the illuminated

side) and a back-sensitive (η_{coll} increases towards back of the active layer) device (SI, Figure 3.13).

We first consider the 300 – 750 nm region, where both components of the heterojunction can be photoexcited. Without an external bias voltage, the observed EQE resembles the simulated photoresponse of a front-sensitive device, suggesting that the device performance is limited by the collection of holes at the front electrode (Figure 3.4e, green lines). If a reverse bias is applied, however, the EQE spectrum transforms into the photoresponse of a back-sensitive device, indicating that under these conditions the collection of electrons at the back electrode becomes the limiting factor (Figure 3.4e, red lines). Here, the incident light has been attenuated by the optically thick COF:PC₇₁BM film and hence the spectrum resembles the inverse of the absorption spectrum.^[39, 40] This voltage-switchable spectral response is fully reversible (SI, Figure 3.12c)

In the longer-wavelength region, where only the COF can be photoexcited, the EQE spectrum exhibits a relatively sharp peak around 840 nm. Optical modelling of the absorbed photons in this region (SI, Figure 3.13a) suggests that rather than corresponding to an absorption feature of the COF, this peak is caused by the balance between the penetration of light deep into the active layer (limiting factor at 750 – 840 nm) and the absorption capabilities of the COF (dominant factor at 840 – 1100 nm). Here, the device is back-sensitive, i.e. limited by the collection of electrons irrespective of the applied bias (Figure 3.4e, right part).

A more detailed analysis of the origin of these device characteristics is beyond the scope of this work and will be the subject of future studies.

3.4 Conclusion

In this work we have developed the first near-infrared-absorbing 2D covalent organic frameworks. The incorporation of donor-acceptor-type isoindigo- and thienoisindigo-based building blocks leads to the formation of strongly light absorbing, stable and porous networks. Growing these materials as an oriented thin film allowed us to construct an interdigitated heterojunction upon infiltration of the COF pores with a soluble fullerene derivative. This heterojunction was successfully applied as the active layer in a UV- to NIR-responsive photodetector. We found that the spectral response of the device could be switched reversibly from blue- and red-sensitive to green- and NIR-sensitive by changing the bias voltage. To the best of our knowledge, this is the first time that such nearly complete inversion of spectral sensitivity has been observed. This effect could lead to potential applications in information

3 Spectrally Switchable Photodetection with Near-Infrared-Absorbing Covalent Organic Frameworks

technology or spectral imaging. Future work will be dedicated to developing a more quantitative understanding of the COF photophysics.

3.5 Supporting Information

Abbreviations

Bn	benzyl
BET	Brunauer-Emmett-Teller
dba	<i>trans,trans</i> -dibenzylideneacetone
DCE	1,2-dichloroethane
DCM	dichloromethane
DFT	density functional theory
DMF	<i>N,N</i> -dimethylformamide
DMSO	dimethyl sulfoxide
EI	electron ionization
eq.	equivalents
GISAXS	grazing-incidence small angle X-ray scattering
HOMO	highest occupied molecular orbital
HRMS	high resolution mass spectrometry
LUMO	lowest unoccupied molecular orbital
NBS	<i>N</i> -bromosuccinimide
NIR	near-infrared
NIS	<i>N</i> -iodosuccinimide
NMR	nuclear magnetic resonance
PCBM	[6,6]-phenyl-C ₆₁ -butyric acid methyl ester
PC ₇₁ BM	[6,6]-phenyl-C ₇₁ -butyric acid methyl ester
PFN	poly[(9,9-bis(3-(<i>N,N</i> -dimethylamino)propyl)fluorene)- <i>alt</i> -(9,9-dioctylfluorene)]
PL	photoluminescence
PMMA	poly(methyl methacrylate)
PXRD	powder X-ray diffraction
QSDFE	quenched solid density functional theory
rt	room temperature
TEM	transmission electron microscopy
TFP	tri(2-furyl)phosphine
THF	tetrahydrofuran
TLC	thin layer chromatography

Section A – Methods

Nuclear magnetic resonance (NMR) spectra were recorded on Bruker AV 400 and AV 400 TR spectrometers. Chemical shifts are expressed in parts per million (δ scale) and are calibrated using residual undeuterated solvent peaks as an internal reference (^1H : CDCl_3 : 7.26, $\text{DMSO-}d_6$: 2.50, $\text{DMF-}d_7$: 8.03; ^{13}C : CDCl_3 : 77.16, $\text{DMSO-}d_6$: 39.52, $\text{DMF-}d_7$: 163.15). Data for ^1H NMR spectra are reported in the following way: chemical shift (δ ppm) (multiplicity, coupling constant/Hz, integration). Multiplicities are reported as follows: s = singlet, d = doublet, t = triplet, q = quartet, m = multiplet, or combinations thereof.

High resolution electron ionization (EI) **mass spectra** (MS) were recorded with a Thermo Finnigan MAT 95 instrument.

Powder X-ray diffraction (PXRD) measurements were performed using a Bruker D8 Discover with Ni-filtered Cu K_α radiation and a LynxEye position-sensitive detector.

2D grazing-incidence small angle X-ray scattering (GISAXS) data were recorded with an Anton Paar SAXSpace system equipped with a GeniX Cu K_α microsource and a Dectris Eiger R 1M detector. The samples were positioned at 200 mm sample-detector distance and at a tilt angle of 2.3° with respect to the incident beam.

The **structure models of the COFs** were constructed using the Accelrys Materials Studio software package. For each COF structure we applied the space group with the highest possible symmetry, taking into account the rotation of the phenylenes versus the pyrene core. Structure refinements using the Rietveld or Pawley method were carried out as implemented in the Reflex module of the Materials Studio software. Pseudo-Voigt peak profiles were used and peak asymmetry was corrected using the Finger-Cox-Jephcoat method. Connolly surfaces were generated using an N_2 -sized probe ($r = 0.368$ nm) at a 0.025 nm grid interval.^[36]

DFT-based geometry optimizations were performed with the CASTEP code using the generalized-gradient-approximation PBE functional. The energy cutoff for the plane wave basis set was set to 340.0 eV, ions were represented with ultra-soft pseudopotentials and k-point sampling was performed with a $1 \times 1 \times 4$ Monkhorst-Pack grid. The correction scheme of Tkatchenko and Scheffler was used to account for dispersion interactions.

Transmission electron microscopy (TEM) was performed on an FEI Titan Themis equipped with a field emission gun operated at 300 kV.

The **nitrogen sorption isotherms** were recorded on a Quantachrome Autosorb 1 at 77 K. Prior to the measurement of the sorption isotherm, the samples were outgassed for 24 h at 120°C under high vacuum. For the evaluation of the surface area, the BET model was applied in the ranges $0.05 \leq p/p_0 \leq 0.21$ (**Py-pII COF**), $0.07 \leq p/p_0 \leq 0.18$ (**Py-pTII COF**), and $0.07 \leq p/p_0 \leq$

0.20 (**Py-tTH COF**). The calculations for obtaining the pore size distribution were performed using the QSDFT equilibrium model with a carbon kernel for cylindrical pores.

Infrared (IR) spectra were recorded on a Perkin Elmer Spectrum BX II FT-IR system equipped with a diamond attenuated total reflection unit.

UV-VIS spectra were recorded using a Perkin-Elmer Lambda 1050 spectrometer equipped with a 150 mm InGaAs integrating sphere. The transmission absorbance of the COF:PC₇₁BM heterojunction was recorded with the sample placed close to the center of the integrating sphere, using an ITO/MoO_x substrate coated with a 450 – 480 nm thick PMMA layer as reference.

Diffuse reflectance spectra were collected with a Praying Mantis accessory and were referenced to barium sulfate powder as white standard. The specular reflection of the sample surface was removed from the signal using apertures that allow only light scattered at angles > 20° to pass.

The **spectral response and external quantum efficiency (EQE)** measurements of the photodetector devices were performed under pulsed ($f = 17$ Hz) quasi-monochromatic (FWHM < 5 nm) illumination generated from a 150 W Xe arc lamp via a monochromator (Horiba Jobin Yvon microHR). The monochromatic light intensity was below 2 mW cm⁻² at all wavelengths and did not cause any measurable thermal drift of the device under test. The photocurrent was detected via a lock-in amplifier (Signal Recovery SR7230) with a low-noise pre-amplifier (Femto DLPCA-200), and referenced to a Si photodiode with NIST traceable calibration.

Section B - Building Block syntheses

All reactions were performed in oven-dried glassware under argon atmosphere using standard Schlenk and glovebox techniques. Reagents and anhydrous solvents were obtained from commercial suppliers and used as received. All other solvents were obtained in high-purity grades and were dried and saturated with argon before use.

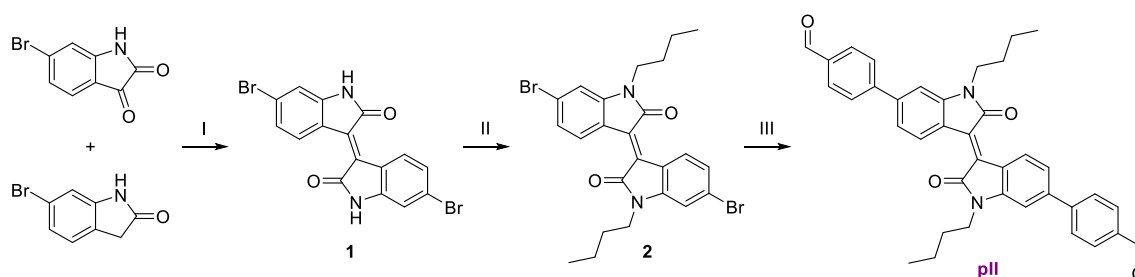
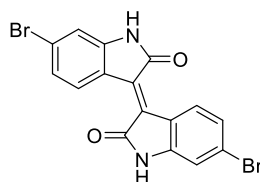


Figure 3.5. Synthesis of the pII building block. **(I)** HOAc/HCl, reflux, 80%. **(II)** 1-bromobutane, K₂CO₃, DMF, 100 °C, 79%. **(III)** 4-formylphenylboronic acid, Pd(OAc)₂, CsOH·H₂O, XPhos, 1-butanol/H₂O, 50 °C, 52%.

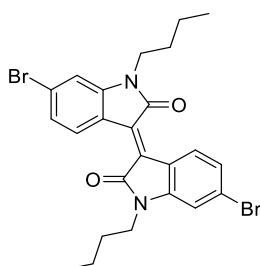
6,6'-dibromoisoindigo (1)^[41]



Under argon, 0.2 mL of concentrated aqueous hydrochloric acid (37%) was added to a suspension of 6-bromoisoindigo (1.07 g, 4.72 mmol, 1.0 eq.) and 6-bromooxindole (1.00 g, 4.72 mmol, 1.0 eq.) in 30 mL glacial acetic acid in a 100 mL Schlenk flask. The reaction mixture was heated under reflux (135 °C) for 48 h. After cooling to room temperature, the precipitate was collected by filtration and washed with water, ethanol, and ethyl acetate (20 mL each). After drying in high vacuum, 6,6'-dibromoisoindigo was obtained as a brown solid (1.58 g, 3.77 mmol, 80%).

¹H NMR (400 MHz, DMF-*d*₇): 11.07 (s, 2H), 9.12 (d, *J* = 8.6 Hz, 2H), 7.22 (dd, *J* = 8.6, 2.0 Hz, 2H), 7.14 (d, *J* = 1.9 Hz, 2H).

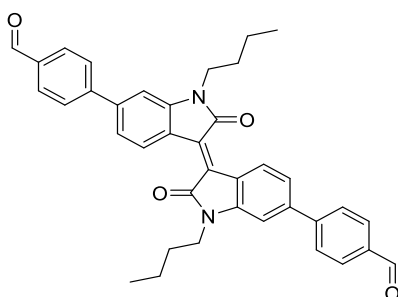
¹³C NMR (101 MHz, DMF-*d*₇): 170.3, 147.1, 134.0, 132.3, 127.0, 125.2, 122.4, 113.7.

6,6'-dibromo-*N,N'*-dibutyl-isoindigo (2)

1-Bromobutane (1.14 g, 0.89 mL, 8.29 mmol, 2.2 eq.) was added to a solution of **1** (1.58 g, 3.77 mmol, 1.0 eq.) and potassium carbonate (2.61 g, 18.9 mmol, 5.0 eq.) in anhydrous DMF (50 mL). The reaction mixture was stirred overnight at 100 °C. After cooling, the reaction mixture was poured into water. The product was extracted with CHCl₃ (4x50 mL), washed with brine, and dried over magnesium sulfate. The solvent was removed under reduced pressure and the residue was purified by column chromatography (silica gel, DCM/*n*-hexane 3:1), yielding the title compound as a deep red solid (1.59 g, 2.99 mmol, 79%).

¹H NMR (400 MHz, CDCl₃): 9.06 (d, *J* = 8.6 Hz, 2H), 7.16 (dd, *J* = 8.6, 1.9 Hz, 2H), 6.92 (d, *J* = 1.8 Hz, 2H), 3.73 (t, *J* = 7.4 Hz, 4H), 1.61 – 1.72 (m, 4H), 1.48 – 1.35 (m, 4H), 0.97 (t, *J* = 7.3 Hz, 6H).

¹³C NMR (101 MHz, CDCl₃): 167.9, 146.0, 132.8, 131.4, 126.9, 125.3, 120.6, 111.5, 40.2, 29.7, 20.5, 14.0.

6,6'-bis(4-formylphenyl)-*N,N'*-dibutyl-isoindigo (pII)

Following a modified literature protocol,^[42] compound **2** (27 mg, 0.050 mmol, 1.0 eq.), Pd(OAc)₂ (0.5 mg, 0.002 mmol, 4 mol%), XPhos (1.1 mg, 0.0024 mmol, 4.8 mol%), and 4-formylphenylboronic acid (23 mg, 0.15 mmol, 3.0 eq.) were dissolved in 280 μL 1-butanol and stirred for 15 min. Then, a solution of CsOH·H₂O (29 mg, 0.17 mmol, 3.4 eq.) in 70 μL degassed H₂O was added. After stirring at 50 °C for 48 h, the mixture was poured into water and extracted with CHCl₃ (4x10 mL). The organic phase was washed with brine and dried over

magnesium sulfate. The solution was concentrated under reduced pressure and the crude product was purified by column chromatography (silica gel, CHCl₃), yielding the title compound as a dark brown solid (16 mg, 0.026 mmol, 52%).

¹H NMR (400 MHz, CDCl₃): 10.09 (s, 2H), 9.31 (d, *J* = 8.3 Hz, 2H), 8.00 (d, *J* = 8.3 Hz, 4H), 7.81 (d, *J* = 8.2 Hz, 4H), 7.33 (dd, *J* = 8.4, 1.7 Hz, 2H), 7.02 (d, *J* = 1.7 Hz, 2H), 3.88 (t, *J* = 7.3 Hz, 4H), 1.83 – 1.70 (m, 4H), 1.52 – 1.41 (m, 4H), 1.00 (t, *J* = 7.3 Hz, 6H).

¹³C NMR (101 MHz, CDCl₃): 191.8, 168.2, 146.5, 145.7, 143.8, 136.0, 133.1, 130.8, 130.5, 127.9, 122.1, 121.5, 106.7, 40.1, 29.8, 20.5, 14.0.

HR-EI-MS: *m/z* 582.67 (M⁺, calculated for C₃₈H₃₄N₂O₄: 582.70).

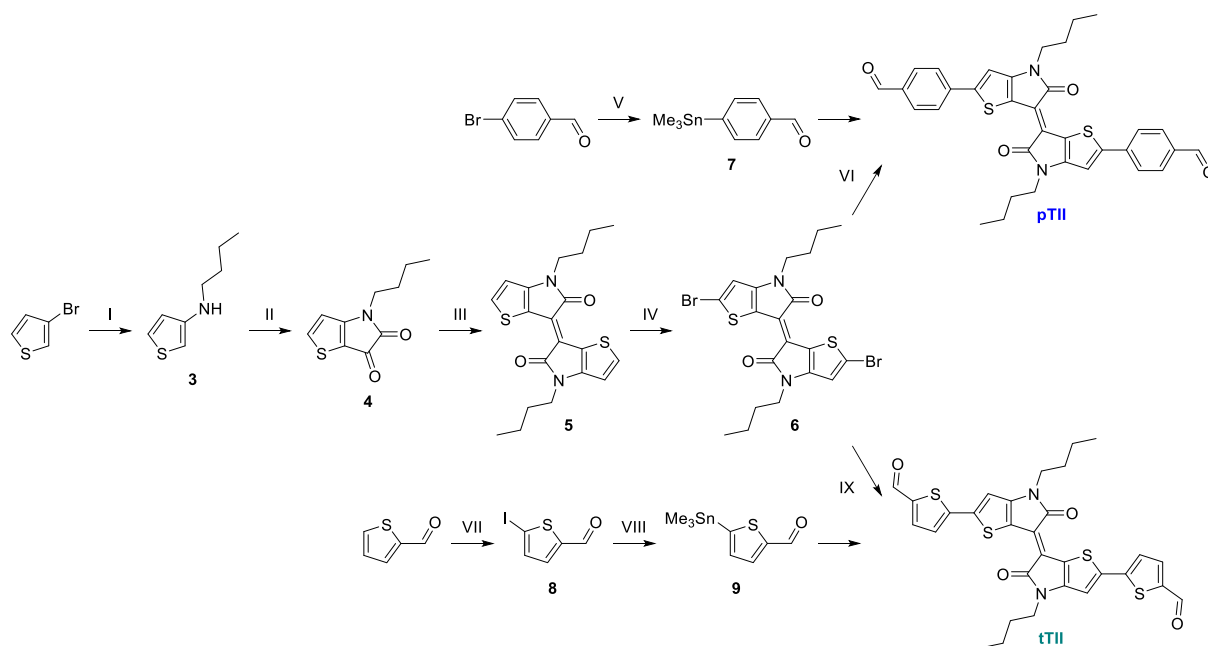
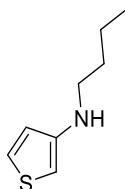


Figure 3.6. Synthesis of the **pTII** and **tTII** building blocks. (I) *n*-butylamine, Cu, CuI, K₃PO₄, 2-dimethylaminoethanol, 80 °C, 60%. (II) oxalyl chloride, Et₃N, DCM, -15 °C/0 °C/rt, 52%. (III) Lawesson's Reagent, toluene, 100 °C, 49%. (IV) NBS, THF, 0 °C, 85%. (V) (SnMe₃)₂, Pd(PPh₃)₄, toluene, 100 °C, 37%. (VI) Pd(dba)₂, TFP, toluene, 85 °C, 57%. (VII) NIS, *p*-toluenesulfonic acid, EtOH, 50 °C, 96%. (VIII) (SnMe₃)₂, Pd(PPh₃)₄, toluene, 85 °C, 48%. (IX) Pd(dba)₂, TFP, toluene, 85 °C, 36%.

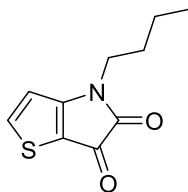
3-(butylamino)thiophene (**3**)^[43]



In a glovebox, a reaction mixture containing 3-bromothiophene (12.2 g, 75 mmol, 1.0 eq.), *n*-butylamine (8.23 g, 113 mmol, 1.5 eq.), copper (480 mg, 7.5 mmol, 10 mol%), CuI (1.43 g, 7.5 mmol, 10 mol%), and K₃PO₄ (31.8 g, 150 mmol, 2.0 eq.) in anhydrous 2-dimethylaminoethanol (75 mL) was heated to 80 °C for 48 h. After cooling to room temperature, the supernatant was decanted and the solids were washed with THF (3x25 mL). The combined liquids were concentrated under reduced pressure. The product was purified by high vacuum distillation (10⁻² mbar, 61 °C), yielding a colorless, highly air-sensitive liquid (6.94 g, 44.7 mmol, 60%).

¹H NMR (400 MHz, CDCl₃): 7.15 (dd, *J* = 5.1, 3.0 Hz, 1H), 6.61 (dd, *J* = 5.1, 1.5 Hz, 1H), 5.95 (dd, *J* = 3.0, 1.5 Hz, 1H), 3.57 (s, 1H), 3.07 (t, *J* = 5.8 Hz, 2H), 1.56 – 1.66 (m, 2H), 1.37 – 1.49 (m, 2H), 0.96 (t, *J* = 7.3 Hz, 3H).

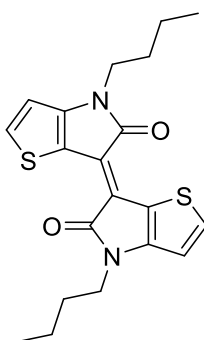
¹³C NMR (101 MHz, CDCl₃): 149.4, 125.5, 120.4, 95.7, 46.5, 32.2, 20.8, 14.4.

4-butyl-4*H*-thieno[3,2-*b*]pyrrole-5,6-dione (4)

A solution of oxalyl chloride (2.70 g, 21.3 mmol, 1.6 eq.) in 14 mL of anhydrous DCM was cooled to $-15\text{ }^{\circ}\text{C}$ in a 100 mL Schlenk flask. Compound 3 (2.07 g, 13.3 mmol, 1.0 eq.) in 23 mL DCM was added slowly via a syringe over 20 minutes, followed by the dropwise addition of triethylamine (4.40 g, 5.57 mL, 39.9 mmol, 3.0 eq.). The reaction mixture was stirred at $0\text{ }^{\circ}\text{C}$ for 1 h, allowed to warm to room temperature, and stirred overnight. After completion, the reaction was quenched by the addition of H_2O , and the product was extracted with DCM (4x50 mL). The combined organic phases were washed with brine, dried over MgSO_4 , and concentrated under reduced pressure. The product was purified by column chromatography (silica gel, DCM/THF 100:3), yielding the title compound as a red oil (1.44 g, 6.86 mmol, 52%).

^1H NMR (400 MHz, CDCl_3): 8.00 (d, $J = 5.0$ Hz, 1H), 6.79 (d, $J = 5.0$ Hz, 1H), 3.66 (t, $J = 7.2$ Hz, 2H), 1.71 – 1.60 (m, 2H), 1.44 – 1.32 (m, 2H), 0.95 (t, $J = 7.4$ Hz, 3H).

^{13}C NMR (101 MHz, CDCl_3): 173.2, 165.3, 161.6, 144.0, 113.1, 111.2, 42.0, 30.4, 20.1, 13.8.

***N,N'*-dibutyl-thienoisindigo (5)^[44]**

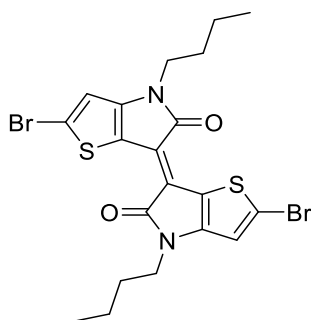
A solution of compound 4 (1.91 g, 9.14 mmol, 2.0 eq.) in 73 mL of dry toluene was added to Lawesson's Reagent (1.85 g, 4.57 mmol, 1.0 eq.) in a 250 mL three-neck flask at room temperature. The reaction mixture was stirred at $100\text{ }^{\circ}\text{C}$ for 5 minutes in a pre-heated oil bath. After cooling to room temperature, all volatiles were removed under high vacuum. The residue

was purified by column chromatography (silica gel, DCM), yielding the title compound as a dark purple powder (860 mg, 2.23 mmol, 49%).

^1H NMR (400 MHz, CDCl_3): 7.53 (d, $J = 5.2$ Hz, 2H), 6.81 (d, $J = 5.2$ Hz, 2H), 3.81 (t, $J = 7.3$ Hz, 4H), 1.77 – 1.66 (m, 4H), 1.46 – 1.34 (m, 4H), 0.95 (t, $J = 7.4$ Hz, 6H).

^{13}C NMR (101 MHz, CDCl_3): 171.2, 151.4, 134.5, 121.3, 114.3, 111.3, 41.7, 30.8, 20.3, 13.9.

5,5'-dibromo-*N,N'*-dibutyl-thienoisindigo (6)

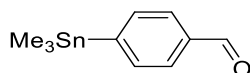


N-bromosuccinimide (449 mg, 2.52 mmol, 2.1 eq.) was added to a solution of compound **5** (464 mg, 1.20 mmol, 1.0 eq.) in 55 mL of anhydrous THF at 0 °C. The reaction mixture was stirred at this temperature for 1 h in the dark, followed by the addition of H_2O and extraction with CHCl_3 (3x50 mL). The combined organic phases were washed with brine, dried over MgSO_4 , and concentrated under reduced pressure. Purification via column chromatography (silica gel, CHCl_3) yielded the title compound as a dark blue powder (555 mg, 1.02 mmol, 85%).

^1H NMR (400 MHz, CDCl_3): 6.82 (s, 2H), 3.74 (t, $J = 7.2$ Hz, 4H), 1.74 – 1.62 (m, 4H), 1.44 – 1.31 (m, 4H), 0.91 (t, $J = 7.4$ Hz, 6H).

^{13}C NMR (101 MHz, CDCl_3): 170.2, 150.0, 123.3, 119.8, 115.0, 114.8, 41.8, 30.8, 20.3, 13.9.

4-(trimethylstannyl)benzaldehyde (7)



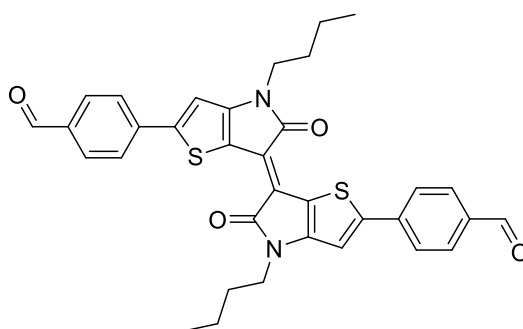
A reaction mixture containing 4-bromobenzaldehyde (1.48 g, 8.0 mmol, 1.0 eq.), hexamethylditin (3.14 g, 9.6 mmol, 1.2 eq.), and $\text{Pd}(\text{PPh}_3)_4$ (462 mg, 0.4 mmol, 5 mol%) in 40 mL of dry toluene was heated to 100 °C for 24 h. After completion, all volatiles were removed under high vacuum at 50 °C. The residue was taken up in diethyl ether and filtered

through neutral alumina. All volatiles were removed under reduced pressure, yielding an orange oil. Slow cooling to 10 °C yielded the title compound as colorless needles (788 mg, 2.93 mmol, 37%).

^1H NMR (400 MHz, CDCl_3): 10.00 (s, 1H), 7.81 (d, $J = 8.0$ Hz, 2H), 7.68 (d, $J = 7.6$ Hz, 2H), 0.34 (s, with Sn coupling, 9H).

^{13}C NMR (101 MHz, CDCl_3): 192.9, 152.6, 136.5, 136.3, 128.7, -9.3.

5,5'-bis(4-formylphenyl)-*N,N'*-dibutyl-thienoisindigo (**pTII**)

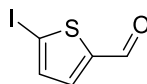


A reaction mixture containing compound **6** (272 mg, 0.50 mmol, 1.0 eq.), compound **7** (323 mg, 1.20 mmol, 2.4 eq.), $\text{Pd}(\text{dba})_2$ (29 mg, 0.05 mmol, 10 mol%), and tri(2-furyl)phosphine (29 mg, 0.125 mmol, 25 mol%) in 5 mL dry toluene was heated to 85 °C for 48 h. After completion, all volatiles were removed under high vacuum at 50 °C. The solid residue was dissolved in CHCl_3 at 60 °C. Purification via repeated column chromatography (silica gel, 1st column CHCl_3 , 2nd column DCM) yielded the title compound as a dark blue solid (169 mg, 0.28 mmol, 57%).

^1H NMR (400 MHz, CDCl_3): 10.03 (s, 2H), 7.94 – 7.88 (m, 8H), 7.19 (s, 2H), 3.88 (t, $J = 7.3$ Hz, 4H), 1.83 – 1.74 (m, 5H), 1.51 – 1.40 (m, 4H), 1.00 (t, $J = 7.4$ Hz, 6H).

Due to the low solubility of this compound in common deuterated solvents, no ^{13}C NMR spectra could be recorded.

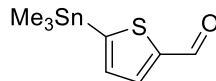
HR-EI-MS: m/z 594.74 (M^+ , calculated for $\text{C}_{34}\text{H}_{30}\text{N}_2\text{O}_4\text{S}_2$: 594.75).

5-iodothiophene-2-carbaldehyde (8)^[45]

Thiophene-2-carbaldehyde (2.24 g, 20 mmol, 1.0 eq.) was dissolved in 40 mL EtOH and heated to 50 °C. *N*-iodosuccinimide (4.95 g, 22 mmol, 1.1 eq.) and *p*-toluenesulfonic acid monohydrate (380 mg, 2 mmol, 10 mol%) were added and the resulting mixture was stirred at 50 °C in the dark for 10 min. After completion, 20 mL 1 M aqueous HCl and 20 mL EtOAc were added. The organic layer was extracted with EtOAc (3x25mL), washed with saturated aqueous Na₂S₂O₃ and Na₂CO₃ solutions (2x20 mL each), dried over MgSO₄, and filtered through a cotton plug. All volatiles were removed under high vacuum, yielding a slightly yellow solid (4.57 g, 19.2 mmol, 96%).

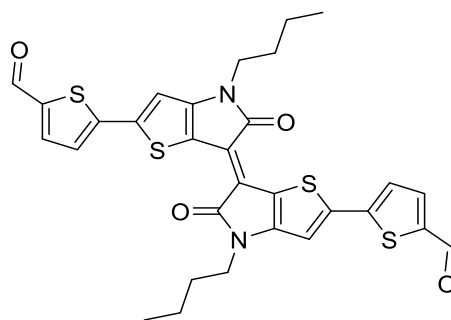
¹H NMR (400 MHz, CDCl₃): 9.77 (s, 1H), 7.39 (s, 2H).

¹³C NMR (101 MHz, CDCl₃): 181.3, 149.8, 138.4, 137.1, 87.9.

5-(trimethylstannyl)thiophene-2-carbaldehyde (9)

A reaction mixture containing compound **8** (472 mg, 2.0 mmol, 1.0 eq.), hexamethylditin (786 mg, 2.4 mmol, 1.2 eq.), and Pd(PPh₃)₄ (116 mg, 0.1 mmol, 5 mol%) in 10 mL of dry toluene was heated to 85 °C for 24 h. After completion, the solution was concentrated under reduced pressure at room temperature to remove the solvent and most of the by-product. The product was purified by sublimation (10⁻³ mbar, 60°C), yielding the title compound as a white crystalline solid (264 mg, 0.96 mmol, 48%).

¹H NMR (400 MHz, CDCl₃): 9.94 (s, 1H), 7.83 (d, *J* = 3.5 Hz, 1H), 7.28 (d, *J* = 3.5 Hz, 1H), 0.42 (s, with Sn coupling, 9H).

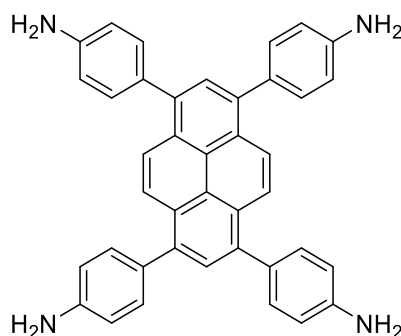
5,5'-bis(2-formylthiophen-5-yl)-*N,N'*-dibutyl-thienoisindigo (tTII)

A reaction mixture containing compound **6** (272 mg, 0.50 mmol, 1.0 eq.), compound **9** (330 mg, 1.20 mmol, 2.4 eq.), Pd(dba)₂ (29 mg, 0.05 mmol, 10 mol%), and tri(2-furyl)phosphine (29 mg, 0.125 mmol, 25 mol%) in 5 mL dry toluene was heated to 85 °C for 48 h. After completion, all volatiles were removed under high vacuum at 50 °C. The solid residue was dissolved in CHCl₃ at 60 °C. Purification via repeated column chromatography (silica gel, 1st column CHCl₃, 2nd column DCM) yielded the title compound as a dark green solid (108 mg, 0.178 mmol, 36%).

¹H NMR (400 MHz, CDCl₃): 9.90 (s, 2H), 7.71 (d, *J* = 4.0 Hz, 2H), 7.45 (d, *J* = 4.0 Hz, 2H), 7.05 (s, 2H), 3.85 (t, *J* = 7.3 Hz, 4H), 1.81 – 1.71 (m, 4H), 1.49 – 1.38 (m, 4H), 0.99 (t, *J* = 7.4 Hz, 6H).

Due to the low solubility of this compound in common deuterated solvents, no ¹³C NMR spectra could be recorded.

HR-EI-MS: *m/z* 606.78 (M⁺, calculated for C₃₀H₂₆N₂O₄S₄: 606.81).

1,3,6,8-tetrakis(4-aminophenyl)pyrene (Py)^[17, 46]

A reaction mixture containing 1,3,6,8-tetrabromopyrene (1482 mg, 2.86 mmol, 1.0 eq.), 4-aminophenylboronic acid pinacol ester (3010 mg, 13.7 mmol, 4.8 eq.), K₂CO₃ (2175 mg, 15.7 mmol, 5.5 eq.), and Pd(PPh₃)₄ (330 mg, 0.29 mmol, 10 mol%) in 32 mL 1,4-dioxane and 8 mL degassed H₂O was heated to reflux (115 °C) for 3 d. After cooling to room temperature,

H₂O (50 mL) was added. The resulting precipitate was collected via filtration and was washed with H₂O (50 mL) and MeOH (100 mL). Recrystallization from 1,4-dioxane, followed by drying under high vacuum furnished the title compound, co-crystallized with approximately 1.5 dioxane molecules per formula unit, as a bright yellow powder (1792 mg, 2.56 mmol, 90%).

¹H NMR (400 MHz, DMSO-*d*₆): 8.13 (s, 4 H), 7.79 (s, 2 H), 7.34 (d, *J* = 8.4 Hz, 8 H), 6.77 (d, *J* = 8.5 Hz, 8 H), 5.30 (s, 8 H), 3.56 (s, 12 H, dioxane).

¹³C NMR (100 MHz, DMSO-*d*₆): 148.2, 137.1, 131.0, 129.0, 127.6, 126.7, 126.1, 124.4, 113.9, 66.3 (dioxane).

Section C – COF syntheses

All COF syntheses were performed under argon atmosphere. Solvents and acetic acid were obtained in high purity grade from commercial suppliers and were, unless shipped under argon, degassed and saturated with argon prior to use.

Py-pII COF

1,3,6,8-tetrakis(4-aminophenyl)pyrene dioxane adduct (**Py**; 14.0 mg, 20 μmol , 1.0 eq.) and 6,6'-bis(4-formylphenyl)-*N,N'*-dibutylisoindigo (**pII**; 23.3 mg, 40 μmol , 2.0 eq.) were filled into a 6 mL reaction tube, followed by the addition of mesitylene (333 μL), 1,4-dioxane (667 μL), and 6 M acetic acid (100 μL). The tube was sealed and the reaction mixture was heated at 120 $^{\circ}\text{C}$ for 4 d. After cooling to room temperature, the precipitate was collected by filtration and slowly dried in air for 24 h, yielding the **Py-pII COF** as a dark purple, hard and brittle powder.

Elemental analysis (calculated, found for $\text{C}_{232}\text{H}_{180}\text{N}_{16}\text{O}_8$): C (83.93, 82.47), H (5.46, 5.71), N (6.75, 6.31).

Py-pTII COF

Py (14.0 mg, 20 μmol , 1.0 eq.) and 5,5'-bis(4-formylphenyl)-*N,N'*-dibutyl-thienoisindigo (**pTII**; 23.8 mg, 40 μmol , 2.0 eq.) were filled into a 6 mL reaction tube, followed by the addition of mesitylene (333 μL), 1,4-dioxane (667 μL), and 6 M acetic acid (100 μL). The tube was sealed and the reaction mixture was heated at 120 $^{\circ}\text{C}$ for 4 d. After cooling to room temperature, the precipitate was collected by filtration and slowly dried in air for 24 h, yielding the **Py-pTII COF** as a dark blue, hard powder.

Elemental analysis (calculated, found for $\text{C}_{216}\text{H}_{164}\text{N}_{16}\text{O}_8\text{S}_8$): C (77.02, 75.77), H (4.91, 5.11), N (6.65, 6.25), S (7.61, 7.41).

Py-tTII COF

Py (7.0 mg, 10 μmol , 1.0 eq.) and 5,5'-bis(2-formylthiophen-5-yl)-*N,N'*-dibutyl-thienoisindigo (**tTII**; 12.1 mg, 20 μmol , 2.0 eq.) were filled into a 6 mL reaction tube, followed by the addition of mesitylene (167 μL), 1,4-dioxane (333 μL), and 6 M acetic acid (50 μL). The tube was sealed and the reaction mixture was heated at 120 $^{\circ}\text{C}$ for 4 d. After cooling to room

temperature, the precipitate was collected by filtration and slowly dried in air for 24 h, yielding the **Py-tTH COF** as a dark green, hard and brittle powder.

Elemental analysis (calculated, found for $C_{200}H_{148}N_{16}O_8S_{16}$): C (70.31, 70.46), H (4.37, 4.79), N (6.56, 5.91), S (15.01, 13.81).

Py-tTH COF film growth and device fabrication

Indium-tin-oxide (ITO) coated glass substrates (VisionTec, 12 – 15 ohms/sq) were patterned by etching with Zn and 5 M aqueous HCl. A 10 nm thick hole-selective MoO_x layer was deposited by thermal evaporation at 3×10^{-6} mbar.

A 20 mL teflon-lined autoclave was charged with **Py** (40 μ mol, 28 mg, 1.0 eq.) and **tTH** (80 μ mol, 48.5 mg, 2.0 eq.), 2 mL of a mesitylene/1,4-dioxane 1:2 mixture, and 200 μ L of 6 M acetic acid. The substrate was placed in this reaction mixture with the conductive side facing down and at sufficient height that the substrate did not touch the solid precursors. After heating at 120 °C for 4 d, the autoclave was allowed to cool to room temperature. The COF film was removed from the reaction solution, rinsed with MeCN, dried in air, and transferred to an argon-filled glovebox.

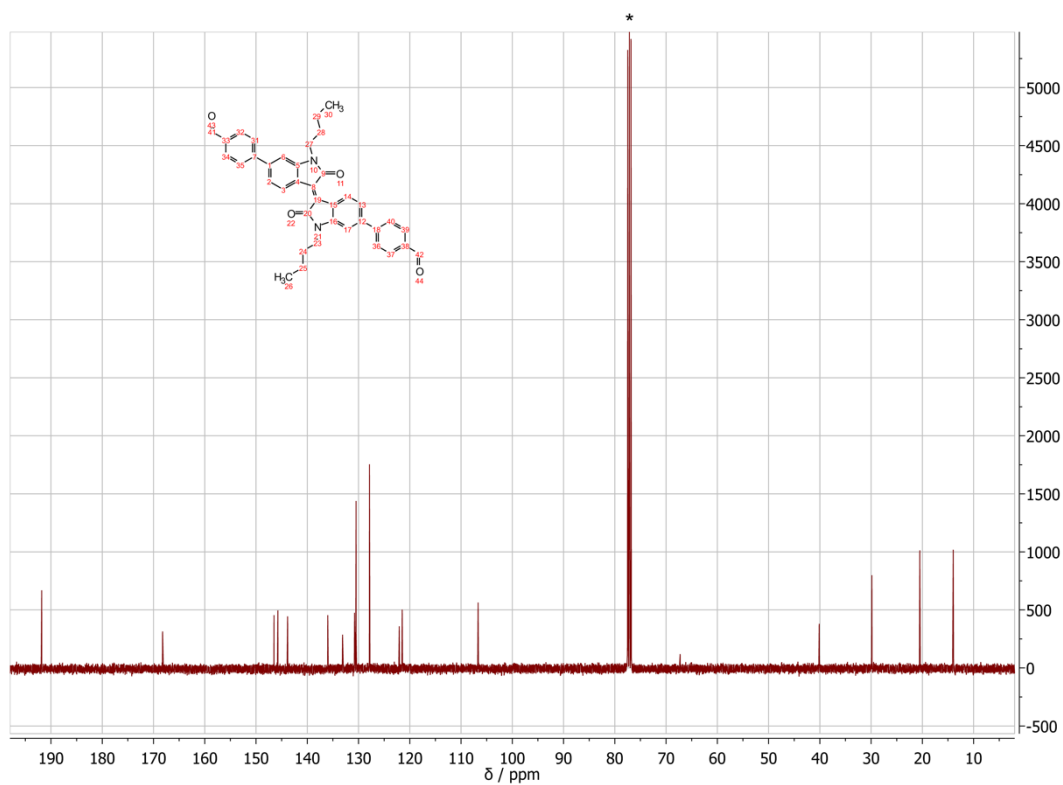
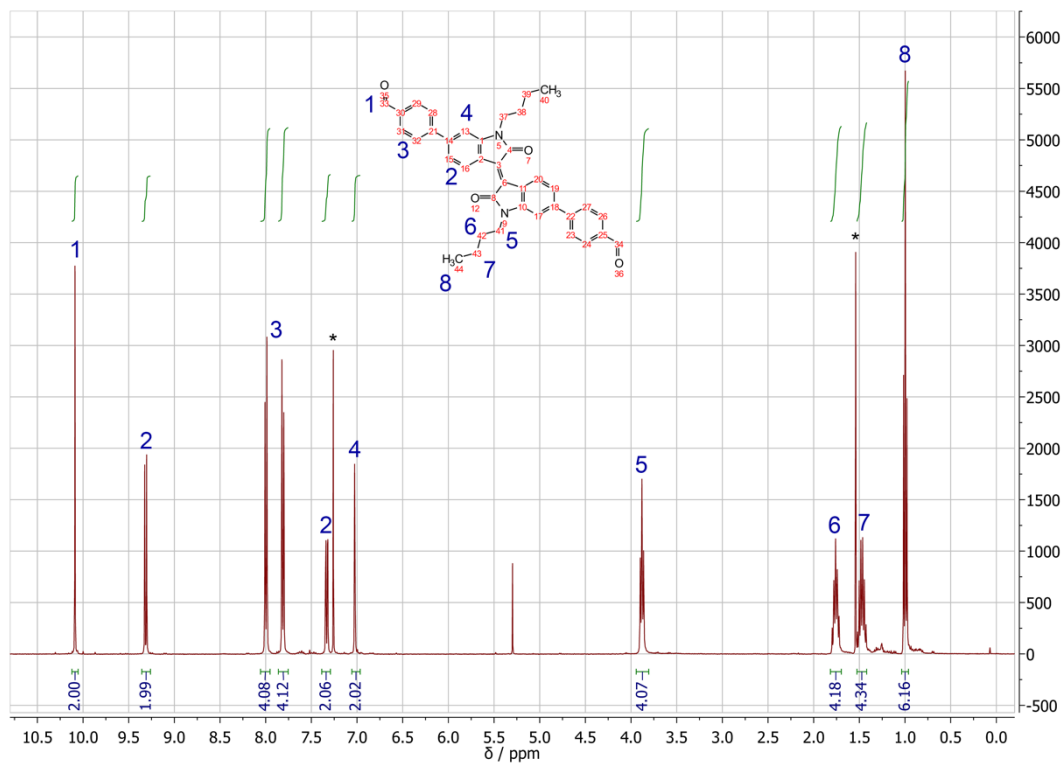
The device was completed by spin-coating a 10 mg mL^{-1} solution of PC₇₁BM in chlorobenzene (60 s soaking, then 40 s @ 1000 rpm) and a 2 mg mL^{-1} PFN solution in methanol with 5 μ L mL^{-1} HOAc (40 s @ 1000 rpm), followed by thermal evaporation of 120 nm Ag. The active area of 3x3 mm² was defined by the overlap of the ITO front and the Ag back electrode. For the non-infiltrated device, the PC₇₁BM coating step was skipped and the PFN layer was deposited directly onto the COF.

Device measurements were performed in a sealed sample holder under argon atmosphere and using a 2.8x2.8 mm² laser-cut shadow mask.

Section D – NMR spectra of the building blocks

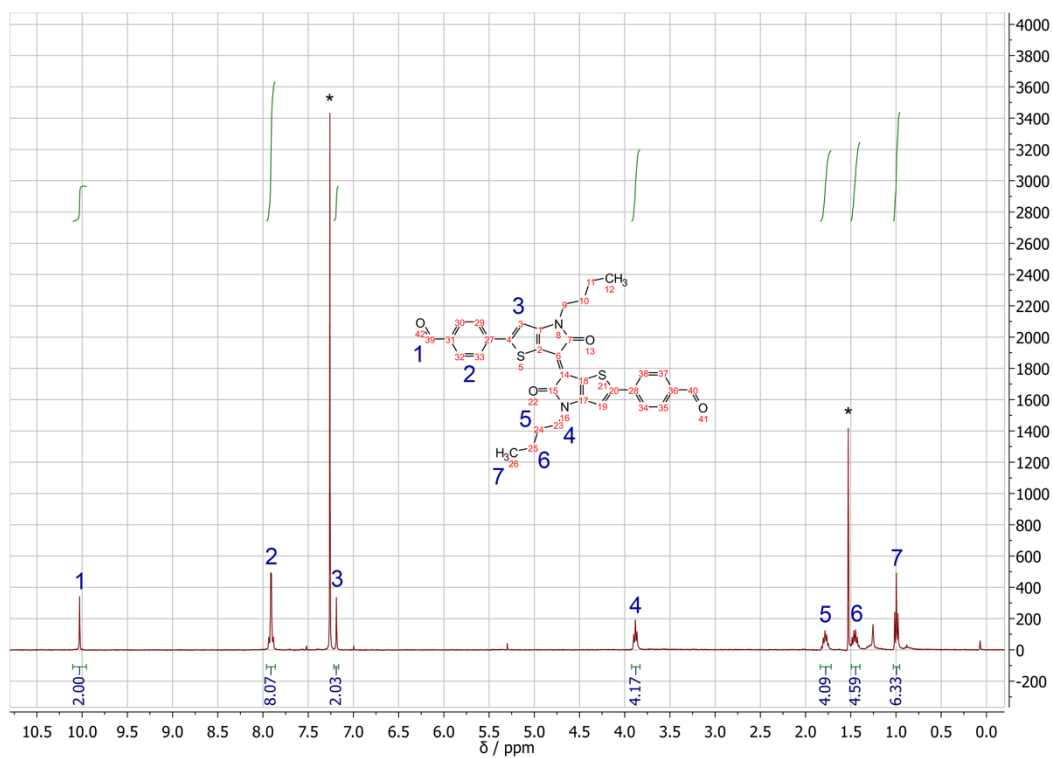
^1H and ^{13}C NMR spectra. Residual (undeuterated) solvent peaks and $\text{H}_2\text{O}/\text{HDO}$ are marked with asterisks.

pH

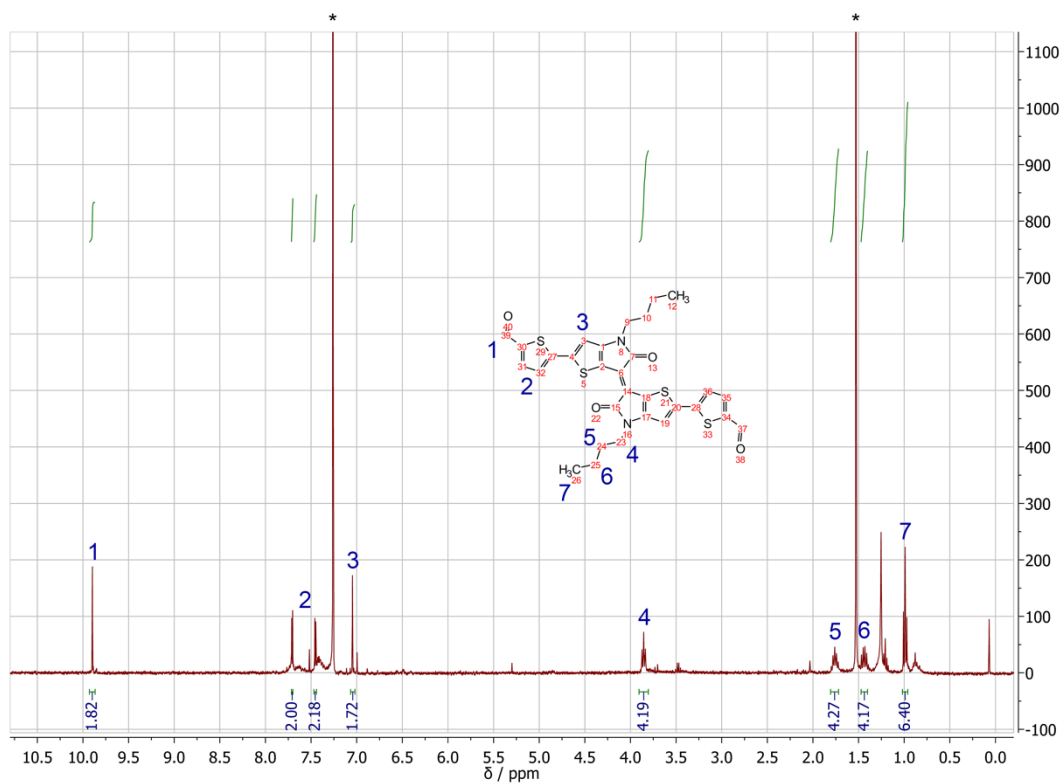


3 Spectrally Switchable Photodetection with Near-Infrared-Absorbing Covalent Organic Frameworks

pTH

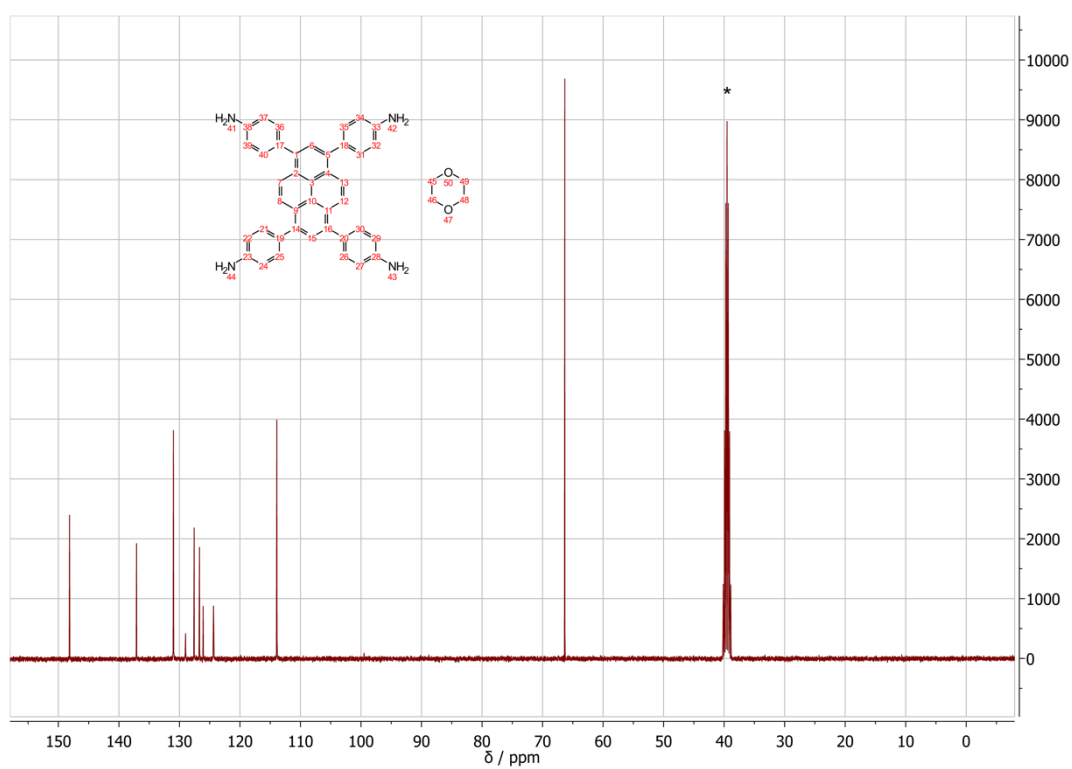
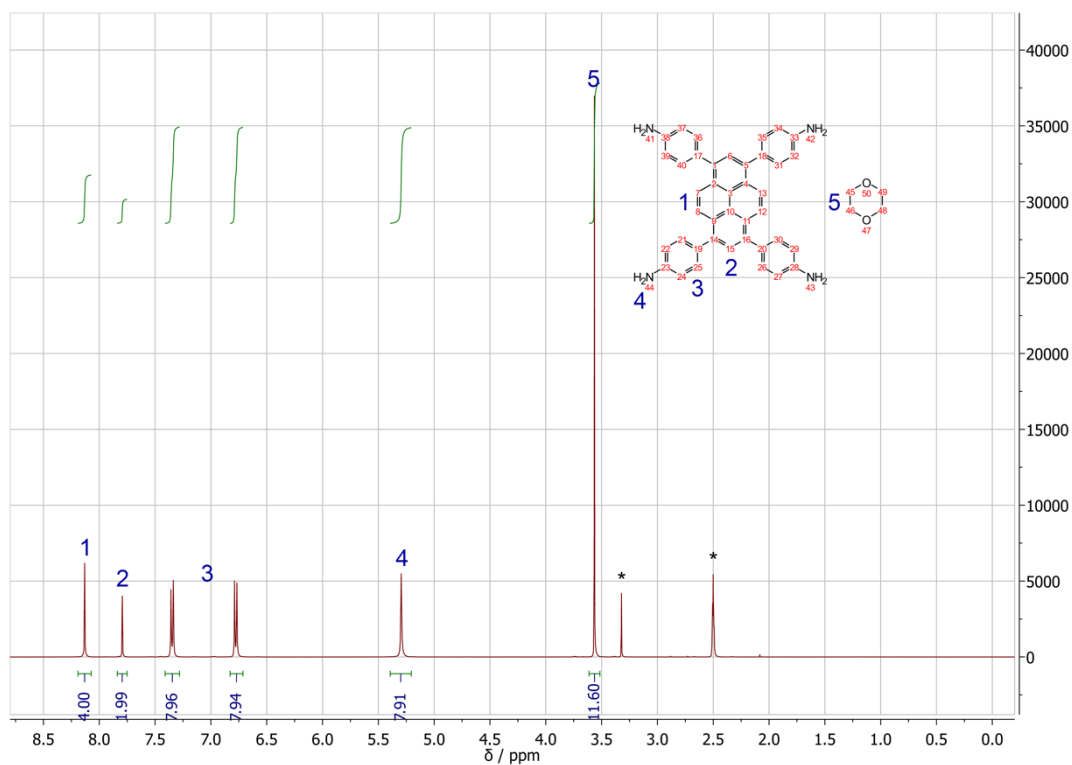


tTH



3 Spectrally Switchable Photodetection with Near-Infrared-Absorbing Covalent Organic Frameworks

Py



Section E – HRMS analysis of the building blocks

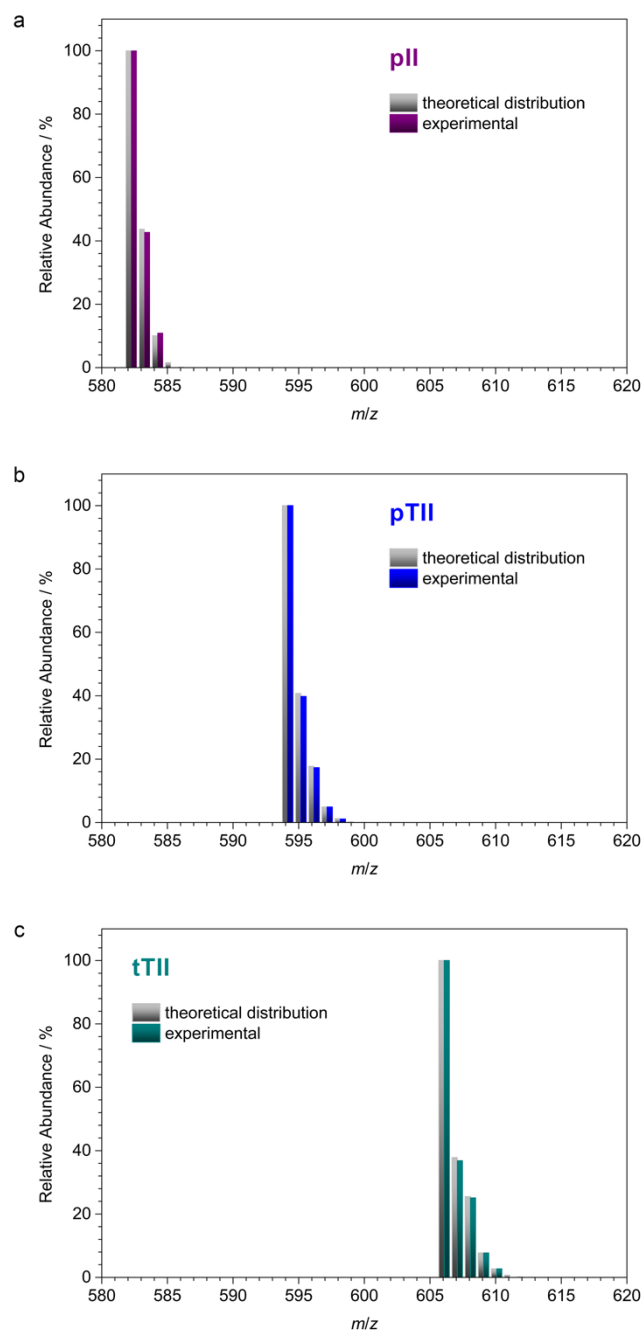


Figure 3.7. Comparison between the theoretical (gray) and the experimental (colored) HR-EI-MS patterns of the three isoidindigo-derived building blocks. The patterns correspond to the respective single positively charged molecules (M^+).

Section F – IR spectroscopy

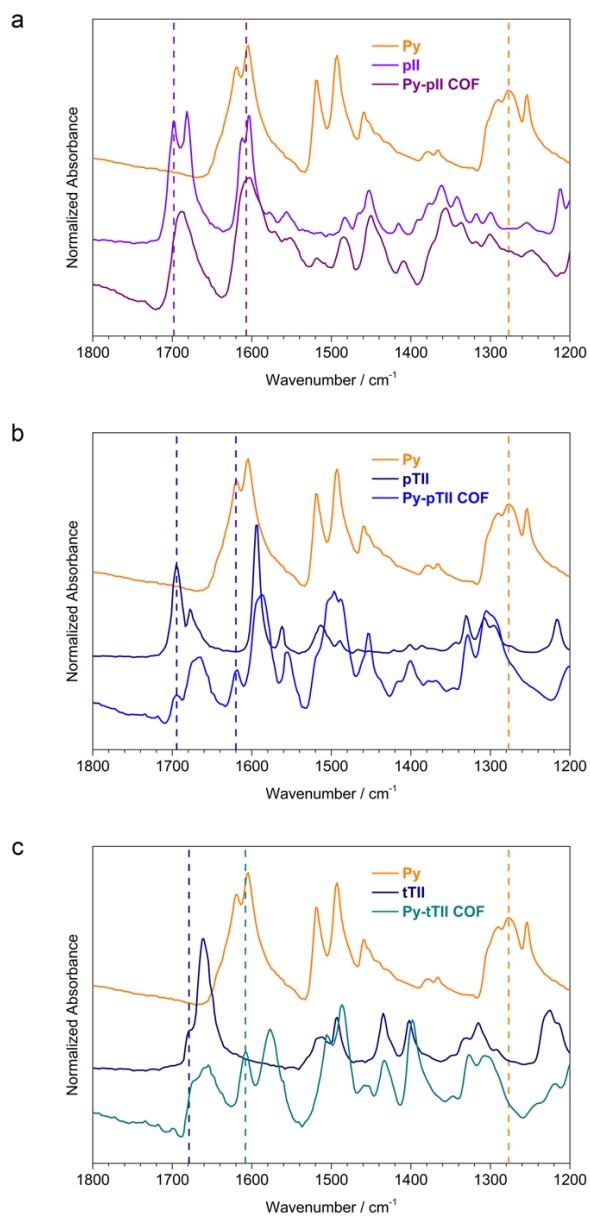


Figure 3.8. IR spectra of the building blocks and COFs.

	Wavenumber / cm^{-1}	Assignment
Py	1277	C-N stretching
pII	1698	C=O stretching
Py-pII COF	1607	C=N stretching
pTII	1695	C=O stretching
Py-pTII COF	1620	C=N stretching
tTII	1679	C=O stretching
Py-tTII COF	1608	C=N stretching

Section G – UV-VIS spectroscopy

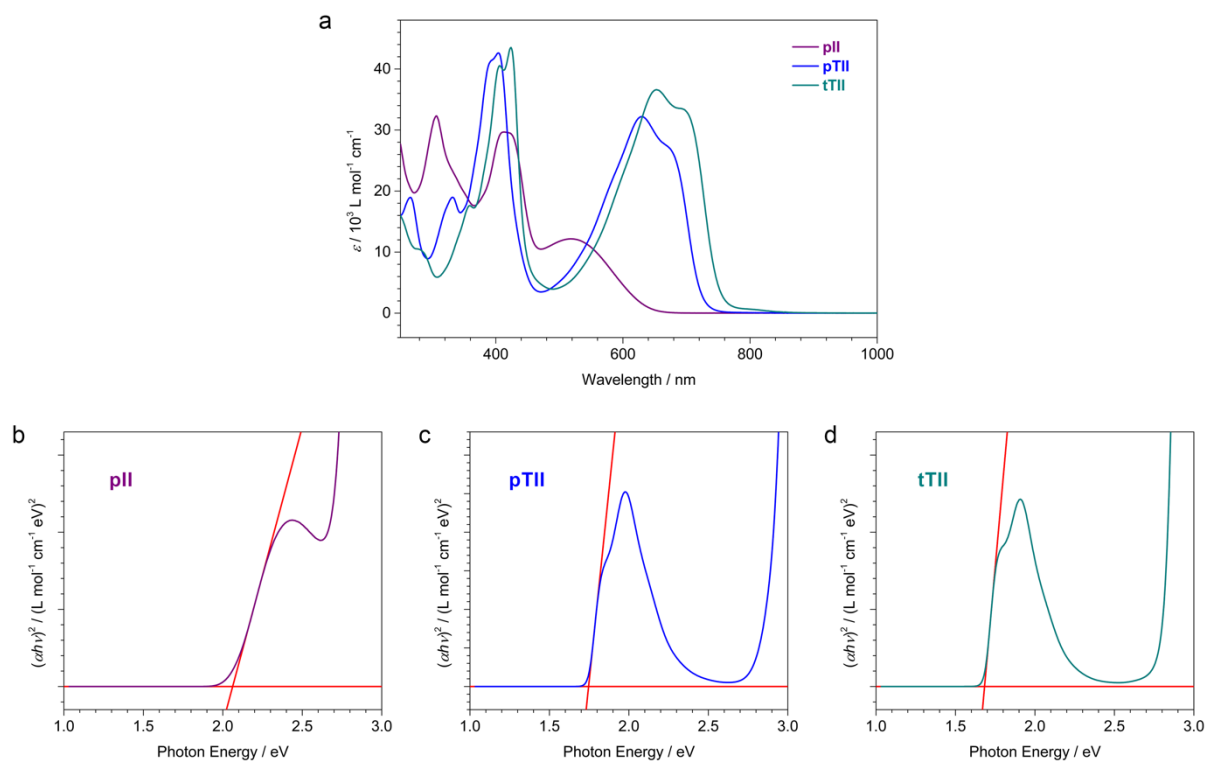


Figure 3.9. (a) UV-vis-NIR absorption spectra of the isoindigo and thienoisoindigo building blocks dissolved in chloroform. (b-d) The corresponding Tauc plots for direct optical band gaps, with linear fits to their respective absorption edges.

3 Spectrally Switchable Photodetection with Near-Infrared-Absorbing Covalent Organic Frameworks

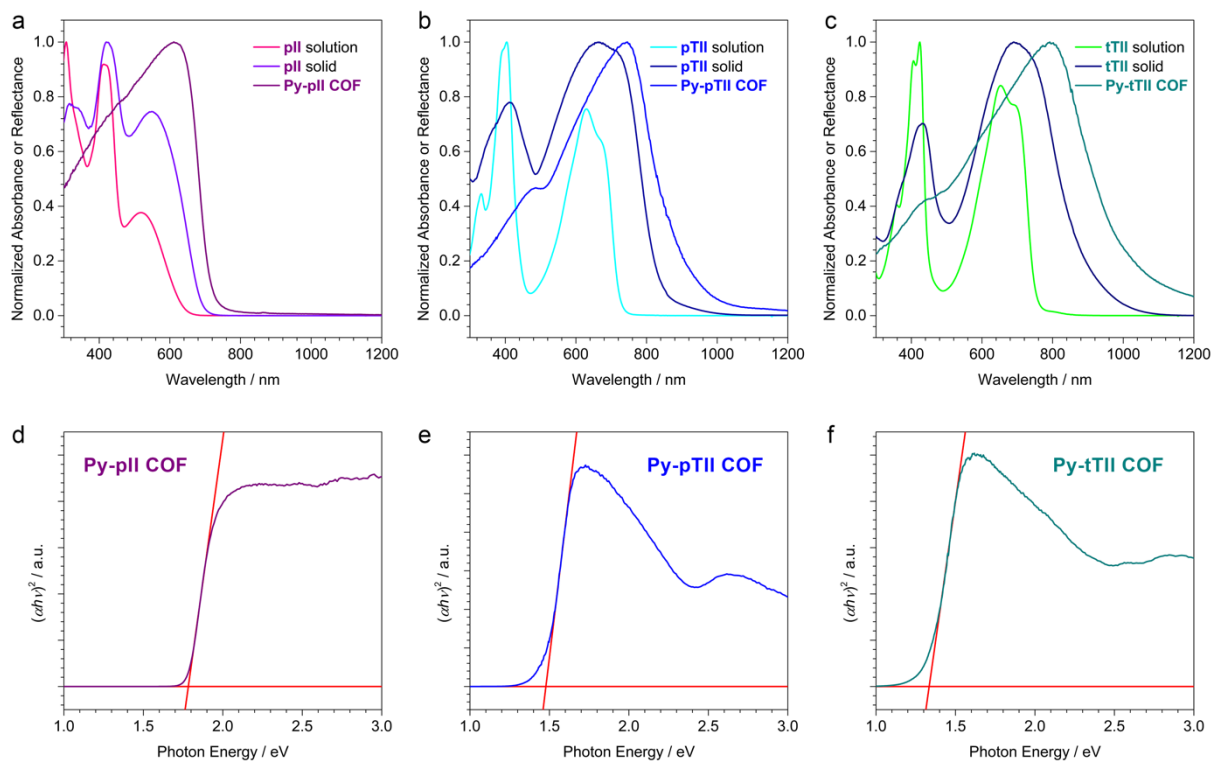


Figure 3.10. (a-c) Comparison of the absorption and diffuse reflectance spectra (in Kubelka-Munk units) of the COFs and the respective building blocks in chloroform solution and as solids. (d-f) The Tauc plots of the COFs assuming direct optical band gaps, with linear fits to their respective absorption edges.

Section H – GISAXS analysis of the COF thin film

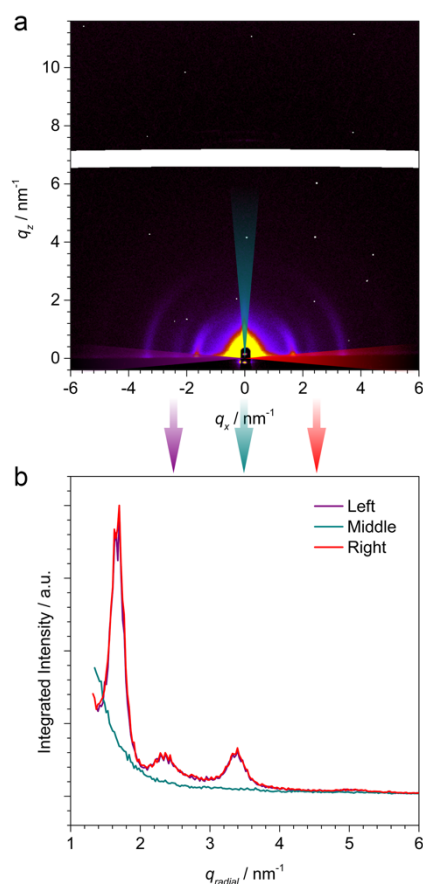


Figure 3.11. (a) GISAXS pattern of a **Py-tTH COF** film grown on ITO/MoO_x. (b) Radial integration over the purple, green, and red segments (10° opening) shows that most of the intensity of the 110, 020 and 200, 220, and 330 reflections appears directly above the sample horizon (purple and red lines). The intensity of these *hk0* reflections is below the noise level in the segment perpendicular to the sample horizon (green line), confirming the distinct texture of the COF.

Section I – Additional device data

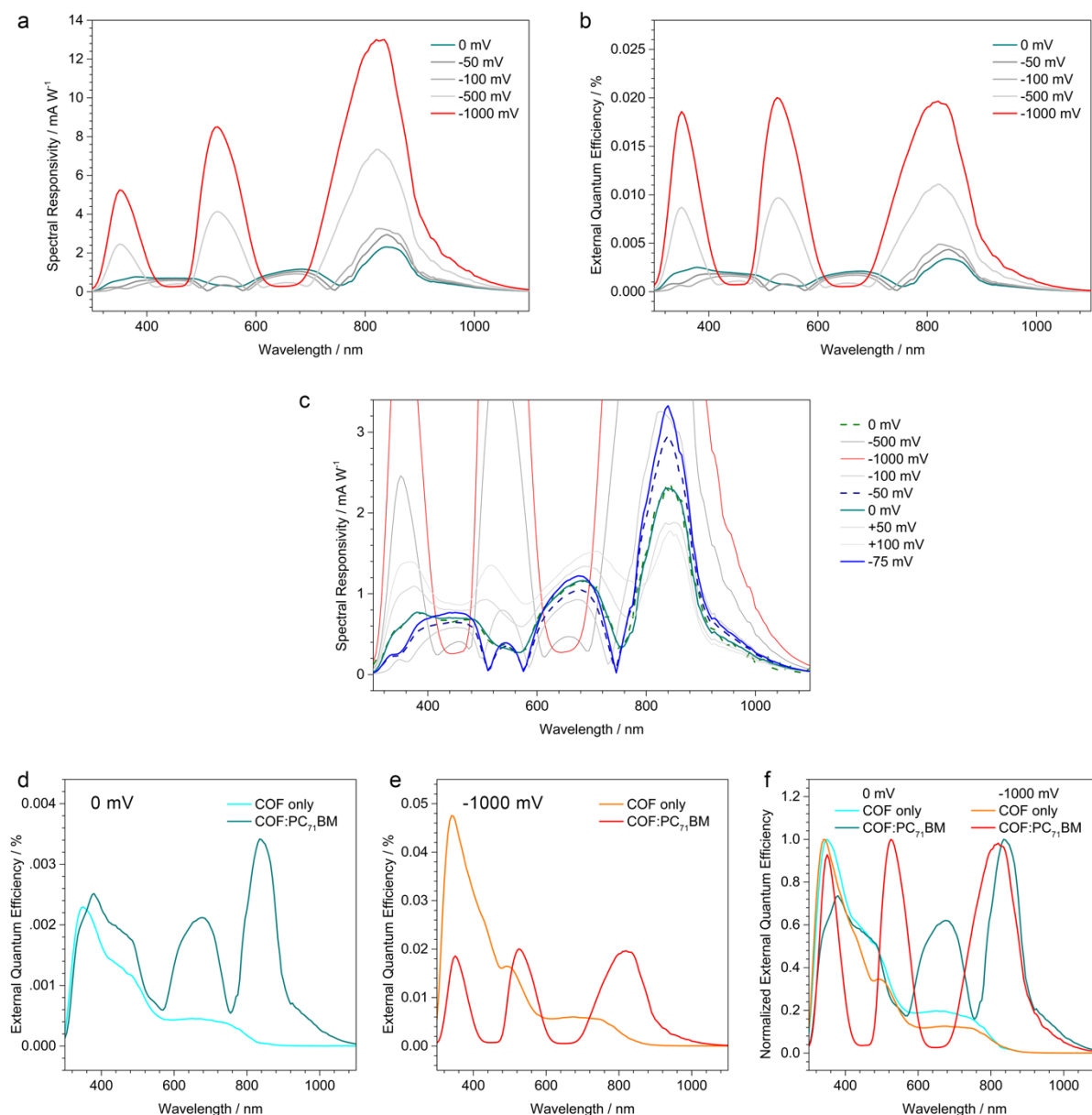


Figure 3.12. (a,b) Spectral responsivity and EQE spectra of the **Py-tTH COF**-based photodetector at various bias voltages. (c) The bias-dependent spectral responsivity measurements in chronological order: 0 mV bias \rightarrow -500 mV \rightarrow -1000 mV \rightarrow -100 mV \rightarrow -50 mV \rightarrow 0 mV \rightarrow +50 mV \rightarrow +100 mV \rightarrow -75 mV. The reversibility of the spectral changes is best apparent when comparing the two curves recorded at 0 mV (green dashed and solid lines), and the spectra recorded at -50 mV and -75 mV (blue dashed and solid lines). (d,e) Comparison between the EQE spectra of the COF:PC₇₁BM photodetector and a PC₇₁BM-free, otherwise identical device under short-circuit conditions and at 1000 mV reverse bias, respectively. The formation of an interdigitated COF:PC₇₁BM heterojunction boosts the device efficiency particularly in the red-to-NIR region that is dominated by the **tTH** ICT band absorption (dark green and red lines), indicating that the PC₇₁BM acceptor phase is vital for exciton splitting and electron transport. This finding provides strong evidence for the successful infiltration of the PC₇₁BM throughout the entire COF film. (f) Normalized representation of the EQE spectra at short-circuit and under reverse bias. In contrast to the COF:PC₇₁BM device (green and red lines), the spectral sensitivity profile of the COF-only device is almost bias-independent (cyan and orange lines).

Section J – Optical modelling

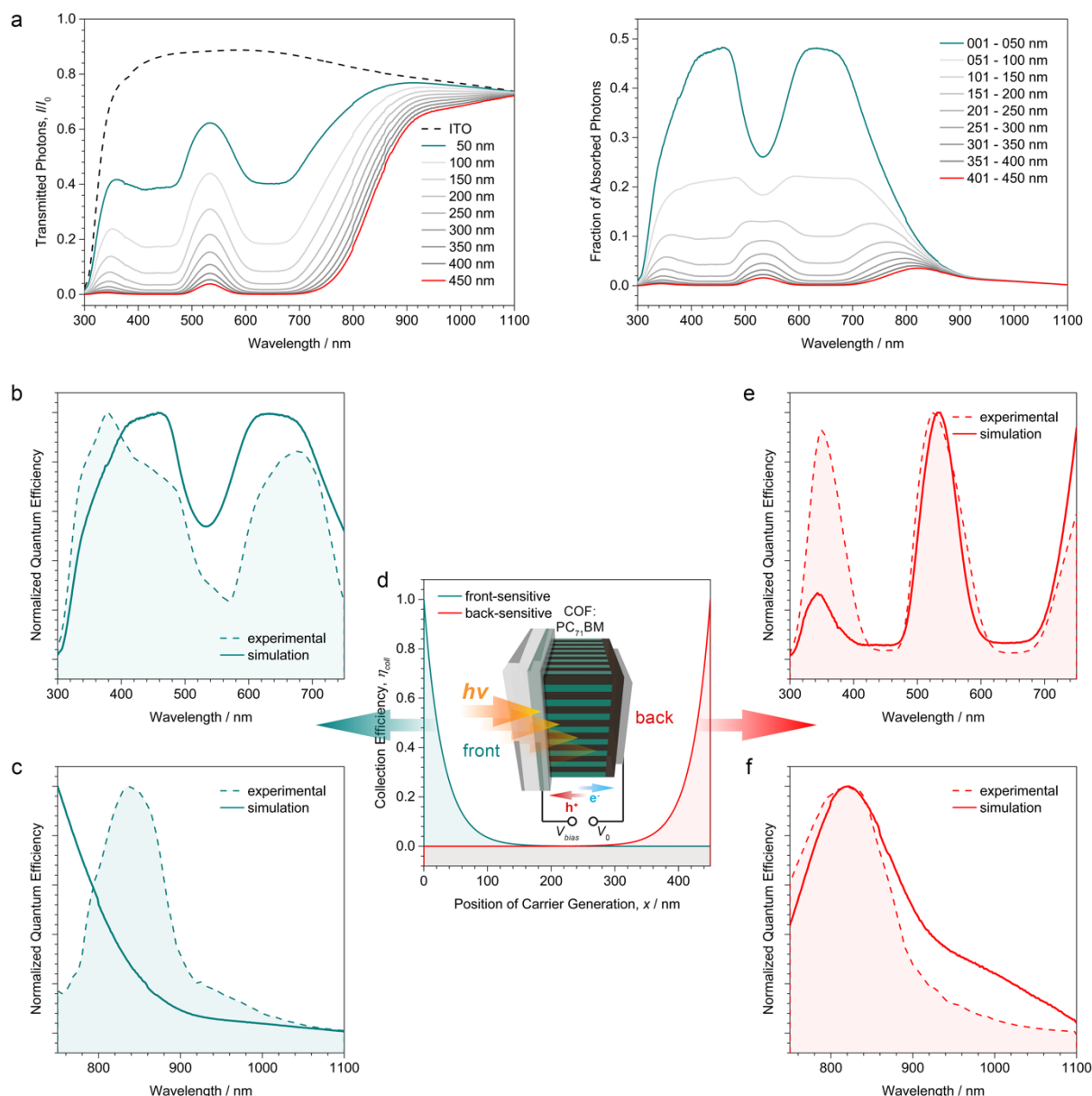


Figure 3.13 (a) Left, the simulated light intensity throughout the active layer, and right, the corresponding fraction of photons absorbed in the respective slices. (b,c) Comparison of the EQE spectra simulated for a front-sensitive device with the experimental EQE spectrum recorded at 0 mV bias. (d) The collection efficiency profiles used for the simulations of the EQE spectra. Inset, illustration of the **Py-tTH COF**-based photodetector. (e,f) Comparison of the simulated EQE spectra of a back-sensitive device with the experimental EQE spectrum recorded at -1000 mV bias.

The conversion of incident light into a measurable current relies on a series of processes:

- (1) An incident photon needs to be absorbed inside the active layer by either the COF or the PC₇₁BM, producing the initial photoexcited state.
- (2) An electron-hole pair must be generated from this photoexcitation.
- (3) Both charge carriers need to diffuse to the respective selective electrodes (in our device layout holes to the front, electrons to the back electrode). The

probability $\eta(\lambda, x)$ for a photon of wavelength λ to be converted at the depth x within the active layer into a measurable current can therefore be described as

$$\eta(\lambda, x) = \eta_{abs}(\lambda, x)\eta_{gen}\eta_{coll}(x)$$

(1) The absorption efficiency $\eta_{abs}(\lambda, x)$ depends on the absorption coefficient and the light intensity at the respective position. Assuming the light reflection at internal interfaces in the device to be negligible, and not taking into account the light reflection at the back electrode (the device is optically thick over a wide spectral range), the light intensity $I(\lambda, x)$ is given by the Beer-Lambert law

$$I(\lambda, x) = I_{ITO} 10^{-\alpha(\lambda)x}$$

Here, I_{ITO} is the light intensity after passing the ITO front electrode, and $\alpha(\lambda)$ is the extinction coefficient per unit thickness, derived from absorption spectroscopy (Figure 3.13a). We thus can express $\eta_{abs}(\lambda, x)$ as

$$\eta_{abs}(\lambda, x) = I(x)(1 - 10^{-\alpha(\lambda)x})$$

(2) The carrier pair generation efficiency η_{gen} is assumed to be constant throughout the active layer, and to be wavelength-independent in a first approximation.

(3) The collection efficiency $\eta_{coll}(x)$, however, depends on where inside the active layer the carrier pair has been generated. For charge carrier pairs created close to the front electrode, the hole needs to diffuse only a short distance in order to be collected at the front electrode. For each collected hole, an electron travels through the active layer and is collected at the back electrode. If the charge carrier pair is generated at the back of the active layer, the transport distance is relatively short for the electron, whereas the hole can make its way through the active layer to the front electrode before getting trapped or recombining.

A non-uniform collection efficiency throughout the active layer indicates an imbalance in the mobility-lifetime products of electrons and holes, whereby the device is limited by the species that need to be generated closer to their respective electrode in order to be collected efficiently (i.e. front-sensitive: holes, back-sensitive: electrons). Such limits might be due to trapping and recombination inside the active layer, or could be caused by barriers at the electrodes that impede extraction.

We treat $\eta_{coll}(x)$ as wavelength-independent over wavelength ranges where the device physics is not expected to change considerably. The transition from the 300 – 750 nm range, in which both components of the heterojunction can be photoexcited, to the 750 – 1100 nm range, in

which only the COF absorbs light, however, represents a significant change. We thus treat these wavelength ranges individually throughout the following discussion.

The external quantum efficiency (EQE) is defined as the fraction of collected charge carrier pairs per incident photon.

$$EQE(\lambda) = \frac{n_e}{n_{ph}(\lambda)}$$

Following the above considerations, we can express the EQE as the sum of $\eta(\lambda, x)$ over the thickness of the active layer.

$$EQE(\lambda) = \sum_{x=0 \text{ nm}}^{x=450 \text{ nm}} \eta_{abs}(\lambda, x) \eta_{gen} \eta_{coll}(x)$$

and

$$EQE(\lambda) \propto \sum_{x=0 \text{ nm}}^{x=450 \text{ nm}} \eta_{abs}(\lambda, x) \eta_{coll}(x)$$

This proportionality allows us to draw conclusions about where the majority of collected charge carriers are generated under short-circuit and reverse bias conditions.

Since in most organic heterojunctions the collection efficiency drops with increasing distance from the electrodes, we simulated the two extreme cases of front-sensitive ($\eta_{coll}(x)$ drops exponentially with distance from the hole-selective front electrode) and back-sensitive devices ($\eta_{coll}(x)$ drops exponentially with distance from the electron-selective back contact) (Figure 3.13d).

A comparison between the simulated and experimental EQE spectra suggests that across the 300 – 750 nm range, the **Py-fTH-COF**:PC₇₁BM-based photodetector is front-sensitive without external bias (Figure 3.13b), and becomes increasingly back-sensitive as the reverse bias is applied. At –1000 mV, the collected charge carriers seem to originate almost exclusively from a thin region at the back of the device, whereas all charge carrier pairs originating from the rest of the active layer recombine before they can be collected at the electrodes (Figure 3.13e). The device is thus most efficient at wavelengths where the absorption is low and enough photons are available at the back of the active layer, resulting in an inversion of the sensitivity profile of the photosensor.

The same considerations apply for the 750 – 1100 nm range. We find, however, that in this wavelength region, the device is back-sensitive regardless of the applied bias (Figures 3.13c,

f). The observed sensitivity peak results from the balance between light availability at the back of the device and light absorption (Figure 3.13a, right).

Differences between the experimental and the simulated EQE spectra are mainly due to the simplifications made in our model, in particular the assumption of a wavelength-independent generation efficiency and neglecting reflected light.

3.6 References

- [1] A. P. Côte, A. I. Benin, N. W. Ockwig, M. O'Keeffe, A. J. Matzger, O. M. Yaghi, *Science* **2005**, *310*, 1166-1170.
- [2] F. J. Uribe-Romo, J. R. Hunt, H. Furukawa, C. Klöck, M. O'Keeffe, O. M. Yaghi, *J. Am. Chem. Soc.* **2009**, *131*, 4570-4571.
- [3] D. Beaudoin, T. Maris, J. D. Wuest, *Nature Chem.* **2013**, *5*, 830-834.
- [4] E. L. Spitler, W. R. Dichtel, *Nature Chem.* **2010**, *2*, 672-677.
- [5] S. Duhović, M. Dincă, *Chem. Mater.* **2015**, *27*, 5487-5490.
- [6] N. Huang, X. Ding, J. Kim, H. Ihee, D. Jiang, *Angew. Chem. Int. Ed.* **2015**, *54*, 8704-8707.
- [7] Q. Fang, Z. Zhuang, S. Gu, R. B. Kaspar, J. Zheng, J. Wang, S. Qiu, Y. Yan, *Nature Commun.* **2014**, *5*, 4503.
- [8] M. G. Rabbani, A. K. Sekizkardes, Z. Kahveci, T. E. Reich, R. Ding, H. M. El-Kaderi, *Chem. Eur. J.* **2013**, *19*, 3324-3328.
- [9] M. Calik, T. Sick, M. Dogru, M. Döblinger, S. Datz, H. Budde, A. Hartschuh, F. Auras, T. Bein, *J. Am. Chem. Soc.* **2016**, *138*, 1234-1239.
- [10] S. Lin, C. S. Diercks, Y.-B. Zhang, N. Kornienko, E. M. Nichols, Y. Zhao, A. R. Paris, D. Kim, P. Yang, O. M. Yaghi, C. J. Chang, *Science* **2015**, *349*, 1208-1213.
- [11] H. Furukawa, O. M. Yaghi, *J. Am. Chem. Soc.* **2009**, *131*, 8875-8883.
- [12] D. B. Shinde, S. Kandambeth, P. Pachfule, R. R. Kumar, R. Banerjee, *Chem. Commun.* **2015**, *51*, 310-313.
- [13] V. S. Vyas, F. Haase, L. Stegbauer, G. Savasci, F. Podjaski, C. Ochsenfeld, B. V. Lotsch, *Nature Commun.* **2015**, *6*, 8508.
- [14] G. H. V. Bertrand, V. K. Michaelis, T.-C. Ong, R. G. Griffin, M. Dinca, *Proc. Natl. Acad. Sci. USA* **2013**, *110*, 4923-4928.
- [15] L. Chen, K. Furukawa, J. Gao, A. Nagai, T. Nakamura, Y. Dong, D. Jiang, *J. Am. Chem. Soc.* **2014**, *136*, 9806-9809.
- [16] N. Keller, D. Bessinger, S. Reuter, M. Calik, L. Ascherl, F. C. Hanusch, F. Auras, T. Bein, *J. Am. Chem. Soc.* **2017**, *139*, 8194-8199.
- [17] F. Auras, L. Ascherl, A. H. Hakimioun, J. T. Margraf, F. C. Hanusch, S. Reuter, D. Bessinger, M. Döblinger, C. Hettstedt, K. Karaghiosoff, S. Herbert, P. Knochel, T. Clark, T. Bein, *J. Am. Chem. Soc.* **2016**, *138*, 16703-16710.
- [18] L. Ascherl, T. Sick, J. T. Margraf, S. H. Lapidus, M. Calik, C. Hettstedt, K. Karaghiosoff, M. Döblinger, T. Clark, K. W. Chapman, F. Auras, T. Bein, *Nature Chem.* **2016**, *8*, 310-316.

- [19] D. D. Medina, V. Werner, F. Auras, R. Tautz, M. Dogru, J. Schuster, S. Linke, M. Döblinger, J. Feldmann, P. Knochel, T. Bein, *ACS Nano* **2014**, *8*, 4042-4052.
- [20] S. Jin, M. Supur, M. Addicoat, K. Furukawa, L. Chen, T. Nakamura, S. Fukuzumi, S. Irle, D. Jiang, *J. Am. Chem. Soc.* **2015**, *137*, 7817-7827.
- [21] D. D. Medina, M. L. Petrus, A. N. Jumabekov, J. T. Margraf, S. Weinberger, J. M. Rotter, T. Clark, T. Bein, *ACS Nano* **2017**, *11*, 2706-2713.
- [22] M. Dogru, M. Handloser, F. Auras, T. Kunz, D. Medina, A. Hartschuh, P. Knochel, T. Bein, *Angew. Chem. Int. Ed.* **2013**, *52*, 2920-2924.
- [23] M. Calik, F. Auras, L. M. Salonen, K. Bader, I. Grill, M. Handloser, D. D. Medina, M. Dogru, F. Löbermann, D. Trauner, A. Hartschuh, T. Bein, *J. Am. Chem. Soc.* **2014**, *136*, 17802-17807.
- [24] J. Guo, Y. Xu, S. Jin, L. Chen, T. Kaji, Y. Honsho, M. A. Addicoat, J. Kim, A. Saeki, H. Ihee, S. Seki, S. Irle, M. Hiramoto, D. Jiang, *Nature Commun.* **2013**, *4*, 2736.
- [25] J. Peet, J. Y. Kim, N. E. Coates, W. L. Ma, D. Moses, A. J. Heeger, G. C. Bazan, *Nature Mater.* **2007**, *6*, 497-500.
- [26] M. S. Chen, J. R. Niskala, D. A. Unruh, C. K. Chu, O. P. Lee, J. M. J. Fréchet, *Chem. Mater.* **2013**, *25*, 4088-4096.
- [27] W. Yue, R. S. Ashraf, C. B. Nielsen, E. Collado-Fregoso, M. R. Niazi, S. A. Yousaf, M. Kirkus, H.-Y. Chen, A. Amassian, J. R. Durrant, I. McCulloch, *Adv. Mater.* **2015**, *27*, 4702-4707.
- [28] G. Kim, S.-J. Kang, G. K. Dutta, Y.-K. Han, T. J. Shin, Y.-Y. Noh, C. Yang, *J. Am. Chem. Soc.* **2014**, *136*, 9477-9483.
- [29] I. Meager, M. Nikolka, B. C. Schroeder, C. B. Nielsen, M. Planells, H. Bronstein, J. W. Rumer, D. I. James, R. S. Ashraf, A. Sadhanala, P. Hayoz, J.-C. Flores, H. Sirringhaus, I. McCulloch, *Adv. Funct. Mater.* **2014**, *24*, 7109-7115.
- [30] M. Matsumoto, R. R. Dasari, W. Ji, C. H. Feriante, T. C. Parker, S. R. Marder, W. R. Dichtel, *J. Am. Chem. Soc.* **2017**, *139*, 4999-5002.
- [31] R. Stalder, J. Mei, J. R. Reynolds, *Macromolecules* **2010**, *43*, 8348-8352.
- [32] Y. K. Voronina, D. B. Krivolapov, A. V. Bogdanov, V. F. Mironov, I. A. Litvinov, *J. Struct. Chem* **2012**, *53*, 413-416.
- [33] X. Chen, N. Huang, J. Gao, H. Xu, F. Xu, D. Jiang, *Chem. Commun.* **2014**, *50*, 6161-6163.
- [34] Y. Wu, H. Xu, X. Chen, J. Gao, D. Jiang, *Chem. Commun.* **2015**, *51*, 10096-10098.
- [35] M. S. Lohse, J. M. Rotter, J. T. Margraf, V. Werner, M. Becker, S. Herbert, P. Knochel, T. Clark, T. Bein, D. D. Medina, *CrystEngComm* **2016**, *18*, 4295-4302.

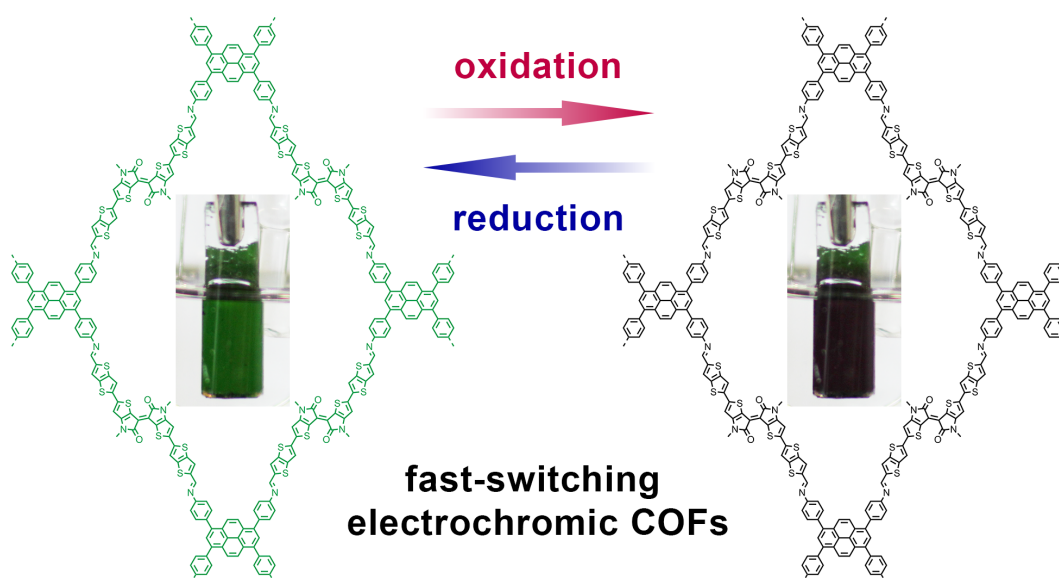
- [36] T. Düren, F. Millange, G. Férey, K. S. Walton, R. Q. Snurr, *J. Phys. Chem. C* **2007**, *111*, 15350-15356.
- [37] G. W. P. Van Pruissen, F. Gholamrezaie, M. M. Wienk, R. A. J. Janssen, *J. Mater. Chem.* **2012**, *22*, 20387.
- [38] G. K. Dutta, A.-R. Han, J. Lee, Y. Kim, J. H. Oh, Y. Changduk, *Adv. Funct. Mater.* **2013**, *23*, 5317-5325.
- [39] Y. Li, F. Auras, F. Löbermann, M. Döblinger, J. Schuster, L. Peter, D. Trauner, T. Bein, *J. Am. Chem. Soc.* **2013**, *135*, 18513-18519.
- [40] M. Kubo, T. Kaji, M. Hiramoto, *AIP Adv.* **2011**, *1*, 032177.
- [41] J. Mei, K. R. Graham, R. Stalder, J. R. Reynolds, *Org. Lett.* **2010**, *12*, 660-663.
- [42] J. Yang, S. Liu, J.-F. Zheng, J. S. Zhou, *Eur. J. Org. Chem.* **2012**, 6248-6259.
- [43] Y. Koizumi, M. Ide, A. Saeki, C. Vijayakumar, B. Balan, M. Kawamotoa, S. Seki, *Polym. Chem.* **2013**, *4*, 484-494.
- [44] M. Karakawa, Y. Aso, *Macromol. Chem. Phys.* **2013**, *214*, 2388-2397.
- [45] J. Grolleau, P. Frère, F. Gohier, *Synthesis* **2015**, *47*, 3901-3906.
- [46] S. Jin, T. Sakurai, T. Kowalczyk, S. Dalapati, F. Xu, H. Wei, X. Chen, J. Gao, S. Seki, S. Irle, D. Jiang, *Chem. Eur. J.* **2014**, *20*, 14608-14613.

4 Fast-Switching Vis-IR Electrochromic Covalent Organic Frameworks

This chapter is based on the following publication:

Derya Bessinger, Katharina Muggli, Michael Beetz, Florian Auras*, and Thomas Bein*

J. Am. Chem. Soc. **2021**, *143*, 7351–7357



Copyright 2021, Derya Bessinger, Katharina Muggli, Michael Beetz, Florian Auras, and Thomas Bein

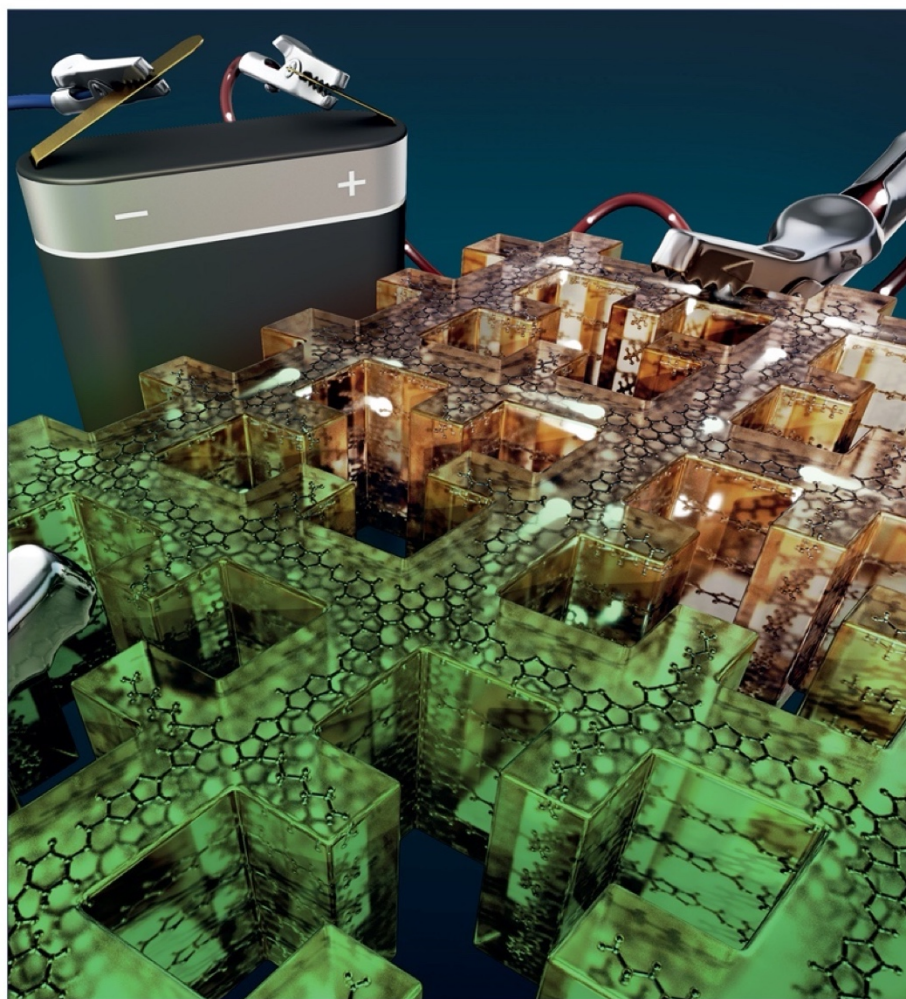
* corresponding authors

The article was published with the Supplementary Cover Art in issue 19 from May 2021.

May 19, 2021
Volume 143
Number 19
pubs.acs.org/JACS

J | A | C | S

JOURNAL OF THE AMERICAN CHEMICAL SOCIETY



 ACS Publications
Most Trusted. Most Cited. Most Read.

www.acs.org

Cover artwork: Vera Hiendl (e-conversion cluster)

based on an idea of F. Auras, D. Bessinger, and V. Hiendl

4.1 Abstract

Electrochromic coatings are promising for applications in smart windows or energy-efficient optical displays. However, classical inorganic electrochromic materials such as WO_3 suffer from low coloration efficiency and slow switching speed. We have developed highly efficient and fast-switching electrochromic thin films based on fully organic, porous covalent organic frameworks (COFs). The low-bandgap COFs have strong Vis-NIR absorption bands in the neutral state, which shift significantly upon electrochemical oxidation. Fully reversible absorption changes by close to 3 OD can be triggered at low operating voltages and low charge per unit area. Our champion material reaches an electrochromic coloration efficiency of $858 \text{ cm}^2 \text{ C}^{-1}$ at 880 nm and retains >95% of its electrochromic response over 100 oxidation/reduction cycles. Furthermore, the electrochromic switching is extremely fast with response times below 0.4 s for the oxidation and around 0.2 s for the reduction, outperforming previous COFs by at least an order of magnitude and rendering these materials some of the fastest-switching frameworks to date. This combination of high coloration efficiency and very fast switching reveals intriguing opportunities for applications of porous organic electrochromic materials.

4.2 Introduction

Since their first development in 2005, covalent organic frameworks (COFs) have emerged into a very active research field of tailor-made functional nanostructures.^[1-3] Constructed from rigid organic building blocks, COFs combine high crystallinity with a precisely defined porosity and large internal surface area.^[4-6] A wide range of functional building blocks enable the design of bespoke networks with well-defined catalytic, optical and electronic properties.^[7-11]

Electrochromism describes reversible color changes of a material in response to an external electronic stimulus. Electrochromic materials have been applied in smart windows, optical displays, and molecular imaging.^[12-14] In addition to well-established inorganic electrochromic materials such as WO_3 , research focuses increasingly on organic molecular compounds and polymers.^[15-17] Organic materials offer higher coloration efficiencies and better tunability owing to their broad range of possible chemical modifications, while the higher diffusion rates of charge-compensating counterions allow for faster switching times.^[18, 19]

Due to their permanent porosity on a molecular length scale, every building block throughout a COF domain can be brought into contact with an electrolyte, enabling very fast and efficient electrochromic switching. However, first examples of electrochromic COFs based on triphenylamine dyes have not yet reached their full potential as they show only moderate coloration efficiencies and switching speeds.^[20, 21]

Here we present a series of fast-switching electrochromic 2D-COFs with panchromatic UV-Vis-IR response and high coloration efficiency. Key to this performance is our linker design strategy where we combine a central thienoisindigo moiety with more electron-rich units while fully retaining its favorable stacking interactions (Figure 1). This donor-acceptor-donor electronic setup promotes intramolecular charge transfer, leading to strong light absorption across the visible and near IR regions and an increased sensitivity of the absorption spectra towards electrochemical oxidation. COFs constructed from the new building blocks are highly crystalline frameworks with large one-dimensional pores for optimal accessibility of every building block throughout the material. Oriented COF thin films of the best-performing framework are stable over at least 200 oxidation/reduction cycles. They retain >95% of their electrochromic response over 100 cycles, show very rapid switching with response times below 0.4 s (oxidation) and around 0.2 s (reduction), and have coloration efficiencies of up to 858 cm² C⁻¹.

4.3 Results

In order to maximize the electrochromic response across the visible and near-infrared (NIR) spectral regions, we constructed building blocks with a donor-acceptor-donor (D-A-D) electronic configuration. This design not only provides a sufficiently small bandgap to push the absorption onset well into the NIR (Supporting Information, Figure 4.11), but also renders the charge-transfer (CT) and π - π^* transitions very sensitive to electronic changes such that significant electrochromic response can be expected over a wide spectral range.^[18, 22-24] We chose the highly electron-deficient thienoisindigo (TII) unit as the acceptor and combined it with the more electron-rich thienothiophene (TT) or naphthalene (N) donors, yielding the extended, NIR-absorbing ttTII(CHO)₂ and nTII(CHO)₂ building blocks, respectively (Figure 4.1). For comparison purposes, we also constructed the dicarboxaldehyde building blocks of the individual components (TII, TT, and N).

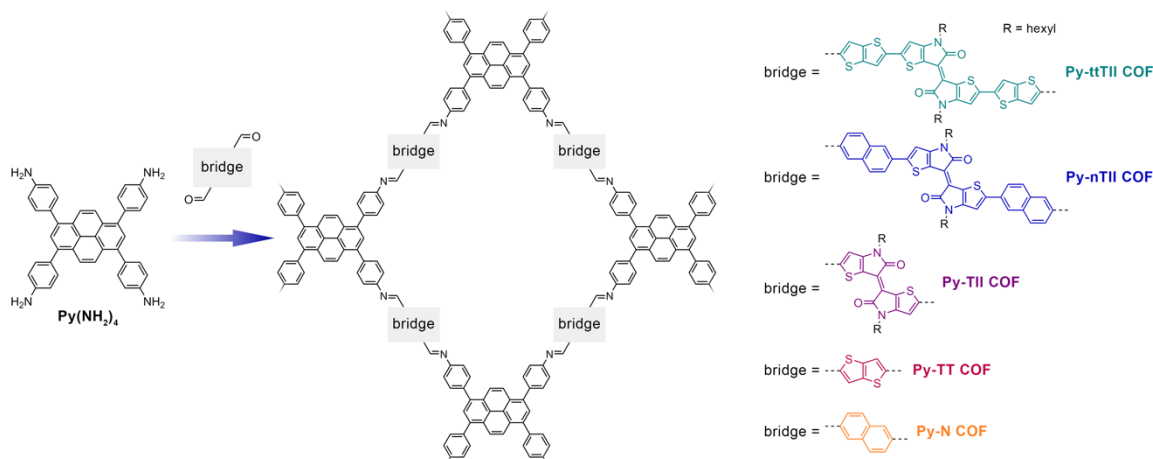


Figure 4.1. Construction of the new thienoisindigo COFs and the Py-TT and Py-N COF reference materials. The co-condensation of the linear dicarboxaldehydes with the pyrene tetraaniline yields a series of isostructural frameworks with a pseudosquare geometry and slip-stacked 2D layers.

For COF construction we selected the well-established pyrene tetraaniline (Py(NH₂)₄) as the tetradentate counterpart. This building block is known to generate exceptionally crystalline and stable 2D-COFs with a broad range of linear linkers and, most importantly, is compatible with heteroaromatic moieties where strong electrostatic interactions enforce slip-stacked arrangements.^[25-27] Moreover, the pyrene building block enables the synthesis of very well-oriented COF films on a variety of substrates.^[28, 29]

The Py-ttTII, Py-nTII, Py-TII, Py-TT, and Py-N COFs were synthesized under solvothermal conditions with aqueous acetic acid as the catalyst (see the SI, Section B for experimental details). The isorecticular COFs feature a pseudosquare geometry with slip-stacked 2D layers.

When synthesized as a bulk material, the Py-ttTII COF is a dark green powder. Its powder X-ray diffraction pattern exhibits a series of sharp reflections with only minimal background, confirming the formation of a highly crystalline framework (Figure 4.2a). Rietveld refinement carried out in the monoclinic space group *C2/m* and using the structure model shown in Figure 4.2b provides a very good fit to the experimental pattern. The refined lattice parameters are $a = 6.33 \pm 0.02$ nm, $b = 5.89 \pm 0.02$ nm, $c = 0.39 \pm 0.02$ nm, and $\beta = 60 \pm 5^\circ$. Due to the large number of atoms per unit cell and the inherent flexibility of the COF backbone and alkyl chains, it is not possible to refine individual atom positions. Thus, slight differences between the structure model and the actual COF structure are unavoidable, causing the deviations in intensity observed for some of the higher-index reflections.

4 Fast-Switching Vis-IR Electrochromic Covalent Organic Frameworks

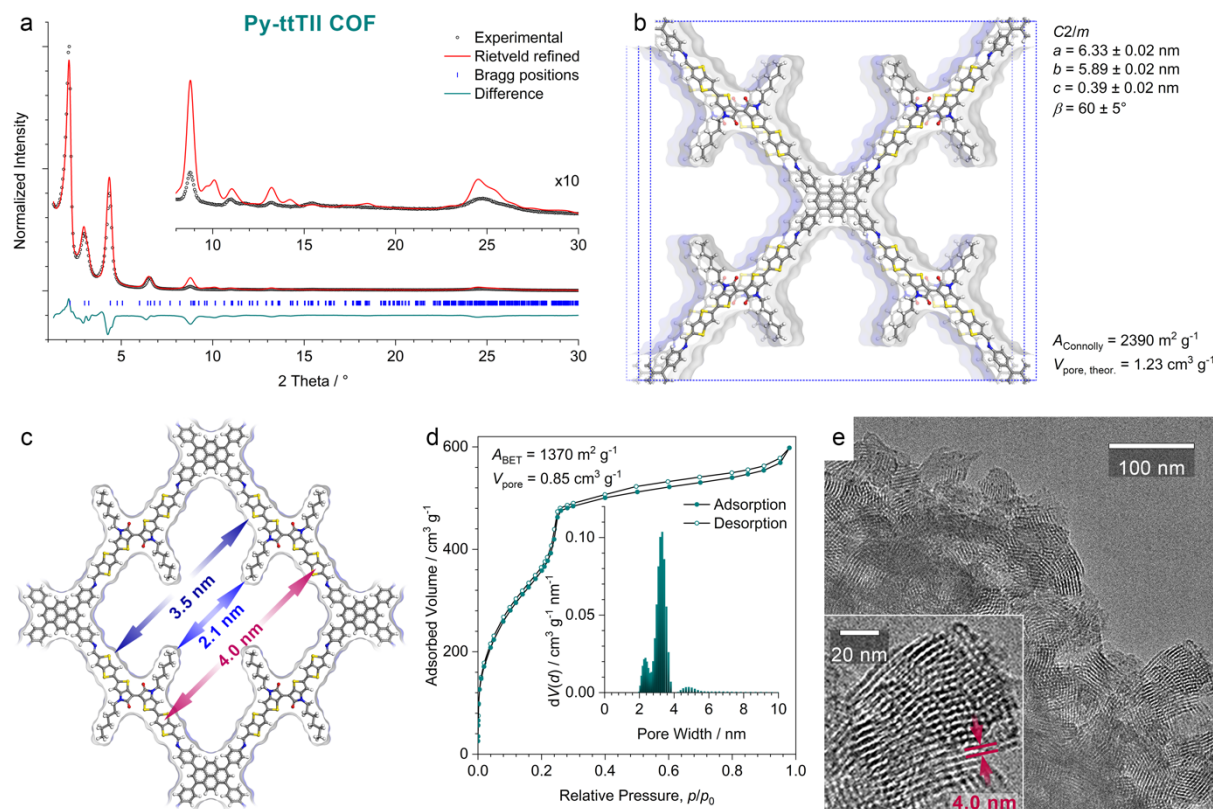


Figure 4.2. Structure analysis of the Py-ttTII COF. **(a)** Experimental PXRD pattern of the Py-ttTII COF bulk material (black dots). Rietveld refinement (red line) using the monoclinic (space group $C2/m$) structure model displayed in **(b)** provides a good fit with only minor differences between the experimental and refined patterns (green line) arising mainly from the flexibility of the alkyl chains. $R_{wp} = 12.3\%$, $R_p = 20.9\%$. Bragg positions are indicated by blue ticks. Inset: Magnified view of the $2\theta > 8^\circ$ region. **(b)** The Rietveld-refined structure model of the Py-ttTII COF viewed perpendicular to the crystallographic a - b plane. The COF has a pseudosquare geometry with slip-stacked layers. The structure is highly porous with a Connolly surface area of $2390 \text{ m}^2 \text{ g}^{-1}$ and a pore volume of $1.23 \text{ cm}^3 \text{ g}^{-1}$. **(c)** Illustration of the pore structure of the COF viewed along the c -axis. The structure refinement indicates that in this COF the alkyl chains extend relatively straight into the pores, producing a shamrock-shaped pore cross section. The wall-to-wall distances (blue arrows) are 2.1 nm and 3.5 nm including and excluding the alkyl chains, respectively. The periodicity of the COF in this orientation is 4.0 nm (red arrows). **(d)** Nitrogen sorption isotherm recorded at 77 K. Inset: Fitting the isotherm with a QSDFT equilibrium model for cylindrical pores produces a bimodal pore size distribution (PSD) with peaks at 2.3 nm and 3.4 nm. These values are in good agreement with the wall-to-wall distances including and excluding the alkyl chains derived from the refined structure model, confirming the shamrock-shaped pore cross section. **(e)** High-resolution TEM image of a Py-ttTII COF bulk powder sample showing crystallites of approximately 50 nm diameter. Inset: A crystallite viewed along the pores (i.e., along the crystallographic c -axis) showing a periodicity of 4.0 nm in excellent agreement with the structure model.

While the refinement of individual atoms is not possible, the data quality is sufficient to refine the overall orientation of the alkyl chains. In the case of the Py-ttTII COF, the alkyl chains were found to extend straight into the pores, creating a shamrock-shaped pore cross section with wall-to-wall distances of 3.5 nm and 2.1 nm without and with alkyl chains, respectively (Figure 4.2c). This configuration is very similar to the geometries found in molecular crystals of thienoisindigos with linear alkyl chains, and is further supported by gas sorption analysis (see below).^[30, 31]

The nitrogen sorption isotherm recorded at 77 K exhibits a type IVb isotherm shape with a sharp step at $p/p_0 = 0.24$, confirming the mesoporosity of the framework (Figure 4.2d).^[32] Analysis of the isotherm using the quenched solid density functional theory (QSDFT) method and an equilibrium model for cylindrical pores yields a bimodal pore size distribution (PSD). Bimodal PSDs have been observed previously for alkyl-containing COFs and are the result of the QSDFT method trying to describe a non-cylindrical pore shape.^[27] The maxima at 2.3 nm and 3.4 nm are in very good agreement with the wall-to-wall distances with and without alkyl chains, respectively, and further confirm the shamrock-shaped pore cross section with two predominant diagonals. The Py-ttTII COF has a Brunauer-Emmett-Teller (BET) surface area of $1370 \text{ m}^2 \text{ g}^{-1}$ with a total pore volume of $0.85 \text{ cm}^3 \text{ g}^{-1}$. The experimental surface area is about 60% of the Connolly surface area calculated from the idealized structure model. This reduction in porosity is frequently observed for alkyl-chain containing COFs and is mainly attributed to the enhanced trapping of oligomers due to the complex pore shape.^[27, 33] However, at 60% of the theoretical porosity, the accessibility throughout the framework is expected to be sufficient for efficient electrochemical switching (see below).

High-resolution transmission electron microscopy (TEM) images reveal the nanocrystalline morphology of the Py-ttTII COF powder with domain sizes of 50 – 100 nm (Figure 4.2e). Crystallites that are oriented with their crystallographic *c*-axis (i.e., along the pores) parallel to the viewing direction confirm the pseudo-square topology with a periodicity of 4.0 nm, which is in excellent agreement with the refined structure model.

The naphthalene-containing Py-nTII COF has a very similar structure and features the same shamrock-shaped pore cross section (SI, Figure 4.5). In contrast, due to the shorter TII(CHO)₂ building block, the alkyl chains of the Py-TII COF cannot extend straight into the pore, but are forced to collapse onto the pore walls (SI, Figures 4.6, 4.7). Hence, this COF has significantly narrower pores with a single maximum in the corresponding PSD. The Py-N and Py-TT COFs are highly crystalline frameworks with very similar overall topology but relatively small diamond-shaped pores (SI, Figure 4.9).^[28]

For the electrochemistry and spectroelectrochemistry experiments, oriented COF thin films were grown on transparent and conductive indium-tin-oxide (ITO) coated glass (Py-ttTII, Py-TII, Py-TT and Py-N COFs) or 10 nm Au on glass (Py-nTII COF) substrates using modified solvothermal protocols (see the SI, section B for details).

2D grazing-incidence wide-angle X-ray scattering (GIWAXS) measurements confirm that the COF films are crystalline and strongly textured (Figure 4.3a and SI, Figures 4.12, 4.13). For all COFs, the $hk0$ reflections show the highest intensity close to the sample horizon, indicating a preferred orientation of the a - b plane parallel to the substrate surface. Consistently, the intensity of the 001 and other low-index $hk1$ reflections is concentrated within a 60° segment centered at $q_x = 0 / q_z = 18 \text{ nm}^{-1}$. This preferential orientation is highly desired, as the COF pores extend towards the film surface and are fully accessible.

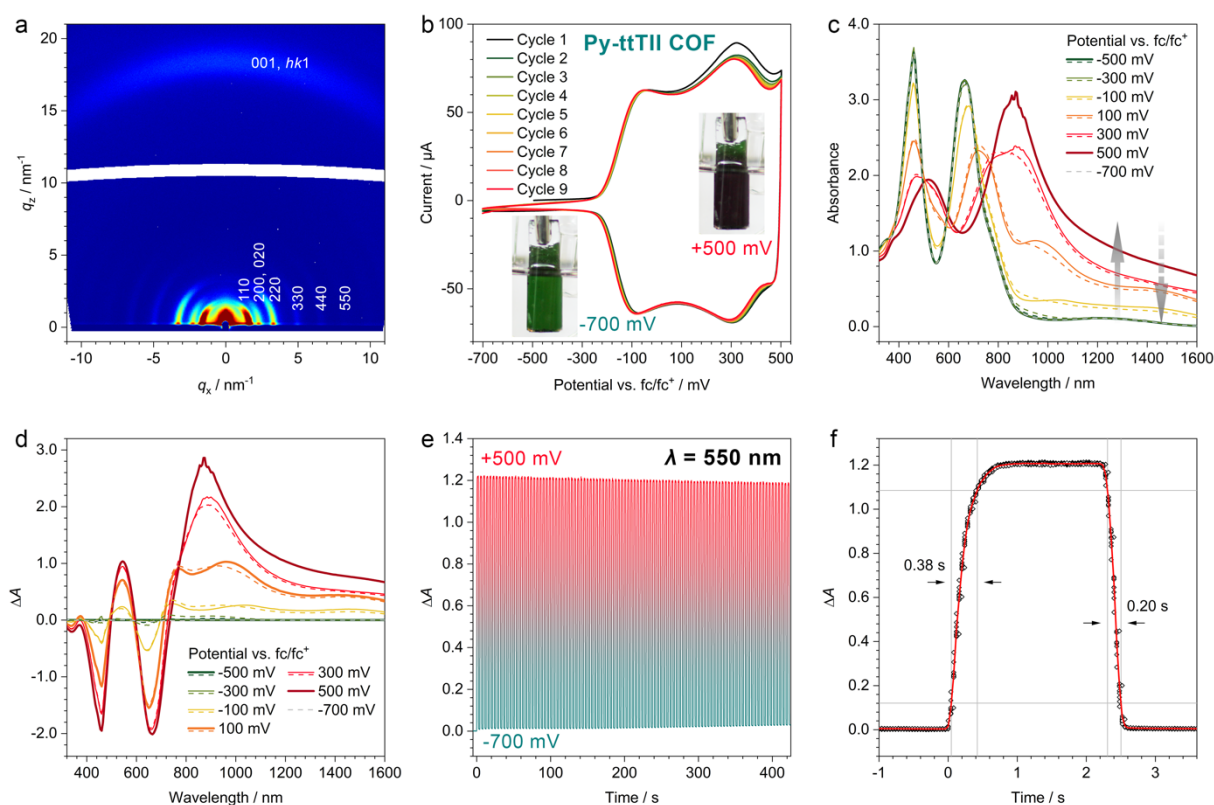


Figure 4.3. Electrochromism of Py-ttTII COF thin films. **(a)** GIWAXS pattern of a 430 nm thick Py-ttTII COF film grown on ITO/glass. Color scaling is logarithmic. The intensities of the $hk0$ reflections are concentrated directly above the sample horizon, confirming the anticipated strong texture with a predominant orientation of crystallites with their a - b plane parallel to the substrate surface. The 001 and other low-index $hk1$ reflections form an arc with the highest intensity in the middle segment close to the substrate normal. **(b)** Cyclic voltammograms of a Py-ttTII film on ITO/glass recorded at a scan rate of 20 mV s^{-1} in a three-electrode-setup. The COF shows two very well-defined oxidation waves at -100 and $+300 \text{ mV vs. fc/fc}^+$, respectively, with negligible drift over nine oxidation/reduction cycles. Insets: Photographs of the COF film in the neutral (-700 mV) and oxidized ($+500 \text{ mV}$) states. **(c)** Spectroelectrochemical characterization of a Py-ttTII COF film. UV-Vis-NIR spectra are recorded at increasing (oxidation; solid lines) and decreasing (reduction; dashed lines) potentials. The electrochromic color changes are fully reversible with only minimal hysteresis. After reduction back to the neutral state (-700 mV ; grey dashed line), the spectrum is indistinguishable from the initial spectrum (green). **(d)** Plot of the absorption difference between the spectra shown in (c) after stepwise oxidation and the initial spectrum. The first oxidation step produces an absorption band at 1000 nm (orange line), which is replaced by an even stronger band at 900 nm after the second oxidation step (dark red). The emergence of the new absorption bands is accompanied by two strong bleach bands that correspond to the absorption of the neutral Py-ttTII COF at 450 and 650 nm . **(e)** Electrochromic switching stability over 100 oxidation/reduction cycles. The applied potential is switched between -700 and $+500 \text{ mV}$ with 2 s dwell time after each potential step. Upon oxidation, the absorbance at 550 nm changes by 1.2 OD with only minimal drift ($<5\%$) over 100 cycles. **(f)** Switching speed at 550 nm extracted from ten oxidation/reduction cycles (symbols: data points, red line: average). The electrochromic response of the Py-ttTII

COF film is very fast with 0.38 s for the oxidation and 0.20 s for the reduction, determined between 10% and 90% ΔA thresholds.

The optical properties of the thienoisindigo COFs are largely dominated by the strong absorption features of the ttTII, nTII, and TII building blocks (SI, Figure 4.11). The higher-energy absorption bands between 350 and 500 nm can be attributed to $\pi-\pi^*$ transitions, while the longer-wavelength absorption is due to intramolecular charge transfer (ICT) between the electron-rich and -deficient moieties of the building blocks.^[23, 34] Both $\pi-\pi^*$ and ICT bands appear red-shifted and broadened compared to the respective building blocks due to aggregation effects across the closely-packed, slip-stacked layers in the COF.^[35]

In order to study the electrochromic behavior of our COFs, we integrated the COF thin film coated electrodes in a three-electrode electrochemical setup with a Pt wire as the counter electrode and a Ag/AgCl reference electrode (see the SI, section A for details). 0.1 M tetrabutylammonium hexafluorophosphate (TBAPF₆) in acetonitrile was used as the electrolyte. The applied potentials were calibrated against the ferrocene fc/fc⁺ redox couple.

Cyclic voltammetry (CV) scans of the Py-ttTII COF show two very well-defined oxidation waves at around -100 and +300 mV, respectively, which appear mirrored when the scan direction is reversed (Figure 4.3b). The respective anodic and cathodic peak positions are shifted by only about 20 mV, suggesting that the redox processes in the COF are fully reversible with fast electron transfer kinetics. The reversibility is further illustrated by the absence of any major drift or changes in curve shape during repeated redox cycles.

Electrochemical oxidation of the Py-ttTII COF film causes a gradual color change from initially dark green to black (SI, Figure 4.14). The corresponding UV-Vis-NIR spectra recorded in 200 mV intervals reveal the progressive bleaching of the two main absorption bands of the neutral COF, accompanied by the appearance of a new feature around 550 nm and a massive absorption band in the near-infrared (Figures 4.3c, d). The first oxidation step (-100 to +100 mV) produces a spectral feature at 1000 nm, which is replaced by an even stronger absorption band around 900 nm after the second oxidation step. The spectral changes are fully reversible with only minimal hysteresis. The spectrum recorded at -700 mV is indistinguishable from the initial spectrum of the neutral COF.

The charge density extracted from a 430 nm thick COF film during the oxidation scan is 0.0032 C cm⁻², which is very close to the theoretical charge density of 0.0030 C cm⁻² calculated for the two-electron oxidation of every ttTII unit in the COF film (see the SI, section I). We

thus can assign the two oxidation waves in the CV scans and the corresponding 1000 nm and 900 nm absorption features to the ttTII^+ and ttTII^{2+} species, respectively.

The two-electron oxidation leads to very strong absorption and bleach bands (absorption changes of up to 2.8 OD), and requires only slightly more charge per unit area than the theoretical limit discussed above. Thus, the electrochromic color changes are highly efficient with coloration efficiencies (CEs) of $318 \text{ cm}^2 \text{ C}^{-1}$ at 550 nm, $620 \text{ cm}^2 \text{ C}^{-1}$ at 660 nm, and $858 \text{ cm}^2 \text{ C}^{-1}$ at 880 nm, respectively (see the SI, section I). These values are several times higher than the CEs of previously reported electrochromic COFs,^[20, 21] rendering the Py-ttTII COF, to the best of our knowledge, the most efficient electrochromic organic framework to date.^[36, 37]

In order to further investigate the stability and response times, we alternated the applied potential between +500 mV (oxidized COF) and -700 mV (neutral COF). The Py-ttTII COF retains >95% of its initial electrochromic response over 100 oxidation/reduction cycles (Figure 4.3e and SI, Figure 4.19), and >85% over 200 cycles (SI, Figure 4.21). Furthermore, the framework crystallinity remains unaffected during these experiments. GIWAXS patterns of the COF film before and after 200 oxidation/reduction cycles are virtually identical (SI, Figure 4.12).

The response to step changes in the applied potential is extremely fast with response times of 0.38 s for the oxidation (coloration) and 0.2 s for the reduction (bleaching) at 550 nm (Figure 4.3f). Response times at 660 nm and 900 nm are similarly fast (SI, Figure 4.19e). To the best of our knowledge, the Py-ttTII COF is the fastest electrochromic framework to date, outcompeting published COFs and inorganic competitors such as WO_3 by more than an order of magnitude.^[20, 21, 38]

As an illustration for a potential application of our electrochromic COFs, we employed a Py-ttTII COF film as an electrochromic window that can rapidly switch between transmitting (neutral COF) and blocking (oxidized COF) light from a green LED. A video of this is included as Supporting Information (viewable at: <https://doi.org/10.1021/jacs.0c12392>).

The electronically and topologically very similar Py-nTII COF shows an overall comparable electrochromic performance, but with slightly less defined oxidation and reduction waves, and weaker coloring due to its reduced film thickness (SI, Figure 4.15). Owing to their more electron-deficient and/or wider band gap building blocks, the Py-TII, Py-TT and Py-N COFs require more positive potentials for oxidation (SI, Figures 4.16, 4.17, 4.18). Moreover, the color changes are much less pronounced and there is significant drift in the CV curves.

4.4 Discussion

Comparing the five electrochromic COFs, we can formulate a set of design rules:

(I) Response and coloration efficiency critically depend on a building block design that combines high extinction coefficients with significant spectral differences between the neutral building block and its oxidized forms. The D-A-D electronic configuration of the ttTII and nTII building blocks has proven very efficient in fulfilling both criteria.

(II) Framework stability during repeated oxidation/reduction seems to depend on two factors. There is a general trend that for a given linker length the more rigid building blocks generate more robust frameworks. This factor works in favor of the flat and almost linear ttTII building block over the slightly non-planar, more flexible nTII and the angled TII. Moreover, stability over repeated electrochromic switching cycles seems to depend critically on the pore size. The COF pores need to be sufficiently large to accommodate the counterions required for overall charge neutrality (i.e., four counter ions per pore and COF layer for the two-electron oxidation of every bridge unit). They must also enable fast diffusion of electrolyte ions into and out of the pores during the electrochemical oxidation and reduction. Among the frameworks in this study, the Py-ttTII and Py-nTII COFs fulfil this criterion, whereas the smaller-pore COFs show significant drift during repeated CV scans, likely due to a build-up of ions in the pores.

(III) Rapid response requires unimpeded diffusion of ions in the pores as well as electronic connectivity throughout the COF film. The Py-ttTII COF films have a unique pillar-like morphology (SI, Figure 4.12c). Every pillar appears to be a continuous COF nanocrystal, ensuring best possible electronic coupling to the ITO electrode and uninterrupted pores for fast electrolyte diffusion.

4.5 Conclusion

We have developed highly efficient, fast-switching and stable electrochromic covalent organic frameworks based on modified thienoisindigo building blocks. With a donor-acceptor-donor electronic setup, the low-bandgap COFs have strong Vis-NIR absorption bands in the neutral state, which shift significantly upon electrochemical oxidation. Absorption changes by close to 3 OD can be triggered at low operating voltages and are fully reversible. The champion Py-ttTII COF reaches an electrochromic coloration efficiency of $858 \text{ cm}^2 \text{ C}^{-1}$ at 880 nm and retains >95% of its electrochromic response over 100 oxidation/reduction cycles. Furthermore, the electrochromic switching of our oriented COF films is extremely fast with response times below

4 Fast-Switching Vis-IR Electrochromic Covalent Organic Frameworks

0.4 s for the oxidation and around 0.2 s for the reduction, outperforming previous COFs by at least an order of magnitude and rendering these materials, to the best of our knowledge, the fastest-switching frameworks to date.

4.6 Supporting Information

Abbreviations

BET	Brunauer-Emmett-Teller
CV	cyclic voltammetry
dba	dibenzylideneacetone
DCM	dichloromethane
DMF	<i>N,N</i> -dimethylformamide
DMSO	dimethyl sulfoxide
eq.	equivalents
fc	ferrocene
ICT	intramolecular charge transfer
ITO	indium tin oxide
LDA	lithium diisopropylamide
NBS	<i>N</i> -bromosuccinimide
NIR	near-infrared
OD	optical density
PSD	pore size distribution
PTFE	poly(tetrafluoroethylene)
QSDFt	quenched solid density functional theory
rt	room temperature
SPhos	dicyclohexylphosphino-2',6'-dimethoxybiphenyl
TBAPF ₆	tetrabutylammonium hexafluorophosphate
TFA	trifluoroacetic acid
THF	tetrahydrofuran
tol	tolyl

COF building blocks

Py(NH ₂) ₄	1,3,6,8-tetrakis(4-aminophenyl)pyrene
N(CHO) ₂	naphthalene-2,6-dicarbaldehyde
nTII(CHO) ₂	5,5'-bis(2-formylnaphthalen-6-yl)- <i>N,N'</i> -dihexyl-thienoisindigo
TII(CHO) ₂	5,5'-diformyl- <i>N,N'</i> -dihexyl-thienoisindigo
TT(CHO) ₂	thieno[3,2- <i>b</i>]thiophene-2,5-dicarbaldehyde
ttTII(CHO) ₂	5,5'-bis(2-formylthienothiophen-5-yl)- <i>N,N'</i> -dihexyl-thienoisindigo

Section A – Methods

Nuclear magnetic resonance (NMR) spectra were recorded on Bruker Avance III HD spectrometers. Proton chemical shifts are expressed in parts per million (δ scale) and are calibrated using residual undeuterated solvent peaks as an internal reference (^1H NMR: CDCl_3 : 7.26, $\text{DMSO-}d_6$: 2.50; ^{13}C NMR: CDCl_3 : 77.2, $\text{DMSO-}d_6$: 39.5). Data for ^1H NMR spectra are reported in the following way: chemical shift (δ ppm) (multiplicity, coupling constant, integration). Multiplicities are reported as follows: s = singlet, d = doublet, t = triplet, q = quartet, m = multiplet, or combinations thereof.

Solid-state ^{13}C cross-polarization magic angle spinning (CP-MAS) NMR spectra were recorded with a Bruker Avance III-500 spectrometer using 4 mm diameter ZrO_2 rotors at a spinning frequency of 12 kHz.

Powder X-ray diffraction (PXRD) patterns were measured on a Bruker D8 Advance diffractometer equipped with a $\text{Cu K}\alpha$ source (0.1 mm divergence slit, knife edge air scatter screen) and a LynxEye detector. $\text{K}\beta$ radiation was attenuated with a 0.0125 mm Ni filter.

2D grazing-incidence wide angle X-ray scattering (GIWAXS) data were recorded with an Anton Paar SAXSpoint 2.0 system equipped with a Primux 100 micro $\text{Cu K}\alpha$ source and a Dectris EIGER R 1M detector. The COF films were positioned at a sample-detector distance of 140 mm and were measured with an incidence angle of 0.2° .

The **structure models of the COFs** were constructed using the Accelrys Materials Studio software package. For each COF, the highest possible symmetry was applied considering the rotation of the bridge units vs. the pyrene cores. The structure models were optimized using the Forcite module with the Dreiding force-field. **Structure refinements** were carried out with the Reflex module using the Rietveld method. Pseudo-Voigt peak profiles were used, and peak asymmetry was corrected using the Finger-Cox-Jephcoat method. **Connolly surfaces** and accessible surfaces were generated using a N_2 -sized probe ($r = 0.184$ nm) at a 0.025 nm grid interval.^[39]

Nitrogen sorption isotherms were recorded with Quantachrome Autosorb 1 and Autosorb iQ instruments at 77 K. The samples were extracted with supercritical CO_2 for 1 h, followed by degassing at 100°C under high vacuum for 1 h prior to the measurements. BET areas were calculated based on the pressure range $0.05 \leq p/p_0 \leq 0.2$. Pore size distributions were calculated using the QSDFT equilibrium model (desorption) with a carbon kernel for cylindrical pores.

Scanning electron microscopy (SEM) images were obtained with an FEI Helios NanoLab G3 UC microscope equipped with a Schottky field-emission electron source operated at 1 – 30 kV.

Transmission electron microscopy (TEM) images were obtained with an FEI Titan Themis microscope equipped with a field emission gun operated at 300 kV.

Infrared (IR) spectra were recorded on a Thermo Scientific Nicolet iN10 FT-IR spectrometer equipped with a MicroTip attenuated total reflection (ATR) unit and an MCT-detector. The spectra were analyzed with the OMNIC software package.

UV-Vis-NIR spectra were recorded on a Perkin-Elmer Lambda 1050 spectrometer equipped with a 150 mm InGaAs integrating sphere. Absorbance spectra of the starting materials were measured with 50 μM chloroform solutions. **Diffuse reflectance spectra** were recorded with a Harrick Praying Mantis accessory kit and were referenced to barium sulfate powder as the white standard.

Electrochemical measurements were performed with a Metrohm Autolab PGSTAT potentiostat/galvanostat. **Cyclic voltammetry (CV)** scans were recorded with the respective COF film on ITO or Au/glass as the working electrode, a Pt wire counter electrode and a Ag/AgCl reference electrode. 0.1 M tetrabutylammonium hexafluorophosphate (TBAPF₆) in MeCN was chosen as the electrolyte. 0.1 mM ferrocene solution was used as a standard in control experiments with a blank ITO working electrode. All potentials are referenced to the fc/fc^+ redox pair ($V_{\text{fc}/\text{fc}^+} = +0.50 \text{ V vs. Ag/Ag}^+$).

For the **spectroelectrochemical measurements**, the COF films were placed inside a fused silica cuvette (20 mm path length) equipped with a Pt wire counter electrode, Ag/AgCl (3 M NaCl) reference electrode and 0.1 M TBAPF₆/MeCN electrolyte. The potential was increased/decreased in 200 mV intervals using a 20 mV s^{-1} ramp and then held constant for the duration of the UV-Vis scan (ca. 5 min per spectrum). For the **stability and response time measurements**, the applied potential was switched between -200 mV and $+1 \text{ V}$ vs. Ag/AgCl and held constant for 2 s between each step. In order to reduce the instrument response time, absorption changes were tracked with the Lambda 1050 photomultiplier tube (Vis) and InGaAs (NIR) detectors set to fixed gain mode.

Section B – COF syntheses

Reagents and solvents were obtained in high-purity grades from commercial suppliers and were, unless shipped under argon, degassed and saturated with argon prior to use. The COF building blocks were synthesized as detailed in Section C. Thieno[3,2-*b*]thiophene-2,5-dicarbaldehyde (TT(CHO)₂) was obtained from Merck and purified by recrystallization from hot DMF. 1,3,6,8-tetrakis(4-aminophenyl)pyrene (Py(NH₂)₄(dioxane)_{1.5}) and naphthalene-2,6-dicarbaldehyde (N(CHO)₂) were synthesized according to published procedures.^[25, 29] Please refer to page 103 for a list of abbreviations for the COF building blocks and solvents.

COF bulk powder syntheses were performed under argon atmosphere in PTFE-sealed glass reaction tubes (6 mL volume).

COF thin films were synthesized in 100 mL autoclaves equipped with a 28 mm diameter glass liner. ITO-coated glass substrates were cleaned in detergent solution (Hellmanex III, 0.5% v/v), water, acetone, and isopropanol, and activated with an O₂-plasma for 5 min directly before use. Semi-transparent gold substrates were prepared by thermal evaporation of a 3 nm Ti layer, followed by a 10 nm Au layer. The gold substrates were activated with an O₂-plasma for 5 min directly before use. For the COF thin film syntheses, substrates were placed horizontally in PTFE sample holders with the activated surface face-down.

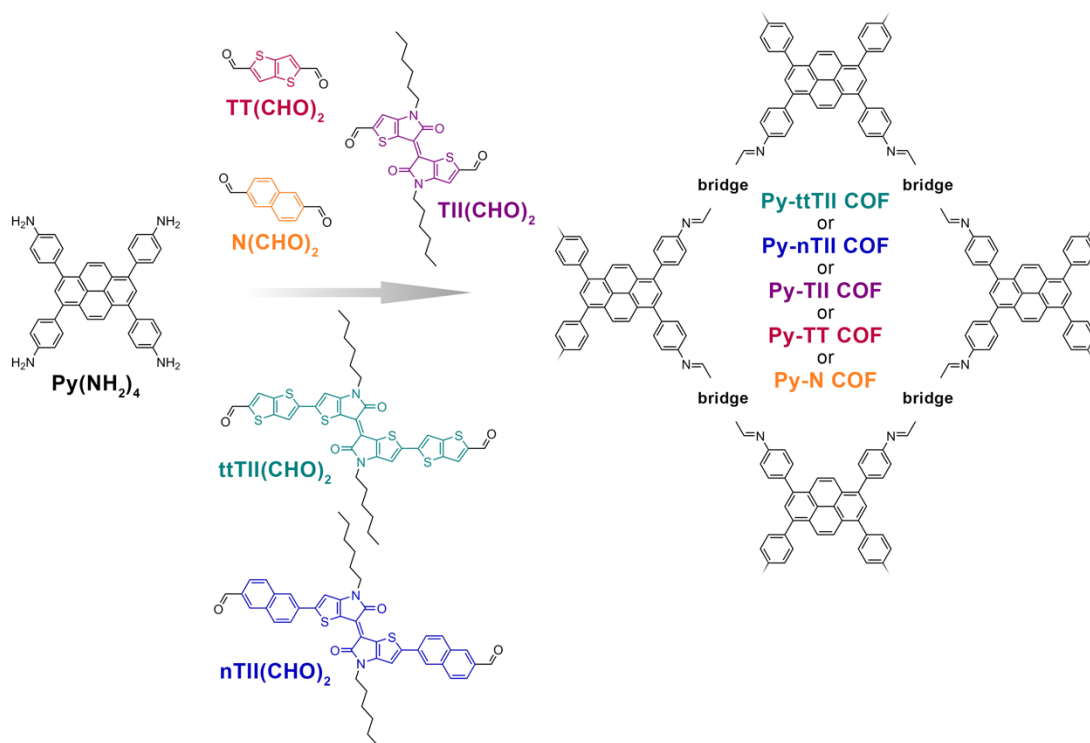


Figure 4.4. Construction of the new thienoindigo-based COFs and smaller-pore reference materials. The co-condensation of the tetradentate $\text{Py}(\text{NH}_2)_4$ with the linear dialdehyde building blocks yields the Py-ttTII, Py-nTII, Py-TII, Py-TT and Py-N COFs, respectively.

Py-ttTII COF. $\text{Py}(\text{NH}_2)_4(\text{dioxane})_{1.5}$ (14.0 mg, 20 μmol , 1.0 eq.) and $\text{ttTII}(\text{CHO})_2$ (31.0 mg, 40 μmol , 2.0 eq.) were filled into a 6 mL reaction tube, followed by the addition of mesitylene (667 μL), benzyl alcohol (333 μL), and 6 M acetic acid (100 μL). The tube was sealed and heated at 120 $^\circ\text{C}$ for 6 d. After cooling to room temperature, the precipitate was collected by filtration, washed with MeCN and dried in air. Extraction with supercritical CO_2 for 1 h yielded the COF as a dark green powder.

Elemental analysis (calculated, found for $\text{C}_{232}\text{H}_{180}\text{N}_{16}\text{O}_8\text{S}_{24}$): C (68.14, 67.48), H (4.44, 4.53), N (5.48, 5.23), S (18.81, 18.37).

Py-ttTII COF films. An autoclave was charged with $\text{Py}(\text{NH}_2)_4(\text{dioxane})_{1.5}$ (3.5 mg, 5 μmol , 1.0 eq.), $\text{ttTII}(\text{CHO})_2$ (7.8 mg, 10 μmol , 2.0 eq.), mesitylene (1333 μL) and benzyl alcohol (667 μL). An ITO/glass substrate was inserted, followed by the addition of 6 M acetic acid (200 μL). The autoclave was sealed and heated at 120 $^\circ\text{C}$ for 3 d. After cooling to room temperature, the COF film was rinsed with dry MeCN and dried with a stream of nitrogen. The COF film thickness is 430 ± 30 nm (determined by cross-sectional SEM, sample-to-sample variation by UV-Vis).

Py-nTII COF. Py(NH₂)₄(dioxane)_{1.5} (14.0 mg, 20 μmol, 1.0 eq.) and nTII(CHO)₂ (30.0 mg, 40 μmol, 2.0 eq.) were filled into a 6 mL reaction tube, followed by the addition of mesitylene (333 μL), 1,4-dioxane (667 μL), and 6 M acetic acid (100 μL). The tube was sealed and heated at 120 °C for 6 d. After cooling to room temperature, the precipitate was collected by filtration, washed with MeCN and dried in air. Extraction with supercritical CO₂ for 1 h yielded the COF as a dark green powder.

Elemental analysis (calculated, found for C₂₆₄H₂₁₂N₁₆O₈S₈): C (79.41, 77.13), H (5.35, 5.36), N (5.61, 5.35), S (6.42, 6.47).

Py-nTII COF films. An autoclave was charged with Py(NH₂)₄(dioxane)_{1.5} (3.5 mg, 5 μmol, 1.0 eq.), nTII(CHO)₂ (7.5 mg, 10 μmol, 2.0 eq.), mesitylene (1333 μL) and benzyl alcohol (667 μL). A gold/glass substrate was inserted, followed by the addition of 6 M acetic acid (200 μL). The autoclave was sealed and heated at 120 °C for 3 d. After cooling to room temperature, the COF film was immersed in dry MeCN for 2 min and dried with a stream of nitrogen.

The COF film thickness is 280 ± 30 nm (determined by cross-sectional SEM; sample-to-sample variation by UV-Vis).

Py-TII COF. Py(NH₂)₄(dioxane)_{1.5} (14.0 mg, 20 μmol, 1.0 eq.) and TII(CHO)₂ (20.0 mg, 40 μmol, 2.0 eq.) were filled into a 6 mL reaction tube, followed by the addition of mesitylene (667 μL), benzyl alcohol (333 μL), and 6 M acetic acid (100 μL). The tube was sealed and heated at 120 °C for 6 d. After cooling to room temperature, the precipitate was collected by filtration, washed with MeCN and extracted with supercritical CO₂ for 1 h to yield the COF as a dark teal powder.

Elemental analysis (calculated, found for C₁₈₄H₁₆₄N₁₆O₈S₈): C (74.06, 72.28), H (5.54, 5.49), N (7.51, 7.02), S (8.60, 8.35).

Py-TII COF films. An autoclave was charged with Py(NH₂)₄(dioxane)_{1.5} (3.5 mg, 5 μmol, 1.0 eq.), TII(CHO)₂ (5.0 mg, 10 μmol, 2.0 eq.), mesitylene (1333 μL) and benzyl alcohol (667 μL). An ITO/glass substrate was inserted, followed by the addition of 6 M acetic acid (200 μL). The autoclave was sealed and heated at 120 °C for 3 d. After cooling to room temperature, the COF film was immersed in dry MeCN for 2 min and dried with a stream of nitrogen.

Py-TT COF. This COF was prepared according to literature procedures.^[28]

Py-TT COF films. COF thin films were prepared according to literature procedures.^[28]

Py-N COF. Py(NH₂)₄(dioxane)_{1.5} (14.0 mg, 20 μmol, 1.0 eq.) and N(CHO)₂ (7.4 mg, 40 μmol, 2.0 eq.) were filled into a 6 mL reaction tube, followed by the addition of mesitylene (667 μL), benzyl alcohol (333 μL), and 6 M acetic acid (100 μL). The tube was sealed and heated at 120 °C for 6 d. After cooling to room temperature, the precipitate was collected by filtration, washed with MeCN and dried in air. Extraction with supercritical CO₂ for 1 h yielded the COF as an orange-red powder.

Elemental analysis (calculated, found for C₁₂₈H₇₆N₈): C (89.07, 86.90), H (4.44, 4.29), N (6.49, 6.21)

Py-N COF films. An autoclave was charged with Py(NH₂)₄(dioxane)_{1.5} (3.5 mg, 5 μmol, 1.0 eq.), N(CHO)₂ (1.8 mg, 10 μmol, 2.0 eq.), mesitylene (1333 μL) and benzyl alcohol (667 μL). An ITO/glass or fused silica substrate was inserted, followed by the addition of 6 M acetic acid (200 μL). The autoclave was sealed and heated at 120 °C for 3 – 4 d. After cooling to room temperature, the COF film was immersed in dry MeCN for 2 min and dried with a stream of nitrogen.

Section C – COF structure analysis

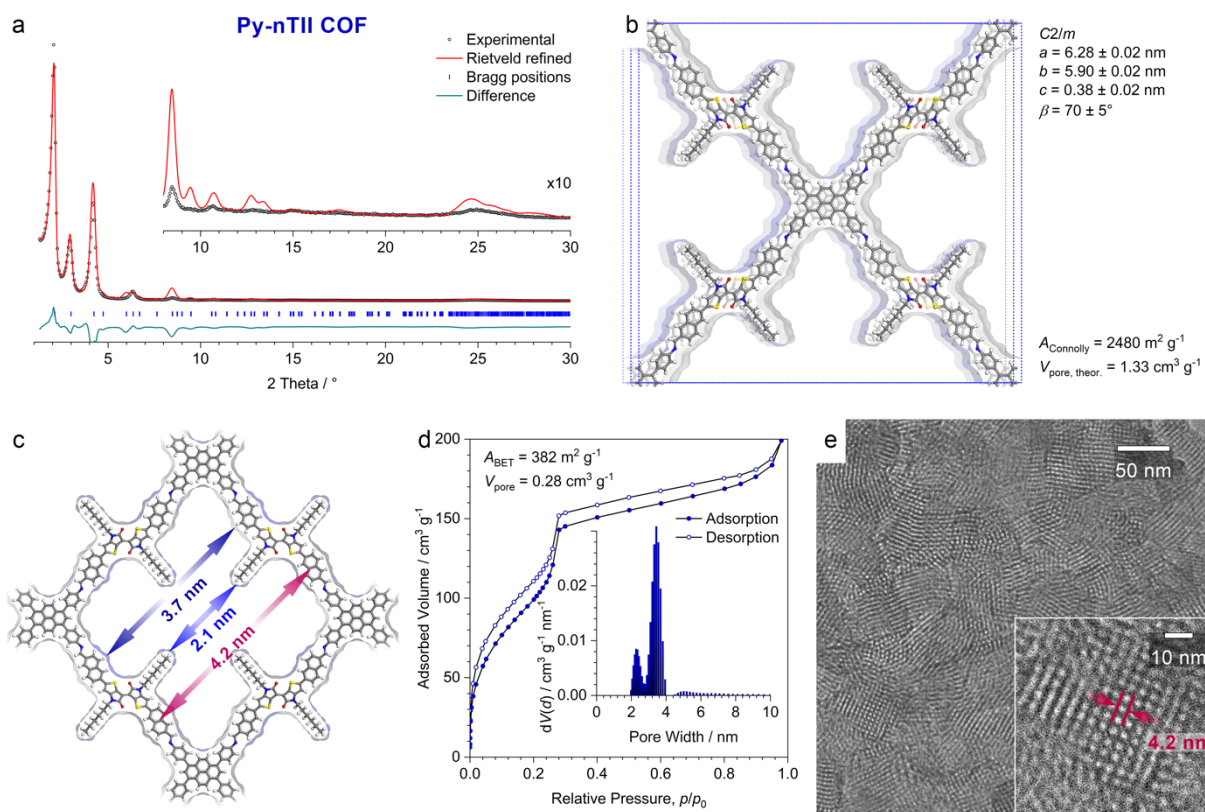


Figure 4.5. Structure analysis of the Py-nTII COF.

(a) PXRD pattern of the Py-nTII COF bulk material (black dots). Rietveld refinement (red line) using the monoclinic (space group $C2/m$) structure model shown on the right provides a good fit, with only small differences between the experimental and refined patterns (green line) arising mainly from the flexibility of the alkyl chains. $R_{wp} = 13.7\%$, $R_p = 23.5\%$. Bragg positions are indicated by blue ticks. Inset: Magnified view of the $2\theta > 8^\circ$ region.

(b) The Rietveld-refined structure model of the Py-nTII COF viewed perpendicular to the crystallographic a - b plane. The COF has a pseudo-square geometry with slip-stacked layers. The structure is highly porous with a Connolly surface of $2480 \text{ m}^2 \text{ g}^{-1}$ and a pore volume of $1.33 \text{ cm}^3 \text{ g}^{-1}$.

(c) Illustration of the pore structure of the COF viewed along the c -axis. The structure refinement indicates that in this COF the alkyl chains extend relatively straight into the pores, producing a shamrock-shaped pore cross section. The wall-to-wall distances (blue arrows) are 2.1 nm and 3.7 nm including and excluding the alkyl chains, respectively. The periodicity of the COF in this orientation is 4.2 nm (red arrows).

(d) Nitrogen sorption isotherm recorded at 77 K. The BET area and total pore volume are reduced compared to the structure model, most likely due to oligomeric fragments that were enclosed in the pores during the synthesis. This is a common challenge for COFs based on extended, bulky building blocks with low solubility.^[9] Inset: Fitting the isotherm with a QSDFT equilibrium model for cylindrical pores produces a bimodal pore size distribution (PSD) with peaks at 2.3 nm and 3.5 nm. While unexpected at first glance, this PSD is a result of the algorithm trying to express the non-cylindrical pores as a superposition of cylindrical pores with the two contributions being in good agreement with the wall-to-wall distances including and excluding the alkyl chains. Bimodal PSDs have been observed previously for alkyl-containing COFs.^[27] The sorption data and PSD analysis hence confirm the shamrock-shaped pore cross section and provide an independent validation of the XRD-derived structure model of the Py-nTII COF.

(e) High-resolution TEM image of a Py-nTII COF bulk powder sample showing crystallites of 50 – 100 nm diameter. Inset: Magnified image of a crystallite viewed along the pores (i.e., along the crystallographic c -axis) showing a periodicity of 4.2 nm in excellent agreement with the structure model.

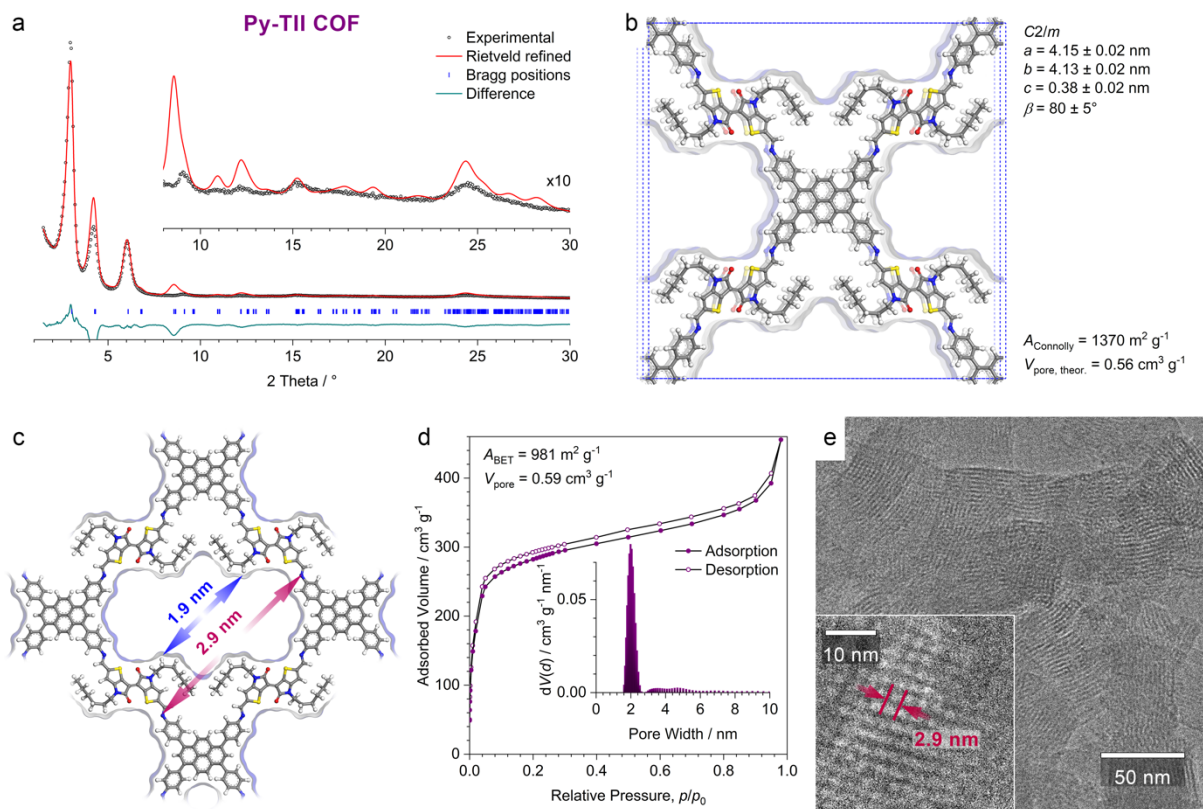


Figure 4.6. Structure analysis of the Py-TII COF.

(a) PXRD pattern of the COF bulk material (black dots). Rietveld refinement (red line) using the monoclinic (space group $C2/m$) structure model shown on the right provides a good fit, with only small differences between the experimental and refined patterns (green line). $R_{wp} = 15.3\%$, $R_p = 23.9\%$. Bragg positions are indicated by blue ticks. Inset: Magnified view of the $2\theta > 8^\circ$ region.

(b) The Rietveld-refined structure model of the Py-TII COF viewed perpendicular to the crystallographic a - b plane. The COF has a pseudo-square geometry with slip-stacked layers. The PXRD data quality is sufficient to refine the location of groups of atoms such as the hexyl chains. In this COF, the alkyl chains do not extend straight into the pore but collapse towards the neighboring pyrene units. This arrangement might be favorable because it avoids close contacts between the alkyl chains and the division of the pores into four small compartments. The COF is porous with a Connolly surface of $1370 \text{ m}^2 \text{ g}^{-1}$ and a pore volume of $0.56 \text{ cm}^3 \text{ g}^{-1}$.

(c) Illustration of the pore structure viewed along the c -axis. The collapsed alkyl chains produce a pore with 1.9 nm wall-to-wall distance (blue arrows). The periodicity of the COF in this orientation is 2.9 nm (red arrows).

(d) Nitrogen sorption isotherm recorded at 77 K . The BET area and pore volume are in good agreement with the porosity expected from the structure model. Inset: Fitting the isotherm with a QSDFT equilibrium model for cylindrical pores yields a narrow PSD with a maximum at 2.0 nm , in excellent agreement with the structure model. The fact that, in contrast to the larger Py-ttTII and Py-nTII COFs, the QSDFT analysis does not produce a bimodal distribution validates the XRD-derived structure model and confirms that the hexyl chains are collapsed to the pore walls in this COF.

(e) High-resolution TEM image of a Py-TII COF bulk powder sample showing crystallites of about 50 nm diameter. Inset: Magnified image of a crystallite viewed along the pores (i.e., along the crystallographic c -axis) showing a periodicity of 2.9 nm in excellent agreement with the structure model.

4 Fast-Switching Vis-IR Electrochromic Covalent Organic Frameworks

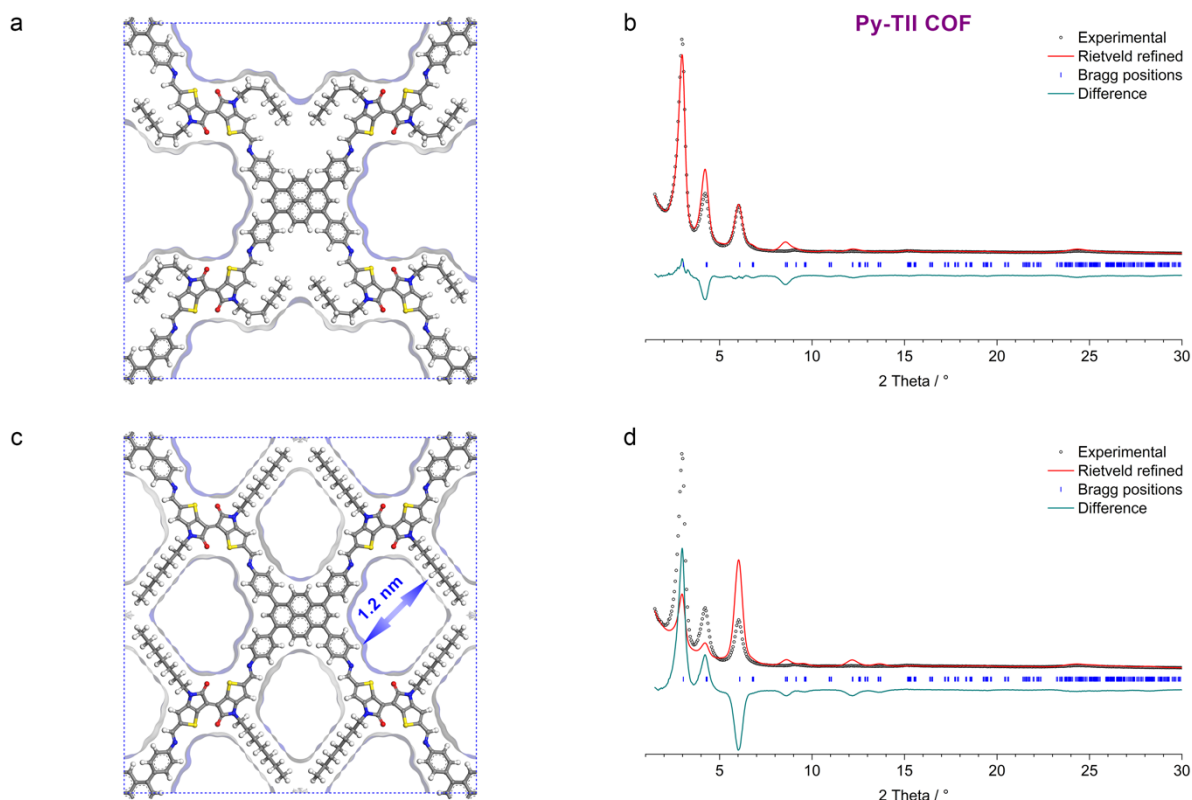


Figure 4.7. Comparison between the Py-TII COF structure models.

(a) Structure model of the Py-TII COF with collapsed alkyl chains. The Connolly surface calculated for an N₂-sized molecule is shown in blue. This arrangement of the alkyl chains leads to a large, slightly slit-like pore.

(b) This structure model provides a good fit to the experimental PXRD data and is further supported by the nitrogen sorption data (Figure 4.6d).

(c) Hypothetical structure model of the COF with the alkyl chains extending straight into the pore. In contrast to the larger COFs, this configuration would divide the pore of the Py-TII COF into four microporous compartments.

(d) Due to the very different distribution of electron density in the pores, this structure would lead to significantly different reflection intensities (red line) which do not match the experimental pattern. Moreover, straight alkyl chains can be excluded based on the nitrogen sorption, which clearly shows a pore width of around 2 nm (Figure 4.6d).

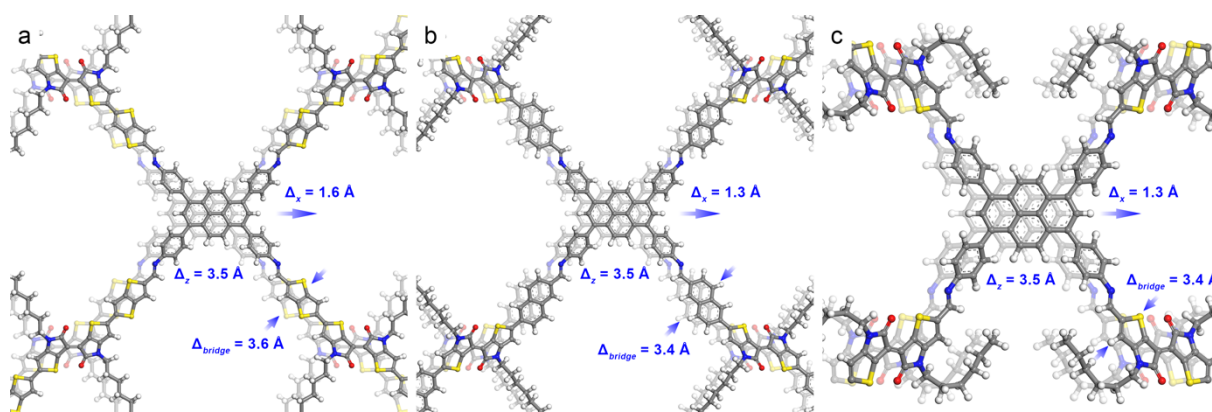


Figure 4.8. Stacking distances in the thienoindigo COFs. (a) Py-ttTII COF, (b) Py-nTII COF, (c) Py-TII COF.

In all COFs, the pyrene-to-pyrene π -stacking distance (Δ_z ; measured perpendicular to the pyrene planes) is 3.5 Å. The distance between the thienoindigo bridge units (measured perpendicular to the TII planes) ranges from 3.4 to 3.6 Å, confirming that also these moieties are closely packed in all three COFs. The lateral layer offset ranges from 1.3 Å in the Py-nTII and Py-TII COFs to 1.6 Å for the Py-ttTII COF. Given the very similar packing geometries, the electronic coupling across the COF layers is expected to be comparable in all three COFs.

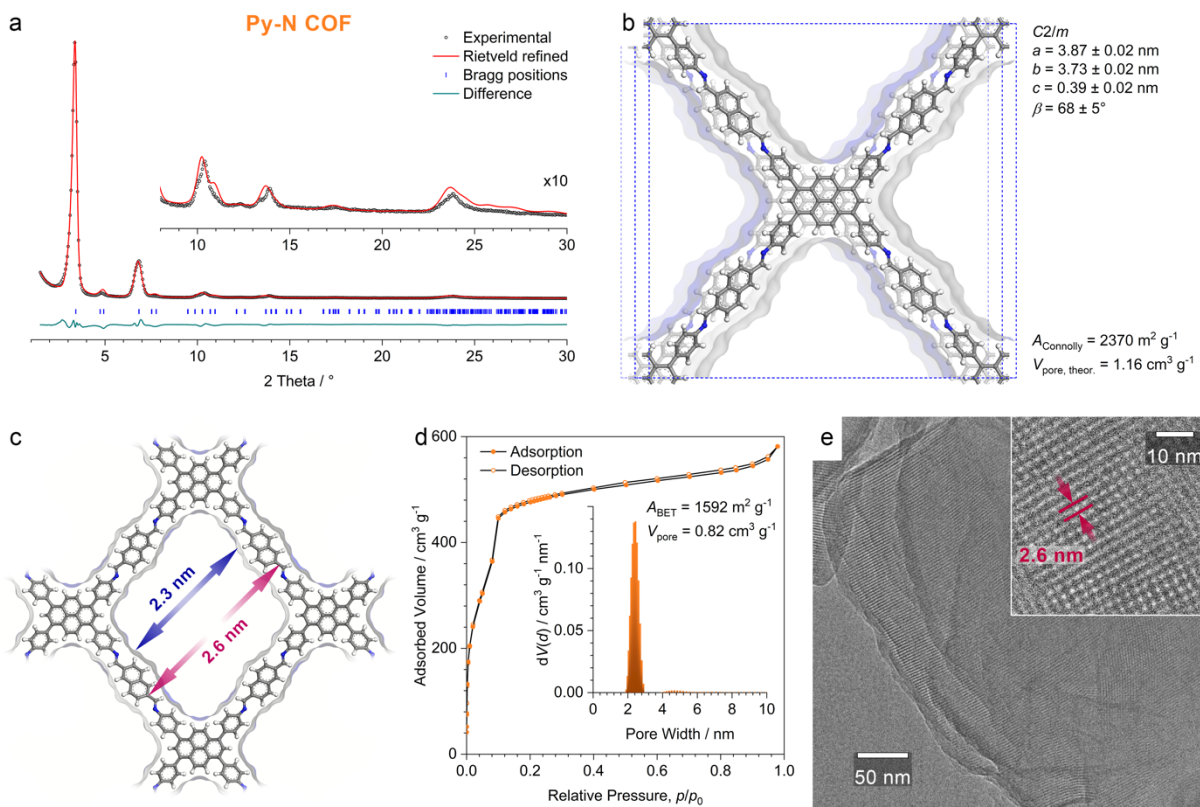


Figure 4.9. Structure analysis of the Py-N COF.

(a) PXRD pattern of the COF bulk material (black dots). Rietveld refinement (red line) using the monoclinic (space group $C2/m$) structure model shown on the right provides a very good fit, with only minimal differences between the experimental and refined patterns (green line). $R_{wp} = 4.0\%$, $R_p = 12.5\%$. Bragg positions are indicated by blue ticks. Inset: Magnified view of the $2\theta > 8^\circ$ region.

(b) The Rietveld-refined structure model of the Py-N COF viewed perpendicular to the crystallographic a - b plane. The COF has a pseudo-square geometry with slip-stacked layers. The COF is highly porous with a Connolly surface of $1910 \text{ m}^2 \text{ g}^{-1}$ and a pore volume of $0.61 \text{ cm}^3 \text{ g}^{-1}$.

(c) Illustration of the pore structure viewed along the c -axis. The pores have a pseudo-square cross section with a wall-to-wall distance of 2.3 nm . The periodicity of the COF in this orientation is 2.6 nm (red arrows).

(d) Nitrogen sorption isotherm recorded at 77 K . The BET area and pore volume are in good agreement with the porosity expected from the structure model. Inset: Fitting the isotherm with a QSDFT equilibrium model for cylindrical pores yields a narrow PSD with a maximum at 2.4 nm , which is in excellent agreement with the structure model.

(e) High-resolution TEM image of a Py-N COF bulk powder sample showing large crystal domains of about 400 nm . Inset: Magnified image of a crystallite viewed along the pores (i.e., along the crystallographic c -axis) showing a periodicity of 2.6 nm in excellent agreement with the structure model.

Other COFs:

See the manuscript for the structure analysis of the Py-ttTII COF.

The structure analysis of the Py-TT COF has been published previously.^[28]

Section D – IR spectroscopy

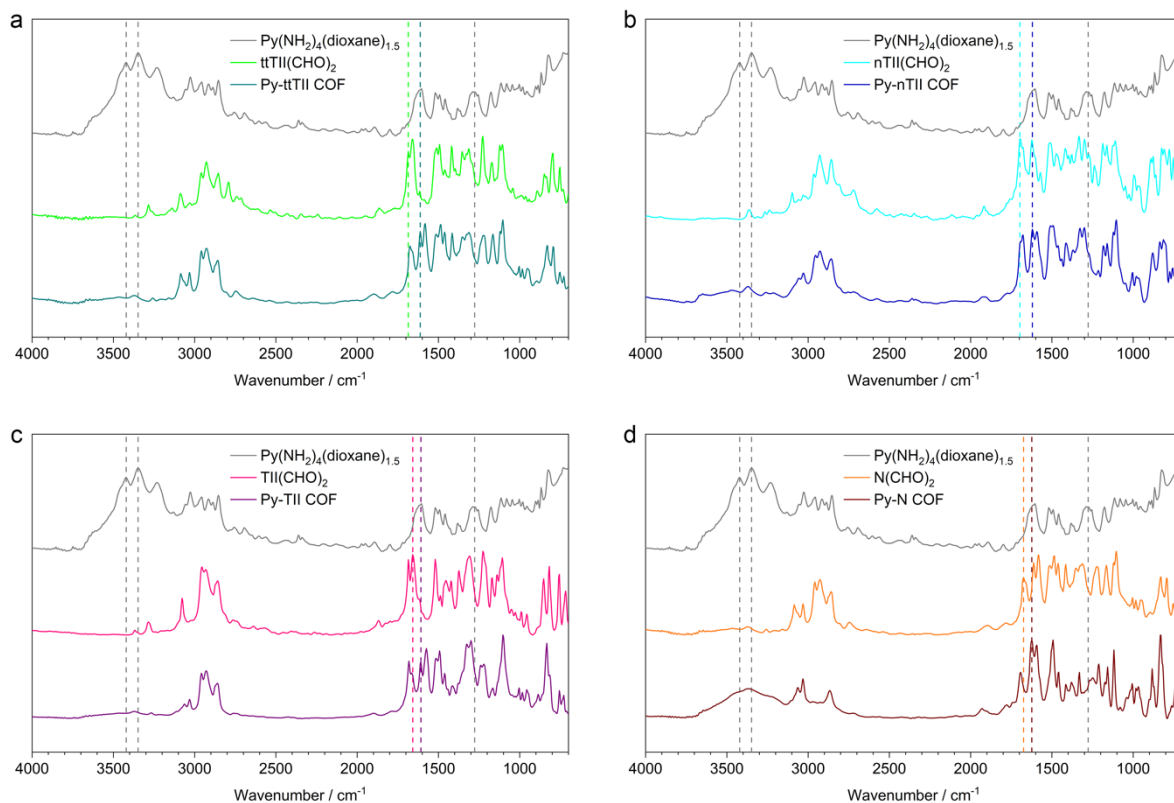


Figure 4.10. Comparison of IR spectra of the precursors and their COF powders. The IR spectra of the building blocks show the characteristic C-NH₂ and C=O stretching vibrations of the amine (Py(NH₂)₄) and aldehyde (linear precursors) functional groups, respectively. The attenuation of these absorption signals and the evolution of the C=N stretching vibrations of the imine bonds at around 1610 cm⁻¹ confirm the successful COF formation.

Table 4.1. Assignments of selected IR signals.

	Wavenumber / cm ⁻¹	Assignment
Py(NH ₂) ₄ (dioxane) _{1.5}	1277	C-NH ₂ stretching
	3348	N-H stretching
	3421	N-H stretching
ttTII(CHO) ₂	1686	C=O stretching
Py-ttTII COF	1612	C=N stretching
nTII(CHO) ₂	1697	C=O stretching
Py-nTII COF	1620	C=N stretching
TII(CHO) ₂	1658	C=O stretching
Py-TII COF	1608	C=N stretching
N(CHO) ₂	1674	C=O stretching
Py-N COF	1624	C=N stretching

Section E – UV-Vis spectroscopy

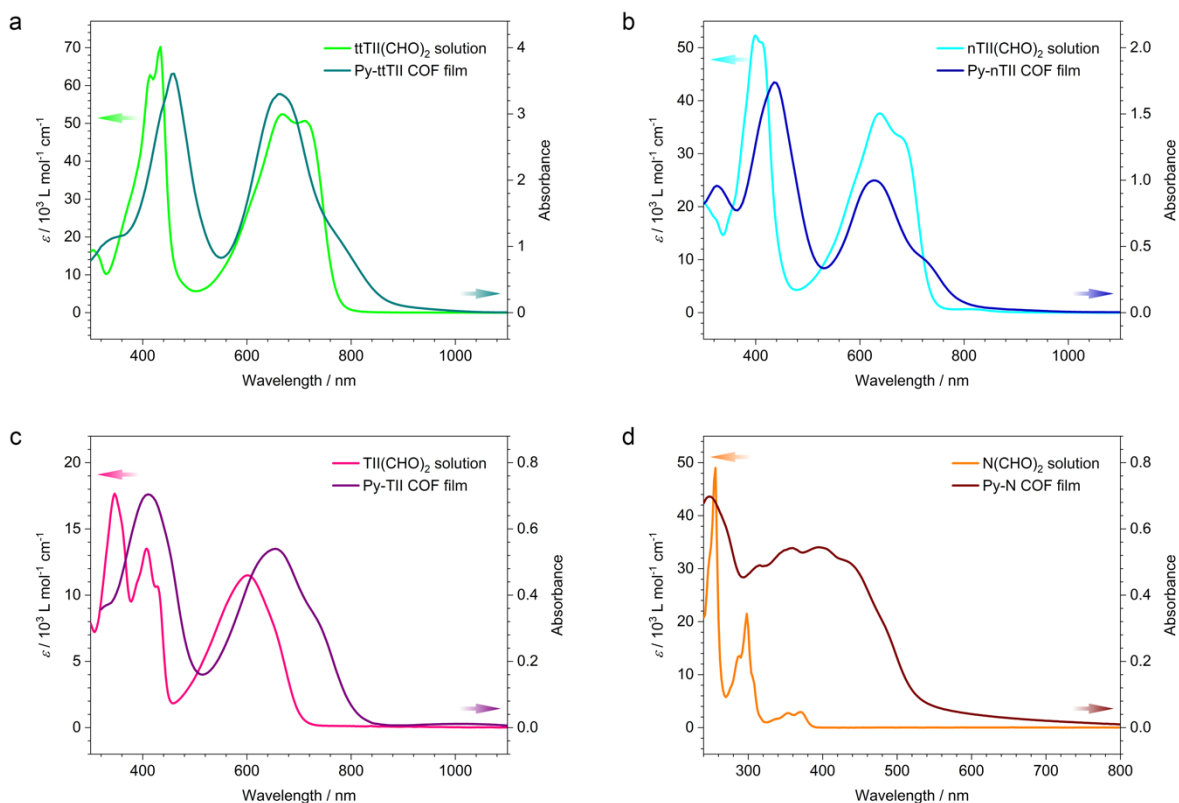


Figure 4.11. Comparison of the absorption spectra of the building blocks (50 μM solutions in CHCl_3) and the corresponding COF thin films. (a) Py-ttTII COF grown on ITO, (b) Py-nTII COF on a 10 nm Au layer, (c) Py-TII COF on ITO, (d) Py-N COF on fused silica.

The thienoindigo-containing building blocks have two characteristic absorption bands. The higher-energy band between 330 and 500 nm can be attributed to $\pi-\pi^*$ transitions, whereas the strong absorption at longer wavelengths starting at 500 nm and ranging into the NIR is due to intramolecular charge transfer (ICT) between electron-rich and -deficient moieties. These ICT transitions are enabled by the structure design of the TII-based building blocks with their strongly electron-accepting ketopyrrole cores and the electron-donating fused thiophenes in the TII, or the coupled thienothiophenes and naphthalenes in the ttTII and nTII building blocks, respectively.

Section F – COF films GIWAXS analysis

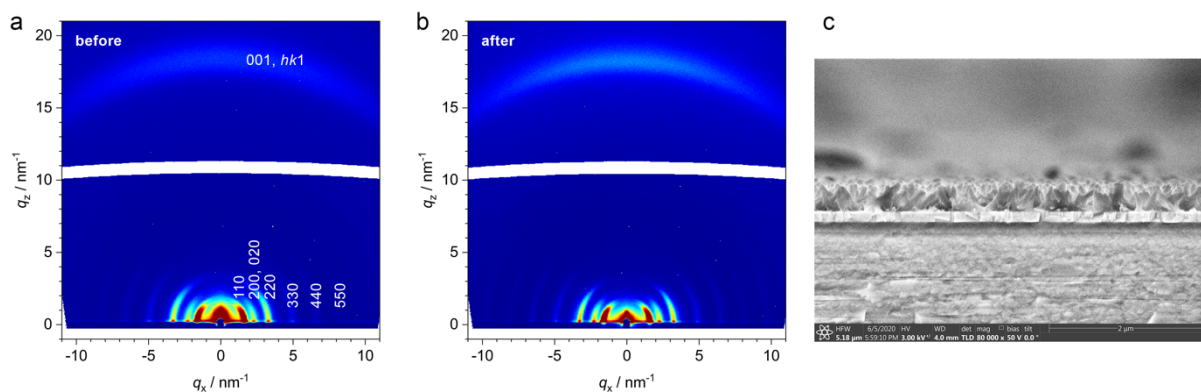


Figure 4.12. 2D GIWAXS patterns of a Py-ttTII COF film on ITO (a) before and (b) after 200 electrochemical oxidation/reduction cycles. The film is polycrystalline and highly textured with the COF *a-b* planes predominantly aligned parallel to the substrate. The crystallinity and orientation are fully retained during the electrochemical switching. (c) SEM cross-section of a Py-ttTII COF film. In contrast to other COFs, films of this COF are not dense, but have a pillar-like morphology.

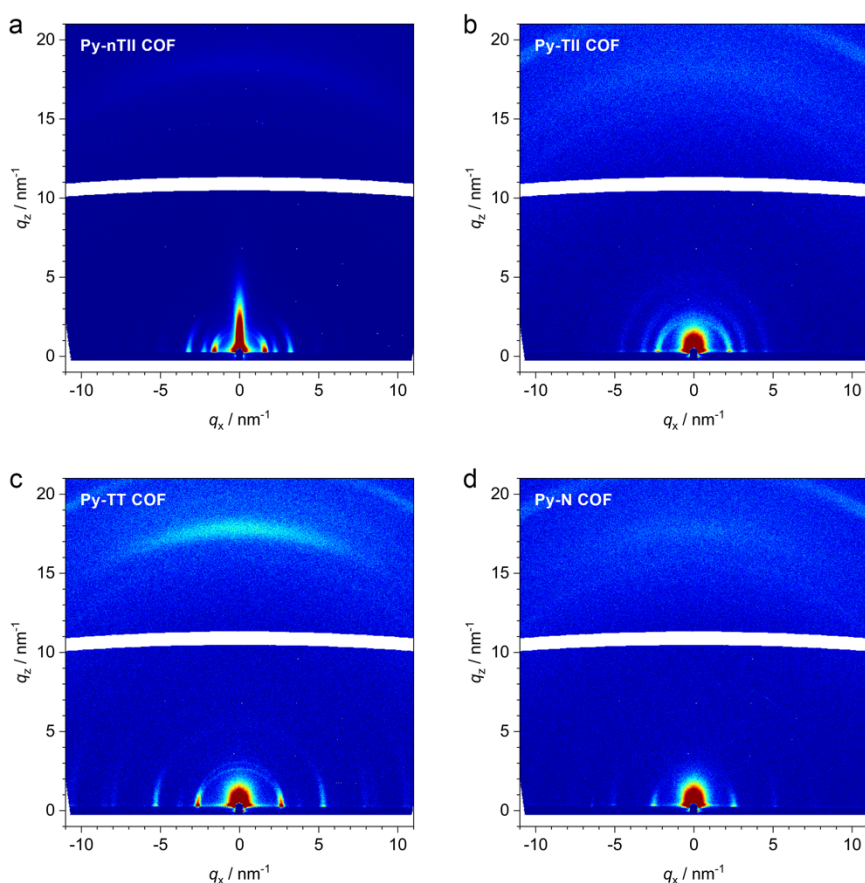


Figure 4.13. 2D GIWAXS patterns of the other COFs after ten oxidation/reduction cycles. (a) Py-nTII COF on a 10 nm Au/glass substrate. (b) Py-TII COF on ITO. (c) Py-TT COF on ITO. (d) Py-N COF on ITO. The COF films are polycrystalline and strongly textured with the *a-b* planes predominantly parallel to the substrate surface. Thus, the pores extend towards the film surface and are accessible.

Section G – Spectroelectrochemistry

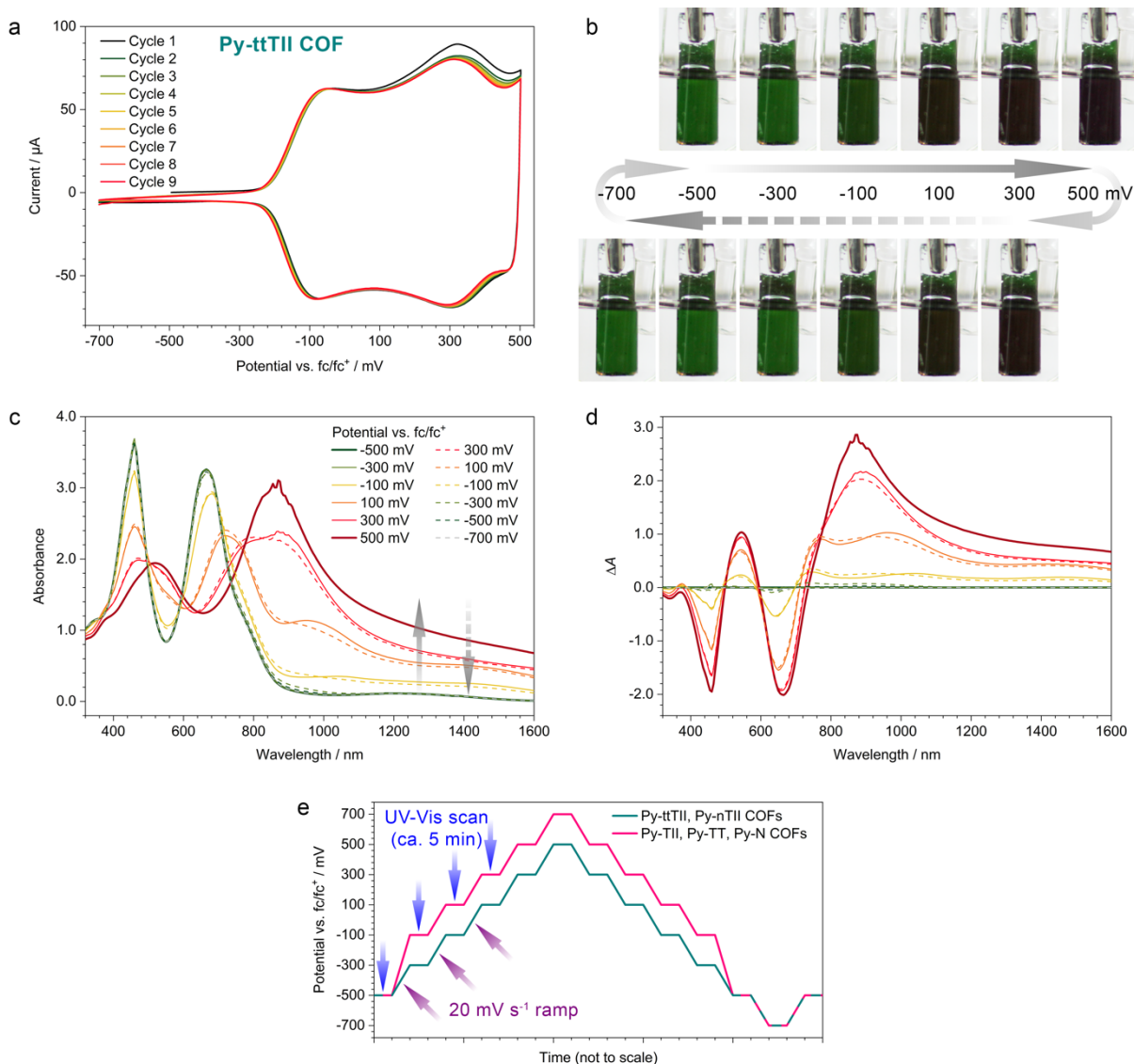


Figure 4.14. Electrochromic properties of the Py-ttTII COF. (a) Cyclic voltammograms of a COF film on ITO recorded at a scan rate of 20 mV s^{-1} . See the Methods section for experimental details. The Py-ttTII COF has two very well-defined oxidation waves at around -100 and $+300$ mV vs. fc/fc⁺, respectively, and shows almost no drift over nine oxidation/reduction cycles. The stability of this COF over more oxidation/reduction cycles is analyzed in the next section.

(b) Photographs of the COF film taken during an oxidation (top row, left to right) / reduction (bottom row, right to left) cycle illustrating the electrochromic color changes.

(c) UV-Vis-NIR spectra recorded at different potentials using the ramp/dwell program shown in (e). The solid and dashed lines refer to spectra recorded at increasing (oxidation) and decreasing (reduction) potentials, respectively. The first oxidation step ($+100$ mV, orange line) produces a new absorption feature at 1000 nm, which is replaced by a strong absorption at 900 nm after the second oxidation step ($+500$ mV, dark red). The electrochromic color changes of the Py-ttTII COF are fully reversible with only minimal hysteresis (dashed lines). At -700 mV, the spectrum is indistinguishable from the initial spectrum (dashed grey line).

(d) Plot of the absorption difference between the oxidized COF and the initial spectrum. Oxidation of the Py-ttTII COF leads to the evolution of strong NIR absorption bands and a minor contribution at 550 nm, accompanied by two bleach bands at 450 and 650 nm.

(e) The voltage ramp programs used for the potential-dependent UV-Vis scans. Each UV-Vis scan (the first four scans are indicated by blue arrows) is followed by a 20 mV s^{-1} voltage ramp to the next potential (purple arrows). The larger-bandgap and/or more electron-deficient Py-TII, Py-TT and Py-N COFs require more positive potentials for oxidation. Hence, the potentials for the UV-Vis scans after the initial measurement are shifted by 200 mV (pink line).

4 Fast-Switching Vis-IR Electrochromic Covalent Organic Frameworks

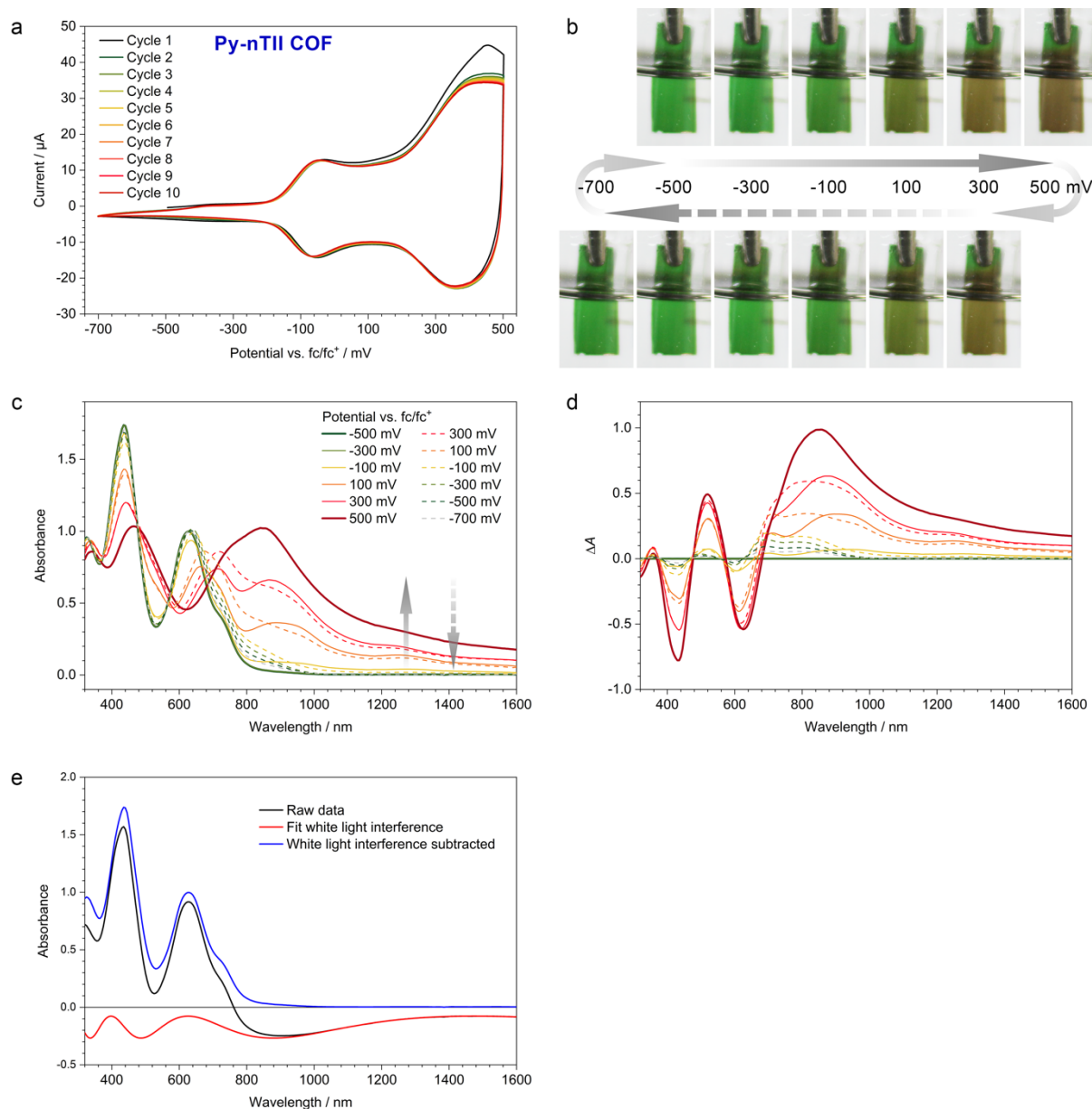


Figure 4.15. Electrochromic properties of the Py-nTII COF.

(a) Cyclic voltammograms of a COF film on a 10 nm Au/glass substrate, recorded at a scan rate of 20 mV s^{-1} . See the Methods section for experimental details. The Py-nTII COF has two very well-defined oxidation waves at around -50 and $+350 \text{ mV vs. } fc/fc^+$, respectively, and shows almost no drift over ten oxidation/reduction cycles.

(b) Photographs of the COF film taken during an oxidation (top row, left to right) / reduction (bottom row, right to left) cycle illustrating the electrochromic color changes.

(c) UV-Vis-NIR spectra recorded at different potentials. The solid and dashed lines refer to spectra recorded at increasing (oxidation) and decreasing (reduction) potentials, respectively. The first oxidation step ($+100 \text{ mV}$, orange line) produces a new absorption feature at 950 nm , which is replaced by a strong absorption at 900 nm after the second oxidation step ($+500 \text{ mV}$, dark red line). The electrochromic color changes of the Py-nTII COF are almost fully reversible, however, with some hysteresis (dashed lines). At -700 mV , the spectrum follows the initial spectrum except for a minor residual absorption around 800 nm .

The effect of white light interference, which is pronounced for this sample due to the Au substrate, was removed from the absorption spectra (see below).

(d) Plot of the absorption difference between the oxidized COF and the initial spectrum. Oxidation of the Py-nTII COF leads to the evolution of strong NIR absorption bands and a minor contribution at 550 nm , accompanied by two bleach bands at 450 and 650 nm .

(e) Background correction of the spectra. White light interference (red line) was approximated by the expression $A = 0.095 \cos(4\pi \cdot 544/\lambda + 1.64) - 0.176$ and subtracted from all spectra. For clarity, only the spectrum at -500 mV is displayed.

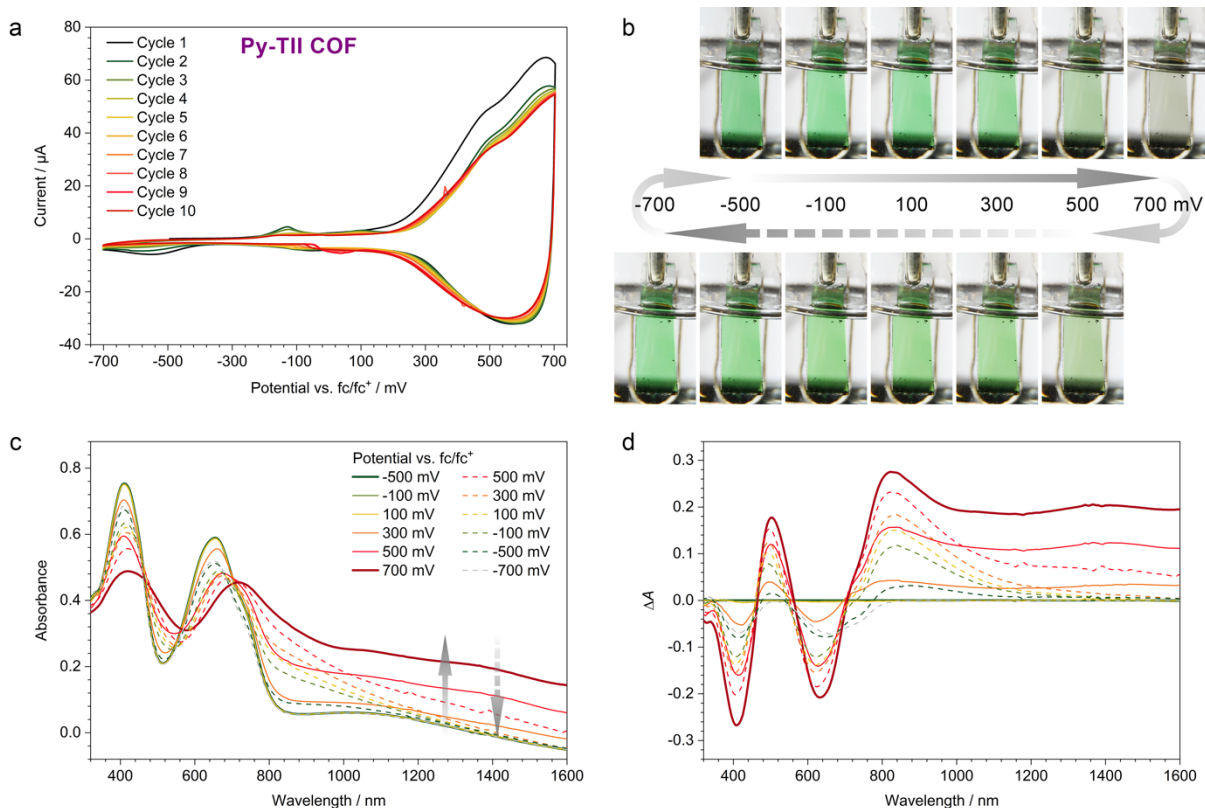


Figure 4.16. Electrochromic properties of the Py-TII COF.

(a) Cyclic voltammograms of a Py-TII COF film on ITO recorded at a scan rate of 20 mV s^{-1} . See the Methods section for experimental details. The Py-TII COF shows one oxidation wave at around +500 mV vs. fc/fc^+ and only moderate drift over ten oxidation/reduction cycles.

(b) Photographs of the COF film taken during an oxidation (top row, left to right) / reduction (bottom row, right to left) cycle illustrating the electrochromic color changes.

(c) UV-Vis-NIR spectra recorded at different potentials. The solid and dashed lines refer to spectra recorded at increasing (oxidation) and decreasing (reduction) potentials, respectively. Oxidation of the COF shifts the lowest-energy absorption band to about 800 nm and produces an additional very broad IR absorption that extends beyond the measurement range. In contrast to the COFs based on the larger and more electron-rich ttTII and nTII building blocks, the electrochromic color changes are not entirely reversible, probably due to pore blocking and a partial delamination of COF layers (see the manuscript for discussion).

(d) Plot of the absorption difference between the oxidized COF and the initial spectrum. Oxidation of the Py-TII COF leads to the evolution of strong NIR absorption bands and a minor contribution at 500 nm, accompanied by two bleach bands at 400 and 650 nm.

4 Fast-Switching Vis-IR Electrochromic Covalent Organic Frameworks

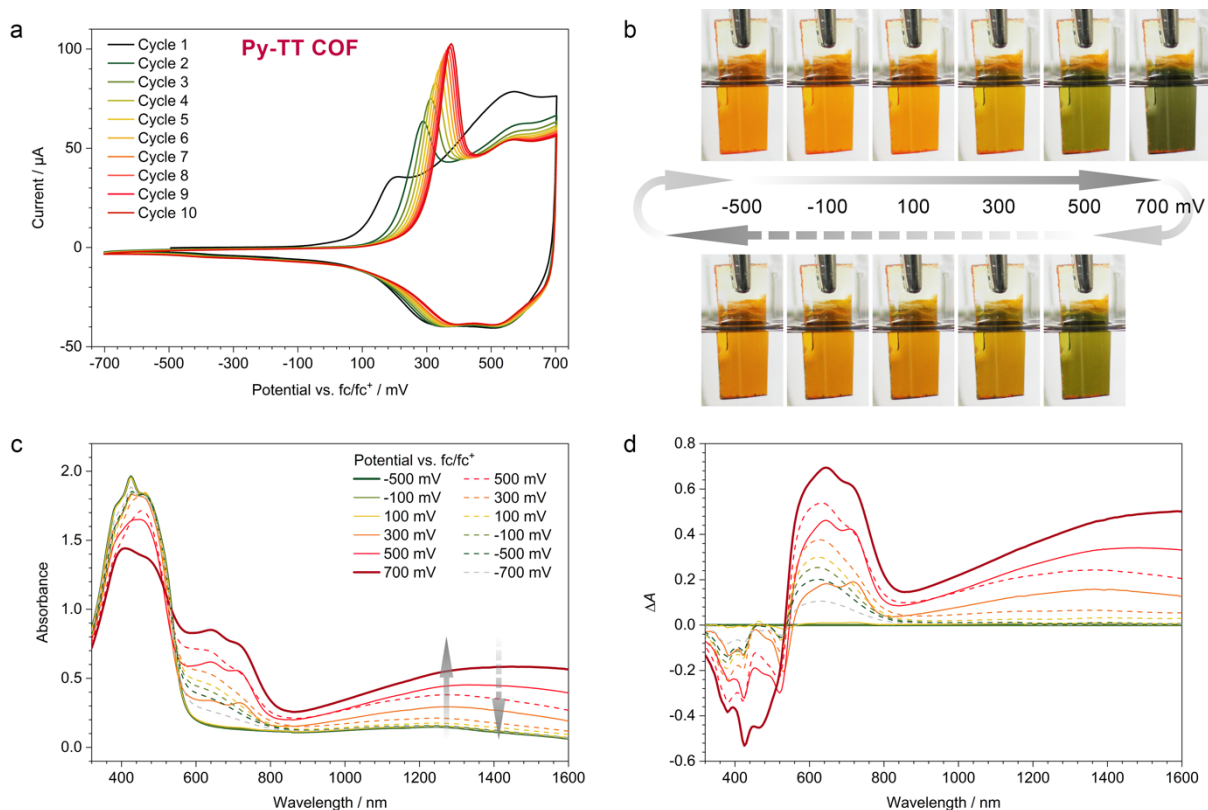


Figure 4.17. Electrochromic properties of the Py-TT COF.

(a) Cyclic voltammetry scans of a Py-TT COF film on ITO recorded at a scan rate of 20 mV s^{-1} . See the Methods section for experimental details. The Py-TT COF shows a well-defined oxidation wave at +200 mV during the first oxidation/reduction cycle, which shifts to higher potentials with every measurement cycle. We attribute this effect to limited diffusion of the electrolyte ions and a build-up of charged species in the considerably smaller pores of this COF (see the manuscript for discussion).

(b) Photographs of the COF film taken during an oxidation (top row, left to right) / reduction (bottom row, right to left) cycle illustrating the electrochromic color changes.

(c) UV-Vis-NIR spectra recorded at different potentials. The solid and dashed lines refer to spectra recorded at increasing (oxidation) and decreasing (reduction) potentials, respectively. Oxidation of the COF causes the evolution of two new absorption features between 600 and 800 nm as well as a broad IR absorption that extends beyond the measurement range. Unlike the large-pore Py-tTII and Py-nTII COFs, the electrochromic color changes of the Py-TT COF are not entirely reversible, most likely due to pore blocking and a partial delamination of COF layers (see the manuscript for discussion).

(d) Plot of the absorption difference between the oxidized COF and the initial spectrum. Oxidation of the Py-TT COF leads to the evolution of a new absorption band between 600 and 800 nm that is accompanied by a bleach band around 400 nm.

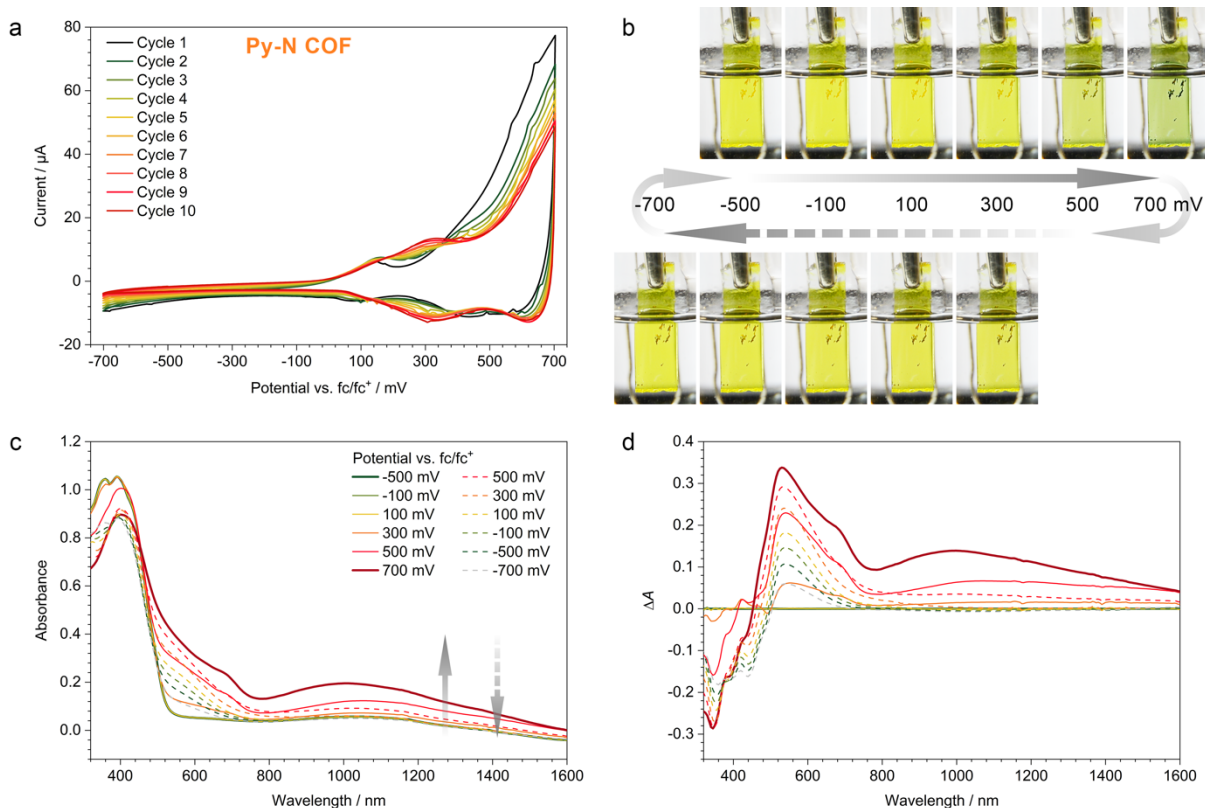


Figure 4.18. Electrochromic properties of the Py-N COF.

(a) Cyclic voltammograms of a Py-N COF film on ITO recorded at a scan rate of 20 mV s^{-1} . See the Methods section for experimental details. This COF shows an oxidation onset between 500 and 700 mV, which gradually shifts with every measurement cycle towards higher potentials. We attribute this effect to limited diffusion of the electrolyte ions and a build-up of charged species in the relatively small pores of this COF (see the manuscript for discussion). The small features at lower potentials are probably due to impurities or defects in the COF film.

(b) Photographs of the COF film taken during an oxidation (top row, left to right) / reduction (bottom row, right to left) cycle illustrating the electrochromic color changes.

(c) UV-Vis-NIR spectra recorded at different potentials. The solid and dashed lines refer to spectra recorded at increasing (oxidation) and decreasing (reduction) potentials, respectively. Oxidation of the COF causes the evolution of a new absorption feature around 600 nm as well as a broad IR absorption around 1000 nm. Unlike the large-pore Py-tfTII and Py-nTII COFs, the electrochromic color changes of the Py-N COF are not entirely reversible, most likely due to pore blocking and a partial delamination of COF layers (see the manuscript for discussion).

(d) Plot of the absorption difference between the oxidized COF and the initial spectrum. Oxidation of the Py-N COF leads to the evolution of a new absorption band around 600 nm that is accompanied by a bleach band around 380 nm.

Section H – Switching speed and stability

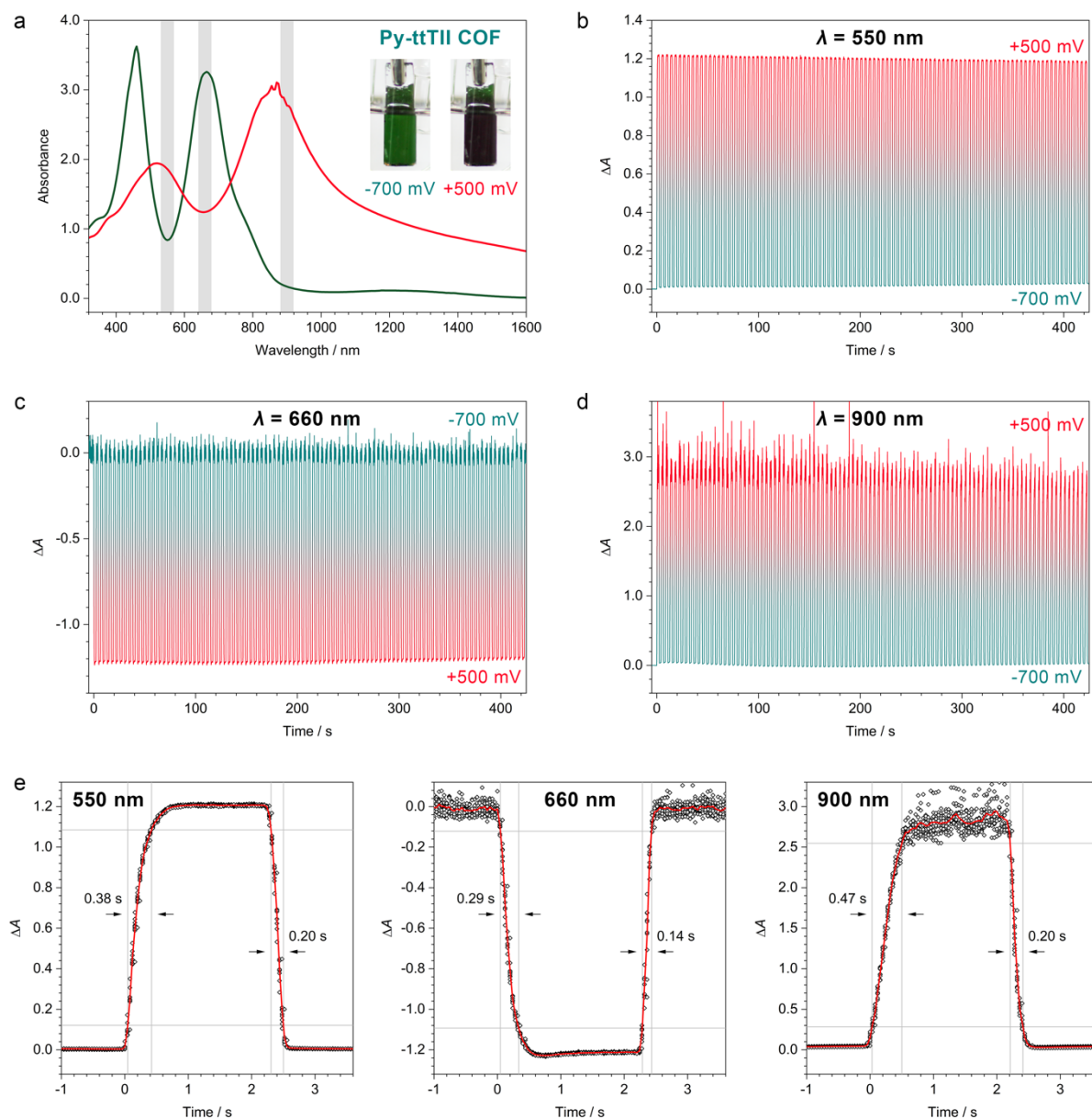


Figure 4.19. Electrochromic switching of the Py-ttTII COF. To avoid any “burn-in” effects, the switching experiments have been conducted with three freshly synthesized Py-ttTII COF samples from the same batch (one for each wavelength). Thus, time = 0 s corresponds to the first time that the samples are oxidized. Any differences between the ΔA values in (a) and (b)/(c)/(d) are due to slight variations in film thicknesses.

(a) Absorption spectra of a Py-ttTII COF film on ITO at -700 mV (green line) and $+500$ mV vs. fc/fc^+ (red line). The wavelengths used for the electrochromic switching experiments are indicated by grey lines. Inset: Photographs of the COF film.

(b) Electrochromic switching between the neutral and oxidized form of a Py-ttTII COF film over 100 cycles. The applied potential is switched between -700 and $+500$ mV vs. fc/fc^+ and held constant for 2 s after each potential step. The change of the absorbance is monitored at 550 nm. At this wavelength, the absorbance increases by 1.2 OD units upon oxidation with almost no degradation over 100 cycles.

(c) Electrochromic switching over 100 cycles recorded at 660 nm. At this wavelength, the absorbance of the Py-ttTII COF is reduced by ca. 1.2 OD upon oxidation.

(d) Electrochromic switching over 100 cycles monitored at 900 nm. Upon oxidation, the absorbance increases by almost 3 OD.

(e) Switching speed of the Py-ttTII COF films in response to potential steps at 550 nm (left), 660 nm (middle) and 900 nm (right). The respective datasets (black dots) of the first ten switching cycles shown in (b)/(c)/(d) are

averaged (red lines). The response is extremely fast with response times of 0.29 – 0.47 s (coloration) and 0.14 – 0.20 s (bleaching) between the 10% and 90% boundaries (grey lines).

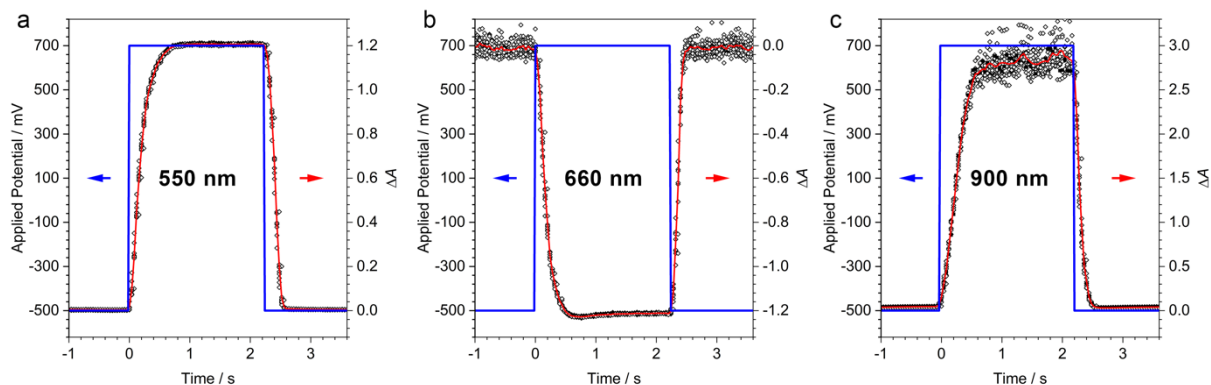


Figure 4.20. Overlay of the applied potential (blue, left y-axis) and the electrochromic response (black symbols and red line, right y-axis) of the Py-ttTII COF films at (a) 550 nm, (b) 660 nm, and (c) 900 nm.

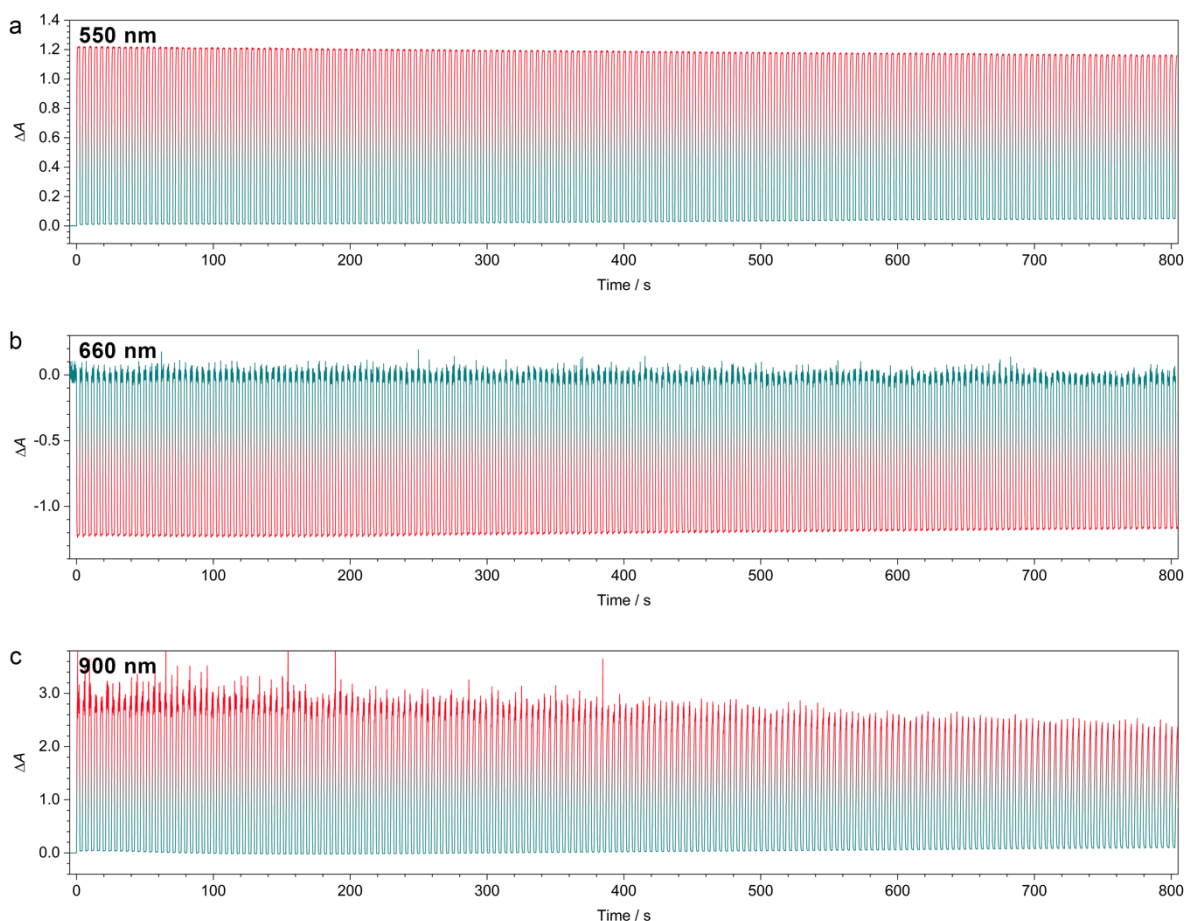


Figure 4.21. Electrochromic switching of the Py-ttTII COF over 200 cycles recorded at (a) 550 nm, (b) 660 nm, and (c) 900 nm. To avoid any “burn-in” effects, the switching experiments have been conducted with three freshly synthesized Py-ttTII COF samples from the same batch (one for each wavelength). Thus, time = 0 s corresponds to the first time that the samples are oxidized. The applied potential is switched between -700 and $+500$ mV vs. fc/fc^+ and held constant for 2 s after each potential step.

Section I – Coloration efficiency and extracted charge

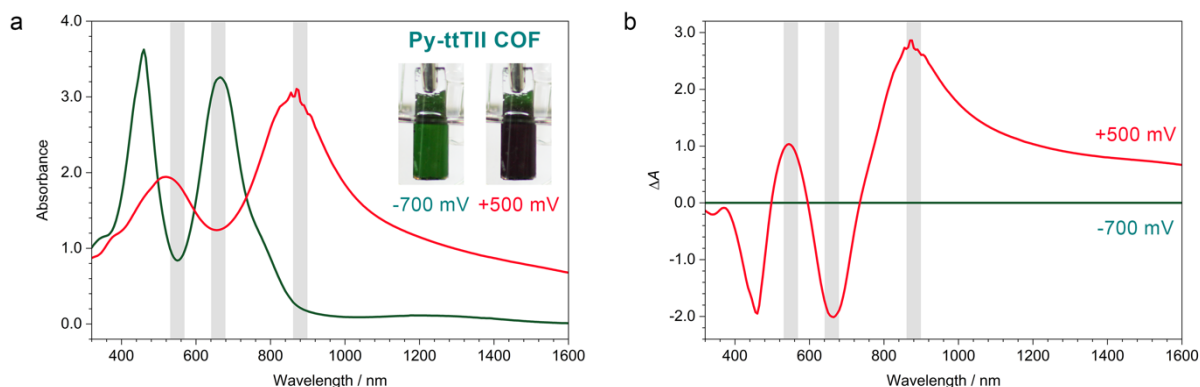


Figure 4.22. Spectra of the Py-ttTII COF in the neutral (green) and the 2x oxidized state (red). **(a)** Absorption spectra. **(b)** Absorption difference between the neutral and the oxidized COF. The wavelengths used for the calculation of the coloration efficiency are indicated by grey lines.

The electrochromic coloration efficiency (CE) relates the absorption change to the injected or extracted charge per unit area.

$$CE(\lambda) = \frac{\Delta A(\lambda)}{Q/A}$$

ΔA is the absorption difference at the respective wavelength λ (Figure 4.22b).

$$\Delta A(550 \text{ nm}) = 1.03 \quad \Delta A(660 \text{ nm}) = 2.01 \quad \Delta A(880 \text{ nm}) = 2.78$$

A is the electrode area in contact with the electrolyte.

$$A = 11 \text{ mm} \times 6.3 \text{ mm} = 0.69 \text{ cm}^2$$

Q is the extracted charge, calculated from the oxidation scan shown in Figures 4.3b and 4.14a.

$$Q = 0.00223 \text{ C} \quad (0.00324 \text{ C cm}^{-2}) \text{ for the two oxidation waves } (-500 \text{ to } +470 \text{ mV vs. fc/fc}^+).$$

Using the above expression, the Py-ttTII COF has the following wavelength-dependent coloration efficiencies:

$$CE(550 \text{ nm}) = 318 \pm 32 \text{ cm}^2 \text{ C}^{-1}$$

$$CE(660 \text{ nm}) = 620 \pm 62 \text{ cm}^2 \text{ C}^{-1}$$

$$CE(880 \text{ nm}) = 858 \pm 86 \text{ cm}^2 \text{ C}^{-1}$$

These values are several times higher than the CEs of previous electrochromic COFs.^[20, 21]

How much charge is extracted per unit cell?

The 430 nm thick Py-ttTII COF film has a volume of $2.95 \times 10^{-11} \text{ m}^3$ using the electrode dimensions stated above and assuming a pinhole-free film with 70% density due to its unique pillar-like morphology (Figure 4.12c). Using the refined unit cell parameters ($V = 1.27 \times 10^{-26} \text{ m}^3$), this relates to 1.63×10^{15} unit cells. Hence, the maximum charge that can be extracted by oxidation of every ttTII unit (the unit cell contains four) is

$$Q_{ox1} = 4Ne = 0.00104 \text{ C (} 0.00152 \text{ C cm}^{-2}\text{)}$$

$$Q_{ox2} = 4Ne \times 2 = 0.00209 \text{ C (} 0.00304 \text{ C cm}^{-2}\text{)}$$

N is the number of unit cells per film (corresponding to $4N$ ttTII units).

e is the elementary charge ($1.602 \times 10^{-19} \text{ C}$).

Q_{ox1} and Q_{ox2} refer to the one-electron and two-electron oxidation, respectively.

This calculation confirms our assignment of the two oxidation waves in the CV scans and the two distinct absorption spectra at different potentials to the one-electron and two-electron oxidation steps. The charge determined from the measured electrical current is slightly higher than the theoretical value, because there is a non-zero current flow through the electrochemical cell under applied bias.

Coloration efficiencies of the other COFs

$$CE(\lambda) = \frac{\Delta A(\lambda)}{Q/A}$$

Py-nTII COF

$$\Delta A(520 \text{ nm}) = 0.490 \quad \Delta A(630 \text{ nm}) = 0.547 \quad \Delta A(850 \text{ nm}) = 0.992$$

$$A = 10 \text{ mm} \times 6.7 \text{ mm} = 0.67 \text{ cm}^2 \quad Q = 0.000814 \text{ C (0.00122 C cm}^{-2}\text{)}$$

$$CE(520 \text{ nm}) = 400 \pm 60 \text{ cm}^2 \text{ C}^{-1}$$

$$CE(630 \text{ nm}) = 450 \pm 70 \text{ cm}^2 \text{ C}^{-1}$$

$$CE(850 \text{ nm}) = 820 \pm 120 \text{ cm}^2 \text{ C}^{-1}$$

Py-TII COF

$$\Delta A(500 \text{ nm}) = 0.179 \quad \Delta A(630 \text{ nm}) = 0.208 \quad \Delta A(820 \text{ nm}) = 0.275$$

$$A = 13 \text{ mm} \times 5.8 \text{ mm} = 0.75 \text{ cm}^2 \quad Q = 0.00103 \text{ C (0.00137 C cm}^{-2}\text{)}$$

$$CE(500 \text{ nm}) = 130 \pm 20 \text{ cm}^2 \text{ C}^{-1}$$

$$CE(630 \text{ nm}) = 150 \pm 20 \text{ cm}^2 \text{ C}^{-1}$$

$$CE(820 \text{ nm}) = 200 \pm 30 \text{ cm}^2 \text{ C}^{-1}$$

Py-TT COF

$$\Delta A(645 \text{ nm}) = 0.692$$

$$A = 11 \text{ mm} \times 7.5 \text{ mm} = 0.83 \text{ cm}^2 \quad Q = 0.00163 \text{ C (0.00198 C cm}^{-2}\text{)}$$

$$CE(645 \text{ nm}) = 350 \pm 35 \text{ cm}^2 \text{ C}^{-1}$$

Py-N COF

$$\Delta A(530 \text{ nm}) = 0.336$$

$$A = 12 \text{ mm} \times 6.5 \text{ mm} = 0.78 \text{ cm}^2 \quad Q = 0.000738 \text{ C (0.000946 C cm}^{-2}\text{)}$$

$$CE(530 \text{ nm}) = 360 \pm 50 \text{ cm}^2 \text{ C}^{-1}$$

The CEs of the Py-ttTII and Py-nTII COFs, which are based on donor-acceptor-donor building blocks, are significantly higher than the CEs of the other frameworks, highlighting the importance of a suitable electronic design.

Section J – Building block syntheses

All reactions were performed in oven-dried glassware under argon atmosphere using standard Schlenk and glovebox techniques. Reagents and solvents were obtained in high-purity grades from commercial suppliers and were, unless shipped under argon, degassed and saturated with argon prior to use. Flash column chromatography was performed using silica gel (Acros Organics, 60 Å, 35 – 70 μm) and was continuously monitored via thin layer chromatography (TLC) using silica gel coated aluminum plates (Merck, 60 Å, F254).

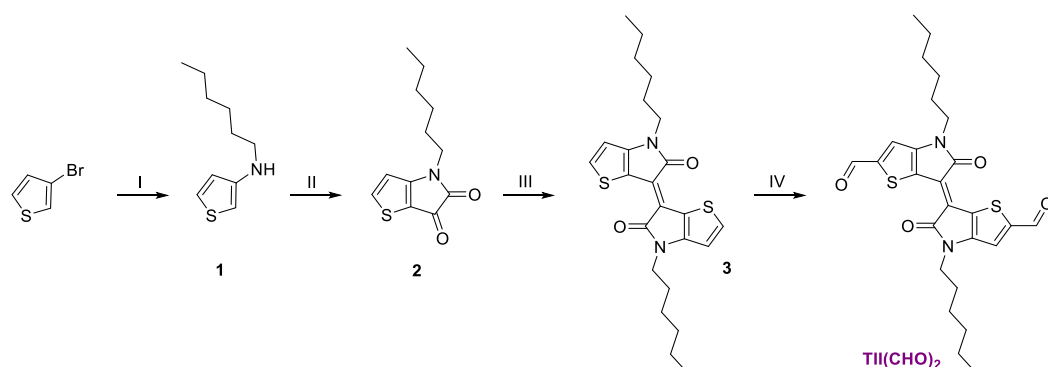
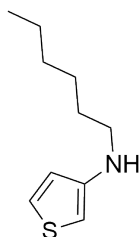


Figure 4.23. Syntheses of the hexyl-alkylated thienoisoindigo-core **3** and the TII(CHO)₂ building block. Reagents and conditions: **(I)** *n*-hexylamine, Cu, CuI, K₃PO₄, 2-dimethylaminoethanol, 80 °C, 65%. **(II)** oxalyl chloride, triethylamine, DCM, -15 °C/0 °C/rt, 53%. **(III)** Lawesson's reagent, toluene, 100 °C, 5 min, 51%. **(IV)** LDA, DMF, THF, -78 °C/rt, 39%.

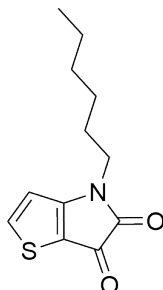
3-(hexylamino)thiophene (**1**)^[27, 40]



A reaction mixture containing 3-bromothiophene (12.2 g, 7.03 mL, 75.0 mmol, 1.0 eq.), *n*-hexylamine (11.4 g, 14.9 mL, 113 mmol, 1.5 eq.), copper powder (477 mg, 7.50 mmol, 10 mol%), CuI (1.43 g, 7.50 mmol, 10 mol%) and K₃PO₄ (31.8 g, 150 mmol, 2.0 eq.) in anhydrous 2-dimethylaminoethanol (75 mL) were stirred under argon at 80 °C for 48 h. After cooling to room temperature, the supernatant was decanted and collected, and the solid residue was washed with anhydrous THF (4x 20 mL). The combined liquids were concentrated under reduced pressure. Purification via high vacuum distillation (10⁻² mbar, 68 °C) yielded the title compound as a colorless and highly air-sensitive liquid (8.98 g, 49.0 mmol, 65%).

Due to the high air- and moisture-sensitivity, no NMR spectra were recorded and the product was used directly in the following step.

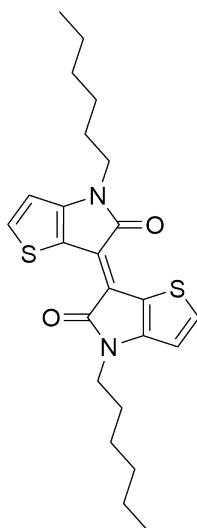
4-hexyl-4*H*-thieno[3,2-*b*]pyrrole-5,6-dione (2)



A solution of oxalyl chloride (9.95 g, 6.72 mL, 78.4 mmol, 1.6 eq.) in 49 mL of anhydrous DCM was cooled to $-15\text{ }^{\circ}\text{C}$. Compound 1 (8.98 g, 49.0 mmol, 1.0 eq.) in 84 mL anhydrous DCM was slowly added via a syringe over 20 minutes under argon atmosphere. After the dropwise addition of triethylamine (14.9 g, 20.4 mL, 147 mmol, 3.0 eq.) at $-15\text{ }^{\circ}\text{C}$, the resulting suspension was stirred for 1 h at $0\text{ }^{\circ}\text{C}$ and allowed to warm to room temperature overnight. The reaction mixture was quenched with H_2O , and the product was extracted with DCM. The combined organic phases were washed with brine three times, dried over MgSO_4 , and concentrated under reduced pressure. The product was purified by column chromatography (silica gel, DCM + 0.5% THF) to yield the title compound as a red oil (6.12 g, 25.8 mmol, 53%).

$^1\text{H-NMR}$ (400 MHz, CDCl_3): 7.99 (d, $J = 5.0$ Hz, 1H), 6.78 (d, $J = 5.0$ Hz, 1H), 3.65 (t, $J = 7.2$ Hz, 2H), 1.73 – 1.61 (m, 2H), 1.41 – 1.24 (m, 6H), 0.88 (t, $J = 7.1$ Hz, 3H).

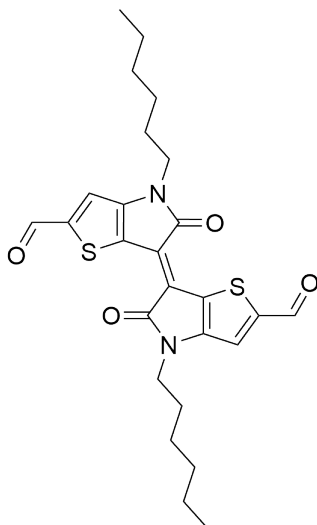
$^{13}\text{C-NMR}$ (101 MHz, CDCl_3): 173.2, 165.3, 161.6, 144.0, 113.1, 111.2, 42.3, 31.5, 28.3, 26.6, 22.6, 14.1.

***N,N'*-dihexyl-thienoisindigo (3)**

Compound **2** (4.68 g, 19.7 mmol, 2.0 eq.) was dissolved in 158 mL anhydrous toluene and added to Lawesson's reagent (3.99 g, 9.87 mmol, 1.0 eq.) under argon atmosphere at room temperature. In a preheated oil bath, the reaction mixture was stirred at 100 °C for 5 minutes. After cooling to room temperature, the product was concentrated under reduced pressure and all volatiles were removed under high vacuum. The crude product was purified by column chromatography (silica gel, DCM/*n*-hexane 2:1) to yield the title compound as a dark violet powder (2.23 g, 5.04 mmol, 51%).

¹H-NMR (400 MHz, CDCl₃): 7.53 (d, *J* = 5.2 Hz, 2H), 6.81 (d, *J* = 5.2 Hz, 2H), 3.80 (t, *J* = 7.3 Hz, 4H), 1.78 – 1.67 (m, 4H), 1.40 – 1.24 (m, 12H), 0.87 (t, *J* = 7.1 Hz, 6H).

¹³C-NMR (101 MHz, CDCl₃): 171.1, 151.4, 134.5, 121.3, 114.3, 111.3, 42.0, 31.6, 28.7, 26.7, 22.7, 14.2.

5,5'-diformyl-*N,N'*-dihexyl-thienoisindigo (TH(CHO)₂)

Following a literature procedure,^[41] a solution of compound **3** (443 mg, 1.0 mmol, 1.0 eq.) in 40 mL anhydrous THF was added dropwise to a 1.0 M solution of LDA in THF/hexane (8.0 mmol, 8.0 eq.) cooled at $-78\text{ }^{\circ}\text{C}$ under argon atmosphere. The reaction mixture was stirred for 2 h at $-78\text{ }^{\circ}\text{C}$. Anhydrous DMF (0.92 mL, 12 mmol, 12 eq.) was added dropwise and the resulting solution was stirred overnight, allowing the mixture to slowly warm to room temperature. The reaction was quenched with 100 mL of 0.5 M aqueous HCl, stirred for 1 h and extracted with DCM. The organic phase was washed with brine (2x), dried over MgSO_4 and concentrated under reduced pressure. The product was purified via column chromatography (silica gel, DCM + 2% EtOAc) to yield the title compound as an indigo blue solid (194 mg, 0.39 mmol, 39%).

^1H NMR (400 MHz, CDCl_3): 9.93 (s, 2H), 7.40 (s, 2H), 3.84 (t, $J = 7.3$ Hz, 4H), 1.80 – 1.70 (m, 4H), 1.42 – 1.26 (m, 12H), 0.89 (t, $J = 7.1$ Hz, 6H).

^{13}C NMR (101 MHz, CDCl_3): 183.0, 169.8, 152.3, 149.5, 123.8, 122.4, 115.1, 42.2, 31.5, 28.4, 26.7, 22.7, 14.1.

HR-EI-MS: m/z 498.16 (M^+ , calculated for $\text{C}_{26}\text{H}_{30}\text{N}_2\text{O}_4\text{S}_2$: 498.16).

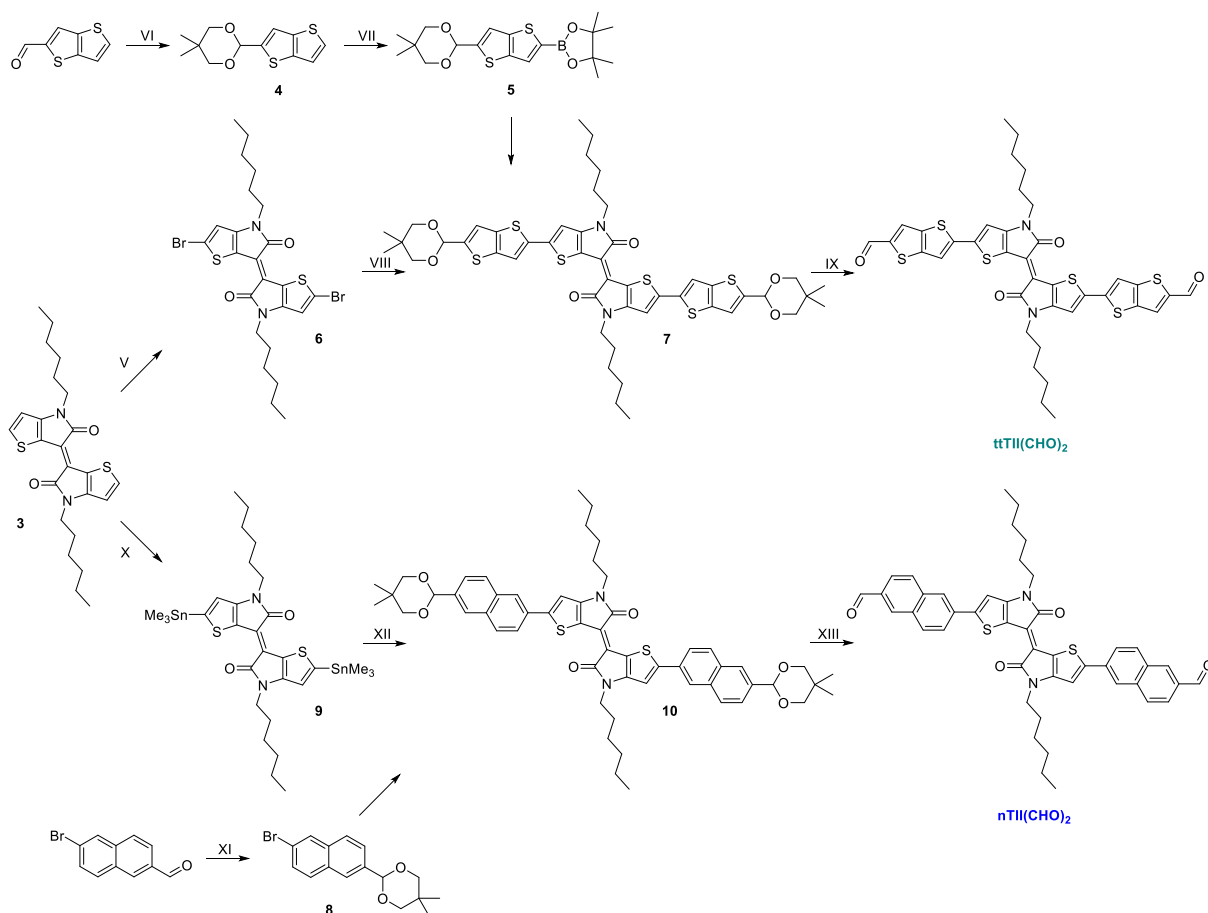
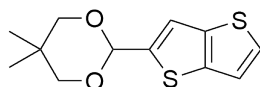


Figure 4.24. Syntheses of the new ttII(CHO)₂ and nII(CHO)₂ building blocks. Reagents and conditions: (V) NBS, THF, 0 °C, 84%. (VI) *p*-toluenesulfonic acid monohydrate, 2,2-dimethyl-1,3-propanediol, toluene, reflux, 97%. (VII) *n*-BuLi, 2-isopropoxy-4,4,5,5-tetramethyl-1,3,2-dioxaborolane, THF, -78 °C/rt, 58%. (VIII) Pd₂(dba)₃·CHCl₃, SPhos, K₂CO₃, *o*-xylene/H₂O, 100 °C, 74%. (IX) TFA, H₂O, rt, 76%. (X) LDA, Me₃SnCl, THF, -78 °C/rt, 83%. (XI) *p*-toluenesulfonic acid monohydrate, 2,2-dimethyl-1,3-propanediol, toluene, reflux, 83%. (XII) Pd₂(dba)₃, P(*o*-tol)₃, toluene, 110 °C, 84%. (XIII) TFA, H₂O, CHCl₃, rt, 81%.

5,5-dimethyl-2-(thieno[3,2-*b*]thiophen-2-yl)-1,3-dioxane (4)

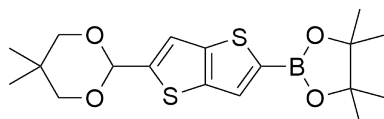


A reaction mixture containing thieno[3,2-*b*]thiophene-2-carboxaldehyde (1000 mg, 5.94 mmol, 1.0 eq.), 2,2-dimethyl-1,3-propanediol (1175 mg, 11.3 mmol, 1.9 eq.) and *p*-toluenesulfonic acid monohydrate (91.3 mg, 0.48 mmol, 8 mol%) in 59 mL toluene was refluxed at 110 °C for 2.5 h. After cooling to room temperature, the reaction mixture was poured into water, extracted with DCM and washed with brine (3x). The organic phase was dried over MgSO₄ and concentrated under reduced pressure. Purification via column chromatography (silica gel, DCM/*n*-hexane 3:2) yielded the title compound as a white powder (1468 mg, 5.77 mmol, 97%).

¹H NMR (400 MHz, CDCl₃): 7.35 (d, *J* = 5.2 Hz, 1H), 7.32 (s, 1H), 7.24 (d, *J* = 5.3 Hz, 1H), 5.68 (s, 1H), 3.78 (d, *J* = 11.3 Hz, 2H), 3.66 (d, *J* = 10.8 Hz, 2H), 1.29 (s, 3H), 0.81 (s, 3H).

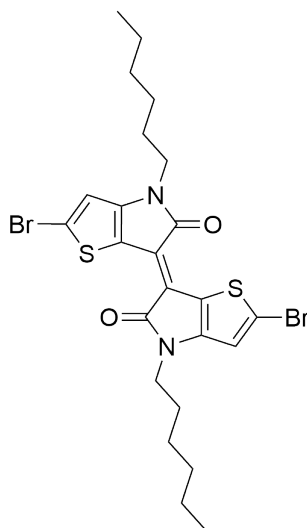
^{13}C NMR (101 MHz, CDCl_3): 143.4, 139.4, 138.5, 127.5, 119.7, 117.7, 98.5, 77.7, 30.4, 23.1, 22.0.

2-(5-(5,5-dimethyl-1,3-dioxan-2-yl)thieno[3,2-*b*]thiophen-2-yl)-4,4,5,5-tetramethyl-1,3,2-dioxaborolane (5)



Compound **4** (715 mg, 2.81 mmol, 1.0 eq.) was dissolved in 23.5 mL THF and cooled to $-78\text{ }^\circ\text{C}$. *n*-BuLi (2.0 M in cyclohexane, 4.22 mmol, 1.5 eq.) was added dropwise and the solution was stirred for 1.5 h at $-78\text{ }^\circ\text{C}$. Subsequently, 2-isopropoxy-4,4,5,5-tetramethyl-1,3,2-dioxaborolane (785 mg, 0.86 mL, 4.22 mmol, 1.5 eq.) was added and the reaction mixture was stirred for 1 h at $-78\text{ }^\circ\text{C}$. The resulting suspension was allowed to warm to room temperature and stirred overnight. The reaction was quenched with H_2O (25 mL) and stirred for 15 minutes. The product was extracted with diethyl ether and washed with brine three times. The organic phase was dried over MgSO_4 and concentrated under reduced pressure. The product was purified via recrystallization from *n*-hexane (75 mL, $70\text{ }^\circ\text{C}$ to room temperature), collected by filtration and dried under high vacuum to yield the title compound as colorless needles (612 mg, 1.61 mmol, 58%).

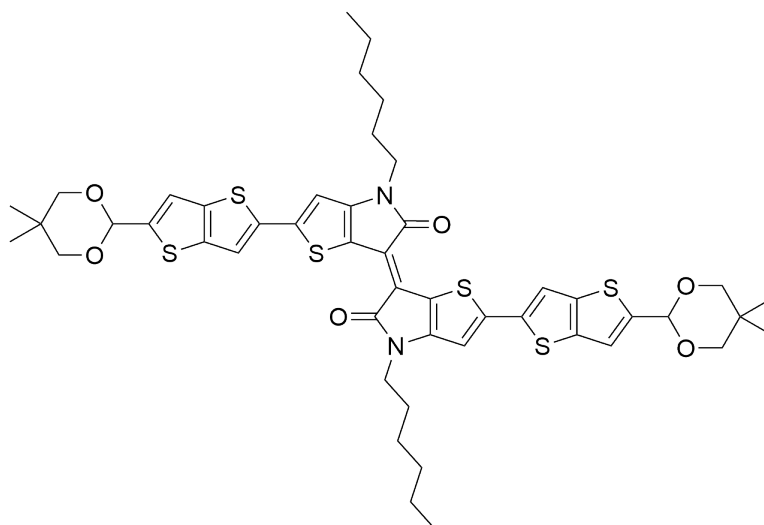
^1H NMR (400 MHz, CDCl_3): 7.73 (s, 1H), 7.33 (s, 1H), 5.68 (s, 1H), 3.78 (d, $J = 11.3\text{ Hz}$, 2H), 3.66 (d, $J = 10.7\text{ Hz}$, 2H), 1.35 (s, 12H), 1.28 (s, 3H), 0.81 (s, 3H).

5,5'-dibromo-*N,N'*-dihexyl-thienoisindigo (6)

A solution of compound **3** (2230 mg, 5.04 mmol, 1.0 eq.) in 231 mL anhydrous THF was cooled to 0 °C. *N*-Bromosuccinimide (1883 mg, 10.6 mmol, 2.1 eq.) was added and the reaction mixture was stirred for 1.5 h at 0 °C in the dark. The reaction was quenched with H₂O, extracted with CHCl₃, and washed with brine (2x). The organic phase was dried over MgSO₄ and concentrated under reduced pressure. Purification via column chromatography (silica gel, CHCl₃/cyclohexane 1:1) yielded the title compound as a dark blue powder (2547 mg, 4.24 mmol, 84%).

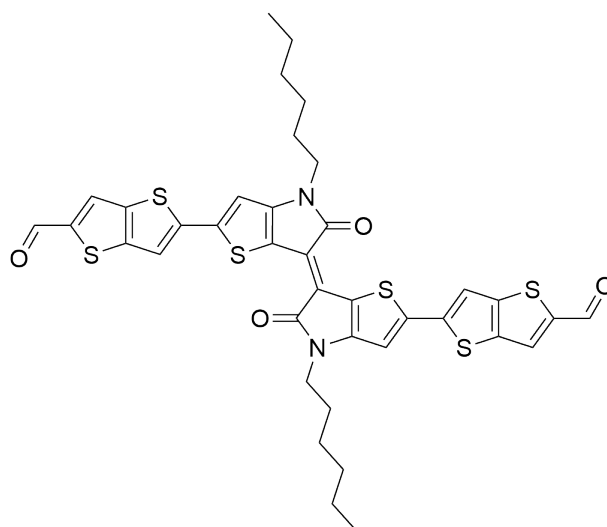
¹H NMR (400 MHz, CDCl₃): 6.84 (s, 2H), 3.74 (t, *J* = 7.3 Hz, 4H), 1.75 – 1.63 (m, 4H), 1.40 – 1.24 (m, 12H), 0.88 (t, *J* = 7.1 Hz, 6H).

¹³C NMR (101 MHz, CDCl₃): 170.2, 150.0, 123.4, 119.9, 115.0, 114.8, 42.0, 31.6, 28.7, 26.7, 22.7, 14.2.

5,5'-bis(5-(5,5-dimethyl-1,3-dioxane-2-yl)thienothiophen-2-yl)-*N,N'*-dihexylthienoindigo (7)

A reaction mixture containing compound **6** (143 mg, 0.24 mmol, 1.0 eq.), compound **5** (217 mg, 0.57 mmol, 2.4 eq.), Pd₂(dba)₃·CHCl₃ (24.6 mg, 0.024 mmol, 10 mol%), SPhos (19.5 mg, 0.05 mmol, 20 mol%), and K₂CO₃ (132 mg, 0.95 mmol, 4 eq.) in 7.6 mL *o*-xylene and 1.9 mL H₂O was stirred at 100 °C for 20 h under argon atmosphere. After cooling to room temperature, the mixture was poured into water and extracted with DCM. The organic phase was dried over MgSO₄ and concentrated under reduced pressure. Purification by column chromatography (silica gel, DCM) yielded the title compound as a dark green powder (168 mg, 0.18 mmol, 74%).

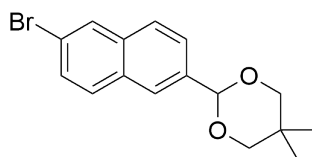
¹H NMR (400 MHz, CDCl₃): 7.53 (s, 2H), 7.29 (s, 2H), 6.91 (s, 2H), 5.68 (s, 2H), 3.86 – 3.75 (m, 8H), 3.67 (d, *J* = 11.0 Hz, 4H), 1.80 – 1.70 (m, 4H), 1.45 – 1.31 (m, 12H), 1.29 (s, 6H), 0.89 (t, *J* = 7.1 Hz, 6H), 0.82 (s, 6H).

5,5'-bis(2-formylthienothiophen-5-yl)-*N,N'*-dihexyl-thienoindigo (ttTII(CHO)₂)

To a solution of compound **7** (160 mg, 0.17 mmol, 1.0 eq.) dissolved in 25 mL CHCl₃, trifluoroacetic acid (5 mL) and H₂O (0.5 mL) were added dropwise and left to stir at room temperature for 4 h under argon atmosphere. The reaction mixture was slowly added into saturated aqueous NaHCO₃ (100 mL) and extracted with CHCl₃. The combined organic phase was washed with brine, dried over MgSO₄ and concentrated to about 100 mL under reduced pressure. The product was precipitated by addition of MeOH (100 mL), collected by filtration, washed with CHCl₃ (20 mL) and dried under high vacuum to yield the title compound as a dark green powder (99 mg, 0.13 mmol, 76%).

¹H NMR (400 MHz, CDCl₃): 9.96 (s, 2H), 7.90 (s, 2H), 7.59 (s, 2H), 7.01 (s, 2H), 3.85 (t, *J* = 7.4 Hz, 4H), 1.83 – 1.73 (m, 4H), 1.41 – 1.29 (m, 12H), 0.90 (t, *J* = 7.0 Hz, 6H).

HR-EI-MS: *m/z* 774.08 (M⁺, calculated for C₃₈H₃₄N₂O₄S₆: 774.08).

2-(6-bromonaphthalen-2-yl)-5,5-dimethyl-1,3-dioxane (8**)**

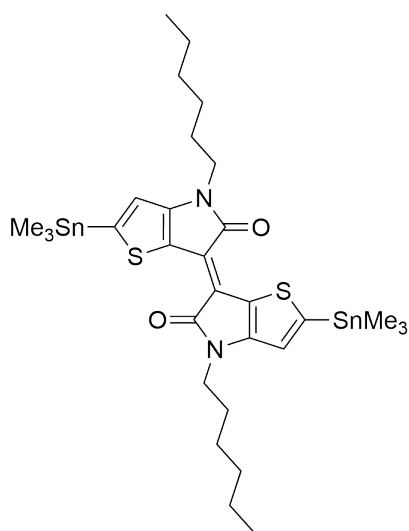
A reaction mixture containing 6-bromo-2-naphthaldehyde (500 mg, 2.1 mmol, 1.0 eq.), *p*-toluenesulfonic acid monohydrate (32.3 mg, 0.17 mmol, 8 mol%) and 2,2-dimethyl-1,3-propanediol (421 mg, 4.0 mmol, 1.9 eq.) in anhydrous toluene (21 mL) were refluxed at 110 °C for 2.5 h under argon atmosphere. After cooling to room temperature, the reaction mixture was poured into water, extracted with DCM and washed with brine (3x). The organic phase was

dried over MgSO_4 , concentrated under reduced pressure, and purified via column chromatography (silica gel, DCM/cyclohexane 1:1) to yield the title compound as a white powder (589 mg, 1.83 mmol, 86%).

^1H NMR (400 MHz, CDCl_3): 8.00 (s, 1H), 7.95 (s, 1H), 7.79 – 7.70 (m, 4H), 7.65 (dd, $J = 8.5$, 1.7 Hz, 1H), 7.54 (dd, $J = 8.7$, 2.0 Hz, 1H), 5.54 (s, 1H), 3.82 (d, $J = 11.3$, 2H), 3.72 (d, $J = 10.6$, 2H), 1.33 (s, 3H), 0.83 (s, 3H).

^{13}C NMR (101 MHz, CDCl_3): 136.6, 134.8, 131.6, 130.2, 129.9, 129.6, 127.4, 125.6, 125.1, 120.4, 101.7, 30.5, 27.1, 23.3, 22.1.

5,5'-bis(trimethylstannyl)-*N,N'*-dihexyl-thienoindigo (9)^[41]

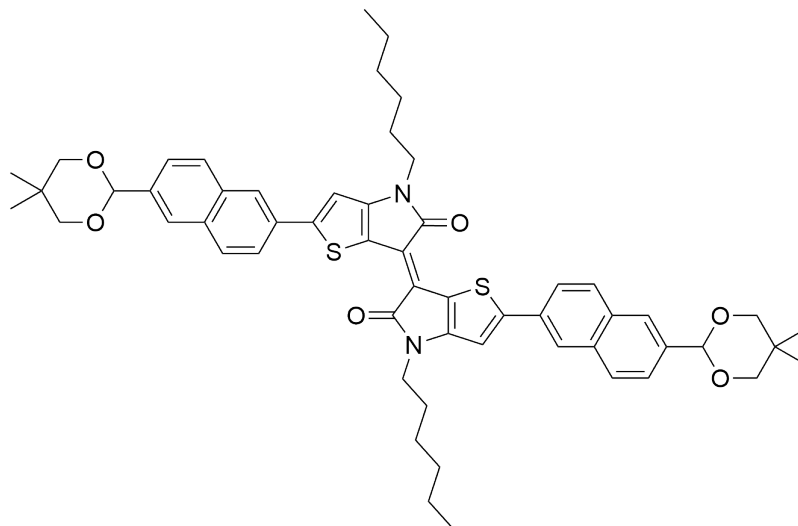


Compound **3** (443 mg, 1.0 mmol, 1 eq.) was dissolved in 50 mL anhydrous THF and added dropwise to LDA (1.0 M in THF/hexane, 8.0 mmol, 8.0 eq.) precooled to $-78\text{ }^\circ\text{C}$ under argon atmosphere. After stirring for 2 h at this temperature, Me_3SnCl (1.0 M in THF, 12 mmol, 12.0 eq.) was added and the reaction mixture was allowed to slowly warm to room temperature overnight. The reaction was quenched with H_2O and all volatiles were removed under high vacuum at $70\text{ }^\circ\text{C}$. The residue was dissolved in DCM, washed with brine (3x), dried over MgSO_4 , and the solvent was removed under reduced pressure. The product was washed with MeOH (200 mL), filtrated and dried under high vacuum to yield the title compound as a purple powder (639 mg, 0.83 mmol, 83%).

^1H NMR (400 MHz, CDCl_3): 6.83 (s, 2H), 3.81 (t, $J = 7.4$ Hz, 4H), 1.79 – 1.68 (m, 4H), 1.42 – 1.24 (m, 12H), 0.88 (t, $J = 7.1$ Hz, 6H), 0.43 (s, with Sn coupling, 18H).

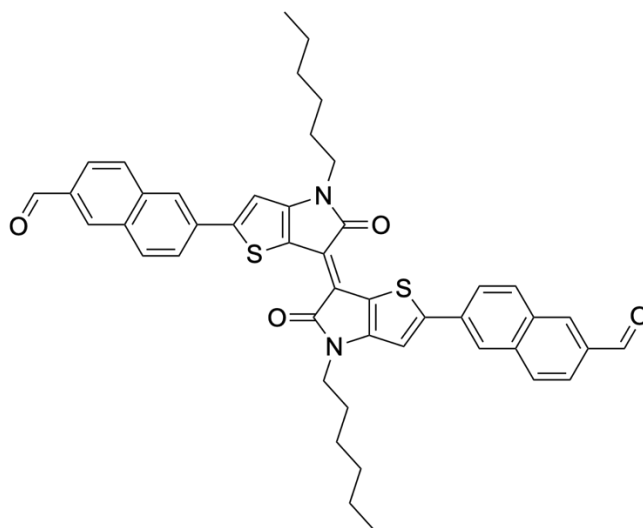
^{13}C NMR (101 MHz, CDCl_3): 171.8, 152.5, 151.1, 120.4, 120.2, 117.8, 42.0, 31.7, 28.8, 26.8, 22.7, 14.2, -7.9.

5,5'-bis(6-(5,5-dimethyl-1,3-dioxane-2-yl)naphthalen-2-yl)-*N,N'*-dihexyl-thienoindigo (10)



A reaction mixture containing compound **9** (230 mg, 0.3 mmol, 1.0 eq.), compound **8** (212 mg, 0.66 mmol, 2.2 eq.), $\text{Pd}_2(\text{dba})_3$ (13.7 mg, 0.015 mmol, 5 mol%) and tri(*o*-tolyl)phosphine (36.5 mg, 0.12 mmol, 0.4 eq.) in 10 mL anhydrous toluene was heated to 110 °C for 4 d. After cooling to room temperature, all volatiles were removed under high vacuum at 60 °C. The solid residue was dissolved in DCM and purified by column chromatography (silica gel, DCM) to yield the title compound as a blue-green powder (234 mg, 0.25 mmol, 84%).

^1H NMR (400 MHz, CDCl_3): 8.22 (s, 2H), 7.96 (s, 2H), 7.91 – 7.81 (m, 6H), 7.67 (dd, $J = 8.5$, 1.7 Hz, 2H), 7.17 (s, 2H), 5.56 (s, 2H), 3.89 (t, $J = 7.3$ Hz, 4H), 3.84 (d, $J = 11.2$ Hz, 4H), 3.72 (d, $J = 10.9$ Hz, 4H), 1.88 – 1.77 (m, 4H), 1.42 – 1.29 (m, 18H), 0.91 (t, $J = 7.1$ Hz, 6H), 0.85 (s, 6H).

5,5'-bis(2-formylnaphthalen-6-yl)-*N,N'*-dihexyl-thienoisindigo (nTII(CHO)₂)

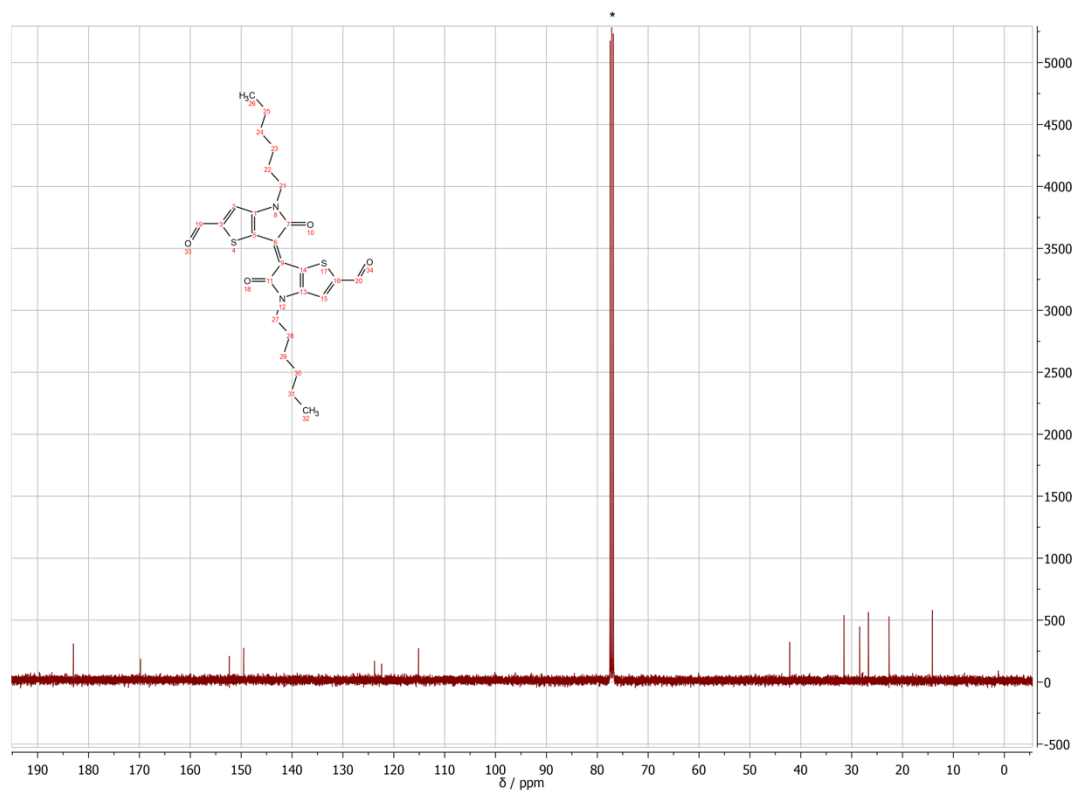
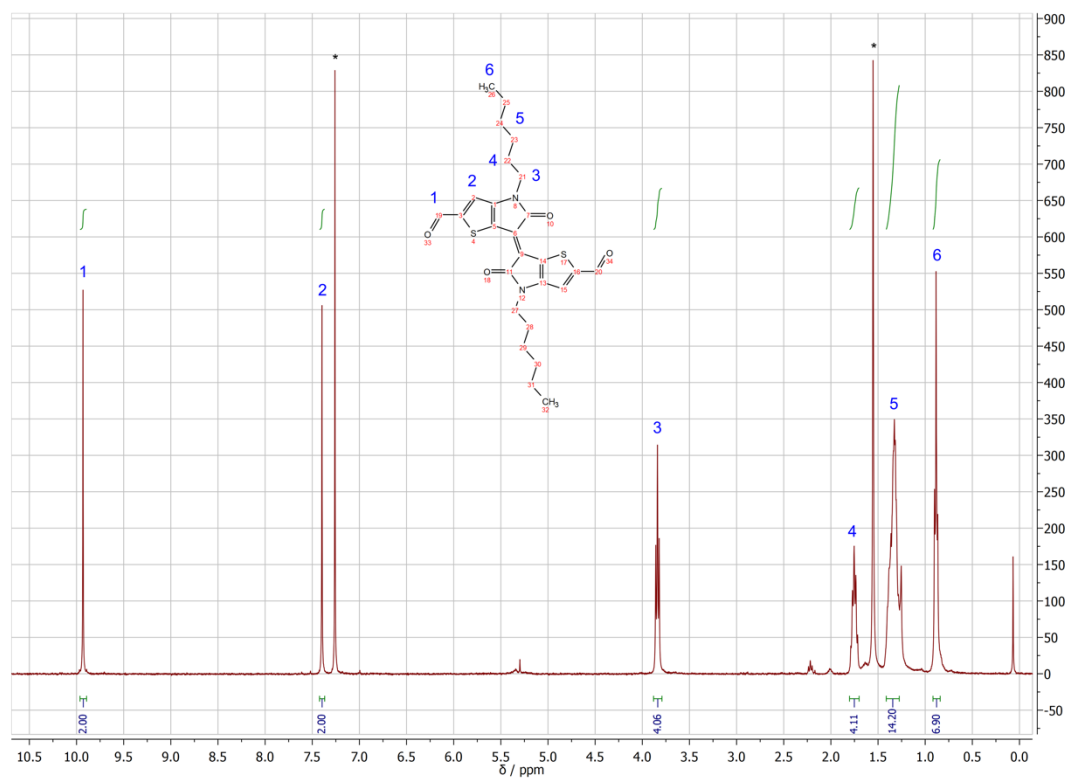
To a solution of compound **10** (572 mg, 0.62 mmol, 1.0 eq.) dissolved in 60 mL CHCl₃, trifluoroacetic acid (12 mL) and H₂O (1.2 mL) were added dropwise and left to stir at room temperature for 4 h under argon atmosphere. The reaction was neutralized by the dropwise addition into saturated aqueous NaHCO₃ (150 mL) and extracted with CHCl₃. The product was precipitated by the addition of MeOH (50 mL), collected by filtration, and washed with H₂O (200 mL), acetone (30 mL) and CHCl₃ (20 mL). Drying under high vacuum yielded the title compound as a dark green powder (375 mg, 0.50 mmol, 81%).

¹H NMR (400 MHz, CDCl₃): 10.15 (s, 2H), 8.30 (s, 2H), 8.25 (s, 2H), 8.03 – 7.90 (m, 8H), 7.24 (s, 2H), 3.90 (t, *J* = 7.3 Hz, 4H), 1.87 – 1.77 (m, 4H), 1.42 – 1.28 (m, 12H), 0.91 (t, *J* = 7.0 Hz, 6H).

HR-EI-MS: *m/z* 750.26 (M⁺, calculated for C₄₆H₄₂N₂O₄S₂: 750.26).

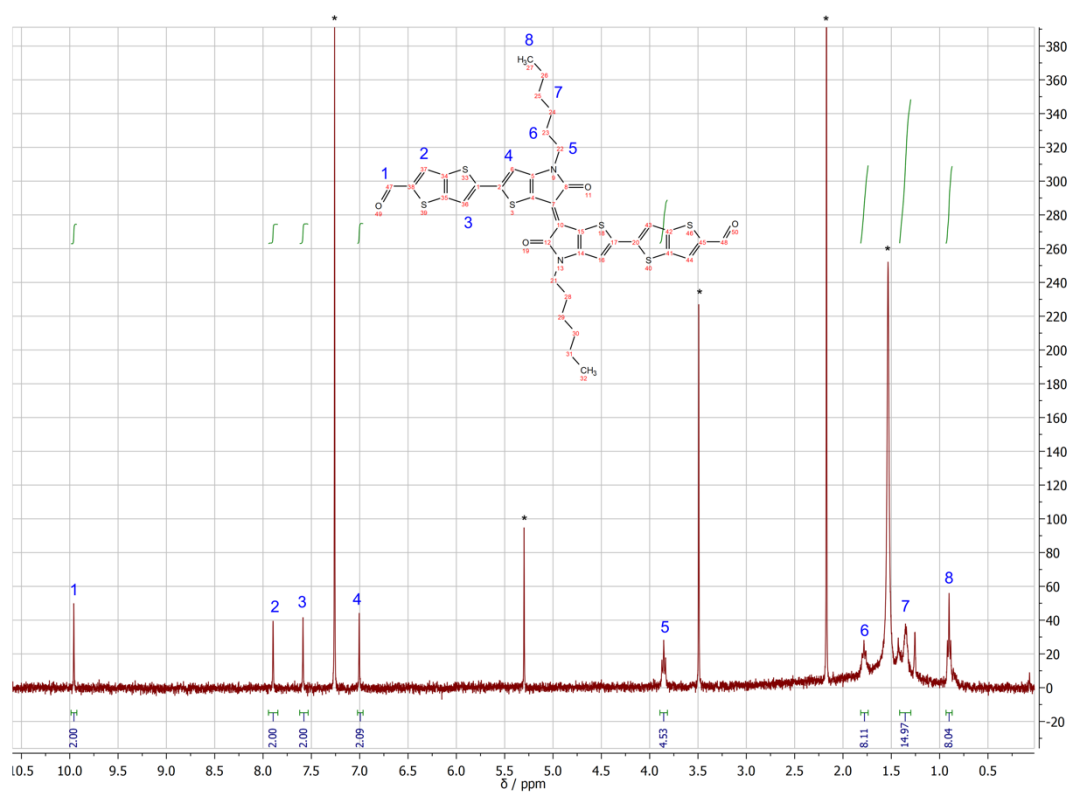
Section K – NMR spectra of the TII building blocks

^1H and ^{13}C NMR spectra. Residual (undeuterated) solvent peaks and $\text{H}_2\text{O}/\text{HDO}$ are marked with asterisks.

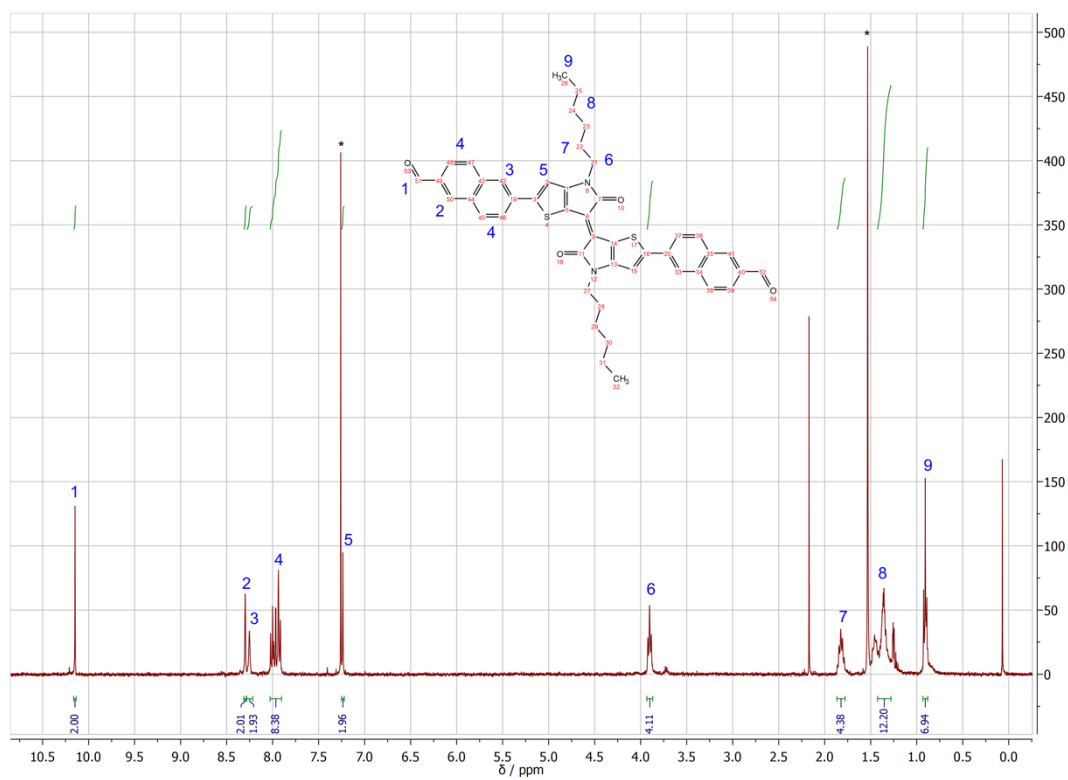
TII(CHO) $_2$ 

4 Fast-Switching Vis-IR Electrochromic Covalent Organic Frameworks

ttTII(CHO)₂



nTII(CHO)₂



Section L – Solid-state NMR spectra

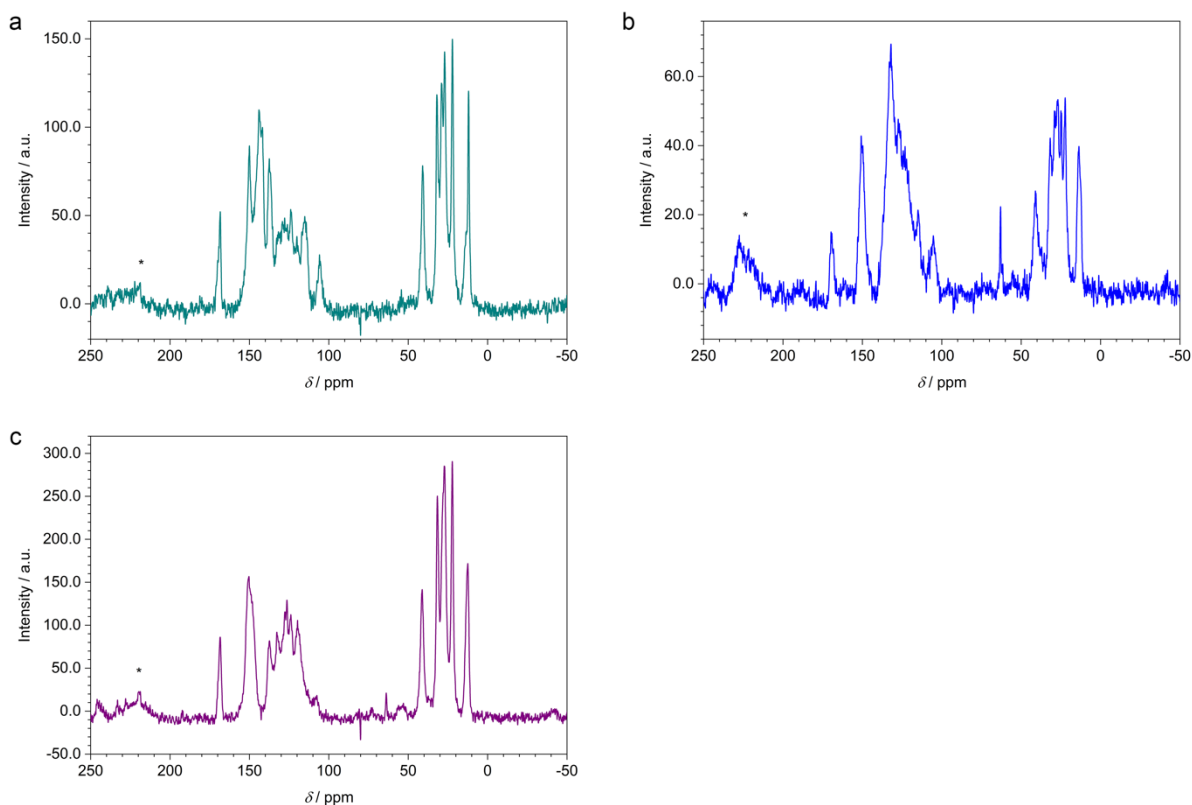


Figure 4.25. Solid-state ^{13}C cross-polarization magic angle spinning (CP-MAS) NMR spectra of the thienoindigo COFs. **(a)** Py-ttTII COF, **(b)** Py-nTII COF, **(c)** Py-TII COF. The appearance of the characteristic imine C=N resonance at around 170 ppm and the absence of residual aldehyde signals around 190 ppm confirm the successful COF formation.^[42] The signals in the 100-150 ppm range originate from the (hetero)aromatic framework backbone, while the six well-resolved signals below 50 ppm are due to the hexyl chains. Spinning sidebands are marked with asterisks.

4.7 References

- [1] A. P. Côte, A. I. Benin, N. W. Ockwig, M. O'Keeffe, A. J. Matzger, O. M. Yaghi, *Science* **2005**, *310*, 1166-1170.
- [2] E. Jin, M. Asada, Q. Xu, S. Dalapati, M. A. Addicoat, M. A. Brady, H. Xu, T. Nakamura, T. Heine, Q. Chen, D. Jiang, *Science* **2017**, *357*, 673-676.
- [3] T. Ma, E. A. Kapustin, S. X. Yin, L. Liang, Z. Zhou, J. Niu, L.-H. Li, Y. Wang, J. Su, J. Li, X. Wang, W. D. Wang, W. Wang, J. Sun, O. M. Yaghi, *Science* **2018**, *361*, 48-52.
- [4] H. Xu, J. Gao, D. Jiang, *Nat. Chem.* **2015**, *7*, 905-912.
- [5] R. L. Li, N. C. Flanders, A. M. Evans, W. Ji, I. Castano, L. X. Chen, N. C. Gianneschi, W. R. Dichtel, *Chem. Sci.* **2019**, *10*, 3796-3801.
- [6] L. Ascherl, T. Sick, J. T. Margraf, S. H. Lapidus, M. Calik, C. Hettstedt, K. Karaghiosoff, M. Döblinger, T. Clark, K. W. Chapman, F. Auras, T. Bein, *Nat. Chem.* **2016**, *8*, 310-316.
- [7] E. L. Spitler, W. R. Dichtel, *Nat. Chem.* **2010**, *2*, 672-677.
- [8] M. Dogru, M. Handloser, F. Auras, T. Kunz, D. Medina, A. Hartschuh, P. Knochel, T. Bein, *Angew. Chem. Int. Ed.* **2013**, *52*, 2920-2924.
- [9] M. Calik, F. Auras, L. M. Salonen, K. Bader, I. Grill, M. Handloser, D. D. Medina, M. Dogru, F. Löbermann, D. Trauner, A. Hartschuh, T. Bein, *J. Am. Chem. Soc.* **2014**, *136*, 17802-17807.
- [10] L. Stegbauer, K. Schwinghammer, B. V. Lotsch, *Chem. Sci.* **2014**, *5*, 2789-2793.
- [11] X. Wang, L. Chen, C. S. Y., M. A. Little, Y. Wu, W.-H. Zhu, R. Clowes, Y. Yan, M. A. Zwijnenburg, R. S. Sprick, A. I. Cooper, *Nat. Chem.* **2018**, *10*, 1180-1189.
- [12] R. D. Rauh, *Electrochim. Acta* **1999**, *44*, 3165-3176.
- [13] C.-P. Cheng, Y. Kuo, C.-P. Chou, C.-H. Cheng, T. P. Teng, *Appl. Phys. A* **2014**, *116*, 1553-1559.
- [14] L. Wu, Y. Sun, K. Sugimoto, Z. Luo, Y. Ishigaki, K. Pu, T. Suzuki, H.-Y. Chen, D. Ye, *J. Am. Chem. Soc.* **2018**, *140*, 16340-16352.
- [15] E. P. Knott, M. R. Craig, D. Y. Liu, J. E. Babiarez, A. L. Dyer, J. R. Reynolds, *J. Mater. Chem.* **2012**, *22*, 4953-4962.
- [16] H. Gu, S. Ming, K. Lin, S. Chen, X. Liu, B. Lu, J. Xu, *Electrochim. Acta* **2018**, *260*, 772-782.
- [17] J. B. Arockiam, H. Son, S. H. Han, G. Balamurugan, Y.-H. Kim, J. S. Park, *ACS Appl. Energy Mater.* **2019**, *2*, 8416-8424.
- [18] P. M. Beaujuge, S. Ellinger, J. R. Reynolds, *Nat. Mater.* **2008**, *7*, 795-799.

- [19] S. A. Sapp, G. A. Sotzing, J. R. Reynolds, *Chem. Mater.* **1998**, *10*, 2101-2108.
- [20] Q. Hao, Z.-J. Li, C. Lu, B. Sun, Y.-W. Zhong, L.-J. Wan, D. Wang, *J. Am. Chem. Soc.* **2019**, *141*, 19831-19838.
- [21] F. Yu, W. Liu, S.-W. Ke, M. Kurmoo, J.-L. Zuo, Q. Zhang, *Nat. Commun.* **2020**, *11*, 5534.
- [22] P. M. Beaujuge, C. M. Amb, J. R. Reynolds, *Acc. Chem. Res.* **2010**, *43*, 1396-1407.
- [23] R. Stalder, J. Mei, J. R. Reynolds, *Macromolecules* **2010**, *43*, 8348-8352.
- [24] C.-C. Ho, C.-A. Chen, C.-Y. Chang, S. B. Darling, W.-F. Su, *J. Mater. Chem. A* **2014**, *2*, 8026-8032.
- [25] F. Auras, L. Ascherl, A. H. Hakimiooun, J. T. Margraf, F. C. Hanusch, S. Reuter, D. Bessinger, M. Döblinger, C. Hettstedt, K. Karaghiosoff, S. Herbert, P. Knochel, T. Clark, T. Bein, *J. Am. Chem. Soc.* **2016**, *138*, 16703-16710.
- [26] N. Keller, D. Bessinger, S. Reuter, M. Calik, L. Ascherl, F. C. Hanusch, F. Auras, T. Bein, *J. Am. Chem. Soc.* **2017**, *139*, 8194-8199.
- [27] D. Bessinger, L. Ascherl, F. Auras, T. Bein, *J. Am. Chem. Soc.* **2017**, *139*, 12035-12042.
- [28] L. Ascherl, E. W. Evans, M. Hennemann, D. Di Nuzzo, A. G. Hufnagel, M. Beetz, R. H. Friend, T. Clark, T. Bein, F. Auras, *Nat. Commun.* **2018**, *9*, 3802.
- [29] L. Ascherl, E. W. Evans, J. Gorman, S. Orsborne, D. Bessinger, T. Bein, R. H. Friend, F. Auras, *J. Am. Chem. Soc.* **2019**, *141*, 15693-15699.
- [30] T. Hasegawa, M. Ashizawa, H. Matsumoto, *RSC Adv.* **2015**, *5*, 61035-61043.
- [31] D. Yoo, T. Hasegawa, M. Ashizawa, T. Kawamoto, H. Masunaga, T. Hikima, H. Matsumoto, T. Mori, *J. Mater. Chem. C* **2017**, *5*, 2509-2512.
- [32] K. A. Cychosz, R. Guillet-Nicolas, J. García-Martínez, M. Thommes, *Chem. Soc. Rev.* **2017**, *46*, 389-414.
- [33] M. Matsumoto, R. R. Dasari, W. Ji, C. H. Feriante, T. C. Parker, S. R. Marder, W. R. Dichtel, *J. Am. Chem. Soc.* **2017**, *139*, 4999-5002.
- [34] G. K. Dutta, A.-R. Han, J. Lee, Y. Kim, J. H. Oh, C. Yang, *Adv. Funct. Mater.* **2013**, *23*, 5317-5325.
- [35] A. Oleson, T. Zhu, I. S. Dunn, D. Bialas, Y. Bai, W. Zhang, M. Dai, D. R. Reichman, R. Tempelaar, L. Huang, F. C. Spano, *J. Phys. Chem. C* **2019**, *123*, 20567-20578.
- [36] J. f. Feng, T. F. Liu, R. Cao, *Angew. Chem. Int. Ed.* **2020**, *59*, 22392-22396.
- [37] C. R. Wade, M. Li, M. Dincă, *Angew. Chem. Int. Ed.* **2013**, *52*, 13377-13381.
- [38] G. Cai, M. Cui, V. Kumar, P. Darmawan, J. Wang, X. Wang, A. L.-S. Eh, K. Qian, P. S. Lee, *Chem. Sci.* **2016**, *7*, 1373-1382.

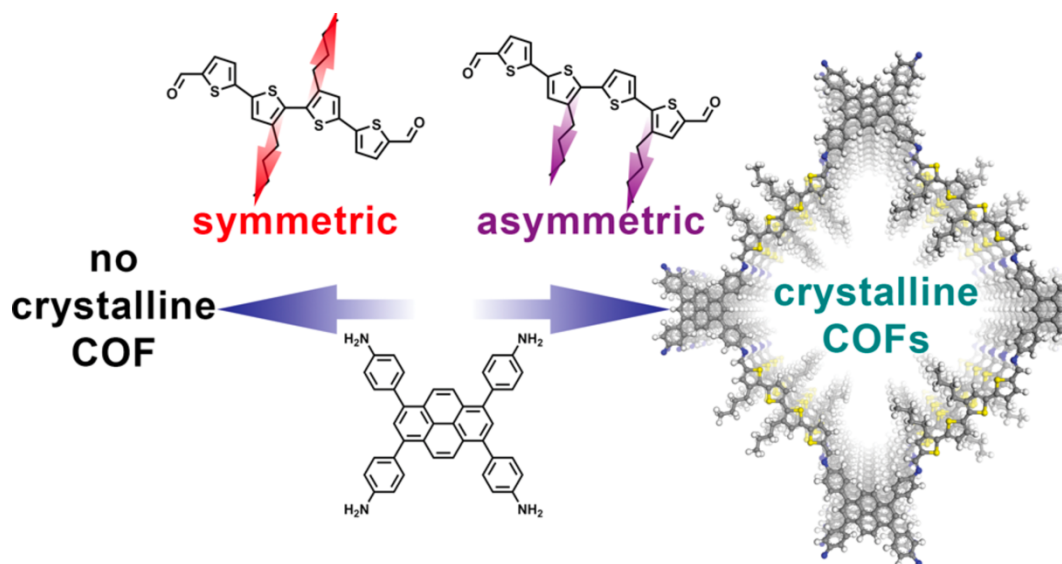
- [39] T. Düren, F. Millange, G. Férey, K. S. Walton, R. Q. Snurr, *J. Phys. Chem. C* **2007**, *111*, 15350-15356.
- [40] Y. Koizumi, M. Ide, A. Saeki, C. Vijayakumar, B. Balan, M. Kawamotoa, S. Seki, *Polym. Chem.* **2013**, *4*, 484-494.
- [41] T. Hasegawa, M. Ashizawa, J. Hiyoshi, S. Kawauchi, J. Mei, Z. Bao, H. Matsumoto, *Polym. Chem.* **2016**, *7*, 1181-1190.
- [42] H. L. Nguyen, C. Gropp, Y. Ma, C. Zhu, O. M. Yaghi, *J. Am. Chem. Soc.* **2020**, *142*, 20335-20339.

5 Oligothiophene-Bridged Conjugated Covalent Organic Frameworks

This chapter is based on the following publication:

Niklas Keller, Derya Bessinger, Stephan Reuter, Mona Calik, Laura Ascherl, Fabian C. Hanusch, Florian Auras*, and Thomas Bein*

J. Am. Chem. Soc. **2017**, *139*, 8194–8199



Copyright 2017, American Chemical Society

The synthesis of the Pyrene building block for the COFs of this project was carried out by D. Bessinger. Furthermore, D. Bessinger contributed to this work with the complete development and synthesis of the short-chain oligothiophene a4T_{Me} and the consequent COF formation that produced the nitrogen sorption data confirming the porosity and accessibility of the crystalline frameworks.

*corresponding authors

5.1 Abstract

Two-dimensional covalent organic frameworks (2D-COFs) are crystalline, porous materials comprising aligned columns of π -stacked building blocks. With a view toward the application of these materials in organic electronics and optoelectronics, the construction of oligothiophene-based COFs would be highly desirable. The realization of such materials, however, has remained a challenge, in particular with respect to laterally conjugated imine-linked COFs. We have developed a new building block design employing an asymmetric modification on an otherwise symmetric backbone that allows us to construct a series of highly crystalline quaterthiophene-derived COFs with tunable electronic properties. Studying the optical response of these materials, we have observed for the first time the formation of a charge transfer state between the COF subunits across the imine bond. We believe that our new building block design provides a general strategy for the construction of well-ordered COFs from various extended building blocks, thus greatly expanding the range of applicable molecules.

5.2 Introduction

Since the development of the first covalent organic frameworks (COFs) in 2005,^[1] these materials have attracted considerable scientific interest for applications in gas storage and separation,^[2, 3] in photocatalysis,^[4, 5] as proton conducting materials,^[6, 7] and in optoelectronics.^[8, 9] Cross-linking multidentate organic building blocks via reversible covalent bond formation into a crystalline porous framework allows for the construction of robust materials with tunable functionality based on the selection of their building blocks.^[10-16] This way, a great variety of highly ordered materials can be realized having specific combinations of properties that can offer advantages over already established materials, such as zeolites or conductive polymers. With a view on optoelectronic properties, sheet-like 2D-COFs are of particular interest.^[17] In these materials, the covalently linked layers are tightly π -stacked, thus forming columns with significant electronic overlap that enable efficient migration of excitations and charge carriers.^[18-20]

Oligo- and polythiophene-based materials, such as 2,2':5',2'':5'',2'''-quaterthiophene (4T), α -sexithiophene (6T), and poly(3-hexylthiophene-2,5-diyl) (P3HT), are among the most

prominent molecular semiconductors in organic field effect transistors (OFETs) and organic photovoltaics (OPV).^[21-23] These materials benefit from high intrinsic charge carrier mobilities of both electrons and holes, typically broad optical absorption throughout the visible spectrum, and good chemical stability.^[24-26]

The incorporation of this important class of molecular semiconductors into a COF, however, has remained a challenge. Only the smallest thiophene-based building blocks, i.e., thiophene, bithiophene (2T),^[27] and small fused thiophenes such as thieno[3,2-*b*]thiophene (TT)^[8, 11] and benzo[1,2-*b*:4,5-*b'*]dithiophene (BDT),^[28-30] have been applied as COF building blocks to date, and mostly in boronate-linked COFs that lack electronic conjugation within the COF layers.

With a view on COFs for optoelectronics, it would thus be highly desirable to develop a method to integrate larger oligothiophenes (nT , $n \geq 4$) that allow for significant π -overlap and spectral coverage into a conjugated COF.

As flat, extended conjugated building blocks typically suffer from very low solubility in all common solvents, solubilizing groups such as alkyl chains are required for tuning the solubility into the optimal regime for COF growth.^[30, 31] However, even short alkyl chains can severely impede the close face-on oriented packing that is a prerequisite for the formation of conductive 2D-COFs.

In this work, we have developed a building block design concept that allows us to overcome these limitations through an asymmetric functionalization of an otherwise C_2 -symmetric 4T backbone. This way, we can incorporate solubilizing alkyl chains and allow them to integrate into the COF lattice at sufficiently large distances, while maintaining the desirable close contacts between the thiophene layers. We then extended this concept to electronic modifications of the backbone via the incorporation of thiophene-based acceptor units, such as 4*H*-thieno[3,4-*c*]pyrrole-4,6(5*H*)-dione (TPD) and thieno[3,4-*b*]thiophene (TT). Combining these modified 4T building blocks with pyrene-based moieties, we synthesized a first series of highly crystalline quaterthiophene-linked COFs with tunable optical absorption and emission properties.

5.3 Results and Discussion

Starting from commercially available 3-bromothiophene, we synthesized the quaterthiophene (4T) dialdehyde building blocks via Ni- and Pd-catalyzed Kumada and Suzuki cross-coupling reactions [see the Supporting Information (SI) for details]. In order to study the effect of the configuration of the alkyl chains, we synthesized a symmetric and an asymmetric version of the dibutyl-4T, in which the alkyl chains are attached to the 3-positions of the second and third (s4T) and the first and third thiophene units (a4T), respectively (Figure 5.1a).

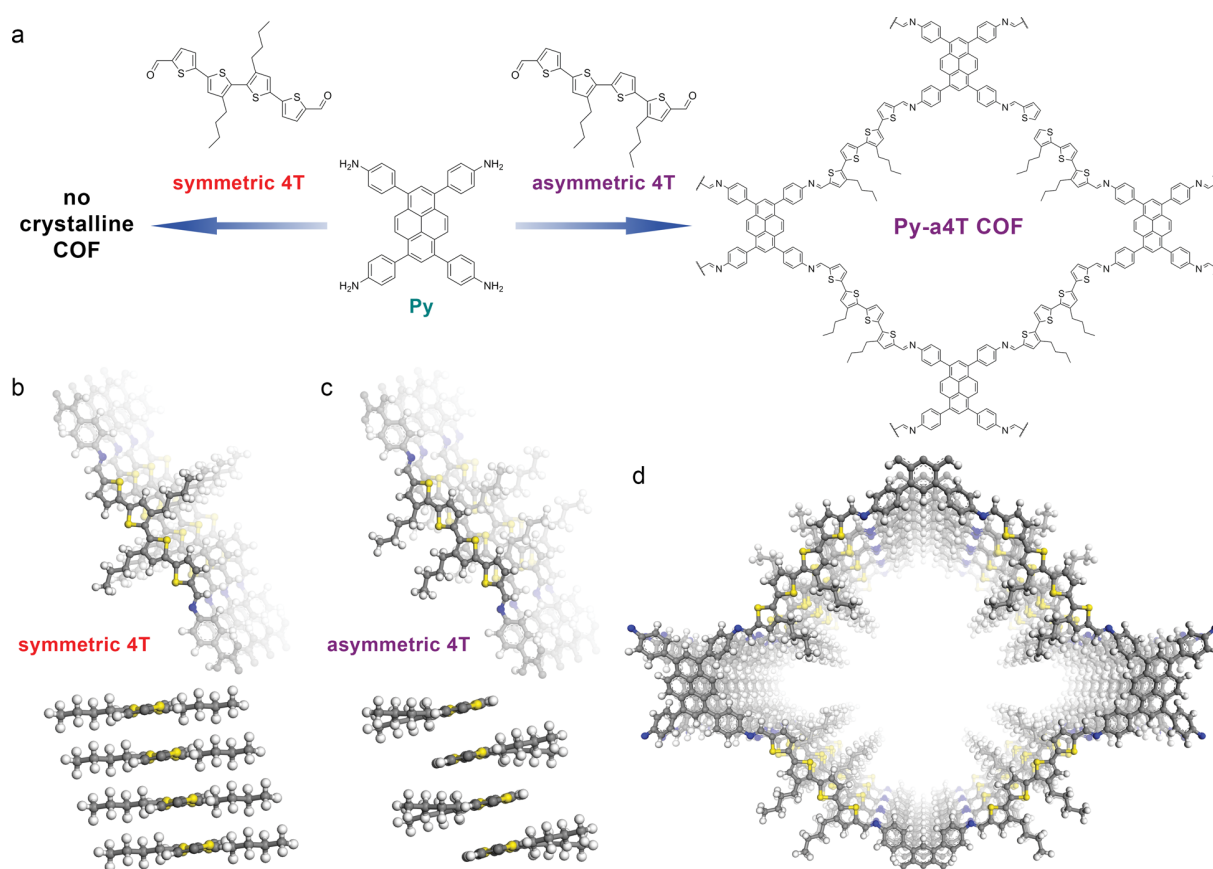


Figure 5.1. (a) Co-condensation of 1,3,6,8-tetrakis(4-aminophenyl)pyrene (Py) with 2 equiv of the quaterthiophene dialdehyde bearing asymmetric butyl chains (a4T) leads to the formation of the Py-a4T COF. When employing a quaterthiophene dialdehyde with a symmetric configuration of the alkyl chains (s4T), however, no crystalline material can be obtained. (b) Cut-out of the DFT-optimized hypothetical Py-s4T COF structure. Slipped cofacial stacking of the s4T building block would place the alkyl chains of adjacent layers in close vicinity, causing considerable steric repulsion and impeding the close packing required for 2D-COF formation. (c) This steric repulsion can be avoided by attaching the alkyl chains to the first and third thiophene unit (a4T) instead, allowing for sufficiently spaced alternating alkyl chains while a close-packed cofacial arrangement of the thiophene backbone is supported. (d) DFT-optimized structure of the Py-a4T COF with alternating orientation of the alkyl chains viewed along the pseudoquadratic pore.

For constructing the imine-linked COFs, we followed a synchronized offset stacking approach.^[15] This COF design uses geometrically interlocked layers for superior crystallinity while enabling close-packed arrangements of both subunits and is perfectly compatible with

the quasi C₂-symmetric flat geometry of the 4T bridges. The quaterdentate 1,3,6,8-tetrakis(4-aminophenyl)pyrene (Py) has previously been applied in the synthesis of several imine-linked frameworks and has proven to generate stable and exceptionally crystalline 2D-COFs.^[15, 32, 33] Pyrene-based frameworks feature a quasi-quadratic geometry comprising close-packed, slightly slip-stacked pyrene columns and equally close-packed, slip-stacked linear bridges, thus providing the ideal geometric environment for our new 4T building blocks.

On the basis of published pyrene COF structures and density functional theory (DFT) simulations, we expect the 4T unit to be incorporated as face-on oriented stacks, whereby each layer is slipped by about 0.1 nm, mainly perpendicular to the 4T axis (Figures 5.1b, c). In the case of s4T, this would bring the alkyl chains of adjacent layers very close together and most likely cause considerable steric repulsion, forcing the framework into a less closely stacked conformation and sacrificing in part the π - overlap between the thiophenes. On the other hand, a4T can stack with the butyl chains alternating on both sides of the stack, thus allowing for much larger spacing between these alkyl chains while maintaining a close-packed face-on orientation of the 4T backbone (Figures 5.1c, d).

Acid-catalyzed solvothermal synthesis using a4T and Py in a 2:1 molar ratio yielded the anticipated Py-a4T COF as a dark red powder (see the SI for details). The successful formation of a crystalline material was confirmed by powder X-ray diffraction (PXRD; Figure 5.2a).

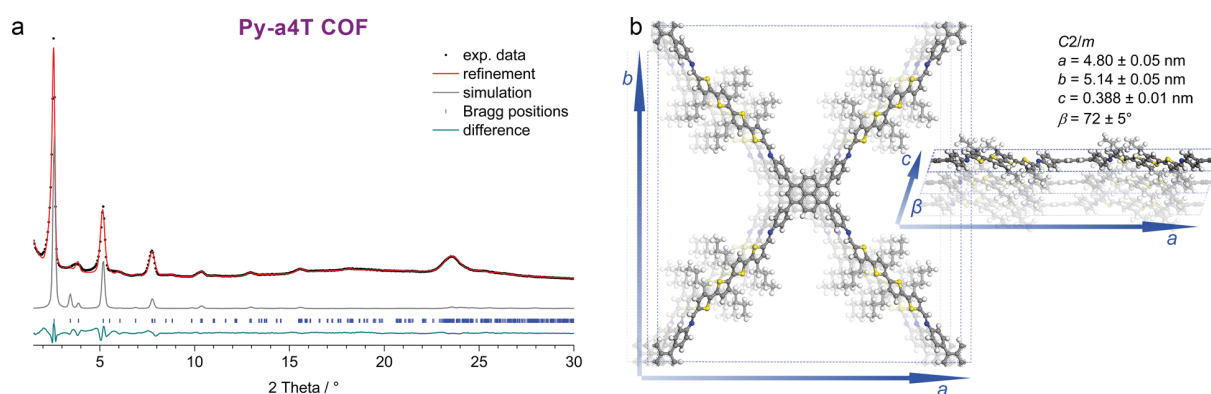


Figure 5.2. (a) Experimental PXRD data (black dots) of Py-a4T COF. Pawley refinement (red line) using the *C₂/m* symmetric structure model shown in part **b** provides a very good fit to the experimental pattern with only minimal differences (the green line shows the difference plot between the experimental and refined patterns; $R_{wp} = 7.5\%$, $R_p = 13.4\%$). Bragg positions are indicated with blue ticks. The alkyl chains of the a4T building block were treated in the refinement as a superposition of both possible orientations with 50% occupancy each (both shown in the figure). The simulated PXRD pattern based on the *C₂/m* symmetric unit cell (gray line) is in very good agreement with the experimental and the refined pattern. Differences in the peak intensities, in particular the altered intensity ratios between lower- and higher-angle reflections, might stem from small oligomeric fragments that are trapped in the large COF pores (the attenuation of peak intensities due to this will be strongest at small 2θ angles).

The presence of multiple higher-order reflections reveals the high degree of long-range order present in this new COF. Pawley refinement using a force-field- optimized $C2/m$ symmetric structure model (Figure 5.2b) provides a very good fit to the experimental data and produced the lattice parameters $a = 4.80 \pm 0.05$ nm, $b = 5.14 \pm 0.05$ nm, $c = 0.388 \pm 0.01$ nm, and $\beta = 72^\circ \pm 5^\circ$. From the above discussion and the computational modeling, we anticipate an alternating sequence of the alkyl chains as the predominant stacking motif within a single a4T stack. The four a4T stacks that constitute the walls of a COF pore, however, are separated well enough such that they will not form an ordered superstructure. We thus treated the alkyl chains in the Pawley refinement and the simulation of the PXRD pattern as a superposition of both possible orientations with 50% occupancy each.

The formation of an ordered porous framework was further confirmed by transmission electron microscopy (TEM) (SI, Figure 5.18). The contrast of the pore channels is visible for a number of crystallites with a projected periodicity of 3.4 nm, which corresponds very well to the channel repeat distance of 3.45 nm in the refined structure.

In order to probe the influence of the alkyl chain length on the resulting framework, we synthesized a short-chain analogue of the a4T building block bearing two methyl groups instead of the butyl chains. Due to the significantly lower solubility of this a4T_{Me} building block, the COF synthesis required a 2.5 times more dilute reaction mixture. The resulting framework is isostructural to the original a4T COF, with a slightly smaller unit cell (SI, Figure 5.19).

Under identical synthetic conditions as those chosen for the Py-a4T COF and under all other solvent combinations and concentrations tested, the reaction between Py and 2 equiv of s4T yielded only orange-red, fully amorphous networks. This observation confirms our above conclusions drawn from the structure modeling and highlights the importance of the building block design.

The asymmetric modification strategy also allows us to extend one of the thiophene units into a more-electron-deficient fused heterocycle, thus forming a donor–acceptor (D–A) building block with modified optical and electronic properties while retaining the overall geometry of the 4T backbone.

Incorporation of a single 4*H*-thieno[3,4-*c*]pyrrole-4,6(5*H*)-dione (TPD) or thieno[3,4-*b*]thiophene (TT) via sequential Stille coupling reactions yielded the 4T_{TPD} and 4T_{TT} building blocks, respectively (Figure 5.3a; see the SI for experimental details). For the best possible crystallinity, the 4T_{TT} building block was synthesized as an isomer-pure material with the orientation of the TT subunit as shown in Figure 5.3a. In both cases, the asymmetric

incorporation enables the 4T derivatives to stack in a close-packed alternating sequence despite the sterically demanding acceptor moieties (Figures 5.3b, c).

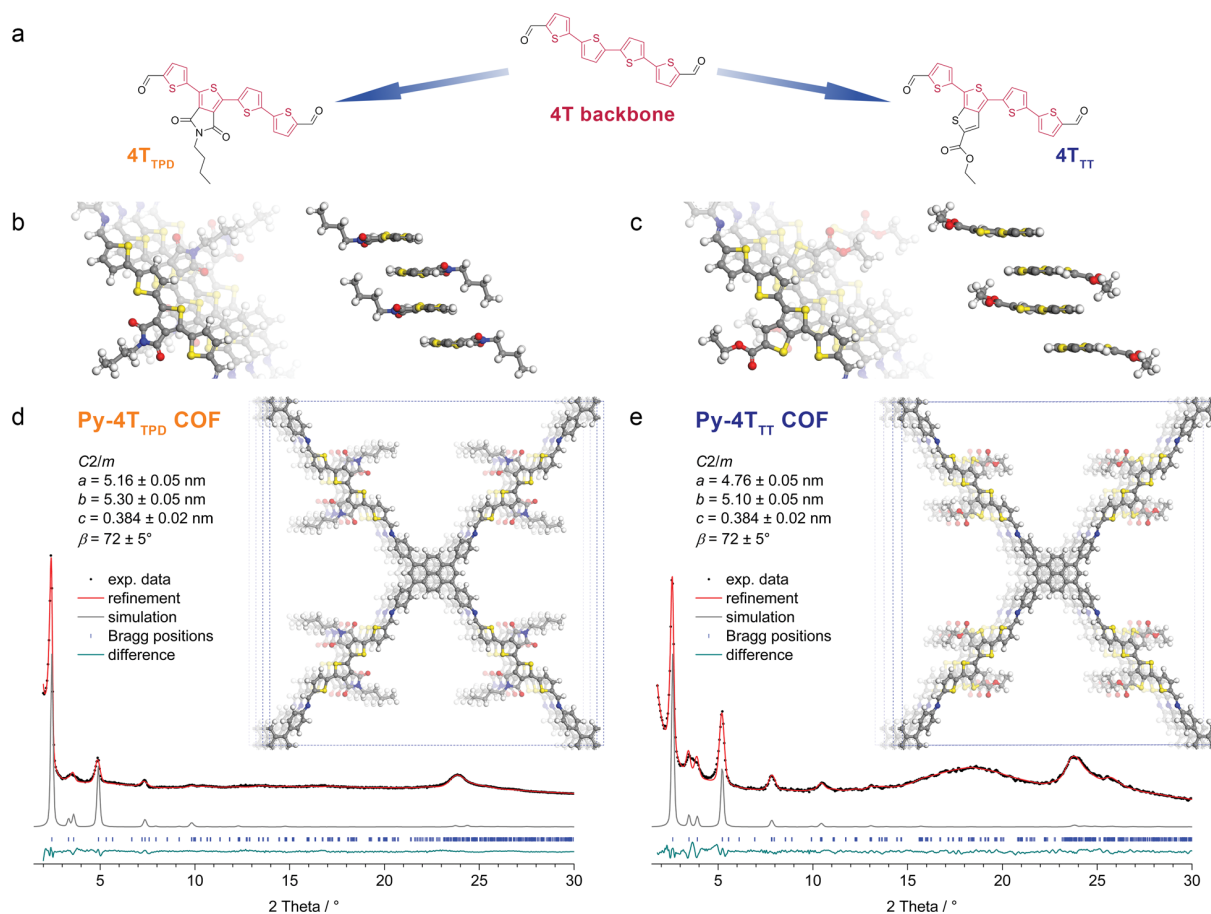


Figure 5.3. (a) The asymmetric modification approach can also be used to construct quaterthiophene-based donor–acceptor building blocks, in which one thiophene is replaced by an electron-deficient 3,4-extended thiophene. (b, c) Despite the increased steric demands of these subunits, a close-packed cofacial arrangement of the asymmetric building blocks is possible via alternating orientation of the electron-deficient moieties. (d, e) Experimental PXRD data (black dots) of the Py-4T_{TPD} and Py-4T_{TT} COFs, respectively, and corresponding Pawley-refined patterns (red lines) and difference plots (green lines; $R_{wp} = 5.2\%$, $R_p = 14.3\%$ and $R_{wp} = 9.3\%$, $R_p = 16.1\%$, respectively). Bragg positions are indicated with blue ticks. The acceptor moieties (TPD and TT) were treated in the refinements as a superposition of both possible orientations with 50% occupancy each (both shown in the representations of the unit cells). The simulated PXRD patterns (gray lines) based on the *C2/m* symmetric unit cells (insets) agree very well with the experimental and refined patterns of the respective frameworks. Differences in the peak intensities, in particular the altered intensity ratios between lower- and higher-angle reflections, might stem from unreacted precursor materials or small fragments adsorbed in the COF pores (the attenuation of peak intensities due to this is strongest at small 2θ angles).

The acid-catalyzed reaction of Py with 2 equiv of the modified 4T building blocks under solvothermal conditions yielded the Py-4T_{TPD} and Py-4T_{TT} COFs, respectively. The formation of crystalline frameworks was confirmed by PXRD analysis (Figures 5.3d, e). Pawley refinements of the Py-4T_{TPD} and Py-4T_{TT} COFs using the force-field-optimized structure models displayed as insets in Figures 5.3d, e reproduced the experimental patterns very well. Following the same reasoning as for the simulation and refinement of the Py-a4T COF (see

above), the asymmetric 4T_{TPD} and 4T_{TT} building blocks were approximated as a superposition of both possible orientations with 50% occupancy each. The refined unit cell parameters are $a = 5.16 \pm 0.05$ nm, $b = 5.30 \pm 0.05$ nm, $c = 0.384 \pm 0.02$ nm, and $\beta = 72^\circ \pm 5^\circ$ for the Py-4T_{TPD} COF and $a = 4.76 \pm 0.05$ nm, $b = 5.10 \pm 0.05$ nm, $c = 0.384 \pm 0.02$ nm, and $\beta = 72^\circ \pm 5^\circ$ for the Py-4T_{TT} COF. The longer pore diagonals a and b in these COFs compared to the Py-a4T COF can be attributed to a slight variation in the optimal stacking offset perpendicular to the 4T axis and the resulting differences in the tilt of the 4T columns versus the pyrene core. The length of the crystallographic c axis, on the other hand, is dominated by the stacking of the pyrene units and, thus, hardly affected by the tilt of the 4T bridge.

The new 4T-based COFs are intensely colored powders that are capable of absorbing most of the visible spectrum (Figure 5.4a).

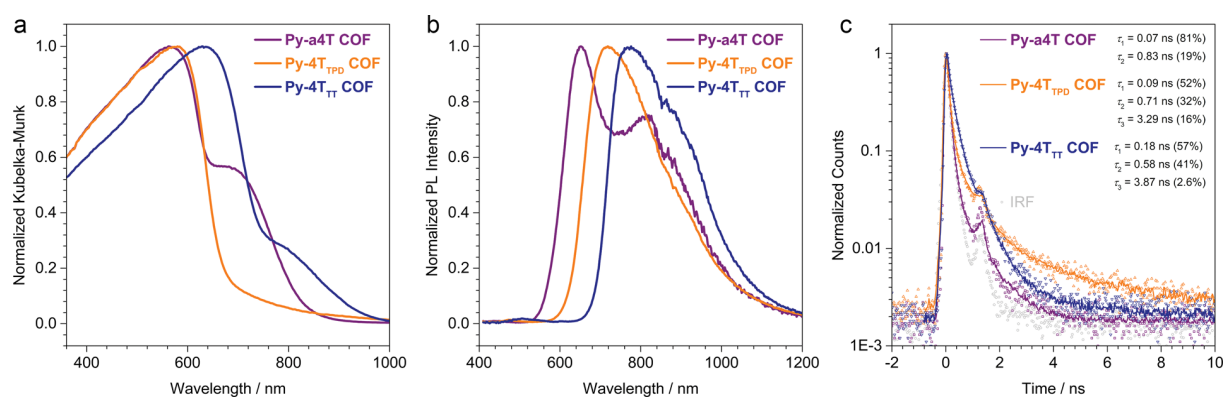


Figure 5.4. (a) UV-vis-NIR absorption of the three thiophene-bridged COFs, calculated from the diffuse reflectance spectra of the COF powders dispersed in BaSO₄. (b) PL spectra measured with pulsed 378 nm excitation and (c) the corresponding TCSPC traces recorded at the respective emission maximum of each COF. The lines represent exponential deconvolution fits taking into account the instrument response function and scattering (see the SI for details; the rise at 1.35 ns originates from the diode laser). The COFs exhibit fast biexponential (Py-a4T) or triexponential (Py-4T_{TPD} and Py-4T_{TT}) decays with sub-nanosecond components. The fractional intensities, i.e., the fractions of collected photons corresponding to the respective lifetimes, are stated in brackets.

The optical bandgaps estimated from Tauc plots are 1.57, 1.17 (indirect), and 1.40 eV for the Py-a4T, Py-4T_{TPD}, and Py-4T_{TT} COFs, respectively (SI, Figure 5.12). Electronic integration of the 4T subunit is apparent from the strong red-shift of the absorption in comparison to previously reported pyrene COFs with small acene bridges. Furthermore, the increased absorption capabilities of the D-A building blocks (SI, Figure 5.10 and Figure 5.11) translate to red-shifted absorption maxima of the corresponding COFs (Py-a4T COF, 563 nm; Py-4T_{TPD} COF, 580 nm; Py-4T_{TT} COF, 638 nm). All three COFs feature an additional absorption band below the energy of the main π - π^* transition that is relatively weak for the Py-4T_{TPD} and

strongest for the Py-a4T COF. This might indicate the formation of a charge transfer state between the electron-rich pyrene and the slightly electron-deficient 4T subunits (see below).

The photoluminescence (PL) spectra follow the same trends as the absorption spectra with emission maxima of the COFs at 654, 718, and 773 nm, respectively (Figure 5.4b and SI, Figure 5.13 and Figure 5.14).

The hypothesis of a photoinduced charge transfer between the two imine-linked building blocks is supported by the time-correlated single photon counting (TCSPC) traces of the COFs (Figure 5.4c). Dilute solutions of the 4T building blocks exhibit monoexponential decay curves with lifetimes of about 0.5 ns (a4T, 4T_{TT}) or 1 ns (4T_{TPD}) (SI, Figure 5.16 and Figure 5.17). In the solid state, the PL lifetimes of the pure building blocks are increased to $\tau_1 \sim 0.5$ ns and $\tau_2 \sim 1$ ns (biexponential decays). The Py building block shows even longer lifetimes of above 2 ns in solution and a main component of >1 ns in the solid state. If integrated into a COF, however, the PL lifetimes are drastically reduced. The fastest component, which represents more than 50% of the emitted photons, drops to below 200 ps (Py-4T_{TT}) or even below 100 ps (Py-a4T, Py-4T_{TPD}). This indicates that the imine-linked pairing with the tetraphenylpyrene has opened up a new pathway for fast and efficient conversion of the COF π^* excited state, potentially via electron transfer to the quaterthiophenes and hole transfer to the pyrene. This is further supported by comparison with the PL lifetimes reported for electron-rich acene-bridged pyrene COFs that do not enable strong intramolecular charge transfer.^[15] In these materials, the lifetimes are much longer, ranging from 0.35 ns to well above 1 ns.

The existence of an efficient charge transfer pathway that competes effectively with the radiative recombination of the COF π^* excited state is additionally supported by the quenching of the 4T PL upon incorporation into the COF (SI, Figure 5.15). This effect is most significant for the Py-a4T COF, which is consistently the material that exhibits the strongest charge transfer absorption band in the diffuse reflectance spectrum. To the best of our knowledge, this is the first observation of the formation of a charge transfer state between the subunits of an imine-linked COF.

5.4 Conclusion

In this work, we have developed the first quaterthiophene-based 2D covalent organic frameworks comprising ordered π -stacked columns of 4T and pyrene moieties. Following an asymmetric functionalization strategy of the otherwise C_2 -symmetric 4T backbone allowed us to incorporate alkyl chains for optimized solubility while fully retaining the ability of the building blocks to form close-packed face-on stacked thiophene columns. We demonstrate that this strategy also provides a facile route for modifying the electronic properties of the 4T backbone via incorporation of electron-deficient subunits, thus forming donor-acceptor type molecules. The absorption and emission spectra confirm that the 4T-based building blocks are electronically integrated into the framework. Spectral features below the energy of the π - π^* transition and the analysis of the corresponding emission decay time traces reveal the fast and efficient formation of a charge transfer state between the imine-linked pyrene and quaterthiophene subunits. We believe that our new asymmetric building block design provides a general strategy for the construction of well-ordered COFs from various extended building blocks. This will greatly expand the range of applicable molecules for realizing frameworks with tailor-made optoelectronic properties.

5.5 Supporting Information

Abbreviations

Ac	acetyl
Bn	benzyl
dba	<i>trans,trans</i> -dibenzylideneacetone
DCB	1,2-dichlorobenzene
DCE	1,2-dichloroethane
DCM	dichloromethane
DFT	density functional theory
DMF	<i>N,N</i> -dimethylformamide
DMSO	dimethyl sulfoxide
dppp	1,3-bis(diphenylphosphino)propane
EI	electron ionization
eq.	equivalents
Et	ethyl
HRMS	high resolution mass spectroscopy
IRF	instrument response function
NBS	<i>N</i> -bromosuccinimide
PL	photoluminescence
PXRD	powder X-ray diffraction
rt	room temperature
TCSP	time-correlated single photon counting
TEM	transmission electron microscopy
TFP	tri(2-furyl)phosphine
THF	tetrahydrofuran

Section A – Methods

Nuclear magnetic resonance (NMR) spectra were recorded on Bruker AV 400 and AV 400 TR spectrometers. Chemical shifts are expressed in parts per million (δ scale) and are calibrated using residual (undeuterated) solvent peaks as an internal reference ($^1\text{H-NMR}$: CDCl_3 : 7.26, $\text{DMSO-}d_6$: 2.50, $\text{DMF-}d_7$: 8.03; $^{13}\text{C-NMR}$: CDCl_3 : 77.16, $\text{DMSO-}d_6$: 39.52, $\text{DMF-}d_7$: 163.15). Data for ^1H NMR spectra are reported in the following way: chemical shift (δ ppm) (multiplicity, coupling constant/Hz, integration). Multiplicities are reported as follows: s = singlet, d = doublet, t = triplet, q = quartet, m = multiplet, or combinations thereof.

High resolution electron ionization (EI) **mass spectra (MS)** were recorded with a Thermo Finnigan MAT 95 instrument.

Powder X-ray diffraction (PXRD) measurements were performed using a Bruker D8 Discover with Ni-filtered Cu K_α radiation and a LynxEye position-sensitive detector.

The **structure models of the COFs** were built using the Forcite module of the Accelrys Materials Studio software package. For each COF structure, we applied the space group with the highest possible symmetry, taking into account the rotation of the phenylenes versus the pyrene core. Structure refinements using the Pawley method were carried out as implemented in the Reflex module of the Materials Studio software. Pseudo-Voigt peak profiles were used, and peak asymmetry was corrected using the Finger-Cox-Jephcoat method. A crystallite domain size of 100 nm along a , b and c , and lattice strain parameters of 0.5%, 0.5% and 0.2% along a , b , c , respectively, were assumed throughout the refinements. The asymmetric linear building blocks were treated as a superposition of both possible orientations, both having 50% occupancy.

DFT-based geometry optimizations were performed with the CASTEP code using the generalized-gradient-approximation PBE functional. The energy cutoff for the planewave basis set was set to 310.0 eV, ions were represented with ultra-soft pseudopotentials and k-point sampling was performed with a $1 \times 1 \times 4$ Monkhorst-Pack grid ($1 \times 1 \times 2$ for the Py-a4T COF double layer). The correction scheme of Tkatchenko and Scheffler was used to account for dispersion interactions.

The **nitrogen sorption isotherms** were recorded on a Quantachrome Autosorb 1 at 77 K in a pressure range from $p/p_0 = 0.001$ to 0.999. For the evaluation of the surface area, the BET model was applied between 0.069 and 0.132 p/p_0 . The pore size distribution was calculated from the adsorption branch using a QSDFT model with a carbon kernel for cylindrical pores.

Transmission electron microscopy (TEM) was performed on an FEI Titan Themis instrument equipped with a field emission gun operated at 300 kV.

Infrared (IR) spectra were recorded on a Perkin Elmer Spectrum BX II FT-IR system equipped with a diamond attenuated total reflection unit.

UV-VIS-NIR spectra were recorded using a Perkin-Elmer Lambda 1050 spectrometer equipped with a 150 mm integrating sphere and photomultiplier tube (PMT) and InGaAs detectors. **Diffuse reflectance** spectra were collected with a Praying Mantis (Harrick) accessory and were referenced to barium sulfate powder as white standard. The specular reflection of the sample surface was removed from the signal using apertures that allow only light scattered at angles $> 20^\circ$ to pass.

Photoluminescence (PL) measurements were performed using a home-built setup consisting of a Horiba Jobin Yvon iHR 320 monochromator equipped with a photomultiplier tube and a liquid N₂-cooled InGaAs detector. The samples were illuminated with a 378 nm diode laser (pulse power 0.99 nJ cm⁻², pulse rate 40 MHz).

Time-correlated single photon counting (TCSPC) measurements were performed using a PicoQuant FluoTime 300 spectrometer equipped with a 378 nm picosecond diode laser (pulse power 0.99 nJ cm⁻², pulse rate 40 MHz).

Section B – Building block syntheses

All reactions were performed in oven-dried glassware under argon atmosphere using standard Schlenk techniques. Reagents and solvents were obtained in high purity grades from commercial suppliers and used as received.



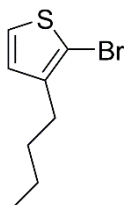
Figure 5.5. Synthesis of the s4T, a4T and a4T_{Me} building blocks.

3-butylthiophene (1)

A solution of BuMgCl (2.0 M in THF, 100 mmol, 1.25 eq.) was slowly added to a solution of 3-bromothiophene (13.0 g, 80 mmol, 1.0 eq.) and Ni(dppp)Cl₂ (867 mg, 1.6 mmol, 2 mol%) in 120 mL THF. During the addition, the reaction mixture was maintained at room temperature by a water bath. After stirring at 30 °C overnight, the reaction mixture was quenched by the addition of 50 mL of 2 M HCl, extracted with Et₂O, washed with brine, dried over MgSO₄, and concentrated under reduced pressure. Vacuum distillation (10⁻¹ mbar, 35 °C) furnished the title compound as a colorless liquid (8.02 g, 57.2 mmol, 71%).

^1H NMR (400 MHz, CDCl_3): 7.24 (dd, $J = 4.9, 2.9$ Hz, 1H), 6.94 (dd, $J = 4.9, 1.3$ Hz, 1H), 6.93 – 6.91 (m, 1H), 2.67 – 2.62 (m, 2H), 1.66 – 1.57 (m, 2H), 1.42 – 1.31 (m, 2H), 0.93 (t, $J = 7.3$ Hz, 3H).

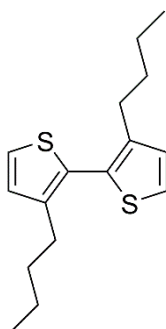
2-bromo-3-butylthiophene (**2**)



N-bromosuccinimide (10.7 g, 60 mmol, 1.05 eq.) was added to a solution of compound **1** (8.02 g, 57.2 mmol, 1.0 eq.) in 60 mL CHCl_3 . The reaction mixture was cooled to 0 °C, followed by the addition of 60 mL glacial acetic acid. The solution was allowed to warm to room temperature over the course of several hours and stirred for 2 d in the dark. The slightly yellow solution was poured onto 200 mL H_2O , extracted with DCM, washed with saturated NaHCO_3 solution, dried over MgSO_4 , and concentrated under reduced pressure. High vacuum distillation (10^{-3} mbar, 33 °C) furnished the title compound as a colorless liquid (11.2 g, 51.1 mmol, 89%).

^1H NMR (400 MHz, CDCl_3): 7.18 (d, $J = 5.6$ Hz, 1H), 6.80 (d, $J = 5.6$ Hz, 1H), 2.60 – 2.55 (m, 2H), 1.61 – 1.52 (m, 2H), 1.41 – 1.31 (m, 2H), 0.94 (t, $J = 7.3$ Hz, 3H).

3,3'-dibutyl-2,2'-bithiophene (**3**)^[34]



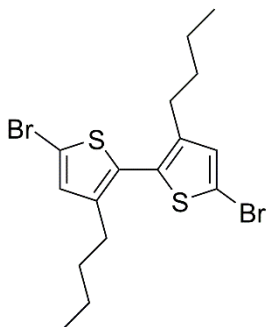
A Grignard reagent, prepared by sonication of compound **2** (1.10 g, 5.0 mmol, 1.1 eq.), 1,2-dibromoethane (939 mg, 5.0 mmol, 1.1 eq.) and Mg (243 mg, 10 mmol, 2.2 eq.) in 14 mL of dry Et_2O , was slowly added to a solution containing compound **2** (986 mg, 4.5 mmol, 1.0 eq.) and $\text{Ni}(\text{dppp})\text{Cl}_2$ (81 mg, 0.15 mmol, 3 mol%) in 21 mL of dry Et_2O . The reaction mixture was heated to reflux for 20 h. Upon completion, the reaction was quenched by the addition of EtOH

and a few droplets of 2 M HCl, and concentrated under reduced pressure. The crude product was purified via column chromatography (silica gel, heptane), yielding the title compound as a colorless oil (772 mg, 2.77 mmol, 62%).

^1H NMR (400 MHz, CDCl_3): 7.29 (d, $J = 5.2$ Hz, 2H), 6.97 (d, $J = 5.2$ Hz, 2H), 2.53 – 2.48 (m, 4H), 1.58 – 1.49 (m, 4H), 1.34 – 1.23 (m, 4H), 0.86 (t, $J = 7.3$ Hz, 6H).

^{13}C NMR (101 MHz, CDCl_3): 142.4, 128.9, 125.4, 33.0, 28.6, 22.6, 14.1.

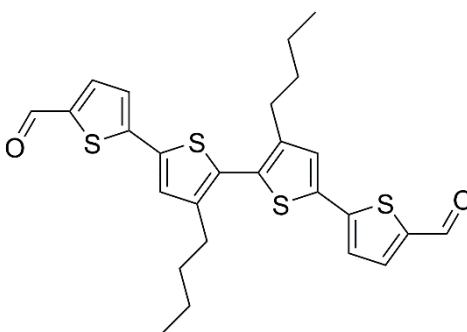
5,5'-dibromo-3,3'-dibutyl-2,2'-bithiophene (4)



Compound **3** (772 mg, 2.77 mmol, 1.0 eq.) was dissolved in 6 mL CHCl_3 and cooled to 0 °C. *N*-bromosuccinimide (1.04 g, 5.82 mmol, 2.1 eq.) and glacial acetic acid (6 mL) were added and the solution was allowed to slowly warm up to room temperature. After stirring at room temperature for 2 d in the dark, the reaction mixture was poured onto H_2O , extracted with DCM, washed with saturated NaHCO_3 solution, dried over MgSO_4 , and concentrated under reduced pressure. The crude product was purified by column chromatography (silica gel, cyclohexane), yielding a colorless oil (1.17 g, 2.68 mmol, 97%).

^1H NMR (400 MHz, CDCl_3): 6.91 (s, 2H), 2.47 – 2.41 (m, 4H), 1.54 – 1.44 (m, 4H), 1.33 – 1.22 (m, 4H), 0.86 (t, $J = 7.3$ Hz, 6H).

^{13}C NMR (101 MHz, CDCl_3): 143.9, 131.6, 129.0, 112.5, 32.8, 28.6, 22.5, 14.0.

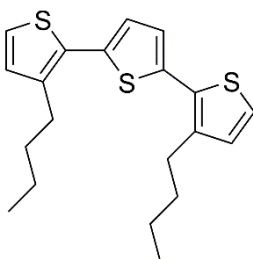
3',3''-dibutyl-[2,2':5',5'':2'',2'''-quaterthiophene]-5,5'''-dicarbaldehyde (s4T)

Following a procedure by Yang *et al.*,^[35] compound **4** (1.08 g, 2.48 mmol, 1.0 eq.) was stirred with Pd(OAc)₂ (23 mg, 0.10 mmol, 4 mol%) and XPhos (57 mg, 0.12 mmol, 4.8 mol%) in 14 mL n-butanol until complete dissolution of the solids (ca. 15 min). Next, a solution containing CsOH·H₂O (1.42 g, 8.43 mmol, 3.4 eq.) in 3.5 mL H₂O was added, followed by the addition of 5-formyl-2-thienylboronic acid (1.16 g, 7.44 mmol, 3.0 eq.). The resulting mixture was stirred for 2 d at 35 °C. After completion, H₂O was added and the product was extracted with DCM, dried over MgSO₄ and concentrated under reduced pressure. Purification via column chromatography (silica gel, DCM) furnished the title compound as a bright red powder (697 mg, 1.40 mmol, 56%).

¹H NMR (400 MHz, CDCl₃): 9.86 (s, 2H), 7.67 (d, *J* = 4.0 Hz, 2H), 7.24 (d, *J* = 3.9 Hz, 2H), 7.23 (s, 2H), 2.59 – 2.51 (m, 4H), 1.63 – 1.52 (m, 4H), 1.38 – 1.27 (m, 4H), 0.89 (t, *J* = 7.3 Hz, 6H).

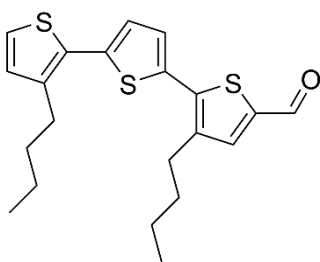
¹³C NMR (101 MHz, CDCl₃): 182.6, 146.9, 144.4, 141.9, 137.4, 136.1, 129.8, 127.8, 124.3, 32.8, 28.8, 22.6, 14.0.

HR-EI-MS: *m/z* 498.74 (M⁺, calculated for C₂₆H₂₆O₂S₄: 498.75).

3,3''-dibutyl-2,2':5',2''-terthiophene (5)^[34]

A Grignard reagent, prepared by sonication of compound **2** (4.38 g, 20 mmol, 2.9 eq.), 1,2-dibromoethane (3.76 g, 20 mmol, 2.9 eq.) and Mg (972 mg, 40 mmol, 5.7 eq.) in 56 mL of dry Et₂O, was slowly added to a solution containing 2,5-dibromothiophene (1.69 g, 7.0 mmol, 1.0 eq.) and Ni(dppp)Cl₂ (325 mg, 0.6 mmol, 3 mol%) in 50 mL dry Et₂O. The reaction mixture was heated to reflux for 40 h. Upon completion, the reaction was quenched by the addition of 1 M HCl (50 mL), extracted with DCM, washed with H₂O, dried over MgSO₄, and concentrated under reduced pressure. The crude product was purified via column chromatography (silica gel, heptane), yielding the title compound as a slightly yellow oil (2.47 g, 6.84 mmol, 98%).

¹H NMR (400 MHz, CDCl₃): 7.18 (d, *J* = 5.2 Hz, 2H), 7.06 (s, 2H), 6.94 (d, *J* = 5.2 Hz, 2H), 2.79 (t, *J* = 7.8 Hz, 4H), 1.69 – 1.59 (m, 4H), 1.46 – 1.35 (m, 4H), 0.94 (t, *J* = 7.3 Hz, 6H).

3,3''-dibutyl-5-formyl-2,2':5',2''-terthiophene (6)

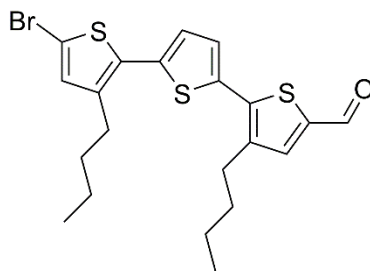
A Vilsmeier reagent, prepared by the addition of POCl₃ (1.57 g, 10.3 mmol, 1.5 eq.) to 6.5 mL of dry DMF at 0 °C, was added to a solution of compound **5** (2.47 g, 6.84 mmol, 1.0 eq.) in 96 mL DCE at 0 °C. The reaction mixture was stirred overnight at 70 °C. Subsequently, H₂O was added and the pH was adjusted to 8.5–9 with 1 M NaOH. The product was extracted with DCM, dried over MgSO₄ and concentrated under reduced pressure. Purification via column chromatography (silica gel, DCM/n-hexane 3:2) furnished the product as a slightly yellow solid (1.95 g, 5.02 mmol, 73%).

¹H NMR (400 MHz, CDCl₃): 9.83 (s, 1H), 7.60 (s, 1H), 7.24 (d, *J* = 3.8 Hz, 1H), 7.22 (d, *J* = 5.2 Hz, 1H), 7.11 (d, *J* = 3.8 Hz, 1H), 6.96 (d, *J* = 5.2 Hz, 1H), 2.87 – 2.81 (m, 2H),

2.82 – 2.76 (m, 2H), 1.73 – 1.60 (m, 4H), 1.49 – 1.36 (m, 4H), 0.97 (t, $J = 7.4$ Hz, 3H), 0.94 (t, $J = 7.3$ Hz, 3H).

^{13}C NMR (101 MHz, CDCl_3): 182.7, 141.3, 140.5, 140.4, 140.4, 139.2, 138.6, 134.6, 130.4, 129.9, 127.9, 126.5, 124.6, 33.0, 32.6, 29.3, 29.2, 22.8, 22.7, 14.1, 14.1.

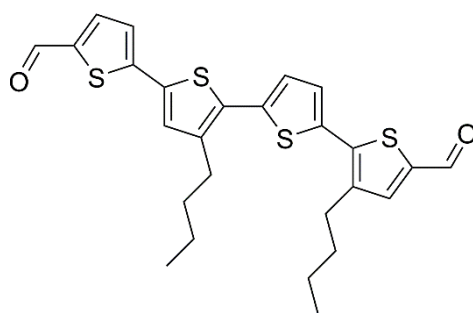
5-bromo-3,3''-dibutyl-5''-formyl-2,2':5',2''-terthiophene (7)



Compound 6 (1.95 g, 5.02 mmol, 1.0 eq.) was dissolved in 15 mL CHCl_3 and cooled to 0 °C. NBS (938 mg, 5.27 mmol, 1.05 eq.) and glacial acetic acid (15 mL) were added and the solution was allowed to slowly warm up to room temperature. After stirring at room temperature for 2 d in the dark, the reaction mixture was poured onto H_2O , extracted with DCM, washed with saturated NaHCO_3 solution, dried over MgSO_4 , and concentrated under reduced pressure. The crude product was purified by column chromatography (silica gel, DCM/cyclohexane 3:2), yielding an orange solid (2.20 g, 4.71 mmol, 94%).

^1H NMR (400 MHz, CDCl_3): 9.83 (s, 1H), 7.60 (s, 1H), 7.22 (d, $J = 3.8$ Hz, 1H), 7.05 (d, $J = 3.8$ Hz, 1H), 6.92 (s, 1H), 2.85 – 2.79 (m, 2H), 2.76 – 2.70 (m, 2H), 1.73 – 1.56 (m, 4H), 1.49 – 1.33 (m, 4H), 0.96 (t, $J = 7.3$ Hz, 3H), 0.94 (t, $J = 7.3$ Hz, 3H).

^{13}C NMR (101 MHz, CDCl_3): 182.7, 141.1, 140.9, 140.6, 140.6, 139.1, 137.1, 135.2, 133.0, 131.4, 127.9, 126.9, 111.4, 32.9, 32.6, 29.3, 29.2, 22.7, 22.7, 14.0, 14.0.

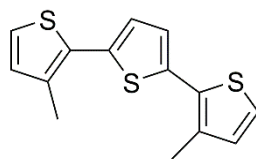
3,3''-dibutyl-[2,2':5',5'':2'',2''''-quaterthiophene]-5,5''-dicarbaldehyde (a4T)

Following a procedure by Yang *et al.*,^[35] compound **7** (2.20 g, 4.71 mmol, 1.0 eq.) was stirred with Pd(OAc)₂ (21 mg, 0.094 mmol, 2 mol%) and XPhos (54 mg, 0.113 mmol, 2.4 mol%) in 26.4 mL n-butanol until complete dissolution of the solids (ca. 15 min). Next, a solution containing CsOH·H₂O (1.58 g, 9.42 mmol, 2.0 eq.) in 6.6 mL H₂O was added. Subsequently, 5-formyl-2-thienylboronic acid (1.32 g, 8.48 mmol, 1.8 eq.) was added and the resulting mixture was stirred for 18 h at room temperature. After completion, H₂O was added and the product was extracted with CHCl₃, dried over MgSO₄ and concentrated under reduced pressure. Purification via column chromatography (silica gel, CHCl₃), followed by recrystallization from hot DCE furnished the title compound as a dark red microcrystalline powder (2.15 g, 4.29 mmol, 91%).

¹H NMR (400 MHz, CDCl₃): 9.86 (s, 1H), 9.84 (s, 1H), 7.67 (d, *J* = 4.0 Hz, 1H), 7.60 (s, 1H), 7.26 (d, *J* = 3.8 Hz, 1H), 7.24 (d, *J* = 4.0 Hz, 1H), 7.20 (s, 1H), 7.16 (d, *J* = 3.9 Hz, 1H), 2.86 – 2.82 (m, 2H), 2.82 – 2.77 (m, 2H), 1.74 – 1.63 (m, 4H), 1.50 – 1.39 (m, 4H), 0.97 (t, *J* = 7.4 Hz, 3H), 0.97 (t, *J* = 7.3 Hz, 3H).

¹³C NMR (101 MHz, CDCl₃): 182.6, 182.5, 146.7, 142.0, 141.6, 140.7, 140.7, 140.7, 139.1, 137.4, 137.4, 135.5, 134.3, 131.9, 129.3, 128.0, 126.9, 124.4, 32.8, 32.6, 29.4, 29.3, 22.8, 22.7, 14.1, 14.0.

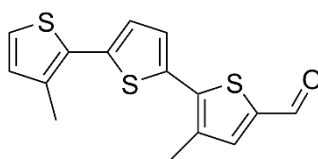
HR-EI-MS: *m/z* 498.73 (M⁺, calculated for C₂₆H₂₆O₂S₄: 498.75).

3,3''-dimethyl-2,2':5',2''-terthiophene (5_{Me})

A Grignard reagent, prepared by sonication of 2-bromo-3-methylthiophene (1.126 mL, 10.0 mmol, 2.9 eq.), 1,2-dibromoethane (0.862 mL, 10.0 mmol, 2.9 eq.), and Mg (477.7 mg, 19.6 mmol, 5.7 eq.) in 30 mL dry Et₂O was slowly added to a solution containing 2,5-dibromothiophene (389 μL, 3.5 mmol, 1.0 eq.) and Ni(dppp)Cl₂ (162.6 mg, 0.3 mmol, 3 mol%) in 20 mL dry Et₂O. The reaction mixture was heated to reflux for 40 h. Upon completion, the reaction was quenched by the addition of 30 mL 1 M HCl, extracted with DCM and washed with H₂O. The organic phase was then dried over MgSO₄ and concentrated under reduced pressure. The crude product was purified via column chromatography (silica gel, pentane), yielding the title compound as a slightly yellow oil, which crystallized slowly (492 mg, 1.78 mmol, 51%).

¹H NMR (400 MHz, CDCl₃): 7.15 (d, *J* = 5.1 Hz, 2H), 7.08 (s, 2H), 6.89 (d, *J* = 5.1 Hz, 2H), 2.42 (s, 6H).

¹³C NMR (101 MHz, CDCl₃): 136.7, 134.5, 131.9, 131.3, 126.2, 123.8, 15.9.

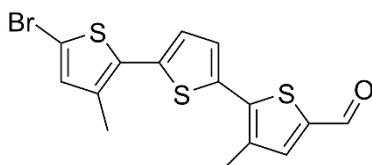
5-formyl-3,3''-dimethyl-2,2':5',2''-terthiophene (6_{Me})

A Vilsmeier reagent, prepared by the addition of POCl₃ (283 mg/ 168 μL, 1.8 mmol, 1.3 eq.) to 1.343 mL of dry DMF, was added to a solution of compound 5_{Me} (391.8 mg, 1.4 mmol, 1.0 eq.) in 28 mL DCE. The reaction mixture was stirred overnight at 70 °C. Subsequently, 50 mL H₂O was added and the pH was adjusted to 8.5–9 with 1 M NaOH. The product was extracted with DCM, dried over MgSO₄ and concentrated under reduced pressure. Purification via column chromatography (silica gel, chloroform) furnished the product as a slightly yellow solid (397 mg, 1.3 mmol, 92%).

¹H NMR (400 MHz, CDCl₃): 9.82 (s, 1H), 7.54 (s, 1H), 7.28 (d, *J* = 3.9 Hz, 1H), 7.19 (d, *J* = 5.1 Hz, 1H), 7.13 (d, *J* = 3.9 Hz, 1H), 6.91 (d, *J* = 5.1 Hz, 1H), 2.48 (s, 3H), 2.43 (s, 3H).

^{13}C NMR (101 MHz, CDCl_3): 182.5, 141.7, 140.5, 139.8, 139.0, 134.9, 134.9, 134.8, 131.8, 130.4, 127.8, 126.1, 124.2, 16.0, 15.7.

5-bromo-5''-formyl-3,3''-dimethyl-2,2':5',2''-terthiophene (7_{Me})

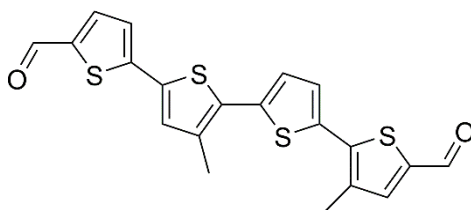


Compound 6_{Me} (397 mg, 1.3 mmol, 1.0 eq.) was dissolved in a mixture of 12.5 mL CHCl_3 and 12.5 mL glacial acetic acid and cooled to $0\text{ }^\circ\text{C}$. *N*-bromosuccinimide (255 mg, 1.4 mmol, 1.1 eq.) was added in the dark and the solution was allowed to slowly warm up to room temperature. After stirring at room temperature for 3 d in the dark, the reaction mixture was poured onto H_2O , extracted with DCM, washed with brine, dried over MgSO_4 , and concentrated under reduced pressure. The crude product was purified by column chromatography (silica gel, gradient eluent: *n*-hexane with 2% – 25% EtOAc), yielding a bright yellow solid (438 mg, 1.14 mmol, 90%).

^1H NMR (400 MHz, CDCl_3): 9.82 (s, 1H), 7.54 (s, 1H), 7.26 (d, $J = 4.0$ Hz, 1H), 7.07 (d, $J = 3.9$ Hz, 1H), 6.88 (s, 1H), 2.47 (s, 3H), 2.37 (s, 3H).

^{13}C NMR (101 MHz, CDCl_3): 182.5, 141.3, 140.4, 140.1, 137.5, 135.4, 135.4, 135.0, 134.3, 131.9, 127.7, 126.5, 111.0, 16.0, 15.6.

3,3''-dimethyl-[2,2':5',5'':2'',2'''-quaterthiophene]-5,5'''-dicarbaldehyde ($a4T_{\text{Me}}$)



Following a procedure by Yang et al.,^[35] compound 7_{Me} (232 mg, 0.6 mmol, 1.0 eq.) was stirred with $\text{Pd}(\text{OAc})_2$ (2.71 mg, 0.012 mmol, 2 mol%) and XPhos (6.91 mg, 0.015 mmol, 2.4 mol%) in 3.4 mL *n*-butanol (ca. 15 min). Next, a solution containing $\text{CsOH}\cdot\text{H}_2\text{O}$ (203 mg, 1.21 mmol, 2.0 eq.) in 846 μL H_2O was added, followed by the addition of 5-formyl-2-thienylboronic acid (170 mg, 1.09 mmol, 1.8 eq.). The resulting mixture was stirred for 2 d at room temperature and 1 d at $50\text{ }^\circ\text{C}$. After completion, H_2O was added and the product was extracted with CHCl_3 ,

washed with brine 3 times, dried over MgSO_4 , and concentrated under reduced pressure. Purification via column chromatography (silica gel, chloroform/EtOAc 99:1) furnished the title compound as a bright red powder (205 mg, 0.494 mmol, 82%).

^1H NMR (400 MHz, CDCl_3): 9.86 (s, 1H), 9.83 (s, 1H), 7.67 (d, $J = 4.0$ Hz, 1H), 7.55 (s, 1H), 7.30 (d, $J = 3.9$ Hz, 1H), 7.23 (d, $J = 4.0$ Hz, 1H), 7.19 (d, $J = 3.9$ Hz, 1H), 7.18 (s, 1H), 2.49 (s, 3H), 2.45 (s, 3H).

^{13}C NMR (101 MHz, CDCl_3): 182.5, 146.6, 142.0, 141.2, 140.4, 140.2, 137.8, 137.5, 136.0, 135.8, 135.1, 133.9, 132.4, 130.6, 127.9, 126.7, 124.4, 16.1, 15.9.

HR-EI-MS: m/z 414.56 (M^+ , calculated for $\text{C}_{20}\text{H}_{14}\text{O}_2\text{S}_4$: 414.57).

5 Oligothiophene-Bridged Conjugated Covalent Organic Frameworks

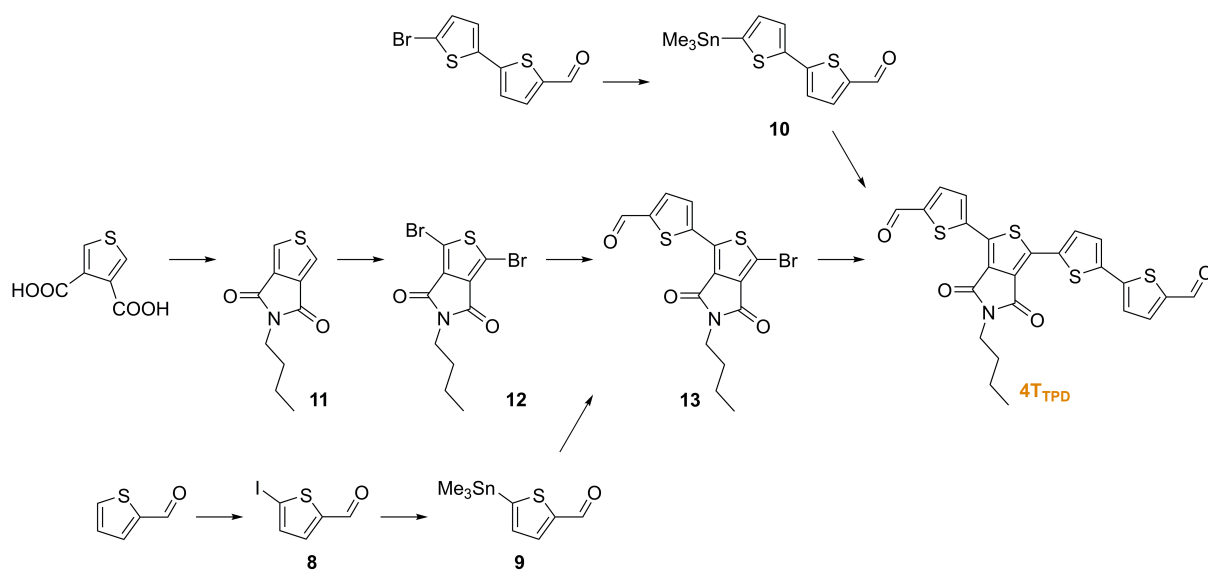
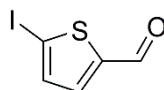


Figure 5.6. Synthesis of the 4T_{TPD} building block.

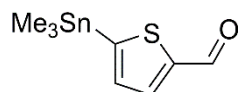
5-iodothiophene-2-carbaldehyde (8)^[36]



Thiophene-2-carbaldehyde (2.24 g, 20 mmol, 1.0 eq.) was dissolved in 40 mL EtOH and heated to 50 °C. *N*-iodosuccinimide (4.95 g, 22 mmol, 1.1 eq.) and *p*-toluenesulfonic acid monohydrate (380 mg, 2 mmol, 10 mol%) were added and the resulting mixture was stirred at 50 °C in the dark for 10 min. After completion, 20 mL of 1 M aqueous HCl and 20 mL EtOAc were added. The organic layer was extracted with EtOAc, washed with saturated aqueous Na₂S₂O₃ and Na₂CO₃ solutions, dried over MgSO₄, and filtered through a cotton plug. All volatiles were removed under high vacuum, yielding a slightly yellow solid (4.57 g, 19.2 mmol, 96%).

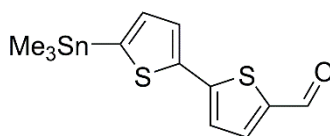
¹H NMR (400 MHz, CDCl₃): 9.77 (s, 1H), 7.39 (s, 2H).

¹³C NMR (101 MHz, CDCl₃): 181.3, 149.8, 138.4, 137.1, 87.9.

5-(trimethylstannyl)thiophene-2-carbaldehyde (9)

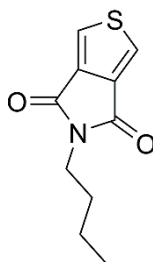
A reaction mixture containing compound **8** (472 mg, 2.0 mmol, 1.0 eq.), hexamethylditin (786 mg, 2.4 mmol, 1.2 eq.), and Pd(PPh₃)₄ (116 mg, 0.1 mmol, 5 mol%) in 10 mL of dry toluene was heated to 85 °C for 24 h. After completion, the solution was concentrated under reduced pressure at room temperature to remove the solvent and most of the by-product. The product was purified by sublimation (10⁻³ mbar, 60 °C), yielding the title compound as a white crystalline solid (264 mg, 0.96 mmol, 48%).

¹H NMR (400 MHz, CDCl₃): 9.94 (s, 1H), 7.83 (d, *J* = 3.5 Hz, 1H), 7.28 (d, *J* = 3.5 Hz, 1H), 0.42 (s, with Sn coupling, 9H).

5'-(trimethylstannyl)-[2,2'-bithiophene]-5-carbaldehyde (10)

A reaction mixture containing 5'-bromo-[2,2'-bithiophene]-5-carbaldehyde (1.00 g, 3.66 mmol, 1.0 eq.), hexamethylditin (1.44 g, 4.4 mmol, 1.2 eq.), and Pd(PPh₃)₄ (208 mg, 0.18 mmol, 5 mol%) in 20 mL of dry toluene was heated to 85 °C for 24 h. After completion, all volatiles were removed under high vacuum at 40 °C. The brown residue was dissolved in toluene, washed with saturated aqueous KCl, dried over Na₂SO₄, passed through a neutral alumina plug and evaporated to dryness, yielding a yellow solid (920 mg, 2.58 mmol, 70%), which was used in the next step without further purification.

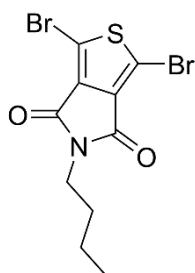
¹H NMR (400 MHz, CDCl₃): 9.85 (s, 1H), 7.66 (d, *J* = 4.0 Hz, 1H), 7.45 (d, *J* = 3.4 Hz, 1H), 7.24 (d, *J* = 4.0 Hz, 1H), 7.14 (d, *J* = 3.4 Hz, 1H), 0.41 (s, with Sn coupling, 9H).

5-butyl-4*H*-thieno[3,4-*c*]pyrrole-4,6(5*H*)-dione (11)^[37, 38]

Thiophene-3,4-dicarboxylic acid (3.29 g, 19.1 mmol, 1.0 eq.) and 3 Å molecular sieve (~200 mg) were dispersed in 40 mL acetic anhydride and heated to 140 °C for 24 h. After cooling to room temperature, the solution was decanted and evaporated to dryness. The resulting light grey solid was dried under high vacuum and re-dissolved in 60 mL of dry toluene. Butylamine (2.01 g, 28.7 mmol, 1.5 eq.) was added, and the solution was heated to reflux for 24 h. All volatiles were removed under high vacuum, yielding a faint brownish powder. SOCl₂ (120 mL) was added and the mixture was heated to reflux (88 °C) overnight. The SOCl₂ was distilled off at ambient pressure, leaving behind a dark crystalline solid. Purification via column chromatography (silica gel, DCM), followed by recrystallization from Et₂O afforded the title compound as colorless platelets (3.06 g, 14.6 mmol, 77%).

¹H NMR (400 MHz, CDCl₃): 7.80 (s, 2H), 3.67 – 3.57 (m, 2H), 1.67 – 1.58 (m, 2H), 1.41 – 1.30 (m, 2H), 0.94 (t, *J* = 7.4 Hz, 3H).

¹³C NMR (101 MHz, CDCl₃): 162.8, 136.9, 125.6, 38.4, 30.7, 20.2, 13.8.

1,3-dibromo-5-butyl-4*H*-thieno[3,4-*c*]pyrrole-4,6(5*H*)-dione (12)^[39]

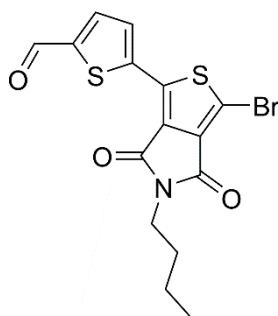
Compound **11** (2.64 g, 12.6 mmol, 1.0 eq.) was dissolved in a mixture of conc. H₂SO₄ (18.9 mL) and trifluoroacetic acid (63 mL) at 0 °C. *N*-bromosuccinimide (6.73 g, 37.8 mmol, 3.0 eq.) was added and the reaction mixture was allowed to slowly warm to room temperature. After stirring in the dark for 2 d, the solution was poured onto H₂O, extracted with CHCl₃, dried over MgSO₄, and concentrated under reduced pressure. The product was purified by column

chromatography (silica gel, toluene/DCM/heptane 3:1:1), yielding a slightly yellow solid (3.18 g, 8.65 mmol, 69%).

^1H NMR (400 MHz, CDCl_3): 3.60 (t, $J = 7.2$ Hz, 2H), 1.66 – 1.57 (m, 2H), 1.40 – 1.29 (m, 2H), 0.94 (t, $J = 7.3$ Hz, 3H).

^{13}C NMR (101 MHz, CDCl_3): 160.5, 135.0, 113.1, 38.7, 30.5, 20.2, 13.7.

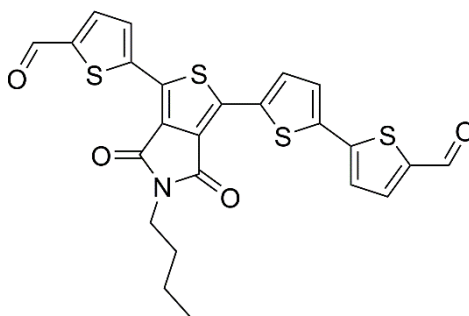
compound 13



A reaction mixture containing compound **12** (602 mg, 1.64 mmol, 1.0 eq.), compound **9** (451 mg, 1.64 mmol, 1.0 eq.), $\text{Pd}(\text{dba})_2$ (47 mg, 0.082 mmol, 5 mol%), and tri(2-furyl)phosphine (47 mg, 0.20 mmol, 12 mol%) in 20 mL dry toluene was heated to 85 °C for 48 h. After completion, all volatiles were removed under high vacuum at 50 °C. Purification via column chromatography (silica gel, CHCl_3) yielded the title compound as a yellow solid (171 mg, 0.43 mmol, 26%).

^1H NMR (400 MHz, CDCl_3): 9.94 (s, 1H), 8.08 (d, $J = 4.0$ Hz, 1H), 7.75 (d, $J = 4.1$ Hz, 1H), 3.66 (t, $J = 7.2$ Hz, 2H), 1.71 – 1.60 (m, 2H), 1.42 – 1.32 (m, 2H), 0.95 (t, $J = 7.4$ Hz, 3H).

TPD-modified quaterthiophene (4T_{TPD})



A reaction mixture containing compound **13** (80 mg, 0.20 mmol, 1.0 eq.), compound **10** (86 mg, 0.24 mmol, 1.2 eq.), $\text{Pd}(\text{dba})_2$ (12 mg, 0.020 mmol, 10 mol%), and tri(2-

furyl)phosphine (12 mg, 0.050 mmol, 25 mol%) in 2 mL dry toluene was heated to 85 °C for 24 h. After completion, all volatiles were removed under high vacuum at 50 °C. Purification via column chromatography (silica gel, DCM), followed by recrystallization from DCE/Et₂O afforded the title compound as an orange solid (89 mg, 0.174 mmol, 87%).

¹H NMR (400 MHz, CDCl₃): 9.94 (s, 1H), 9.90 (s, 1H), 8.19 (d, *J* = 4.0 Hz, 1H), 7.98 (d, *J* = 4.0 Hz, 1H), 7.77 (d, *J* = 4.0 Hz, 1H), 7.71 (d, *J* = 4.0 Hz, 1H), 7.36 (d, *J* = 4.0 Hz, 2H), 3.70 (t, *J* = 7.3 Hz, 2H), 1.74 – 1.64 (m, 2H), 1.46 – 1.35 (m, 2H), 0.97 (t, *J* = 7.4 Hz, 3H).

¹³C NMR (101 MHz, CDCl₃): 182.7, 182.6, 162.5, 162.3, 145.5, 144.9, 143.0, 140.6, 139.8, 137.3, 137.2, 136.8, 134.8, 133.1, 131.8, 131.6, 130.6, 129.8, 127.2, 125.6, 38.7, 30.7, 20.3, 13.8.

HR-EI-MS: *m/z* 511.63 (M⁺, calculated for C₂₄H₁₇NO₄S₄: 511.64).

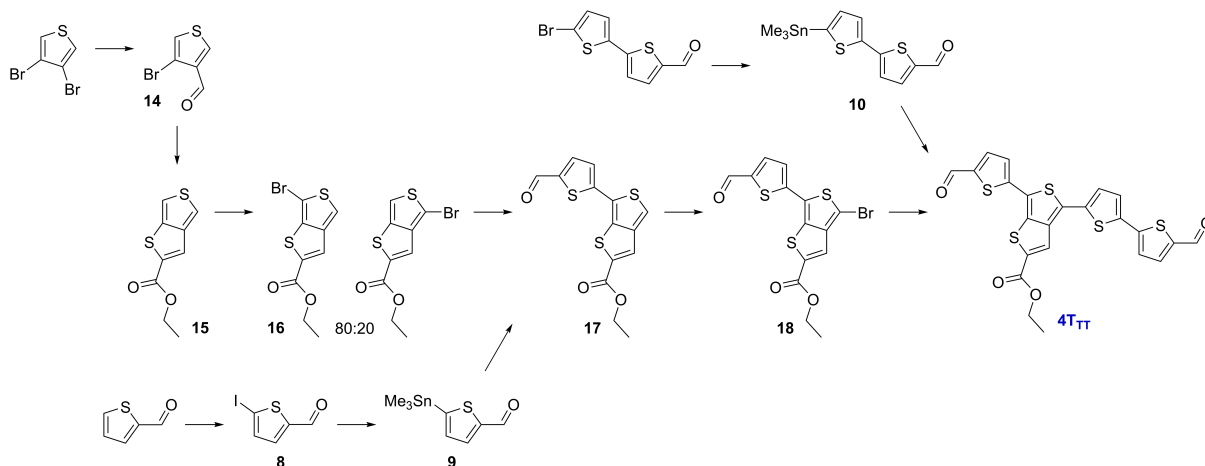
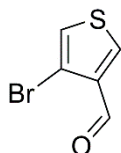


Figure 5.7. Synthesis of the 4TT building block.

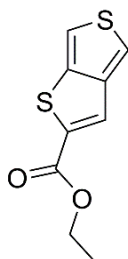
4-bromothiophene-3-carbaldehyde (14)



A solution of 3,4-dibromothiophene (5.4 g, 22.3 mmol, 1.0 eq.) in 15 mL of dry Et₂O was cooled to $-78\text{ }^{\circ}\text{C}$ and *n*-BuLi (2.0 M in cyclohexane, 22.3 mmol, 1.0 eq.) was slowly added. After stirring for 15 min, DMF (1.63 g, 22.3 mmol, 1.0 eq.) was added. The reaction mixture was stirred for 3 h at $-78\text{ }^{\circ}\text{C}$ and then allowed to slowly warm to room temperature. H₂O was added to quench the reaction, and the solution was extracted with DCM, dried over Na₂SO₄, and evaporated to dryness. Purification via high vacuum distillation (10^{-3} mbar, $65\text{ }^{\circ}\text{C}$) afforded the title compound as a faint yellowish, air-sensitive liquid (2.29 g, 12.0 mmol, 54%).

¹H NMR (400 MHz, CDCl₃): 9.95 (s, 1H), 8.15 (d, *J* = 3.4 Hz, 1H), 7.36 (d, *J* = 3.4 Hz, 1H).

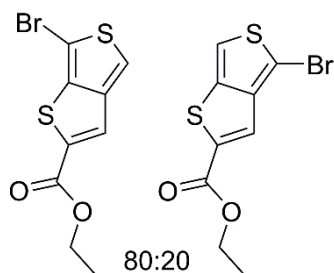
¹³C NMR (101 MHz, CDCl₃): 184.8, 137.7, 134.7, 125.2, 111.5.

ethyl thieno[3,4-*b*]thiophene-2-carboxylate (15)^[40]

Ethyl mercaptoacetate (1.59 g, 13.2 mmol, 1.1 eq.) was added dropwise to a solution of compound 14 (2.29 g, 12.0 mmol, 1.0 eq.), K₂CO₃ (2.49 g, 18.0 mmol, 1.5 eq.), and CuO nanopowder (< 50 nm particle size, 28 mg, 0.36 mmol, 3 mol%) in 24 mL DMSO at 60 °C. The reaction mixture was stirred overnight at 60 °C. After completion, H₂O and brine were added, and the product was extracted with DCM. The combined organic phase was washed with brine, dried over Na₂SO₄, and concentrated under reduced pressure. Purification via column chromatography (silica gel, DCM/heptane 2:1) yielded the title compound as a slightly yellowish powder (1.50 g, 7.08 mmol, 59%).

¹H NMR (400 MHz, CDCl₃): 7.70 (d, *J* = 0.8 Hz, 1H), 7.59 (d, *J* = 2.6 Hz, 1H), 7.28 (dd, *J* = 2.7, 0.8 Hz, 1H), 4.38 (q, *J* = 7.1 Hz, 2H), 1.39 (t, *J* = 7.1 Hz, 3H).

¹³C NMR (101 MHz, CDCl₃): 163.3, 146.1, 140.0, 140.0, 123.6, 116.7, 111.5, 61.8, 14.5.

ethyl 6-bromothieno[3,4-*b*]thiophene-2-carboxylate (16)^[41]

Compound **15** (1.34 g, 6.31 mmol, 1.0 eq.) was dissolved in 45 mL DMF and stirred at 0 °C in the dark. A solution of *N*-bromosuccinimide (1.12 g, 6.31 mmol, 1.0 eq.) in 45 mL DMF was added over the course of 6 h via an addition funnel (approximately one drop every 10 s). Upon completion, the reaction mixture was allowed to warm up to room temperature over the course of 12 h. All volatiles were removed under reduced pressure. Purification via column chromatography (silica gel, CHCl₃/cyclohexane 1:1) afforded a slightly pink solid (1.68 g, 5.78 mmol, 92%). The product was found to be a 80:20 mixture of the 6-bromo- and the 4-bromothieno[3,4-*b*]thiophene-2-carboxylate that could not be separated at this stage.

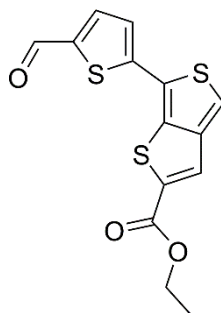
^1H NMR (400 MHz, CDCl_3): 7.56 (d, $J = 0.9$ Hz, 1H), 7.24 (d, $J = 0.9$ Hz, 1H), 4.38 (q, $J = 7.1$ Hz, 2H), 1.41 (t, $J = 7.1$ Hz, 3H).

Isomer: 7.66 (s, 1H), 7.52 (s, 1H), 4.38 (q, $J = 7.1$ Hz, 2H), 1.39 (t, $J = 7.1$ Hz, 3H).

^{13}C NMR (101 MHz, CDCl_3): 162.7, 145.9, 140.8, 138.9, 122.5, 112.6, 102.8, 61.9, 14.3.

Isomer: 162.7, 145.3, 140.4, 124.2, 123.2, 118.0, 97.9, 61.8, 14.3.

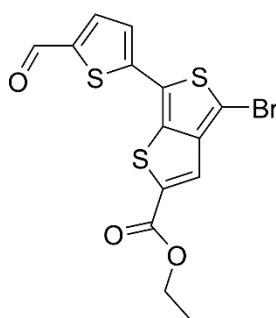
compound 17



A reaction mixture containing compound **16** (730 mg, 2.5 mmol, 1.0 eq.), compound **9** (825 mg, 3.0 mmol, 1.2 eq.), $\text{Pd}(\text{dba})_2$ (144 mg, 0.25 mmol, 10 mol%), and tri(2-furyl)phosphine (145 mg, 0.625 mmol, 25 mol%) in 25 mL dry toluene was heated to 85 °C for 20 h. After completion, all volatiles were removed under high vacuum at 50 °C. Purification via column chromatography (silica gel, DCM/cyclohexane 5:1) afforded the title compound as a yellow-green solid (470 mg, 1.46 mmol, 58%). The product was found to be a 90:10 mixture of the 6-thienyl and 4-thienyl isomers.

^1H NMR (400 MHz, CDCl_3): 9.90 (s, 1H), 7.99 (d, $J = 0.8$ Hz, 1H), 7.73 (d, $J = 4.0$ Hz, 1H), 7.36 (d, $J = 4.0$ Hz, 1H), 7.33 (d, $J = 0.8$ Hz, 1H), 4.42 (q, $J = 7.1$ Hz, 2H), 1.43 (t, $J = 7.1$ Hz, 3H).

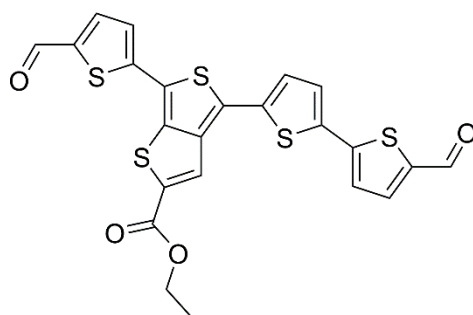
^{13}C NMR (101 MHz, CDCl_3): 182.4, 162.6, 145.3, 143.2, 142.4, 142.3, 141.3, 137.1, 126.8, 124.8, 122.9, 112.8, 62.0, 14.3.

compound 18

Compound **17** (470 mg, 1.46 mmol, 1.0 eq.) was dissolved in 30 mL CHCl_3 . *N*-bromosuccinimide (312 mg, 1.75 mmol, 1.2 eq.) was added and the resulting mixture was stirred at room temperature in the dark for 2 d. After completion, the solution was poured onto H_2O and extracted with DCM. The organic phase was dried over Na_2SO_4 and concentrated under reduced pressure. Purification via column chromatography (silica gel, DCM/cyclohexane 4:1) afforded the isomer-pure title compound as an orange solid (501 mg, 1.25 mmol, 86%). The 4-thienyl isomer is slightly slower on the column and thus could be fully removed from the product.

^1H NMR (400 MHz, CDCl_3): 9.91 (s, 1H), 7.96 (s, 1H), 7.71 (d, $J = 4.0$ Hz, 1H), 7.28 (d, $J = 4.0$ Hz, 1H), 4.42 (q, $J = 7.1$ Hz, 2H), 1.43 (t, $J = 7.1$ Hz, 3H).

^{13}C NMR (101 MHz, CDCl_3): 182.5, 162.4, 144.3, 143.0, 142.9, 142.8, 142.4, 137.2, 128.3, 125.2, 123.8, 100.1, 62.4, 14.5.

TT-modified quaterthiophene (4T_{TT})

A reaction mixture containing compound **18** (321 mg, 0.8 mmol, 1.0 eq.), compound **10** (343 mg, 0.96 mmol, 1.2 eq.), $\text{Pd}(\text{dba})_2$ (46 mg, 0.08 mmol, 10 mol%), and tri(2-furyl)phosphine (46 mg, 0.20 mmol, 25 mol%) in 8 mL dry toluene was heated to 85 °C for 20 h. After completion, all volatiles were removed under high vacuum at 50 °C. Purification

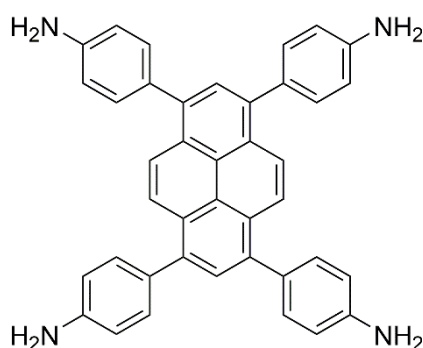
via column chromatography (silica gel, DCM), followed by precipitation from $\text{CHCl}_3/\text{Et}_2\text{O}$ afforded the title compound as a deep red solid (266 mg, 0.517 mmol, 65%).

^1H NMR (400 MHz, CDCl_3): 9.92 (s, 1H), 9.89 (s, 1H), 8.03 (s, 1H), 7.75 (d, $J = 4.1$ Hz, 1H), 7.71 (d, $J = 4.1$ Hz, 1H), 7.39 (d, $J = 3.8$ Hz, 1H), 7.38 (d, $J = 3.8$ Hz, 1H), 7.32 (d, $J = 4.1$ Hz, 1H), 7.29 (d, $J = 4.0$ Hz, 1H), 4.46 (q, $J = 7.1$ Hz, 2H), 1.46 (t, $J = 7.2$ Hz, 3H).

^{13}C NMR data could not be recorded for this compound due to its low solubility.

HR-EI-MS: m/z 514.61 (M^+ , calculated for $\text{C}_{23}\text{H}_{14}\text{O}_4\text{S}_5$: 514.61).

1,3,6,8-tetrakis(4-aminophenyl)pyrene (Py)^[15, 42]



A reaction mixture containing 1,3,6,8-tetrabromopyrene (1482 mg, 2.86 mmol, 1.0 eq.), 4-aminophenylboronic acid pinacol ester (3010 mg, 13.7 mmol, 4.8 eq.), K_2CO_3 (2175 mg, 15.7 mmol, 5.5 eq.), and $\text{Pd}(\text{PPh}_3)_4$ (330 mg, 0.29 mmol, 10 mol%) in 32 mL 1,4-dioxane and 8 mL H_2O was heated to reflux (115 °C) for 3 d. After cooling to room temperature, H_2O was added. The resulting precipitate was collected via filtration and was washed with H_2O and MeOH. Recrystallization from 1,4-dioxane, followed by drying under high vacuum furnished the title compound, co-crystallized with approximately 1.5 dioxane molecules per formula unit, as a bright yellow powder (1792 mg, 2.56 mmol, 90%).

^1H NMR (400 MHz, $\text{DMSO}-d_6$): 8.13 (s, 4 H), 7.79 (s, 2 H), 7.34 (d, $J = 8.4$ Hz, 8 H), 6.77 (d, $J = 8.5$ Hz, 8 H), 5.30 (s, 8 H), 3.56 (s, 12 H, dioxane).

^{13}C NMR (100 MHz, $\text{DMSO}-d_6$): 148.2, 137.1, 131.0, 129.0, 127.6, 126.7, 126.1, 124.4, 113.9, 66.3 (dioxane).

Section C – COF syntheses

All COF syntheses were performed under argon atmosphere in PTFE-sealed glass reaction tubes (6 mL volume). Solvents and acetic acid were obtained in high purity grade from commercial suppliers and were, unless shipped under argon, degassed and saturated with argon prior to use.

Py-a4T COF

1,3,6,8-tetrakis(4-aminophenyl)pyrene dioxane adduct (Py; 14.0 mg, 20 μmol , 1.0 eq.) and 3,3''-dibutyl-[2,2':5',5'':2'',2'''-quaterthiophene]-5,5'''-dicarbaldehyde (a4T; 20 mg, 40 μmol , 2.0 eq.) were filled into a reaction tube, followed by the addition of mesitylene (133 μL), BnOH (67 μL), and 6 m acetic acid (20 μL). The tube was sealed and the reaction mixture was heated at 120 °C for 4 d. After cooling to room temperature, the precipitate was collected by filtration and slowly dried in air for 24 h, yielding the Py-a4T COF as a dark red powder (19 mg, 64%). Following the same synthesis protocol, but employing the s4T building block instead, did not lead to the formation of a crystalline network. Other solvent mixtures (mesitylene/dioxane, mesitylene/BnOH, DCB/dioxane, DCB/BnOH; ratios from 2:1 to 1:9) and concentrations were tested as well, but the resulting solids did not show any sign of long-range order.

Py-a4T_{Me} COF

1,3,6,8-tetrakis(4-aminophenyl)pyrene dioxane adduct (Py; 14.0 mg, 20 μmol , 1.0 eq.) and 3,3''-dimethyl-[2,2':5',5'':2'',2'''-quaterthiophene]-5,5'''-dicarbaldehyde (a4T_{Me}; 17 mg, 40 μmol , 2.0 eq.) were filled into a reaction tube, followed by the addition of mesitylene (333 μL), BnOH (167 μL), and 6 m acetic acid (50 μL). The tube was sealed and the reaction mixture was heated at 120 °C for 4 d. After cooling to room temperature, the precipitate was collected by filtration, slowly dried in an argon atmosphere overnight, and extracted with supercritical CO₂ for 2 h, yielding the Py-a4T_{Me} COF as a dark red powder.

Py-4T_{TPD} COF

Py (7.0 mg, 10 μmol , 1.0 eq.) and the TPD-modified quaterthiophene (4T_{TPD}; 10.2 mg, 20 μmol , 2.0 eq.) were filled into a reaction tube, followed by the addition of mesitylene (167 μL), 1,4-dioxane (333 μL), and 6 m acetic acid (50 μL). The tube was sealed and the reaction mixture was heated at 120 $^{\circ}\text{C}$ for 4 d. After cooling to room temperature, the precipitate was collected by filtration and slowly dried in air, yielding the Py-4T_{TPD} COF as an orange powder.

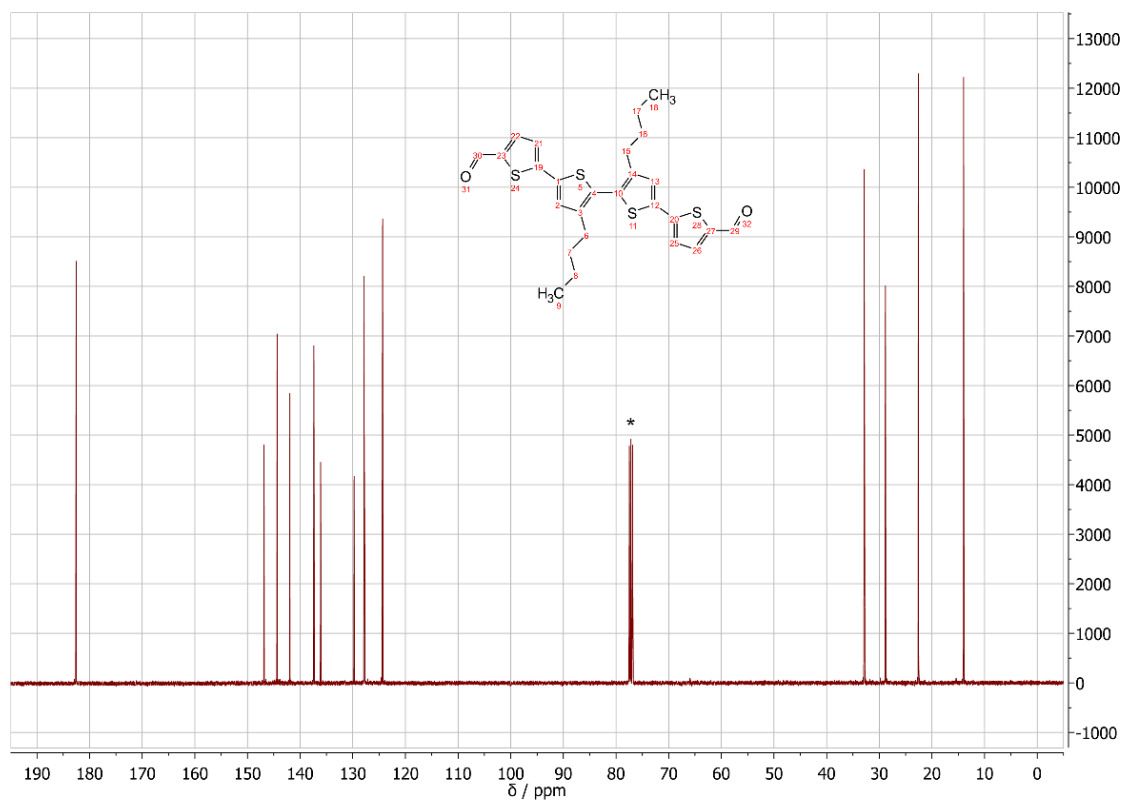
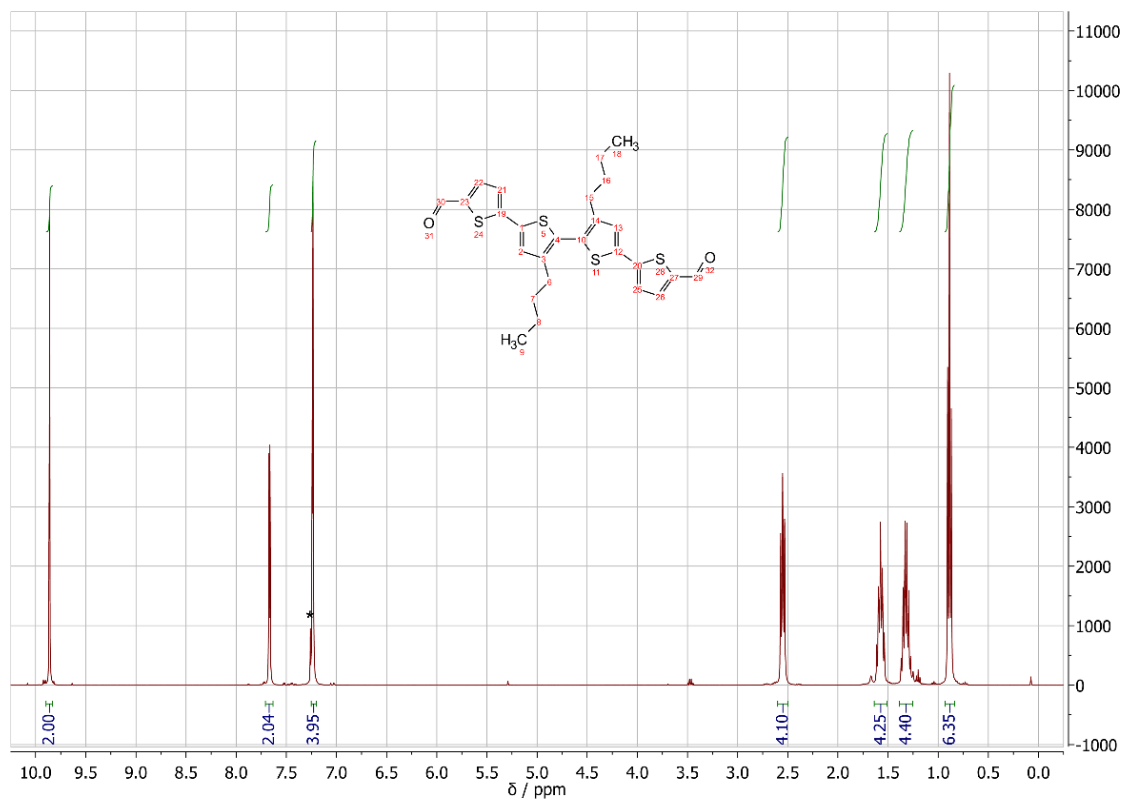
Py-4T_{TT} COF

Py (14.0 mg, 20 μmol , 1.0 eq.) and TT-modified quaterthiophene (4T_{TT}; 20.6 mg, 40 μmol , 2.0 eq.) were filled into a reaction tube, followed by the addition of mesitylene (667 μL), BnOH (333 μL), and 6 m acetic acid (100 μL). The tube was sealed and the reaction mixture was heated at 120 $^{\circ}\text{C}$ for 4 d. After cooling to room temperature, the precipitate was collected by filtration and slowly dried in air for 24 h, yielding the Py-4T_{TT} COF as a very dark purple powder (26 mg, 85%).

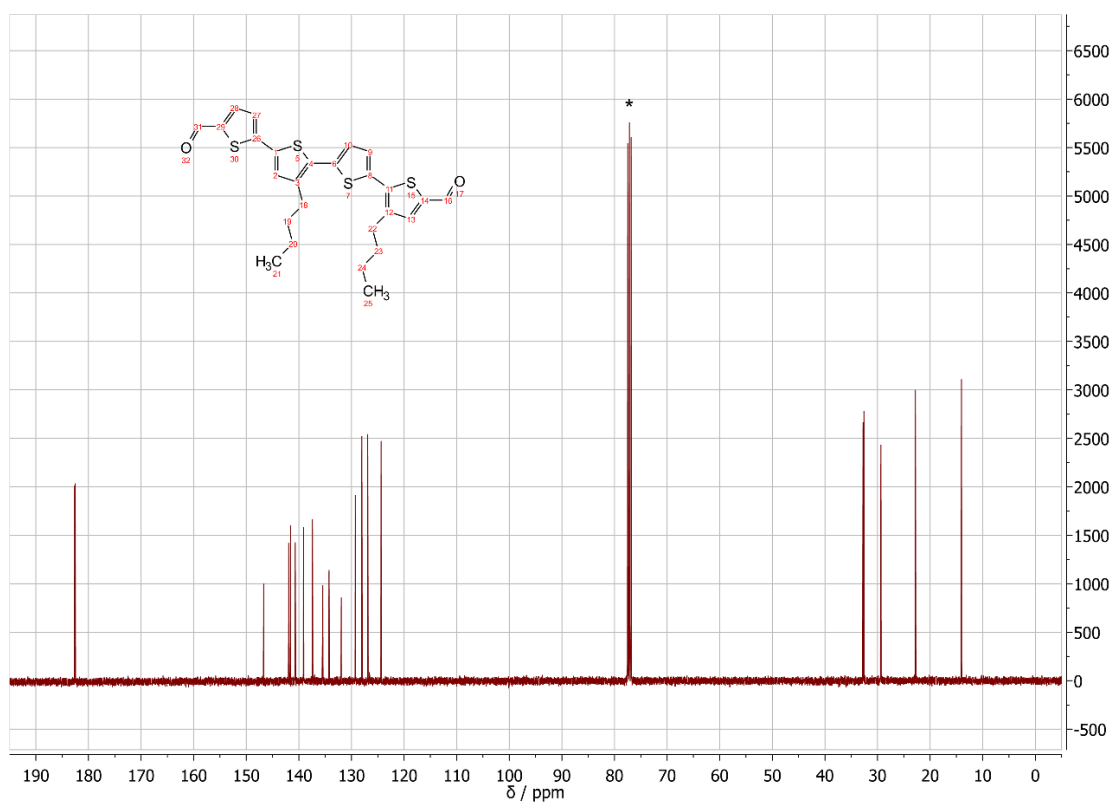
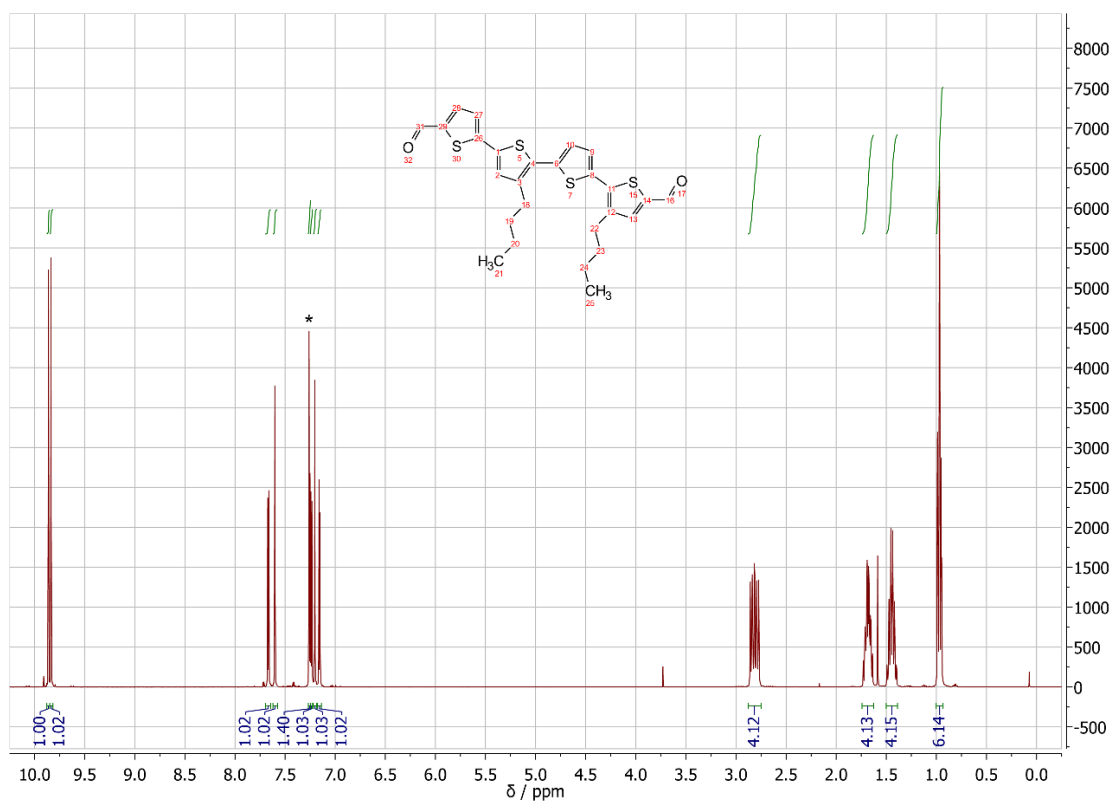
Section D- NMR spectra of the building blocks

^1H and ^{13}C NMR spectra. Residual (undeuterated) solvent peaks are marked with asterisks.

s4T

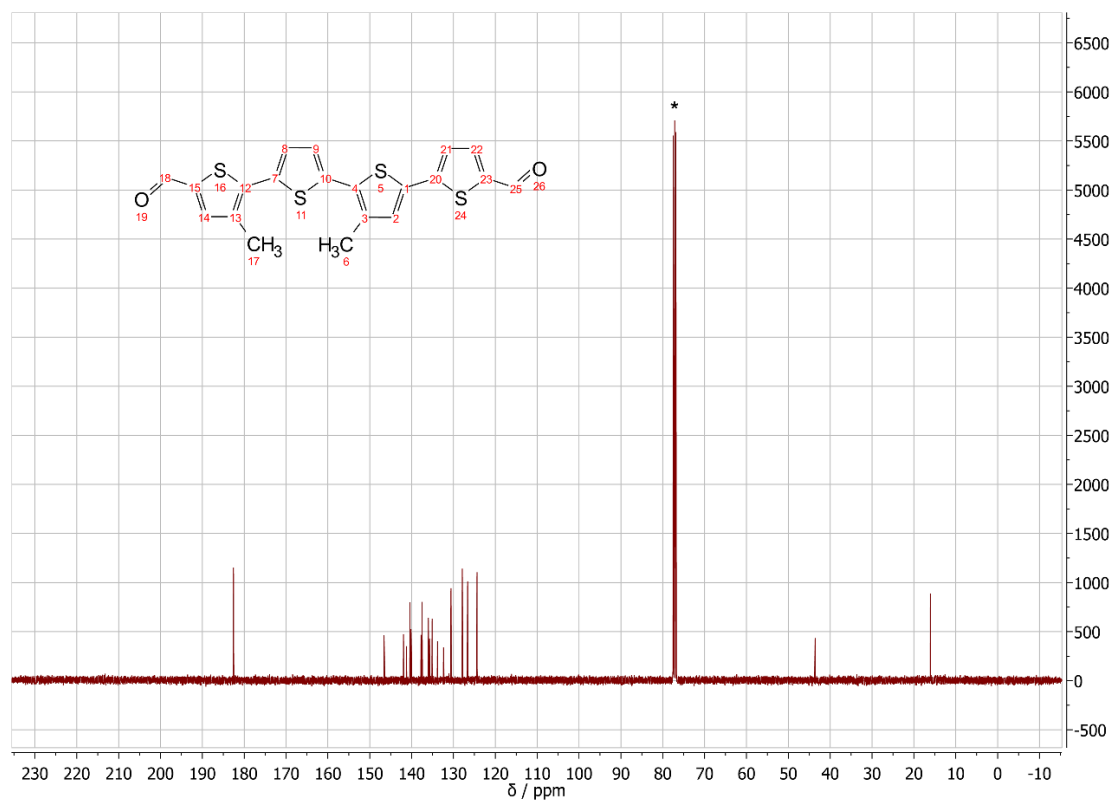
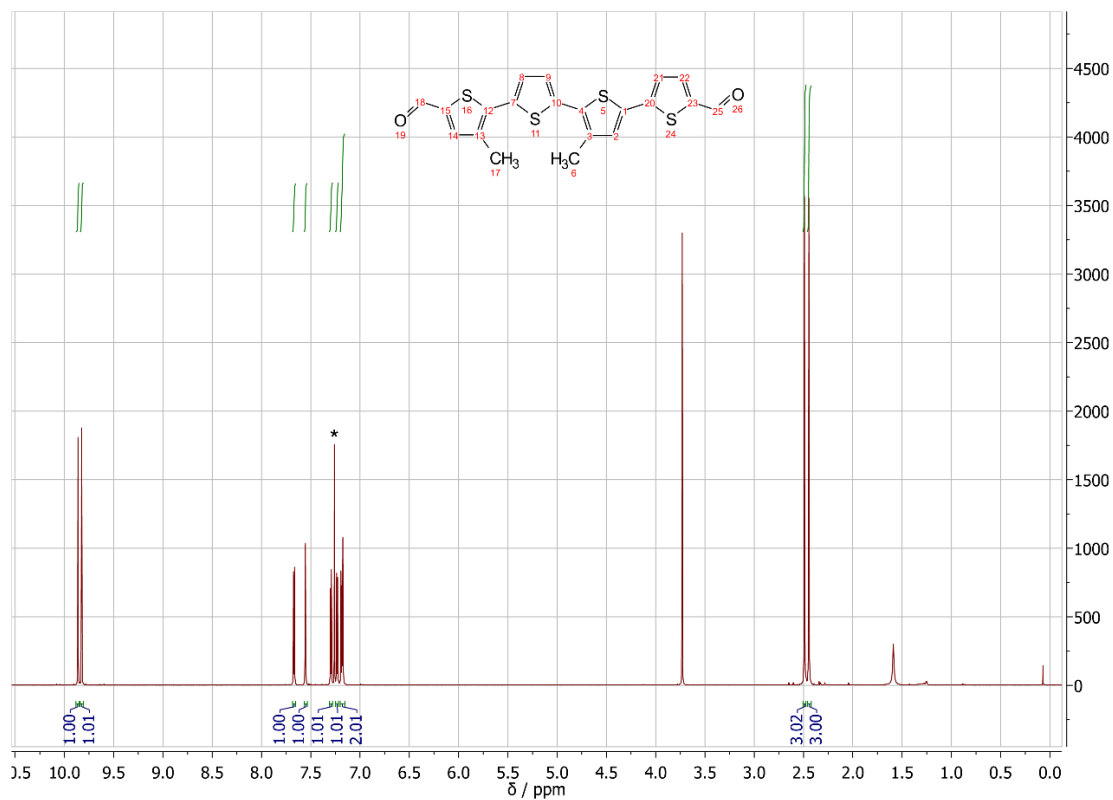


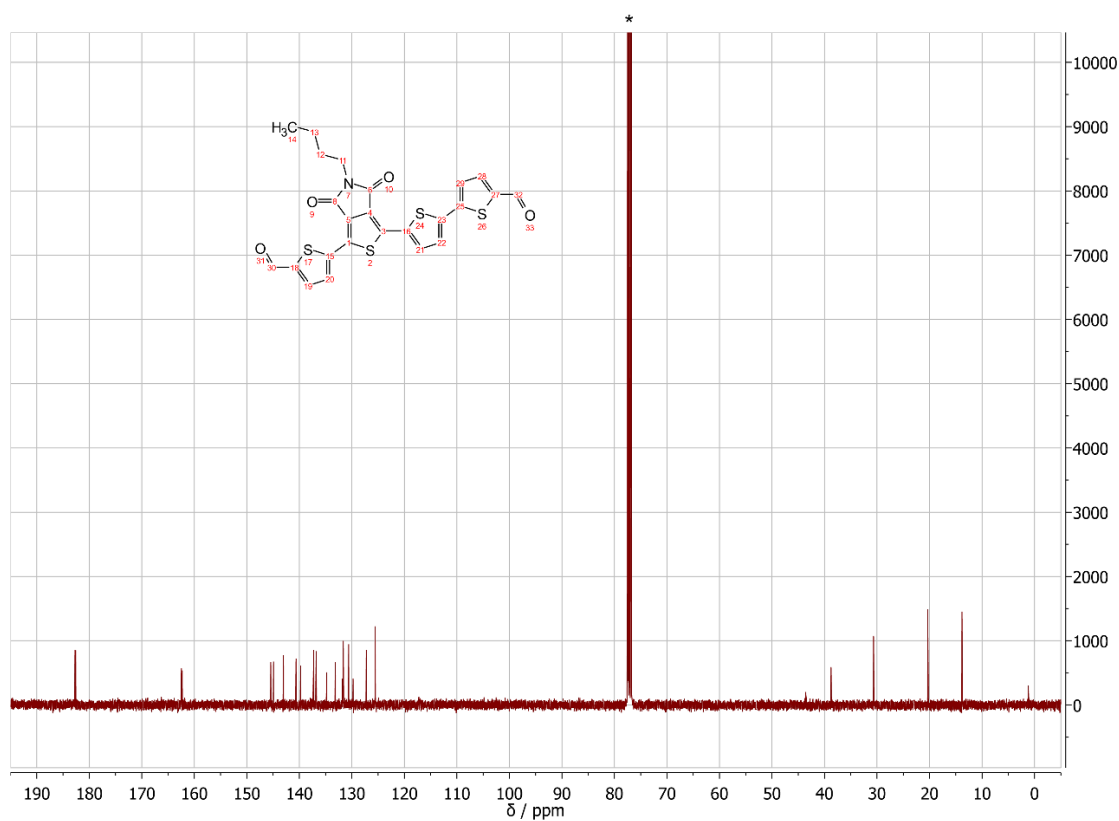
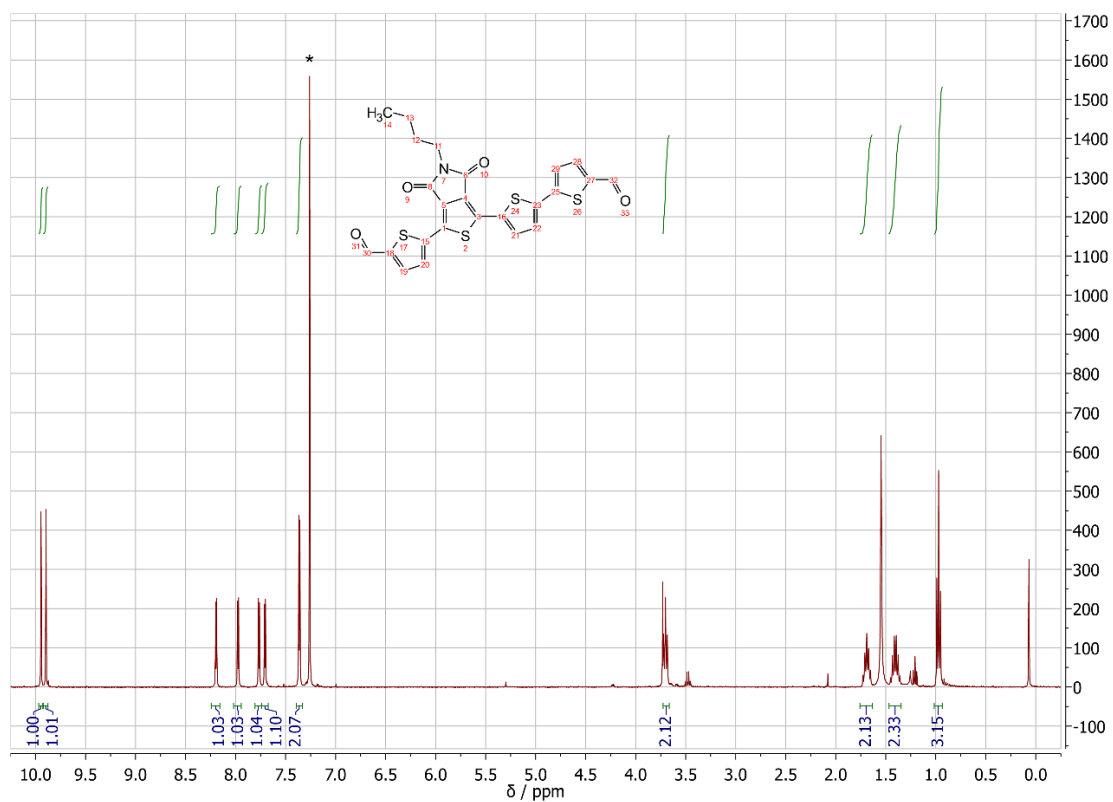
a4T

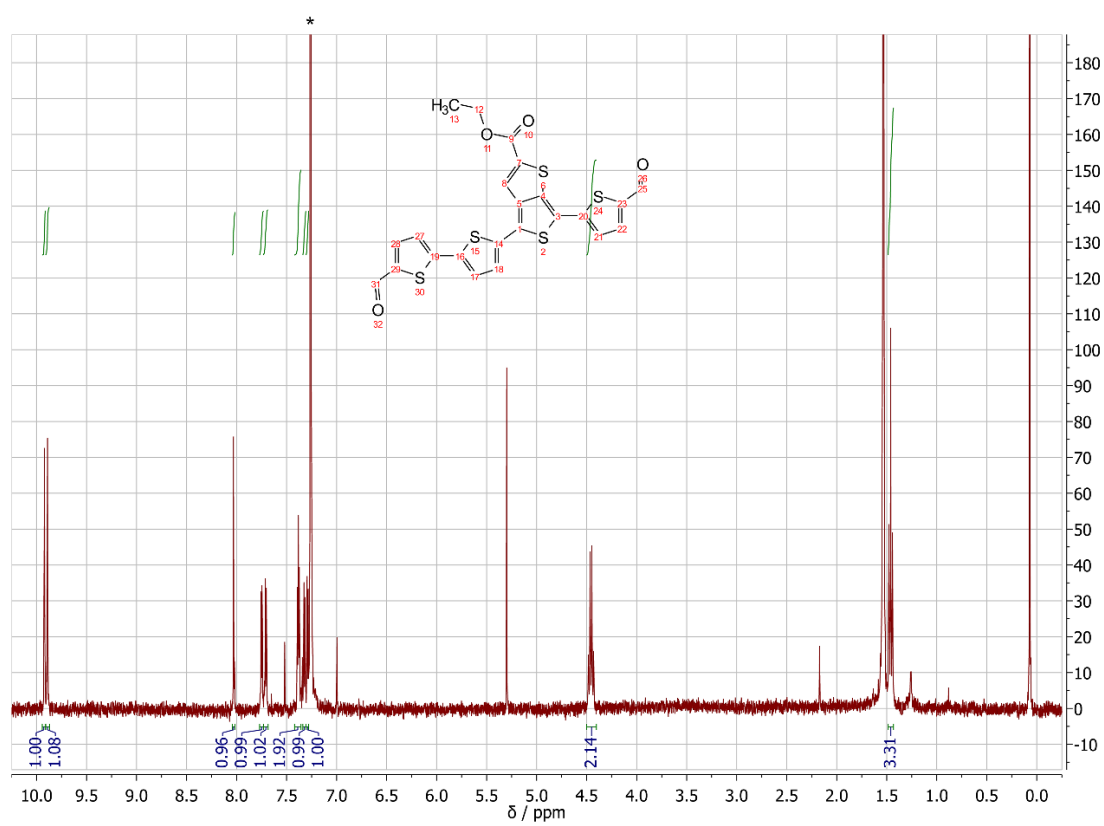


5 Oligothiophene-Bridged Conjugated Covalent Organic Frameworks

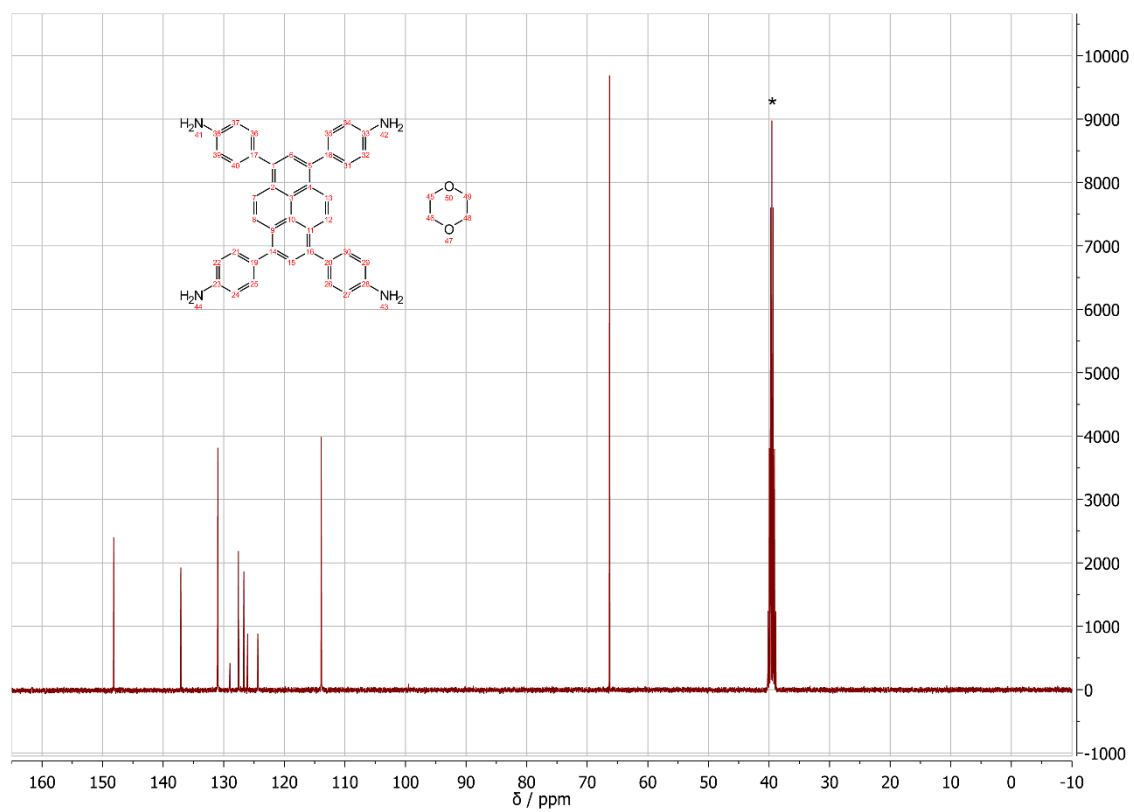
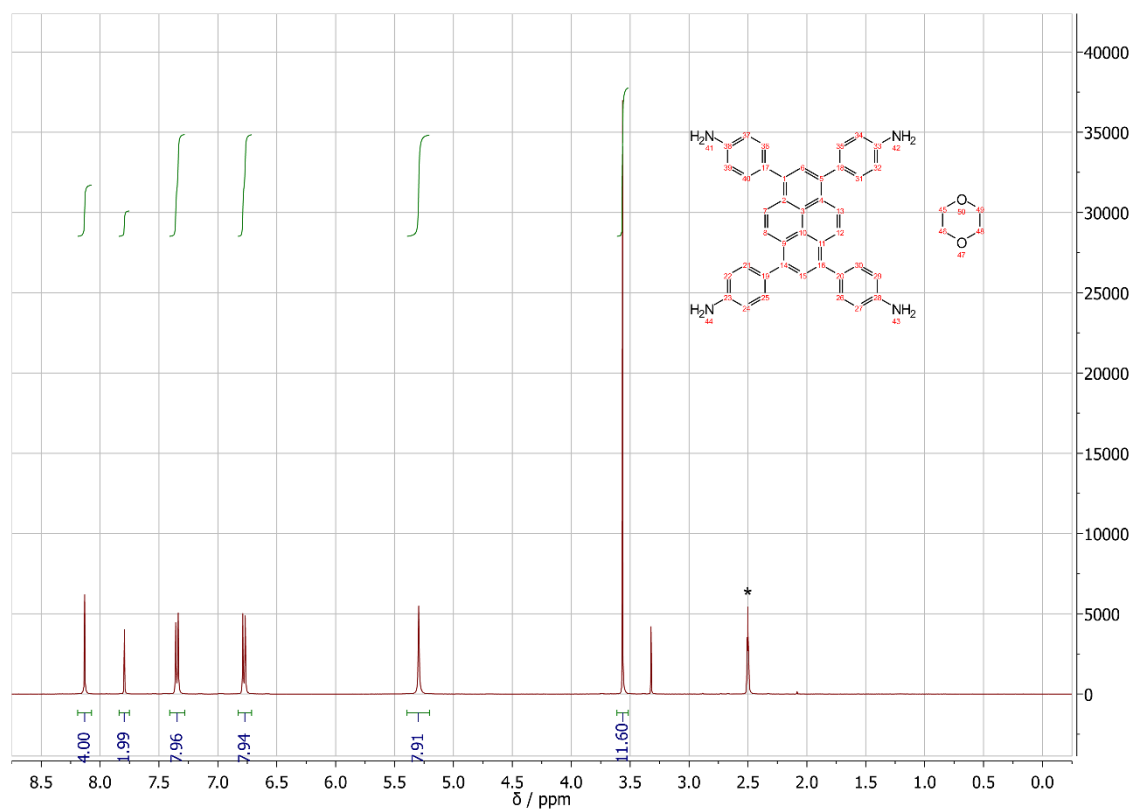
a4T_{Me}



4T_{TPD}

4T_{TT}

Py



Section E – HRMS analysis of the building blocks

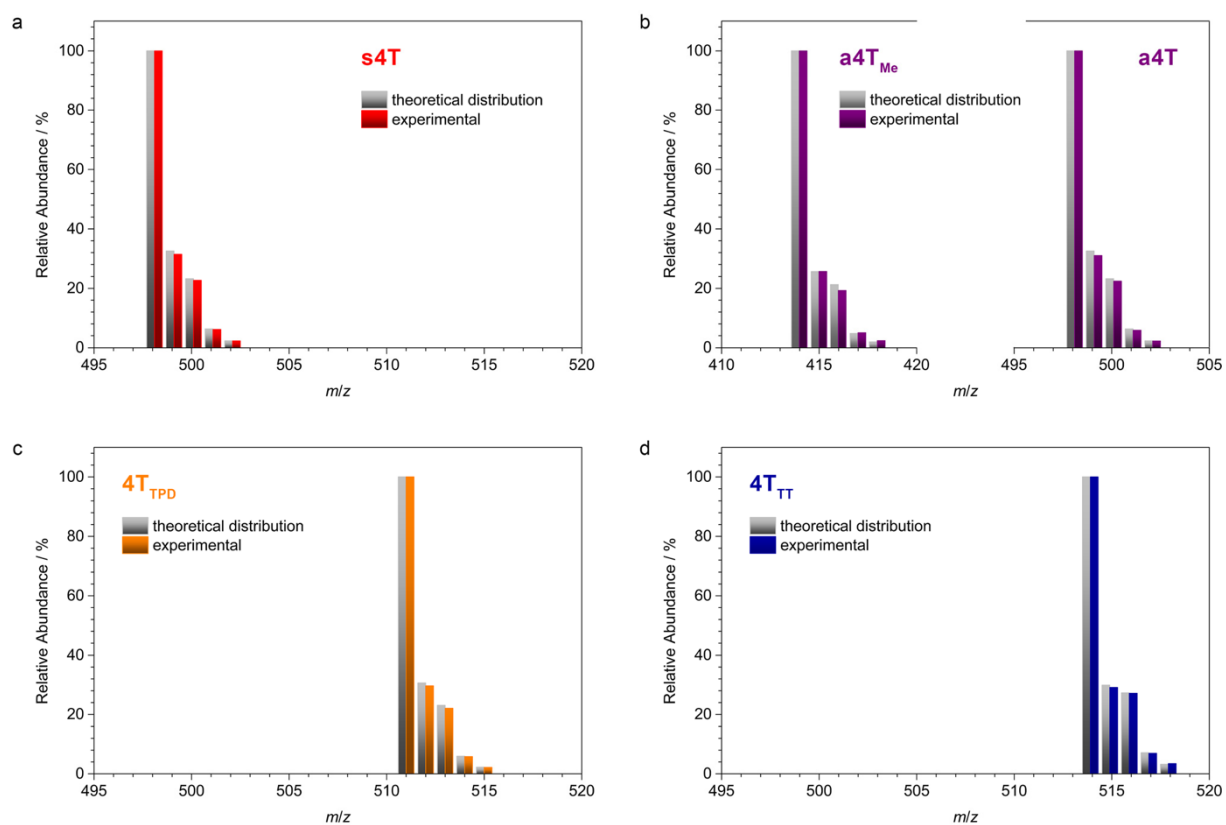


Figure 5.8. Comparison between the theoretical (grey) and the experimental (colored) HR-EI-MS patterns of the four quaterthiophene-derived building blocks. The patterns correspond to the respective singly positively charged molecules (M^+).

Section F – IR spectroscopy

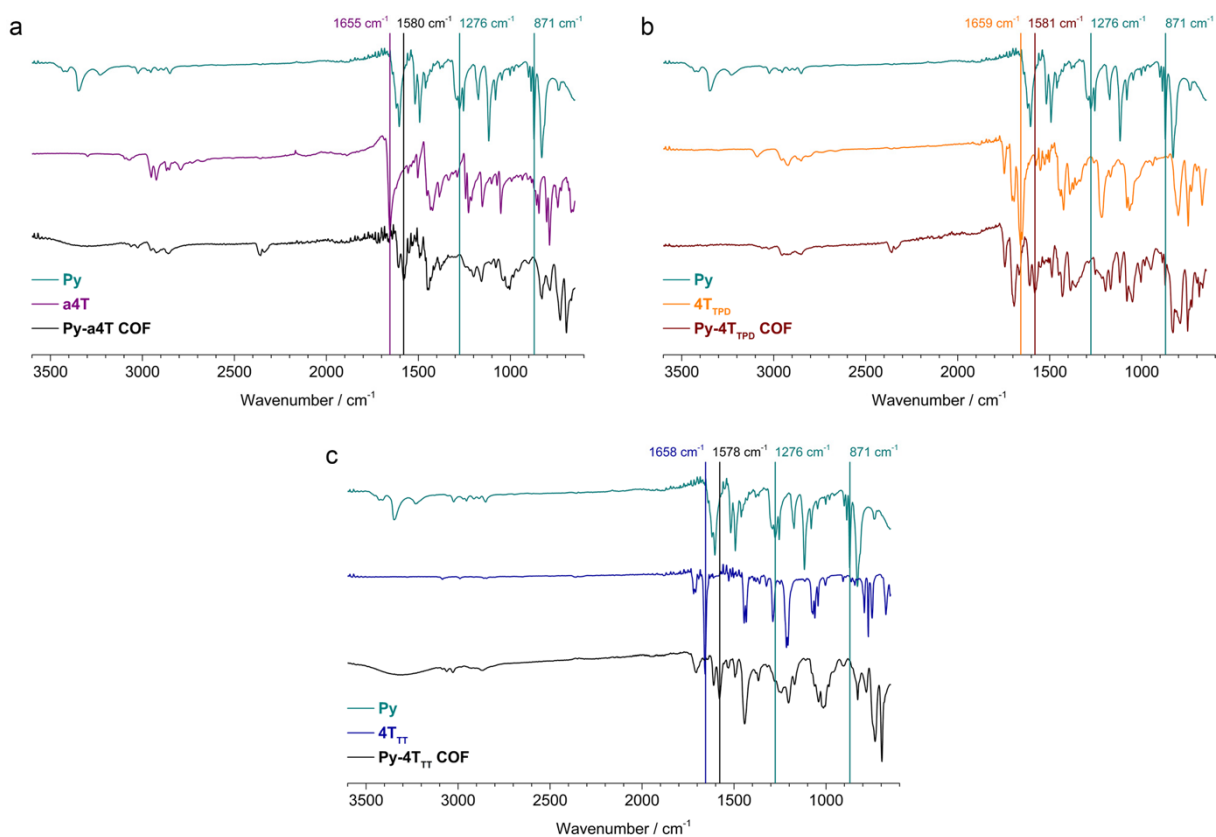


Figure 5.9. IR spectra of the building blocks and the quaterthiophene-based COFs.

Table 5.1 Assignments of the IR signals.

	Wavenumber / cm^{-1}	Vibration mode
Py	1276	C-N stretching mode
	871	N-H wag vibration
a4T	1655	C=O stretching vibration
Py-a4T COF	1580	C=N stretching mode
4T _{TPD}	1659	C=O stretching vibration
Py-4T _{TPD} COF	1581	C=N stretching mode
4T _{TT}	1658	C=O stretching vibration
Py-4T _{TT} COF	1578	C=N stretching mode

Section G – UV-VIS-NIR spectroscopy

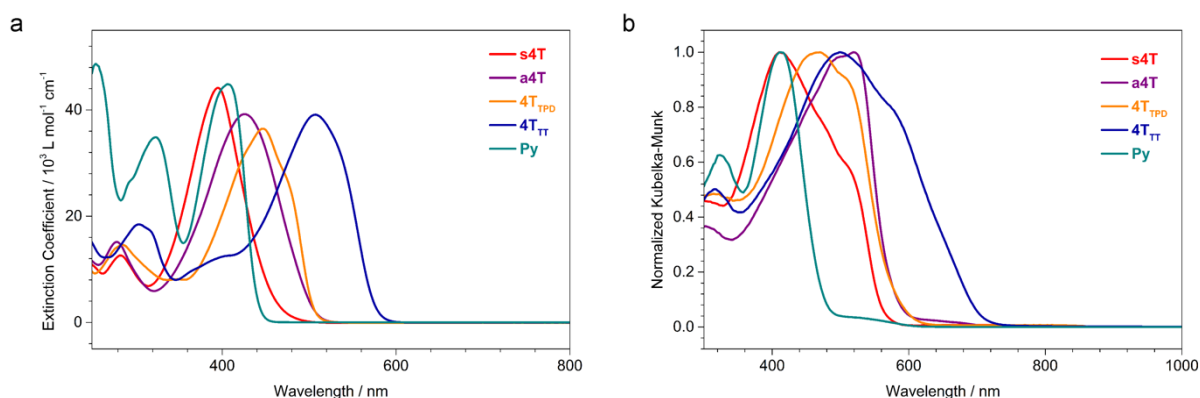


Figure 5.10. Comparison of the absorption spectra of the COF building blocks. (a) Transmission absorption spectra measured for 50 μM solutions in CHCl_3 (s4T, a4T, 4T_{TPD}, 4T_{TT}) or 1,4-dioxane (Py). (b) Corresponding diffuse reflectance spectra measured for the respective powders dispersed in BaSO_4 .

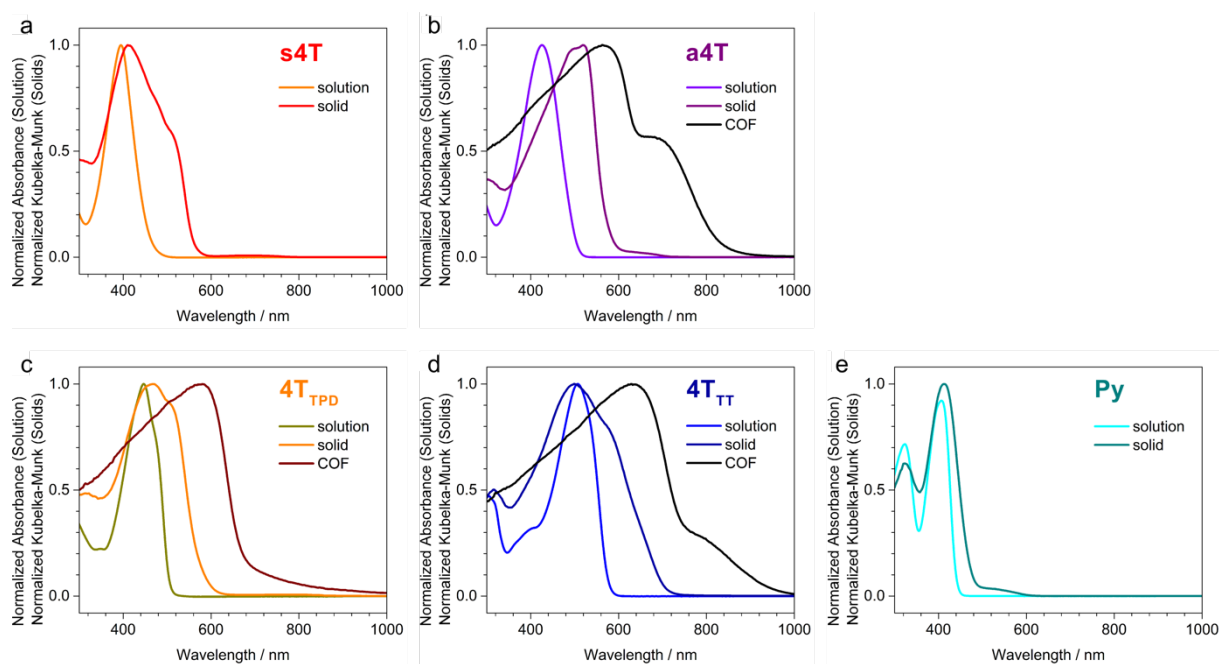


Figure 5.11. Comparison of the absorption and diffuse reflectance spectra of the building blocks in solution, as a solid, and (for a4T, 4T_{TPD}, 4T_{TT}) incorporated into the pyrene-linked COF.

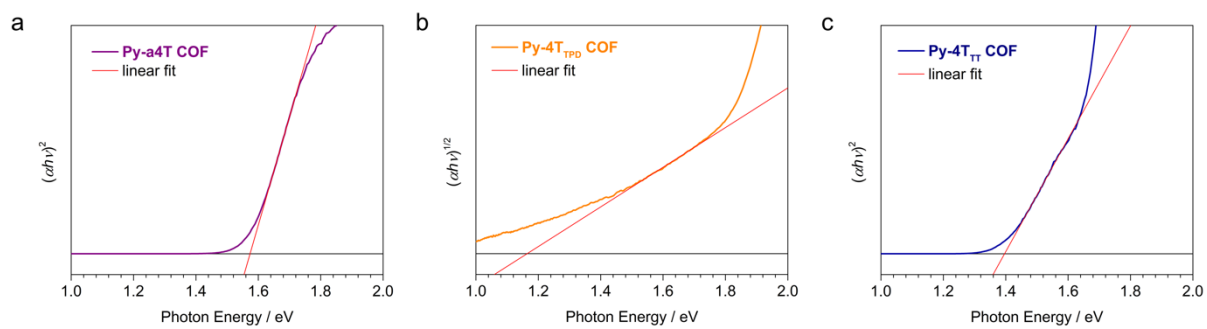


Figure 5.12. Tauc plots of the 4T-based COFs suggesting direct (Py-a4T and Py-4T_{TT} COFs) and indirect optical bandgaps (Py-4T_{TPD} COF).

Section H – PL spectroscopy

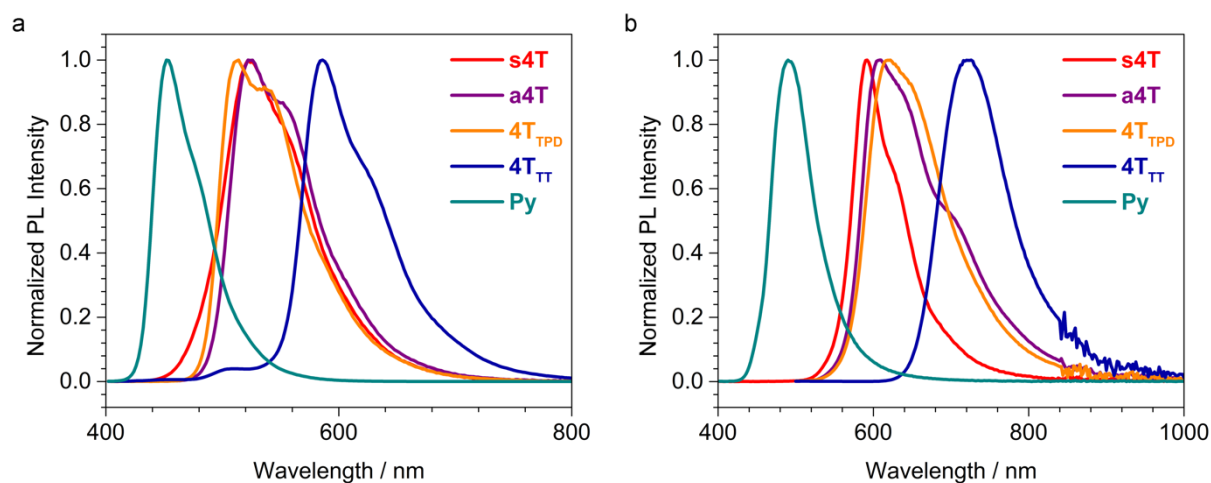


Figure 5.13. PL spectra of the COF building blocks measured (a) as 50 μM solutions in CHCl_3 (s4T, a4T, 4T_{TPD} , 4T_{TT}) or 1,4-dioxane (Py), and (b) as solids. $\lambda_{\text{exc}} = 378 \text{ nm}$.

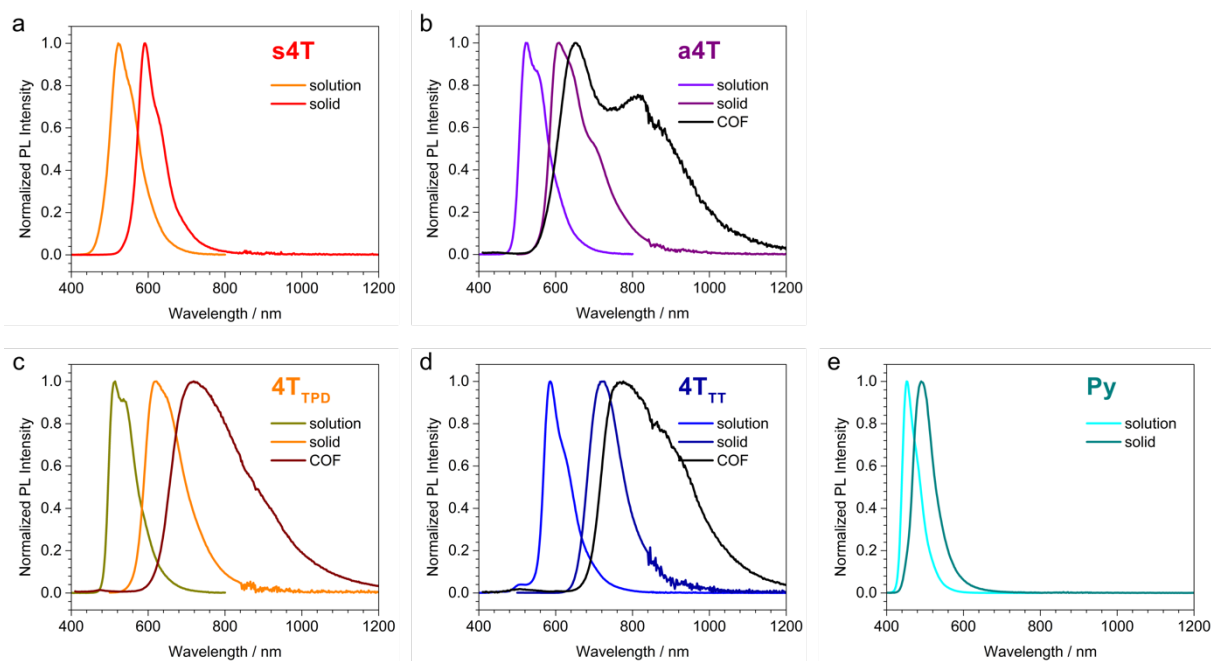


Figure 5.14. Comparison of the PL spectra of the building blocks in solution, as a solid, and (for a4T, 4T_{TPD} , 4T_{TT}) incorporated into the pyrene-linked COF. $\lambda_{\text{exc}} = 378 \text{ nm}$.

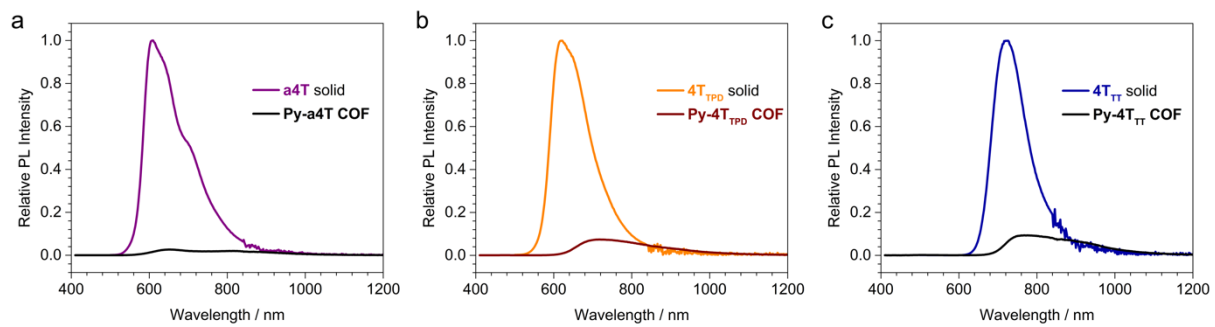


Figure 5.15. Comparison of the relative PL intensities of the 4T building blocks and the corresponding COFs.

Section I – Time-correlated single photon counting

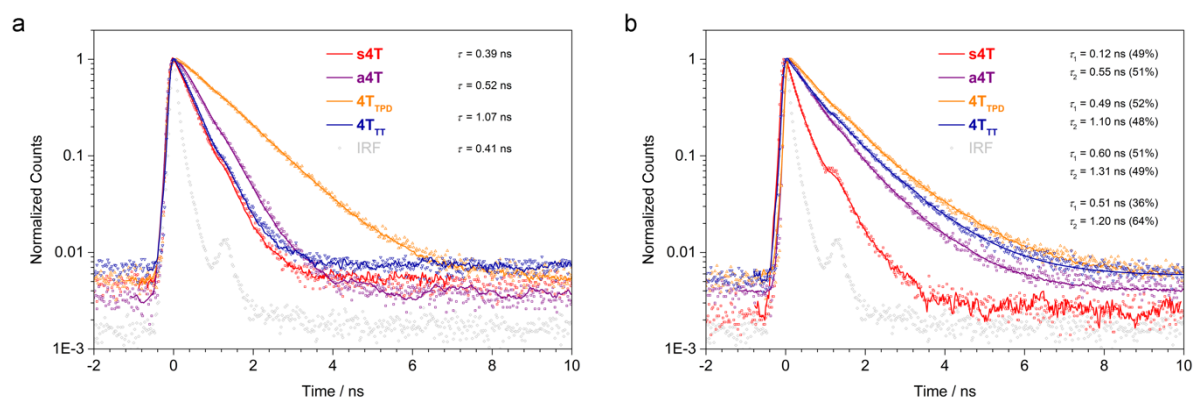


Figure 5.16. TCSPC traces of the building blocks (a) in 50 μM CHCl₃ solution and (b) as solids, recorded at their respective emission maximum. $\lambda_{exc} = 378$ nm. The lifetimes were obtained from exponential deconvolution fits (solid lines).

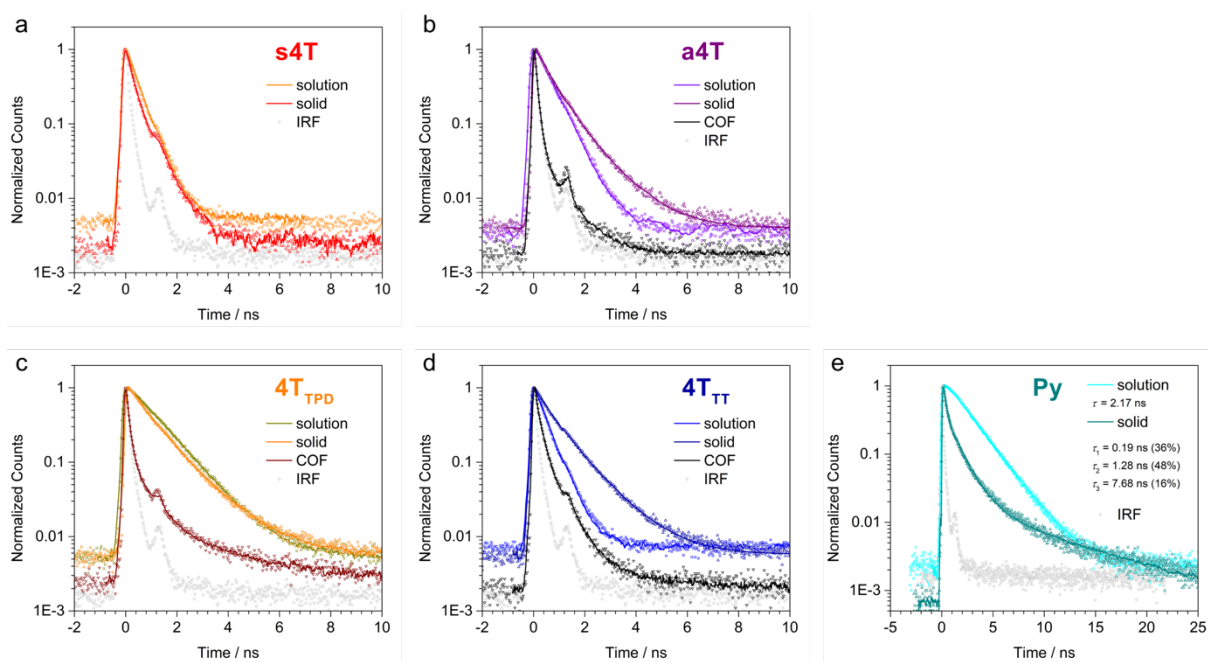


Figure 5.17. Comparison of the TCSPC traces of the building blocks in solution, as a solid, and (for a4T, 4T_{TPD}, 4T_{TT}) incorporated into the pyrene-linked COF.

Section J – Transmission electron microscopy

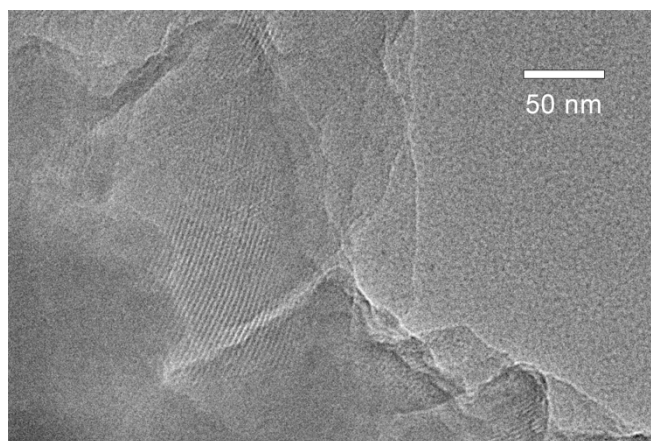


Figure 5.18. High-resolution TEM image of the Py-a4T COF. The parallel-aligned pores are visible for a number of individual COF crystallites (visibility depends on crystal orientation relative to the electron beam).

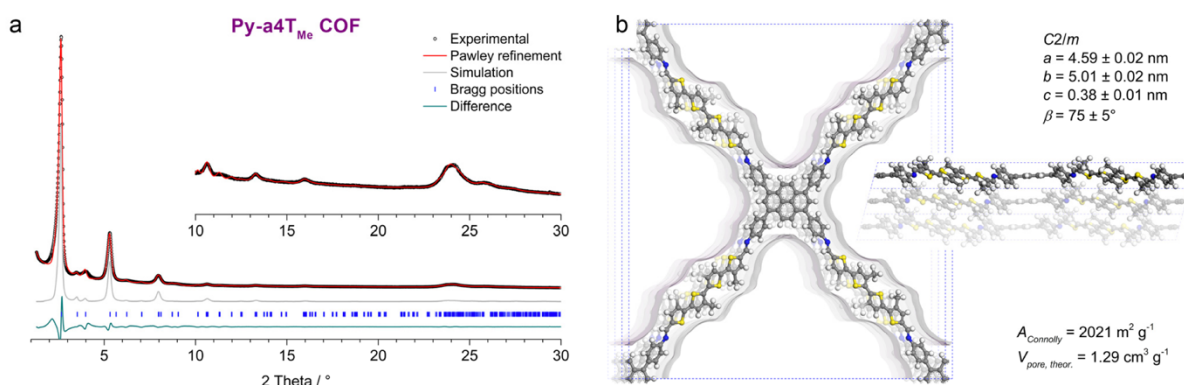
Section K – Py-a4T_{Me} COF XRD

Figure 5.19. (a) Experimental PXRD pattern (black dots) of the short-chain Py-a4T_{Me} COF. Pawley refinement (red line) in the space group *C2/m* provides an excellent fit to the experimental data. Inset, magnified view of the $2\theta > 10^\circ$ region. The simulated PXRD pattern (grey lines) based on the structure model shown in (b) agrees very well with the experimental and refined patterns of the framework. For the pattern simulation, the methyl groups were treated as a superposition of both possible orientations with 50% occupancy. The minimal differences in the peak intensities might stem from slight differences between the simulated and the actual COF structure. (b) The Py-a4T_{Me} COF unit cell with the viewing direction normal to the *a-b* plane (left) and along *b* (right), and the Connolly surface calculated for a nitrogen-sized probe molecule.

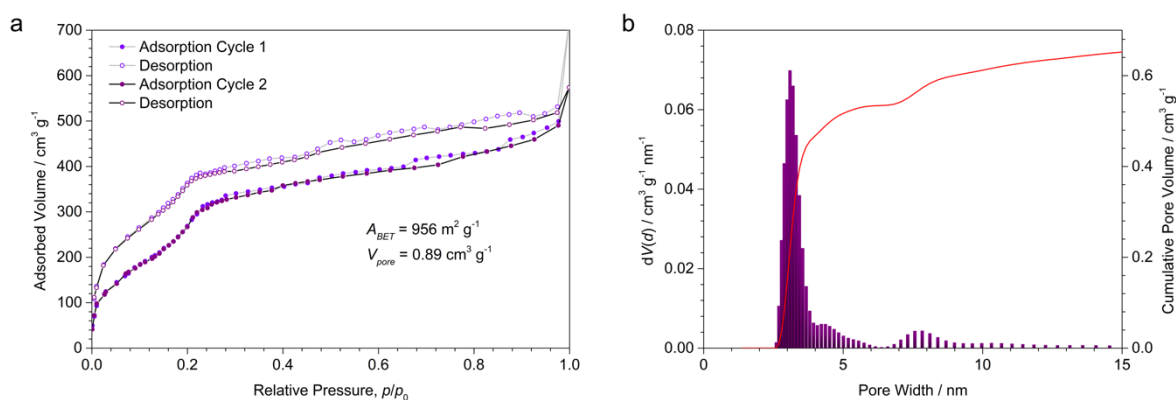
Section L – Nitrogen sorption of the Py-a4T_{Me} COF

Figure 5.20. (a) Nitrogen sorption isotherms recorded at 77 K. Two adsorption-desorption cycles were recorded using the same sample to test the stability of the framework. (b) QSDFT calculation using the adsorption branch yields a narrow pore size distribution with a maximum at 3.1 nm, in excellent agreement with the pore diagonal of 3.06 nm in the Py-a4T_{Me} COF structure.

The Py-a4T_{Me} COF is porous with a BET surface close to 1000 m² g⁻¹, and the maximum of the pore size distribution agrees very well with the pore diagonal when taking into account the methyl groups.

Due to the length and inherent flexibility of the 4T based building blocks, the frameworks described in this study are quite fragile. Thus, the COFs bearing longer alkyl chains have a tendency to deform as a response to the adsorption of probe molecules during the nitrogen

sorption experiments, leading to inconsistent isotherms. The shorter chains of the Py-a4T_{Me} COF, however, seem to reduce the forces onto the COF walls during the sorption cycle and therefore this COF yields consistent and reproducible sorption results (Figure 5.20).

5.6 References

- [1] A. P. Côté, A. I. Benin, N. W. Ockwig, M. O'Keeffe, A. J. Matzger, O. M. Yaghi, *Science* **2005**, *310*, 1166-1170.
- [2] H. Furukawa, O. M. Yaghi, *J. Am. Chem. Soc.* **2009**, *131*, 8875-8883.
- [3] C. J. Doonan, D. J. Tranchemontagne, T. G. Glover, J. R. Hunt, O. M. Yaghi, *Nat. Chem.* **2010**, *2*, 235-238.
- [4] L. Stegbauer, K. Schwinghammer, B. V. Lotsch, *Chem. Sci.* **2014**, *5*, 2789-2793.
- [5] S. Lin, C. S. Diercks, Y.-B. Zhang, N. Kornienko, E. M. Nichols, Y. Zhao, A. R. Paris, D. Kim, P. Yang, O. M. Yaghi, C. J. Chang, *Science* **2015**, *349*, 1208-1213.
- [6] S. Chandra, T. Kundu, S. Kandambeth, R. BabaRao, Y. Marathe, S. M. Kunjir, R. Banerjee, *J. Am. Chem. Soc.* **2014**, *136*, 6570-6573.
- [7] D. B. Shinde, H. B. Aiyappa, M. Bhadra, B. P. Biswal, P. Wadge, S. Kandambeth, B. Garai, T. Kundu, S. Kurungot, R. Banerjee, *J. Mater. Chem. A* **2016**, *4*, 2682-2690.
- [8] M. Dogru, M. Handloser, F. Auras, T. Kunz, D. Medina, A. Hartschuh, P. Knochel, T. Bein, *Angew. Chem. Int. Ed.* **2013**, *52*, 2920-2924.
- [9] J. Guo, Y. Xu, S. Jin, L. Chen, T. Kaji, Y. Honsho, M. A. Addicoat, J. Kim, A. Saeki, H. Ihee, S. Seki, S. Irie, M. Hiramoto, J. Gao, D. Jiang, *Nat. Commun.* **2013**, *4*, 2736.
- [10] M. Calik, T. Sick, M. Dogru, M. Döblinger, S. Datz, H. Budde, A. Hartschuh, F. Auras, T. Bein, *J. Am. Chem. Soc.* **2016**, *138*, 1234-1239.
- [11] L. Ascherl, T. Sick, J. T. Margraf, S. H. Lapidus, M. Calik, C. Hettstedt, K. Karaghiosoff, M. Döblinger, T. Clark, K. W. Chapman, F. Auras, T. Bein, *Nat. Chem.* **2016**, *8*, 310-316.
- [12] D. N. Bunck, W. R. Dichtel, *Angew. Chem. Int. Ed.* **2012**, *51*, 1885-1889.
- [13] D. B. Shinde, S. Kandambeth, P. Pachfule, R. R. Kumar, R. Banerjee, *Chem. Commun.* **2015**, *51*, 310-313.
- [14] L. Chen, K. Furukawa, J. Gao, A. Nagai, T. Nakamura, Y. Dong, D. Jiang, *J. Am. Chem. Soc.* **2014**, *136*, 9806-9809.
- [15] F. Auras, L. Ascherl, A. H. Hakimioun, J. T. Margraf, F. C. Hanusch, S. Reuter, D. Bessinger, M. Döblinger, C. Hettstedt, K. Karaghiosoff, S. Herbert, P. Knochel, T. Clark, T. Bein, *J. Am. Chem. Soc.* **2016**, *138*, 16703-16710.
- [16] G. Lin, H. Ding, D. Yuan, B. Wang, C. Wang, *J. Am. Chem. Soc.* **2016**, *138*, 3302-3305.
- [17] S. Wan, F. Gándara, A. Asano, H. Furukawa, A. Saeki, S. K. Dey, L. Liao, M. W. Ambrogio, Y. Y. Botros, X. Duan, S. Seki, J. F. Stoddart, O. M. Yaghi, *Chem. Mater.* **2011**, *23*, 4094-4097.

- [18] S. Jin, X. Ding, X. Feng, M. Supur, K. Furukawa, S. Takahashi, M. Addicoat, M. E. El-Khouly, T. Nakamura, S. Irle, S. Fukuzumi, A. Nagai, D. Jiang, *Angew. Chem. Int. Ed.* **2013**, *52*, 2017-2021.
- [19] M. Calik, F. Auras, L. M. Salonen, K. Bader, I. Grill, M. Handloser, D. D. Medina, M. Dogru, F. Löbermann, D. Trauner, A. Hartschuh, T. Bein, *J. Am. Chem. Soc.* **2014**, *136*, 17802-17807.
- [20] S.-L. Cai, Y.-B. Zhang, A. B. Pun, B. He, J. Yang, F. M. Toma, I. D. Sharp, O. M. Yaghi, J. Fan, S.-R. Zheng, W.-G. Zhang, Y. Liu, *Chem. Sci.* **2014**, *5*, 4693-4700.
- [21] J. Y. Kim, S. H. Kim, H.-H. Lee, K. Lee, W. Ma, X. Gong, A. J. Heeger, *Adv. Mater.* **2006**, *18*, 572-576.
- [22] M. D. Irwin, D. B. Buchholz, A. W. Hains, R. P. H. Chang, T. J. Marks, *Proceedings of the National Academy of Sciences* **2008**, *105*, 2783-2787.
- [23] K. Cnops, B. P. Rand, D. Cheyons, B. Verreert, M. A. Empl, P. Heremans, *Nat. Commun.* **2014**, *5*, 3406.
- [24] B. Kan, M. Li, Q. Zhang, F. Liu, X. Wan, Y. Wang, W. Ni, G. Long, X. Yang, H. Feng, Y. Zuo, M. Zhang, F. Huang, Y. Cao, T. P. Russell, Y. Chen, *J. Am. Chem. Soc.* **2015**, *137*, 3886-3893.
- [25] Z. Li, G. He, X. Wan, Y. Liu, J. Zhou, G. Long, Y. Zuo, M. Zhang, Y. Chen, *Adv. Energy Mater.* **2012**, *2*, 74-77.
- [26] Q. Zhang, B. Kan, F. Liu, G. Long, X. Wan, X. Chen, Y. Zuo, W. Ni, H. Zhang, M. Li, Z. Hu, F. Huang, Y. Cao, Z. Liang, M. Zhang, T. P. Russell, Y. Chen, *Nature Photonics* **2014**, *9*, 35.
- [27] G. H. V. Bertrand, V. K. Michaelis, T.-C. Ong, R. G. Griffin, M. Dincă, *Proc. Natl. Acad. Sci. U.S.A.* **2013**, *110*, 4923-4928.
- [28] D. D. Medina, V. Werner, F. Auras, R. Tautz, M. Dogru, J. Schuster, S. Linke, M. Döblinger, J. Feldmann, P. Knochel, T. Bein, *ACS Nano* **2014**, *8*, 4042-4052.
- [29] D. D. Medina, J. M. Rotter, Y. Hu, M. Dogru, V. Werner, F. Auras, J. T. Markiewicz, P. Knochel, T. Bein, *J. Am. Chem. Soc.* **2015**, *137*, 1016-1019.
- [30] J. I. Feldblyum, C. H. McCreery, S. C. Andrews, T. Kurosawa, E. J. G. Santos, V. Duong, L. Fang, A. L. Ayzner, Z. Bao, *Chem. Commun.* **2015**, *51*, 13894-13897.
- [31] M. S. Lohse, J. M. Rotter, J. T. Margraf, V. Werner, M. Becker, S. Herbert, P. Knochel, T. Clark, T. Bein, D. D. Medina, *CrystEngComm* **2016**, *18*, 4295-4302.
- [32] M. G. Rabbani, A. K. Sekizkardes, Z. Kahveci, T. E. Reich, R. Ding, H. M. El-Kaderi, *Chem. Eur. J.* **2013**, *19*, 3324-3328.
- [33] X. Chen, N. Huang, J. Gao, H. Xu, F. Xu, D. Jiang, *Chem. Commun.* **2014**, *50*, 6161-6163.
- [34] P. T. Henderson, D. M. Collard, *Chem. Mater.* **1995**, *7*, 1879-1889.

- [35] J. Yang, S. Liu, J.-F. Zheng, J. Zhou, *Eur. J. Org. Chem.* **2012**, 2012, 6248-6259.
- [36] J. Grolleau, P. Frère, F. Gohier, *Synthesis* **2015**, 24, 3901-3906.
- [37] Y.-T. Song, P.-H. Lin, C.-Y. Liu, *Adv. Synth. Catal.* **2014**, 356, 3761-3768.
- [38] A. Najari, S. Beaupré, P. Berrouard, Y. Zou, J.-R. Pouliot, C. Lepage-Pérusse, M. Leclerc, *Adv. Funct. Mater.* **2011**, 21, 718-728.
- [39] C. B. Nielsen, T. Bjørnholm, *Org. Lett.* **2004**, 6, 3381-3384.
- [40] M.-J. Baek, S.-H. Lee, K. Zong, Y.-S. Lee, *Synth. Met.* **2010**, 160, 1197-1203.
- [41] B. Carsten, J. M. Szarko, H. J. Son, W. Wang, L. Lu, F. He, B. S. Rolczynski, S. J. Lou, L. X. Chen, L. Yu, *J. Am. Chem. Soc.* **2011**, 133, 20468-20475.
- [42] S. Jin, T. Sakurai, T. Kowalczyk, S. Dalapati, F. Xu, H. Wei, X. Chen, J. Gao, S. Seki, S. Irle, D. Jiang, *Chem. Eur. J.* **2014**, 20, 14608-14613.

6 Extension of Oligothiophene Backbones in Covalent Organic Frameworks

This chapter is based on the following manuscript:

Niklas Keller,[‡] Derya Bessinger,[‡] Andreas C. Jakowetz, and Thomas Bein*

to be submitted.

based on the manuscript initially published in:

N. Keller, *PhD Thesis*, Ludwig-Maximilians-Universität München, **2020**

N. Keller and D. Bessinger designed and prepared the project and synthesized the compounds that were subject of research, followed by the subsequent structural and optical characterization and data evaluation. The TCSPC measurements were conducted and evaluated by N. Keller and A. Jakowetz.

[‡] These authors contributed equally.

6.1 Abstract

The intriguing properties of oligothiophenes are already being successfully utilized for applications in organic optoelectronics and recently also in the field of covalent organic frameworks (COFs). In this work, we followed up on the recent advances of quaterthiophene-based building blocks and developed different variations of oligothiophenes that were then embedded in the solid matrix defined by two-dimensional COFs. Modifications, like the functionalization with alkyl chains, are often a prerequisite for processability, e.g. to increase the solubility of the molecular building blocks, or are specifically introduced to tune the characteristics of the resulting frameworks. It would be highly desirable to study the impact of slight changes to the backbone without varying too many other parameters. Therefore, we developed a series of oligothiophene building blocks with two adjustable options that allow for modulations of their COFs with the aim to ultimately derive design rules. Both, the length of the alkyl chains attached to the thiophene bridges and the number of thiophene units coupled to form the oligothiophene building block were varied and their impact on the COFs' properties was subsequently examined. Variation of the backbone length allowed us to tune the fundamental COF metrics, which define structural parameters such as the pore size, and optical studies revealed an additional correlation between the photoluminescence (PL) lifetimes and the oligothiophene modifications with two opposing trends: backbone extension increases the PL lifetimes with the excited states becoming more stabilized and alkyl chain elongation decreases the lifetimes potentially due to competing non-radiative decay pathways. The findings of our work serve as a guiding principle to tackle future studies more efficiently and highlight the importance of elaborate building block design for the construction of COFs.

6.2 Introduction

One benefit of reticular chemistry is the possibility to adjust the building blocks and translate these changes directly into the macroscopic structure. This potential becomes evident for COFs, a relatively new class of porous material. In the case of 2D COFs, building blocks of different geometries are linked by slightly reversible condensation reactions to form 2D sheets that stack in the 3rd dimension in the case of 2D COFs, yielding highly ordered, porous and light-weight materials.^[1, 2] The stacked sheets build ordered columns of packed nodes and bridges enabling electronic overlap between adjacent COF layers that promote charge carrier mobility along the stacks.^[3, 4] The possibility of synthesizing tailor-made organic building blocks paves the way

to a vast diversity of COFs that are deliberately designed to meet the optimal requirements for specific future applications, for example in gas storage or separation,^[5-7] as well as for the uptake of guest molecules,^[8-11] control of π -density,^[12] and enabling access for postsynthetic modifications^[13, 14] or catalysis.^[15, 16] Nevertheless, tailoring the properties of COFs can sometimes be challenging and becomes even more demanding when extending their characteristics beyond just structural changes. Therefore, it is highly desirable to obtain basic knowledge about critical COF construction rules. Using a well-defined and stable framework as a starting point and incorporating gradual changes into it provides valuable insights in order to formulate general design rules for linker–structure–property relationships. By adjusting one structural feature at a time, the resulting effect can be directly attributed to this specific modification. As an example, the extension of building units to extend the pore size is a straightforward technique for a simple but well-developed design principle.^[17, 18] However, transferring one adjustment to other characteristics or even a different COF system, i.e. proposing a comprehensive linker–structure–property relationship, still remains challenging in the field of COFs.

Aiming to adopt the advantages of electroactive oligo- or polythiophenes, which were already applied as well-studied components of prominent semiconductors in organic optoelectronics,^[19-21] to the field of COFs, first frameworks bearing thiophenes, bithiophenes,^[22] thieno[3,2-*b*]thiophenes (TT),^[8] and benzo[1,2-*b*:4,5-*b'*]dithiophenes (BDT)^[23] have been realized.

Another approach in this context utilized the conducting properties of polythiophenes by creating a host–guest system with poly(3,4-ethylenedioxythiophene) (PEDOT) infiltrated into COF pores and thus forming electron-conducting pathways and enhancing the electrical conductivity.^[24, 25]

An asymmetric functionalization strategy enabled the extension of the oligothiophene backbone successfully implemented into a COF to four fused thiophenes.^[26] The resulting quaterthiophene (4T)-based COFs showed the photoinduced formation of a charge transfer state between the imine-linked subunits and associated effects on the electronic and optical characteristics.

Here, we investigate how these properties of oligothiophene-based COFs can be further tuned by systematically modifying the structure of their bridging building blocks. A series of bithiophene, quaterthiophene, and sexithiophene building blocks was developed to cover a broad and representative range of oligothiophenes while still maintaining synthetic feasibility and chemical functionality necessary for the successful condensation reactions to form the corresponding COFs. Both the impact of the number of fused thiophene rings within the

respective building blocks and the influence of attached alkyl chains of varying length on structural and optical properties were examined. Different from previous work of our group,^[26] the oligothiophene backbone was not extended by sterically demanding electron-deficient moieties to form a donor-acceptor building block for the sake of simplicity. For the quaterthiophene series, the attached alkyl chains were kept at the same 3-positions of the first and third thiophene since this asymmetric configuration empirically promoted the crystallinity of the 4T-based COFs. The resulting COF structures provide the same $C2/m$ space group for all molecular variations. Therefore, measurable deviations of the structure can be directly compared and correlated to the other frameworks of the series.

6.3 Results and Discussion

While pyrene-based building blocks have been extensively studied as tetragonal node in 2D COFs, oligothiophenes (nT) have only been applied in few reports as linear building blocks with a length of up to $n = 4$, denoted as 4T.^[22, 26] Herein, we extend this concept to sexithiophenes ($n = 6$) to complete the series of 2T and 4T backbones, all containing terminal dialdehyde groups. Upon co-condensation with the 1,3,6,8-tetrakis(4-aminophenyl)pyrene (Py) counterpart, the resulting COFs form pseudoquadratic pores. Figure 6.1 schematically illustrates an overview of the developed molecular building blocks of this project and the chemical structures of the resulting oligothiophene-bridged COFs.

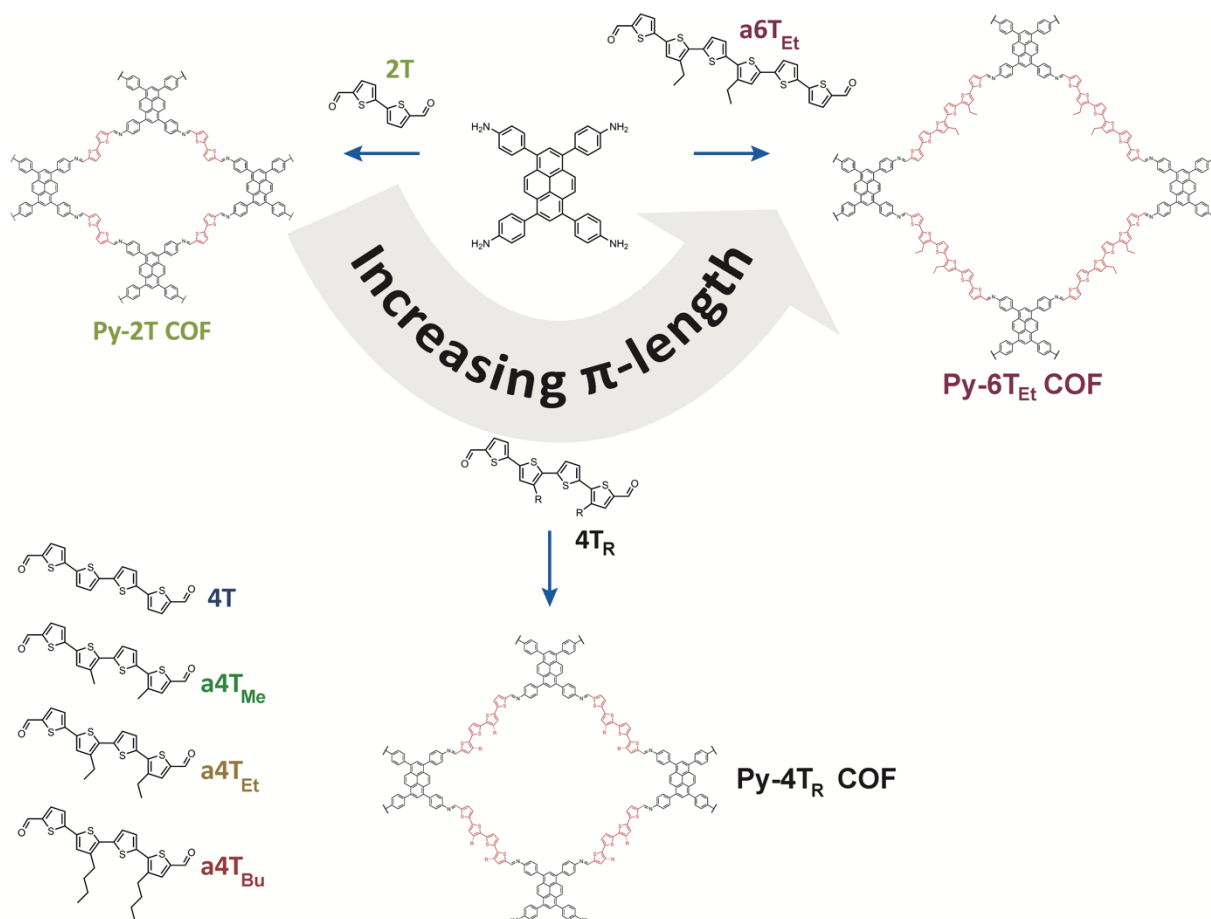


Figure 6.1. Overview of the oligothiophene-based COF series. Thiophene-oligomers of three different lengths functionalized with aldehyde groups were introduced into periodic frameworks via co-condensation with 1,3,6,8-tetrakis(4-aminophenyl)pyrene (Py), leading to Py-2T, Py-4T_R, and Py-6T_{Et} COFs. For the quaterthiophene series, the side groups connected to the first and third thiophene ring were varied from hydrogen (4T) to methyl (4T_{Me}), ethyl (4T_{Et}), and butyl chains (4T_{Bu}). All variations of oligothiophenes formed COFs with pseudoquadratic pores.

The oligothiophenes were synthesized by following the asymmetric functionalization approach developed in our group^[26] to allow for closely stacked bridging units during framework formation and promoting the π -conjugation between the 2D COF layers. Incorporated into the crystalline framework, the steric repulsion of the alkyl chains is minimized by an alternating stacking behavior analogous to the literature-known a4T_{Bu} COF (Figure 6.2). The 4T building blocks bear alkyl chains of methyl (4T_{Me}), ethyl (4T_{Et}), and butyl (4T_{Bu}) on the first and third thiophene, whereas the 6T_{Et} component was functionalized with ethyl chains on the second and fourth thiophene unit. Since the solubility continuously decreases with growing number of linked thiophene units of the oligothiophenes, the extended 6T building block was not synthesized as a bare backbone. The impact of extending the π -conjugation by larger thiophene backbones was investigated by comparing the 2T-, 4T- and 6T_{Et}-containing pyrene COFs while the different quaterthiophene variations provide information on the effect of different alkyl groups (Figure 6.1).

The imine-linked COFs were synthesized via an acid-catalyzed solvothermal co-condensation of the respective oligothiophenes-dialdehydes with half the equivalent of the tetradentate amine-functionalized pyrene building block (see the Supporting Information (SI) for details on the synthesis procedures).

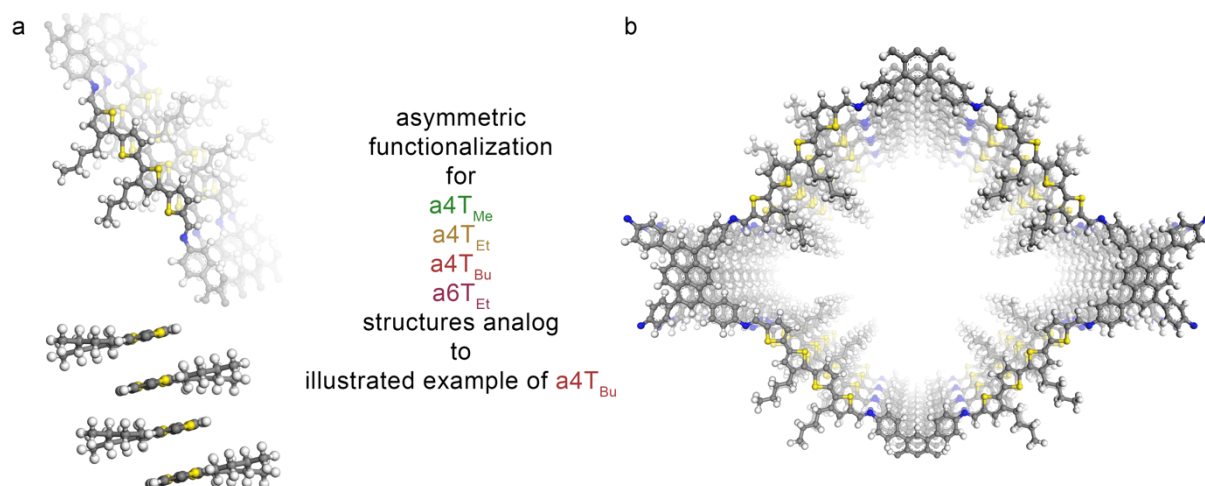


Figure 6.2. Exemplary illustration of the asymmetric configuration of the alkyl chains attached to the oligothiophenes for the Py-4T_{Bu} COF.^[26] (a) The cut out structure model shows the alternating alkyl chains between adjacent 2D COF layers leaving sufficient spacing and thus facilitating the unimpeded stacking. The COFs with the oligothiophenes of different asymmetric modifications feature structures similar to the depicted structural simulation in (b). In the structural refinement analysis, the alkyl chains of the listed oligothiophene building blocks were treated as a superposition of both possible orientations with 50% occupancy each.

Powder X-ray diffraction patterns confirm the successful formation of crystalline COFs constructed with the oligothiophene building block series (Figure 6.3). The sharp reflections that reach into the higher-order region demonstrate the formation of highly crystalline structures. Pawley refinements of the simulated COF structures revealed excellent fits with the experimental data. On the basis of our previous studies on pyrene-containing COFs^[27, 28] and particularly the Py-a4T_{Bu} COF simulations,^[26] we continued to simulate the COF structures in the space group $C2/m$ and approximated the asymmetrically attached alkyl chains as a superposition of both possible orientations with 50% occupancy each.

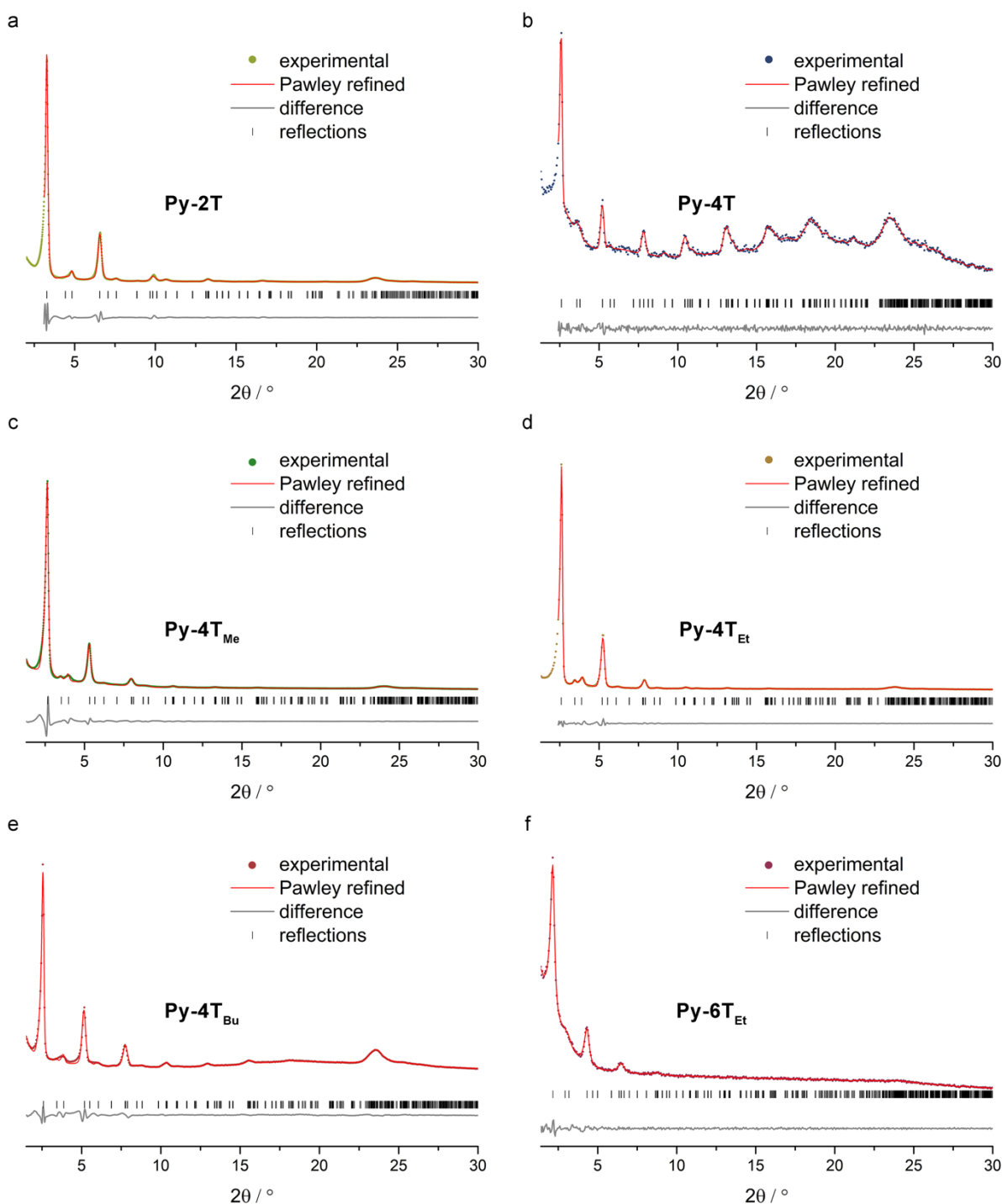


Figure 6.3. Experimental powder XRD data (dots) and Pawley-refined XRD patterns (red line) of the oligothiophene-bridged COF series of (a) Py-2T, (b) Py-4T, (c) Py-4T_{Me}, (d) Py-4T_{Et}, (e) Py-4T_{Bu}, and (f) Py-6T_{Et}. The Pawley refinements carried out in the $C2/m$ space group provide a very good fit to the experimental data and show only minimal differences visualized by the difference plot (grey line). The corresponding refined structure model simulations are shown in Section E of the SI. Bragg positions are indicated with black ticks.

When comparing the refined COF unit cells containing different numbers of fused thiophene units, i.e. the 2T, 4T, and 6T building blocks, it is evident that their cell parameters increase in directions a and b by about 1 nm for each system (see the SI, Section E for details). These findings are consistent with the anticipated extension of the COF structure and therefore its

pore size by elongating each linear building block by two thiophenes that correspond to an additional length of about 7.7 Å.^[29] In contrast, the impact of the alkyl chain length on the structural features is not as distinct and no clear trend can be derived due to the sufficient spacing between the chains which is a result of the effective asymmetric modification strategy. These results demonstrate that direct pore size modulation is possible by fusing more thiophene units to the linear backbone while maintaining the same overall geometry. Since the alkyl chain functionalization has no significant effect on the structure and stability of the 4T_R-containing frameworks, a direct comparison of their optical features is possible.

The ordered structure of the synthesized porous COFs was confirmed with transmission electron microscopy (TEM). Well-ordered and porous crystalline domains were observed by clearly visible lattice fringes (see the SI, Section I).

In order to study the effect of structural modifications in the framework on the optical properties, UV-Vis diffuse reflectance spectra of the COFs were recorded. The extension of the linear bridge of the Py-2T COF by another bithiophene moiety leads to the Py-4T COF and induces a slight red-shift of the absorption band, accompanied by a distinct additional feature below the energy of the main π - π^* transition at around 750 nm (Figure 6.4a). This absorption feature was attributed to the photoinduced generation of a charge transfer state between the electron-rich pyrene and the more electron-deficient oligothiophene building units in our previous report.^[26]

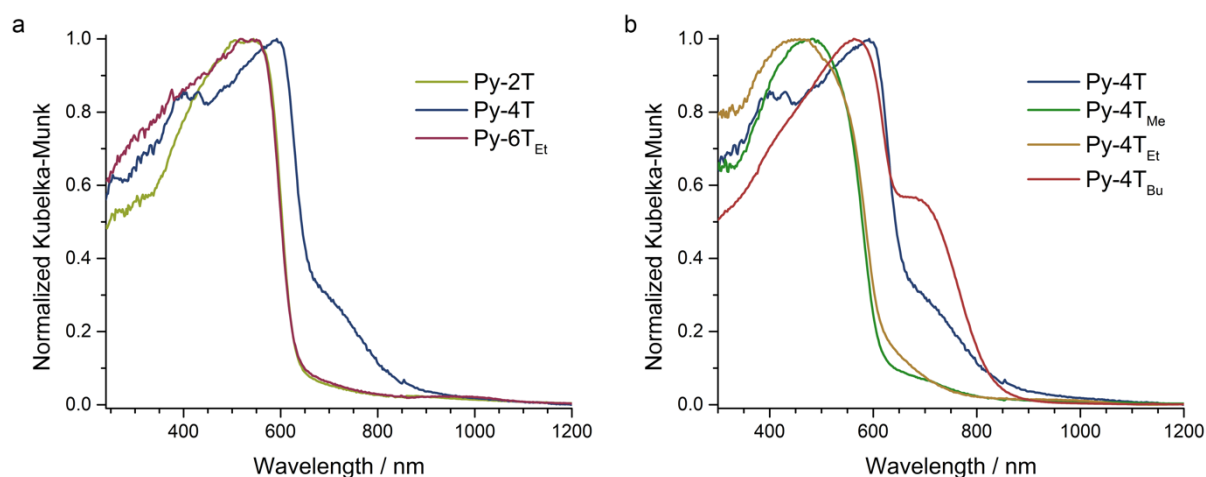


Figure 6.4. (a) Diffuse reflectance spectra of the Py-2T, Py-4T and Py-6T_{Et} COFs and (b) of the Py-4T_R COF series, all measured as solid powders dispersed in BaSO₄.

Surprisingly, the addition of yet another bithiophene moiety did not lead to the expected bathochromic shift of the Py-6T_{Et} COF despite the extended π -conjugation in theory, but in contrast led to a blue shift compared to the Py-4T COF. At 544 nm, the absorption maximum of the Py-6T_{Et} COF is in the same region as the Py-2T COF absorption maximum. Since the absorption characteristics of the molecular 6T_{Et} building block, which comprises the longest π -conjugated backbone, are indeed furthest red-shifted (see the SI, Section F), the contradictory blue-shift of the respective COF may be attributed to its reduced conjugation due to structural factors. The experimental PXRD data of the Py-6T_{Et} COF (Figure 6.3f) exhibits the lowest reflection to background ratio and the smallest number of sharp signals of the oligothiophene series, indicating that the long-range growth of a highly ordered and stable framework was impeded by the inherent flexibility of the extended linear subunit. The loss of conjugation in Py-6T_{Et} eventually influences the optical features, shifting its absorption towards shorter wavelengths with respect to the Py-4T_R COFs with long-range crystallographic order.

The Py-4T_R COF series containing different alkyl chains attached to the 4T backbone reveals their influence on the absorption properties of the bulk materials. The attached methyl and ethyl chains blue-shift the absorption maxima by more than 100 nm from 592 nm (Py-4T) to 484 nm and 458 nm for Py-4T_{Me} and Py-4T_{Et}, respectively. In contrast, extending the alkyl chain length further to butyl groups red-shifts the absorption maximum of Py-4T_{Bu} back to 564 nm, which is in close vicinity to the peak of the Py-4T COF with the bare backbone. For a deeper understanding and a better evaluation of the optical data, absorption spectra of thin oriented COF films grown on fused silica substrates could provide more precise insights. Instead of measuring the diffuse reflectance of nonuniformly dispersed bulk material and applying the Kubelka-Munk theory for interpretation, the absorption characteristics of controllable thin COF films are here directly measured via transmission, allowing accurate conclusions on their intrinsic optical properties.

However, crystalline and oriented film growth was challenging and only realizable for two COFs of the series, as seen in the GIWAXS data shown in Figure 6.5.

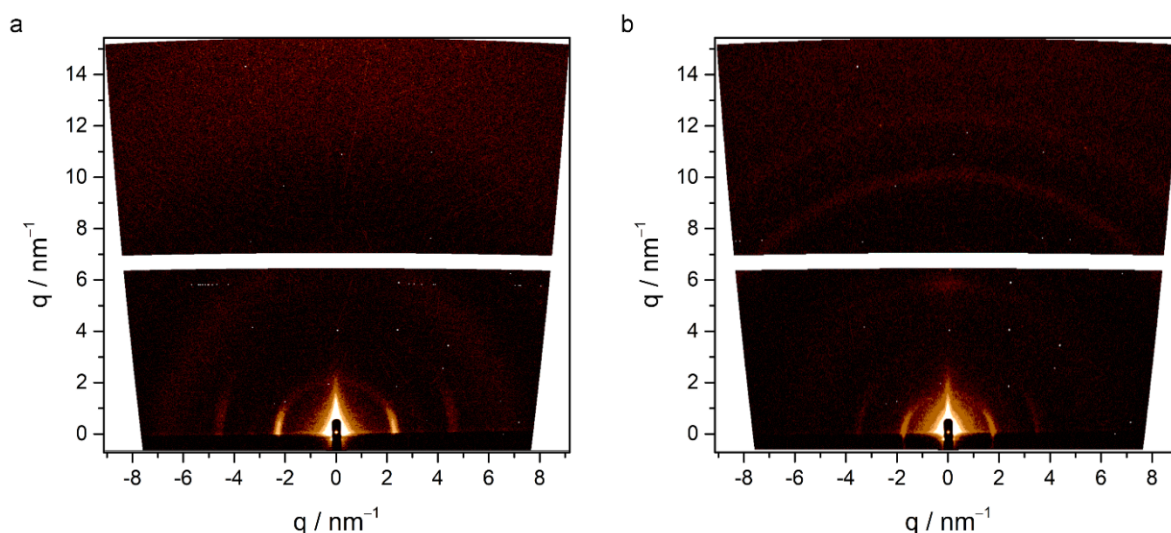


Figure 6.5. GIWAXS analysis of (a) Py-2T and (b) Py-4T_{Et} thin films grown in an oriented and crystalline manner on ITO-coated glass substrates.

Extensive screening of synthesis conditions and substrate types led to successful film growth of Py-2T and Py-4T_{Et} COF thin films on ITO-coated glass substrates. The other COFs of the oligothiophene series resulted in amorphous films on the different substrates examined (glass, ITO-coated glass, fused SiO₂). Nevertheless, first absorption measurements were performed on crystalline Py-4T_{Et} COF thin films and compared to amorphous but well-covered Py-4T, Py-4T_{Me} and Py-4T_{Bu} thin films. For these thin films, the absorption maxima were found to be around 450 nm (SI, Figure 6.19) and the peak profiles are quite similar. Since especially the optical spectra of the Py-4T and Py-4T_{Bu} films significantly differ from their optical powder measurements and lack absorption features in the low-energy part of the spectrum, crystalline COF films ultimately have to be realized in order to derive conclusive results.

Another advantage of oriented COF films is the potential of gathering more information about the optoelectronic properties by sensitive spectroscopic methods such as time-resolved microwave conductivity for charge carrier transport and transient absorption spectroscopy for exciton dynamics. Additionally, the processability as thin films opens a new pathway for applications and allows for the possibility to develop COF-based devices.

The photoluminescence (PL) measurements of the oligothiophene-based COF series showed similar trends as found for the absorption spectra (Figure 6.6). For the bithiophene-containing Py-2T COF, the emission peak was observed at 634 nm. The extension of the linear bridge to quaterthiophene causes a red-shift of the PL maximum to about 690 nm with a slight shoulder at lower energies at about 800 nm.

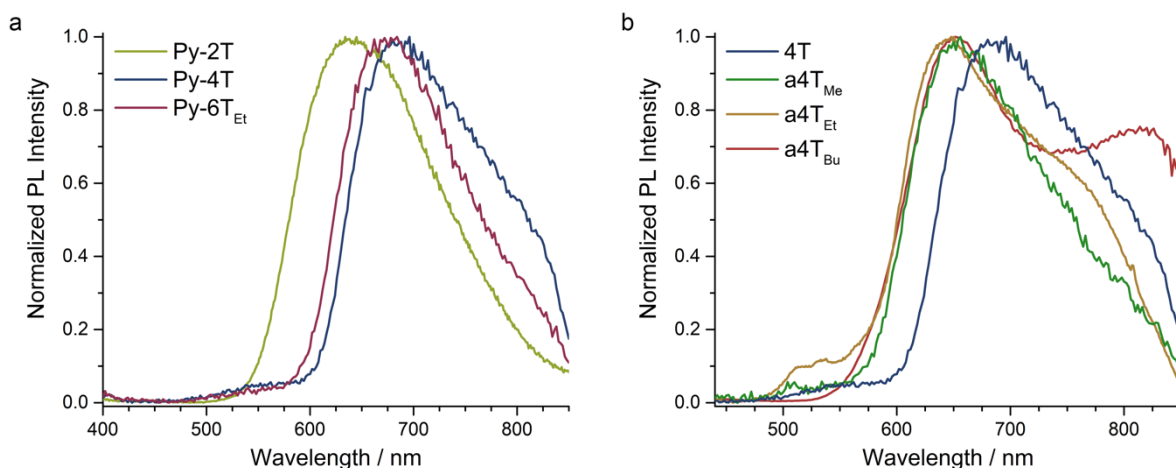


Figure 6.6. (a) Photoluminescence spectra of Py-2T, Py-4T, and Py-6T_{Et} and (b) of the Py-4T_R COFs measured as solids under inert atmosphere ($\lambda_{exc} = 378$ nm).

Similar to the absorption spectra, the additional feature could be again assigned to the photoinduced charge transfer state. When the linear building unit was extended further to 6T_{Et}, the corresponding COF showed a narrower emission peak at about 680 nm (Figure 6.6a). This follows the same trend of the absorption spectra with the larger Py-6T_{Et} COF, which should hypothetically possess an extended π -conjugation, blue-shifted to the Py-4T COF. Again, this can be attributed to the reduced conjugation due to the higher flexibility of the extended COF. The PL spectra of the linear monomers however show the largest oligothiophene 6T_{Et} furthest red-shifted, as anticipated (SI, Figures 6.16b and 6.18b).

Regarding the impact of the alkyl chain functionalization, it would be interesting whether the PL trends found for the monomers also translate to the corresponding COFs. For closer comparison, the optical characteristics of the oligothiophene building blocks were measured in 50 μ M CHCl₃ solution and as solids (see the SI, Section F). An increasing chain length led to a slightly greater Stokes shift for the diluted monomers by blue-shifting their absorption maxima and red-shifting their emission maxima (SI, Figure 6.15). However, for both absorption and photoluminescence, the spectroscopic data obtained from the COF bulk materials do not follow these trends. The PL spectrum of the non-alkyl-functionalized Py-4T COF exhibits a peak at around 700 nm which thus appears at higher wavelengths than the COFs with alkyl chains attached (Figure 6.6b). The photoluminescence maxima of the methyl-, ethyl-, and butyl-modified COFs are all in the same region whereas the shoulder towards higher wavelengths becomes more defined with increasing chain length. Since differences in optical properties between the 4T building blocks are already more significant when comparing the spectra of the molecules in solution and as solids (SI, Section F), it is not surprising that 2D COFs with their

ordered π -stacking of layers and defined molecular distances tend to optically differ even further from their subunits.

To further understand these PL characteristics, it would be again of great interest to investigate preferentially ordered COF thin films. This is especially critical for the quaterthiophene series where the differences are so minor that the sample composition should be kept as constant as possible for better comparability. These findings could then be complemented and verified by electrochemical experiments on crystalline films and theoretical calculations to learn more about the band structure.

The PL decay histograms were recorded with time-correlated single photon counting (TCSPC) of the COF bulk materials under inert atmosphere and revealed bi- and tri-exponential decay curves (Figure 6.7).

Considering the effect of the varied number of coupled thiophenes, a slight increase of the lifetimes can be observed. The longer fluorescence lifetimes τ_1 show a clear extension from 4.06 ns via 5.72 ns to 6.80 ns for Py-2T, Py-4T and Py-6T_{Et}, respectively. This increase in PL lifetimes cannot be directly transferred to their faster decay components (τ_2 and τ_3) that represent the larger fraction of the decay dynamics. Nevertheless, the contribution of the slower fluorescence decay τ_2 increases with backbone extension. The PL lifetimes of the respective oligothiophene monomers 2T, 4T, and 6T_{Et} measured in dilute solutions increase with the number of thiophenes in the molecule, observable in the increasing decay times and the weighted average PL lifetimes of 0.28 ns, 0.77 ns, and 1.08 ns, respectively. These findings show that integrating extended oligothiophenes into COFs results in more stabilized excited states in the framework. We attribute these to an increased delocalization of the excited state over extended π -conjugated backbones.

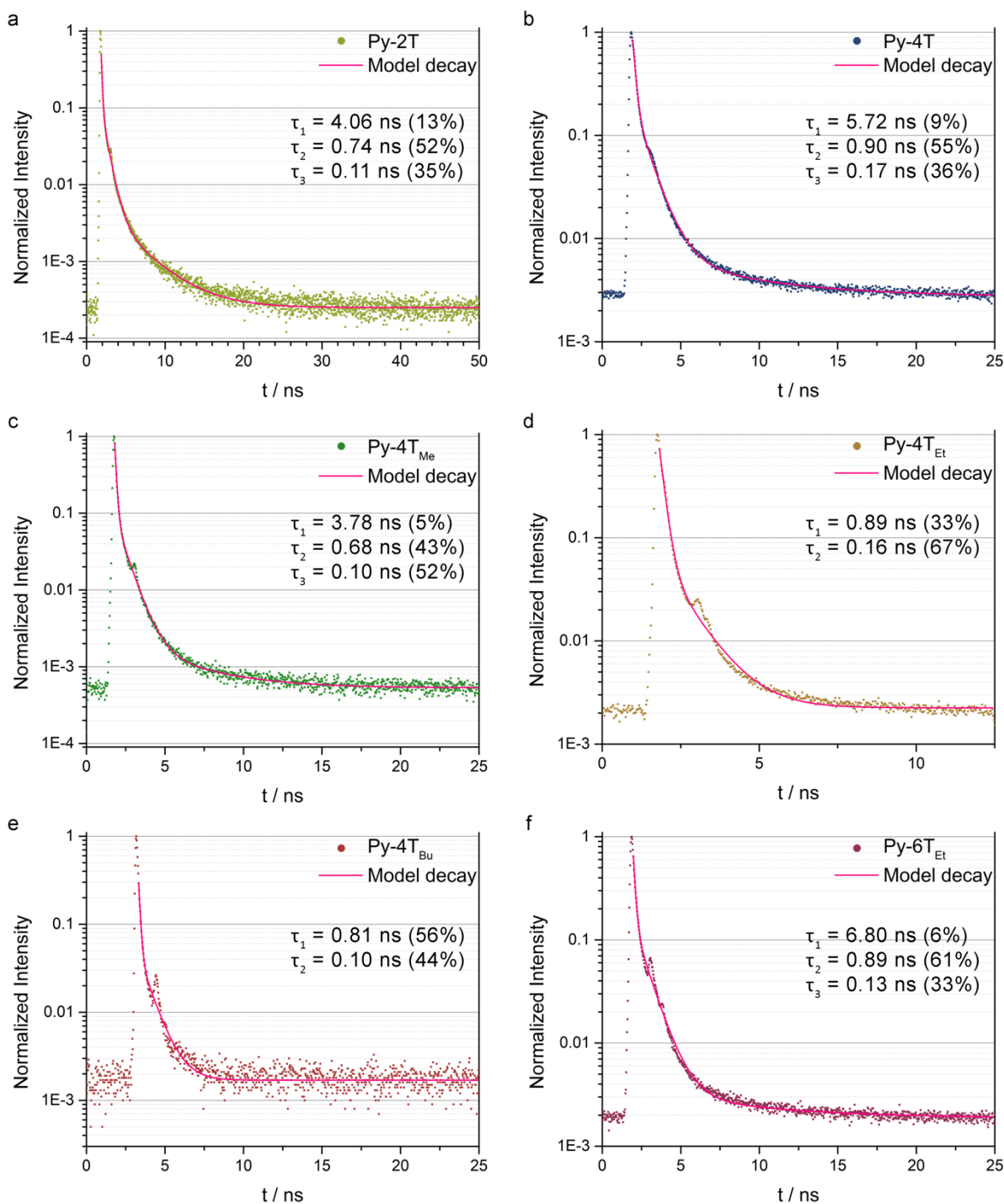


Figure 6.7. Photoluminescence decay data of (a) Py-2T at 640 nm, (b) Py-4T at 690 nm, (c) Py-4T_{Me} at 646 nm, (d) Py-4T_{Et} at 650 nm, (e) Py-4T_{Bu} at 654 nm, and (f) Py-6T_{Et} at 666 nm emission, respectively. The decays were recorded at the respective peaks of the PL spectra, using TCSPC with 378 nm excitation. Experimental decay: dots in respective color, tri-exponential or bi-exponential fit of the decay: pink line.

Investigating the influence of the alkyl chain length, a significant shift towards accelerated fluorescence decays was observed. By introducing methyl groups to the backbone, the PL lifetimes decrease to 3.78 ns for the slowest component τ_1 , 0.68 ns for τ_2 , and 0.10 ns for τ_3 . Further extending the chain length to ethyl and butyl results in a model with a bi-exponential

decay fit and decay times below 1 ns each. The TCSPC traces of the respective building blocks follow this trend, revealing faster bi-exponential decay components with extending chain length (SI, Figure 6.20). It can therefore be concluded that extension of the alkyl functionalization does influence the PL lifetimes. The longer alkyl chains might enhance competing non-radiative decay pathways due to facilitated vibrational relaxation.

Future work could further help to support these findings by modifying the alkyl chain length of the 2T and 6T backbones accordingly and then investigating and comparing the characteristics of their resulting pyrene-based COF systems. Further theoretical calculations of the oligothiophenes' charge density distributions might additionally help to better understand the influence of the alkyl chains.

6.4 Conclusion

In this work, we have developed an isostructural oligothiophene-based COF series which was constructed from a tetragonal pyrene node and chemically modified linear subunits. These linear subunits comprised aldehyde-functionalized oligothiophene building blocks of different length with various numbers of fused thiophene units, specifically bithiophene, quaterthiophene, and sexithiophene. The length of the alkyl chains attached asymmetrically to the quaterthiophene backbone was varied from methyl via ethyl to butyl. This way, the effect of both factors on structural and optical properties could be investigated. The extension of the linear bridge length was indeed observable in the experimental structural data with increasing unit cells of the refined structure models. However, the alkyl chain variations showed only minor impact on the unit cell parameters which highlights the asymmetric modification strategy leaving enough spacing between the chains.

We observed a correlation between the length of the oligothiophene bridging unit and the resulting photoluminescence lifetimes in the COF. Extending the backbone induces a lifetime increase with more stabilized excited states. Additionally, the length of the attached alkyl chains influenced the excited state dynamics in the COF. The longer chains led to a faster photoluminescence decay with the shortest lifetimes found for the COF with the largest alkyl group of the series, Py-4T_{Bu}, which indicates more accessible non-radiative decay pathways enabled by increased vibrational relaxation.

This study highlights the advantage of the modular construction principle of COFs, where modifications of their subunits can strongly affect their fundamental characteristics. We

demonstrated that slight variations of the integrated linear building blocks had an effect on their characteristics and derived a first guiding principle for tuning the excited state dynamics in COFs. We believe that further development based on these findings with expansion to other COF systems could help to establish general rules regarding building block modifications and to gain increasing control of optoelectronic processes in COFs.

6.5 Supporting Information

Section A – Methods

Nuclear magnetic resonance (NMR) spectra were recorded on Bruker AV 400 and AV 400 TR spectrometers. Chemical shifts are expressed in parts per million (δ scale) and are calibrated using residual (undeuterated) solvent peaks as an internal reference ($^1\text{H-NMR}$: CDCl_3 : 7.26, $\text{DMSO-}d_6$: 2.50, $^{13}\text{C-NMR}$: CDCl_3 : 77.16, $\text{DMSO-}d_6$: 39.52). Data for ^1H NMR spectra are reported in the following way: chemical shift (δ ppm) (multiplicity, coupling constant/Hz, integration). Multiplicities are reported as follows: s = singlet, d = doublet, t = triplet, q = quartet, m = multiplet, or combinations thereof.

High resolution electron ionization (EI) **mass spectra (MS)** were recorded with a Thermo Finnigan MAT 95 instrument.

The **nitrogen sorption** isotherms were recorded on a Quantachrome Autosorb 1 at 77 K in a pressure range from $p/p_0 = 0.001$ to 0.98. Prior to the measurement of the sorption isotherm, the sample was heated for 24 h at 120 °C under turbomolecular pump vacuum. For the evaluation of the surface area, the BET model was applied between 0.05 and 0.2 p/p_0 . The calculation of the pore size distribution was done using the QSDFT equilibrium model with a carbon kernel for cylindrical pores on the adsorption branch. The Connolly surface area differs from the experimental data, usually due to the non-ideal composition and structure of the COF sample. Grain boundaries and the displacement of COF layers may also lead to defects in the crystalline structure and to blocked pores and thus lower experimental values. Residual, adsorbed molecular/oligomeric fragments may also decrease the accessible surface area.

Powder X-ray diffraction (PXRD) measurements were performed using a Bruker D8 Discover with Ni-filtered Cu K_α radiation and a LynxEye position-sensitive detector. **Two-dimensional grazing-incidence wide angle X-ray scattering (2D GIWAXS)** data were collected using an Anton-Paar SAXSpace system equipped with a Cu K_α microfocus source operated at 50 kV and 1 mA and an Eiger Dectris R 1M 2D detector.

Transmission electron microscopy (TEM) measurements were performed on a probe-corrected FEI Titan Themis 60-300 kV (FEI Company/Thermo Fisher Scientific Inc., USA) electron microscope equipped with a Super-X windowless EDX (four quadrant SDD EDX detection) and a X-FEG high-brightness gun with monochromator (energy spread <0.2 eV).

UV-Vis spectra were recorded using a Perkin-Elmer Lambda 1050 spectrometer equipped with a 150 mm integrating sphere. **Diffuse reflectance spectra** were collected with a Praying Mantis (Harrick) accessory and were referenced to barium sulfate powder as white standard.

Photoluminescence (PL) measurements were performed using a home-built setup consisting of a Horiba Jobin Yvon iHR 320 monochromator equipped with a photomultiplier tube and a liquid N₂-cooled InGaAs detector. The samples were illuminated with a pulsed (83 Hz) 365 nm or 405 nm LED at a light intensity of 500 mW cm⁻².

Time-resolved PL measurements were acquired using a **time-correlated single photon counting (TCSPC)** setup (FluoTime 300, PicoQuant GmbH). The samples were photo-excited using lasers with suitable wavelengths according to the sample absorption, i.e. 378 nm, 403 nm or 507 nm wavelength (LDH-P-C-375, LDH-P-C-405, and LDH-P-C-510, respectively, all from PicoQuant GmbH) pulsed at 500 kHz, with a pulse duration of ~100 ps and fluence of ~300 nJcm⁻²/pulse. The samples were exposed to the pulsed light source set at 0.3 μJcm⁻²/pulse fluence for ~10 minutes prior to measurement to ensure stable sample emission. The PL was collected using a high-resolution monochromator and photomultiplier detector assembly (PMA-C 192-N-M, PicoQuant GmbH).

Section B – Building block syntheses

All reactions were carried out with magnetic stirring, and if moisture or air sensitive, under argon atmosphere using standard Schlenk techniques in oven-dried glassware. Liquid reagents and solvents were added by syringes or oven-dried stainless-steel cannulas through rubber septa. Chemicals were purchased from commercial suppliers and used without further purification. The solvents were of reagent grade or purified by distillation. Yields refer to isolated homogeneous and spectroscopically pure materials, unless otherwise specified.

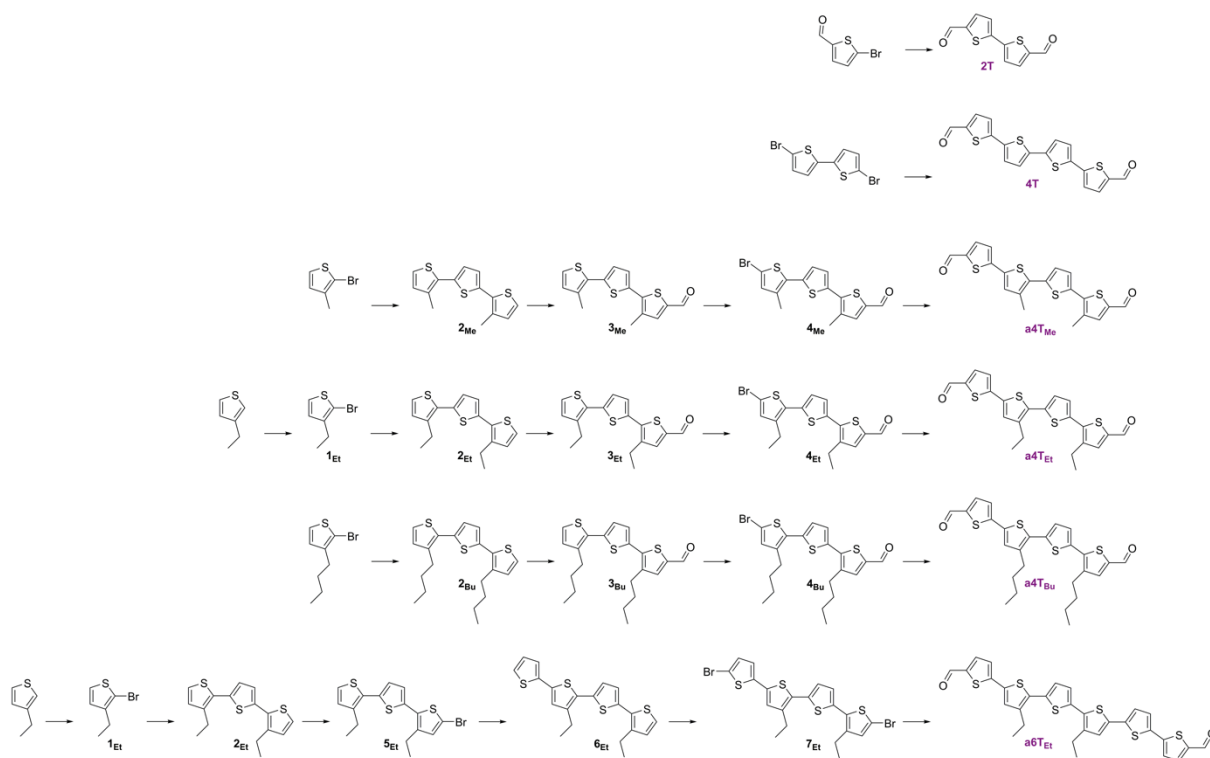
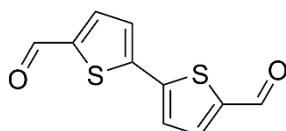


Figure 6.8. Synthesis of the oligothiophene series, 2T, 4T, a4T_{Me}, a4T_{Et}, a4T_{Bu}, and a6T_{Et}.

[2,2'-bithiophene]-5,5'-dicarbaldehyde (2T)



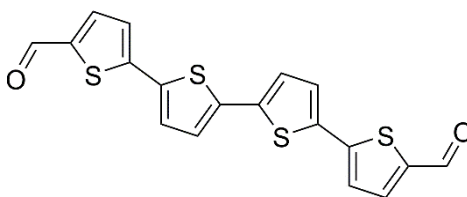
A solution of 5-bromo-2-thiophenecarboxaldehyde (1.910 g, 10 mmol, 1 eq), Pd(OAc)₂ (89.8 mg, 0.4 mmol, 0.04 eq), XPhos (228.8 mg, 0.48 mmol, 0.048 eq) in 56 mL 1-butanol was stirred for 15 min under argon at room temperature. Then a solution of CsOH·H₂O (3.358 g, 20 mmol, 2 eq.) in 14 mL water was prepared and added to the reaction suspension, followed by the addition of 5-formyl-2-thienylboronic acid (2.807 g, 18 mmol, 1.8 eq.). After stirring for 48 h at ambient conditions, the yellow-brown suspension was quenched by the addition of

400 mL of H₂O. The mixture was extracted with CHCl₃, dried over MgSO₄ and concentrated under reduced pressure. The crude product was purified via column chromatography (silica gel, DCM), yielding the title compound as a yellow powder (1.795 g, 8.1 mmol, 81%).

¹H NMR (400 MHz, CDCl₃): 9.92 (s, 2H), 7.72 (d, *J* = 4.0 Hz, 2H), 7.42 (d, *J* = 4.0 Hz, 2H).

¹³C NMR (101 MHz, CDCl₃): 182.7, 145.0, 144.1, 137.0, 126.6.

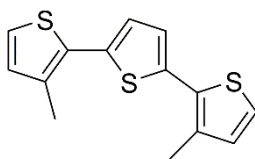
[2,2':5',2'':5'',2''':5''']-quaterthiophene]-5,5'''-dicarbaldehyde (4T)



Following a procedure by Yang et al.,^[30] 5,5'-dibromo-2,2'-bithiophene (1.0 g, 3.09 mmol, 1.0 eq.) was stirred with Pd(OAc)₂ (27.6 mg, 0.123 mmol, 4 mol%) and XPhos (70.6 mg, 0.148 mmol, 4.8 mol%) in 18 mL *n*-butanol for 15 min at room temperature. Next, a solution containing CsOH·H₂O (1.762 g, 10.5 mmol, 3.4 eq.) in 4.4 mL H₂O was added. Subsequently, 5-formyl-2-thienylboronic acid (1.444 g, 9.26 mmol, 3 eq.) was added and the resulting mixture was stirred for 48 h at room temperature. After completion, H₂O was added and the suspension was filtered and washed with *n*-hexane (100 mL) and CHCl₃ (20 mL). The organic phase was dried over MgSO₄ and concentrated under reduced pressure. The crude product was purified via recrystallization from THF and furnished the title compound as a dark red powder (754 mg, 1.95 mmol, 63%).

¹H NMR (400 MHz, DMSO-*d*₆): 9.90 (s, 2H), 8.02 (d, *J* = 4.0 Hz, 2H), 7.63 (d, *J* = 3.9 Hz, 2H), 7.60 (d, *J* = 4.0 Hz, 2H), 7.51 (d, *J* = 3.9 Hz, 2H).

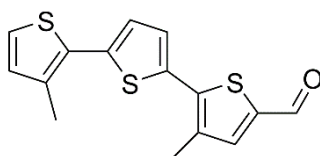
HR-EI-MS: *m/z* 385.95 (M⁺, calculated for C₂₆H₂₆O₂S₄: 385.95).

3,3''-dimethyl-2,2':5',2''-terthiophene (2_{Me})

A Grignard reagent, prepared by sonication of 2-bromo-3-methylthiophene (5.06 g, 28.6 mmol, 2.9 eq.), 1,2-dibromoethane (5.38 g, 28.6 mmol, 2.9 eq.) and Mg (1.37 mg, 56.1 mmol, 5.7 eq.) in 85 mL of dry Et₂O, was slowly added to a solution containing 2,5-dibromothiophene (2.39 g, 10.0 mmol, 1.0 eq.) and Ni(dppp)Cl₂ (465.4 mg, 0.86 mmol, 3 mol%) in 57 mL dry Et₂O. The reaction mixture was heated to reflux for 40 h. Upon completion, the reaction was quenched by the addition of 2 M HCl (100 mL), extracted with DCM, washed with H₂O, dried over MgSO₄, and concentrated under reduced pressure. The crude product was purified via column chromatography (silica gel, *n*-pentane), yielding the title compound as yellow crystals (2.47 g, 6.84 mmol, 69%).

¹H NMR (400 MHz, CDCl₃): 7.15 (d, *J* = 5.1 Hz, 2H), 7.08 (s, 2H), 6.89 (d, *J* = 5.1 Hz, 2H), 2.42 (s, 6H).

¹³C NMR (101 MHz, CDCl₃): 136.7, 134.5, 131.9, 131.3, 126.2, 123.8, 15.9.

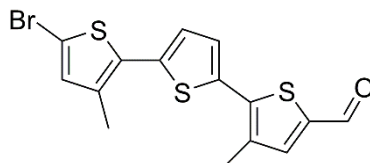
3,3''-dimethyl-5-formyl-2,2':5',2''-terthiophene (3_{Me})

A Vilsmeier reagent, prepared by the addition of POCl₃ (1.39 g, 8.83 mmol, 1.3 eq.) to 6.6 mL of dry DMF, was added to a solution of compound 2_{Me} (1.90 g, 6.87 mmol, 1.0 eq.) in 140 mL DCE. The reaction mixture was stirred overnight at 70 °C. Subsequently, H₂O (250 mL) was added and the pH was adjusted to 8.5-9 with 2 M NaOH. The product was extracted with DCM, dried over MgSO₄ and concentrated under reduced pressure. Purification via column chromatography (silica gel, CHCl₃) furnished the product as a yellow powder (1.72 g, 5.65 mmol, 82%).

¹H NMR (400 MHz, CDCl₃): 9.82 (s, 1H), 7.55 (s, 1H), 7.28 (d, *J* = 3.9 Hz, 1H), 7.19 (d, *J* = 5.1 Hz, 1H), 7.13 (d, *J* = 3.9 Hz, 1H), 6.91 (d, *J* = 5.1 Hz, 1H), 2.48 (s, 3H), 2.43 (s, 3H).

^{13}C NMR (101 MHz, CDCl_3): 182.5, 141.7, 140.5, 139.8, 139.0, 134.9, 134.9, 134.8, 131.8, 130.4, 127.8, 126.1, 124.2, 16.0, 15.7.

5-bromo-3,3''-dimethyl-5''-formyl-2,2':5',2''-terthiophene (4_{Me})

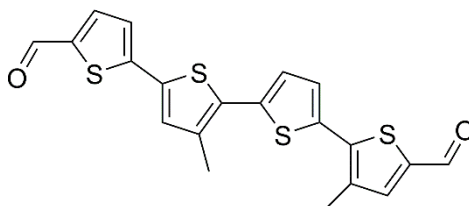


Compound 3_{Me} (1.72 g, 5.6 mmol, 1.0 eq.) was dissolved in 55 mL CHCl_3 and cooled to 0 °C. NBS (1.10 mg, 6.2 mmol, 1.1 eq.) and glacial acetic acid (55 mL) were added and the solution was allowed to slowly warm up to room temperature. After stirring at room temperature for 2 d in the dark, the reaction mixture was poured onto H_2O , extracted with DCM, washed with saturated NaHCO_3 solution, dried over MgSO_4 , and concentrated under reduced pressure. The crude product was purified by column chromatography (silica gel, *n*-hexane with 2% - 25% EtOAc), yielding the title compound as a bright yellow solid (1.844 g, 4.81 mmol, 86%).

^1H NMR (400 MHz, CDCl_3): 9.82 (s, 1H), 7.55 (s, 1H), 7.26 (d, $J = 3.8$ Hz, 1H), 7.07 (d, $J = 3.8$ Hz, 1H), 6.88 (s, 1H), 2.47 (s, 3H), 2.37 (s, 3H).

^{13}C NMR (101 MHz, CDCl_3): 182.5, 141.3, 140.4, 140.1, 137.5, 135.4, 135.4, 135.0, 134.3, 131.9, 127.7, 126.5, 111.0, 16.0, 15.6.

3,3''-dimethyl-[2,2':5',5'':2'',2''']-quaterthiophene]-5,5'''-dicarbaldehyde ($a4\text{T}_{\text{Me}}$)



Following a procedure by Yang et al.,^[30] compound 4_{Me} (1.04 g, 2.7 mmol, 1.0 eq.) was stirred with $\text{Pd}(\text{OAc})_2$ (12.2 mg, 0.05 mmol, 2 mol%) and XPhos (31.0 mg, 0.067 mmol, 2.4 mol%) in 32 mL *n*-butanol (ca. 15 min). Next, a solution containing $\text{CsOH}\cdot\text{H}_2\text{O}$ (911.5 mg, 5.4 mmol, 2.0 eq.) in 7.8 mL H_2O was added, followed by the addition of 5-formyl-2-thienylboronic acid (170 mg, 1.09 mmol, 1.8 eq.). The resulting mixture was stirred for 3 d at room temperature. After completion, H_2O was added and the product was extracted with CHCl_3 , washed with brine 3 times, dried over MgSO_4 , and concentrated under reduced pressure. Purification via column

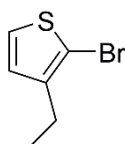
chromatography (silica gel, chloroform/EtOAc 99:1) furnished the title compound as a bright red powder (205 mg, 0.494 mmol, 82%).

^1H NMR (400 MHz, CDCl_3): 9.86 (s, 1H), 9.83 (s, 1H), 7.67 (d, $J = 4.0$ Hz, 1H), 7.55 (s, 1H), 7.30 (d, $J = 3.9$ Hz, 1H), 7.23 (d, $J = 4.0$ Hz, 1H), 7.19 (d, $J = 3.9$ Hz, 1H), 7.18 (s, 1H), 2.49 (s, 3H), 2.45 (s, 3H).

^{13}C NMR (101 MHz, CDCl_3): 182.5, 146.6, 142.0, 141.2, 140.4, 140.2, 137.8, 137.5, 136.0, 135.8, 135.1, 133.9, 132.4, 130.6, 127.9, 126.7, 124.4, 16.1, 15.9.

HR-EI-MS: m/z 414.56 (M^+ , calculated for $\text{C}_{20}\text{H}_{14}\text{O}_2\text{S}_4$: 414.57).

2-bromo-3-ethylthiophene (1_{Et})

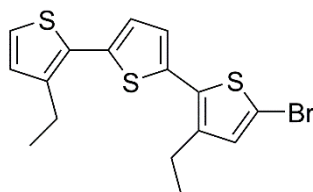


N-bromosuccinimide (8.3 g, 46.8 mmol, 1.05 eq.) was added to a solution of 2-ethylthiophene (5.0 g, 44.6 mmol, 1.0 eq.) in 47 mL CHCl_3 . The reaction mixture was cooled to 0 °C, followed by the addition of 47 mL glacial acetic acid. The solution was allowed to warm to room temperature over the course of several hours and stirred for 2 d in the dark. The slightly yellow solution was poured onto 200 mL H_2O , extracted with DCM, washed with saturated NaHCO_3 solution, dried over MgSO_4 , and concentrated under reduced pressure. High vacuum distillation (31 mbar, 33 °C) furnished the title compound as a colorless liquid (7.47 g, 39.1 mmol, 89%).

^1H NMR (400 MHz, CDCl_3): 7.19 (d, $J = 5.6$ Hz, 1H), 6.82 (d, $J = 5.6$ Hz, 1H), 2.59 (q, $J = 7.6$ Hz, 2H), 1.19 (t, $J = 7.6$ Hz, 3H).

^{13}C NMR (101 MHz, CDCl_3): 143.3, 127.9, 125.4, 108.5, 23.0, 14.3.

The consecutive compounds (2_{Et} , 3_{Et} , 4_{Et} , $a4\text{T}_{\text{Et}}$, 2_{Bu} , 3_{Bu} , 4_{Bu} , $a4\text{T}_{\text{Bu}}$) were synthesized analogous to the products listed above (2_{Me} , 3_{Me} , 4_{Me} , $a4\text{T}_{\text{Me}}$).

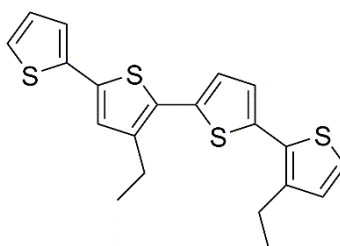
5-bromo-3,3''-diethyl-2,2':5',2''-terthiophene (5_{Et})

Compound **2_{Et}** (5.13 g, 16.8 mmol, 1.0 eq.) was dissolved in CHCl₃ (34 ml) and cooled to 0 °C. *N*-bromosuccinimide (3.15 g, 17.7 mmol, 1.05 eq.) and glacial acetic acid (34 ml) were added and the solution was allowed to slowly warm up to room temperature. After stirring at room temperature for 3 d in the dark, the reaction mixture was poured onto 100 mL water, extracted with CH₂Cl₂, washed with sat. NaHCO₃ solution, dried over MgSO₄, and concentrated under reduced pressure. The crude product was purified by flash column chromatography (silica, 2-methylpentane) yielding compound **5_{Et}** (3.667 g, 9.6 mmol, 57%) as a yellow oil.

¹H NMR (400 MHz, CDCl₃): 7.20 (d, *J* = 5.2 Hz, 1H), 7.05 (d, *J* = 3.7 Hz, 1H), 7.00 (d, *J* = 3.7 Hz, 1H), 6.97 (d, *J* = 5.2 Hz, 1H), 6.93 (s, 1H), 2.81 (q, *J* = 7.5 Hz, 2H), 2.75 (q, *J* = 7.5 Hz, 2H), 1.27 (t, *J* = 7.6 Hz, 3H), 1.25 (t, *J* = 7.6 Hz, 3H).

¹³C NMR (101 MHz, CDCl₃): 141.5, 141.2, 136.7, 134.6, 132.2, 131.6, 129.8, 129.6, 126.5, 126.0, 124.1, 110.6, 22.5, 22.5, 15.1, 15.0.

HR-EI-MS: *m/z* 382.14 (M⁺, calculated for C₁₆H₁₅BrS₃: 381.95).

3,3''-diethyl-2,2':5',2'':5'',2'''-quaterthiophene (6_{Et})

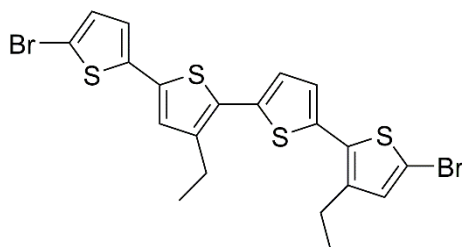
A solution of CsOH·H₂O (1.219 g, 7.26 mmol, 2 eq.) and water (5.1 ml) was added to a stirring suspension of compound **5_{Et}** (1.391 g, 3.628 mmol, 1.0 eq.), palladium acetate (32.6 mg, 0.145 mmol, 4 mol%), XPhos (83.0 mg, 0.174 mmol, 4.8 mol%) and *n*-butanol (20 ml). After addition of 5-formyl-2-thienylboronic acid (836 mg, 6.53 mmol, 1.8 eq.) the slurry was stirred at room temperature for 2 d. Water (50 ml) and CH₂Cl₂ (100 ml) was added to the slurry. The aqueous phase was extracted by CH₂Cl₂ and the combined extracts were washed with sat. NaHCO₃ and brine. The solution was dried over Na₂SO₄ and concentrated under reduced

pressure. The residue was purified by flash column chromatography (silica, 0% → 20% CH₂Cl₂ in *n*-pentane), yielding compound **6_{Et}** (407 mg, 1.05 mmol, 29%) as an orange oil.

¹H NMR (400 MHz, CDCl₃): 7.22 (dd, *J* = 5.1, 1.1 Hz, 1H), 7.20 (d, *J* = 5.2 Hz, 1H), 7.17 (dd, *J* = 3.6, 1.1 Hz, 1H), 7.08 (d, *J* = 3.8 Hz, 1H), 7.06 (d, *J* = 3.8 Hz, 1H), 7.05 (s, 1H), 7.02 (dd, *J* = 5.1, 3.6 Hz, 1H), 6.98 (d, *J* = 5.2 Hz, 1H), 2.82 (p, *J* = 7.5 Hz, 4H), 1.31 (t, *J* = 7.6 Hz, 3H), 1.28 (t, *J* = 7.6 Hz, 3H).

HR-EI-MS: *m/z* 386.22 (M⁺, calculated for C₂₀H₁₈S₄: 386.03).

5,5'''-dibromo-3,3''-diethyl-2,2':5',2'':5'',2'''-quaterthiophene (**7_{Et}**)



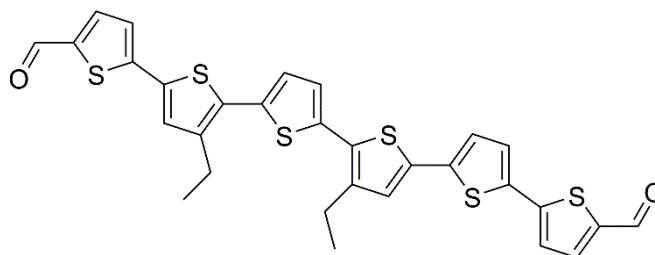
A solution of *N*-bromosuccinimide (439 mg, 2.46 mmol, 2.0 eq.) and dry DMF (3 ml) was added to a solution of compound **6_{Et}** (477 mg, 1.23 mmol, 1.0 eq.) in DMF (13 ml) at 80 °C. After stirring at 80 °C for 3 h, the reaction mixture was poured onto water (100 ml), extracted with CH₂Cl₂, washed with water, dried over MgSO₄, and concentrated under reduced pressure. The crude product was purified by flash column chromatography (silica, 0% → 15% CHCl₃ in isohexane) yielding compound **7_{Et}** (539 mg, 990 μmol, 80 %) as an orange solid.

¹H NMR (400 MHz, CDCl₃): 7.06 (d, *J* = 3.8 Hz, 1H), 7.01 (d, *J* = 3.8 Hz, 1H), 6.97 (s, 1H), 6.97 (d, *J* = 3.9 Hz, 1H), 6.93 (s, 1H), 6.90 (d, *J* = 3.9 Hz, 1H), 2.78 (q, *J* = 7.6 Hz, 2H), 2.75 (q, *J* = 7.6 Hz, 2H), 1.29 (t, *J* = 7.6 Hz, 3H), 1.25 (t, *J* = 7.6 Hz, 3H).

¹³C NMR (101 MHz, CDCl₃): 142.0, 141.8, 138.8, 136.1, 135.0, 134.6, 132.4, 131.6, 130.9, 129.5, 126.7, 126.5, 126.2, 123.9, 111.2, 110.9, 22.9, 22.7, 15.1, 15.0

HR-EI-MS: *m/z* 541.84 (M⁺, calculated for C₂₀H₁₆Br₂S₄: 541.84).

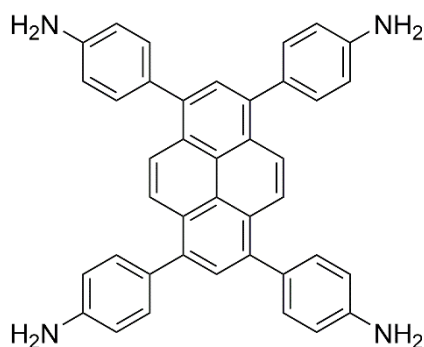
3''',4'-diethyl-[2,2':5',2'':5'',2''':5''',2''':5''''',2''''':5''''''-sexithiophene]-5,5''''''-dicarbaldehyde
(a6T_{Et})



A solution of CsOH·H₂O (185 mg, 1.10 mmol, 2.0 eq.) and water (0.77 ml) was added to a stirring suspension of compound 7_{Et} (300 mg, 551 μmol, 1.0 eq.), palladium acetate (5.0 mg, 22 μmol, 4 mol%), XPhos (12.6 mg, 27 μmol, 4.8 mol%) and *n*-butanol (6.2 ml). After addition of 5-formyl-2-thienylboronic acid (253 mg, 1.65 mmol, 3.0 eq.) the slurry was stirred at 50 °C for 2 d. Water (100 ml) and CH₂Cl₂ (200 ml) was added to the slurry. The aqueous phase was extracted by CH₂Cl₂ and the combined extracts were washed with sat. NaHCO₃ and brine. The organic layers were dried over Na₂SO₄ and concentrated under reduced pressure. Purification of the residue by flash column chromatography (silica, CH₂Cl₂) yielded 116 mg product (191 μmol, 35%). Recrystallization from DCE and vacuum drying afforded **a6T_{Et}** (99 mg, 163 μmol, 30%) as deep dark purple crystals.

¹H NMR (400 MHz, CDCl₃): 9.90 (s, 2H), 8.02 (d, *J* = 2.4 Hz, 1H), 8.01 (d, *J* = 2.4 Hz, 1H), 7.61 (d, *J* = 3.9 Hz, 1H), 7.59 (s, 1H), 7.58 (d, *J* = 2.7 Hz, 1H), 7.57 (d, *J* = 2.7 Hz, 1H), 7.43 (s, 1H), 7.43 (d, *J* = 3.8 Hz, 1H), 7.34 (d, *J* = 3.9 Hz, 1H), 7.31 (d, *J* = 3.9 Hz, 1H), 2.81 (q, *J* = 7.5 Hz, 2H), 2.80 (q, *J* = 7.5 Hz, 2H), 1.28 (t, *J* = 7.5 Hz, 6H)

HR-EI-MS: *m/z* 605.99 (M⁺, calculated for C₃₀H₂₂O₂S₆: 605.99).

1,3,6,8-tetrakis(4-aminophenyl)pyrene (Py)^[27, 31]

A reaction mixture containing 1,3,6,8-tetrabromopyrene (1482 mg, 2.86 mmol, 1.0 eq.), 4-aminophenylboronic acid pinacol ester (3010 mg, 13.7 mmol, 4.8 eq.), K_2CO_3 (2175 mg, 15.7 mmol, 5.5 eq.), and $Pd(PPh_3)_4$ (330 mg, 0.29 mmol, 10 mol%) in 32 mL 1,4-dioxane and 8 mL H_2O was heated to reflux (115 °C) for 3 d. After cooling to room temperature, H_2O was added. The resulting precipitate was collected via filtration and was washed with H_2O and MeOH. Recrystallization from 1,4-dioxane, followed by drying under high vacuum furnished the title compound, co-crystallized with approximately 1.5 dioxane molecules per formula unit, as a bright yellow powder (1792 mg, 2.56 mmol, 90%).

1H NMR (400 MHz, $DMSO-d_6$): 8.13 (s, 4 H), 7.79 (s, 2 H), 7.34 (d, $J = 8.4$ Hz, 8 H), 6.77 (d, $J = 8.5$ Hz, 8 H), 5.30 (s, 8 H), 3.56 (s, 12 H, dioxane).

^{13}C NMR (100 MHz, $DMSO-d_6$): 148.2, 137.1, 131.0, 129.0, 127.6, 126.7, 126.1, 124.4, 113.9, 66.3 (dioxane).

Section C – COF syntheses

COF bulk material syntheses were carried out under argon atmosphere in PTFE-sealed 6 mL glass tubes. High purity solvents and acetic acid were sourced from commercial suppliers and degassed and saturated with argon prior to use unless shipped under argon.

Py-2T

1,3,6,8-tetrakis(4-aminophenyl)pyrene dioxane adduct (Py; 7.0 mg, 10 μmol , 1.0 eq.) and [2,2'-bithiophene]-5,5'-dicarbaldehyde (2T; 4.5 mg, 20 μmol , 2.0 eq.) were filled into a reaction tube, followed by the addition of mesitylene (333 μl), benzyl alcohol (167 μl) and 6 M acetic acid (70 μL). The tube was sealed and the reaction mixture was heated at 120 $^{\circ}\text{C}$ for 3 d. After cooling to room temperature, the precipitate was collected by filtration, and extracted with supercritical CO_2 for 2 h, yielding the Py-2T COF as a red powder.

Py-4T COF

1,3,6,8-tetrakis(4-aminophenyl)pyrene dioxane adduct (Py; 10.5 mg, 15 μmol , 1.0 eq.) and [2,2':5',2'':5'',2''':5''']-quaterthiophene]-5,5''-dicarbaldehyde (4T; 11.6 mg, 30 μmol , 2.0 eq.) were filled into a reaction tube, followed by the addition of 1,2-dichlorobenzene (167 μl), benzyl alcohol (83 μl) and 6 M acetic acid (25 μL). The tube was sealed and the reaction mixture was heated at 120 $^{\circ}\text{C}$ for 3 d. After cooling to room temperature, the precipitate was collected by filtration, slowly dried in an argon atmosphere overnight, and extracted with supercritical CO_2 for 2 h, yielding the Py-4T COF as a dark red to black powder.

Py-4T_{Me} COF

1,3,6,8-tetrakis(4-aminophenyl)pyrene dioxane adduct (Py; 14.0 mg, 20 μmol , 1.0 eq.) and 3,3''-dimethyl-[2,2':5',5'':2'',2''']-quaterthiophene]-5,5''-dicarbaldehyde (a4T_{Me}; 17 mg, 40 μmol , 2.0 eq.) were filled into a reaction tube, followed by the addition of mesitylene (333 μL), BnOH (167 μL), and 6 M acetic acid (50 μL). The tube was sealed and the reaction mixture was heated at 120 $^{\circ}\text{C}$ for 4 d. After cooling to room temperature, the precipitate was collected by filtration, slowly dried in an argon atmosphere overnight, and extracted with supercritical CO_2 for 2 h, yielding the Py-4T_{Me} COF as a dark red powder.

Py-4T_{Et} COF

1,3,6,8-tetrakis(4-aminophenyl)pyrene dioxane adduct (Py; 7.0 mg, 10 μmol , 1.0 eq.) and 3,3''-diethyl-[2,2':5',5'':2'',2'''-quaterthiophene]-5,5'''-dicarbaldehyde (a4T_{Et}; 8.9 mg, 20 μmol , 2.0 eq.) were filled into a reaction tube, followed by the addition of mesitylene (187 μL), BnOH (63 μL), and 6 M acetic acid (50 μL). The tube was sealed and the reaction mixture was heated at 120 °C for 4 d. After cooling to room temperature, the precipitate was collected by filtration, slowly dried in an argon atmosphere overnight, and extracted with supercritical CO₂ for 2 h, yielding the Py-4T_{Me} COF as a dark red powder.

Py-4T_{Bu} COF

1,3,6,8-tetrakis(4-aminophenyl)pyrene dioxane adduct (Py; 14.0 mg, 20 μmol , 1.0 eq.) and 3,3''-dibutyl-[2,2':5',5'':2'',2'''-quaterthiophene]-5,5'''-dicarbaldehyde (a4T_{Bu}; 20 mg, 40 μmol , 2.0 eq.) were filled into a reaction tube, followed by the addition of mesitylene (133 μL), BnOH (67 μL), and 6 M acetic acid (20 μL). The tube was sealed and the reaction mixture was heated at 120 °C for 4 d. After cooling to room temperature, the precipitate was collected by filtration and slowly dried in air for 24 h, yielding the Py-4T_{Bu} COF as a dark red powder.

Py-6T_{Et} COF

1,3,6,8-tetrakis(4-aminophenyl)pyrene dioxane adduct (Py; 7.0 mg, 10 μmol , 1.0 eq.) and 3''',4'-diethyl-[2,2':5',2'':5'',2''':5''',2''':5''',2''''-sexithiophene]-5,5''''-dicarbaldehyde (a6T_{Et}; 12.1 mg, 20 μmol , 2.0 eq.) were filled into a reaction tube, followed by the addition of mesitylene (167 μL), BnOH (83 μL), and 6 M acetic acid (25 μL). The tube was sealed and the reaction mixture was heated at 120 °C for 3 d. After cooling to room temperature, the precipitate was collected by filtration and slowly dried in an argon atmosphere overnight, and extracted with supercritical CO₂ for 2 h, yielding the Py-6T_{Et} COF as a dark red powder.

COF thin film syntheses were carried out under argon atmosphere in PTFE-sealed 100 mL glass containers equipped with a glass liner. The COF films were grown on quartz substrates cleaned in Hellmanex solution, water, acetone, and isopropanol prior to use. The substrates were placed in a PTFE holder in the reaction solution.

Py-2T thin film

1,3,6,8-tetrakis(4-aminophenyl)pyrene dioxane adduct (Py; 10.5 mg, 15 μmol , 1.0 eq.) and [2,2'-bithiophene]-5,5'-dicarbaldehyde (2T; 6.7 mg, 30 μmol , 2.0 eq.) were filled into a glass container, followed by the addition of mesitylene (1333 μl), benzyl alcohol (667 μl) and 6 M acetic acid (150 μL). The quartz substrate was placed in the reaction solution and the glass vessel was sealed and heated at 120 $^{\circ}\text{C}$ for 1 d. After cooling to room temperature, the substrate was cleaned with acetonitrile, and dried at 60 $^{\circ}\text{C}$ for 30 min, yielding the crystalline and oriented Py-2T COF as a red thin film.

Py-4T_{Et} thin film

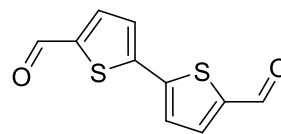
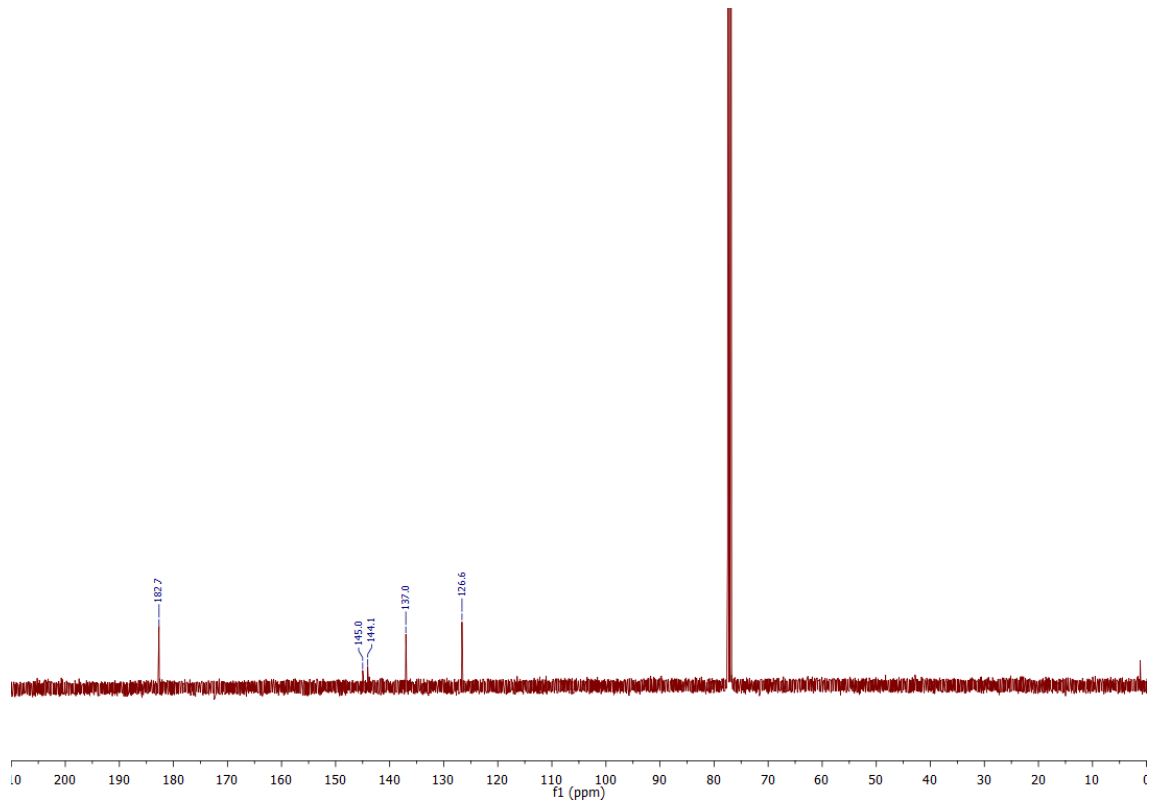
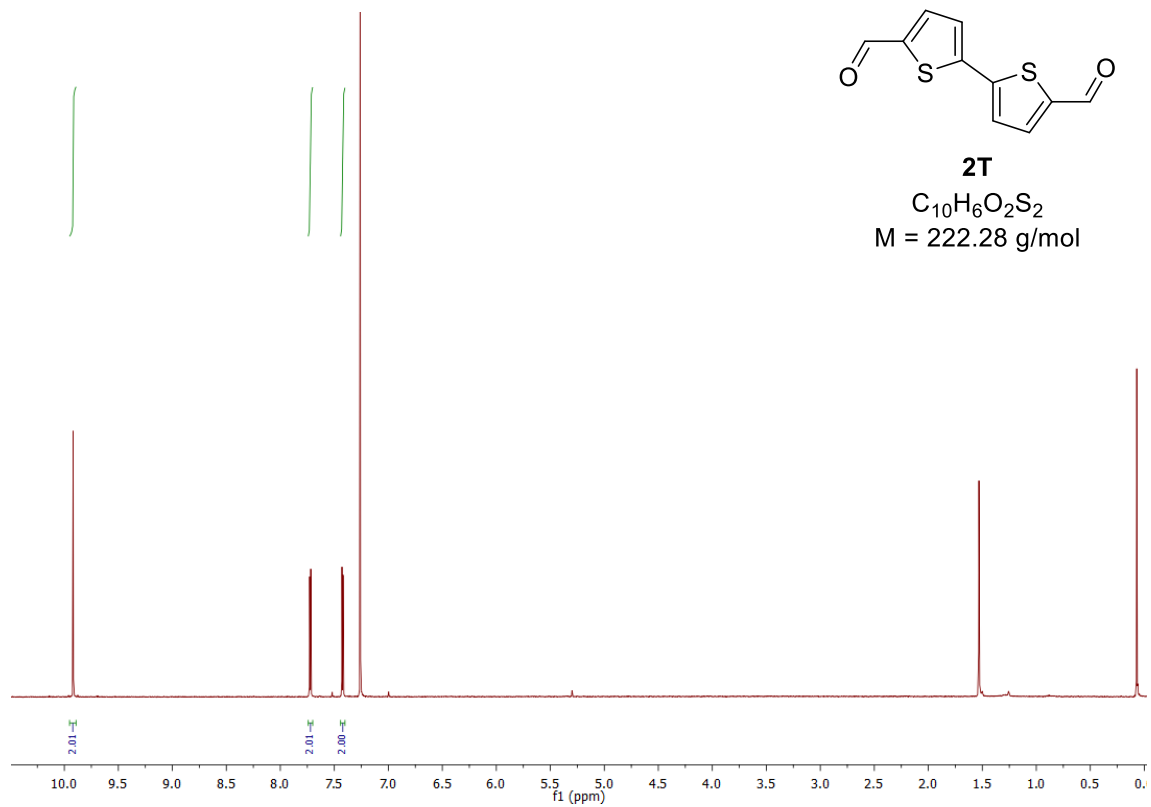
1,3,6,8-tetrakis(4-aminophenyl)pyrene dioxane adduct (Py; 14.0 mg, 20 μmol , 1.0 eq.) and 3,3"-diethyl-[2,2':5',5":2",2"'-quaterthiophene]-5,5"'-dicarbaldehyde (a4T_{Et}; 17 mg, 40 μmol , 2.0 eq.) were filled into a glass container, followed by the addition of mesitylene (1333 μl), benzyl alcohol (667 μl) and 6 M acetic acid (150 μL). The quartz substrate was placed in the reaction solution and the glass vessel was sealed and heated at 120 $^{\circ}\text{C}$ for 1 d. After cooling to room temperature, the substrate was cleaned with acetonitrile, and dried at 60 $^{\circ}\text{C}$ for 30 min, yielding the crystalline and oriented Py-4T_{Et} as a red thin film.

Amorphous thin films of Py-4T, Py-4T_{Me}, Py-4T_{Bu}

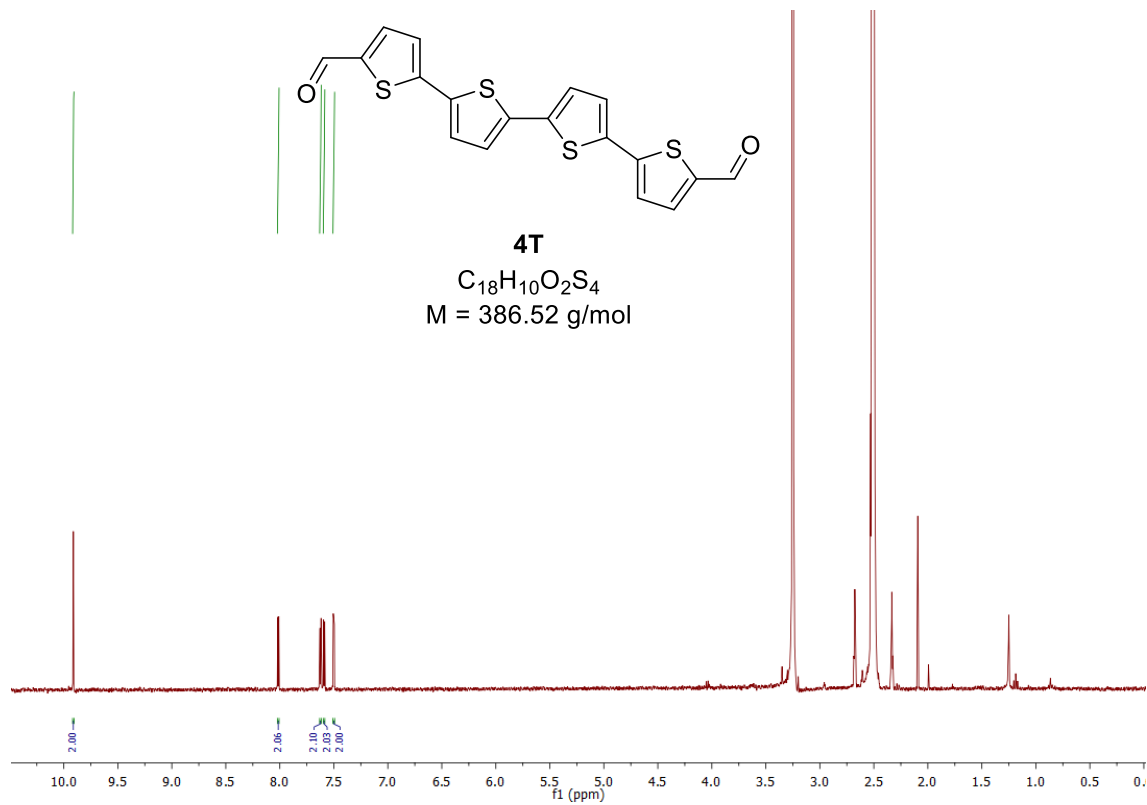
1,3,6,8-tetrakis(4-aminophenyl)pyrene dioxane adduct (Py; 10.5 mg, 15 μmol , 1.0 eq.) and the corresponding quaterthiophene-dicarbaldehyde (4T, 4T_{Me}, 4T_{Bu}; 30 μmol , 2.0 eq.) were filled into a glass container, followed by the addition of mesitylene (1333 μl), benzyl alcohol (667 μl) and 6 M acetic acid (150 μL). The quartz substrate was placed in the reaction solution and the glass vessel was sealed and heated at 120 $^{\circ}\text{C}$ for 1-3 d. Extensive screening of the parameters did not yield a crystalline material yet but resulted in Py-4T/-4T_{Me}/-4T_{Bu} thin films that did not show crystallinity in the GIWAXS measurements.

Section D – NMR of the oligothiophene building blocks

2T

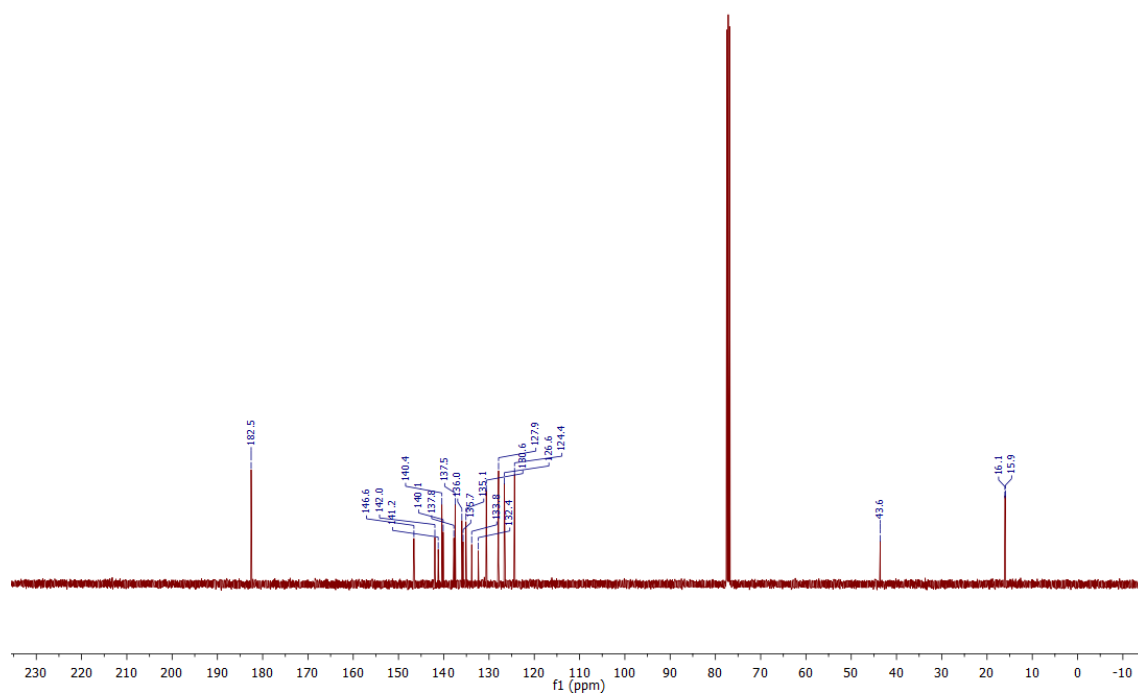
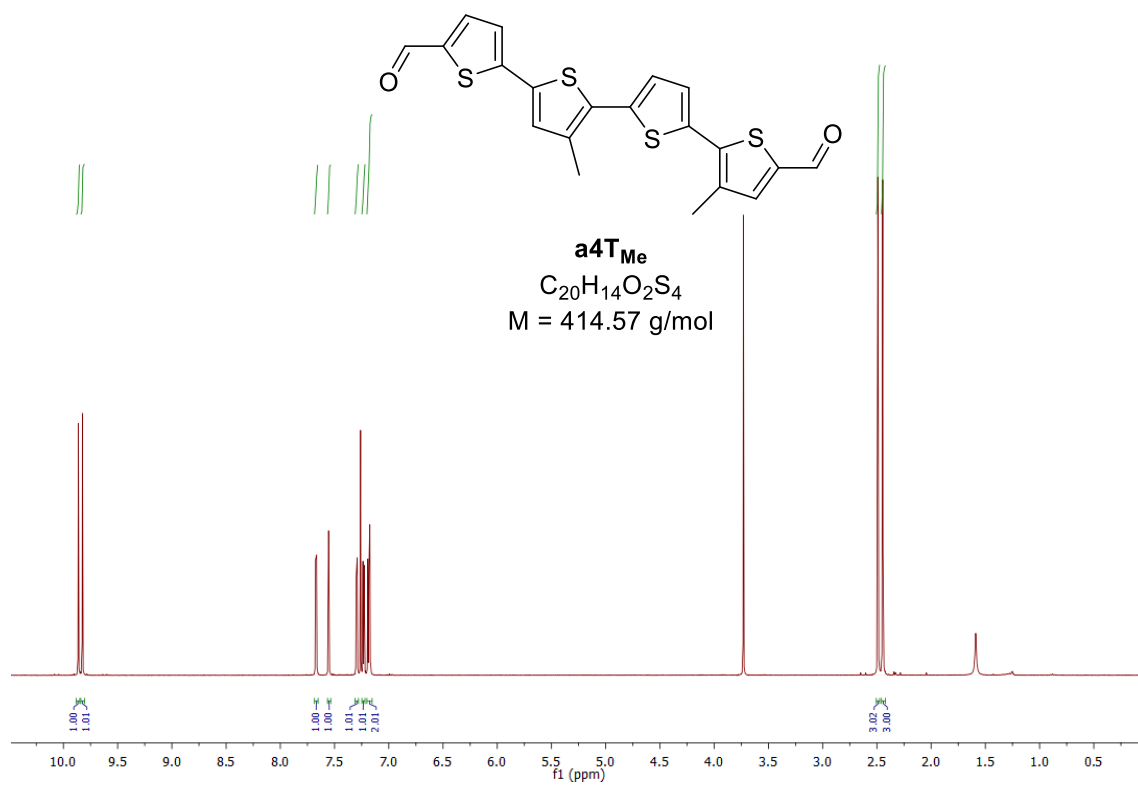
**2T** $C_{10}H_6O_2S_2$
M = 222.28 g/mol

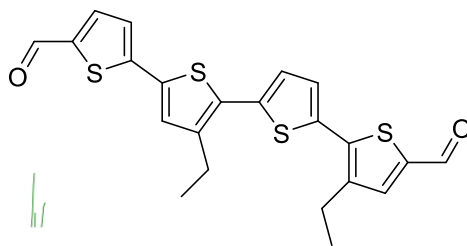
4T



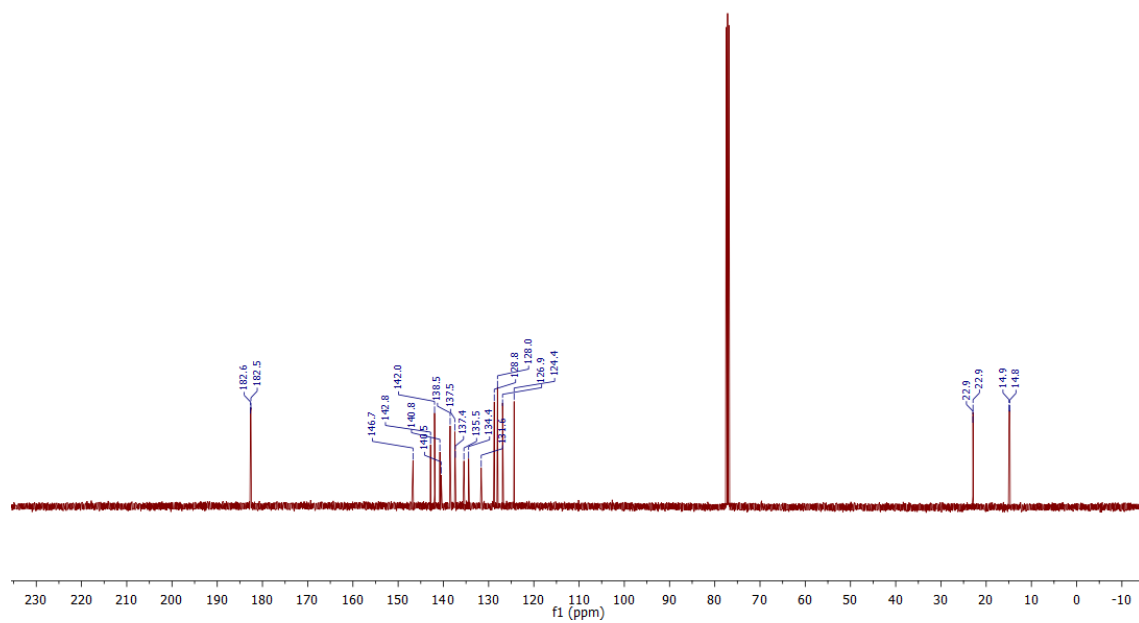
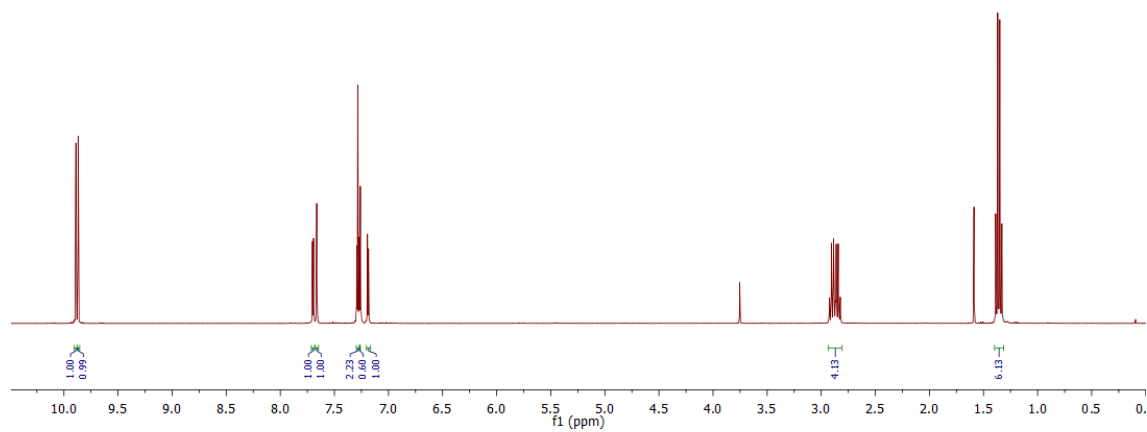
6 Extension of Oligothiophene Backbones in Covalent Organic Frameworks

a4T_{Me}



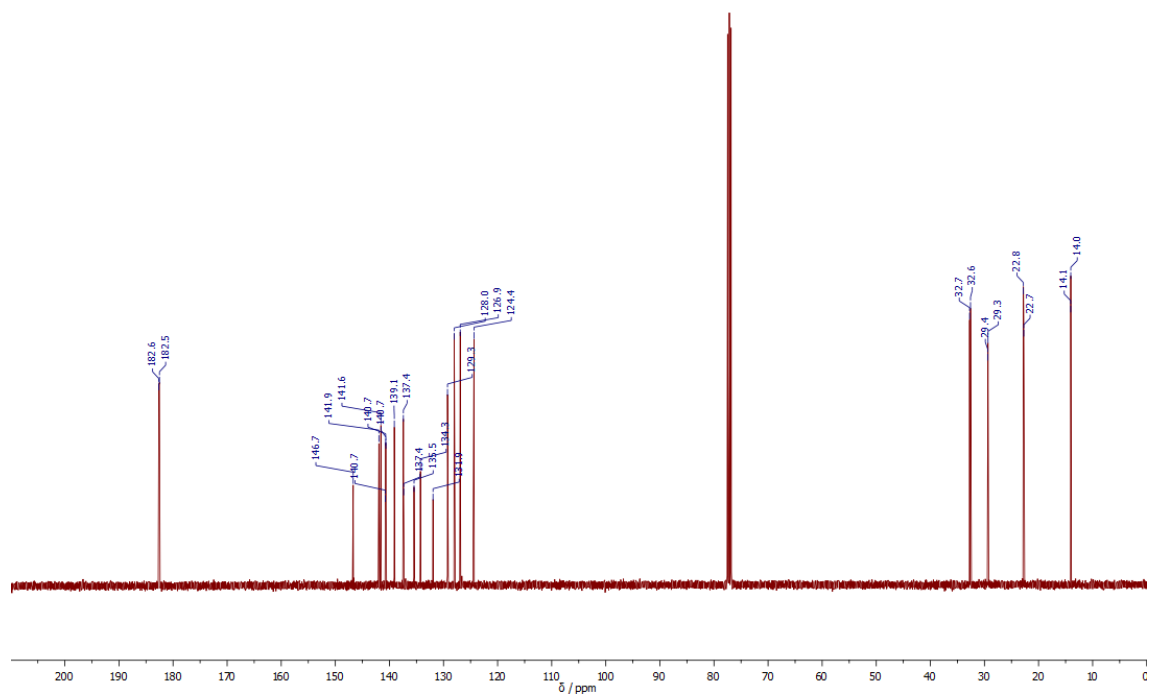
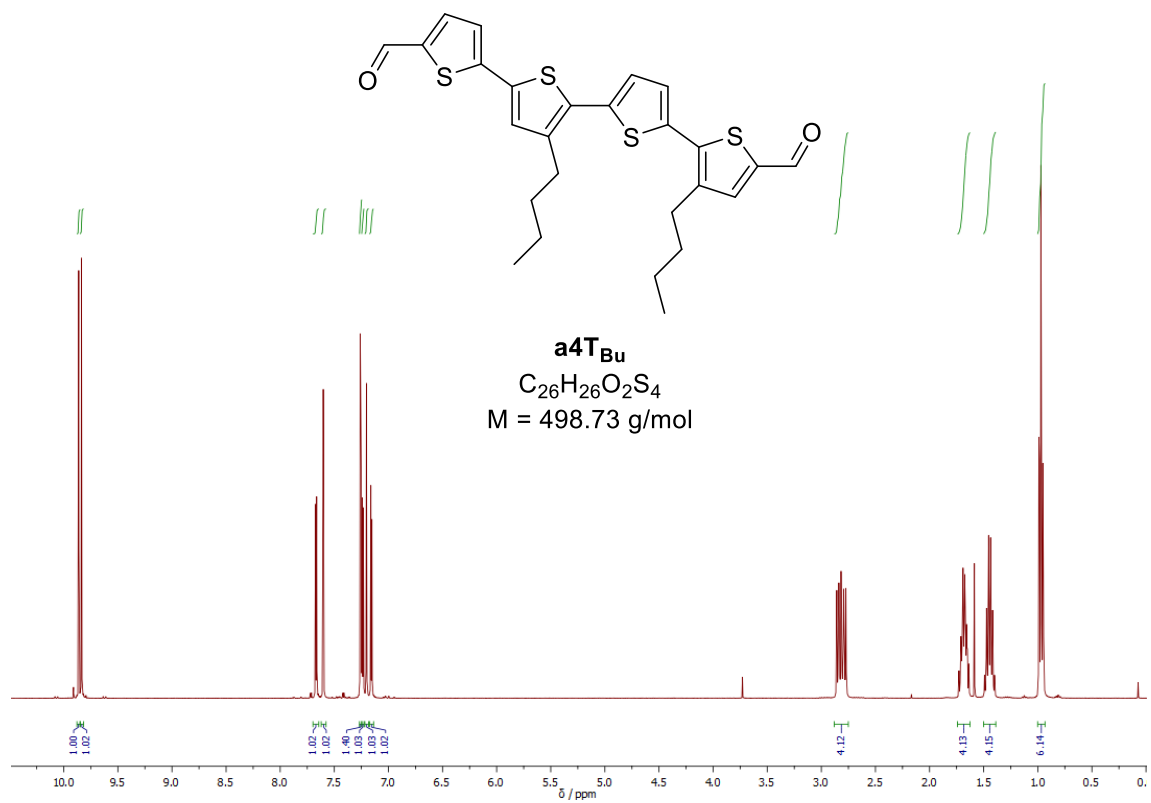
a4T_{ET}

a4T_{ET}
 $C_{22}H_{18}O_2S_4$
 $M = 442.62 \text{ g/mol}$

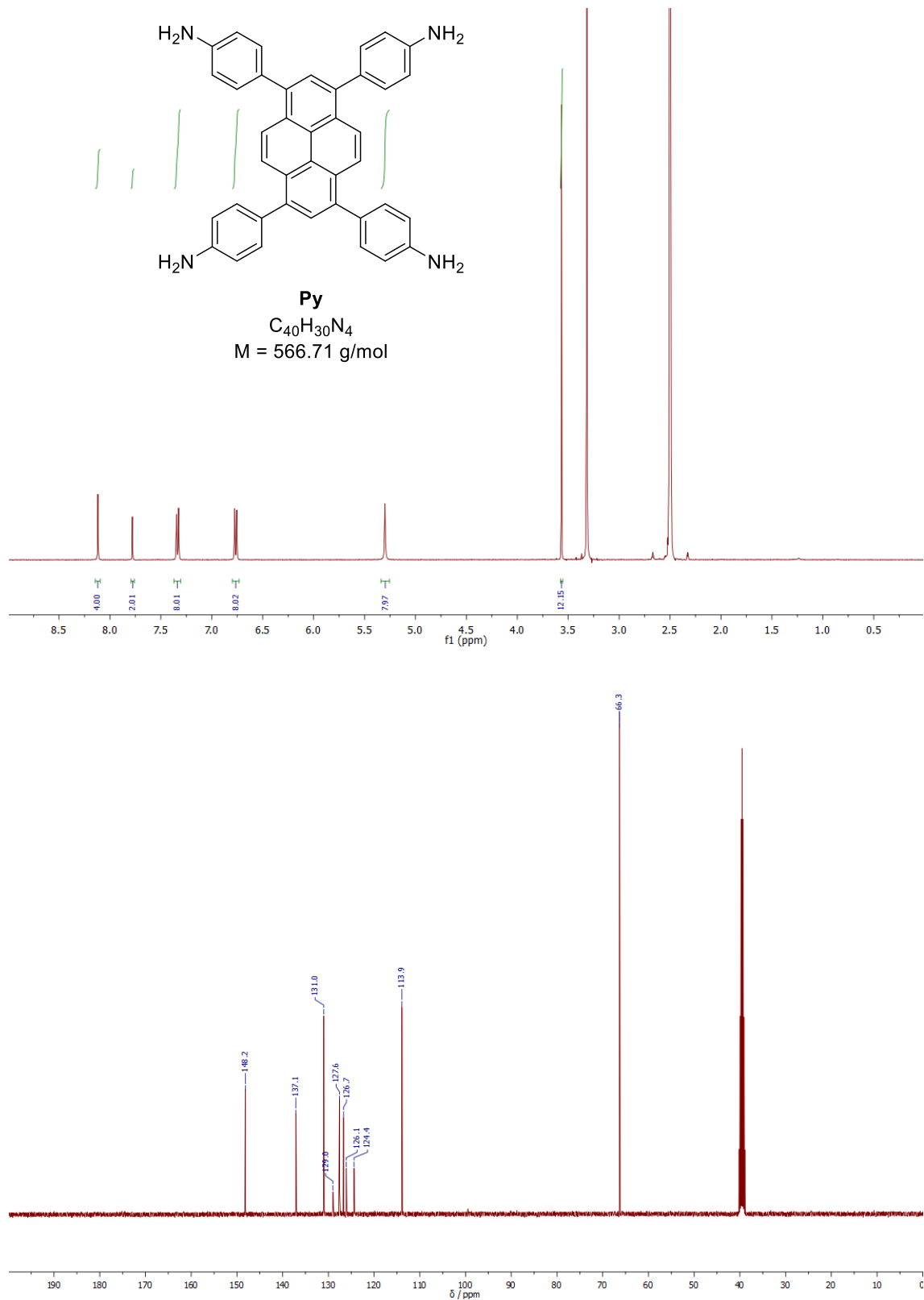


6 Extension of Oligothiophene Backbones in Covalent Organic Frameworks

a4T_{Bu}



Py



Section E – X-Ray diffractograms and refinements

We note that the oligothiophenes twist with nearly the same angle as the phenylene of the pyrene node. This results in a nearly planar bridge between adjacent pyrene nodes.

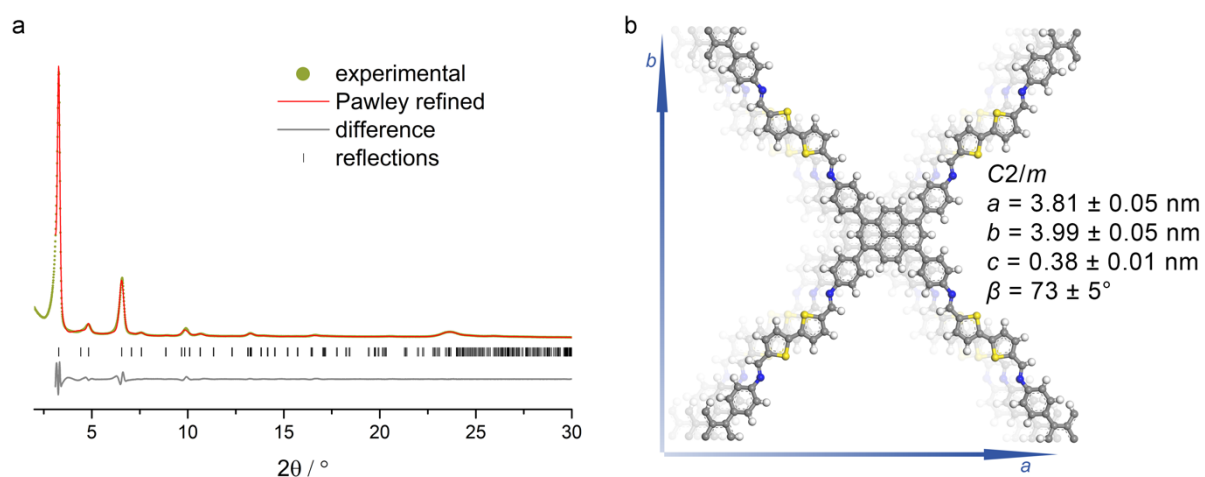


Figure 6.9. (a) Experimental PXRD data (light green dots) of Py-2T COF. Pawley refinement (red line) using the $C2/m$ symmetric structure model shown in (b) provides a very good fit to the experimental pattern with only minimal differences (grey line: difference between experimental and refined patterns; $R_{wp} = 8.2\%$, $R_p = 6.3\%$). Bragg positions are indicated by black ticks.

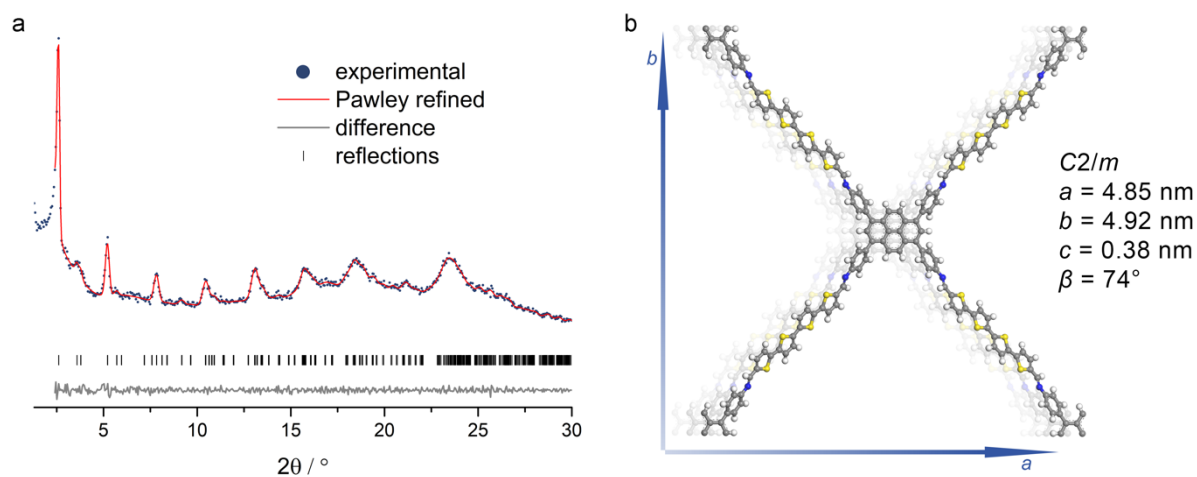


Figure 6.10. (a) Experimental PXRD data (blue dots) of Py-4T COF. Pawley refinement (red line) using the $C2/m$ symmetric structure model shown in (b) provides a very good fit to the experimental pattern with only minimal differences (grey line: difference between experimental and refined patterns; $R_{wp} = 3.5\%$, $R_p = 2.8\%$). Bragg positions are indicated by black ticks.

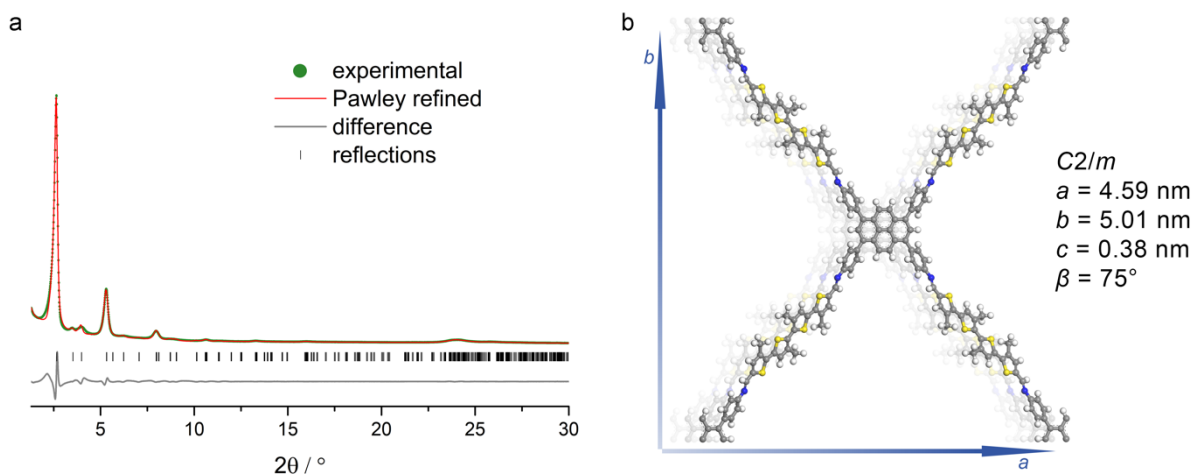


Figure 6.11. (a) Experimental PXRD data (green dots) of Py-4T_{Me} COF. Pawley refinement (red line) using the $C2/m$ symmetric structure model shown in (b) provides a very good fit to the experimental pattern with only minimal differences (grey line: difference between experimental and refined patterns; $R_{wp} = 10.2\%$, $R_p = 12.5\%$). Bragg positions are indicated by black ticks. The methyl groups of the a4T_{Me} building block were treated in the refinement as a superposition of both possible orientations with 50% occupancy each (both shown in the figure).

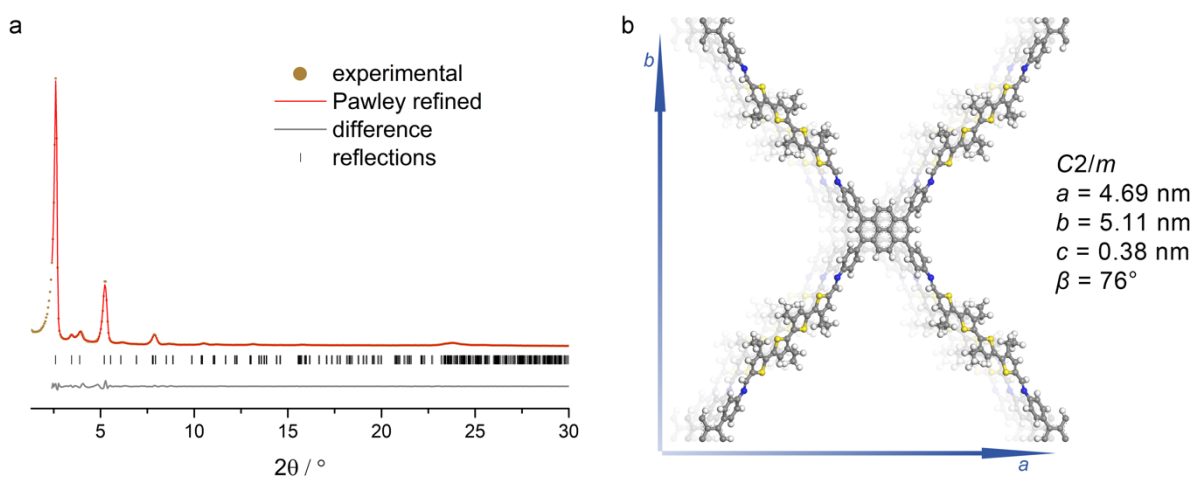


Figure 6.12. (a) Experimental PXRD data (brown dots) of Py-4T_{Et} COF. Pawley refinement (red line) using the $C2/m$ symmetric structure model shown in (b) provides a very good fit to the experimental pattern with only minimal differences (grey line: difference between experimental and refined patterns; $R_{wp} = 5.8\%$, $R_p = 3.9\%$). Bragg positions are indicated by black ticks. The alkyl chains of the a4T_{Et} building block were treated in the refinement as a superposition of both possible orientations with 50% occupancy each (both shown in the figure).

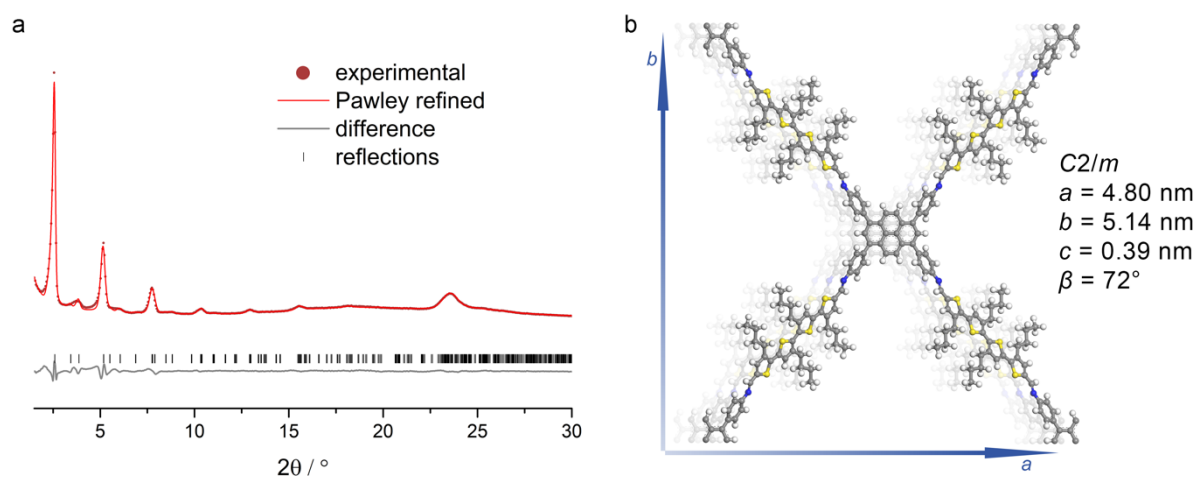


Figure 6.13. (a) Experimental PXRD data (red dots) of Py-4T_{Bu} COF. Pawley refinement (red line) using the $C2/m$ symmetric structure model shown in (b) provides a very good fit to the experimental pattern with only minimal differences (grey line: difference between experimental and refined patterns; $R_{wp} = 7.5\%$, $R_p = 13.4\%$). Bragg positions are indicated by black ticks. The alkyl chains of the a4T_{Bu} building block were treated in the refinement as a superposition of both possible orientations with 50% occupancy each (both shown in the figure).

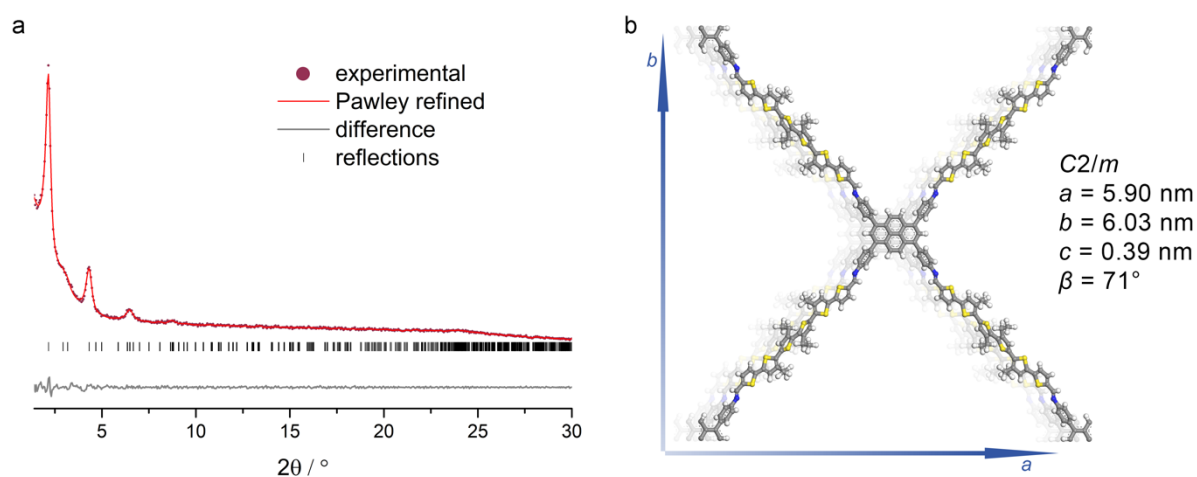


Figure 6.14. (a) Experimental PXRD data (dark red dots) of Py-6T_{Et} COF. Pawley refinement (red line) using the $C2/m$ symmetric structure model shown in (b) provides a very good fit to the experimental pattern with only minimal differences (grey line: difference between experimental and refined patterns; $R_{wp} = 3.2\%$, $R_p = 2.6\%$). Bragg positions are indicated by black ticks. The alkyl chains of the a6T_{Et} building block were treated in the refinement as a superposition of both possible orientations with 50% occupancy each (both shown in the figure).

Section F – UV-Vis and PL spectroscopy of the building blocks

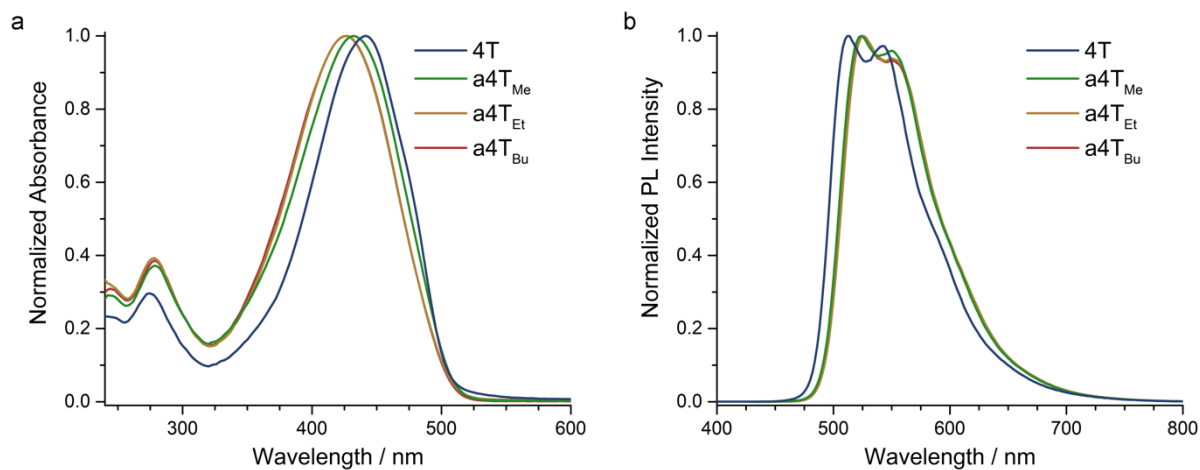


Figure 6.15. (a) Optical absorption spectra and (b) PL ($\lambda_{exc} = 378$ nm) spectra of the 4T monomers measured in solution (50 μ M in CHCl_3).

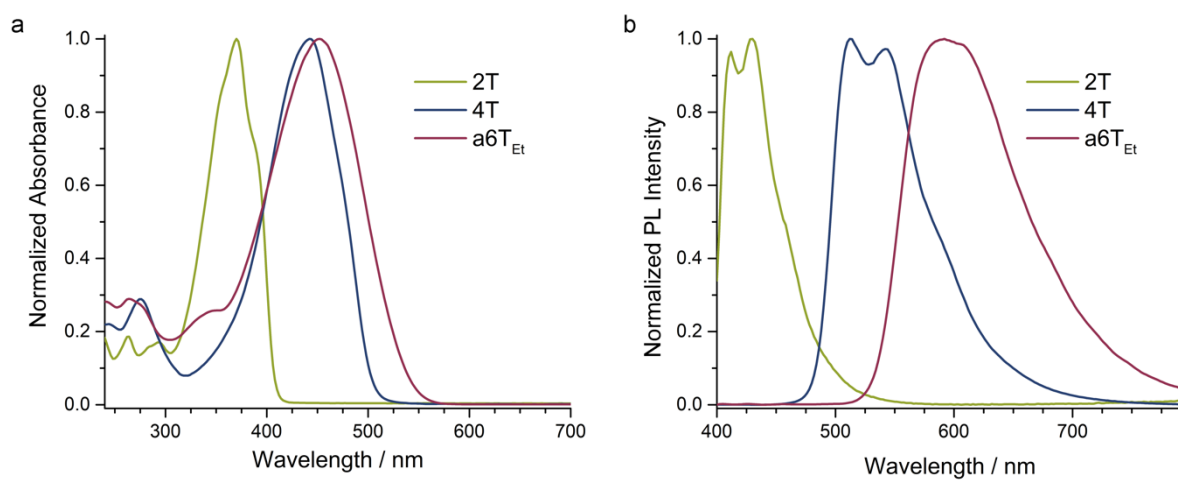


Figure 6.16. (a) Optical absorption spectra and (b) PL ($\lambda_{exc} = 378$ nm) spectra of 2T, 4T and a6T_{Et} monomers measured in solution (50 μ M in CHCl_3).

6 Extension of Oligothiophene Backbones in Covalent Organic Frameworks

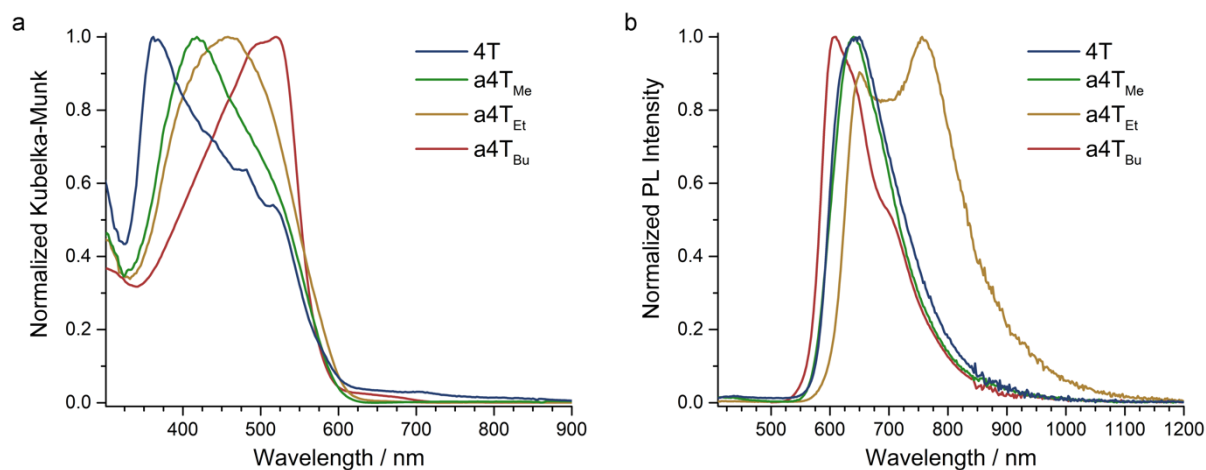


Figure 6.17. (a) Optical absorption spectra and (b) PL ($\lambda_{exc} = 378$ nm) spectra of the 4T monomers measured as solids. Diffuse reflectance spectra measured for the respective powders dispersed in BaSO₄.

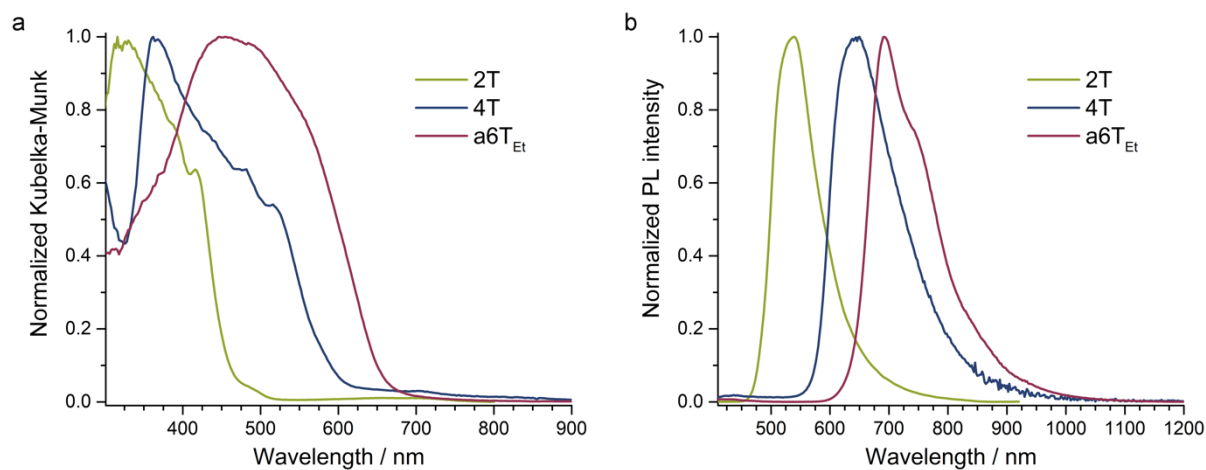


Figure 6.18. (a) Optical absorption spectra and (b) PL ($\lambda_{exc} = 378$ nm) spectra of 2T, 4T and a6T_{Et} monomers measured as solids. Diffuse reflectance spectra measured for the respective powders dispersed in BaSO₄.

Section G - PL spectroscopy of the COFs

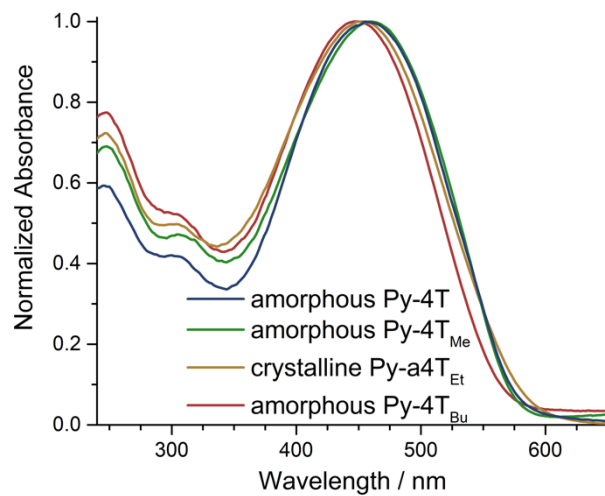


Figure 6.19. Optical absorption spectra of thin films of the 4T COF series. Since extensive screening did not result in crystalline and oriented thin films for all COFs, the spectra of Py-4T, Py-4T_{Me} and Py-4T_{Bu} were recorded from amorphous films.

Section H – TCSPC of the building blocks

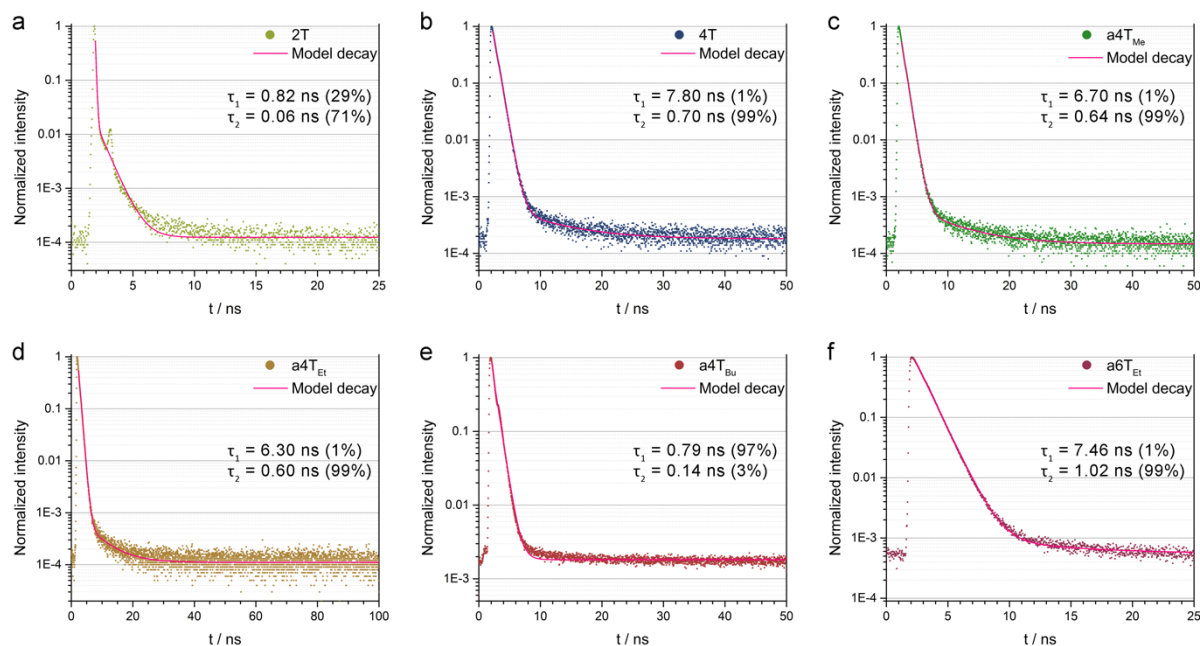


Figure 6.20. PL decay histograms of the monomers measured in solution (50 μM in CHCl_3). Excitation at 378 nm and emission recorded at the respective emission maximum. (a) 2T: emission at 430 nm. (b) 4T: emission at 512 nm. (c) a4T_{Me}: emission at 524 nm. (d) a4T_{Et}: emission at 526 nm. (e) a4T_{Bu}: emission at 525 nm. (f) a6T_{Et}: emission at 590 nm. Experimental decay: dots in respective color shown, bi-exponential fit of the decay: pink line.

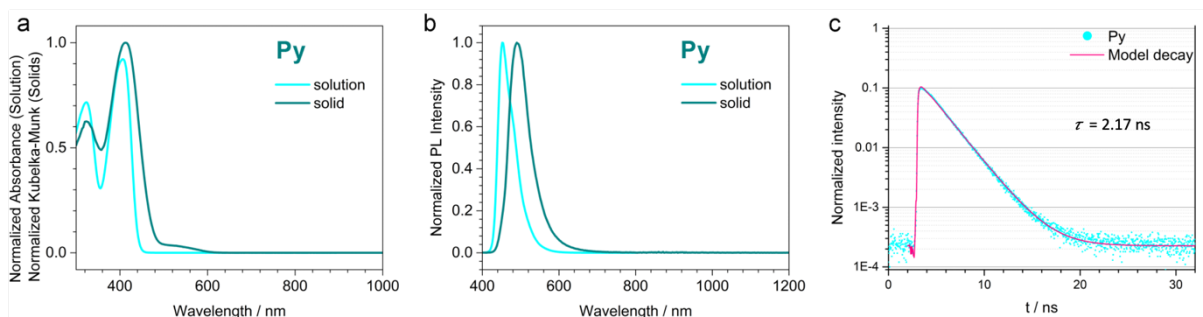


Figure 6.21. (a) Optical absorption spectra and (b) PL ($\lambda_{exc} = 378$ nm) spectra of the Py monomer measured in solution (50 μM in CHCl_3) and as solid.^[26] (c) PL decay histograms of Py measured in solution (50 μM in CHCl_3). Excitation at 378 nm and emission recorded at the emission maximum (455 nm). Experimental decay: dots in respective color, mono-exponential fit of the decay: pink line.

Section I – Transmission electron microscopy

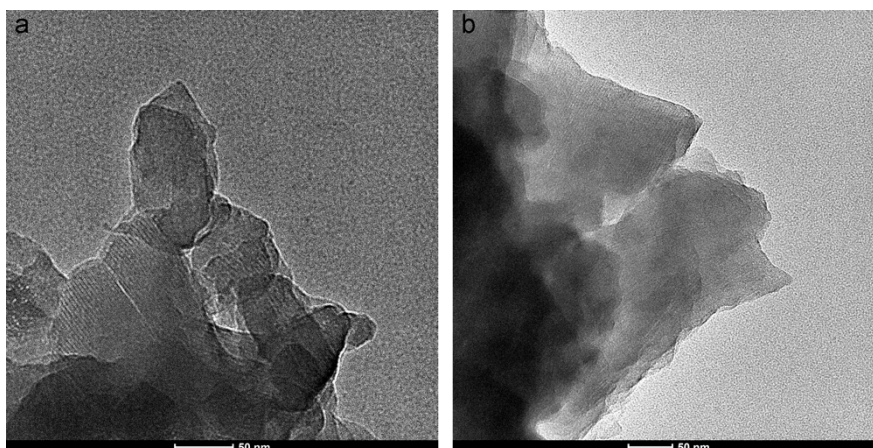


Figure 6.22. HRTEM images of the Py-4T COF bulk powder revealing periodic fringes of the crystalline domains.

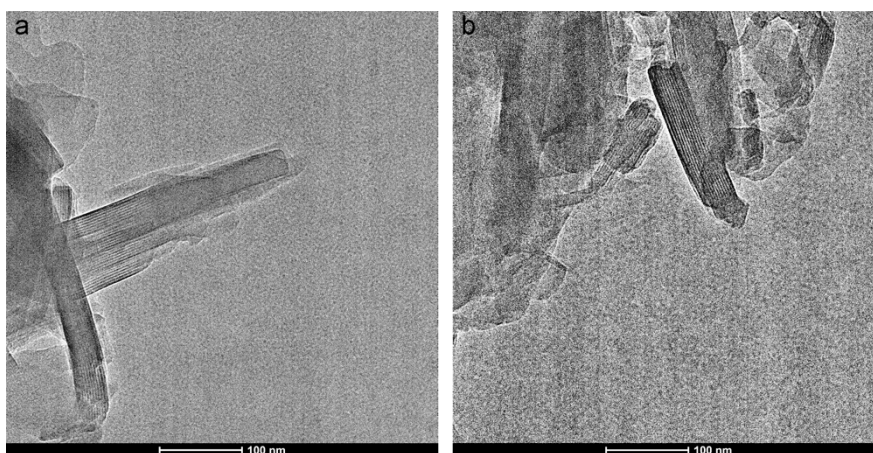


Figure 6.23. HRTEM images of the Py-4TEt COF bulk powder showing the lattice fringes of single crystallites.

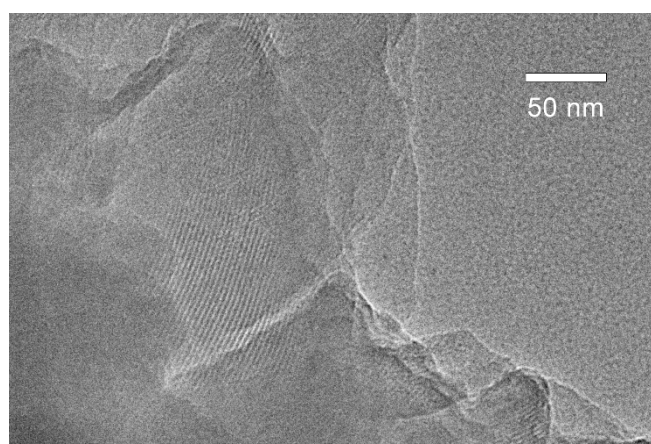


Figure 6.24. HRTEM images of the Py-4TBu COF bulk powder revealing ordered single crystallites with parallel-aligned lattice fringes.^[26]

Section J – Nitrogen sorption

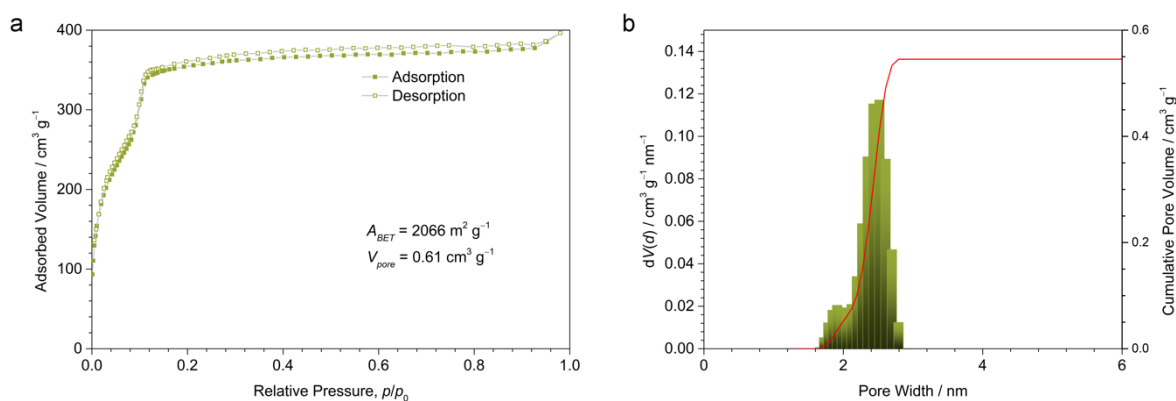


Figure 6.25. (a) Nitrogen sorption isotherms of the Py-2T COF recorded at 77 K. (b) QSDFT calculation using the adsorption branch and desorption branch yields a pore size distribution with the maximum at 2.5 nm with a tail to smaller pore width, in excellent agreement with the pore diagonal of 2.47 nm in the Py-2T structure model.

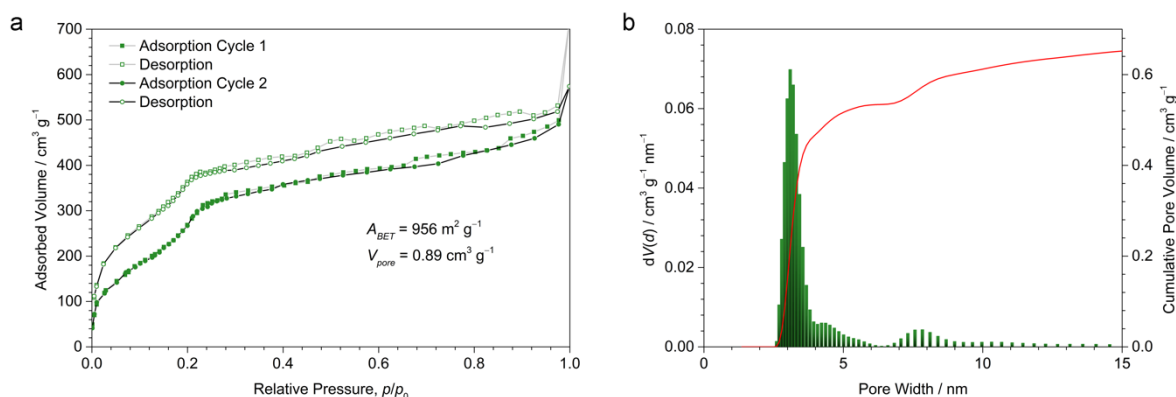


Figure 6.26. (a) Nitrogen sorption isotherms of Py-4T_{Me} COF recorded at 77 K. Two adsorption-desorption cycles were recorded using the same sample to test the stability of the framework. (b) QSDFT calculation using the adsorption branch yields a narrow pore size distribution with a maximum at 3.1 nm, in excellent agreement with the pore diagonal of 3.06 nm in the Py-4T_{Me} structure model.

The other oligothiophene-bridged COFs from the series were also investigated in terms of nitrogen sorption but it was not possible to generate reproducible data from these experiments. These issues have been observed in previous reports on oligothiophene-based COFs and are presumably attributed to the increased flexibility of backbones bearing longer alkyl chains. The respective COFs seem to be unstable towards the adsorption of probe molecules during the nitrogen sorption experiments, leading to inconsistent isotherms.^[26] Similarly, for the Py-4T COF without any alkyl chain modification, nitrogen sorption analysis did not produce reliable data. This can again be attributed to the increased interaction between the COF material and guest molecules, which can also be observed for the extraction with supercritical CO₂ leading to the loss of crystallinity and long-range order.

6.6 References

- [1] C. S. Diercks, O. M. Yaghi, *Science* **2017**, *355*, eaal1585.
- [2] J. W. Colson, W. R. Dichtel, *Nat. Chem.* **2013**, *5*, 453-465.
- [3] S. Patwardhan, A. A. Kocherzhenko, F. C. Grozema, L. D. A. Siebbeles, *J. Phys. Chem. C* **2011**, *115*, 11768-11772.
- [4] S. Jin, X. Ding, X. Feng, M. Supur, K. Furukawa, S. Takahashi, M. Addicoat, M. E. El-Khouly, T. Nakamura, S. Irle, S. Fukuzumi, A. Nagai, D. Jiang, *Angew. Chem. Int. Ed.* **2013**, *52*, 2017-2021.
- [5] G.-Y. Lee, J. Lee, H. T. Vo, S. Kim, H. Lee, T. Park, *Sci. Rep.* **2017**, *7*, 557.
- [6] S.-Y. Ding, W. Wang, *Chem. Soc. Rev.* **2013**, *42*, 548-568.
- [7] H. Furukawa, O. M. Yaghi, *J. Am. Chem. Soc.* **2009**, *131*, 8875-8883.
- [8] M. Dogru, M. Handloser, F. Auras, T. Kunz, D. Medina, A. Hartschuh, P. Knochel, T. Bein, *Angew. Chem. Int. Ed.* **2013**, *52*, 2920-2924.
- [9] L. Chen, K. Furukawa, J. Gao, A. Nagai, T. Nakamura, Y. Dong, D. Jiang, *J. Am. Chem. Soc.* **2014**, *136*, 9806-9809.
- [10] Q. Liao, C. Ke, X. Huang, G. Zhang, Q. Zhang, Z. Zhang, Y. Zhang, Y. Liu, F. Ning, K. Xi, *J. Mater. Chem. A* **2019**, *7*, 18959-18970.
- [11] J. Sun, X. Zhou, S. Lei, *Chem. Commun.* **2016**, *52*, 8691-8694.
- [12] S. Dalapati, M. Addicoat, S. Jin, T. Sakurai, J. Gao, H. Xu, S. Irle, S. Seki, D. Jiang, *Nat. Commun.* **2015**, *6*, 7786.
- [13] F. Haase, E. Troschke, G. Savasci, T. Banerjee, V. Duppel, S. Dörfler, M. M. J. Grundei, A. M. Burow, C. Ochsenfeld, S. Kaskel, B. V. Lotsch, *Nat. Commun.* **2018**, *9*, 2600.
- [14] P. J. Waller, Y. S. AlFaraj, C. S. Diercks, N. N. Jarenwattananon, O. M. Yaghi, *J. Am. Chem. Soc.* **2018**, *140*, 9099-9103.
- [15] L. Stegbauer, K. Schwinghammer, B. V. Lotsch, *Chem. Sci.* **2014**, *5*, 2789-2793.
- [16] T. Sick, A. G. Hufnagel, J. Kampmann, I. Kondofersky, M. Calik, J. M. Rotter, A. Evans, M. Döblinger, S. Herbert, K. Peters, D. Böhm, P. Knochel, D. D. Medina, D. Fattakhova-Rohlfing, T. Bein, *J. Am. Chem. Soc.* **2018**, *140*, 2085-2092.
- [17] E. L. Spitler, J. W. Colson, F. J. Uribe-Romo, A. R. Woll, M. R. Giovino, A. Saldivar, W. R. Dichtel, *Angew. Chem. Int. Ed.* **2012**, *51*, 2623-2627.
- [18] L. Ascherl, T. Sick, J. T. Margraf, S. H. Lapidus, M. Calik, C. Hettstedt, K. Karaghiosoff, M. Döblinger, T. Clark, K. W. Chapman, F. Auras, T. Bein, *Nat. Chem.* **2016**, *8*, 310-316.

- [19] M. D. Irwin, D. B. Buchholz, A. W. Hains, R. P. H. Chang, T. J. Marks, *Proc. Natl. Acad. Sci. U.S.A.* **2008**, *105*, 2783-2787.
- [20] K. Cnops, B. P. Rand, D. Cheyns, B. Verreet, M. A. Empl, P. Heremans, *Nat. Commun.* **2014**, *5*, 3406.
- [21] B. Kan, M. Li, Q. Zhang, F. Liu, X. Wan, Y. Wang, W. Ni, G. Long, X. Yang, H. Feng, Y. Zuo, M. Zhang, F. Huang, Y. Cao, T. P. Russell, Y. Chen, *J. Am. Chem. Soc.* **2015**, *137*, 3886-3893.
- [22] G. H. V. Bertrand, V. K. Michaelis, T.-C. Ong, R. G. Griffin, M. Dincă, *Proc. Natl. Acad. Sci. U.S.A.* **2013**, *110*, 4923-4928.
- [23] D. D. Medina, V. Werner, F. Auras, R. Tautz, M. Dogru, J. Schuster, S. Linke, M. Döblinger, J. Feldmann, P. Knochel, T. Bein, *ACS Nano* **2014**, *8*, 4042-4052.
- [24] C. R. Mulzer, L. Shen, R. P. Bisbey, J. R. McKone, N. Zhang, H. D. Abruña, W. R. Dichtel, *ACS Cent. Sci.* **2016**, *2*, 667-673.
- [25] Y. Wu, D. Yan, Z. Zhang, M. M. Matsushita, K. Awaga, *ACS Appl. Mater. Interfaces* **2019**, *11*, 7661-7665.
- [26] N. Keller, D. Bessinger, S. Reuter, M. Calik, L. Ascherl, F. C. Hanusch, F. Auras, T. Bein, *J. Am. Chem. Soc.* **2017**, *139*, 8194-8199.
- [27] F. Auras, L. Ascherl, A. H. Hakimoun, J. T. Margraf, F. C. Hanusch, S. Reuter, D. Bessinger, M. Döblinger, C. Hettstedt, K. Karaghiosoff, S. Herbert, P. Knochel, T. Clark, T. Bein, *J. Am. Chem. Soc.* **2016**, *138*, 16703-16710.
- [28] D. Bessinger, L. Ascherl, F. Auras, T. Bein, *J. Am. Chem. Soc.* **2017**, *139*, 12035-12042.
- [29] R. Lin, M. Galili, U. J. Quaade, M. Brandbyge, T. Bjørnholm, A. D. Esposti, F. Biscarini, K. Stokbro, *J. Chem. Phys.* **2002**, *117*, 321-330.
- [30] J. Yang, S. Liu, J.-F. Zheng, J. Zhou, *Eur. J. Org. Chem.* **2012**, *2012*, 6248-6259.
- [31] S. Jin, T. Sakurai, T. Kowalczyk, S. Dalapati, F. Xu, H. Wei, X. Chen, J. Gao, S. Seki, S. Irle, D. Jiang, *Chem. Eur. J.* **2014**, *20*, 14608-14613.

7 Highly Crystalline and Fully Conjugated 3D Cyclooctatetrathiophene-based Covalent Organic Frameworks as Bulk and Thin Film Materials

This chapter is based on the following manuscript:

Derya Bessinger,[‡] Stephan Reuter,[‡] Ignacio Muñoz Alonso, Niklas Keller, Marcella Günther, Dana Medina, and Thomas Bein*

to be submitted

[‡] These authors contributed equally.

7.1 Abstract

While a large number of two-dimensional, conjugated covalent organic frameworks (COFs) have been developed in recent years, access to fully conjugated three-dimensional covalent organic frameworks (COFs) has been challenging. Such fully conjugated 3D COFs present an intriguing goal due to their expected advantages of extended electron delocalization throughout the whole framework, which could be enabling for diverse applications in optoelectronics. To address this challenge, a new extended pseudo-tetrahedral node based on cyclooctatetrathiophene (COTh), which consists of a saddle-shaped annulene skeleton with 8 π -electrons, was recently used for the synthesis of fully conjugated 3D COFs. We have developed a novel compact derivative of the COTh building block with functional groups directly attached to the fused thiophenes of the core. Implementing a modulation approach with mono-functionalized inhibitors yielded the novel COTh-1P COF with remarkable crystallinity and permanent porosity. Transferring the elaborated modulation strategy and improved synthesis conditions to the solvothermal growth of thin films produced the first preferentially oriented conjugated 3D COF films on various substrates without prior surface modification. Conductivity measurements of these films resulted in room temperature conductivities of around $9 \times 10^{-6} \text{ S cm}^{-1}$. The synthesis of crystalline and oriented films of fully π -conjugated COTh-based COFs is expected to encourage future research regarding the optoelectronic properties of fully conjugated 3D COFs.

7.2 Introduction

Linking rigid organic building blocks in condensation reactions according to the principle of reticular chemistry defines a new category of materials with open porous frameworks. The so-formed covalent organic frameworks (COFs) can either be two-^[1-3] or three-dimensional^[4, 5] depending on the selection of the molecular precursors and the resulting topologies.

Since the pioneering discovery of three-dimensional covalent organic frameworks (COFs) by Yaghi and co-workers in 2007,^[6] the field of 3D COFs has increasingly gained in importance due to their broad applicability and intriguing properties. For example, these porous and chemically stable frameworks have been utilized in the fields of gas storage and separation,^[7-10] dye removal,^[11, 12] ion exchange,^[12, 13] drug delivery,^[14] and catalysis.^[15-17] Most of the building blocks of 3D COFs comprise tetrahedral nodes, such as tetraphenylmethane,^[6, 18] tetraphenylsilane,^[7, 19] and adamantane,^[15, 20] which are linked to multidentate counterparts of

various geometries leading to frameworks of different topologies. However, these tetrahedral cores with sp^3 -hybridized carbon or silicon atoms are not fully π -conjugated, thereby disrupting electron delocalization and thus limiting their potential use in optoelectronics. In order to overcome these limitations and to construct a fully conjugated 3D network, the pseudo-tetrahedral cyclooctatraphiophene (COTh) node with an sp^2 carbon-conjugated structure was recently integrated into COFs.^[21-23] The saddle-shaped building block was initially reported by Kauffmann *et al.* in 1978^[24] and has been further investigated.^[25-28] COTh exhibits a central [8]annulene as a non-planar 8π -conjugated skeleton formed by four thiophenes fused at the 2- and 3-positions. The saddle shape of COTh was confirmed by single crystal X-ray analysis,^[29-31] which renders this and related molecules promising new building units for the development of fully conjugated COFs.

While COTh-based building blocks have been integrated into first 3D COFs (in powder form) showing high electron mobility values but moderate conductivity,^[21, 22] the development of preferentially oriented thin films has not been addressed yet. However, transferring the intriguing features of fully conjugated 3D COTh-COFs to well-defined thin films is key for exploring potential optoelectronic applications in devices.

Growing COFs as oriented thin films already enabled their implementation as the active material in various applications for 2D COFs, such as photovoltaics,^[32-34] watersplitting,^[35] photodetection,^[36] acidochromism,^[37] solvatochromism,^[38] and electrochromism.^[39] However, preferentially oriented thin films of conjugated 3D COFs have not been reported to date. Furthermore, the few existing 3D COF membranes on substrates are mainly fabricated with functionalized substrate surfaces bearing functional groups for COF growth.^[40, 41] Since many electrochemical and electronic applications require direct contact of COF material with strong electronic connectivity to a conductive surface, oriented growth of ordered structures on non-functionalized substrates would be highly desirable.

One of the great merits of crystalline COFs is the ability to define and control their structure with atomic precision. Since the functionality of COFs is often strongly dependent on their degree of order, it is highly desirable to adjust the reaction conditions in a way that a controlled and nearly defect-free crystal growth is possible. Many applications that require a highly-ordered and open porous structure, e.g. in the field of gas separation and storage,^[8, 42, 43] catalysis,^[44, 45] filtration,^[46] sensors,^[37, 47] electrochromism,^[39] and optoelectronics,^[34, 48-50] are affected by the structural definition and defect density of their active COF materials.

In order to better control the morphology and improve the crystallization processes of COFs, so-called modulating agents have been added to the synthesis.^[5] These mono-functionalized

modulators dynamically end-cap the COF growth and compete with the multifunctional constituents of the framework during the formation process and therefore decelerate the crystal growth rate. The slowed COF formation in combination with facilitated defect correction processes ultimately decreases the fraction of precipitated amorphous components and increases the controlled growth of well-ordered and highly crystalline domains or even single crystals. This modulation approach was already successfully applied in the syntheses of two- and three-dimensional COFs and showed a strongly positive effect on the crystallinity of the respective COFs.^[5, 51-53] Alternatively, controlled nucleation was also employed in a seeded growth approach to produce single-crystalline 2D COFs.^[54] Here, the slow addition of monomers to preformed nanoparticles in a second polymerization step increased the single crystal domain size, emphasizing the importance of controlled COF formation.

In this work, we developed highly crystalline 3D COFs with incorporated sp^2 carbon-conjugated COTh building blocks serving as pseudo-tetrahedral nodes. In addition to extended building blocks with bridging phenylene moieties attached to the core, we designed a smaller version of the COTh building block with the functional groups required for the COF imine bond formation directly fused to the four thiophenes of the [8]annulene core, producing compact and fully conjugated 3D frameworks with reduced flexibility. We then transferred the modulation approach to the solvothermal 3D COF thin film fabrication in order to slow down the nucleation rate, impede the fast precipitation of bulk material and therefore promote the controlled growth of crystalline COF on the substrate surface. This led to the first preferentially oriented and conjugated 3D COF films on various substrates showing promising electrical characteristics.

7.3 Results and Discussion

For the construction of the sp^2 carbon-conjugated 3D COFs, two different variants of tetrahedral COTh building blocks were synthesized. The shorter version COTh(CHO)₄ with the formyl groups directly fused to the thiophenes of the core and an extended version COTh(P-NH₂)₄ which is amine-functionalized by attaching aniline groups at the C2 positions of the core. These terminal aldehyde and amine functionalities enable the reversible imine bond formation during the COF syntheses, respectively.

The saddle-shaped building blocks were generated by different synthetic pathways (SI, Figures 7.4 and 7.5). Both start from di- or tetrabrominated bithiophenes which are then protected at the α -positions and fused at the vacant bromine-positions via cyclodimerization. For COTh(P-NH₂)₄, 3,3'-dibromo-2,2'-bithiophene was treated with lithium diisopropylamide to attach trimethyl-silane protecting groups at the 5-positions, yielding compound **1**.^[55] Following the literature procedure, the addition of *n*-BuLi and anhydrous copper(II) chloride yielded the central trimethylsilyl (TMS)-protected COTh core (**2**).^[56] Subsequent selective bromination using *N*-bromosuccinimide (NBS) yielded the 2,5,8,11-tetrabromo-cyclooctatetrathiophene (**3**) followed by a four-fold Suzuki cross-coupling reaction with 4-(4,4,5,5-tetramethyl-1,3,2-dioxaborolan-2-yl)aniline, successfully generating COTh(P-NH₂)₄ in a four-step protocol with sufficient yields overall. The synthesis of the shorter COTh(CHO)₄ variant was also conducted in a four-step protocol, starting with selective formylation of 3,3',5,5'-tetrabromo-2,2'-bithiophene in the presence of *n*-BuLi, yielding compound **4**.^[57] Acetal protection of the aldehyde groups via neopentyl glycol produced compound **5** and allowed for the formation of the central acetal-protected COTh motif (**6**) that was then deprotected with trifluoroacetic acid thus affording the novel tetra-aldehyde building block COTh(CHO)₄ in overall good yields. The successful synthesis and purity of both building blocks was confirmed by ¹H NMR (see the SI, Section C).

The chemical diversity introduced by the straightforward condensation of aldehydes and primary amines, forming imine bonds between respective building blocks, allows for the combination of the tetrahedral node with a variety of complementary counterparts. Therefore, both COTh-based building blocks were imine-linked to linear para-substituted benzene rings or a modified benzene unit with incorporated methoxy-groups at the 2- and 5-positions (Figure 7.1).

7 Highly Crystalline and Fully Conjugated 3D Cyclooctatetrathiophene-based Covalent Organic Frameworks as Bulk and Thin Film Materials

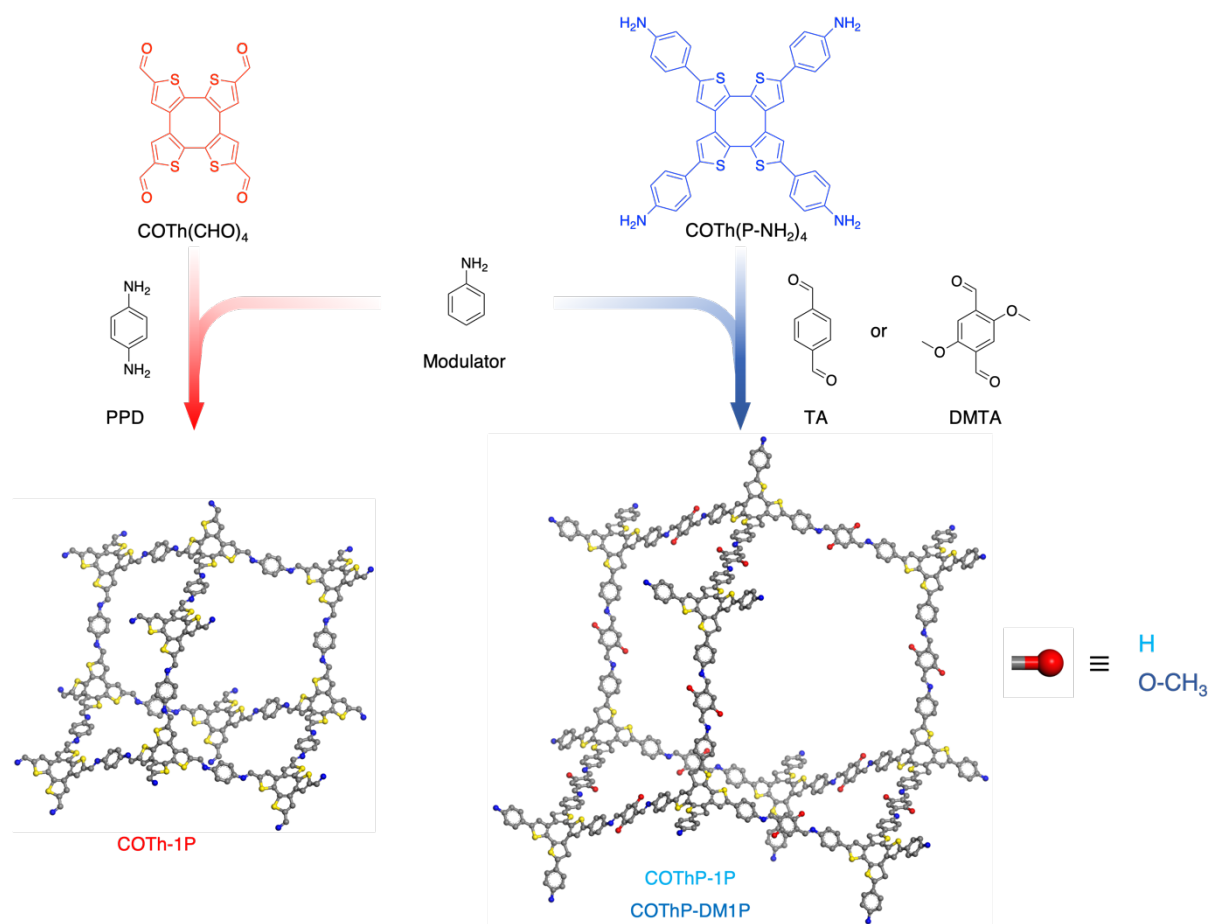


Figure 7.1. Synthesis of the new COTh-based COFs. The co-condensation of the tetrahedral building blocks $\text{COTh}(\text{CHO})_4$ or $\text{COTh}(\text{P-NH}_2)_4$ with p -phenylenediamine (PPD), terephthalaldehyde (TA) or 2,5-dimethoxyterephthalaldehyde (DMTA) led to the 3D COTh-1P, COThP-1P, and COThP-DM1P COFs, respectively. To enhance the crystallinity, the COF growth was controlled by adding the mono-functionalized modulator aniline to the synthesis. The resulting frameworks crystallize in the diamond topology and are constructed from interpenetrated adamantane-like cages (color scheme: C grey, S yellow, N blue).

The 3D COFs were synthesized via acid-catalyzed polycondensation of $\text{COTh}(\text{P-NH}_2)_4$ and terephthalaldehyde (TA) or 2,5-dimethoxyterephthalaldehyde (DMTA) in a 1:2 molar ratio, yielding the red-colored COThP-1P and COThP-DM1P COFs, respectively (Figure 7.1). Similar solvothermal conditions yielded the COTh-1P COF as a red powder by co-condensation of the $\text{COTh}(\text{CHO})_4$ and p -phenylenediamine (PPD) building units in a 1:2 molar ratio. In order to enhance the crystallinity of our new framework materials, we added mono-functionalized benzene molecules, i.e. aniline, as modulator to the COF synthesis. The best results were achieved by first partially dissolving the modulator and the corresponding aldehyde-containing counterpart in benzyl alcohol solvent and then adding the acetic acid at room temperature. Subsequently, the second building block of the final framework was added and the sealed reaction tube was exposed to solvothermal conditions at 120 °C. We assume that this modulation technique slows down the COF formation, thus enhancing error corrections.^[58] It

hereby favors the thermodynamic equilibrium state and helps to avoid kinetic traps,^[52] supporting the controlled crystal growth of the COF. Indeed, the high crystallinity of all three COTh-based COFs synthesized with this modulation approach could be validated by powder X-ray diffraction (PXRD) showing several high-intensity reflections, especially towards lower diffraction angles (Figure 7.2a and SI, Figures 7.6a, 7.7a). The well-defined reflections in the higher-order range of the X-ray diffractograms and the absence of visible amorphous background confirm the highly ordered periodic structure. Research on employing aniline as a modulator in the synthesis of imine-linked 3D COFs already showed significant impact regarding control of crystallization.^[5] Here, the COF nucleation is slowed down and dynamic reversible processes are enhanced by the monofunctional reaction competitor that moderates fast imine formation by the multi-functional building units that could otherwise lead to precipitated amorphous or disordered material. Specifically, the excess of added amine monomers increases the concentration of amines in the reaction and thus the overall reversibility of the imine-bond formation during COF synthesis. This ultimately promotes defect correction during framework construction and therefore improves the crystal growth of the COFs. The enhanced crystallinity is distinctly visible when directly comparing the PXRD data of the two synthetic approaches with and without modulator for the COThP-1P COF (SI, Figure 7.15). While the PXRD pattern of the COF obtained via the synthesis method with a modulator shows several sharp reflections and only weak background, the XRD of the COF synthesized without a modulator indicates a low degree of order and a large amount of amorphous material. The loss of crystallinity is clearly visible for the 200-reflection at $2\theta = 3.8^\circ$ showing a drastically decreased intensity compared to the COF obtained via the modulator-containing synthesis. Furthermore, long-range order reflections at higher angles are hardly identifiable in the overall strong background, highlighting the influence of the modulator on the crystal growth.

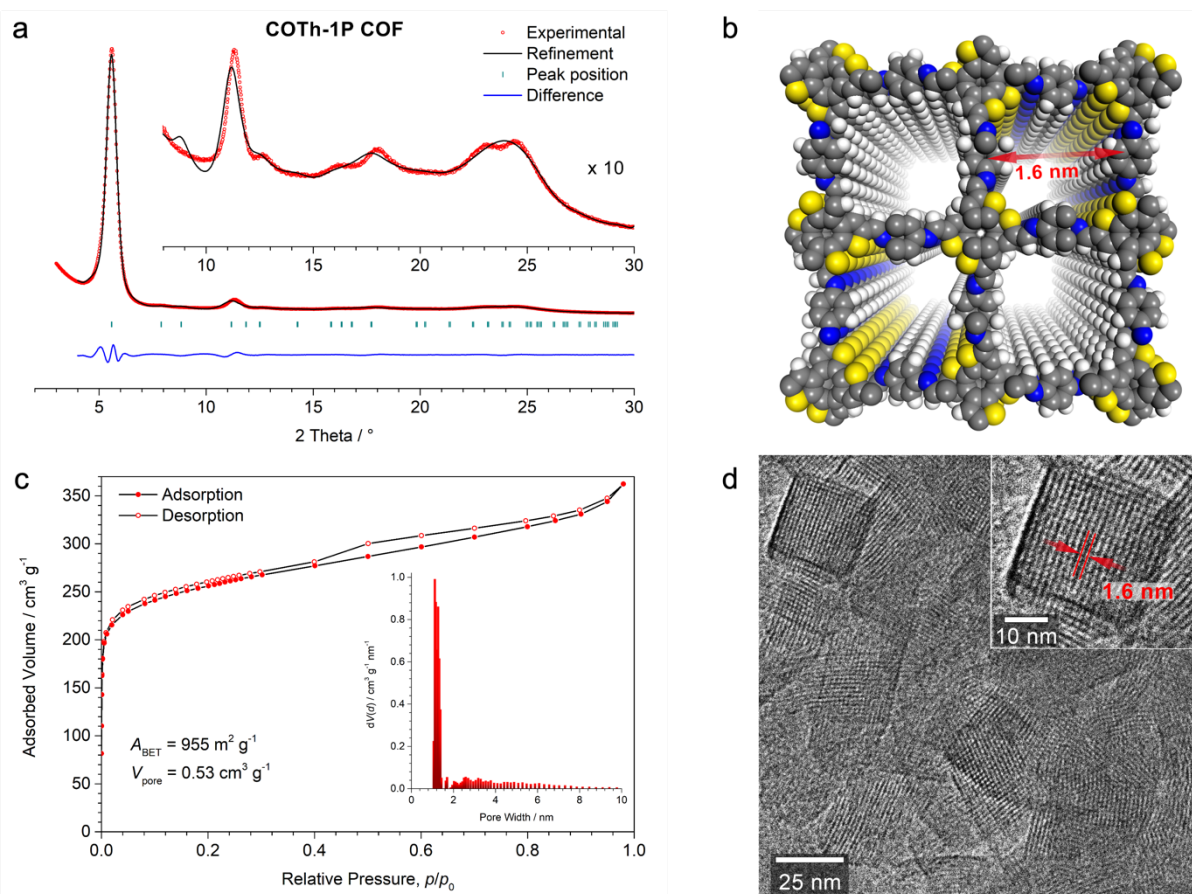


Figure 7.2. Structural characterization of the COTh-1P COF. (a) Experimental PXRD pattern of the COF bulk material (red dots) and Rietveld refinement (black line) using a structure model in the tetragonal $I4_122$ space group. The peak positions are indicated by cyan ticks and the difference plot (blue line) shows an overall good fit between the experimental and refined data ($R_{wp} = 4.82\%$ and $R_p = 3.69\%$). Inset: tenfold magnification of the $8^\circ < 2\theta < 30^\circ$ region. (b) Refined COF structure simulation with a diamond topology showing square-shaped pores when viewed along the c -axis and exhibiting a sevenfold interpenetration ($dia-c7$). (c) Type Ib nitrogen sorption isotherm recorded at 77 K with the NLDFT-based pore size distribution modeled for cylindrical pores showing its maximum at 1.1 nm, which corresponds very well to the simulated average pore distance of 1.2 nm. (d) High-resolution TEM image of the polycrystalline powder. Inset: A well-ordered single crystallite oriented with view along the pore channels in c -direction shows the square-shaped pores and a periodicity of 1.6 nm in excellent agreement with the simulated periodicity of the refined structure (red arrows).

The formation of a highly ordered structure of the novel 3D COTh-1P COF based on the tetrahedral COTh core unit was confirmed by PXRD (Figure 7.2a) and enabled a Rietveld refined structure model with a sevenfold interpenetrated diamond topology ($dia-c7$) (Figure 7.2b and SI, Figure 7.16). The refinement using a tetragonal structure model with $I4_122$ symmetry produces the lattice parameters $a = b = 31.7 \text{ \AA}$, $c = 3.59 \text{ \AA}$ and $\alpha = \beta = \gamma = 90^\circ$. With view along the c -axis, the interweaved diamond net shows square-shaped 1D pore channels with a simulated periodicity of 1.6 nm (Figure 7.2b).

Nitrogen sorption measurements conducted at 77 K confirmed the accessibility of the microporous COTh-1P, revealing a type Ib isotherm with a steep uptake below $p/p_0 = 0.05$ and a Brunauer-Emmett-Teller (BET) surface area of $955 \text{ m}^2 \text{ g}^{-1}$ with a total pore volume of

$0.53 \text{ cm}^3 \text{ g}^{-1}$. The pore size distribution was determined using the nonlocal solid density functional theory (NLDFT) for cylindrical pores and showed a peak pore diameter of 1.1 nm matching the simulated average pore dimension of 1.2 nm.

High-resolution transmission electron microscopy (TEM) images of the polycrystalline COF bulk material show the formation of highly textured crystallites with a size of around 25 nm (Figure 7.2d). Evaluation of a single COF domain with its 1D rectangular pores oriented along the viewing direction reveals a periodicity of 1.6 nm, which is in excellent agreement with the periodicity of the simulated structure model.

The larger COTh-based building block, COTh(P-NH₂)₄, produced the COThP-1P and COThP-DM1P COFs with comparable crystallinity (see the SI, Section E). Compared to the compact COTh-1P COF, the pore dimensions are expected to be larger due to the extended tetrahedral node containing additional phenylene groups between the functional amine groups and the COTh core. The pore sizes experimentally determined via nitrogen sorption corroborate our expectation. The pore size distributions evaluated from the type Ib sorption isotherms by NLDFT calculations show different maxima at 1.9 nm and 1.6 nm for the COThP-1P and COThP-DM1P COF, respectively. The decrease in pore size for the COThP-DM1P is attributed to the attached methoxy side chains which extend into the pores, following the trend observed for previous isostructural 2D and 3D COFs.^[59, 60] The anticipated similar periodicity of both extended COFs, only differing in the methoxy functional groups attached to the same backbone, is confirmed by TEM images of COThP-1P and COThP-DM1P, each showing the porous structure of the polycrystalline bulk materials (Figures 7.6 and 7.7). Refined structure simulations of the extended 3D COFs will help to support the experimental findings and are the aim of future work.

Next, we explored the growth of thin films of the conjugated 3D COFs. The improved nucleation control during the solvothermal synthesis by the modulation approach allowed for the fabrication of homogenous and preferentially oriented 3D COTh-1P COF thin films on various substrates. The modulator again decreases the nucleation rate and slows down the COF formation which reduces the amount of material that would otherwise precipitate quickly and could thus not be deposited as crystalline COF material on the substrate surface. The mono-functionalized inhibitor was added to the synthesis batch prior to the insertion of the substrate with the to-be-coated surface face-down in a polytetrafluoroethylene (PTFE) holder (see the SI, Section D for experimental details). In contrast to previously reported 3D COF thin films,^[40, 61] the substrates do not require modification of the surface for a homogeneously grown COF layer

with controllable and constant thickness. This establishes new possibilities to construct 3D COF coatings on specific substrates required for different applications. We have therefore grown the COF on three substrates, i.e. fused silica, indium tin oxide (ITO), and partially coated ITO, where a part of the ITO coating is chemically etched off, that were then characterized with optical, electrochemical, and electronic measurements (see below). After the solvothermal synthesis, all substrates are covered with homogeneously grown, crystalline COF thin films with a preferential orientation that is confirmed by grazing-incidence wide angle X-ray scattering (GIWAXS, Figure 7.3a). With the intensity maximum at around $q_z = 4.5 \text{ nm}^{-1}$, the GIWAXS pattern indicates a preferentially oriented crystalline film.

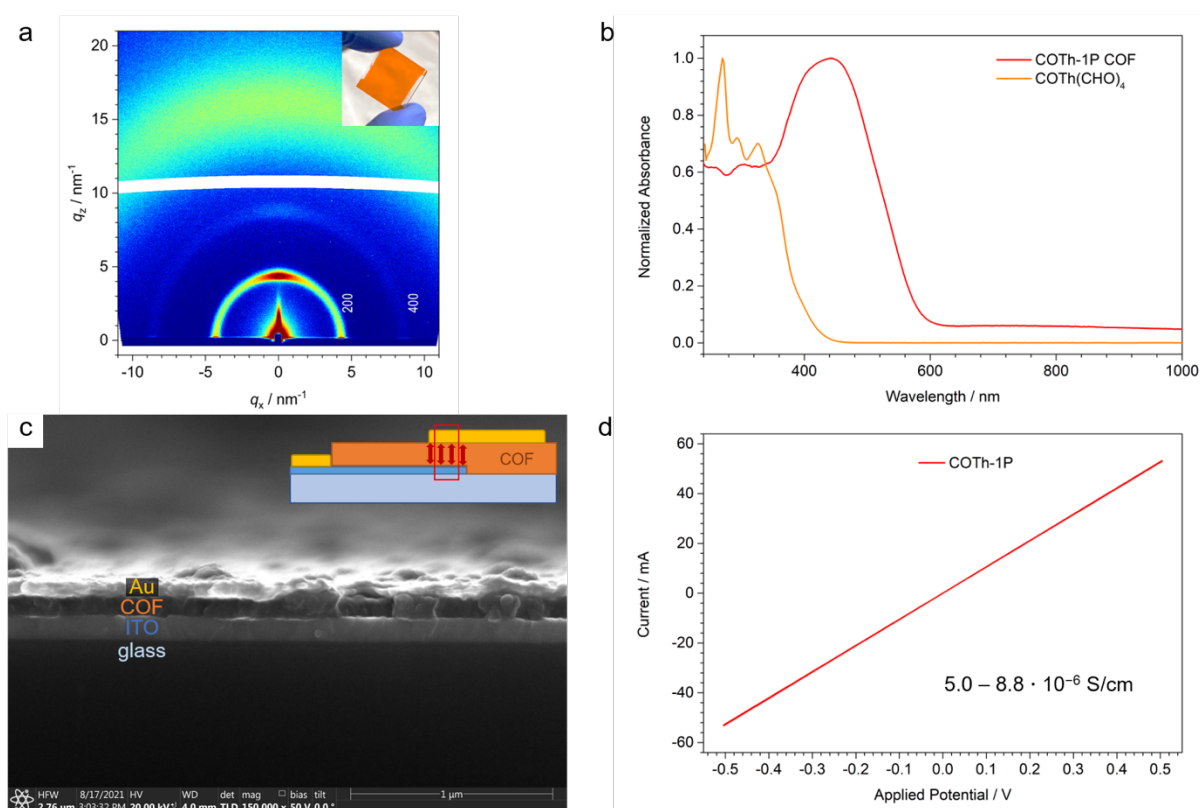


Figure 7.3. Fabrication of COTh-1P thin films. (a) GIWAXS pattern of a COTh-1P film grown on fused silica with the intensity maximum at $q_z = 4.5 \text{ nm}^{-1}$, indicating a preferentially oriented thin film. Inset: Photographic picture of the COTh-1P thin film on a fused silica substrate. (b) UV-Vis absorption spectra of the COTh(CHO)₄ building block (orange) and the COTh-1P COF film (red). The distinctly red-shifted absorption of the COF indicates the successful incorporation of the building block leading to increased electronic conjugation. (c) Cross-sectional SEM image of the COTh-1P device applied for the electrical conductivity measurements. The inset at the top right illustrates its architecture with a 100 nm COF film (orange) grown on partially covered ITO (dark blue)/glass (light blue) substrates. Gold contacts (yellow) with a thickness of 50 nm were evaporated on top of the COF and the ITO. The measuring range and direction is indicated by red arrows. The red box visualizes the segment that is shown on the SEM image which clearly reveals the different layers. (d) $I-V$ curve of the COTh-1P device cycled between -0.5 and $+0.5 \text{ V}$ applied potential. The linear $I-V$ curve indicates an ohmic behavior with conductivities of up to $8.8 \times 10^{-6} \text{ S/cm}$.

Optical characterization via UV-Vis and photoluminescence (PL) measurements shows a broad optical absorption band of the COTh-1P COF with a maximum at 445 nm and a Stokes-shifted PL peak at 716 nm (see the SI, Section F). Comparing the absorption spectra of the COTh(CHO)₄ building block and the COTh-1P COF, a distinct bathochromic shift of the COF absorption is noticeable following the electronic integration into the ordered and conjugated COF structure (Figure 7.3b). The COF's optical band gap was estimated to be 2.32 eV from the absorption onset via Tauc plot for a direct transition (SI, Figure 7.10c).

Top-view and cross-sectional scanning electron microscopy (SEM) images confirm the homogeneous growth of a 100 nm COF thin film on top of the substrate. (SI, Figure 7.14).

Cyclic voltammetry (CV) measurements of the COTh-1P COF thin film were conducted with a three-electrode-setup. The COF was grown on a conductive ITO substrate that was then applied as the working electrode. In our system, a platinum and a silver wire functioned as the counter electrode and the quasi-reference electrode, respectively, and 0.1 M tetrabutylammonium hexafluorophosphate (TBAPF₆) in acetonitrile was used as the electrolyte. The CV curves were recorded at a scan rate of 50 mV s⁻¹ and calibrated against the ferrocene fc/fc⁺ redox couple. The measurements show a well-defined oxidation wave at 0.11 V vs fc/fc⁺ with only minimal drift over four cycles, indicating the stability of the COF material in this potential range (SI, Figure 7.11).

In order to quantify the intrinsic conductivity of the fully π -conjugated COF structure with a high degree of interpenetration, the 100 nm thin COF film was grown on a glass substrate, which was partially coated with a conductive ITO layer. 50 nm thin gold contacts were then evaporated onto the sample using a custom-made mask, completing the device architecture (Figure 7.3c, inset). For the conductivity measurements, the gold was layered on two sides of the substrate: one side comprised blank ITO without COF material (contact area) and the other one included the COF film, which covered the conductive ITO (measuring range) and the non-conductive glass substrate (contact area).

Cross-sectional SEM images at the device position that constitutes parts of the measuring area and thus includes all layers, show the various layers on top of the glass substrate with a dense COF layer grown on the ITO and covered by gold contacts (Figure 7.3c). This enabled measurements of the conductivity in *z*-direction (vertical to the substrate plane) with a cross-sectional area of 3x4 mm. In doing so, we reduce the negative effect of structural defects (e.g. grain boundaries) that would deteriorate lateral electronic coupling in *xy*-direction.

The electrical current was then measured with the applied potentials ranging from -0.5 V to 0.5 V. The linear *I-V* curve shows the characteristic behavior of an ohmic resistor (Figure 7.3d).

Considering Ohm's law with $I = V/R$ and determining the slope of the I - V curve, the electrical resistance R can be calculated. With the resistance R , the known electrode surface and the film thickness, the specific electrical resistance ρ can then be calculated according to the equation

$$\rho = R \frac{A}{l}$$

where A is the surface area of the respective measured electrode and l is the film thickness.

The conductivity σ was determined as the reciprocal value of the specific resistance according to the equation $\sigma = 1/\rho$. The highly crystalline COTh-1P COF shows reproducible conductivity values of up to $8.8 \times 10^{-6} \text{ S cm}^{-1}$, which reflects an increase in conductivity by two orders of magnitude compared to recently reported 3D COTh-based COFs.^[21]

These findings demonstrate the great potential of the modulation approach for growing oriented conjugated 3D COF thin films in a controlled manner on specific substrates which are prerequisite for various optoelectronic applications.

7.4 Conclusion

We have developed highly crystalline conjugated three-dimensional COFs employing the pseudo-tetrahedral and sp^2 carbon-conjugated cyclooctatetrathiophene in modulator-controlled syntheses. We synthesized two COTh-based building blocks of different size and produced three highly ordered COFs via condensation reactions. The novel compact variant of the COTh building blocks functionalized with aldehydes directly connected to the core was covalently linked to linear phenylene connectors to form the COTh-1P COF with high crystallinity. The interpenetrated framework with diamond topology exhibits accessible square-shaped channels, which was confirmed by nitrogen sorption analysis and transmission electron microscopy. The modulation approach for the first time enabled the formation of homogenous 3D COTh-1P COF thin films on various substrates which do not require a previous modification of their surface. The crystal growth of a COF coating with a preferential orientation and controllable thickness allows to directly transfer the intrinsic properties of COTh-1P to specific application fields and therefore increases their versatility.

We thus could investigate the electronic characteristics of the oriented COTh-1P thin film using a sandwich format that reduces the influence of structural defects, and determine a conductivity of $8.8 \times 10^{-6} \text{ S cm}^{-1}$.

With the ability to grow thin films on different substrates in combination with the moderate intrinsic conductivity, a new pathway has been established for many prospective applications of fully conjugated COTh-based 3D COFs in organic optoelectronics, such as organic solar cells. Future work aimed at extending the framework series by various linear counterparts is expected to result in new organic materials featuring omnidirectional conjugation and intriguing optoelectronic properties.

7.5 Supporting Information

Section A – Methods

Nuclear magnetic resonance (NMR) spectra were recorded on Bruker AV 400 and AV 400 TR spectrometers. Proton chemical shifts are expressed in parts per million (δ -scale) and are calibrated using residual non-deuterated solvent peaks as internal reference ($^1\text{H-NMR}$: CDCl_3 : 7.26, $\text{DMSO-}d_6$: 2.50).

UV-Vis spectra were recorded using a Perkin-Elmer Lambda 1050 spectrometer equipped with a 150 mm integrating sphere. Diffuse reflectance spectra were recorded using a Harrick Praying Mantis accessory kit and were referenced to barium sulfate as the white standard.

High resolution electron ionization (EI) **mass spectra (MS)** were recorded with a Thermo Finnigan MAT 95 instrument.

Nitrogen sorption isotherms were recorded on a Quantachrome Autosorb 1 at 77 K within a pressure range of $p/p_0 = 0.001$ to 0.98. Prior to the measurement of the sorption isotherms the samples were heated for 24 h at 120 °C under turbo-pumped vacuum. For the evaluation of the surface area the BET model was applied between 0.0005 and 0.08 p/p_0 . Pore size distributions were calculated using the NLDFT adsorption model for cylindrical pores.

Powder X-ray diffraction (PXRD) measurements were performed using a Bruker D8 Discover with Ni-filtered Cu K_α radiation and a LynxEye position-sensitive detector.

The initial structure models of the COFs were built using the Forcite module of the Accelrys Materials Studio software package. For the COTh-1P COF, we applied a tetragonal crystal system with the highest possible symmetry in the space group $I4_122$. Experimental PXRD data were used for the respective Rietveld refinements to optimize the structure models.

2D grazing-incidence wide angle X-ray scattering (GIWAXS) data were recorded with an Anton Paar SAXSpoint 2.0 system equipped with a Primux 100 micro Cu K_α source and a Dectris EIGER R 1M detector. The COF films were positioned at a sample-detector distance of 140 mm and were measured with an incidence angle of 0.2°.

Transmission electron microscopy (TEM) was performed on a probe-corrected FEI Titan Themis instrument equipped with a field emission gun operated at 300 kV.

Scanning electron microscopy (SEM) images were recorded with an FEI Helios NanoLab G3 UC scanning electron microscope equipped with a field emission gun operated at 3 – 5 kV.

Photoluminescence (PL) data were processed with a FluoTime 300 instrument from PicoQuant GmbH. The samples were photo-excited using lasers with suitable wavelengths according to the sample absorption, in this case 378 nm wavelength (LDH-P-C-375 from PicoQuant GmbH)

pulsed at 40 MHz, with a pulse duration of ~ 100 ps and fluence of ~ 300 nJ cm⁻²/pulse. The PL was collected using a high-resolution monochromator and photomultiplier detector assembly (PMA-C 192-N-M, PicoQuant GmbH).

Cyclic voltammetry measurements were conducted in a three-electrode-setup with a Metrohm Autolab PGSTAT potentiostat/galvanostat and a set scan speed of 50 mV s⁻¹. The COF thin film grown on a conductive ITO substrate was applied as the working electrode and immersed into an electrolyte solution consisting of 0.1 M tetrabutylammonium hexafluorophosphate (TBAPF₆) in MeCN. A Pt wire and a Ag wire were used as the counter electrode and the pseudoreference electrode, respectively. All potentials are referenced to the fc/fc⁺ redox pair.

Section B – Building block syntheses

All reagents were purchased in high-purity grades from commercial suppliers and used as received without further purification, unless stated otherwise. All reactions were conducted in oven-dried glassware under argon atmosphere using standard Schlenk and glovebox techniques.

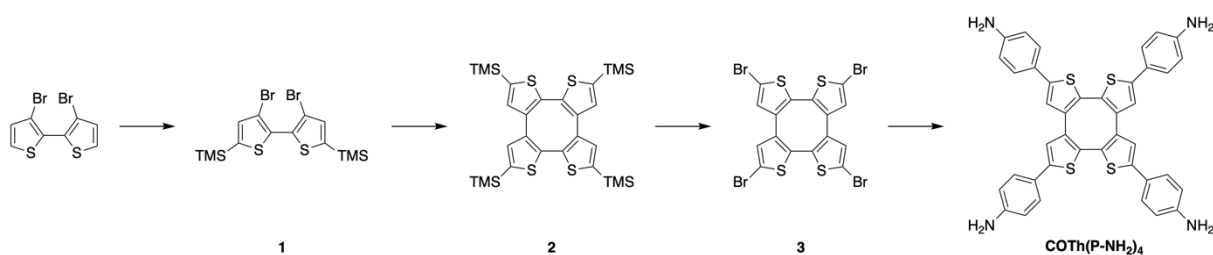
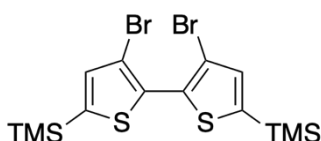


Figure 7.4. Schematic synthesis route for the COTh(P-NH₂)₄ building block.

5,5'-Bis(trimethylsilyl)-3,3'-dibromo-2,2'-bithiophene (1)^[55]

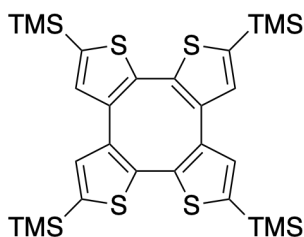


3,3'-Dibromo-2,2'-bithiophene (5.00 g, 15.4 mmol, 1.0 eq.) was dissolved in dry THF (77.2 mL) and cooled to $-78\text{ }^{\circ}\text{C}$. After lithium diisopropylamide (1 M in hexane, 34 mmol, 2.2 eq) was added dropwise over the course of 20 minutes, the resulting white suspension was allowed to warm to $-10\text{ }^{\circ}\text{C}$ and stirred for 30 minutes. Afterwards, the reaction mixture was cooled to $-78\text{ }^{\circ}\text{C}$ and trimethylsilyl chloride (5.66 mL, 4.83 g, 44.5 mmol, 3 eq) was added dropwise. The resulting solution was allowed to warm to room temperature and stirred overnight. The reaction was quenched with water (50 mL) and the product was extracted with diethyl ether, washed with brine and dried over MgSO₄. Solvent removal under reduced pressure and subsequent recrystallization in ethanol furnished compound **1** as a colorless solid (6.06 g, 12.9 mmol, 85%).

¹H NMR (400 MHz, CDCl₃): δ 6.97 (s, 2H), 0.15 (s, 18H).

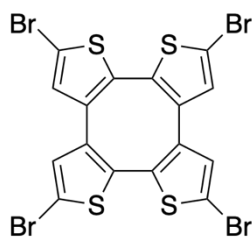
¹³C NMR (400 MHz, CDCl₃): 143.22, 137.38, 134.31, 113.32.

2,5,8,11-Tetrakis(trimethylsilyl)-cyclooctatetrathiophene (2)^[56]



Compound **1** (2.80 g, 5.98 mmol, 1.0 eq.) was dissolved in dry diethyl ether (115 mL) and cooled to $-78\text{ }^{\circ}\text{C}$. *n*-Butyllithium (2.5 M in hexane, 14 mmol, 2.34 eq.) was added dropwise over the course of 30 minutes and the resulting mixture was stirred for 1 h at $-78\text{ }^{\circ}\text{C}$. Dry CuCl_2 (2.40 g, 17.9 mmol, 3.0 eq.) was added and the resulting suspension was allowed to warm to room temperature overnight whilst stirring. After quenching the reaction with water (100 mL), the product was extracted with diethyl ether, washed with brine, dried over Na_2SO_4 and concentrated under reduced pressure. After purification via column chromatography (silica gel, pure hexane), compound **2** was obtained as a colorless solid (802 mg, 1.3 mmol, 44%).

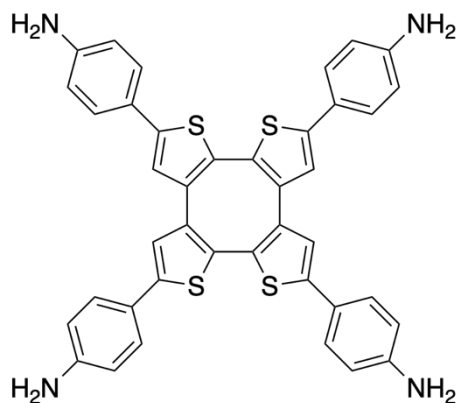
2,5,8,11-Tetrabromo-cyclooctatetrathiophene (3)^[56]



Compound **2** (800 mg, 1.3 mmol, 1.0 eq.) was dissolved in dry THF (26 mL) and cooled to $0\text{ }^{\circ}\text{C}$. *N*-Bromosuccinimide (1.39 g, 7.80 mmol, 6.0 eq.) was added in small portions over the course of 10 minutes and the resulting reaction mixture was allowed to warm to room temperature overnight whilst stirring. The reaction was quenched with water (20 mL) and the product was extracted with dichloromethane. The organic phase was washed with brine, dried over MgSO_4 and concentrated under reduced pressure. Purification via column chromatography (silica gel, pure DCM) yielded compound **3** as a grey solid (556 mg, 0.86 mmol, 66%).

Mass spectra (EI): 644.06 (calculated), 643.6 (experimental).

2,5,8,11-Tetraaniline-cyclooctatetrathiophene (COTh(P-NH₂)₄)



Compound **3** (1.00 g, 1.55 mmol, 1.0 eq.), 4-aminophenyl-boronic acid pinacol ester (9.32 mmol, 2.04 g, 6.0 eq.), Pd(PPh₃)₄ (144 mg, 0.13 mmol, 8 mol%) and K₂CO₃ (2.15 g, 15.6 mmol, 10 eq.) were stirred in 1,4-dioxane (100 mL) and degassed water (6.63 mL). The reaction mixture was then heated to reflux (115 °C) for 72 h. After cooling to room temperature, the product was extracted with dichloromethane and washed with water. Recrystallization using pure ethanol yielded the title compound as a bright yellow powder (560 mg, 0.81 mmol, 52 %).

¹H NMR (400 MHz, DMSO): 7.42 (d, *J* = 8.6 Hz, 8H), 7.33 (s, 4H), 6.66 (d, *J* = 8.5 Hz, 8H), 5.50 (s, 8H).

Mass spectra (EI): 692.12 (calculated), 692.12 (experimental).

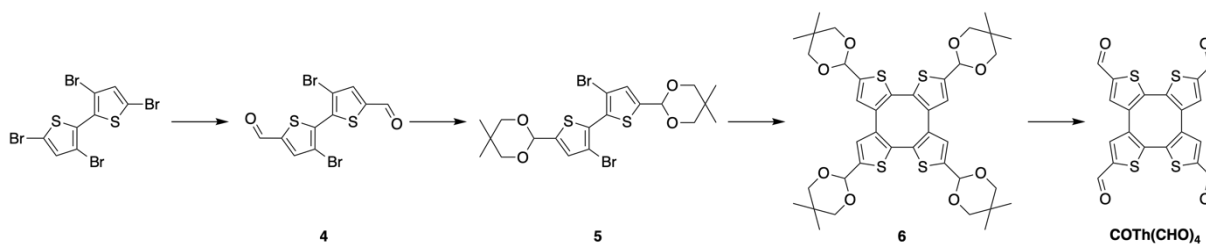
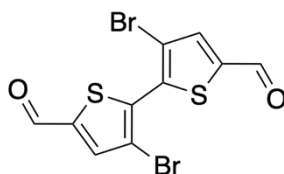


Figure 7.5. Schematic synthesis route for the COTh(CHO)₄ building block.

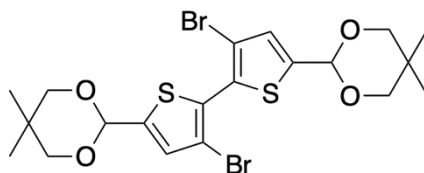
3,3'-Dibromo-[2,2'-bithiophene]-5,5'-dicarbaldehyde (**4**)^[57]



A solution of 3,3',5,5'-tetrabromo-2,2'-bithiophene (5410 mg, 11.2 mmol, 1.0 eq.) in 60 mL anhydrous THF was cooled to $-78\text{ }^{\circ}\text{C}$. *n*-BuLi (2.5 M in hexane, 25.26 mmol, 2.25 eq.) was added dropwise and the solution was stirred for 2 h at $-78\text{ }^{\circ}\text{C}$. Subsequently, anhydrous DMF (2.16 mL, 28.1 mmol, 2.5 eq.) was added and the resulting mixture was allowed to warm to room temperature and stirred overnight. The reaction was then quenched with 80 mL of 6 M HCl and stirred for another hour. The resulting precipitate was collected by filtration, washed with H₂O and recrystallized in 20 mL DMSO at $180\text{ }^{\circ}\text{C}$. After washing with MeOH, the product was dried under high vacuum to yield the title compound as yellowish green needles (2270 mg, 5.97 mmol, 53%).

¹H NMR (400 MHz, DMSO-*d*₆): 9.97 (s, 2H), 8.26 (s, 2H).

2,2'-(3,3'-Dibromo-[2,2'-bithiophene]-5,5'-diyl)bis(5,5-dimethyl-1,3-dioxane) (**5**)



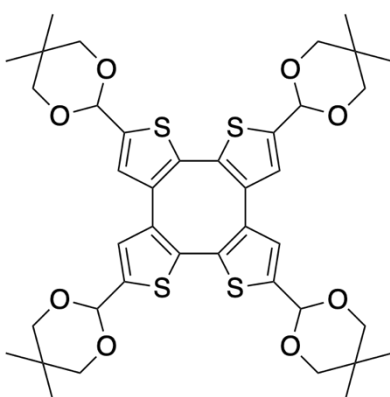
A reaction mixture containing compound **4** (1833 mg, 4.82 mmol, 1.0 eq.), 2,2-dimethyl-1,3-propanediol (5023 mg, 48.2 mmol, 10 eq.), and *p*-toluenesulfonic acid monohydrate (73.4 mg, 0.39 mmol, 8 mol%) in 48 mL benzene was refluxed at $85\text{ }^{\circ}\text{C}$ overnight. After cooling to room temperature, water (50 mL) was added and the product was extracted with DCM and washed with brine three times. The combined organic phases were dried over MgSO₄ and concentrated

under reduced pressure. Purification via column chromatography (silica gel, DCM/n-hexane 2:1) yielded the title compound as a pink powder (2267 mg, 4.10 mmol, 85%).

^1H NMR (400 MHz, CDCl_3): 7.10 (d, $J = 0.7$ Hz, 2H), 5.58 (d, $J = 0.8$ Hz, 2H), 3.76 (d, $J = 11.3$ Hz, 4H), 3.63 (d, $J = 10.7$ Hz, 4H), 1.26 (s, 6H), 0.80 (s, 6H).

^{13}C NMR (101 MHz, CDCl_3): 143.15, 129.21, 128.67, 111.93, 97.55, 77.62, 30.40, 23.10, 21.95.

2,5,8,11-Tetrakis(5,5-dimethyl-1,3-dioxan-2-yl)cyclooctatetrathiophene (6)^[56]

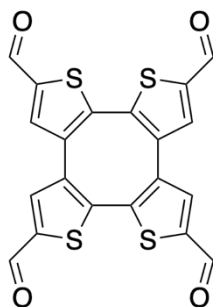


Compound **5** (2267 mg, 4.10 mmol, 1.0 eq.) was dissolved in 40 mL THF and 40 mL diethyl ether. After cooling to -78 °C, $n\text{-BuLi}$ (2.5 M, 9.44 mmol, 2.3 eq.) was added dropwise and the resulting mixture was stirred for 2 hours. Following the addition of anhydrous CuCl_2 (1655 mg, 12.31 mmol, 3.0 eq.), the reaction was allowed to warm to room temperature and stirred overnight. The reaction was quenched with H_2O and stirred for 2 h. The product was extracted with DCM and washed with brine (3x). The organic phase was dried over MgSO_4 and concentrated under reduced pressure. Purification via column chromatography (silica gel, DCM + 1% EtOAc) yielded the product as a yellow powder (1211 mg, 1.54 mmol, 75%).

^1H NMR (400 MHz, CDCl_3): 6.96 (s, 4H), 5.55 (s, 4H), 3.77 – 3.68 (m, 8H), 3.64– 3.53 (m, 8H), 1.25 (s, 12H), 0.78 (s, 12H).

^{13}C NMR (101 MHz, CDCl_3): 142.64, 136.33, 132.78, 127.64, 98.03, 77.53, 30.34, 23.09, 21.99.

**Cycloocta[1,2-b:4,3-b':5,6-b'':8,7-b''']tetrathiophene-2,5,8,11-tetracarbaldehyde
(COTh(CHO)₄)**

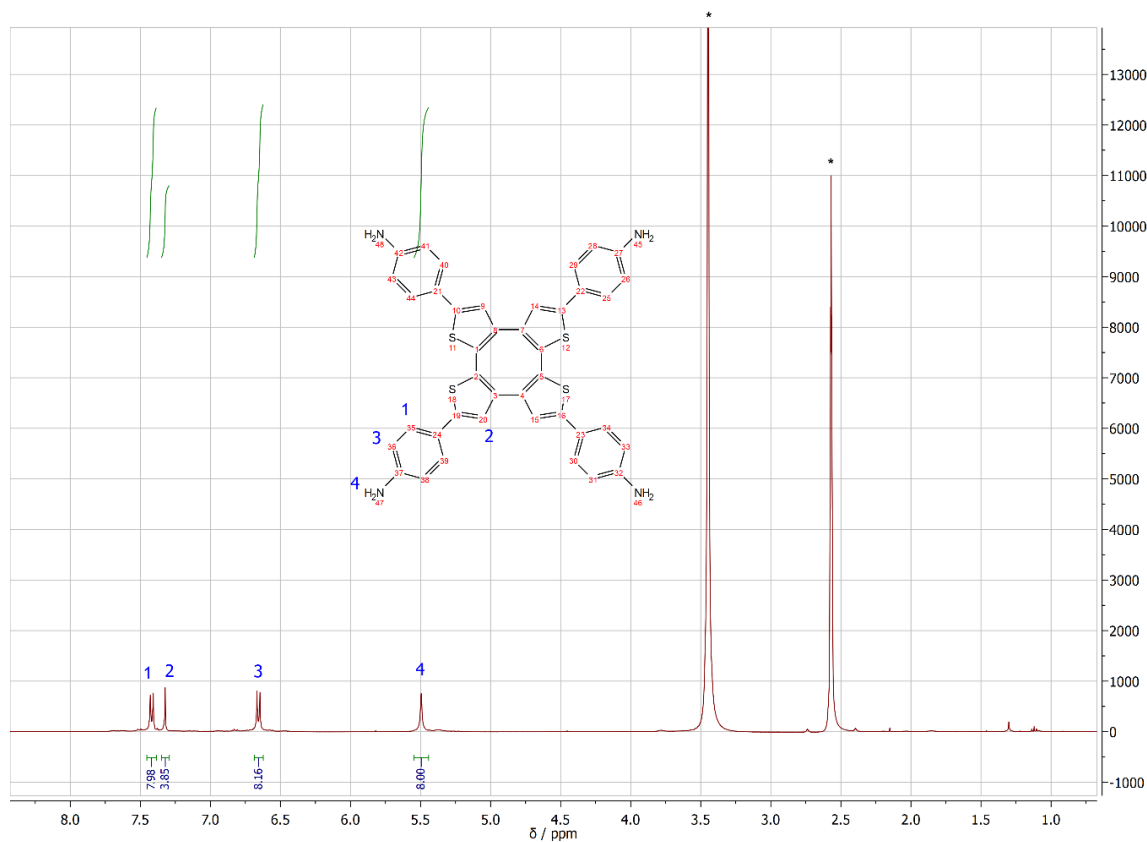


Compound **6** (819 mg, 1.04 mmol, 1.0 eq.) was dissolved in 75 mL CHCl₃. After adding 1.5 mL H₂O and 15 mL trifluoroacetic acid, the reaction mixture was stirred under argon for 2 h. The reaction mixture was then slowly added to 500 mL saturated aqueous NaHCO₃ solution and extracted with DCM. The organic phase was washed with H₂O thoroughly, dried over MgSO₄ and concentrated under reduced pressure. Purification by column chromatography (silica gel, DCM + 7% EtOAc) yielded the title compound as a bright yellow powder (225 mg, 0.51 mmol, 49%).

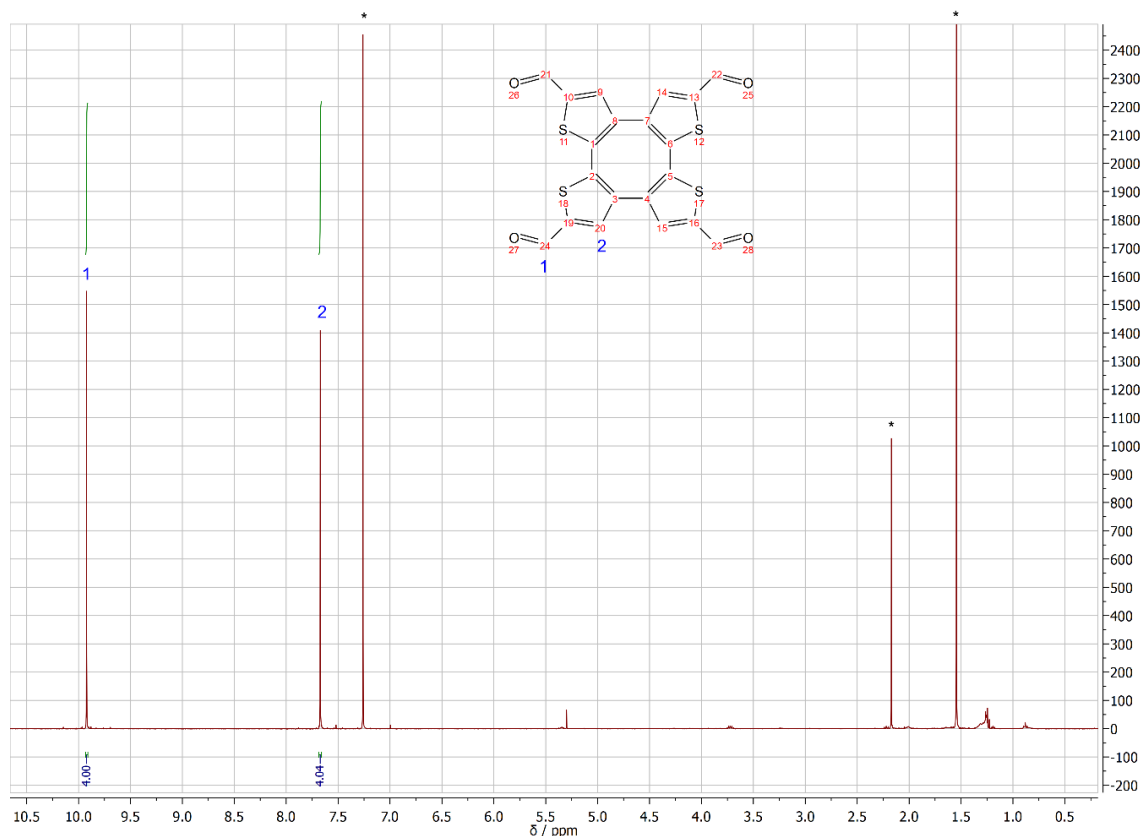
¹H NMR (400 MHz, CDCl₃): 9.92 (s, 4H), 7.67 (s, 4H).

Section C – NMR spectra of the building blocks

COTh(P-NH₂)₄



COTh(CHO)₄



Section D – COF syntheses

The preparation and reactions of all COF syntheses were conducted under argon atmosphere. Solvents and acetic acid were obtained in high purity grade from commercial suppliers and were, unless shipped under inert gas, degassed and flushed under argon prior to use.

COThP-1P COF

Terephthalaldehyde (2.68 mg, 20 μmol , 2.0 eq.) and aniline (13.7 μL , 150 μmol , 15 eq.) were filled into a 6 mL reaction tube. Benzyl alcohol (250 μL) and 6 M acetic acid (50 μL) were added. After COTh(P-NH₂)₄ (6.92 mg, 10 μmol , 1.0 eq.) was dissolved in benzyl alcohol (250 μL) and added quickly, the reaction mixture was subsequently heated at 120 °C for 72 h. After filtration, the red COF powder was washed thoroughly with THF and extracted with supercritical CO₂.

COThP-1P_{Met} COF

2,5-dimethoxyterephthalaldehyde (3.88 mg, 20 μmol , 2.0 eq.) and aniline (13.7 μL , 150 μmol , 15 eq.) were filled into a 6 mL reaction tube. Benzyl alcohol (250 μL) and 6 M acetic acid (50 μL) were added. After COTh(P-NH₂)₄ (6.92 mg, 10 μmol , 1 eq.) was dissolved in benzyl alcohol (250 μL) and added quickly, the reaction mixture was subsequently heated at 120 °C for 72 h. After filtration, the red COF powder was washed thoroughly with THF and extracted with supercritical CO₂.

COTh-1P COF

COTh(CHO)₄ (8.82 mg, 20 μmol , 1.0 eq.), aniline (36.5 μL , 400 μmol , 20 eq.), benzyl alcohol (500 μL) and 6 M acetic acid (100 μL) were filled into a 6 mL reaction tube under inert conditions. Subsequently, *p*-phenylenediamine (40 μL , 40 μmol , 2.0 eq.) and additional 500 μL benzyl alcohol were added. The reaction tube was sealed and heated at 120 °C for 10 d. After cooling to room temperature, the precipitate was filtrated and washed with dry tetrahydrofuran. Extraction with supercritical CO₂ yielded the COTh-1P COF as a dark-red powder.

COTh-1P-COF thin film

COTh(CHO)₄ (2.21 mg, 5 μmol , 1.0 eq.), aniline (9.13 μL , 100 μmol , 20 eq.), benzyl alcohol (1000 μL) and 6 M acetic acid (200 μL) were filled into a 100 mL screw-cap glass autoclave. Following the addition of *p*-phenylenediamine (1.08 mg, 10 μmol , 2.0 eq.), the reaction mixture was dispersed in additional 1000 μL benzyl alcohol. Subsequently, fused silica or ITO/glass

7 Highly Crystalline and Fully Conjugated 3D Cyclooctatetrathiophene-based Covalent Organic Frameworks as Bulk and Thin Film Materials

substrates (1.5 x 1 cm) were inserted horizontally in PTFE holders with the plasma-treated side face-down. Prior to use, the substrates were cleaned in a Hellmanex III detergent solution (0.5% v/v), deionised water, acetone, and isopropanol, and then treated with an O₂-plasma for 5 minutes. The autoclave was sealed and heated at 120 °C for 5 d. After cooling to room temperature, the COF film was removed from the reaction solution, immersed in anhydrous THF and dried with a nitrogen stream.

Section E – Characterization of COThP-based COFs

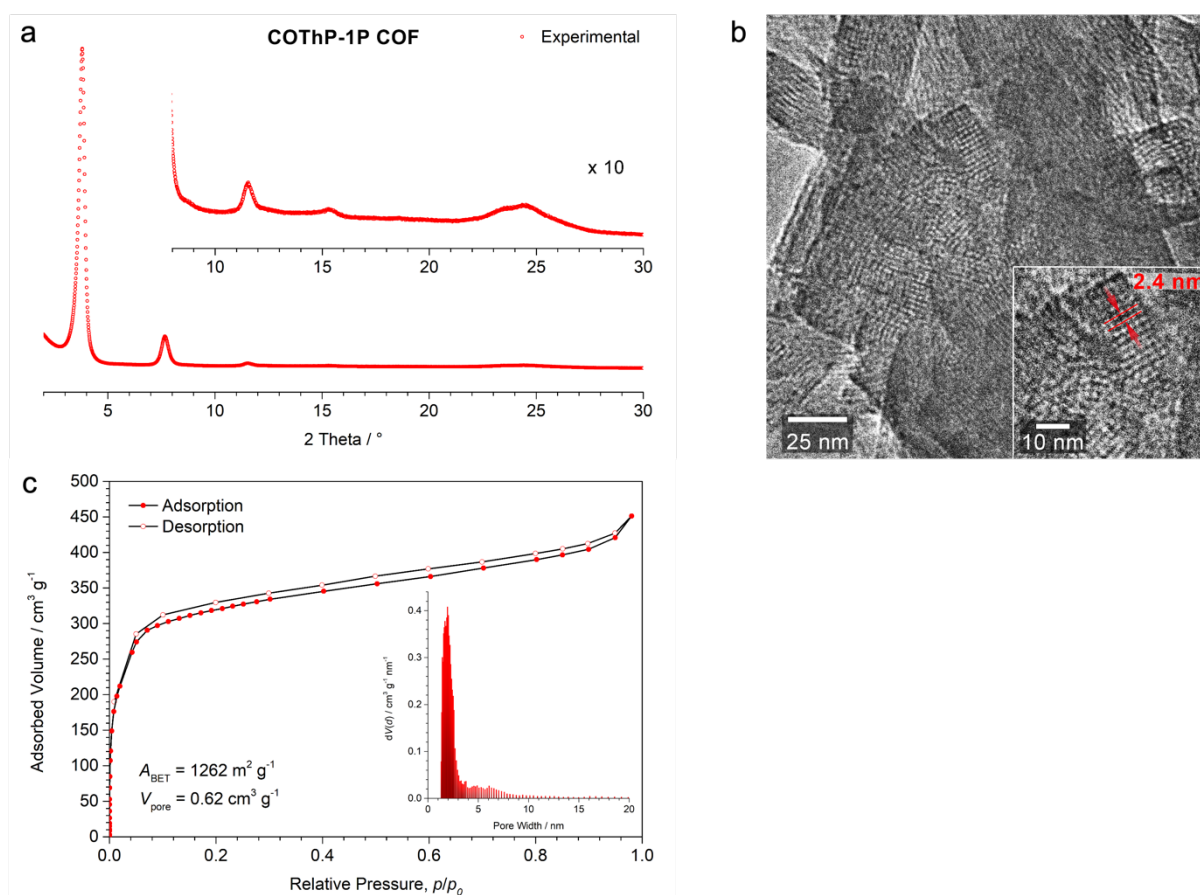


Figure 7.6. Characterization of the COThP-1P COF. (a) Experimental PXRD pattern of the COF bulk material with an inset tenfold magnification of the $8^\circ < 2\theta < 30^\circ$ region. (b) High-resolution TEM image of the polycrystalline powder. Inset: A well-ordered single crystallite oriented with view along the pore channels in *c*-direction shows the square-shaped pores and a periodicity of 2.4 nm. (c) Type Ib nitrogen sorption isotherm recorded at 77 K with the NLDFT-based pore size distribution modeled for cylindrical pores with a maximum at 1.9 nm.

7 Highly Crystalline and Fully Conjugated 3D Cyclooctatetrathiophene-based Covalent Organic Frameworks as Bulk and Thin Film Materials

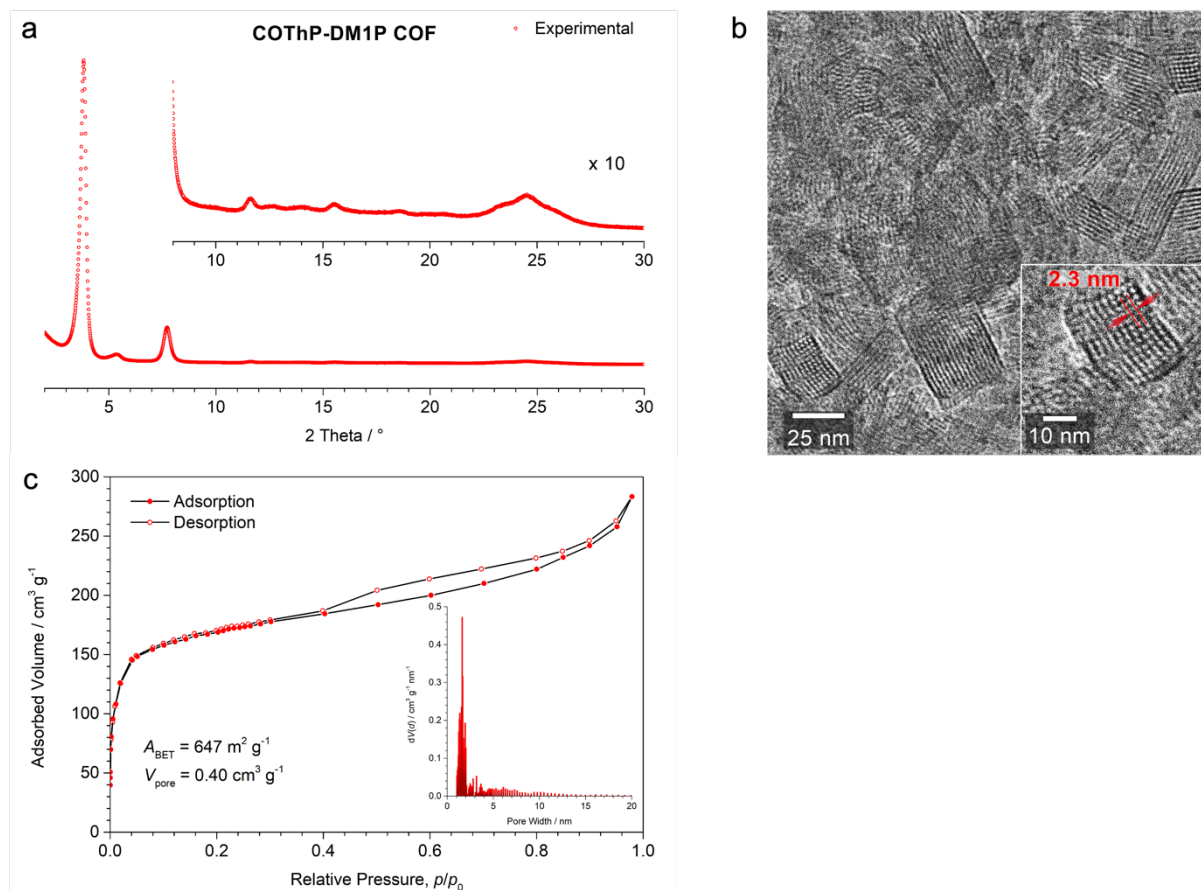


Figure 7.7. Characterization of the COThP-DM1P COF. (a) Experimental PXRD pattern of the COF bulk material with an inset tenfold magnification of the $8^\circ < 2\theta < 30^\circ$ region. (b) High-resolution TEM image of the polycrystalline powder. Inset: A well-ordered single crystallite oriented with view along the pore channels in c -direction shows the square-shaped pores and a periodicity of 2.3 nm. (c) Type Ib nitrogen sorption isotherm recorded at 77 K with the NLDFT-based pore size distribution modeled for cylindrical pores peaking at 1.6 nm.

Section F – Optical characterization

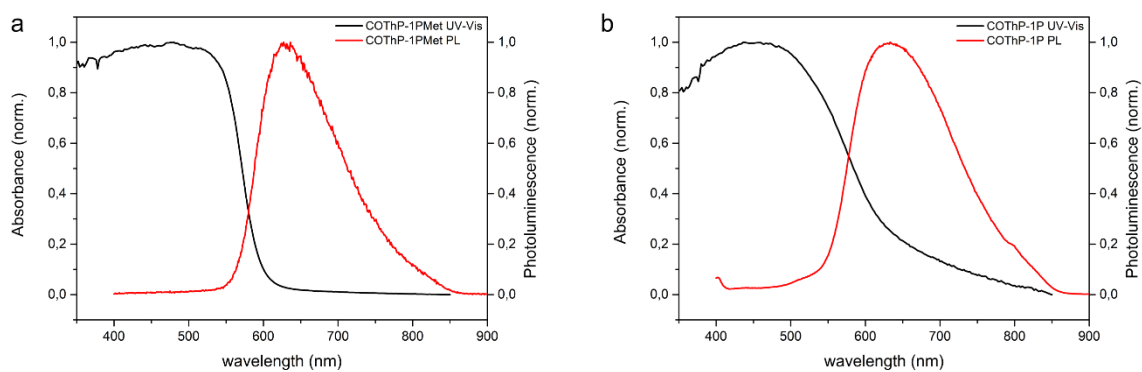


Figure 7.8. Diffuse reflectance and photoluminescence spectra of the COThP-DM1P (a) and COThP-1P (b) COF powder.

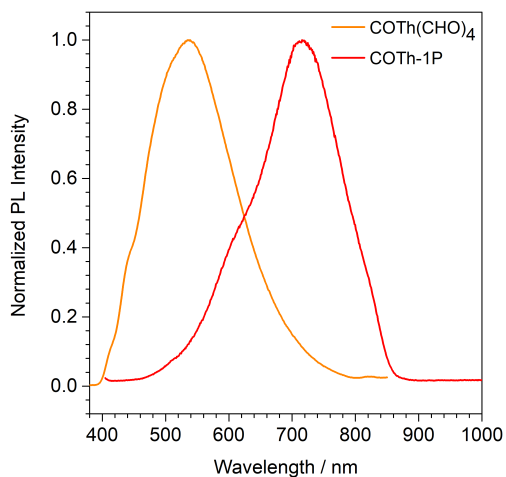


Figure 7.9. Photoluminescence spectra of the COTh(CHO)₄ building block measured in 50 μ M CHCl₃ solution and the COTh-1P COF thin film.

7 Highly Crystalline and Fully Conjugated 3D Cyclooctatraphiophene-based Covalent Organic Frameworks as Bulk and Thin Film Materials

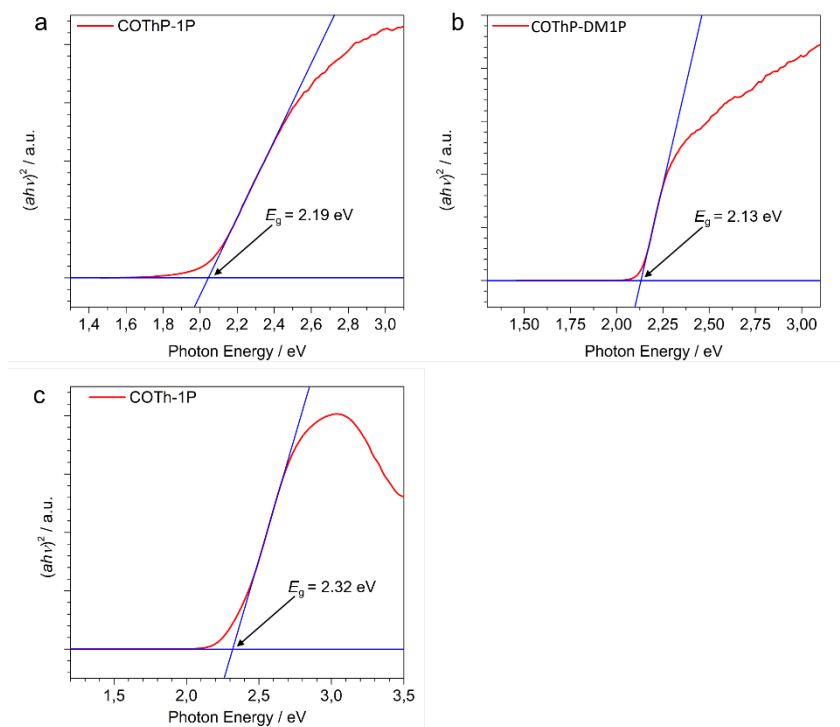


Figure 7.10. Band gap determination via Tauc plots for COThP-1P COF (a), COThP-DM1P COF (b), and COTh-1P COF (c), assuming a direct band gap.

Section G – Electrochemical measurements

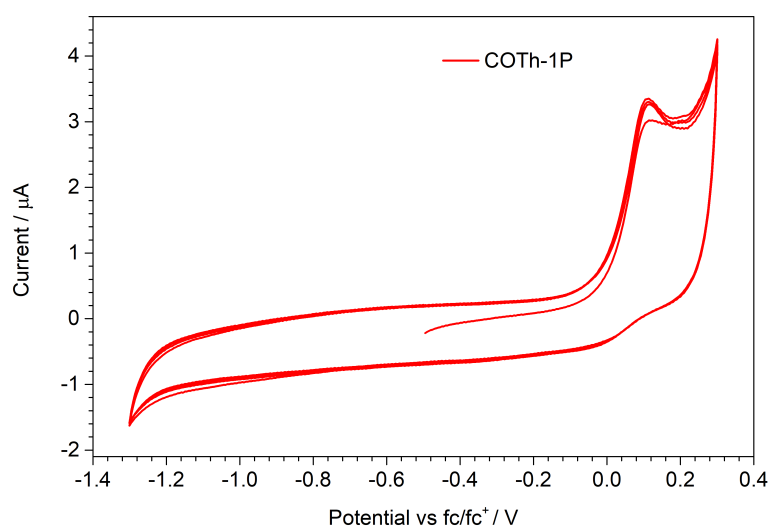


Figure 7.11. Cyclic voltammograms scans of the COTh-1P COF show a distinct oxidation wave at 0.11 mV. Minimal drift over four cycles shows the electrochemical stability of the COF in this potential range.

Section H – Scanning electron microscopy

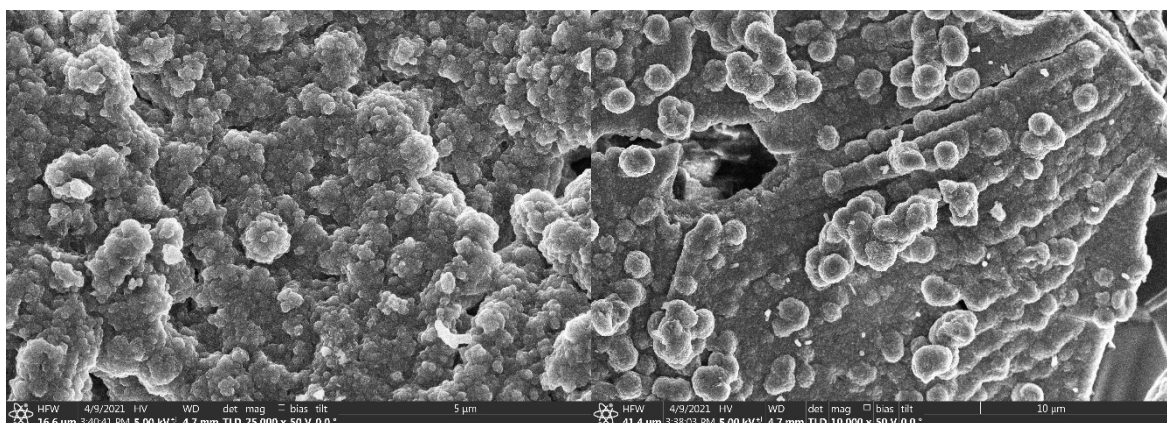


Figure 7.12. SEM images of the COThP-IP COF bulk material.

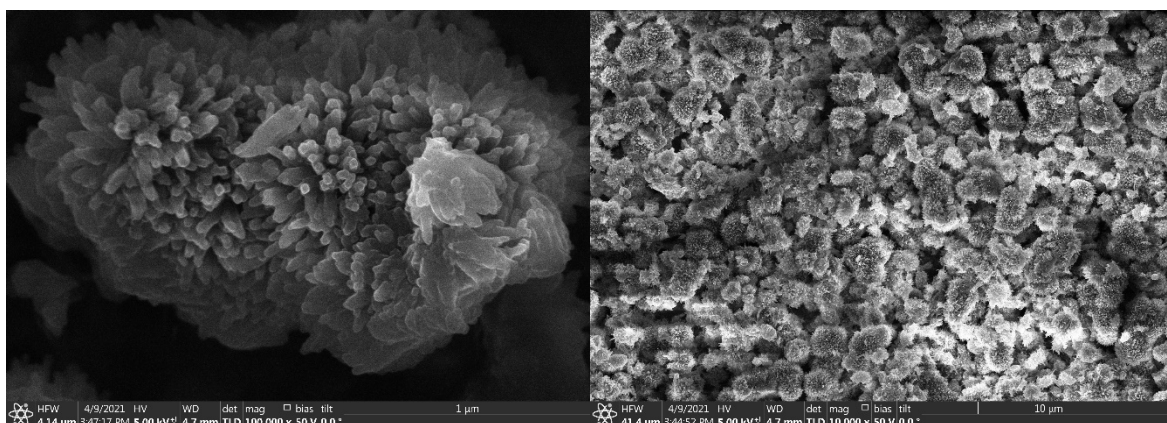


Figure 7.13. SEM images of COThP-DM1P COF powder material.

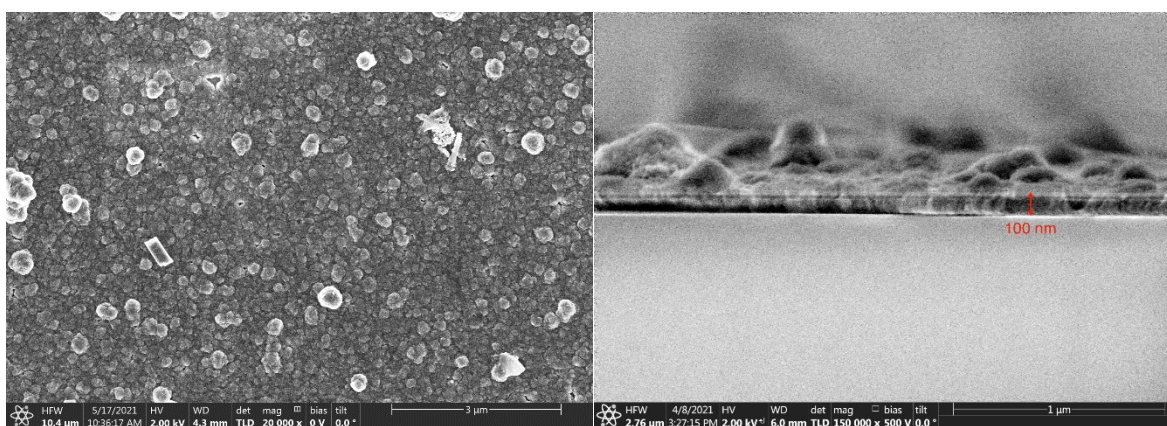


Figure 7.14. Top-view (left) and cross-section (right) SEM images of the COTh-IP COF thin film with 100 nm thickness.

Section I – Modulator impact on the COF synthesis

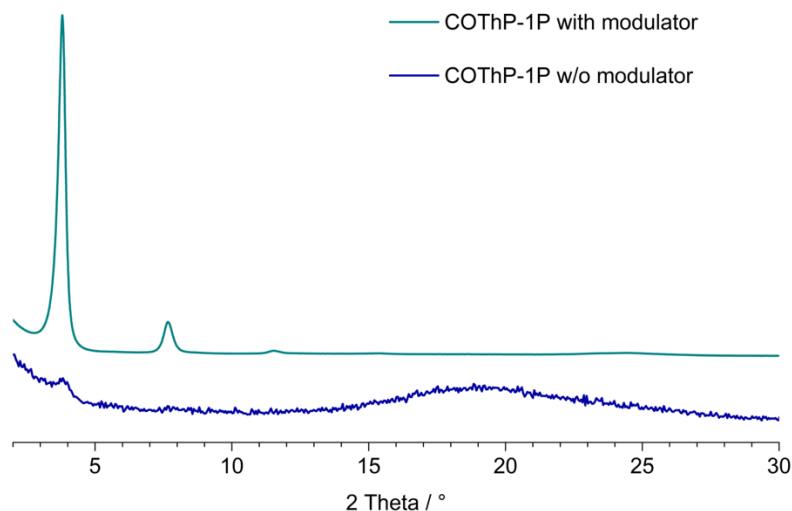


Figure 7.15. Comparison of the PXRD patterns of the COThP-1P COF synthesized via the modulator approach (green line) and without a modulator (blue line). The crystallinity of the COF with a mono-functionalized modulator in the synthesis mixture is distinctly higher revealing well-defined reflections with high intensities at lower angles and virtually no background. In contrast, the COF formed without a modulator almost exclusively shows a visible 200-reflection at $2\theta = 3.8^\circ$ with low intensity and an overall high background indicating the low degree of order.

Section J – Degree of interpenetration

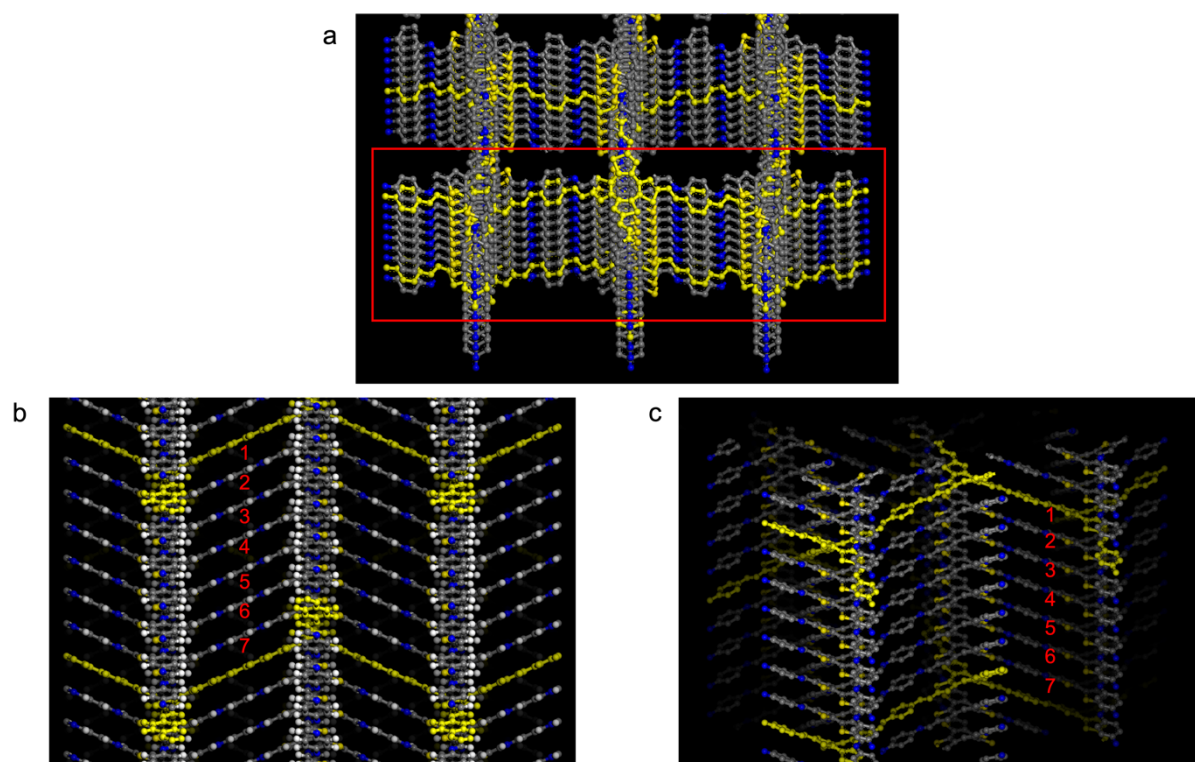


Figure 7.16. Visualization of the interpenetration level of the COTh-1P COF. (a) Tilted side view onto the structure simulation with a single fragment highlighted (yellow). The red box marks the segment that is magnified for determining the degree of interpenetration. The magnified view onto the structure model along the *b*-axis (b) and the tilted view onto the framework edge (c) clearly show the 7-fold interpenetration of the 3D COF.

7.6 References

- [1] A. P. Côté, A. I. Benin, N. W. Ockwig, M. O'Keeffe, A. J. Matzger, O. M. Yaghi, *Science* **2005**, *310*, 1166-1170.
- [2] S. Wan, F. Gándara, A. Asano, H. Furukawa, A. Saeki, S. K. Dey, L. Liao, M. W. Ambrogio, Y. Y. Botros, X. Duan, S. Seki, J. F. Stoddart, O. M. Yaghi, *Chem. Mater.* **2011**, *23*, 4094-4097.
- [3] L. Ascherl, T. Sick, J. T. Margraf, S. H. Lapidus, M. Calik, C. Hettstedt, K. Karaghiosoff, M. Döblinger, T. Clark, K. W. Chapman, F. Auras, T. Bein, *Nat. Chem.* **2016**, *8*, 310-316.
- [4] F. J. Uribe-Romo, J. R. Hunt, H. Furukawa, C. Klöck, M. O'Keeffe, O. M. Yaghi, *J. Am. Chem. Soc.* **2009**, *131*, 4570-4571.
- [5] T. Ma, E. A. Kapustin, S. X. Yin, L. Liang, Z. Zhou, J. Niu, L.-H. Li, Y. Wang, J. Su, J. Li, X. Wang, W. D. Wang, W. Wang, J. Sun, O. M. Yaghi, *Science* **2018**, *361*, 48-52.
- [6] H. M. El-Kaderi, J. R. Hunt, J. L. Mendoza-Cortés, A. P. Côté, R. E. Taylor, M. O'Keeffe, O. M. Yaghi, *Science* **2007**, *316*, 268-272.
- [7] S. S. Han, H. Furukawa, O. M. Yaghi, W. A. Goddard, *J. Am. Chem. Soc.* **2008**, *130*, 11580-11581.
- [8] H. Furukawa, O. M. Yaghi, *J. Am. Chem. Soc.* **2009**, *131*, 8875-8883.
- [9] Y.-X. Ma, Z.-J. Li, L. Wei, S.-Y. Ding, Y.-B. Zhang, W. Wang, *J. Am. Chem. Soc.* **2017**, *139*, 4995-4998.
- [10] X. Guan, Y. Ma, H. Li, Y. Yusran, M. Xue, Q. Fang, Y. Yan, V. Valtchev, S. Qiu, *J. Am. Chem. Soc.* **2018**, *140*, 4494-4498.
- [11] D. N. Bunck, W. R. Dichtel, *Angew. Chem. Int. Ed.* **2012**, *51*, 1885-1889.
- [12] Z. Li, H. Li, X. Guan, J. Tang, Y. Yusran, Z. Li, M. Xue, Q. Fang, Y. Yan, V. Valtchev, S. Qiu, *J. Am. Chem. Soc.* **2017**, *139*, 17771-17774.
- [13] Q. Lu, Y. Ma, H. Li, X. Guan, Y. Yusran, M. Xue, Q. Fang, Y. Yan, S. Qiu, V. Valtchev, *Angew. Chem. Int. Ed.* **2018**, *57*, 6042-6048.
- [14] Q. Fang, J. Wang, S. Gu, R. B. Kaspar, Z. Zhuang, J. Zheng, H. Guo, S. Qiu, Y. Yan, *J. Am. Chem. Soc.* **2015**, *137*, 8352-8355.
- [15] Q. Fang, S. Gu, J. Zheng, Z. Zhuang, S. Qiu, Y. Yan, *Angew. Chem. Int. Ed.* **2014**, *53*, 2878-2882.
- [16] H. Li, Q. Pan, Y. Ma, X. Guan, M. Xue, Q. Fang, Y. Yan, V. Valtchev, S. Qiu, *J. Am. Chem. Soc.* **2016**, *138*, 14783-14788.
- [17] G. Lin, H. Ding, R. Chen, Z. Peng, B. Wang, C. Wang, *J. Am. Chem. Soc.* **2017**, *139*, 8705-8709.

- [18] Y.-B. Zhang, J. Su, H. Furukawa, Y. Yun, F. Gándara, A. Duong, X. Zou, O. M. Yaghi, *J. Am. Chem. Soc.* **2013**, *135*, 16336-16339.
- [19] T. Ma, L. Wei, L. Liang, S. Yin, L. Xu, J. Niu, H. Xue, X. Wang, J. Sun, Y.-B. Zhang, W. Wang, *Nat. Commun.* **2020**, *11*, 6128.
- [20] C. Wang, Y. Wang, R. Ge, X. Song, X. Xing, Q. Jiang, H. Lu, C. Hao, X. Guo, Y. Gao, D. Jiang, *Chem. Eur. J.* **2018**, *24*, 585-589.
- [21] S. Wang, L. Da, J. Hao, J. Li, M. Wang, Y. Huang, Z. Li, Z. Liu, D. Cao, *Angew. Chem. Int. Ed.* **2021**, *60*, 9321-9325.
- [22] S. Wang, X.-X. Li, L. Da, Y. Wang, Z. Xiang, W. Wang, Y.-B. Zhang, D. Cao, *J. Am. Chem. Soc.* **2021**, *143*, 15562-15566.
- [23] M. Wu, Z. Shan, J. Wang, Z. Gu, X. Wu, B. Xu, G. Zhang, *Chem. Commun.* **2021**, *57*, 10379-10382.
- [24] T. Kauffmann, B. Greving, R. Kriegesmann, A. Mitschker, A. Woltermann, *Chem. Ber.* **1978**, *111*, 1330-1336.
- [25] T. Kauffmann, *Angew. Chem. Int. Ed. Engl.* **1979**, *18*, 1-19.
- [26] T. Kauffmann, H. P. Mackowiak, *Chem. Ber.* **1985**, *118*, 3714-3723.
- [27] S. M. H. Kabir, M. Miura, S. Sasaki, G. Harada, Y. Kuwatani, M. Yoshida, M. Iyoda, *Heterocycles* **2000**, *52*, 761-774.
- [28] K. Fukuzumi, Y. Nishii, M. Miura, *Angew. Chem. Int. Ed.* **2017**, *56*, 12746-12750.
- [29] M. J. Marsella, R. J. Reid, *Macromolecules* **1999**, *32*, 5982-5984.
- [30] M. J. Marsella, R. J. Reid, S. Estassi, L.-S. Wang, *J. Am. Chem. Soc.* **2002**, *124*, 12507-12510.
- [31] Y. Wang, D. Gao, J. Shi, Y. Kan, J. Song, C. Li, H. Wang, *Tetrahedron* **2014**, *70*, 631-636.
- [32] M. Dogru, M. Handloser, F. Auras, T. Kunz, D. Medina, A. Hartschuh, P. Knochel, T. Bein, *Angew. Chem. Int. Ed.* **2013**, *52*, 2920-2924.
- [33] M. Calik, F. Auras, L. M. Salonen, K. Bader, I. Grill, M. Handloser, D. D. Medina, M. Dogru, F. Löbermann, D. Trauner, A. Hartschuh, T. Bein, *J. Am. Chem. Soc.* **2014**, *136*, 17802-17807.
- [34] D. D. Medina, V. Werner, F. Auras, R. Tautz, M. Dogru, J. Schuster, S. Linke, M. Döblinger, J. Feldmann, P. Knochel, T. Bein, *ACS Nano* **2014**, *8*, 4042-4052.
- [35] T. Sick, A. G. Hufnagel, J. Kampmann, I. Kondofersky, M. Calik, J. M. Rotter, A. Evans, M. Döblinger, S. Herbert, K. Peters, D. Böhm, P. Knochel, D. D. Medina, D. Fattakhova-Rohlfing, T. Bein, *J. Am. Chem. Soc.* **2018**, *140*, 2085-2092.
- [36] D. Bessinger, L. Ascherl, F. Auras, T. Bein, *J. Am. Chem. Soc.* **2017**, *139*, 12035-12042.

- [37] L. Ascherl, E. W. Evans, J. Gorman, S. Orsborne, D. Bessinger, T. Bein, R. H. Friend, F. Auras, *J. Am. Chem. Soc.* **2019**, *141*, 15693-15699.
- [38] L. Ascherl, E. W. Evans, M. Hennemann, D. Di Nuzzo, A. G. Hufnagel, M. Beetz, R. H. Friend, T. Clark, T. Bein, F. Auras, *Nat. Commun.* **2018**, *9*, 3802.
- [39] D. Bessinger, K. Muggli, M. Beetz, F. Auras, T. Bein, *J. Am. Chem. Soc.* **2021**, *143*, 7351-7357.
- [40] H. Lu, C. Wang, J. Chen, R. Ge, W. Leng, B. Dong, J. Huang, Y. Gao, *Chem. Commun.* **2015**, *51*, 15562-15565.
- [41] J. Fu, S. Das, G. Xing, T. Ben, V. Valtchev, S. Qiu, *J. Am. Chem. Soc.* **2016**, *138*, 7673-7680.
- [42] C. J. Doonan, D. J. Tranchemontagne, T. G. Glover, J. R. Hunt, O. M. Yaghi, *Nat. Chem.* **2010**, *2*, 235-238.
- [43] M. G. Rabbani, A. K. Sekizkardes, Z. Kahveci, T. E. Reich, R. Ding, H. M. El-Kaderi, *Chem. Eur. J.* **2013**, *19*, 3324-3328.
- [44] L. Stegbauer, K. Schwinghammer, B. V. Lotsch, *Chem. Sci.* **2014**, *5*, 2789-2793.
- [45] S.-Y. Ding, J. Gao, Q. Wang, Y. Zhang, W.-G. Song, C.-Y. Su, W. Wang, *J. Am. Chem. Soc.* **2011**, *133*, 19816-19822.
- [46] K. Dey, M. Pal, K. C. Rout, S. Kunjattu H, A. Das, R. Mukherjee, U. K. Kharul, R. Banerjee, *J. Am. Chem. Soc.* **2017**, *139*, 13083-13091.
- [47] L. Chen, L. He, F. Ma, W. Liu, Y. Wang, M. A. Silver, L. Chen, L. Zhu, D. Gui, J. Diwu, Z. Chai, S. Wang, *ACS Appl. Mater. Interfaces* **2018**, *10*, 15364-15368.
- [48] M. Dogru, M. Handloser, F. Auras, T. Kunz, D. Medina, A. Hartschuh, P. Knochel, T. Bein, *Angew. Chem., Int. Ed.* **2013**, *52*, 2920.
- [49] L. Chen, K. Furukawa, J. Gao, A. Nagai, T. Nakamura, Y. Dong, D. Jiang, *J. Am. Chem. Soc.* **2014**, *136*, 9806-9809.
- [50] J. Guo, Y. Xu, S. Jin, L. Chen, T. Kaji, Y. Honsho, M. A. Addicoat, J. Kim, A. Saeki, H. Ihee, S. Seki, S. Irle, M. Hiramoto, J. Gao, D. Jiang, *Nat. Commun.* **2013**, *4*, 2736.
- [51] M. Calik, T. Sick, M. Dogru, M. Döblinger, S. Datz, H. Budde, A. Hartschuh, F. Auras, T. Bein, *J. Am. Chem. Soc.* **2016**, *138*, 1234.
- [52] S. Wang, Z. Zhang, H. Zhang, A. G. Rajan, N. Xu, Y. Yang, Y. Zeng, P. Liu, X. Zhang, Q. Mao, Y. He, J. Zhao, B.-G. Li, M. S. Strano, W.-J. Wang, *Matter* **2019**, *1*, 1592-1605.
- [53] D. Zhu, L. B. Alemany, W. Guo, R. Verduzco, *Polym. Chem.* **2020**, *11*, 4464-4468.
- [54] A. M. Evans, L. R. Parent, N. C. Flanders, R. P. Bisbey, E. Vitaku, M. S. Kirschner, R. D. Schaller, L. X. Chen, N. C. Gianneschi, W. R. Dichtel, *Science* **2018**, *361*, 52-57.

- [55] X. Guo, S. R. Puniredd, M. Baumgarten, W. Pisula, K. Müllen, *J. Am. Chem. Soc.* **2012**, *134*, 8404-8407.
- [56] J. Urieta-Mora, I. García-Benito, I. Zimmermann, J. Aragón, J. Calbo, G. Grancini, A. Molina-Ontoria, E. Ortí, N. Martín, M. K. Nazeeruddin, *J. Mater. Chem. C* **2019**, *7*, 6656-6663.
- [57] A. Bhuwarka, J. F. Mike, J. J. Intemann, A. Ellern, M. Jeffries-El, *Org. Biomol. Chem.* **2015**, *13*, 9462-9470.
- [58] M. Calik, T. Sick, M. Dogru, M. Döblinger, S. Datz, H. Budde, A. Hartschuh, F. Auras, T. Bein, *J. Am. Chem. Soc.* **2016**, *138*, 1234-1239.
- [59] M. S. Lohse, J. M. Rotter, J. T. Margraf, V. Werner, M. Becker, S. Herbert, P. Knochel, T. Clark, T. Bein, D. D. Medina, *CrystEngComm* **2016**, *18*, 4295-4302.
- [60] C. Gao, J. Li, S. Yin, G. Lin, T. Ma, Y. Meng, J. Sun, C. Wang, *Angew. Chem. Int. Ed.* **2019**, *58*, 9770-9775.
- [61] Y. Yang, S. Mallick, F. Izquierdo-Ruiz, C. Schäfer, X. Xing, M. Rahm, K. Börjesson, *Small* **2021**, *17*, 2103152.

8 Conclusion

In this thesis, the focus is on the development of new organic building blocks and their impact on the characteristics of the resulting deliberately designed covalent organic frameworks (COFs). The novel COFs composed of these building blocks could thus be adjusted to specific needs in order to be suitable for various applications.

The first project (Chapter 3) involves the development of a new class of building blocks for two-dimensional COFs, which are already well-established in the field of polymers: isoindigo (II) and thienoisindigo (TII). Given their high planarity, extended π -conjugation, and strong electron-withdrawing character it was possible to produce donor-acceptor-type building blocks by a combination with end-capping electron-donating moieties. These molecules are strongly light absorbing which is owed to their additional intramolecular charge-transfer (ICT) between the electron-deficient and -rich moieties, distinctly reducing the optical bandgap and therefore red-shifting the absorption onset. Implemented into the well-ordered and conjugated structures of COFs, the resulting intensely colored materials acquire the intensive optical features of the II- and TII-based building blocks, extending their absorption into the near-infrared (NIR) region of the electromagnetic spectrum. Structural considerations regarding the planarity and therefore also the effective π -conjugation of the incorporated linear building blocks implied that the chemical modifications made for TII will also affect the optical properties of the respective COFs. These assumptions were confirmed by the distinctly red-shifted absorption spectra of the COFs containing the more planar TII building units. The COF constructed from the subunit with the highest coplanarity, the thienyl-substituted TII (tTII), indeed showed the strongest red-shift of the series.

Utilizing its strong absorption features, the pseudo-quadratic, tTII-containing COF was then applied as the photoactive material in the first COF-based UV- to NIR-responsive photodetector. The device consisting of a COF:fullerene heterojunction showed a switchable photoresponse from blue- and red-sensitive to green- and NIR-responsive by applying a reverse bias. These nearly completely invertible sensitivity characteristics were fully reversible and demonstrated the great potential of TII-based building blocks for COFs.

The series of TII-containing 2D COFs was expanded in the second project of this thesis (Chapter 4). We combined the thienoisindigo-core with thienothiophene (tt) and naphthalene (n) to give the ttTII and nTII building blocks, respectively, further extending their molecular

length while maintaining their strong absorption features due to their donor-acceptor character. Implementation into COFs and growth of crystalline and oriented thin films produced high-performing and fully organic electrochromic materials with very fast switching speeds and high coloration efficiencies.

The direct comparison between TII-containing COFs and additional reference framework materials showed that the best electrochromic performance was achieved by the ttTII-based COF, which meets the optimal requirements for ultrafast and fully reversible color changes. The electrochromic switching speed and framework stability over repeated cycles strongly depend on structural factors such as building block planarity, rigidity, and COF pore size. Thus, the ttTII-containing COF, which contains the more coplanar and less flexible building blocks and larger pore size, facilitates the fast and unimpeded diffusion of charge-balancing counterions in the pores of the robust framework. Based on these design rules, the novel electrochromic framework achieved switching times of 0.4 s for coloration and of 0.2 s for bleaching, while being highly efficient and stable over at least 200 switching cycles.

Additionally, the donor-acceptor electronic configuration of the ttTII building block induces a high coloration efficiency of the resulting framework, which thus combines strong light absorption with significant absorption changes of up to 3 OD in reaction to an external electronic stimulus.

The next chapter covers the incorporation of extended oligothiophenes into the well-ordered environment of COFs. Here, it was necessary to synthetically adjust the linear quaterthiophene building blocks with regard to the position of their solubilizing alkyl chains. The modification strategy to attach alkyl chains asymmetrically instead of symmetrically to the quaterthiophene backbone allowed for an alternating stacking of the alkyl groups in the closely packed arrangement of crystalline COFs, avoiding steric repulsion and hence providing sufficient spacing between them. The same strategy could then be transferred to functionalize the backbones with sterically demanding and electron-deficient moieties in order to tune the optical and electronic properties of the series. Optical investigations of COF systems constructed from these quaterthiophene and pyrene building blocks revealed for the first time the efficient formation of a charge transfer state between the imine-linked subunits. The developed asymmetric building block design of chapter 5 prepared the groundwork for extending the range of possible oligothiophene building blocks in crystalline COFs.

Chapter 6 ties to the insights gained from quaterthiophene-based COFs and investigates the influence of specific modifications of the linear bridging units on the framework characteristics. In this context, a series of oligothiophene building blocks was designed and implemented with two adjusting options for COF modifications: the length of the backbone was extended from two to four to six thiophenes and the alkyl groups attached to the quaterthiophenes were varied from methyl to ethyl to butyl chains. While the alkyl chain variation has virtually no impact on structural properties owing to the asymmetric functionalization strategy with enough spacing between adjacent COF layers, the backbone extension indeed changed the structural COF parameters by expanding the framework and pore size.

Furthermore, studies on the photoluminescence (PL) lifetimes showed that the modification of the linear backbone causes changes of the framework properties following two opposing trends. Extending the building block by more thiophenes induces an increase of the PL lifetimes with a more stabilized excited state. On the contrary, the elongation of the alkyl chain length decreases the lifetimes enabling more competing non-radiative decay pathways due to vibrational relaxation.

With these findings, we could derive a first guiding principle for deliberate building block modifications to tune the properties of COFs. Future studies could ultimately formulate an overarching and comprehensive design rule for various COF systems and thus help to adjust the materials' characteristics specifically by slight changes of the implemented building blocks and to achieve desired optoelectronic functionality.

In the final project (Chapter 7), we focused on a modified variant of the novel pseudo-tetrahedral node cyclooctatetrathiophene (COTh), which has recently been deployed for the formation of three-dimensional COFs. The merit of the COTh building block lies in the central saddle-shaped annulene skeleton with 8 π -electrons and its resulting sp^2 carbon-conjugated structure, enabling fully conjugated 3D COFs. In order to reduce the flexibility of the core building block, we developed a compact variant with the functional groups directly attached to the COTh core consisting of four fused thiophenes. Simultaneous utilization of the modulation approach with mono-functionalized modulators supported the formation of COTh-containing 3D COF material with exceptional crystallinity and permanent porosity. The refined synthesis strategy additionally enabled, for the first time, the homogenous growth of preferentially oriented 3D COF thin films on various substrates without prior surface modification. Conductivity measurements of these crystalline films revealed the benefits of fully conjugated and electronically coupled 3D framework material with promising results of a maximum

intrinsic conductivity of $8.8 \times 10^{-6} \text{ S cm}^{-1}$. With this developed strategy to grow fully conjugated 3D COF material on substrates in an orderly manner and thus fabricate controllable coatings equipped with its intrinsic properties, the foundation was laid for future applications where direct deposition of crystalline 3D frameworks on non-modified substrates is crucial.

In conclusion, this thesis demonstrates the great merits of covalent organic frameworks, specifically with respect to their optoelectronic properties. Starting from a 'blueprint' precisely sketching new periodic structures, which are equipped with specific functionalities and envision future applications, to organic synthesis of advanced molecular building blocks and precisely adjusted condensation reactions, highly crystalline and well-ordered frameworks with bespoke properties are realized. Whether the requirements for these porous materials include strong spectral features and near-infrared absorption, extended pore sizes for fast diffusion processes, incorporation of extended oligothiophene backbones, or fully conjugated coatings, all this could be implemented by the synthetic control and reticular design of COFs. The new functional materials described in this thesis are examples of how the versatile and modifiable structures of COFs are persistently advancing into new fields of application and impressing with their outstanding tailor-made characteristics. The further development of these materials by employing the diverse toolset of organic chemistry promises that a great future lies ahead for COFs and new benchmarks are just waiting to be set.

9 Publications and Presentations

9.1 Publications

1. Spectrally Switchable Photodetection with Near-Infrared-Absorbing Covalent Organic Frameworks

Derya Bessinger, Laura Ascherl, Florian Auras*, and Thomas Bein*
J. Am. Chem. Soc. **2017**, *139*, 12035-12042.

2. Fast-Switching Vis–IR Electrochromic Covalent Organic Frameworks

Derya Bessinger, Katharina Muggli, Michael Beetz, Florian Auras*, and Thomas Bein*
J. Am. Chem. Soc. **2021**, *143*, 7351-7357.

3. Oligothiophene-Bridged Conjugated Covalent Organic Frameworks

Niklas Keller, Derya Bessinger, Stephan Reuter, Mona Calik, Laura Ascherl, Fabian C. Hanusch, Florian Auras*, and Thomas Bein*
J. Am. Chem. Soc. **2017**, *139*, 8194-8199.

4. Perylene-Based Covalent Organic Frameworks for Acid Vapor Sensing

Laura Ascherl, Emrys W. Evans, Jeffrey Gorman, Sarah Orsborne, Derya Bessinger, Thomas Bein, Richard H. Friend, and Florian Auras*
J. Am. Chem. Soc. **2019**, *141*, 15693-15699.

5. Synchronized Offset Stacking: A Concept for Growing Large-Domain and Highly Crystalline 2D Covalent Organic Frameworks

Florian Auras, Laura Ascherl, Amir H. Hakimioun, Johannes T. Margraf, Fabian C. Hanusch, Stephan Reuter, Derya Bessinger, Markus Döblinger, Christina Hettstedt, Konstantin Karaghiosoff, Simon Herbert, Paul Knochel, Timothy Clark, and Thomas Bein*
J. Am. Chem. Soc. **2016**, *138*, 16703–16710.

6. Selective functionalization of the 1H-imidazo[1,2-*b*]pyrazole scaffold. A new potential non-classical isostere of indole and a precursor of push–pull dyes

Kuno Schwärzer, Saroj K. Rout, Derya Bessinger, Fabio Lima, Cara E. Brocklehurst, Konstantin Karaghiosoff, Thomas Bein, and Paul Knochel*

Chem. Sci. **2021**, *12*, 12993-13000.

9.2 Oral Presentations

1. Optoelectronic Properties of Covalent Organic Frameworks with Donor-Acceptor-Type Building Blocks

SolTech Conference 2021, Munich, Germany

2. Fast-Switching Vis-IR Electrochromic Covalent Organic Frameworks

European Conference on Metal Organic Frameworks and Porous Polymers (EuroMOF) 2021, Krakow, Poland – virtual

3. Fast-Switching Vis-IR Electrochromic Covalent Organic Frameworks

Federation of European Zeolite Associations (FEZA) Conference 2021, virtual

4. Fast-Switching Vis-IR Electrochromic Covalent Organic Frameworks

Deutsche Zeolith-Tagung (DZT) 2021, virtual

9.3 Poster Presentations

1. Spectrally Switchable Photodetection with Near-Infrared-Absorbing Covalent Organic Frameworks

European Conference on Metal Organic Frameworks and Porous Polymers (EuroMOF) 2019, Paris, France

2. Spectrally Switchable Photodetection with Near-Infrared-Absorbing Covalent Organic Frameworks

Deutsche Zeolith-Tagung (DZT) 2019, Dresden, Germany

3. Spectrally Switchable Photodetection with Near-Infrared-Absorbing Covalent Organic Frameworks

Center for NanoScience (CeNS) Workshop 2017, Venice, Italy